Springer Series in Materials Science 251

Bing Yan

Photofunctional Rare Earth Hybrid Materials

Springer

Springer Series in Materials Science

Volume 251

The Springer Series in Materials Science covers the complete spectrum of materials research and technology, including fundamental principles, physical properties, materials theory and design. Recognizing the increasing importance of materials science in future device technologies, the book titles in this series reflect the state-of-the-art in understanding and controlling the structure and properties of all important classes of materials.

More information about this series at http://www.springer.com/series/856

Bing Yan

Photofunctional Rare Earth Hybrid Materials

Springer

Bing Yan
School of Chemical Science
and Engineering
Tongji University
Shanghai, China

ISSN 0933-033X ISSN 2196-2812 (electronic)
Springer Series in Materials Science
ISBN 978-981-10-2956-1 ISBN 978-981-10-2957-8 (eBook)
DOI 10.1007/978-981-10-2957-8

Library of Congress Control Number: 2017945272

© Springer Nature Singapore Pte Ltd. 2017
This work is subject to copyright. All rights are reserved by the Publisher, whether the whole or part of the material is concerned, specifically the rights of translation, reprinting, reuse of illustrations, recitation, broadcasting, reproduction on microfilms or in any other physical way, and transmission or information storage and retrieval, electronic adaptation, computer software, or by similar or dissimilar methodology now known or hereafter developed.
The use of general descriptive names, registered names, trademarks, service marks, etc. in this publication does not imply, even in the absence of a specific statement, that such names are exempt from the relevant protective laws and regulations and therefore free for general use.
The publisher, the authors and the editors are safe to assume that the advice and information in this book are believed to be true and accurate at the date of publication. Neither the publisher nor the authors or the editors give a warranty, express or implied, with respect to the material contained herein or for any errors or omissions that may have been made. The publisher remains neutral with regard to jurisdictional claims in published maps and institutional affiliations.

Printed on acid-free paper

This Springer imprint is published by Springer Nature
The registered company is Springer Nature Singapore Pte Ltd.
The registered company address is: 152 Beach Road, #21-01/04 Gateway East, Singapore 189721, Singapore

Preface

Rare earths (REs), as the strategic resources of the twenty-first century, have played a great role in both the industry and economy. Rare earth elements or their compounds are important active components in functional materials for their unique electronic structure and physiochemical properties. Almost all functional materials involve rare earths, especially in electronic, magnetic, optical, and catalytic fields. Their excellent optical behaviors, for example, sharp emission spectra for high color purity, broad emission bands covering the ultraviolet (UV)–visible–near-infrared (NIR) region, wide range of lifetime from the microsecond to the second level, high luminescence quantum efficiencies, and so forth, render rare earths a huge treasury of luminescent materials. Due to these virtues, REs have attracted much attention for a wide variety of applications in the fields of lighting devices (television and computer displays, optical fibers, optical amplifiers, and lasers) and biomedical analysis (medical diagnosis and cell imaging).

Functional hybrid materials consist of both organic and inorganic components, which are assembled for the purpose of generating desirable properties and functionalities. Photofunctional hybrid materials are one of the most active research fields because there are various combinations of photoactive species and hosts. The initial aim is to prepare multicomponent materials and modify their properties, such as thermal or photostability. But now the photofunctional hybrid materials are endowed with abundant connotations. The combination of organic and inorganic components at a molecular or nanometer scale integrates the strengths of organic compounds (easy processing with conventional techniques, elasticity, and functionalities) with the advantages of inorganic components (hardness, thermal and chemical stabilities). All kinds of interaction forces are involved in the complicated hybrid systems, including coordination bonds, covalent bonds, and other interactions. Photofunctional rare earth hybrid materials display special characteristics of both solid-state luminescence and molecular luminescence. These hybrid materials not only involve structural components as building units but also contain photofunctional units, which can be expected to realize the property tuning and function integration.

This book consists of four parts, with seven topics covered in eight chapters. The first part (Chap. 1) is a general introduction to rare earths, rare earth luminescence, luminescent rare earth compounds (phosphors or coordination compounds), and photofunctional rare earth hybrid materials. The second part (Chaps. 2, 3, 4, 5, and 6) gives an overview of the typical photofunctional hybrid materials based on organically modified sol–gel-derived silica, organically modified mesoporous silica, microporous zeolite, metal–organic framework, and polymer or polymer–silica composite. The third part (Chap. 7) sheds light upon photofunctional rare earth hybrid materials with other functional units achieved by multicomponent assembly. The fourth part (Chap. 8) focuses on the photophysical applications of photofunctional rare earth hybrid materials, especially on sensing. The seven topics are chosen here because there are extensive and active reports on them.

Finally, I will express my sincere gratitude to my PhD and master students, whose research works make the main content of this book. And I will also show my appreciation to Professor HJ Zhang, Professor LD Carlos, and Professor HR Li, whose groups have done the valuable works in the relevant fields. I hope that this book will provide readers with insights in the recent developments of photofunctional rare earth hybrid materials.

Shanghai, China Bing Yan

Contents

Part I Introduction

Part II Typical Photofunctional Rare Earth Hybrid Material

Part III Multicomponent Assembly

Part IV Photophysical Application

Part I
Introduction

Chapter 1
Rare Earth, Rare Earth Luminescence, Luminescent Rare Earth Compounds, and Photofunctional Rare Earth Hybrid Materials

Abstract This chapter mainly focuses on the fundamental principles of rare earth luminescence, which are important for the investigation of the photofunctional rare earth hybrid materials. It introduces the rare earth elements and their physiochemical properties, the atomic spectral term and energy level transition of rare earth ions associated with their electronic configuration, and the luminescence and spectroscopy of rare earth ions, rare earth inorganic compounds for phosphors, rare earth coordination compounds for molecular luminescence, and photofunctional rare earth hybrid materials combining the characteristics of both phosphor and molecular luminescence. This chapter provides a basis to understand the contents of the subsequent chapters.

Keywords Rare earth ion • Luminescence • Energy transfer • Phosphor • Complex • Photofunctional hybrid material

1.1 Introduction

Rare earths (REs) are a special group of elements in the periodic table, consisting of sixth-period lanthanides, fourth-period scandium (Sc), and fifth-period yttrium (Y). The lanthanides are a series of elements with atomic numbers from 57 to 71, including lanthanum (La), cerium (Ce), praseodymium (Pr), neodymium (Nd), samarium (Sm), europium (Eu), gadolinium (Gd), terbium (Tb), dysprosium (Dy), holmium (Ho), erbium (Er), thulium (Tm), ytterbium (Yb), and lutetium (Lu). Sc and Y possess the nearly identical chemical properties as lanthanides, although lacking in 4f electrons, so they occur in the same ore bodies and have the same separation difficulties. Therefore, they are usually included in the rare earth category.

The rare earths can be generally divided into two classes, the "light rare earth elements (LREE)" (Ce fraction) and "heavy rare earth elements (HREE)" (Y fraction), i.e., $<4f^7$ and $>4f^7$, respectively. Historically, the two classes were from different ores and studied independently. Y is a heavy rare earth element for its physicochemical property similar to Ho and Er. There are slight differences in physicochemical properties from each other which follow this rule of light and heavy

B. Yan, *Photofunctional Rare Earth Hybrid Materials*,
Springer Series in Materials Science 251, DOI 10.1007/978-981-10-2957-8_1

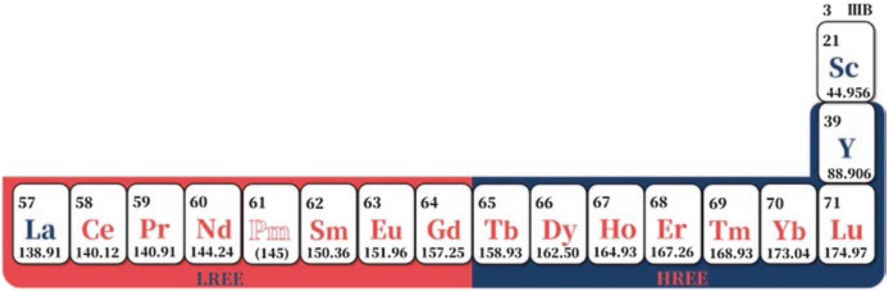

Fig. 1.1 The rare earth elements are often subdivided into light rare earth elements (LREE) and heavy rare earth elements (HREE)

rare earth elements as well. The term “rare earths” has been historically applied to the lanthanides because it was originally believed that these elements were sporadically distributed in nature. But in fact, some elements among them, such as La, Ce, and Y, are relatively abundant (Fig. 1.1) [1].

One important rule correlating structure and physicochemical property of rare earth elements is so-called lanthanide contraction, a term used in chemistry to describe different but closely related concepts associated with smaller than expected atomic radii of the elements in the lanthanide series [2]. In multi-electron atoms, the decrease in radius brought about by increase in nuclear charge is partially offset by electrostatic repulsion among electrons. Particularly, a “shielding effect” operates, i.e., as electrons are added in outer shells, electrons already present shield the outer electrons from nuclear charge, making them a lower effective charge on the nucleus. The shielding effect exerted by the inner electrons decreases in order s > p > d > f. Usually when a particular subshell is filled up in a period, the atomic radii decrease. This effect is particularly pronounced in the case of lanthanides as their 4f subshells are being filled across the period, and they are least able to shield two outer (fifth and sixth) shell electrons. Thus, the shielding effect is least able to counter the decrease in radii caused by the increasing nuclear charge, which leads to “lanthanide contraction.” Radius drops from 1.020 Å in the case of Ce (III) to 0.861 Å in the case of Lu (III) [2]. Since the outer shells of the lanthanides do not change within the group, their chemical behavior is very similar, but the different atomic and ionic radii do affect their chemistry. Without the lanthanide contraction, the chemical separation of lanthanides will be extremely difficult. However, this contraction makes the chemical separation of period 5 and period 6 transition metals of the same group rather difficult. All elements following the lanthanides in the periodic table are influenced by the lanthanide contraction. The period 6 elements have very similar radii compared with the period 5 elements in the same group [2].

Rare earth elements are commonly associated to accessory minerals presenting structures that are large enough. They present high ionic charge and associated large ionic radius. They correspond to transition metals ranging from $4f^0$ to $4f^{14}$, since they progressively fill the $4f$ electronic shell. Chemical properties slowly vary from La to Lu, according to their decreasing ionic radius. The trend usually decreases from LREE to HREE. However, within the 15 elements of the group, the respective ionization potentials present large variations. Values increase first, correlating with the increase in nuclear charge, which in turns increases the repulsion between electrons. However, a break is observed between f^6 and f^7, i.e., Eu and Gd, caused by the exchange of energy resulting from coupling between paired electrons. It represents the half shell effect. Similar effects, but with reduced amplitude, occur at quarter and three-quarter filling of the electronic shell. REE are subdivided to four groups (or tetrads) containing four elements each. The four groups include La to Nd, Pm to Gd, Gd to Ho, and Er to Lu. The four tetrads present specific variations superimposed to the linear trend from LREE to HREE. In each group, the tetrad effect is superimposed on the linear trend and manifested by a curved shape that develops on the four elements. But, depending on the chemical reactions that involve RE elements, those can be more favorably incorporated or not to the mineral assemblage. Two mutually opposite effects are observed, noted W and M types [3].

Here we only give a special example to demonstrate the lanthanide contraction and tetrad effect, which is shown in the cyano-bridged aqua (N,N-dimethylacetamide) (cyanometal) rare earth (Sm, Gd, Ho, Er) nitrate and potassium hexacyanometallate. There are four typical different coordination geometries and crystal structures in these series of complexes with the same terminal ligand N,N-dimethylacetamide (DMA): one-dimensional chain for Sm {$[Sm(DMA)_2(H_2O)_4Fe(CN)_6{\cdot}5H_2O]_n$, $[SmFe]_n$} with approximately parallel transpositioned bridging CN ligands between the Sm and Fe atoms, trinuclear for Gd ($[(Gd(DMA)_3(H_2O)_4)_2Fe(CN)_6][Fe(CN)_6]{\cdot}3H_2O$, Gd_2Fe) with two approximately perpendicular cis-positioned bridging CN ligands between the two Gd and Fe atoms, homonuclear for Ho ($[Ho(DMA)_3(H_2O)_3Fe(CN)_6]{\cdot}3H_2O$, HoFe) with only one bridging CN between the Ho and Fe atom, and ion pair for Er ($[Er(DMA)_3(H_2O)_4][Cr(CN)_6]$, Er-Cr) without any CN bridging between Er and Cr atoms [4, 5].

Besides, there also exists some special phenomenon, which depends on the physiochemical property of rare earth compounds. For example, in the synthesis of $NaRE(MoO_4)_2$ (RE = Y, La, Nd, Eu, Gd, Tb, Er, Yb) and $Na_5Lu(MoO_4)_4$ compounds by a room-temperature solid-state reaction and hydrothermal crystallization process, it indicates that the higher temperature and moisture can speed up the reaction process, and especially the existence of crystalline water molecules in the precursor is necessary for the solid-state reaction at room temperature. It is found that different rare earth nitrate precursors present the different reactivity to sodium molybdate at room temperature. The crystallization degree of the products after room-temperature solid-state reaction depends on the melting point of rare earth nitrate precursors [6].

For rare earth atoms, their electronic configurations are Sc $1s^22s^22p^63s^23p^63d^14s^2$, Y $1s^22s^22p^63s^23p^63d^{10}4s^24p^64d^15s^2$, and Ln $1s^22s^22p^63s^23p^63d^{10}4s^24p^64d^{10}4f^n5s^25p^6 5d^m6s^2$ ($m = 0, 1$; $n = 0$–14). For trivalent rare earth ions, their electronic configurations are Sc(III) $1s^22s^22p^63s^23p^6$, Y(III) $1s^22s^22p^63s^23p^63d^{10}4s^24p^6$, and Ln(III) $1s^22s^22p^63s^23p^63d^{10}4s^24p^64d^{10}4f^n5s^25p^6$ (n = 0–14; among Ln = La, Ce, Gd, and Lu: $5d^1$). Besides the common trivalent state, some rare earth elements can form the divalent (Eu(II), Sm(II), Tm(II), Yb(II)) and tetravalent (Ce(IV) (CeO_2), Pr(IV)

(Pr_6O_{11}), Tb(IV) (Tb_4O_7)) under normal conditions. In aqueous solution, only Ce(IV), Eu(II), and Yb(II) can exist stably.

1.2 Atomic Spectral Term and Energy Level Transition of Rare Earth Ions

The incompletely filled 4f shell of rare earth ions possesses single electrons and produces the non-zero spin quantum number (S). So the spin angular momentum splits and disturbs the orbital angular momentum (L) in the same space region, resulting in the fine splitting of orbital energy levels, so-called the spin–orbit coupling effect. Rare earth ions possess many single electrons and show large quantum number, whose spin–orbit coupling effect is strong. Therefore, the common spectral term ^{2S+1}L-based S and L cannot show the fine energy levels of rare earth ions; we have to consider the strong spin–orbit coupling effect and introduce the angular quantum number (J) originated from L and S. Subsequently, the electron configurations and energy levels of rare earth ions are presented as a spectral sub-term $^{2S+1}L_J$.

For all the rare earth ions, the number of single electrons in the 4f orbital shows the symmetrical distribution centered with Gd^{3+} ion, so there is a rule for their quantum number (L and S). For L and J, a so-called gadolinium breaking effect shows the two different formulas: in front of Gd^{3+}, $J = L\text{-}S$, $L = -1/2(n(n-7))$ and behind Gd^{3+}, $J = L + S$, $L = -1/2((n-7)(n-14))$, where L can be represented as S, P, D, F, G, H, and I, respectively. So being centered with Gd^{3+}, the light rare earth ion and the heavy one show the same L and S symmetrically except for the different J.

Figure 1.2 presents a substantial part of the energy levels originating from the $4f^n$ configuration as a function of n for the trivalent rare earth ions; the width of the bars in the figure gives the order of magnitude of the crystal field splitting. So the number of possible energy level transitions for these rare earth ions is great, revealing that rare earth ions and their compounds are a huge treasure of luminescent materials [7].

1.3 Luminescence and Spectroscopy of Rare Earth Ions

Trivalent rare earth ions such as Sc^{3+}, Y^{3+}, La^{3+}, and Lu^{3+} possess the stable, empty, or filled state, so they are optically inert ions and cannot show the photoactive behavior. Gd^{3+} has half-empty 4f shell and produces a very stable $^8S_{7/2}$ ground state with excitation energy higher than 32,000 cm^{-1}, so the emission of Gd^{3+} is situated in the ultraviolet region (<318 nm). $^8S_{7/2}$ level belongs to non-degenerate orbital and cannot be split by the crystal field, and so its low-temperature emission spectrum only shows a line peak originated from the transition ($^6P_{7/2} \rightarrow {}^8S_{7/2}$). Although Gd^{3+} has the same electron configuration as Eu^{2+}, its $4f^65d$ state is situated at a relatively

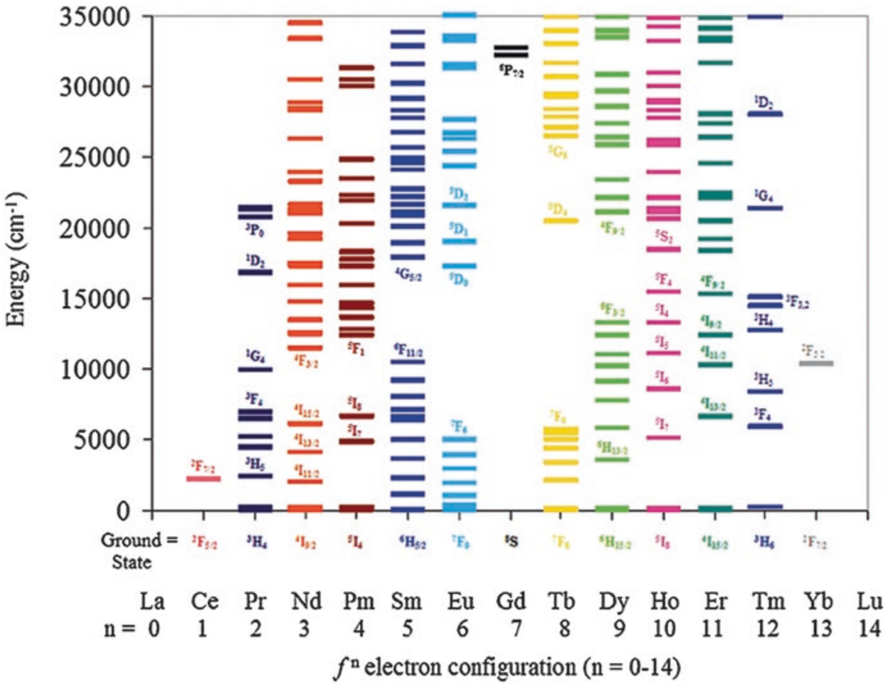

Fig. 1.2 A summary of electronic excited state energy levels for RE^{3+} ions. Reprinted with permission from Ref. [7]. Copyright 2009 the American Chemical Society

high energy state, and it is impossible to observe the band emission from $4f^65d \rightarrow 4f^7$ transition. The luminescence of Gd^{3+} mainly comes from $^6P \rightarrow {}^8S$ transition, a line emission at 313 nm. At its high-energy position, the transition emission can be observed in the host lattice with high-energy optical absorption. Besides, the energy transfer is easy from the ^6P energy level of Gd^{3+} to other rare earth ions or host lattice groups. Therefore, Gd^{3+} generally is considered as an inert ion just like Sc^{3+}, Y^{3+}, La^{3+}, and Lu^{3+} [8, 9].

The emission spectral lines of Eu^{3+} are situated in a red color region, which correspond to the transitions ($4f^6$) from excited state $^5D_0$ to ^7F_J (J = 0, 1, 2, 3, 4, 5, 6). Because the $^5D_0$ level cannot be split by the crystal field (J = 0), the crystal field splitting of ^7F_J levels is produced by the splitting of the emission transitions. Besides, the emission from the higher ^5D energy level ($^5D_1$, $^5D_2$, $^5D_3$) can also be observed. $^5D_0 \rightarrow {}^7F_J$ emission is suitable to determine the spectral features of Eu^{3+}. If Eu^{3+} is located in the lattice with inversion symmetry, electric-dipole transitions between levels of $4f^n$ configuration are strictly forbidden by parity selection rule, and only the weak magnetic-dipole transitions or vibronic electric-dipole transitions occur. If Eu^{3+} is situated in the lattice without inversion symmetry, electric-dipole transition is not strictly forbidden and shows weak spectral lines, so-called forced electric-dipole transition. These transition emissions need two conditions: one is the crystallographic lattice of Eu^{3+} does not have an inversion symmetry center, and the other is the charge transition state which is situated at the low energy level [8, 10].

According to the split number of ^7F_J energy level and the transition number of $^5D_0 \rightarrow {}^7F_J$ transition, it is easy to predict the point group symmetry of the environment where Eu^{3+} is situated: (a) When Eu^{3+} is situated in the lattice with a strict inversion symmetry center, the allowed magnetic-dipole transition $^5D_0 \rightarrow {}^7F_1$ with orange light (about 590 nm) is dominant. (b) When Eu^{3+} is situated in the point group symmetry C_i, C_{2h} and D_{2h}, its $^5D_0 \rightarrow {}^7F_1$ transition shows three spectral lines for the splitting of three states from the completely removed degeneration of $^7F_1$ level in symmetric crystal field. (c) When Eu^{3+} is situated in the point group symmetry C_{4h}, D_{4h}, D_{3d}, S_6, C_{6h}, and D_{6h}, its $^7F_1$ level splits into two states to show two$^5D_0 \rightarrow {}^7F_1$ transition spectral lines. (d) When Eu^{3+} is situated in the point group symmetry T_h and O_h with a high cubic symmetry, $^7F_1$ level only has one split and shows one $^5D_0 \rightarrow {}^7F_1$ transition spectral line.

On the other hand, when Eu^{3+} is situated in the lattice with deviated inversion symmetry center, the forbidden electric-dipole transition $^5D_0 \rightarrow {}^7F_0$ with red light (about 615 nm) is dominant: (a) When Eu^{3+} is situated in the point group symmetry C_s, C_n, and C_{nv}, its $^5D_0 \rightarrow {}^7F_0$ transition emission appears at 580 nm because the expanding crystal field potential energy surface transition needs to involve odd-order crystal field term. (b) $^5D_0 \rightarrow {}^7F_0$ transition of Eu^{3+} cannot be split by the crystal field and shows only one emission peak, and then each peak corresponds to one crystal lattice. Therefore, the number of $^5D_0 \rightarrow {}^7F_1$ emission peaks can be utilized to predict the lattice number of point group symmetry where Eu^{3+} is located (C_s, C_n, and C_{nv}). (c) When Eu^{3+} is situated in point groups with low symmetry, such as triclinic crystal system C_1 and monoclinic crystal system C_s, C_2, $^7F_1$, and $^7F_2$ levels completely remove the degeneration state and are split into three and five sublevels, respectively. Subsequently, there are one $^5D_0 \rightarrow {}^7F_0$ peak, three $^5D_0 \rightarrow {}^7F_1$ peaks, and five $^5D_0 \rightarrow {}^7F_2$ peaks, respectively; among them $^5D_0 \rightarrow {}^7F_2$ transition shows the dominant red emission.

Tb^{3+} emission has originated from its $^5D_4 \rightarrow {}^7F_J$ transition, mainly in the green color region. Besides, the $^5D_3 \rightarrow {}^7F_J$ transition from the high energy level also shows an emission mainly in blue region, which is easily quenched by the crossing relaxation energy transfer process $Tb(^5D_3) + Tb(^7F_6) \rightarrow Tb(^5D_4) + Tb(^7F_6)$. Sm^{3+} emission is situated in the orange–red color region, corresponding to $^4G_{5/2} \rightarrow {}^6H_J$ (J = 5/2, 7/2, 9/2, 11/2, 13/2) [11]. Dy^{3+} shows two main emissions in visible light region, corresponding to $^4F_{9/2} \rightarrow {}^6H_{15/2}$ (470–500 nm, blue region) and $^4F_{9/2} \rightarrow {}^6H_{13/2}$ (570–600 nm, yellow region) [12]. Among them the yellow emission $^4F_{9/2} \rightarrow {}^6H_{13/2}$ (570–600 nm) belongs to hypersensitive transition. The luminescence color of Dy^{3+} often is close to white. When the hypersensitive transition of host lattice is dominant, it shows yellow color emission. The yellow/blue (Y/B) ratio is the important luminescence parameters. The direct excitation of Dy^{3+} in ultraviolet region is not successful because its charge transfer state and 5d energy level are both over 50,000 cm^{-1}. During the energy transfer from host lattice to Dy^{3+}, only YVO_4: Dy^{3+} shows highly effective luminescence.

Pr^{3+} emission color strongly depends on the host lattice of doped Pr^{3+}. Red emission derives from its $^1D_2$ level, and green color emission comes from its $^3P_0$ level. Besides, it can also show blue emission from $^1S_0$ level and visible emission from $^4f^5d$ state [12]. Nd^{3+} ($4f^3$), Er^{3+} ($4f^{11}$), and Yb^{3+} ($4f^{13}$) often show the emission in near-infrared (NIR) region. For Nd^{3+}, its emission is ascribed to three transitions of $^4F_{3/2} \rightarrow {}^4I_J$ (J = 9/2, 11/2, and 13/2) [12]. For Yb^{3+}, it shows the typical emission coming from its $^2F_{5/2} \rightarrow {}^2F_{7/2}$ transition. For Er^{3+}, it exhibits emission in both NIR regions ($^4I_{13/2} \rightarrow {}^4I_{15/2}$) and visible region ($^2H_{11/2} \rightarrow {}^4I_{15/2}$ and $^4S_{3/2} \rightarrow {}^4I_{15/2}$ transition) [12]. Tm^{3+} shows a weak blue emission originating from $^1G_4 \rightarrow {}^3H_6$ transition [12].

Besides the line emission, some rare earth ions also show the wideband emission, such as trivalent ions (Ce^{3+}, Pr^{3+}, and Nd^{3+}) and divalent ions (Eu^{2+}, Sm^{2+}, and Yb^{2+}). Ce^{3+} has only one 4f electron with excited state electron configuration $5d^1$, whose ground state $4f^1$ contains two energy levels ($^2F_{5/2}$ and $^2F_{7/2}$). So Ce^{3+} exhibits two 5d → 4f transition emissions. Ce^{3+} emission generally is situated at ultraviolet or blue region. In few systems, the long wavelength emission in green or red region also can be found, in which the $5d^1$ energy level is relatively low and the crystal field strength is high [13]. The most popular divalent ion is Eu^{2+} ($4f^7$), whose 5d → 4f emission changes in the rage from long wavelength ultraviolet to yellow regions. Eu^{2+} mainly shows the wideband emission due to $4f^65d \rightarrow 4f^7$ transition, which also shows line emission under low-temperature condition [14].

1.4 Rare Earth Phosphors

Rare earth ions and their compounds are a huge treasure of luminescent materials, which can behave as both photoactive ions and host elements. Almost all kinds of rare earth ions can be utilized in phosphors. Rare earth phosphors become the most useful species for commercial applications, due to their typical luminescence processes and mechanisms.

Trivalent rare earth ions have excellent photoactive properties such as sharp emission spectra for high color purity, broad emission bands covering the ultraviolet (UV)-visible–near-infrared (NIR) region, a wide range of lifetimes from the microsecond to the second level, high luminescence quantum efficiencies, etc. These properties have attracted much attention for a wide variety of applications in the fields of lighting devices (television and computer displays, optical fibers, optical amplifiers, lasers) and biomedical analysis (medical diagnosis and cell imaging).

However, it is difficult for rare earth ions to directly behave as luminescent materials because of their poor light absorption abilities. As it is known, the f–f transitions of rare earth ions are spin forbidden, so it is hard to generate efficient emission by direct excitation. The doping of rare earth ions into special matrices such as metallic oxides and oxysalts is traditionally an efficient method to obtain excellent luminescent material. In these kinds of phosphors, the host absorption is the main energy origin for the energy transfer and sensitization of the luminescence of active rare earth ions. Besides, the charge transfer states between rare earth ions and their

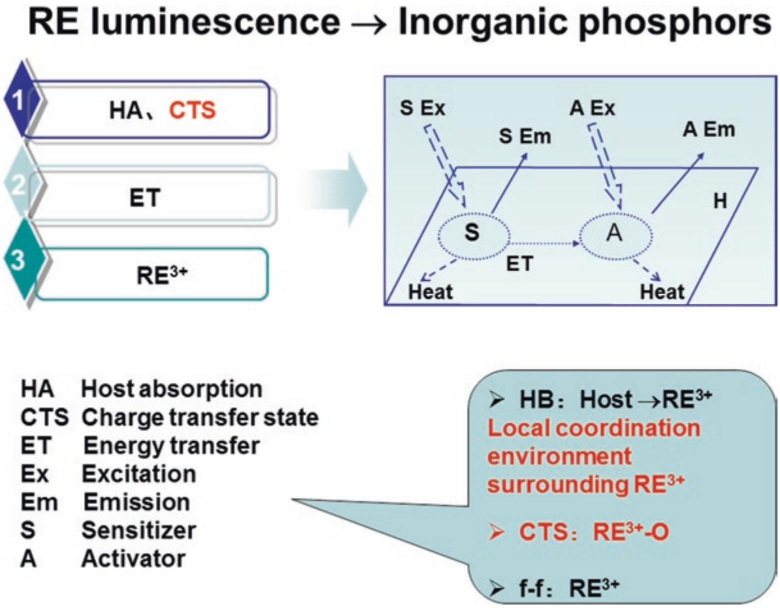

Fig. 1.3 The scheme for the luminescence and energy transfer process in rare earth solid-state phosphors

coordinated oxygen atoms (CTS) also exist in some special phosphor systems. The two main wide energy absorptions can be further excited to activate rare earth ions, resulting in the effective luminescence. Certainly, the f–f transition absorption of rare earth ions themselves also appears (Fig. 1.3).

The binary rare earth compounds used as hosts for the luminescence of rare earth ions mainly include rare earth oxides and fluorides. Among them Y_2O_3:Eu^{3+} is the most famous one because it is used as the red color phosphor for trichromatic lamp. Besides, La_2O_2S:Eu^{3+} is an important cathode ray-luminescent phosphor applied in color television. The binary rare earth fluoride can be used as the host to activate the luminescence of rare earth ions with visible or NIR emission. But their luminescent performance is not satisfied. Recently, the ternary or quaternary fluorides become the important hosts for special luminescence of rare earth ions, including $MREF_4$ (M = Na, Li), $BaREF_5$, $BaMgF_4$, K_3MF_7 (M = Zr, Hf) Na_3ScF_6, M_2NaScF_6 (M = K, Rb, Cs), and $Na_3Li_3Sc_2F_{12}$**,** While the most popular one is the $NaREF_4$ series, especially $NaYF_4$, which is a good host for the upconversion luminescence.

The most extensively used host species are the rare earth oxysalts (complex oxides), which are very abundant and versatile, including silicate, vanadate, niobate, tantalate, titanate, borate, aluminate, tungstate, molybdate, and so on. These oxysalts with oxide polyhedron frameworks can produce the effective host photo-absorption to further sensitize the luminescence of photoactive rare earth ions. In some rare earth ion (such as Eu^{3+})-doped systems, the charge transfer process can occur between Eu^{3+} ion and the oxygen center of the oxide framework, resulting in a wide charge transfer band (CTB). This is beneficial for the energy transfer and luminescence sensitization of rare earth ions. Besides, the characteristic f–f transition of photoactive rare earth ion can also be observed. Some host systems belong to self-activated phosphors, such as tungstate. The doping of activator ions may exhibit the emissions of both host and activator; different luminescence color can be integrated to realize white light output.

Rare earth silicate phosphors include many different types, such as oxygen-rich silicon oxides RE_2SiO_5 (especially Y_2SiO_5), oxyapatites $M_2RE_8(SiO_4)_6O_2$ (M = Mg, Ca, Sr), $Ca_4RE_6(SiO_4)_6O$ (M = Ca, Sr), Zn_2SiO_4, Zr_2SiO_4, $CaSiO_3$, $Sr_3La_6(SiO_4)_6$, $Na_3RESi_3O_9$, $CaAl_2SiO_7$, etc. And also they can form $M_5RE_5(SiO_4)_3(PO_4)_3O_2$ (M = alkali earth) with other oxysalts such as PO_4^{3-}. Rare earth aluminates include $REAlO_3$: Eu^{3+}, $RE_3Al_5O_{12}$, $MREAlO_4$, MAl_2O_4, $BaMgAl_{11}O_{17}$, $Sr_4Al_{14}O_{25}$, MAl_2O_4, $MREAlO_4$, etc. Among them the most important one is yttrium aluminate garnet $Y_3Al_5O_{12}$ (YAG). Besides, the famous green and blue color phosphors are in trichromatic systems, $MAl_{11}O_{19}$:Ce^{3+}, Tb^{3+} (CAT), and $BaMg_2Al_{16}O_{27}$:Eu^{2+}(Mn^{2+}) (BAM). Rare earth borates include $REBO_3$, RE_3BO_6, $Zn_4B_6O_{13}$, MB_6O_{10} (M = alkali earth), $REAl_3(BO_3)_4$, etc. Certainly, both aluminate and borate can be introduced into the same phosphor system, such as $REAl_3(BO_3)_4$, due to their similar physical properties.

The main rare earth vanadates are $REVO_4$ and $M_3RE(VO_4)_3$, respectively. Among them YVO_4: Eu^{3+} is an important phosphor. Certainly, rare earth ions and vanadate ions can be replaced by other similar valence anions or cations, resulting in new phosphors such as $REP_xV_{1-x}O_4$ or $Bi_xRE_{1-x}VO_4$. Rare earth niobate and tantalate phosphors include many systems such as $RENbO_4$, $RETaO_4$, $Zn_3Nb_2O_8$, and $REVTa_2O_9$, respectively. Rare earth phosphates include $REPO_4$, $Zn_3(PO_4)_2$, La_3PO_7, $M_3Ln(PO_4)_3$, NH_4ZnPO_4, etc.

Rare earth tungstates belong to self-activated phosphors, which show strong blue luminescence. The rare earth-doped tungstate phosphors include $M'WO_4$: Eu/Tb (M' = Ca, Sr, Ba, Pb, Zn, Mn, Fe, Cd), RE_2WO_6, Bi_2WO_6, Ag_2WO_4, and $Ag_2W_2O_7$. The most common rare earth molybdate is $NaRE(MoO_4)_2$ (and $Na_5Lu(MoO_4)_4$). Besides, there are other systems, such as $MMoO_4$ (M = Ca, Sr, Ba, Pb, Zn, Mn, Fe, Cd) and $RE_2(MoO_4)_3$. For rare earth titanates, the main host species include $MTiO_3$ (M = Ca, Sr), $RE_2Ti_2O_7$, $RE_2Ti_2O_7$, $NaRETi_2O_6$, and $Na_2RE_2Ti_3O_{10}$, whose main activator ions are Pr^{3+} or Eu^{3+}.

1.5 Luminescent Rare Earth Coordination Compounds

Rare earth coordination compounds or complexes cover different coordination numbers from 3 to 12 and structures from zero-dimensional to three-dimensional for rare earth ions with large ion radius. A majority of them are the complexes with oxygen as the coordinated atom, whose ligands involve carboxylic acids, β-diketones, macrocyclic compounds, etc. Most of these ligands are photoactive due to their localized conjugated structure which can produce the electron transition. β-Diketones possess the double ketone groups linked with methylene group to produce the chelation with rare earth ions. The well-known β-diketones contain acetylacetone (AcAc), trifluoroacetone (TFA), hexafluoroacetone (HFA), 2-thenoyltrifluoroacetone (TTA), dibenzoylmethane (DBM), etc. The introduction of unsymmetrical substituted groups can enhance the photoactive absorption; in particular, TTA is the best ligand to sensitize the luminescence of Eu^{3+}. The coordination interaction is simple between rare earth ions and β-diketones, mainly the chelated coordination. Generally, the β-diketone ligands transform to their enol structure (so-called keto–enol tautomerism) and lose one proton under alkali environment to form β-diketonate, which is coordinated to rare earth ions to form rare earth tris- or tetrais-β-diketonates. The macrocyclic compounds, such as crown ether, calixarene, Schiff base, etc., also can be used as ligands of rare earth ions, whose luminescent performance is not eminent but they can be used for special purposes. The most abundant ligand for rare earth ions is carboxylic acid, especially the aromatic carboxylic acid for the photofunctional application. These ligands contain one or multi-carboxylic groups or other substituted groups, which provide the abundant coordination positions for rare earth ions. Particularly, the complicated coordination modes of carboxylic groups to RE^{3+} endow their complexes with the diverse structures, always resulting in polymeric structures (1D chain, 2D layer, or 3D network). Especially the porous coordination polymers (PCPs) or metal–organic frameworks (MOFs) attract wide interest.

As we all know, all rare earth ions only possess weak light absorption because the molar absorption coefficients of most transitions in the absorption spectra of RE^{3+} are smaller than 10 $Lmol^{-1}$ cm^{-1}; only a very limited amount of radiation is absorbed by direct excitation in the 4f levels to obtain weak luminescence. To overcome this disadvantage, Weissman has discovered *"antenna effect" within the* rare earth complexes of organic ligands, which is based upon the excitation in an absorption band of the organic ligand and the subsequent intramolecular energy transfer between the organic ligands and rare earth ions [15]. Afterward, the mechanism of the energy transfer is studied in detail, putting emphasis on the rare earth β-diketonate complexes, because they are potentially active species in liquid lasers. Combining with luminescence process of organic ligands and the results in rare earth organic complexes, the commonly accepted mechanism by Crosby and Whan is shown in the inset of Fig. 1.4 [16, 17]. Upon irradiation with ultraviolet radiation, organic molecules are excited to a vibrational level of the excited singlet state (S_i) and then may undergo fast internal conversion process (IC) to relax to the lowest vibrational level of the S_1 state, which is a very quick process and easily occurs in solution for the interaction with solvent molecules. Commonly, the excited singlet state of organic molecule can be deactivated radiatively to the ground state, resulting in molecular fluorescence with the spin which allows transition between two electronic states with the same spin multiplicity from S_1 to S_0. On the other hand, the excited singlet state may occur as conversion with different spin multiplicity from singlet S_i to triplet T_i by the microscopic quantum mechanics perturbation, called intersystem crossing (ISC). The excited triplet state of organic molecule can be deactivated radiatively to the singlet ground state, resulting in molecular

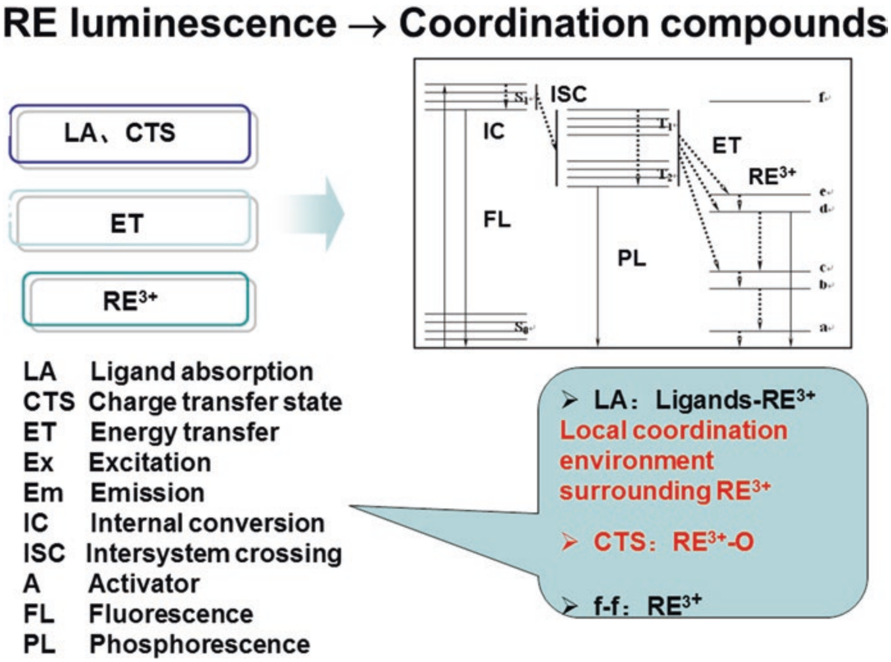

Fig. 1.4 The scheme for the luminescence and energy transfer process in rare earth coordination compounds

phosphorescence with the spin-forbidden transition from T_1 to S_0. When organic molecule behaves like a ligand in rare earth complexes through coordination interaction, the complex may undergo a non-radiative transition from the triplet state to an excited state of the rare earth ion through a so-called intramolecular energy transfer process. The sensitized rare earth ion may undergo a radiative transition to a lower 4f state by characteristic line-like photoluminescence or may be deactivated by non-radiative processes to produce heat. From the emission transition position of common rare earth ions, the certain resonance emission levels can be determined, which are $^4G_{5/2}$ for Sm^{3+} (17,800 cm^{-1}), $^5D_0$ for Eu^{3+} (17,250 cm^{-1}), $^5D_4$ for Tb^{3+} (20,500 cm^{-1}), and $^4F_{9/2}$ for Dy^{3+} (20,960 cm^{-1}), respectively. If the rare earth ion is excited to a non-emitting level, the excitation energy is dissipated via non-radiative processes until a resonance level is reached either directly by excitation in the 4f levels or indirectly by energy transfer. In this case, radiative transitions will compete with the non-radiative processes to display RE^{3+}-centered emission. So the final line emission of rare earth ion depends on the minimization of non-radiative deactivation or other emissions of molecular fluorescence and phosphorescence. To populate a resonance level of a RE^{3+} ion, the necessary prerequisite is the lowest triplet state of the ligand, or the complex is higher than the resonant energy level of the rare earth ion. If not, no effective emission of RE^{3+} is found, and molecular luminescence (fluorescence or phosphorescence) may be observed. So the intramolecular energy transfer within the rare earth complexes may depend on the match between the energy of the lowest triplet level of the ligands or complexes and the resonance level of RE^{3+}. Because the position of the triplet level depends on the type of ligand, it is therefore possible to control the luminescence intensity observed for a given rare earth ion by variation of the ligand.

Sato and Wada have investigated the relationship between the intramolecular energy transfer efficiencies and triplet state energies in the rare earth β-diketones chelates [18]. Gadolinium complexes are selected as model complexes for the determination of the lowest triplet state energies of organic ligands due to their enhanced phosphorescence/fluorescence ratios ($\Phi_{ph}/\Phi_{fl} > 100$) compared to those of other rare earth complexes, and the emitting level energy of Gd^{3+} is so much higher than the triplet state energies of organic ligands; therefore, it cannot be sensitized by ligands. Moreover, the presence of a heavy paramagnetic Gd^{3+} ion enhances the ISC from the singlet to the triplet state because of the mixing of the triplet and singlet states, so-called *paramagnetic effect*. The spin–orbit coupling interaction endows the triplet state a partially singlet character to relax the spectral selection rules. The efficiency of the energy transfer is proportional to the overlap between the phosphorescence spectrum of the ligand and the absorption spectrum of the rare earth ion. The overlap decreases as the triplet state energy increases. Therefore, the intramolecular energy migration efficiency from the organic ligands to the central RE^{3+} is the most important factor influencing the luminescence properties of rare earth complexes, which depends mainly on the two energy transfer processes. One is from the lowest triplet state energy of organic ligand to the resonant energy level by Dexter's resonant exchange interaction theory (Eq. 1.1) [19]:

$$k_{\mathrm{ET}} = 2\pi Z^2 \int F_{\mathrm{d}}(E) F_{\mathrm{a}}(E) \mathrm{dE} \exp(-2R_{\mathrm{da}} / L) \tag{1.1}$$

Where k_{ET} is the rate constant of the intermolecular energy transfer and P_{da} is the transition probability of the resonant exchange interaction. $2\pi Z^2/R$ is the constant relating to the specific mutual distance between the central RE^{3+} ion and its coordinated atoms. $F_{\mathrm{d}}(E)$ and $E_{\mathrm{a}}(E)$ are the experimental luminescent spectrum of energy donor (ligands) and the experimental absorption spectrum of energy acceptor (RE^{3+}), respectively, R_{da} is the intermolecular distance between donor atoms and acceptor atoms, and L is the van der Waals radius. Both R_{da} and L may be considered to be constant in intramolecular transfer processes, so k_{ET} is proportional to the overlap of $F_{\mathrm{d}}(E)$ and $E_{\mathrm{a}}(E)$.

On the other hand, a close match between the energy of the triplet state and the energy of the receiving 4f level of the rare earth ion is not desirable either, because energy back transfer of the rare earth ion to the triplet state can occur. When the energy transfer is not very efficient, it is possible to observe some remaining ligand emission in combination with the rare earth-centered emission. The inverse energy transition by the thermal deactivation mechanism is shown as follows (Eq. 1.2) [20, 21]:

$$k(T) = A\exp(-\Delta E / RT) \tag{1.2}$$

Both of them represent the overlap spectrum of RE^{3+}. With the decrease in the energy difference between the triplet state energy of conjugated carboxylic acid and RE^{3+}, the overlap of $F_d(E)$ and $E_a(E)$ is increased. So from the above equation, it can be concluded that the larger the overlap between the luminescent spectrum of organic ligands and the emissive energy of RE^{3+}, the larger is the intramolecular energy rate constant k_{ET}. On the other hand, the activation energy ΔE in Eq. (1.2) is equal to the energy difference $\Delta E(\text{Tr-RE}^{3+})$, while from the formula, the inverse energy transfer rate constant $k(T)$ increased with decreasing $\Delta E(\text{Tr-RE}^{3+})$ [22–25]. As discussed above, there should exist an optimal energy difference between the triplet position of organic ligands and the emissive energy level RE^{3+}; a larger or a smaller $\Delta E(\text{Tr-RE}^{3+})$ will decrease the luminescence of rare earth complexes.

Another possibility to sensitize rare earth luminescence is via *charge transfer states* [26–28]. This is especially the case for trivalent rare earth ions that can easily be reduced to the divalent state (redox-sensitive rare earth ions) like Sm^{3+}, Eu^{3+}, and Yb^{3+}, where light can be absorbed by an intense ligand-to-metal charge transfer state (LMCT state) from which the excitation energy can be transferred to the 4f levels of the rare earth ion. This process only works well if the LMCT state lies at high-enough energy. For instance, sensitization of Eu^{3+} through a LMCT state is efficient if the LMCT lies above 40,000 cm^{-1}. Low-lying LMCT states will partially or totally quench the luminescence. In the case of Eu^{3+}, metal-centered luminescence is totally quenched if the LMCT energy is less than 25,000 cm^{-1} [29]. Also strongly absorbing chromophores containing d-block metals can be used for sensitizing rare earth luminescence [30]. Because these chromophores absorb in general at longer wavelengths than the most often used organic chromophores (typically in the visible spectral region), *d-block chromophores* are especially useful for sensitizing the near-infrared luminescence of rare earth ions like Nd^{3+}, Er^{3+}, and Yb^{3+}.

Besides, Kleinerman proposes a mechanism of direct transfer of energy from the excited singlet state S_1 to the energy levels of the rare earth ion [31], which is now not considered to be of great importance because it is often not efficient due to the short lifetime of the excited singlet state. In this way, the energetic constraints from the T_1 state of the ligand can be avoided. Horrocks and co-workers later examine the energy transfer processes in rare earth ion-binding proteins and assume that it is the excited singlet state of the chromophore that sensitizes the rare earth examine [6]. However, owing to the lack of information regarding the emission from the excited states of the coordinated ligand and the difficulties in the determination of the ligand-localized triplet–triplet absorption spectra for rare earth chelates, it has been very difficult to prove for certain which state is responsible for the energy transfer process [32]. All the experimental work conducted on the sensitization of rare earth chelate luminescence seems to support the triplet pathway, whereas the singlet pathway for the sensitization of the Eu complex has not been observed experimentally [32]. Yang et al. report the successful extension of the excitation window to the visible region for a Eu complex, which subsequently exhibits highly

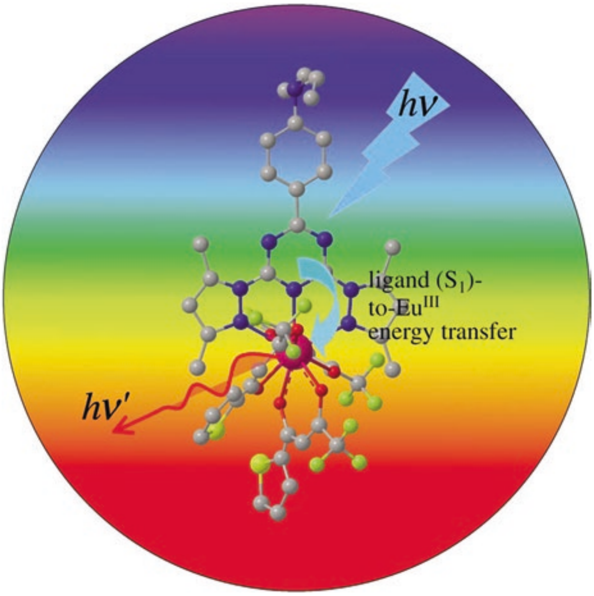

Fig. 1.5 The scheme for the singlet direct energy transfer pathway diagram (bottom) in complex Eu(TTA)3 L (L = N,N-dialkyl aniline moiety-modified dipyrazolyltriazine derivative) (Reprinted with permission from Ref. [32]. Copyright 2004 John Wiley & Sons Ltd)

efficient EuIII-centered luminescence. The sensitization mechanism is shown to take place through the singlet pathway by means of time-resolved luminescence spectroscopic studies. They have demonstrated the first observable case of excitation energy transfer from the ligand to the luminescent states of EuIII ion through the singlet pathway in a visible light-sensitized europium complex. The excitation window for this complex has been extended up to 460 nm (Fig. 1.5).

In addition, in ternary rare earth complexes, there also exists the energy transfer between different ligands. According to the phosphorescent spectra or lifetimes of ternary and binary gadolinium complexes, it can be found that in some ternary rare earth complexes, only one ligand may become the main energy donor for the energy transfer from another ligand to this ligand, whose energy transfer also depends on the triplet state energy level of the two ligands. This phenomenon often occurs in the ternary rare earth complexes with aromatic carboxylic acids and heterocyclic ligands [33]. On the other hand, some inert RE ions (La^{3+}, Gd^{3+}, Y^{3+}, Lu^{3+}) also enhance ultraviolet absorption intensity of ligands and then enhance phosphorescence intensity to improve intersystem crossing efficiency from S_1 to T_1 of ligands. Subsequently, the intramolecular energy transfer efficiency from ligands to RE^{3+} will be increased to obtain the strong luminescence of RE^{3+} [34].

1.6 Photofunctional Rare Earth Hybrid Materials

Photofunctional rare earth hybrid materials are more complicated than molecular systems. The initial aim is to prepare the multicomponent materials and modify their properties, such as thermal stability or photostability. But now the photofunctional hybrid materials are endowed with the abundant connotations. These hybrids display special characteristics of both solid-state luminescence and molecular luminescence. The hybrids not only involve the structural components as the building units but also contain the photofunctional units. The aggregate state and microstructure of the photofunctional hybrid materials have been studied, and the final aim is to realize the property tuning and function integration. In these photofunctional rare earth hybrid systems, all kinds of interaction forces are involved, including coordination bonds, covalent bonds, and other interactions. On the other hand, the composition of hybrid materials is multi-scale, from molecular scale to nanoscale and to bulk materials.

As the above discussion attests, the luminescent rare earth compounds mainly have two types: one is the atomic or ionic system, i.e., rare earth solid-state compounds as phosphors (continuous solids), and the other is the molecular system, i.e., rare earth coordination compounds or complexes (molecular solids). The main distinction between the luminescence of the two kinds of compounds is different energy donors, i.e., host absorption for the former and ligand absorption for the latter. But in fact, the nature of the interaction between photoactive rare earth ions and hosts or ligands is identical, which is the coordination and depends on the coordination environment surrounding rare earth ions. Certainly, the charge transfer state absorption also exists between certain rare earth ions and ligand or host, such as Eu^{3+}-O CTS.

For rare earth photofunctional hybrid materials, the initial aim is only to put photoactive species (mainly rare earth complexes) into some hosts to improve their thermal or photostability [35–39]. The combination of organic and inorganic components at a molecular or nanometer scale integrates certain strong points of organic compounds (easy processing with conventional techniques, elasticity, and organic functionalities) with the advantages of inorganic components (hardness, thermal and chemical stabilities). According to the different interaction forces between the two phases, these hybrid materials are divided into two major classes [40]. Physically doped hybrids have weak interactions (such as hydrogen bonding, van der Waals forces, or weak static effects) between the organic and inorganic phases, which cannot overcome many problems such as clustering of emitters, inhomogeneous dispersion of the components, or leaching of the dopants [41–46]. Chemically bonded hybrids have strong interactions such as covalent, ion–covalent, coordination, or Lewis acid/base bonds, which can graft the rare earth complexes onto hosts [47, 48]. The latter class of hybrids overcome the disadvantages of the former one, since they are homogeneous and can avoid the self-quenching of rare earth ions, which results in increased incorporation concentrations.

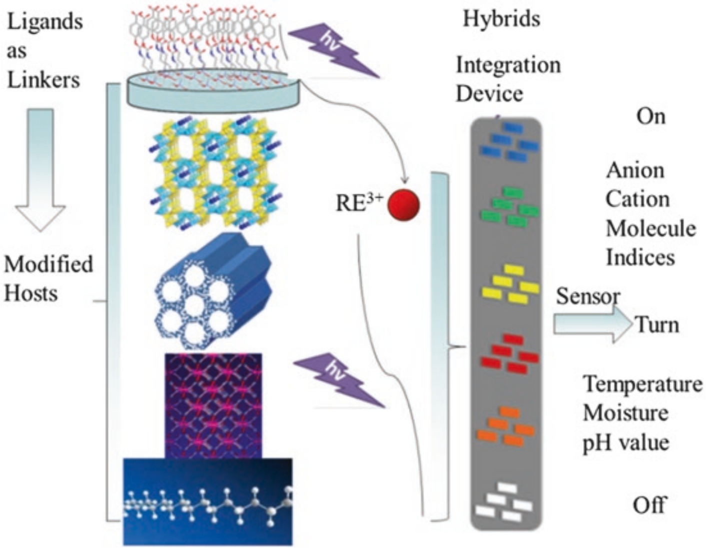

Fig. 1.6 The scheme for the compositions and photophysical applications of photofunctional rare earth hybrid materials

Further, it needs to mention the nature of the luminescence and its significance for photofunctional hybrid materials. The whole photofunctional hybrid material system belongs to the complicated frameworks or networks that contain various kinds of building blocks. The important component is the ligand or linker functionalized host. The scheme of the photofunctional hybrid systems is shown in Fig. 1.6. The linker is a special ligand which plays a key role in producing the antenna effect to transfer energy to sensitize the luminescence of coordinated photoactive RE^{3+}. The linker functionalized host in the hybrid system shows the characteristics of both of the ligand and the host, which integrates the luminescence of solid-state phosphors and molecular complexes. The common hosts include sol–gel-derived silica, which is mainly from organically modified silane, mesoporous silica, microporous zeolite, metal–organic framework or porous coordination polymer, organic polymer or its composites, etc. Certainly, the photo-absorption is often affected by the metal ions coordinated to linker-modified hosts in some systems such as MOFs (or PCPs). The final hybrid system can display multicolor luminescence under energy transfer with antenna effect and also achieve the white color luminescence integration. Some hybrids can be further studied to explore their application in sensing.

In this book, seven topics are discussed in the following chapters. Chapter 2 focuses on photofunctional rare earth hybrid materials based on sol–gel-derived silica, mainly with the organically modified silanes as the linkers. Chapter 3 focuses on photofunctional rare earth hybrid materials based on organically modified mesoporous silica. Chapter 4 focuses on photofunctional rare earth hybrid materials based on microporous zeolite. Chapter 5 focuses on photofunctional rare earth hybrid materials based on metal–organic frameworks. Chapter 6 focuses on photofunctional rare earth hybrid materials based on organic polymer or its composites. Chapter 7 focuses on photofunctional rare earth hybrid materials with other functional units achieved by multicomponent assembly. Chapter 8 focuses on the photophysical applications of photofunctional rare earth hybrid materials, especially on chemical sensing. The seven topics are chosen because there are extensive reports on them.

References

1. Ropp RC (2004) Luminescence and the solid state, 2nd edn. Elsevier Science, Boston
2. Jolly L (1984) Modern inorganic chemistry. McGraw-Hill, New York
3. Kitai A (2008) Luminescent materials and applications. Wiley, Hoboken
4. Yan B, Chen ZD (2001) Cyano-bridged aqua (N,N-dimethylacetamide) (cyanoiron) rare earths from samarium, gadolinium or holmium nitrate and potassium hexacyanoferrate: crystal structure and magnetochemistry. Helv Chim Acta 84:817–829
5. Yan B, Wang SX, Chen ZD (2003) Synthesis, crystal structures and magnetic properties of ion-pair complexes with hydrogen bonding network: $ln(DMA)_n(H_2O)_mCr(CN)_6{\cdot}xH_2O$ (for ln = Sm, Gd: n = 4, m = 3, x = 2; for ln = Er: n = 3, m = 4, x = 0). J Coord Chem 55:573–586
6. JH W, Yan B (2010) Room-temperature solid-state reaction behavior, hydrothermal crystallization and physical characterization of $NaRE(MoO_4)_2$ and $Na_5Lu(MoO_4)_4$ compounds. J Amer Ceram Soc 93:2188–2194
7. Moore EG, Samuel APS, Raymond KN (2009) From antenna to assay: lessons learned in lanthanide luminescence. Acc Chem Res 42:542–552
8. Blasse G, Grabmaier BC (1994) Luminescent materials. Springer, Berlin
9. Blasse G (1992) Vibronic transitions in rare earth spectroscopy. Int Rev Phys Chem 11:71–100
10. Carnall WT, Fields PR, Rajnak K (1968) Electronic energy levels of the trivalent lanthanide aquo ions. IV. Eu^{3+}. J Chem Phys 49:4450–4455
11. Carnall WT, Fields PR, Rajnak K (1968) Electronic energy levels of the trivalent lanthanide aquo ions. III. Tb^{3+}. J Chem Phys 49:4447–4449
12. Carnall WT, Fields PR, Rajnak K (1968) Electronic energy levels in the trivalent lanthanide aquo ions. I. Pr^{3+}, Nd^{3+}, Pm^{3+}, Sm^{3+}, Dy^{3+}, Ho^{3+}, Er^{3+}, and Tm^{3+}. J Chem Phys 49:4424–4442
13. Di Bartolo B (1968) Optical interactionin solids. Wiley, New York
14. Blasse G, Dirksen GJ, Meijerink A (1990) The luminescence of ytterbium(II) in strontium tetraborate. Chem Phys Lett 167:41–44
15. Weissman SI (1942) Intramolecular energy transfer: the fluorescence of complexes of europium. J Chem Phys 10:214–217
16. Crosby GA, Whan RE, Alire RM (1961) Intramolecular energy transfer in rare earth chelates–role of the triplet state. J Chem Phys 34:743–748
17. Crosby GA, Whan RE, Freeman J (1962) Spectroscopic studies of rare earth chelates. J Phys Chem 66:2493–2499
18. Sato S, Wada M (1970) Relations between intramolecular energy transfer efficiencies and triplet state energies in rare earth β-diketone chelates. Bull Chem Soc Jpn 43:1955–1962
19. Dexter DL (1953) A theory of sensitized luminescence in solids. J Chem Phys 21:836–850
20. Brown TD, Shepherd TM (1973) Factors affecting the quantum efficiencies of fluorescent terbium(III) chelates in the solid state. J Chem Soc Dalton Trans:336–341
21. Balzani V, Moggi L, Manfrin MF, Bolletta F (1975) Quenching and sensitization process of coordination compounds. Coord Chem Rev 15:321–433
22. SL W, YL W, Yang YS (1992) Rare earth(iii) complexes with indole-derived acetylacetones II. Luminescent intensity for europium(iii) and terbium(iii) complexes. J Alloys Compd 180:399–402

23. Song YS, Yan B, Chen ZX (2004) Different crystal structure and photophysical properties of rare earth complexes with 5-bromonicotinic acid. J Solid State Chem 177:3805–3814
24. Yan B, Zhou B Photophysical properties of dysprosium complexes with aromatic carboxylic acids by molecular spectroscopy. J Photochem Photobiol A Chem 171:181–186
25. Wang QM, Yan B, Zhang XH (2005) Photophysical properties of novel rare earth complexes with long chain mono-eicosyl *cis*-butene dicarboxylate. J Photochem Photobiol A Chem 174:119–124
26. Petoud S, Bunzli JCG, Glanzman T, Piguet C, Xiang Q, Thummel RP (1999) Influence of charge-transfer states on the Eu(III) luminescence in mononuclear triple helical complexes with tridentate aromatic ligands. J Lumin 82:69–79
27. Faustino WM, Malta OL, de Sa GF (2005) Intramolecular energy transfer through charge transfer state in lanthanide compounds: a theoretical approach. J Chem Phys122:317–325
28. Daleo A, Picot A, Beeby A, Williams JAG, Le Guennic B, Andraud C, Maury O (2008) Efficient sensitization of europium, ytterbium, and neodymium functionalized tris-dipicolinate lanthanide complexes through tunable charge-transfer excited states. Inorg Chem 47:10258–10268
29. Fonger WH, Struck CW (1970) Eu^{3+} ^5D resonance quenching to the charge-transfer states in Y_2O_2S, La_2O_2S, and LaOCl. J Chem Phys 52:6364–6371
30. Ward MD (2007) Transition-metal sensitized near-infrared luminescence from lanthanides in d-f heteronuclear arrays. Coord Chem Rev 251:1663–1677
31. Kleinerman M (1964) Energy migration in lanthanide chelates. Bull Am Phys Soc *9*:265–269
32. Yang C, LM F, Wang Y, Zhang JP, Wong WT, Ai XC, Qiao YF, Zou BS, Gui LL (2004) A highly luminescent europium complex showing visible-light-sensitized red emission: direct observation of the singlet pathway. Angew Chem Int Ed 43:5010–5013
33. Yan B, Zhang HJ, Wang SB, Ni JZ (1998) Intramolecular energy transfer mechanism between ligands in ternary complexes with aromatic acids and 1,10-phenanthroline. J Photochem Photobiol A Chem 116:209–214
34. Yang JH, Zhu GY, Wang H (1989) Application of the co-luminescence effect of rare earths: simultaneous determination of trace amounts of samarium and europium in solution. Analyst 114:1417–1419
35. Carlos LD, Ferreira RAS, Bermudez VD, Ribeiro JLS (2009) Rare earth-containing light-emitting organic–inorganic hybrids: a bet on the future. Adv Mater 21:509534
36. Binnemans K (2009) Rare earth-based luminescent hybrid materials. Chem Rev 109:42834374
37. Yan B (2012) Recent progress on photofunctional rare earth hybrid materials. RSC Adv 2:9304–9324
38. Feng J, Zhang HJ (2013) Hybrid materials based on rare earth organic complexes: a review. Chem Soc Rev 42:387–410
39. Zhang HJ, Niu CJ, Feng J (2014) Rare earth organic-inorganic hybrid luminescent materials. Scientific Press. (in Chinese)
40. Sanchez C, Ribot F (1994) Design of hybrid organic-inorganic materials synthesized via sol-gel chemistry. New J Chem 18:1007–1047
41. Yan B, Zhang HJ, Wang SB, Ni JZ (1997) Luminescence properties of the ternary rare earth complexes with *beta*-diketones and 1,10-phenanthroline incorporated in silica matrix by a sol-gel method. Mater Chem Phys 51:92–96
42. Tanner PA, Yan B, Zhang HJ (2000) Preparation and luminescence properties of sol-gel hybrid materials incorporated with europium complexes. J Mater Chem 35:4325–4328
43. Yan B, Wang QM (2004) In-situ composition and luminescence of terbium coordination polymers/PEMA hybrid thick films. Opt Mater 27:533–537
44. LS F, Meng QG, Zhang HJ, Wang SB, Yang KY, Ni JZ (2000) In situ synthesis of terbium-benzoic acid complex in sol-gel derived silica by a two-step sol-gel method. J Phys Chem Sol 61:1877–1881
45. Dang S, Sun LN, Zhang HJ, Guo XM, Li ZF, Feng J, Guo HD, Guo ZY (2008) Near-infrared luminescence from sol-gel materials doped with holmium(III) and thulium(III) complexes. J Phys Chem C 112:13240–13247

46. Pecoraro E, Ferreira RAS, Molina C, Ribeiro SJL, Messsaddeq Y, Carlos LD (2008) Photoluminescence of bulks and thin films of Eu^{3+}-doped organic/inorganic hybrids. J Alloys Compds 451:136–139
47. Franville AC, Zambon D, Mahiou R (2000) Luminescence behavior of sol−gel-derived hybrid materials resulting from covalent grafting of a chromophore unit to different organically modified alkoxysilanes. Chem Mater 12:428–435
48. Minoofar PN, Hernandez R, Chia S, Dunn B, Zink JI, Franville AC (2002) Placement and characterization of pairs of luminescent molecules in spatially separated regions of nanostructured thin films. J Am Chem Soc 124:14388–14396

Part II

Typical Photofunctional Rare Earth Hybrid Material

Chapter 2

Photofunctional Rare Earth Hybrid Materials Based on Organically Modified Silica

Abstract This chapter mainly focuses on recent research progress in photofunctional rare earth hybrid materials based on organically modified silica, which are obtained through the special chemical linkage of organically modified silanes (ORMOSILs). The content mainly covers the hybrid materials based on aromatic carboxylic acid derivative-modified ORMOSILs, β-diketone and β-diketone analogue derivative-modified ORMOSILs, macrocyclic compound derivative-modified ORMOSILs, heterocyclic ligand derivative-modified ORMOSILs, and the hybrid materials with composite matrices through ORMOSILs. The emphasis is put on the recent research progress of our group.

Keywords Rare earth ion • Photofunctional hybrid material • Organically modified silane • Chemical linkage • Luminescence • Sol–gel-derived silica

2.1 Introduction

Sol–gel process mainly involves two approaches: one is the gelation of a solution of colloidal powders; the other is the hydrolysis and polycondensation of alkoxide or nitrate precursors, followed by either hypercritical drying or aging and drying under ambient atmospheres [1]. Sol–gel system includes different forms such as sols (dispersions of colloidal particles in a liquid), colloids (solid particles with diameters of 1–100 nm), and gels (interconnected, rigid networks with pores of submicrometer dimensions and polymeric chains with an average length greater than a micrometer), respectively. Gels can be classified in four categories by Flory: well-ordered lamellar structures, completely disordered covalent polymeric networks, predominantly disordered polymer networks formed through physical aggregation, and particulate, disordered structures, respectively. The most popular one is silica gel, including versatile organically modified silane (ORMOSIL) derivatives, which forms an interconnected 3D network through the simultaneous hydrolysis and polycondensation of an organometallic precursor (alkoxide). The structures of the main sol–gel products are shown in Fig. 2.1 [2, 3].

The ORMOSILs provide the possibility to prepare sol–gel-derived silica host hybrid materials because they not only behave as the chemical (covalent) linkage

B. Yan, *Photofunctional Rare Earth Hybrid Materials*,
Springer Series in Materials Science 251, DOI 10.1007/978-981-10-2957-8_2

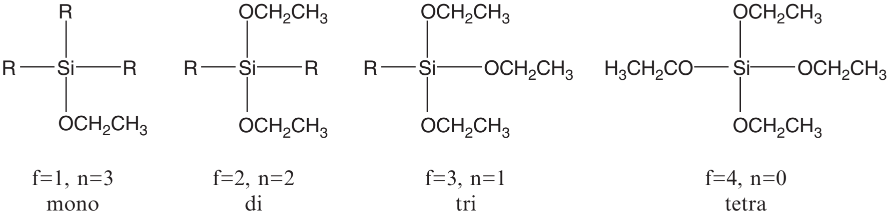

Fig. 2.1 ORMOSIL functionalities. A tetrafunctional silicon alkoxide ($n = 0$) acts as a "network-forming" structure, a trifunctional silicon alkoxide ($n = 1$) behaves as a "cross-linker," a difunctional silicon alkoxide ($n = 2$) behaves as a "bridging" agent, and a monofunctional silicon alkoxide ($n = 4$) can be used as a "terminating" agent. Reprinted with permission from [3]. Copyright 2013 American Chemical Society

but also realize the postsynthetic modification strategy [4, 5]. In fact, the chemical linkers for hybrid materials have a lot of choices, among which the simplest species are the organic ligands with multifunctional groups such as nitrogen heterocyclic-conjugated carboxylates [6, 7]. They possess both coordination and photosensitization capabilities, and some groups are reactive to link all kinds of host materials. Besides, some special ORMOSILs, such as 3-methacryloxypropyltrimethoxysilane (MPTMS) as cross-linking reagent, have carbonyl group with coordination ability and alkoxyl group with condensation polymerization ability [8]. But the absence of conjugate group leads to no apparent photosensitization of RE^{3+}, so another luminescent sensitizer with photoactive molecule-modified ORMOSILs should be introduced into the whole hybrid system to achieve the multicomponent assembly, just like ternary rare earth complexes. Moreover, some cross-linking reagents can be modified together through the addition reaction to obtain the new covalent linkers. For example, 3-(triethoxysilyl)-propyl isocyanate (TESPIC) is modified by (3-aminopropyl)triethoxysilane (APES) to construct the hybrid material [9]. The coupling agent moiety is a convolution of TESPIC and APES through NHC(=O)NH groups which is applied to coordinate to RE^{3+} and further form Si–O backbones after hydrolysis and polycondensation processes. In the same way, two cross-linking reagents, 3-aminopropyl-methyl-diethoxylsiliane ($H_2N(CH_2)_3SiCH_3(OC_2H_5)_2$) and N-2-aminoethyl-3-aminopropyltriethoxylsiliane ($H_2N(CH_2)_2HN(CH_2)_3Si(OC_2H_5)_3$), can be modified by TESPIC to afford two novel cross-linking molecular derivatives as bridge ligands [10]. Then the ternary hybrid system with these linkers and phen ligand are constructed with the two components equipped with covalent bonds.

So it needs to mention that the key procedure in constructing these chemically bonded sol–gel-derived silica hybrid materials is to design the functional bridging molecule (ligand) by grafting; the bridging molecule behaves as a chemical linkage with the functions of coordinating or sensitizing lanthanide ions and forming covalent Si–O networks [11]. The photoactive groups of these bridging molecules are also important in photofunctional hybrids. More general bridging molecules need to be synthesized using modification reactions, named ORMOSILs. Many types of organic ligands have been functionalized and grafted onto silanes in order to achieve

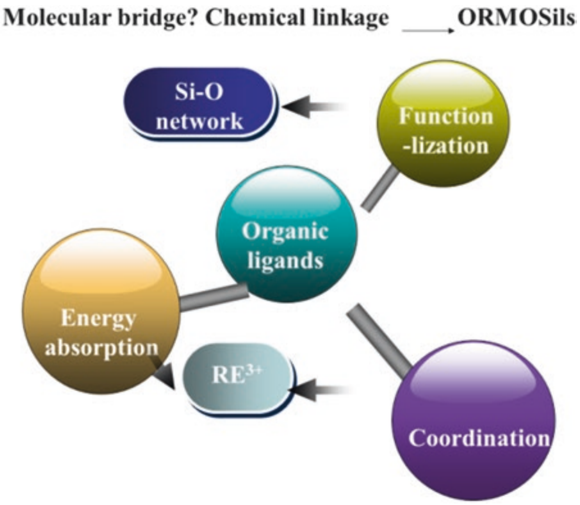

Fig. 2.2 Scheme for the photofunctional rare earth hybrid materials based on ORMOSILs as chemical linkers

various ORMOSILs, whose modification paths can be summarized on the basis of different functional group reactions [11]. The scheme to design or functionalize covalent linkers to assemble the corresponding rare earth hybrid materials is shown in Fig. 2.2 [11]. To design the covalent linkers, two precursors should be considered. One is the typical luminescent ligands to sensitize RE ions, such as beta-diketones or their derivatives, aromatic carboxylic acids and derivatives, and so on. The other is the cross-linking reagent silane or their derivatives, which can be covalently bonded to silica host. The basic strategy is to graft a typical photoactive organic ligand for lanthanide ions onto a special functional silane cross-linking reagent. Subsequently, all kinds of covalent linkers based on ORMOSILS have been designed and synthesized for the construction of photofunctional rare earth hybrid materials.

In this chapter, our focus is on the photofunctional rare earth hybrid materials with ORMOSILs as building block to realize the chemical bonding or linking between rare earth complex species and silica hosts. The classification is made according to the species of organic ligands which functionalize ORMOSILs to be the special chemical linkers. Five classes of these hybrid systems are discussed: hybrids based on aromatic carboxylic acid-derived ORMOSILs, β-diketone and its analogue-derived ORMOSILs, macrocyclic compound-derived ORMOSILs, heterocyclic ligand derivative-modified ORMOSILs, and the hybrid materials with composite matrices through ORMOSILs, respectively.

2.2 Photofunctional Rare Earth Hybrid Materials Based on Aromatic Carboxylic Acid-Modified Silica

Aromatic carboxylic acids play an important role in the rare earth complexes for their complicated coordination modes. All kinds of aromatic carboxylic acid derivatives possess the carboxylic group and other reactive substituted groups, which can be easily modified to ORMOSIL linkers by cross-linking reagent silane. Yan's group has done extensive work on the hybrids with different aromatic carboxylic acids as chemical linkers.

2.2.1 Photofunctional Rare Earth Hybrid Materials Based on Aromatic Carboxylic Acid-Modified Silica Through Carboxylic Group Grafting

Direct modifying of the carboxylic group of aromatic carboxylic acid generally needs a two-step reaction. Firstly, carboxylic acid is transferred to acyl chloride, which is more easily to be modified than carboxylic group. Secondly, the acyl chloride derivative reacts with amino group-substituted silane through the condensation. This method can modify all kinds of aromatic carboxylic acid compounds, but different carboxylic acid ligands may show distinct behaviors because of the different steric hindrances or different positions of the substituted groups [12–22]. The polycarboxylic acid and unsubstituted benzoic acid are hard to modify mainly due to the group competition or weak solubility. Sui et al. have realized the modification of benzoic acid (BA) and used its APES-modified ORMOSILs as linkage to construct the hybrid materials (Fig. 2.3) [12]. It is interesting that the hybrid Tb-BA-APES shows the unexpected micro-lotus rootlike pore morphology. The dimensions of the pores are about 2–3 μm. The special pore microstructure for this hybrid material

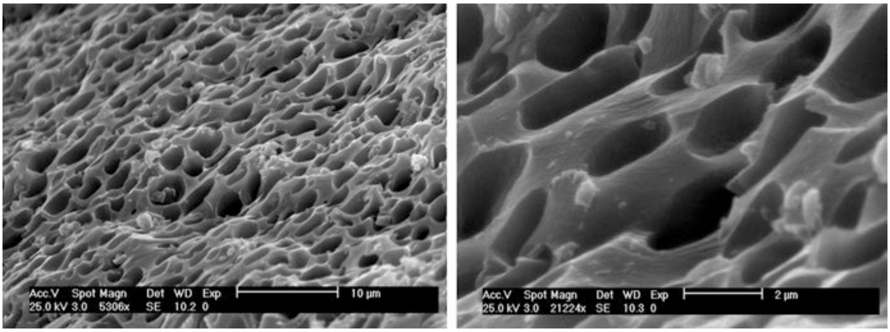

Fig. 2.3 The SEM images for the lotus rootlike morphology of Tb-BA-APES hybrids (Reprinted with permission from Ref. [12]. Copyright 2005 Elsevier)

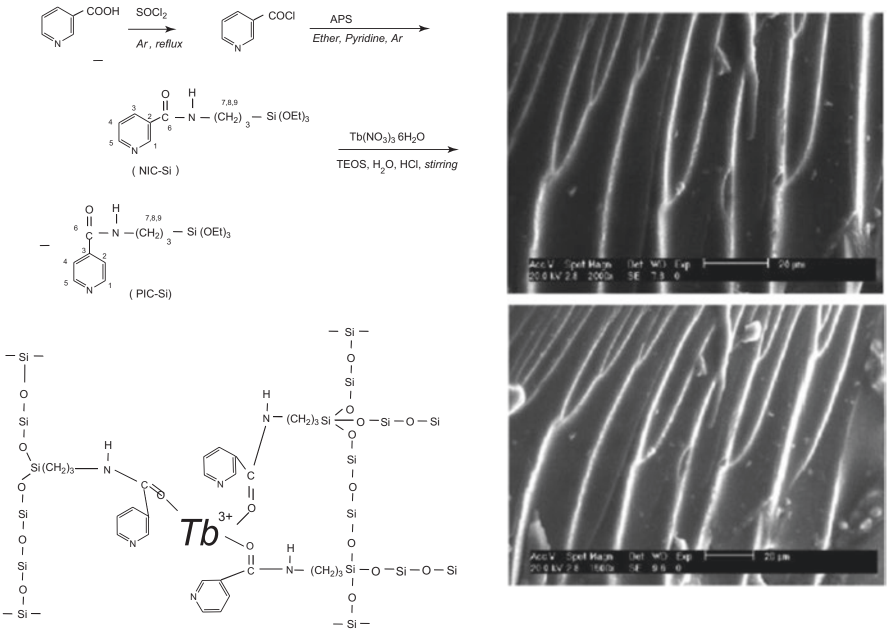

Fig. 2.4 Scheme for the synthesis of hybrid materials Tb-PIC-APES (*Left*) and the selected SEM images of it (*Right*) (Reprinted with permission from [13]. Copyright 2005 the American Chemical Society)

may be due to both the coordination action and covalent bond effect of O–Si–O network backbone.

Wang et al. modify two pyridine carboxylic acids (nicotinic acid and picolinic acid) with APES and prepare the corresponding hybrid materials (Fig. 2.4 (Left)) [13]. From the SEM images in Fig. 2.4 (Right), we can see that some chainlike structures in hybrids appear like the trunk of pine trees. Since the coordination of terbium ions with nicotinic and picolinic acids leads to one-dimensional chainlike coordination polymers, the terbium complexes corresponding to their derivatives should have the tendency to form the polymeric chain, which can compete with the construction of a polymeric network structure of Si–O for the hydrolysis and polycondensation process of silica. Both of their growth liabilities doom the final structure and morphology of the hybrids. In terms of the different steric effects, picolinic acid of four substituted pyridine carboxylate can readily form a chainlike polymeric construction compared with nicotinic acid of a three-substituted one. In this way, the trunk structure is achieved for the dominant growth along the terbium coordination polymer chain in the former, while the latter forms normally homogeneous materials because of less steric hindrance. The research can be extended to the other pyridine carboxylic acid derivative functionalized ORMOSILs hybrid materials, which also show the similar chainlike trunk microstructure in their SEM images [14]. So this is a common phenomenon in aromatic carboxylic acid-derived

ORMOSIL hybrid materials [12–22]. Further, hybrid thin solid films are fabricated via a spin-coating sol–gel process over the quartz substrate [15]. It is a common way to prepare aromatic carboxylic acid-grafted ORMOSIL-derived sol–gel hybrid materials, including the benzoic acid derivatives with various kinds of substituted groups, multi-carboxylic groups, etc. [16–22].

Besides, Wang et al. attempt to predict that the carboxylic groups of *p*-aminobenzoic acid (*p*-ABA, not the amino moiety) will be attacked by TESPIC in terms of intense competition between amino and carboxylic groups, which reveals that the latter is more active in the reaction than the former. NMR and IR data substantiate the structure, and they obtain totally different phosphorescence spectrum compared with the literature [23]. It is estimated that the hydrogen atom of carboxylic acid is less stable than that of amino groups, and it is acidic due to polarization by the carbonyl groups and resonance stabilization of resulting carboxylate. Subsequently, they modify *p*-ABA with functional TESPIC through the hydrogen-transfer addition between the hydroxyl group of *p*-ABA's–COOH and isocyanate. A novel luminescent hybrid material is achieved using *p*-ABA-Si derivative to coordinate to Tb^{3+} [24].

2.2.2 Photofunctional Rare Earth Hybrid Materials Based on Aromatic Carboxylic Acid-Modified Silica Through Amino Group Grafting

The direct functionalization of carboxylate groups involves a two-step reaction and the modification of carboxylate groups to amide (urea) groups, changing their coordination nature which is different from free carboxylic acids. At present, the common approaches are to modify the functional groups except for carboxylic groups, such as amino groups [25–28], hydroxyl groups [29–32], and mecapto groups [33–35], employing the similar hydrogen atom transfer addition reaction between the functional groups and TESPIC. So the strategy is to modify other groups of carboxylic acid while its carboxylic group remains to further coordinate to rare earth ions.

Wang et al. prepare the hybrid material with the linker obtained from a derivative of *meta*-aminobenzoic acid (*m*-ABA) modified by TESPIC [26]. Accordingly, the final hybrid material is formed by a combination of hydrolysis and polycondensation processes of two ethoxy groups (both *m*-ABA-Si and TEOS) (Fig. 2.5 (Left)). In addition, it is interesting to note that many large pores are dispersed on the surface of the materials, mainly through the formation of the backbone of Si–O–Si and its polycondensation (Fig. 2.5 (Right)). This may be related to the mononuclear structure of terbium complex with *m*-ABA, which is different from the chain structure of major rare earth complexes with aromatic carboxylic acid to result in the trunk morphology in their ORMOSIL-derived sol–gel hybrid materials. Similar

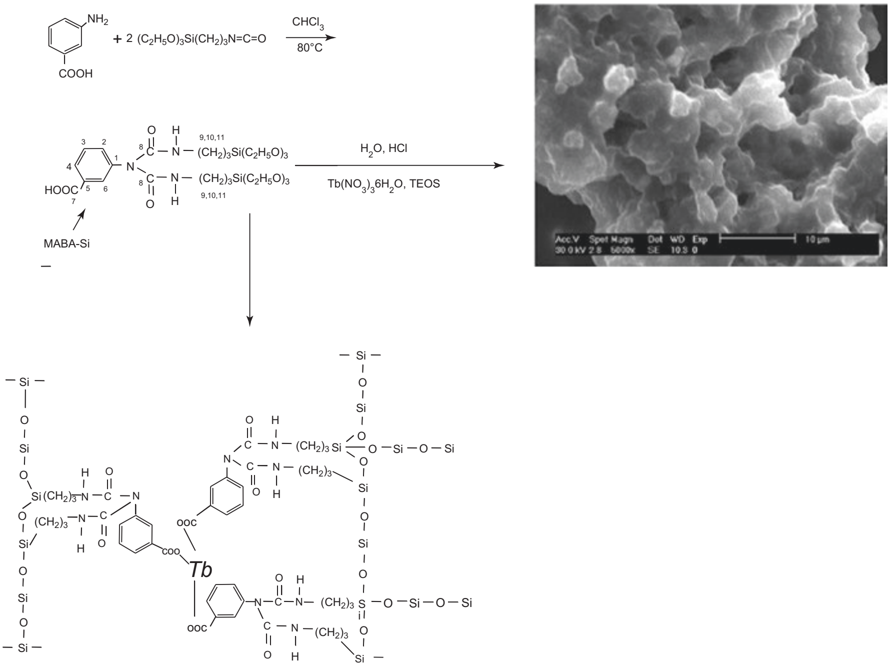

Fig. 2.5 Scheme of hydrolysis and polycondensation processes between *m*-ABA-Si and TEOS (*Left*) and the selected SEM image of the hybrid material (*Right*) (Reprinted with permission from Ref. [26]. Copyright 2012 the Royal Society of Chemistry)

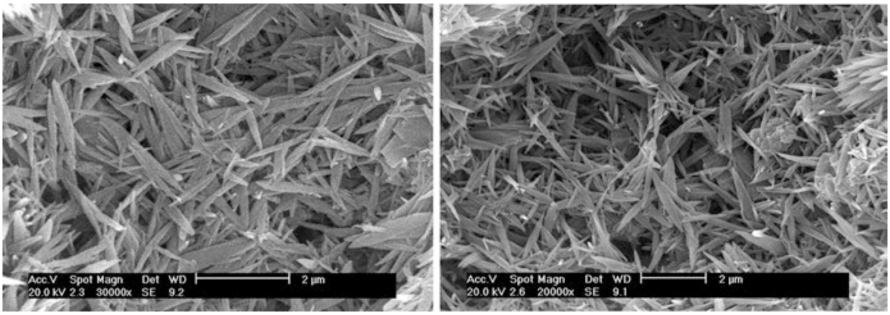

Fig. 2.6 The scanning electron micrographs of the covalently bonded hybrid microparticles: Eu–BMZC–Si (*Left*) and Tb–BMZC–Si (*Right*) (Reprinted with permission from Ref. [28]. Copyright 2009 Elsevier)

result is shown in *ortho*-aminobenzoic acid-grafted ORMOSIL hybrids [25], while it is different for *para*-aminobenzoic acid-grafted ones [23].

Besides the modification of primary amino group of above aminobenzoic acid to prepare ORMOSILs, the second amino group of aromatic carboxylic acids also can be modified with the similar hydrogen atom transfer addition reaction to obtain the covalent ORMOSIL linker [27, 28]. Lu et al. have done related work to modify the second amino group of 2-pyrrolidinone-5-carboxylic acid (PDCA) and benzimidazole-5-carboxylic acid (BMZC) using TESPIC to achieve the covalent linkage (PDCASi and BMZCSi), resulting in the corresponding RE (RE = Eu, Tb) hybrid materials [28]. Especially Eu–BMZC–Si and Tb–BMZC–Si hybrid materials show the uniform leaf-shaped morphology with around 0.1 ~ 0.2 μm dimension (Fig. 2.6). In the sol process, the o/w macro-emulsion is decisive and responsible for the materials' final texture. The texture of lamina is easy to understand because the weak interactions between the organic moieties such as van der Waals, London dispersion, or π–π staking are able to induce an organization in o/w macro-emulsion. The texture of agglomerate in BMZC–Si disappears in Tb(Eu)–BMZC–Si, and the particle size becomes smaller (0.1 ~ 0.2 μm for BMZC–Si hybrids) and more uniform. It may be owed to the coordination between organic groups and rare earth ions, which makes it difficult to form a large organization. It is worth pointing out that the self-assembly phenomenon still exists in the noncrystalline hybrid system through chemical bonds.

2.2.3 Photofunctional Rare Earth Hybrid Materials Based on Aromatic Carboxylic Acid-Modified Silica Through Hydroxyl Group Grafting

Similar to amino groups, the hydroxyl groups also can be modified by the TESPIC through the addition reaction between them, resulting in the hydroxyl aromatic acid-grafted ORMOSIL-derived hybrid silica materials [29–32]. For instance, covalently bonded silica/TESPIC-grafted salicylic acid (SAL) hybrids are prepared from TESPIC-grafted salicylic acid and central metal ions (Tb, Zn) (Fig. 2.7) [29]. The path can be extended to other hydroxyl substituted benzoic acid derivative-grafted ORMOSILs (such as ethyl-*p*-hydroxybenzoate derivatives) modified by TESPIC [30]. Certainly, it is suitable for other kinds of carboxylic acid derivatives with pyridine cycle, such as hydroxynicotinic acid. They can be modified by TESPIC to prepare their corresponding hybrid materials with covalent bonds [31, 32].

2.2.4 Photofunctional Rare Earth Hybrid Materials Based on Aromatic Carboxylic Acid-Modified Silica Through Mercapto Group Grafting

The hydrogen atom transfer addition reaction also can be applied to TESPIC-modified mercapto carboxylic acid to design special ORMOSILS [33–35]. For example, a series of hybrid materials containing photoactive rare earth ions (Eu^{3+}, Tb^{3+}, Sm^{3+}, and Dy^{3+}) have been assembled by the sol–gel process, with the organic

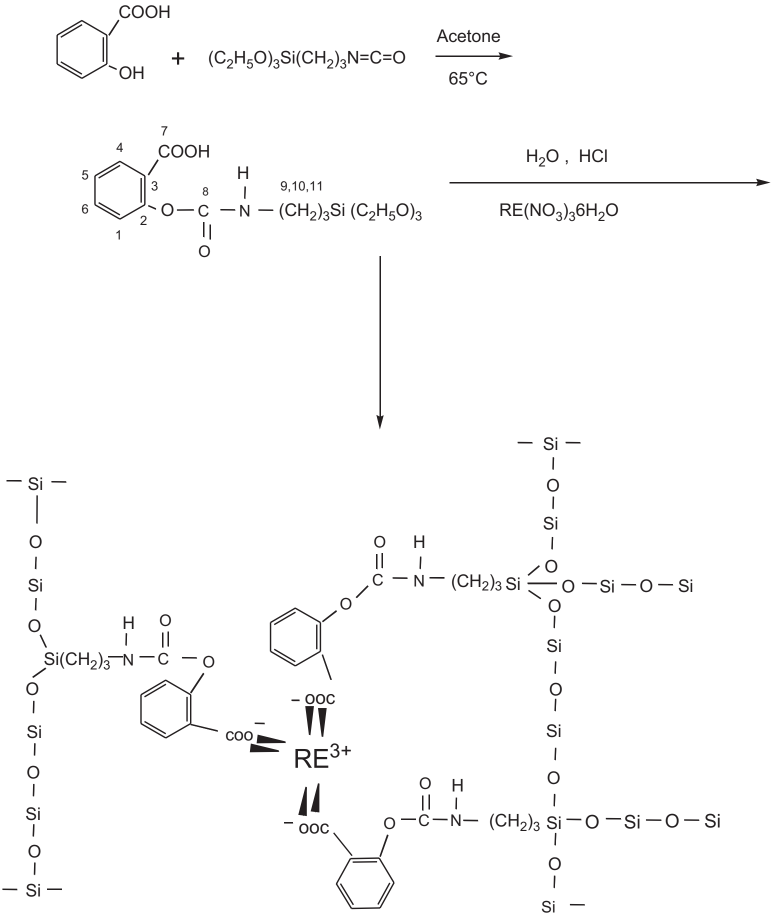

Fig. 2.7 Scheme of the synthesis process of Sal–Si and predicted structure of hybrid materials (Reprinted with permission from Ref. [29]. Copyright 2006 Elsevier B.V)

parts of thiosalicylic acid covalently linked to the inorganic part via sulfide linkage (Fig. 2.8). The organic parts as molecular bridges are obtained from the functionalized thiosalicylic acid (2-mercaptobenzoic acid) by five silane cross-linking reagents, 3-chloropropyltrimethoxysilane, 3-methacryloyloxypropyltrimethoxysilane, (3-aminopropyl)trimethoxysilane, 3-glycidoxypropyltrimethoxysilane, and 3-(triethoxysilyl)propylisocyanate, respectively [33]. The corresponding luminescent spectra obtained from these rare earth hybrids further demonstrate the prediction from the perspective of energy match. Both Tb^{3+} and Eu^{3+} hybrid materials show the effective emission, and Tb^{3+} hybrids possess the higher emission intensity than Eu^{3+} ones. Similarly, the postsynthesis path can be applied to heterocyclic pyridine carboxylic acid with mercapto group [34, 35].

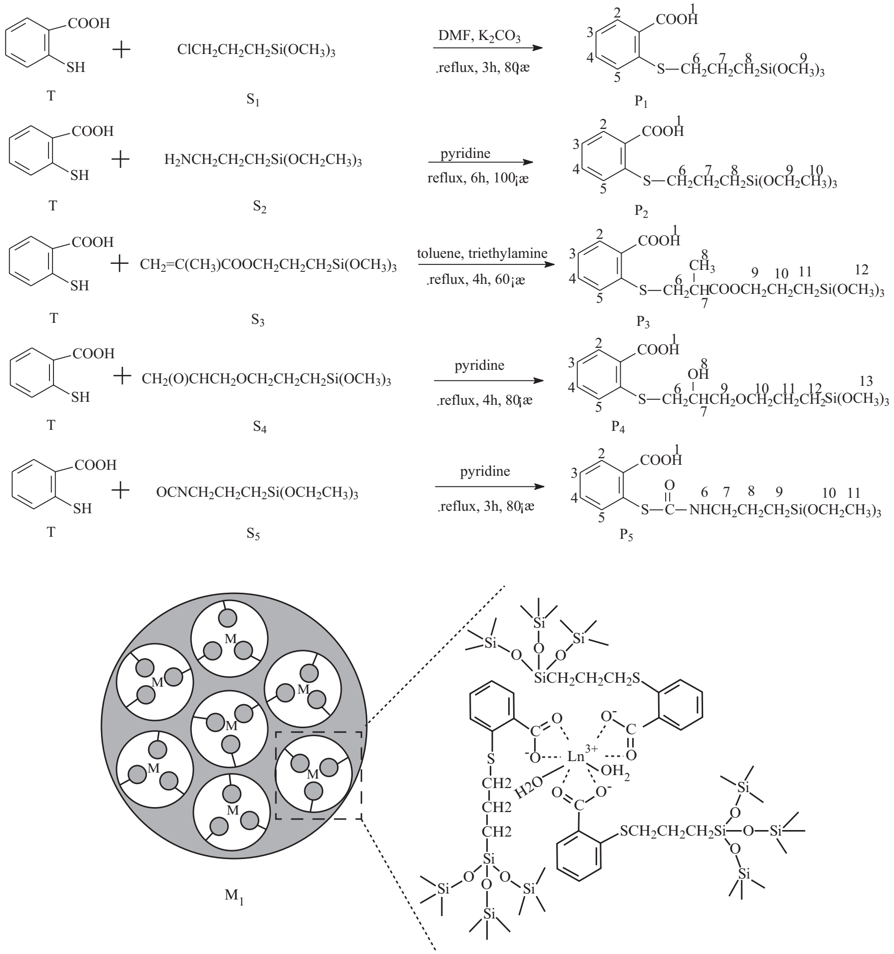

Fig. 2.8 Scheme for synthesis of five precursors on the modification of thiosalicylic acid (*Top*) and for the predicted structure of the hybrid materials (*Bottom*) (Reprinted with permission from Ref. [33]. Copyright 2009 American Chemical Society)

Some typical modification paths for covalent linkers (ORMOSILs) and hybrid materials are introduced above. In fact, aromatic carboxylic acids have abundant substituted groups for modification to design special linkage and assemble the hybrid systems. For example, sulfonamide linkages are selected for linking inorganic and organic parts, since these linkers are stable under acidic and basic conditions and can be converted to sulfonic chlorides [36, 37]. A novel sulfonamide linkage has been constructed, based on the modification of 5-sulfosalicylic acid (SSA) with 3-aminopropylmethyldiethoxysilane (APEMS) or APES, because sulfosalicylic acid has a reactive functionalized sulfo group and an excellent photoactive unit (Fig. 2.9). The above modification path can be used for the modification of

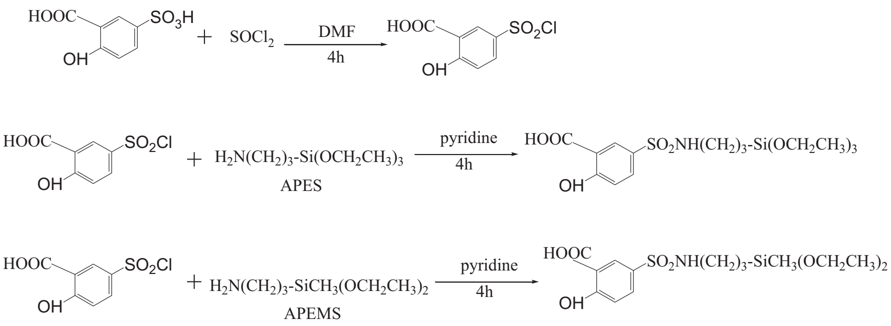

Fig. 2.9 Schemes for synthesis of sulfonamide-derived ORMOSILs. (Reprint with permission from [37]. Copyright 2010 Elsevier)

many kinds of typical ligands for coordination to rare earth ions and further construction of the corresponding hybrid materials [37].

2.3 Photofunctional Rare Earth Hybrid Materials Based on β-Diketone and Its Anaologue Derivative-Modified Silica

β-Diketonate ligands are the most important sensitizers for luminescent rare earth ions, especially for Eu^{3+}, through effective intramolecular energy transfer in their complexes. The property of compounds containing double carbonyl groups mainly depends on the relative position of the two functional groups. The methylene group in middle of the β-diketone ligand shows the stronger acidity than common carbonyl compounds (aldehyde or ketone) because of the influence of the oxygen atoms from double carbonyl groups, which attract electrons. So the methylene group is reactive enough to be easily modified.

2.3.1 Photofunctional Rare Earth Hybrid Materials Based on β-Diketone-Modified Silica

Yan’s group select a partly acidic β-diketonate and consider that its α-hydrogen (the hydrogen atom in the methylene) can be extracted by a base because of the polarization of C–H bonds by the adjacent carbonyl groups. Besides, they perform the modification of one hydrogen atom in the methylene group, which is to decrease the steric hindrance effect of the large silylated groups and to maintain the unsymmetrical structure to obtain effective photoactivity.

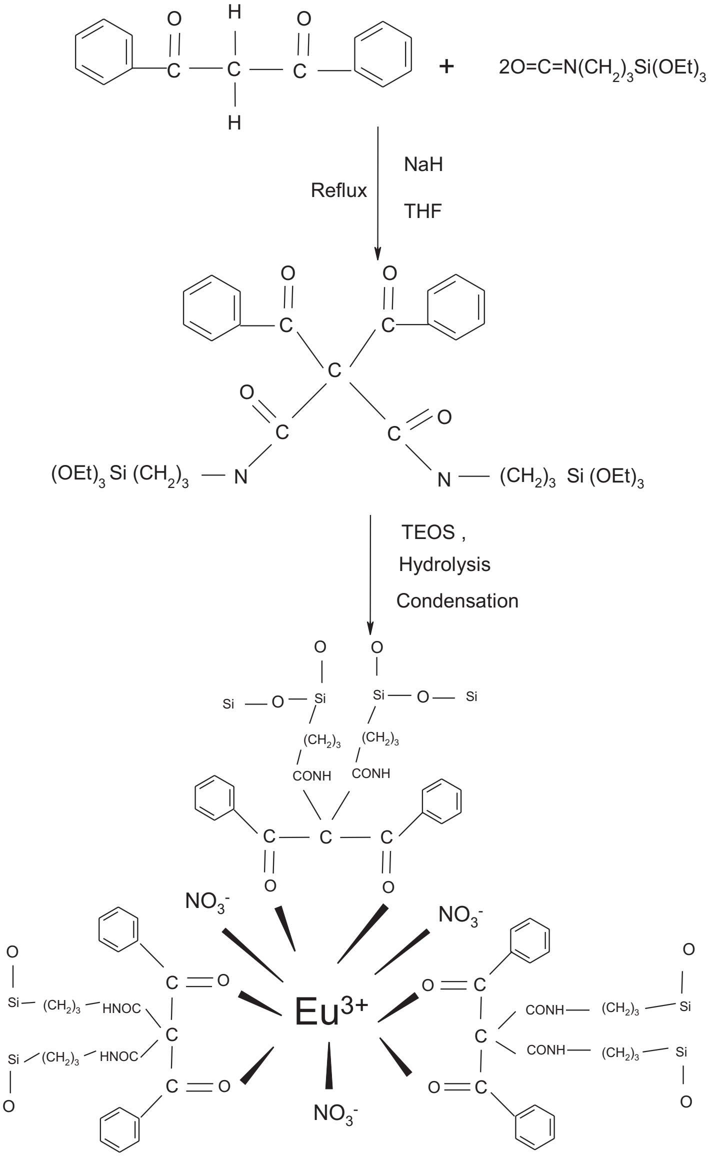

Fig. 2.10 The scheme for predicted structure of europium hybrids through DBM-modified ORMOSILs (Reprinted with permission from Ref. [38]. Copyright 2008 American Chemical Society)

Wang et al. first select dibenzoylmethane (DBM) to modify with the coupling reagent TESPIC, and the as-derived monomers are introduced into inorganic network through covalent bonds (Fig. 2.10) [38]. Subsequently, novel chemically bonded hybrid materials, such as Eu(III)-modified dibenzoylmethane with silica hosts, are prepared and characterized. It is noted that the covalently bonded silicate hybrid material exhibits a stronger red/orange intensity ratio, longer lifetime, and higher quantum efficiency than europium complex of DBM, suggesting that the silica network is suitable for the emissions of covalently bonded hybrids. For the sake of further optimizing the light output and investigating chemical reactivity of carbanions, DBM is considered as partly acidic, and its alpha-hydrogen (the hydrogen atom in the methylene) can be extracted by base because of the polarization of C–H bonds by the adjacent carbonyl groups. The above path is effective to modify all β-diketone ligands to chemical linker ORMOSILs in the preparation of rare earth hybrid materials based on their β-diketonates [39]. Wang et al. obtain the luminescent organosilica microcrystals with rectangular-plate morphology using TTASi with lanthanide ions under reflux without any structure-directing agent [40]. Chen et al. synthesize a TTA-functionalized polyhedral oligomeric silsesquioxane (POSS) [41], which is a viscous liquid at room temperature. Complexation of POSS–TTA with Eu^{3+} ions results in a red-emitting hybrid liquid material, showing significantly improved thermal stability compared with $[Eu(TTA)_3]\cdot 2H_2O$. The long lifetime and high color purity, together with good thermal stability and processability, make it highly promising for use in next-generation organic devices such as flexible displays.

Guo et al. prepare a series of colorless and transparent sol–gel-derived hybrid materials Ln–DBM-Si covalently grafted with $RE(DBM\text{-}OH)_3\cdot 2H_2O$ (where DBM-OH = *o*-hydroxydibenzoylmethane, RE = Eu, Nd, Er, Yb, and Sm) through the primary *β*-diketone ligand DBM-OH [42, 43]. Different from the above modification path of methylene, they modify the hydroxyl group of DBM-OH with TESPIC to achieve the linker DBM-Si. The resultant materials display visible (for Eu) and NIR luminescence (for Nd, Er, Yb, and Sm), respectively. Furthermore, the radiative properties of the Nd^{3+} ion and the Er^{3+} ion in Ln–DBM-Si are evaluated by applying the Judd–Ofelt analysis. The perfect emission band at 1330 nm for Nd–DBM-Si and the broad emission band at 1535 nm for Er–DBM-Si provide the opportunities to develop new materials suitable for optical amplifiers operating at 1.3 and 1.5 μm, the two telecommunication windows. The highly intense emission band at 1060 nm for Nd–DBM-Si offers the possible application in laser systems. Yb–DBM-Si with a strong emission band at 980 nm may be a promising probe for fluoroimmuno-assays and in vivo applications. Especially the Sm–DBM-Si hybrids show three Sm^{3+} excited states, ${}^4G_{7/2}$ (∼20,050 cm^{-1}), ${}^4F_{3/2}$ (∼18,700 cm^{-1}), and ${}^4G_{5/2}$ (∼17,700 cm^{-1}), that can receive energy from the lowest triplet state of the ligand (∼20,325 cm^{-1}), resulting in some emission bands in the NIR region. Intense emission is only observed at the ${}^4G_{5/2}$ level. The reason for this is the close proximity of these three excited states to each other, which causes electrons from the higher states to rapidly relax non-radiatively to the ${}^4G_{5/2}$ level, from which radiative transitions occur. Further, Sun et al. prepare ternary rare earth β-diketonate derivatives covalently bonded to xerogels (Ln-DP xerogel, RE = Sm, Yb, Nd, Er, Pr, Ho) by the above DBM-Si linker [44]. After excitation with visible light (400−410 nm), the xerogels all show characteristic visible (Sm^{3+}) as well as near-infrared (NIR; Sm^{3+}, Yb^{3+}, Nd^{3+}, Er^{3+}, Pr^{3+}, Ho^{3+}) luminescence. It is interesting to observe the NIR

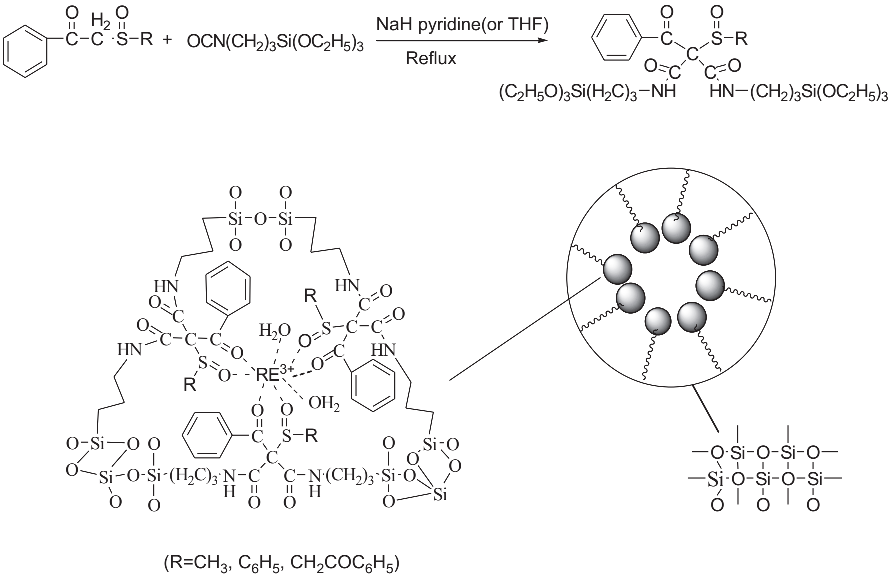

Fig. 2.11 Scheme of synthesis process of the functional sulfoxide molecular bridges and the predicted structure of the hybrid material (Reprinted with permission from Ref. [46]. Copyright 2011 the Royal Society of Chemistry)

luminescence with visible light excitation from xerogels covalently bonded with the Sm^{3+}, Pr^{3+}, and Ho^{3+} derivatives.

Wang et al. prepare hybrid materials with a Eu(III) complex $[(C_2H_5)_4N][Eu(DBM)_3(DBM\text{-}OH)]$ covalently bonded into vinyl-modified silica networks via the similar path to modify the DBM-OH to DBM-Si [45]. The luminescence quantum efficiencies of VTES/TEOS hybrid materials are greatly improved. And it is interesting to find that the luminescent intensity of VTES/TEOS hybrid material is enhanced by optimizing the molar ratio of VTES to TEOS (VTES/TEOS = 4:6) by 3.3 and 2.4 times compared with TEOS-derived hybrid material and pure $[(C_2H_5)_4N][Eu(DBM)_4]$, respectively.

2.3.2 Photofunctional Rare Earth Hybrid Materials Based on Sulfonamide Derivative-Modified Silica

The previous modification path of β-diketonate can also be extended to rare earth hybrids with sulfoxide-derived linkages (ORMOSILs), which have flexibilities and structures similar to those of β-diketonate linkages. Guo et al. prepare three sulfoxide functional bridging molecules (MSAPSi, PPSSi, and BBMSSi) by modification of the methylene groups in sulfoxide ligands (2-(methylsulfinyl) acetophenone(MSAP), phenylphenacylsulfoxide(PPS), and bis(benzoylmethyl)sulfoxide(BBMS)) with

TESPIC, which are used as the ligands of rare earth ions and also as siloxane network precursors (Fig. 2.11) [46]. The triplet state energy of the precursors with different sulfoxide is similar, and the efficiency of the energy transfer for all the hybrids of both series is similar as well, with respect to the value of the quantum efficiency. Subsequently, the distinction of the luminescent intensity for the hybrids with different sulfoxide precursors is not apparent.

2.3.3 Photofunctional Rare Earth Hybrid Materials Based on β-Diketone Analogue-Modified Silica

Lu et al. design a novel molecular precursor (TAM-Si) derived from thioacetamide (TAM) modified by TESPIC though the hydrogen-transfer addition reaction and prepare the covalently bonded RE^{3+} (RE = Eu, Tb) hybrid materials (RE–TAM-Si) [47]. At the same time, the hybrid material of TAM-Si without introduction of RE^{3+} has been obtained as well. The blue emission for TAM-Si hybrids and the narrow-width green and red emissions are achieved for Tb^{3+} and Eu^{3+} ions, respectively. The SEM images of TAM-Si hybrid material and Eu–TAM-Si hybrid material can give some evidence by showing the textures. For TAM-Si hybrids without RE^{3+} ions, in the sol process, the o/w macro-emulsion is decisive and responsible for the final texture of hybrids. It is easy to understand that the isolated sphere is caused by the weak interactions between the organic moieties. The bi-sphere particle may be due to the pervasion between two spheres. The microsphere is in 2–5 μm dimension. The micromorphology of Eu–TAM-Si with europium ions introduced seems to be largely different from TAM-Si, whose particle sizes are in the 50–100 nm dimensions, although they are prepared by the same process. The strong chelation effect between organic groups and rare earth ions makes it difficult to form an organization under the weak interactions.

2.3.4 Photofunctional Rare Earth Hybrid Materials Based on 1,3-Bis(2-Formylphenoxy)-2-Propanol-Modified Silica

Liu et al. synthesize 1,3-bis(2-formylphenoxy)-2-propanol (BFPP) and then graft it to TESPIC to achieve a molecular precursor BFPP-Si through the hydrogen-transfer nucleophilic addition reaction. Then, a chemically bonded binary rare earth hybrids (BFPP-Si-RE) and ternary hybrids (BFPP-Si-bpy-RE and BFPP-Si-phen-RE) are constructed using BFPP-Si as a chemical linker [48]. The ternary rare earth hybrids present stronger luminescent intensities, longer lifetimes, and higher luminescence quantum efficiencies than the binary hybrids, indicating that the introduction of the second ligands can sensitize the luminescence emission of the rare earth ions in the ternary hybrid systems. The quantum efficiencies of the three kinds of europium hybrid materials can be determined in the order: BFPP-Si-bpy-Eu > BFPP-Si-phen-Eu > BFPP-Si-Eu.

2.4 Photofunctional Rare Earth Hybrid Materials Based on Macrocyclic Compound-Modified Silica

Macrocyclic compounds are the typical ligands for rare earth ions, whose unique molecular structure endows them with functional properties for the application in recognition, sensing, separation, etc. So it may have practical value to further functionalize these ligands to ORMOSILs to construct their rare earth hybrid materials. Yan's group has tried the functionalization of some typical macrocyclic derivatives (calixarene, crown ether, porphyrin, and Schiff base) to prepare the ORMOSILs as a linkage and construct the corresponding hybrid materials.

2.4.1 Photofunctional Rare Earth Hybrid Materials Based on Calixarene Derivative-Modified Silica

Due to the attractive cavity in calixarene skeletons, the phenolic groups at the lower rim of the cup in calix[4]arene can be modified with TESPIC. Wang and Lu et al. have found that the hydroxyl groups of the macrocyclic compound *p-tert*-butylcalix[4]arene can be converted into urethanesil (−NH(C = O)O–)-grafted bridges, so Yan et al. modify the calixarene derivatives using TESPIC in molar ratios of 1:3 and 1:1 and find the reaction with 1:1 molar ratio is easier to control using these molar ratios than it is with other molar ratios (Fig. 2.12 (Top)) [49, 50]. Three luminescent colors are checked, blue (BC [4]Si and C [4]Si), green (Tb-BC [4]Si and Tb-C [4]Si), and red (Eu-BC [4]Si and Eu-C [4]Si), respectively, suggesting that the intramolecular energy transfer process takes place within these molecular-based hybrids. Quite few spheroids (with a diameter of approximately 2–3 μm) emerge in the fracture surface, and they predict that both the coupling agent TESPIC and the cuplike macrocyclic calix[4]arene trigger the formation of such attractive morphology (Fig. 2.12 (Bottom)). Tb-BC [4]-Si shows some large sphere-like micromorphology with a dimension of 3–5 micrometer.

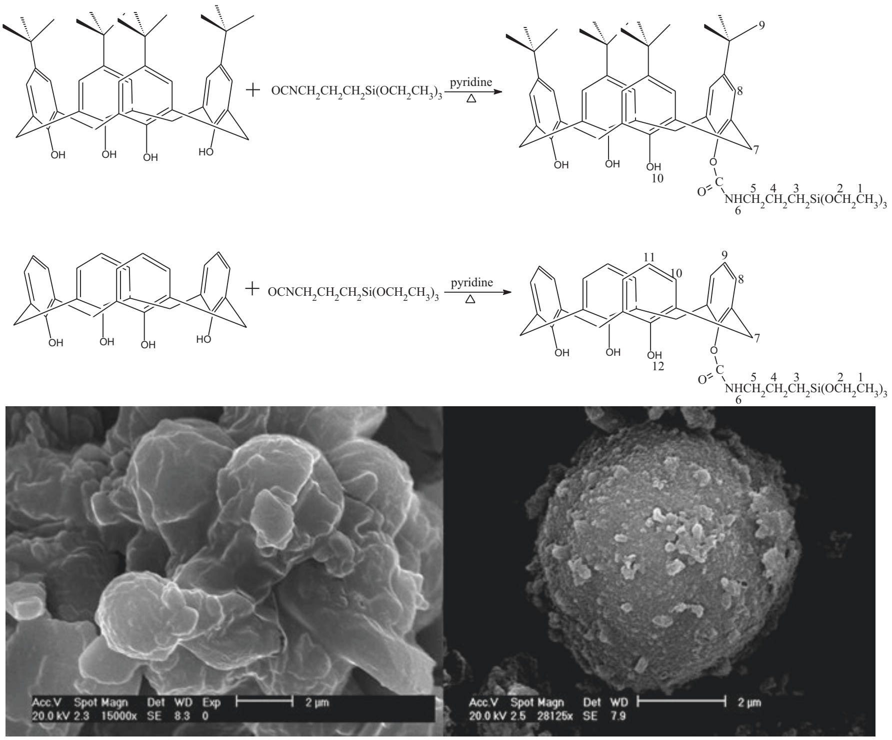

Fig. 2.12 (*Top*) Typical preparation procedures of calix[4]arene-derived ORMOSILs. (*Bottom*) SEM images for Tb covalently bonded hybrids: Tb-Cal-Si (*left*) and Tb-BC[4]-Si (*right*) (Reprinted with permission from [49, 50]. Copyright 2009 American Chemical Society)

2.4.2 Photofunctional Rare Earth Hybrid Materials Based on Crown Derivative-Modified Silica

Liu et al. synthesize a series of hybrid materials (CE-15-Si-Ln, CE-16-Si-Ln, CE-18-Si-Ln) containing a novel aza-crown ether organic component (Fig. 2.13 (Left)) [51]. The hybrids show red emission (Eu), green emission (Tb), and near-infrared (NIR) luminescence (Nd). Three functional molecular precursors (denoted as CE-15-Si, CE-16-Si, and CE-18-Si) are synthesized with two or three N-substituted pendant arms containing chelating groups. The quantum efficiencies of the europium hybrid materials can be determined in the order CE-15-Si-Eu < CE-16-Si-Eu < CE-18-Si-Eu < CE-15-Si-phen-Eu < CE-16-Si-phen-Eu < CE-18-Si-phen-Eu. The quantum efficiencies of CE-18-Si-phen-Eu, CE-16-Si-phen-Eu, and CE-15-Si-phen-Eu are much higher than those of CE-18-Si-Eu, CE-16-Si-Eu, and CE-15-Si-Eu. The select micrographs for the CE-18-Si-Eu (B) and CE-18-Si-Tb (D) hybrid materials (Fig. 2.13 (Right)) show a more spiral chainlike morphology which looks like the cobweb network. The quite uniform

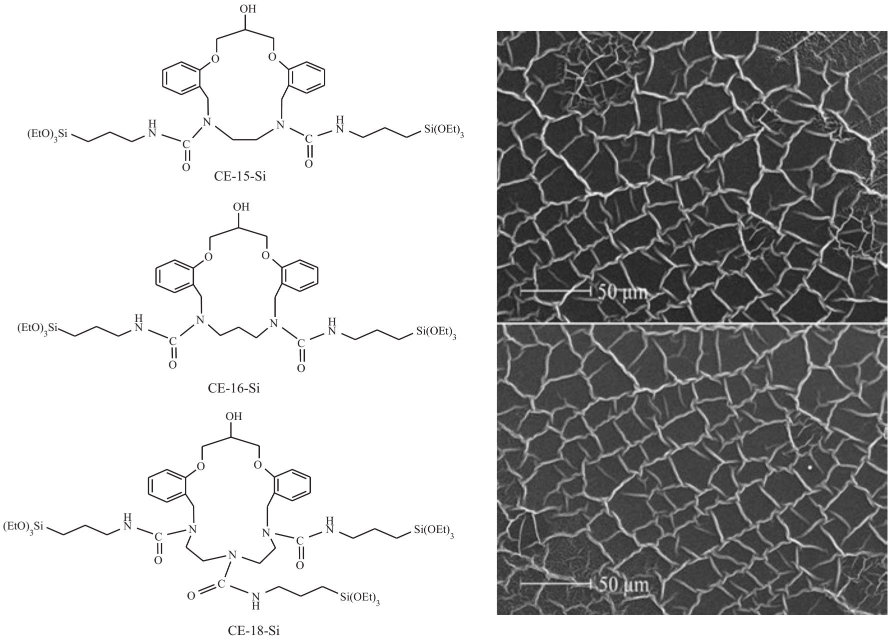

Fig. 2.13 Chemical structure of the silylated precursors containing aza-crown ether rings CE-15-Si, CE-16-Si, and CE-18-Si (*Left*) and selected SEM images of hybrid materials CE-16-Si-Eu (*Top*) and CE-16-Si-Tb (*Bottom*) (*Right*) (Reprinted with permission from Ref. [51]. Copyright 2011 the Royal Society of Chemistry)

frameworks on the surface of these hybrid materials suggest that a self-assembly process might occur during the polymerization reaction. It benefits from the functional bridge silylated precursors which covalently bond the crown ethers' organic constituent into the inorganic Si–O–Si networks. The different microstructures of these samples may be due to the enlarged extent of polycondensation reaction in CE-18-Si-Ln system. Compared with CE-15-Si-RE and CE-16-Si-RE, CE-18-Si-RE system has a larger 18-atom ring and 3 N-substituted pendant arms containing ethoxy silica groups which may readily provide enlarged extent of polycondensation. However, in this study, exchanging the RE^{3+} ion and the addition of the second ligands seem to have little influence on the microstructure.

2.4.3 Photofunctional Rare Earth Hybrid Materials Based on Porphyrin Derivative-Modified Silica

Guo et al. modify the organic macrocycle 5, 10, 15, 20-tetra-(p-hydroxy)phenylporphyrin (THPP) to ORMOSILs through a hydrogen-transfer reaction between OH group of free porphyrin and the organosilane TESPIC and further prepare the covalently bonded NIR luminescent RE-THPP-Si (RE = Nd, Yb) hybrid materials [52]. The entrapment of metalloporphyrins (with Zn^{2+} and Yb^{3+}) in silica microspheres is further achieved by modification of protoporphyrin IX (Pp-IX) molecules with three different organosilane precursors via the sol–gel method [53]. The results reveal that the obtained porphyrin networks are covalently bonded to the inorganic matrix through the bridging action of the functionalized silica microspheres. Furthermore, it has also been observed that porphyrin molecules located in different environments exhibit different photophysical properties in the visible and near-infrared regions.

2.4.4 Photofunctional Rare Earth Hybrid Materials Based on Schiff-Base Derivative Compound-Modified Silica

Liu et al. synthesize three kinds of Schiff-base compounds (denoted as *o*-BASB, *p*-BASB, and *m*-BASB) containing a hydroxyl group and a carboxyl group and prepare the molecular precursor (*o*-BASB-Si, *p*-BASB-Si, and *m*-BASB-Si), and rare earth ions (Eu^{3+} and Tb^{3+}) are coordinated through the carboxyl groups (Fig. 2.14). A series of chemically bonded hybrid materials (*o*-BASB-Si-RE-phen, *o*-BASB-Si-RE-bpy, *p*-BASB-Si-RE-phen, *p*-BASB-Si-RE-bpy, *m*-BASB-Si-RE-phen, and *m*-BASB-Si-RE-bpy, RE = Eu or Tb) are thus constructed [54]. The addition of the second ligand of phen and bpy makes these hybrids present stronger luminescent intensities and higher emission quantum efficiency, especially after the addition of phen. The quantum efficiencies of *p*-BASBSi-Eu-phen (30.7%), *o*-BASB-Si-Eu-phen (27.1%), and *m*-BASB-Si-Eu-phen (23.4%) are much higher than those of *p*-BASB-Si-Eu-bpy (10.0%), *o*-BASB-Si-Eu-bpy (6.9%), and *m*-BASB-Si-Eu-bpy (6.1%). Uniform microstructures of these hybrids are also obtained where the organic and the inorganic compounds are covalently linked through Si–O bonds through a self-assembly process.

2.5 Photofunctional Rare Earth Hybrid Materials Based on Heterocyclic Compound-Modified Silica

Using abovementioned typical ligands (aromatic carboxylic acids, β-diketones, and macrocyclic compounds) of rare earth ions to synthesize the ORMOSIL linkages and their sol–gel hybrid materials, we can obtain abundant modification strategies and paths. In fact, there are still a great number of photoactive organic ligands to be developed, which can be utilized to design special linkages and construct hybrid systems. Here we only give some common examples.

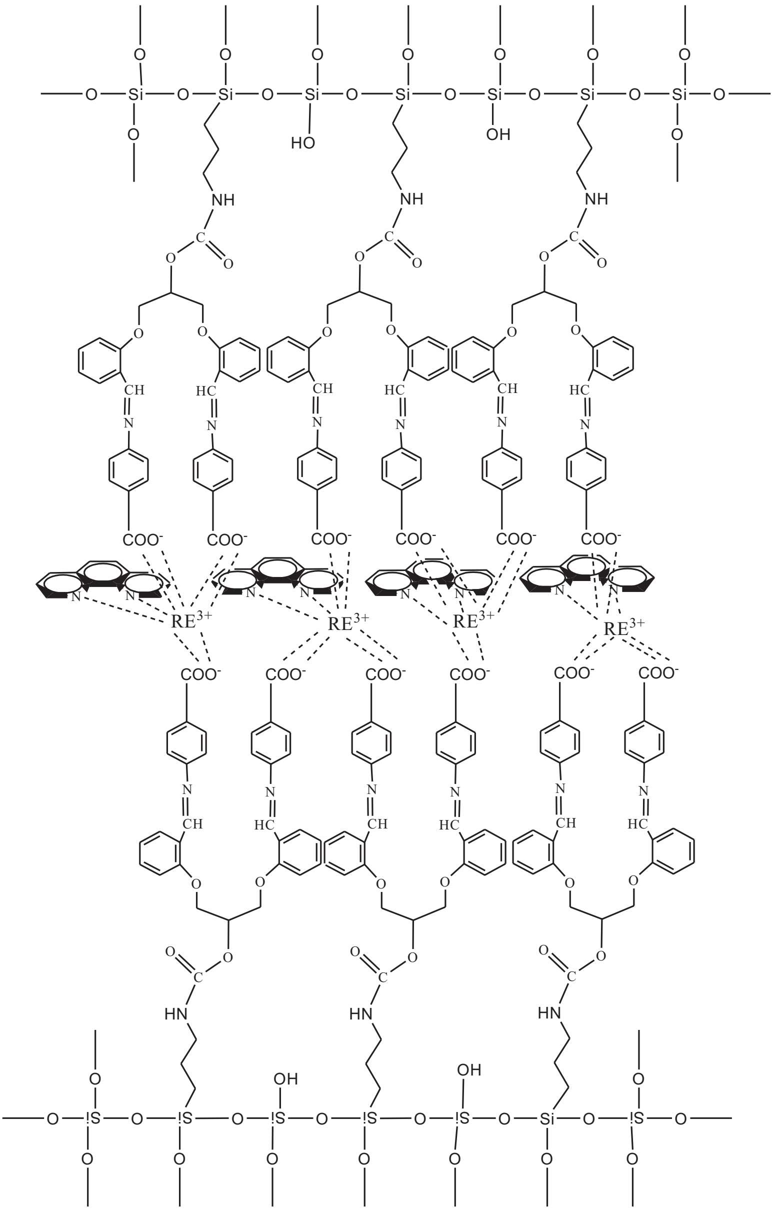

Fig. 2.14 The predicted structure of the ternary hybrids *p*-BASB-Si-Ln-phen

2.5.1 Photofunctional Rare Earth Hybrid Materials Based on Bipyridine Derivative-Modified Silica

Li et al. have done a lot of works on hybrid materials containing ORMOSILs derived from pyridine derivatives (such as phen or bpy) [55–60]. The pyridine derivatives are modified using two paths. One is oxidation to the corresponding pyridylcarboxylic acid derivatives, followed by modification of the carboxylic groups to acyl chloride derivative and then amide condensation reaction with TESPIC. The ORMOSIL bpy-Si is to construct rare earth (Eu^{3+}, Tb^{3+}) hybrid materials through coordination between RE^{3+} and the nitrogen atoms of the pyridine rings [55]. Recently, they report a ternary europium monophase hybrid system with a bis-silylated bpy ligand derived from 4,4′-diamino-2,2′-bpyridine and three TTA ligands, which has a much longer lifetime than that of the pure Eu complex of TTA [56]. A transparent and luminescent ionogel monolith is prepared by hydrolysis and condensation of the silylated bpyridine; it can sensitize the luminescence of Eu^{3+} in the presence of a carboxyl-functionalized ionic liquid in which Eu^{3+} is coordinated to the oxygen atoms of carboxylate groups from the ionic liquid. Graffion et al. report the sol–gel fabrication of bridged silsesquioxane thin films containing trivalent RE^{3+} from a 4,4′-diureido-2,2′-bipyridine bridged organosilane in the presence of Eu^{3+} or Tb^{3+} salts [57]. Crack- and defect-free thin films (~50 nm) of optical quality are deposited on glass substrates by spin coating after optimizing the spinning rate and solvent system. Ellipsometry investigations reveal a significant decrease in the refractive index of the films with aging of the corresponding precursor sols. In contrast, the photoluminescence properties of the films are independent of precursor aging time, although significant differences are observed with respect to the corresponding bulk materials. Compared to the bulk materials, the films exhibit a significant blue shift of the excitation spectra and an increase of the excited state lifetime. The optical conversion efficiencies of some collectors are also determined and potential applications of the coatings in such areas as luminescent solar concentrators are discussed.

The other path consists of modifying the amino-derived phen molecule with TESPIC through an addition reaction. The hybrid materials are assembled after coordination between the nitrogen atoms of the ORMOSILs and RE^{3+} by a sol–gel process [58]. The hybrid materials can be prepared as thin films by dip coating. In addition, because of their strong nucleophilic abilities, the two amino groups of 2,6-diaminopyridine are modified by TESPIC, and the two derived carbonyl groups and the pyridine nitrogen atom provide three coordination locations for lanthanide ions.

Lenaerts et al. synthesize 1,10-phenanthroline-5,6-dione from oxidation of phen and then transform it into the imidazo[4,5-*f*]-1,10-phenanthroline substituted in the two-position by a 4-hydroxyphenyl group. After modification of the phen derivative with an excess TESPIC to a hydrolyzable ORMOSIL containing the imidazo[4,5-*f*]-1,10-phenanthroline moiety, ternary rare earth hybrid materials are prepared with the ORMOSILs and homogeneous distribution of luminescent RE^{3+} TTA complexes

(RE = Pr, Nd, Sm, Eu, Dy, Ho, Er, Tm, Yb) [59]. The corresponding thin films of the silica hybrid material are prepared by the sol–gel method and by spin coating of the gelating solution on glass slides or on oxidized silicon wafers. The luminescence quantum yields of Eu^{3+}-doped thin films exposed to different drying conditions are determined by using an integrating sphere.

Similar to the modification path of phen-Si, Bo et al. design a new ORMOSIL based on the modification 4′-*p*-aminophenyl-2,2′:6′,2″-terpyridine by TESPIC and prepared the rare earth (Er^{3+}, Eu^{3+}, and Tb^{3+}) hybrid materials [60]. For the hybrid Er and hybrid Eu, excitation at the ligand absorption wavelength results in the typical near-IR luminescence (centered at around 1.54 mm) due to the $^4I_{13/2}$–$^4I_{15/2}$ transition of Er^{3+} ions and strong visible region emission of the Eu^{3+} ions ($^5D_0$–^7F_J), which contributes to the efficient energy transfer from terpy to the two ions. Different from Bo's work, Tong et al. synthesize a new monomer-based terpy derivative by the thiol–ene photopolymerization between γ-mercaptopropyltrimethoxysilane and 4′-allyloxy-2,2′:6′,2″-terpyridine [61]. The rare earth hybrid materials exhibit strong red Eu^{3+} and green Tb^{3+} emission due to efficient energy transfer from the ligands to RE^{3+} ions.

2.5.2 Photofunctional Rare Earth Hybrid Materials Based on Amino Compound-Modified Silica

Yan's group first focus on amino aromatic carboxylic acid ligands [28–31] and then extend their work to other amino compounds such as amino acridines, aminopyridines, 2,2′-dipyridylamine, and 2-amino-5-phenylthiazole [62–66]. Guo et al. select a special ligand, 2-amino-5(4)-phenylthiazole, which has reactive hydrogen atoms and can be expected to realize hydrogen-transfer reactions with the silane cross-linking reagent TESPIC. The obtained silylated linkages (ORMOSILs) can be used as siloxane network precursors to construct rare earth hybrids [62]. SEM proves that all of these hybrid materials exhibit homogeneous microstructures, suggesting the occurrence of self-assembly of the inorganic network and organic chain. In addition, the different functional molecular bridges have little influence on the microstructure and the photoluminescence properties such as luminescent lifetimes and quantum efficiencies.

2.5.3 Photofunctional Rare Earth Hybrid Materials Based on Hydroxyl Compound-Modified Silica

The modification of hydroxyl groups of some ligands to synthesize ORMOSILs has been proved to be an effective approach to assemble rare earth hybrid materials, which involves hydroxyl carboxylic acid, hydroxyl β-diketone (DBM-OH), and calixarene with multi-hydroxyls. In fact, it can be adapted to all kinds of hydroxyl compounds. Even for some ligands without apparent coordination ability, they can be modified to embody the carbonyl group to be coordinated with rare earth ions, such as phenol or its derivative, hydroxypyridine, hydroxyquinoline, and tifferron (4, 5-dihydroxy-1,3-benzenedisulfonic acid disodium salt, TF) [67–72].

Qian et al. modify tifferron (TF) by TESPIC to afford a novel functional bridge intermediate (named as TFSi), which is used to coordinate to terbium or zinc ions and further introduced into silica matrixes [70]. Uniform spherical particles can be observed on the surface of the hybrid material, mainly through the formation of the backbone of Si–O–Si and its polycondensation. The microsphere of Tb-TF-Si is located in around 0.5 μm dimension. The micromorphology of Zn-TF-Si seems to be different from Tb-TF-Si, whose particle sizes are in the 2.0 micrometer dimension, although they are prepared by the same process. Because of the different chelation effects between organic groups and Tb^{3+} or Zn^{2+} ions, the configurations of the organosilane are mixed up, and it is difficult to form an organization under the weak interactions such as π–π staking. Tb(Zn)-TF-Si shows the same sphere microstructure with the similar particle size to Zn-TF-Si, suggesting the Zn ions play an important role in the formation of microstructure of Si–O in the sol–gel process. As we know, Tb^{3+} possesses the higher coordination number (8 or 9) than Zn^{2+} (4 or 6), so the chelated ability of Tb^{3+} to TF-Si is stronger than that of Zn^{2+} to TF-Si and can have greater influence on the control of the microstructure of hybrids. Subsequently, the coordination effect intervenes with the normal sol–gel process and limits growth rate and particle size, and especially the Tb-TF-Si presents the smaller particle size. The interpretation has been verified by SEM patterns. Green emission of Tb^{3+} hybrids and violet–blue luminescence of Zn^{2+} hybrids have been achieved by the molecular-based hybrid materials. Besides, both Tb^{3+} and Zn^{2+} are introduced into the same hybrid systems through covalent Si–O bond, whose sphere particle size can be modified. Especially the photoluminescence can be enhanced, suggesting that intramolecular energy transfer takes place between inert Zn^{2+} and Tb^{3+} within the chemically bonded hybrid systems.

2.5.4 Photofunctional Rare Earth Hybrid Materials Based on Mercapto Compounds (3-alkyl-4-amino-5-ylsulfanyl-1,2,4-triazole)-Modified Silica

Liu et al. synthesize a series of hybrid materials in which the triazole heterocyclic organic components are grafted into the silica backbone via covalent bonds through a sol–gel process (Fig. 2.15) [73, 74]. The organic part 3-alkyl-4-amino-5-ylsulfanyl-1,2,4-triazole (O1 and O2) is first prepared by the reaction of thiocarbohydrazide with acetic acid or propionic acid, respectively, and then is functionalized with trialkoxysilyl groups, and the as-obtained silylated monomers (P1–P4) are used as the siloxane network precursors to coordinate to Eu^{3+} or Tb^{3+} and further introduced

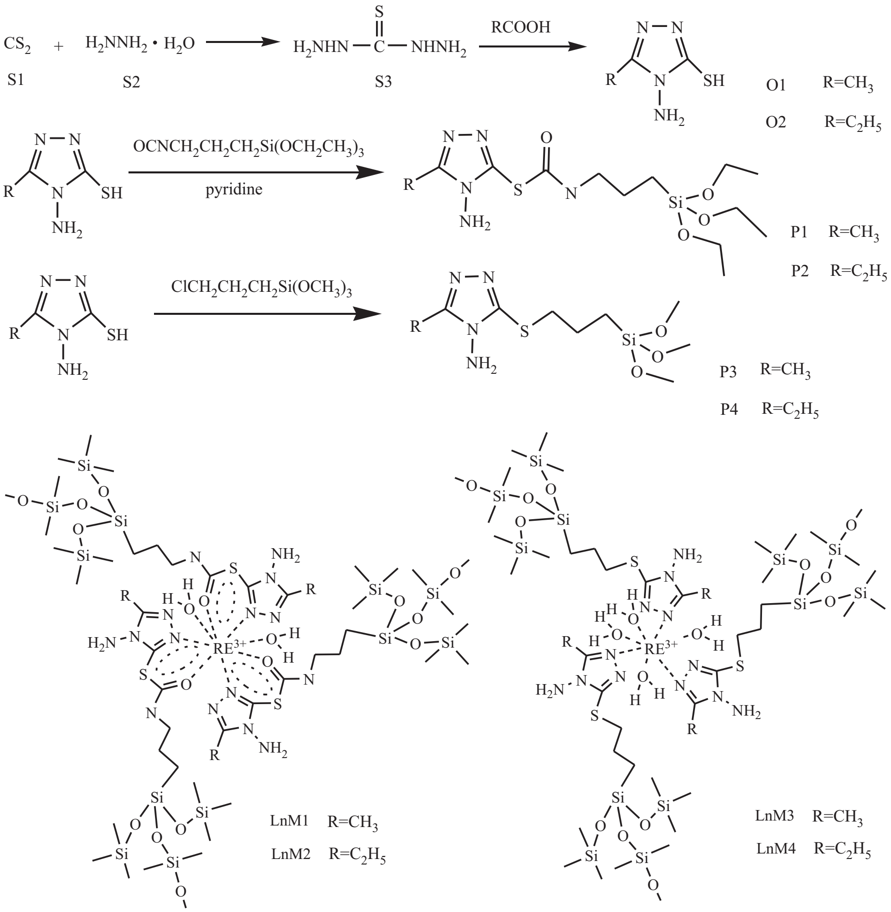

Fig. 2.15 Scheme for synthesis of thiocarbohydrazide organic components and silylated precursors (Reprinted with permission from Ref. [73]. Copyright 2008 the American Chemical Society)

into silica matrices by Si–O bonds after hydrolysis and polycondensation processes. Modifications by different trialkoxysilyl groups (TESPIC or CPTMS (chloropropyltrimethoxysilane)) lead to the different coordination structures and thus influence the absorption efficiency or the ability of the organic ligands to transfer the absorbed energy to RE^{3+} ions and consequently change the luminescence lifetimes and the quantum yield of the emission.

2.5.5 Photofunctional Rare Earth Hybrid Materials Based on Other Special ORMOSIL-Derived Silica

Lu et al. synthesize a functional precursor (PySi) from the hydrosilylation reaction of methyldichlorosilane and 4-vinylpyridine and prepare two series of novel luminescent hybrid materials (RE-PySi, RE = Tb, Dy) [75]. It is found that the sol–gel treatment has an influence on the organization and microstructure of the hybrid materials, indicating that the hybrid material systems derived from different solvents exhibit different textures. They further design two series of acylamido side functionalized polysiloxanes and synthesize from the modifications of amino silane with different acylating agents, resulting in functionalized polysiloxane–RE^{3+} (RE = Tb, Eu, Dy, and Sm) hybrids [76].

Nobre et al. prepare hybrid materials from the sol–gel reactions of bridged silsesquioxane precursor $(EtO)_3Si(CH_2)_3NH(C = O)NH\text{-}(CH_2)_{12}\text{-}NH(C = O)NH\text{-}(CH_2)_3Si(OEt)_3$ in the presence or absence of $EuCl_3{\cdot}6H_2O$ [77]. Supramolecular self-assembly of the growing structure relies primarily on the establishment of strong and ordered hydrogen bonding interactions. In the case of the Eu^{3+}-containing hybrids, the lanthanide ions play a totally unparallel dual role in acting simultaneously as structure-directing agents and structural probes to sense locally morphological alterations. The photoluminescence features as a function of the Eu^{3+} content and acidic- and F^--catalyzed conditions used in the synthesis are compared to address the effect of the morphology in the photoluminescence features of the hybrid materials.

Besides, Lin et al. synthesize a monomer containing large organic bridging groups of complex chemical structure, consisting of a heterocyclic ring integrated through flexible alkyl chains with three trimethoxysilyl groups [78]. Luminescent bridged polysilsesquioxanes possessing the luminescence characteristics of Eu^{3+} and Tb^{3+} ions are obtained by in situ hydrolysis and condensation of the monomer.

2.6 Photofunctional Rare Earth Hybrid Materials Based on Composite Matrices of Silica

In all the above work, the hybrids are mainly based on inorganic silica polymer networks. Recently, some studies have focused on the lanthanide hybrids of other inorganic frameworks such as M–O–M (M = B, Al, Ti) [79–87]. Li's group has prepared lanthanide hybrids of titania with simple organic pyridinecarboxylic acid linkages [79, 80]. They report a facile strategy to tether lanthanide complexes to hybrid titania materials via sol–gel processing by employing chemically modified titanium alkoxide as the precursor where the organic ligand sensitizing the luminescence of lanthanide ions is bonded to titanium [79]. They also employ isonicotinic acid (NIT) to modify titanium alkoxide to graft lanthanide complexes onto titania via adduct formation of tris(TTA) rare earth complexes with the nitrogen atoms from NITRE^{3+}-diketonate complexes (RE = Eu, Nd, Er) immobilized on an NIT-functionalized titania material [80]. The coordinated water molecules are expelled from the first coordination sphere of RE^{3+} ion as revealed by the prolonged lifetime of the hybrid titania material compared with that of the pure Eu^{3+} TTA complex. Depending on the lanthanide ion, the luminescent titania materials are emitted in the visible region (Eu) or in the near-infrared region (Nd, Er).

Guo et al. prepare three different types of hybrid materials formed by Eu^{3+} and Tb^{3+} complexes covalently grafted to silica-, titania-, or silica/titania-based hosts (Fig. 2.16 (Left)) [81]. Since the organic ligand 2-sulfanyl pyridine-3-carboxylic acid (SPC), a derivative of nicotinic acid, exhibits three potential binding sites (pyridine N, sulfhydryl S, and carboxylic O), the multifunctional precursor can be prepared through the reaction of the carboxylic group with titanium alkoxide and the modification of the sulfhydryl group with silane cross-linking reagents. The detailed PL studies show that, compared with the titania-based hybrid materials (Ln-SPC-Ti), the silica- and silica/titania-based hybrid materials (Ln-SPCSi and Ln-SPCSi-Ti) exhibit higher luminescence intensity and emission quantum efficiency. So this strategy can be extended to construct a variety of rare earth hybrids with silica–alumina and silica–titania composite hosts [82, 83].

Wang et al. prepare some ORMOSIL covalently linked rare earth hybrid materials with Si–O–M (M = B or Ti) xerogels as hosts by controlling the hydrolysis rates of alkoxyl compounds (TEOS, titanium butoxide, and tributyl borate) [84–87]. For example, polysilsesquioxane bridges are obtained through the modification of TESPIC by two β-diketone ligands (TTA and trifluoroacetylacetone (TFA)) and then assemble the corresponding hybrid xerogels with composite host [84]. The hybrids with composite Si–O–B xerogels have photoluminescence properties (red emission intensities, lifetimes, and quantum efficiencies) comparable to those of hybrids of the pure silica oxygen network, and the hybrids with Si–O–B or Si–O–Si xerogels both show luminescent performances superior to those of the hybrids with Si–O–Ti xerogels. The single modification by TTA also gives excellent luminescence of the hybrid xerogels, and the luminescence quantum efficiencies of the hybrids with a Si–O–B host show the highest values among all the hosts. B and Si are diagonal elements in the periodic table, and they have similar features and chemical behaviors, as verified by the similar sol–gel processes of their alkoxyl compounds. However, the composite host of the Si–O–B systems shows little distinction from that of the pure Si–O host, and the results show that the hybrid gel with a composite Si–O–B host did not change the luminescence of the final hybrid. Ti is a transition metal and has chemical properties different from Si. This work has been extended to other hybrid systems [85–87].

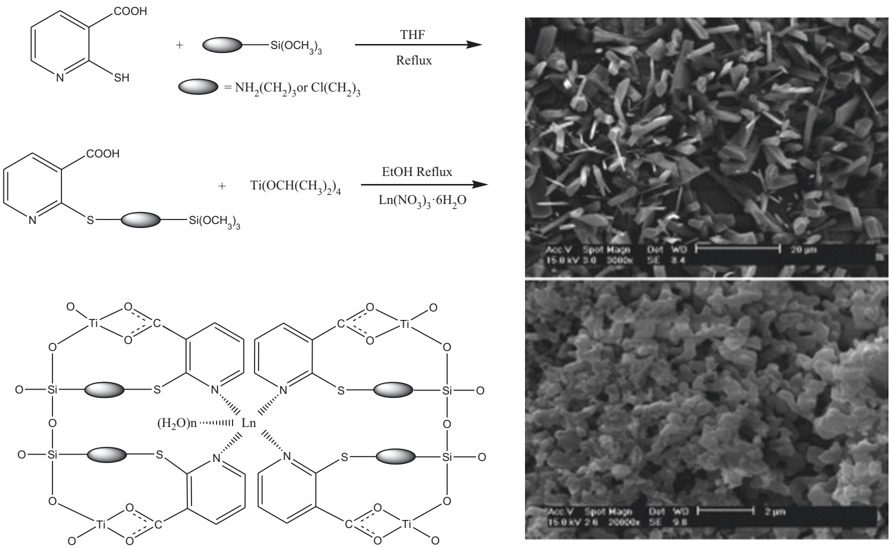

Fig. 2.16 (*Left*) The scheme for synthetic procedure and possible structure of hybrid materials RE-SPCSi-Ti and (*Right*) selected SEM images of Eu-SPC-Ti (*Top*) and Eu-SPCSi-Ti (*Bottom*) (Reprinted with permission from Ref. [81]. Copyright 2011 the Royal Society of Chemistry)

2.7 Conclusion and Outlook

In summary, on the basis of the design of chemical linkage (ORMOSILs) and the assembly of sol–gel-derived rare earth silica hybrid materials, the general strategies and paths are obtained and can be applied to other hybrid materials. These research results provide a useful experience to further explore the new hybrid materials and new applications. In fact, the content of some following chapters is related to the content of this chapter.

References

1. Hench LL, West JK (1990) The sol-gel process. Chem Rev 90:33–72
2. Ciriminna R, Sciortino M, Alonzo G, de Schrijver A, Pagliaro M (2011) From molecules to systems: sol-gel microencapsulation in silica-based materials. Chem Rev 111:765–789
3. Ciriminna R, Fidalgo A, Pandarus V, Béland F, Ilharco LM, Pagliaro M (2013) The sol−gel route to advanced silica-based materials and recent applications. Chem Rev 113:6592−6620
4. Yan B (2012) Recent progress on photofunctional lanthanide hybrid materials. RSC Adv 2:9304–9324
5. Feng J, Zhang HJ (2013) Hybrid materials based on lanthanide organic complexes: a review. Chem Soc Rev 42:387–410

6. Wang YG, Wang L, Li HR, Liu P, Qin DS, Liu BY, Zhang WJ, Deng RP, Zhang HJ (2008) Synthesis and luminescence properties of hybrid organic–inorganic transparent titania thin film activated by in-situ formed lanthanide complexes. J Solid State Chem 181:562–566
7. Yan B, Sheng C, Guo L (2012) Lanthanide (Eu^{3+}, Tb^{3+}, Gd^{3+}) hybrid system with functionalized diethylenetriamine pentaacetic acid ligand: coordination bonding assembly, luminescence and MRI contrast agent property. Inorg Chem Comm 18:43–46
8. Wang QM, Yan B (2004) From molecules to materials: a new way to construct luminescent chemical bonded hybrid systems based with ternary lanthanide complexes of 1,10-phenanthroline. Inorg Chem Comm 7:1124–1127
9. Wang QM, Yan B (2005) Optically hybrid lanthanide ions (Eu^{3+}, Tb^{3+})-centered materials with novel functional di-urea linkages. Appl Organomet Chem 19:952–956
10. Yan B, Wang FF (2007) Molecular design and photo-physics of quaternary hybrid terbium centered systems with novel functional di-urea linkages of strong chemical bonds through hydrogen transfer addition. J Organomet Chem 692:2395–2401
11. Yan B (2014) Assembling photofunctional rare earth hybrid materials using organically modified siloxanes as linkers. J Chin Soc Rare Earths (in Chinese) 32:1–15
12. Yan B, Sui YL (2006) Construction of hybrid material with double chemical bond from functional bridge ligand: molecular modification, lotus root-like micromorphology and strong luminescence. Opt Mater 28:1216–1221
13. Wang QM, Yan B (2005) A novel way to prepare luminescent terbium molecular-scale hybrid materials: modified heterocyclic ligands covalently bonded with silica. Cryst Growth Des 5:497–503
14. Wang QM, Yan B (2005) Construction of lanthanide luminescent molecular-based hybrid material using modified functional bridge chemical bonded with silica. J Photochem Photobiol A Chem 175:159–164
15. Yan B, Sui YL, Liu JL (2009) Photoluminescent hybrid thin films fabricated with lanthanide ions covalently bonded silica. J Alloys Compds 476:826–829
16. Wang QM, Yan B (2005) An unusual way to luminescent terbium molecular-level hybrid materials: modified methyl benzoic acid covalently bonded with silica as a bridge. J Mater Res 20:592–598
17. Yan B, Zhou B, Wang QM (2006) Luminescent lanthanide molecular-based hybrid materials bridged through novel urethane linkages. Appl Organomet Chem 20:835–839
18. Yan B, Zhao LM (2005) Construction of luminescent terbium inorganic/organic molecular-based hybrids from modified functional bridge ligand. Mater Lett 59:795–799
19. Zhao LM, Yan B (2006) The fabrication of rare earth covalent luminescent hybrid materials with potential molecular bridge by in situ sol-gel process. Mater Res Bull 41:1–9
20. Sui YL, Yan B (2006) Luminescent molecular hybrid system derived from 2-furancarboxylic acid and silylated monomer coordinated to rare earth ions. Appl Surf Sci 252:4306–4311
21. Zhao LM, Yan B (2006) Molecular-based smart hybrid material through in situ sol-gel process: artificial assembly of terbium with modified bridge ligand and luminescence. Coll Surf A 275:64–68
22. Yan B, Sui YL (2007) Fabrication and characterization of molecular hybrid materials with lanthanides covalently bonded in silica via sol-gel process. Mater Lett 61:3715–3718
23. Liu FY, Fu LS, Wang J, Liu Z, Li HR, Zhang HJ (2002) Luminescent hybrid films obtained by covalent grafting of terbium complex to silica network. Thin Solid Films 419:178–182
24. Wang QM, Yan B (2007) Molecular assembly and photophysical properties of a novel luminescent terbium hybrid material with modified carboxyl group of *p*-aminobenzoic acid as a functional bridge. Mater Lett 60:3420–3425
25. Wang QM, Yan B (2004) Novel luminescent molecular-based hybrid organic-inorganic terbium complex covalently bonded materials via sol-gel process. Inorg Chem Comm 7:747–750
26. Wang QM, Yan B (2004) Novel luminescent terbium molecular-based hybrids with modified meta-aminobenzoic acid covalently bonded with silica. J Mater Chem 15:2450–2454

27. Yan B, Lu HF (2009) Lanthanide-centered inorganic/organic hybrids from functionalized 2-pyrrolidinone-5-carboxylic acid bridge: covalently bonded assembly and luminescence. J Organomet Chem 694:2597–2603
28. Yan B, Lu HF (2009) Novel leaf-shaped hybrid micro-particles: chemically bonded self-assembly, microstructure and photoluminescence. J Photochem Photobiol A Chem 205:122–128
29. Wang QM, Yan B (2006) Terbium/zinc luminescent hybrid siloxane-oxide materials bridged by novel ureasils linkages. J Organomet Chem 691:545–550
30. Wang QM, Yan B (2006) Designing a family of luminescent hybrid materials by 3-(triethoxysilyl)-propyl isocyanate grafted 2-hydroxynicotinic acid bridge molecules. J Organomet Chem 691:3567–3573
31. Zhao LM, Yan B (2005) A novel path to luminescent hybrid molecular materials: modifying the hydroxyl group of 6-hydroxynicotinic acid by grafting to a silica network. Appl Organomet Chem 19:1060–1064
32. Yan B, Ma DJ (2006) From chemistry to materials, design and photophysics of functional terbium molecular hybrids from assembling covalent chromophore to alkoxysilanes through hydrogen transfer addition. J Solid State Chem 179:2059–2066
33. Yan B, Lu HF (2008) Lanthanide-centered covalently bonded hybrids through sulfide linkage: molecular assembly, physical characterization, and photoluminescence. Inorg Chem 47:5601–5611
34. Yan B, Qian K, Lu HF (2009) Chemically bonded metallic (Eu, Tb, Zn) hybrid materials through sulfide linkage: molecular construction, physical characterization and photophysical properties. J Organomet Chem 694:3160–3166
35. Yan B, Wang XL, Qian K, Lu HF (2010) Coordination bonding assembly, characterization and photophysical properties of lanthanide (Eu, Tb)/zinc centered hybrid materials through sulfide bridge. J Photochem Photobiol A Chem 212:75–80
36. Lu HF, Yan B (2006) Attractive sulfonamide bridging bonds constructing lanthanide centered photoactive covalent hybrids. J Non-cryst Sol 352:5331–5336
37. Qian K, Yan B (2010) Lanthanide/zinc centered photoactive hybrids with functional sulfonamide linkage: coordination bonding assembly, characterization and photophysical properties. Polyhedron 29:226–231
38. Yan B, Wang QM (2008) Two luminescent molecular hybrids composed of bridged Eu(III)-*beta*-diketone chelates covalently trapped in silica and titanate gels. Cryst Growth Des 8:1484–1489
39. Yan B, Kong LL, Zhou B (2009) A luminescent covalently bonded rare earth hybrid material by functionalized trifluoacetylacetone linkage. J Non-Cryst Sol 355:1281–1284
40. Wang Y, Wang YG, Cao PP, Li YN, Li HR (2011) Rectangular-plate like organosilica microcrystals based on silylated β-diketone and lanthanide ions. CrystEngComm 13:177–181
41. Chen XF, Zhang PN, Wang TR, Li HR (2014) The first europium(III) β-diketonate complex functionalized polyhedral oligomeric silsesquioxane. Chem Eur J 20:2551–2556
42. Guo XM, Guo HD, Fu LS, Zhang HJ, Carlos LD, Deng RP, Yu JB (2008) Synthesis and photophysical properties of novel organic–inorganic hybrid materials covalently linked to a europium complex. J Photochem Photobiol A Chem 200:318–324
43. Guo XM, Guo HD, Fu LS, Carlos LD, Ferreira RAS, Sun LN, Deng RP, Zhang HJ (2009) Novel near-infrared luminescent hybrid materials covalently linking with lanthanide [Nd(III), Er(III), Yb(III), and Sm(III)] complexes via a primary β-diketone ligand: synthesis and photophysical studies. J Phys Chem C 113:12538–12545
44. Sun LN, Qiu YN, Liu T, Zhang JZ, Dang S, Feng J, Wang ZJ, Zhang HJ, Shi LY (2013) Near infrared and visible luminescence from xerogels covalently grafted with lanthanide [Sm^{3+}, Yb^{3+}, Nd^{3+}, Er^{3+}, Pr^{3+}, Ho^{3+}] β-diketonate derivatives using visible light excitation. ACS Appl Mater Interf 5:9585–9593
45. Wang YH, Li B, Zhang LM, Zuo QH, Liu LN, Li P (2010) Improved photoluminescence properties of a novel europium(III) complex covalently grafted to organically modified silicates. J Coll Interf Sci 349:505–511

46. Guo L, Yan B, Liu JL (2011) Photofunctional Eu^{3+}/Tb^{3+} hybrids through sulfoxide linkages: coordination bonds construction, characterization and luminescence. Dalton Trans 40:4933–4940
47. Lu HF, Yan B (2008) Covalently assembly and photophysical properties of novel lanthanide centered hybrid materials by functionalized thioacylureas bridge. J Photochem Photobiol A Chem 197:351–358
48. Liu JL, Yan B (2008) Lanthanide (Eu^{3+}, Tb^{3+}) centered hybrid materials using modified functional bridge chemical bonded with silica: molecular design, physical characterization, and photophysical properties. J Phys Chem B 112:10898–10907
49. Yan B, Wang QM, Ma DJ (2009) Molecular construction, characterization, and photophysical properties of supramolecular lanthanide-calix[4]arene covalently bonded hybrid systems. Inorg Chem 48:36–44
50. Lu HF, Yan B, Liu JL (2009) Functionalization of calix[4]arene as a molecular bridge to assemble luminescent chemically bonded rare earth hybrid systems. Inorg Chem 48:3966–3975
51. Liu JL, Yan B, Guo L (2011) Lanthanide-centered organic-inorganic hybrids through a functionalized aza-crown ether bridge: coordination bonding assembly, microstructure and multicolor luminescence. Dalton Trans 40:1961–1968
52. Guo L, Yan B (2011) Bear-infrared luminescent hybrid materials using modified functional lanthanide (Nd^{3+}, Yb^{3+}) porphyrins complexes chemical bonded with silica. Inorg. Chem Comm 14:1833–1837
53. Guo L, Fu LS, Ferreira RAS, Carlos LD, Yan B (2012) Photofunctional hybrid silica microspheres covalently functionalized with metalloporphyrins. J Solid State Chem 194:9–14
54. Liu JL, Yan B, Guo L (2010) Photoactive ternary lanthanide-centered hybrids with Schiff-base functionalized polysilsesquioxanes bridges and N-heterocylic ligands. Eur J Inorg Chem 2290–2296
55. Li HR, Lin J, Zhang HJ, Li HC, Fu LS, Meng QG (2001) Novel, covalently bonded hybrid materials of europium (terbium) complexes with silica. Chem Comm 1212–1213
56. Li HR, Lin NN, Wang Y, Feng Y, Gan QY, Zhang HJ, Dong QL, Chen YH (2009) Construction and photoluminescence of monophase hybrid materials derived from a urea-based bis-silylated bpyridine. Eur J Inorg Chem 519–523
57. Carlos LD, Chi Man MW, Bartlett JR (2012) Luminescent coatings from bpyridine-based bridged silsesquioxanes containing Eu3+ and Tb3+ salts. J Mater Chem 22:13279–13285
58. Li HR, Lin J, Zhang HJ, Fu LS, Meng QG, Wang SB (2002) Preparation and luminescence properties of hybrid materials containing europium(III) complexes covalently bonded to a silica matrix. Chem Mater 14:3651–3655
59. Lenaerts P, Storms A, Mullens J, D'Haen J, Gorller-Walrand C, Binnemans K, Driesen K (2005) Thin films of highly luminescent lanthanide complexes covalently linked to an organic-inorganic hybrid material via 2-2ubstituted imidazo[4,5-*f*]-1,10-phenanthroline groups. Chem Mater 17:5194–5201
60. Bo SH, Liu XH, Zhen Z (2008) Preparation and luminescence properties of hybrid materials containing lanthanide complexes covalently bonded to a terpyridine-functionalized silica matrix. J Lumin 128:1725–1730
61. Tong BH, Wang SJ, Jiao J, Ling FR, Meng XZ, Wang B (2007) Novel luminescent lanthanide complexes covalently linked to a terpyridine-functionalized silica network. J Photochem Photobiol A Chem 191:74–79
62. Guo L, Yan B (2010) Chemically bonding assembly, physical characterization, and photophysical properties of lanthanide hybrids from a functional thiazole bridge. Eur J Inorg Chem 1267–1274
63. Wang QM, Yan B (2006) Molecular assembly of red and green nanophosphors from amine-functionalized covalent linking hybrids with emitting centers Eu^{3+} and Tb^{3+} ions. J Photochem Photobiol A Chem 178:70–75
64. Lu HF, Yan B (2008) Lanthanide-centered luminescent hybrid micro sphere-particles obtained by sol-gel method. J Photochem Photobiol A Chem 194:136–142

65. Liu JL, Yan B (2010) Rare earth (Eu^{3+}, Tb^{3+}) hybrids through amide bridge: chemically bonded self-assembly and photophysical properties. J Organomet Chem 695:580–587
66. Yan B, Zhou B, Wang QM (2007) Novel hybrid materials with covalent bonding and rare earth ions-induced enhancing luminescence of bridged 9-amino acridine. J Lumin 126:556–560
67. Yan B, Qiao XF (2007) Photophysical properties of terbium molecular-based hybrids assembled with novel ureasil linkages. Photochem Photobiol 83:971–978
68. Yan B, Qian K, Lu HF (2007) Molecular assembly and photophysical properties of quaternary molecular hybrid materials with chemical bond. Photochem Photobiol 83:1481–1490
69. Yan B, Qian K (2009) Chemically bonded hybrid systems from functionalized hydroxypyridine molecular bridge: characterization and photophysical properties. Photochem Photobiol 85:1278–1285
70. Yan B, Qian K (2009) Novel chemically bonded Tb/Zn hybrid sphere particles: molecular assembly, microstructure, and photoluminescence. J Photochem Photobiol A Chem 207:217–223
71. Sui YL, Yan B (2006) Fabrication and photoluminescence of molecular hybrid films based on the complexes of 8-hydroxyquinoline with different metal ions via sol–gel process. J Photochem Photobiol A Chem 182:1–6
72. Sun LN, Dang S, Yu JB, Feng J, Shi LY, Zhang HJ (2010) Near-infrared luminescence from visible-light-sensitized hybrid materials covalently linked with tris(8-hydroxyquinolinate)-lanthanide [Er(III), Nd(III), and Yb(III)] derivatives. J Phys Chem B 114:16393–16397
73. Liu JL, Yan B (2008) Molecular construction and photophysical properties of luminescent covalently bonded lanthanide hybrid materials obtained by grafting organic ligands containing 1,2,4-triazole on silica by mercapto modification. J Phys Chem C 112:14168–14178
74. Liu JL, Yan B (2009) Molecular assembly, physical characterization and photophysical properties of ternary lanthanide hybrids containing functional 1,2,4-triazole and 1,10-phenanthroline. J Photochem Photobiol A Chem 206:32–39
75. Lu HF, Wang H, Feng SY (2010) A new way to construct luminescent functionalized silicon hybrid material derived from methyldichlorosilane. J Photochem Photobiol A Chem 210:48–53
76. Lu HF, Wang XC, Wang H, Feng SY (2010) Molecular design and photophysical properties of acylamido side functionalized polysiloxanes with lanthanide ions as luminescent centers. J Photochem Photobiol A Chem 215:46–51
77. Nobre SS, Cattoen X, Sa Ferreira RA, Carcel C, Bermudez VD, Chi Man MW, Carlos LD (2010) Eu^{3+}-assisted short-range ordering of photoluminescent bridged silsesquioxanes. Chem Mater 22:3599–3609
78. Lin NN, Li HR, Wang YG, Feng Y, Qin DS, Gan QY, Chen SD (2008) Luminescent triazine-containing bridged polysilsesquioxanes activated by lanthanide ions. Eur J Inorg Chem 4781–4785
79. Liu P, Li HR, Wang YG, Liu BY, Zhang WJ, Wang YJ, Yan WD, Zhang HJ, Schubert U (2008) Europium complexes immobilization on titania *via* chemical modification of titanium alkoxide. J Mater Chem 18:735–737
80. Li HR, Liu P, Wang YG, Zhang L, JB Y, Zhang HJ, Liu BY, Schubert U (2009) Preparation and luminescence properties of hybrid titania immobilized with lanthanide complexes. J Phys Chem C 113:3945–3949
81. Guo L, Fu LS, Ferreira RAS, Carlos LD, Li QP, Yan B (2011) Novel lanthanide luminescent materials based on multifunctional complexes of 2-sulfanylpyridine-3-carboxylic acid and silica/titania hosts. J Mater Chem 21:15600–15607
82. Guo L, Yan B (2010) New luminescent lanthanide centered Si-O-Ti organic–inorganic hybrid material using sulfoxide linkage. Inorg Chem Comm 13:358–360
83. Guo L, Yan B (2011) Photoluminescent lanthanide inorganic-organic hybrid systems with different metallic alkoxides components through 2-pyrazinecarboxylate linkage. J Photochem Photobiol A Chem 224:141–146

84. Yan B, Wang C, Liu JL, Guo L (2011) Photoactive europium hybrids of β-diketone-modified polysilsesquioxane bridge linking Si-O-B(Ti)-O xerogels. Eur J Inorg Chem 879–887
85. Yan B, Wang C, Guo L, Liu JL (2010) Photophysical properties of Eu(III) center covalently immobilized in Si-O-B and Si-O-Ti composite gels. Photochem Photobiol 86:499–506
86. Yan B, Wang C (2011) Luminescent Eu^{3+}/Tb^{3+} immobilized in 5-amino-iso-phthalate functionalized hybrid gels through di-urea bridge. Inorg Chem Comm 14:1494–1497
87. Wang C, Yan B (2011) Rare earth (Eu^{3+}, Tb^{3+}) entered composite gels Si-O-M (M = B, Ti) through hexafluoroacetyl -acetone building block: sol-gel preparation, characterization and photoluminescence. Mater Res Bull 46:2515–2522

Chapter 3
Photofunctional Rare Earth Hybrid Materials Based on Organically Modified Mesoporous Silica

Abstract This chapter mainly focuses on recent research progress in photofunctional rare earth hybrid materials based on organically modified mesoporous silica. According to the type of mesoporous host, the content includes photofunctional rare earth hybrid materials based on organically functionalized MCM-type mesoporous silica, organically functionalized SBA-type mesoporous silica, organically functionalized POMs-type mesoporous silica, mesoporous silica composite with inorganic host, and mesoporous silica–polymer composite. Herein, it focuses the research progress of our group.

Keywords Rare earth ion • Photofunctional hybrid materials • Luminescence • Mesoporous silica

3.1 Introduction

Compared to the traditional molecular sieves, mesoporous silica possesses high specific surface area and uniform pore diameter distribution, whose pore diameter is large and can be controlled by means of selecting different templates or adding organic compounds [1, 2]. In the field of host–guest chemistry, mesoporous silica is used as the host for large guest molecules. There are a lot of methods to tune the pore diameter of mesoporous silica, whose basic principle is to reduce or enlarge the size or volume of the micelle of precursors [3, 4]. The free Si–OH groups over the mesoporous materials can undergo the silylation reaction. The surface silylation reaction of mesoporous silica not only can change the surface polarity but also can introduce other functional groups such as mecapto or amino groups. Mesoporous materials have no active center; the low chemical reactivity and high stability limit their applications. In this case, chemical modification of mesoporous silica materials to improve their reactivity has become a hot research topic in recent years. Organic groups interact with the Si–OH group of mesoporous silica to form Si–C or Si–O–C bonds, which realize the functionalization of mesoporous materials and modify the hydrophobicity of the pore wall of mesoporous silica. Subsequently, all kinds of hybrid materials based on mesoporous hosts have been developed [5, 6].

B. Yan, *Photofunctional Rare Earth Hybrid Materials*,
Springer Series in Materials Science 251, DOI 10.1007/978-981-10-2957-8_3

Mesoporous materials are analogous nanomaterials with ordered arrays of uniform nanochannels. They can be used as supports for rare earth complexes [7–19]. MCM-41, one member of the M41S family, possesses regular hexagonal arrays of mesopores, a variable pore diameter of 1.5–30 nm, and tailorable interior surfaces [7–9]. These properties, together with its thermal and mechanical stabilities, make it an ideal host for incorporation of active molecules, so some work has already been devoted to this area [7–9]. SBA-15 has also become a very attractive host because of its high hydrothermal stability and the presence of hexagonally ordered large mesopores (*P*6mm symmetry group) interconnected by complementary micropores. Previous results reveal that the obtained materials possess good luminescence properties and photo and thermal stabilities. The mesoporous silica SBA-16 has also been considered as a good support on account of its three-dimensional structure, consisting of ordered interconnected spherical mesopores, which has a cubic cage-like structure with multidirectional and large pore systems allowing good access for both functionalization and adsorption [10–14]. Periodic mesoporous organosilicas (PMOs) possess some obvious advantages over porous sol–gel-derived or grafted hybrid materials, such as highly ordered structures with very uniform pores, homogeneous distribution of functional groups throughout the whole framework, high loading amount, etc. [15–18].

Up to present, as an important functionalization approach, chemical modification has been extensively utilized in all kinds of materials. The main functionalization method for mesoporous materials is postsynthetic modification. Here only two basic methods are introduced, one is grafting, and the other is co-hydrolysis/polydensation [19, 20]. The grafting method is to link the functional group in the channel of mesoporous host to realize the surface modification of them after the formation of mesoporous structure (generally after removing template). The large amount of Si–OH over the surface of mesoporous silica can behave as the anchor point to graft organic functional groups, [21] and then the organic molecules react with Si–OH to introduce the channels which are grafted onto the surface of mesoporous silica host. The grafting method includes three aspects: inert surface group grafting, active surface group grafting, and position selective grafting, respectively. The removal of templates includes two methods: calcination and extraction. Compared to calcination method, extraction method can retain a great amount of Si–OH groups on the surface, which hardly lose and are easy to graft organic groups. In the grafting modification of mesoporous silica, outside surface is more easily to introduce functional groups than inside surface, and the functionalized groups over outside surface exhibit superior reactivity. So it can selectively functionalize the outside surface of mesoporous silica before removing templates. In order to decrease the reactivity of the groups on outside surface and improve the selectivity of reaction, it can first deactivate the outside surface and then functionalize the inside surface of mesoporous silica. For these functionalized mesoporous silica with grafting method, the organic functional groups possess low loading amount, so it is difficult to control the content and position in the channel, and the distribution in the channel is not uniform. Cohydrolysis/polycondensation belongs to one-step direct synthesis, in which silane sources (cross-linking reagents) are added in the sol to synthesize the mesoporous materials [22, 23]. The functionalization and synthesis of mesoporous silica are processed simultaneously. The advantage of this method to synthesize mesoporous materials is that the organic functional groups distribute in the channels uniformly [24].

For photofunctional mesoporous hybrid materials, considering the requirement of photoactivity, the functionalized units or groups should possess the emissive or absorptive property. Single silane source like cross-linking reagents doesn't have apparent photoactivity, so it needs to be modified with photoactive ligands. In Chap. 2, the corresponding modified path has been discussed, which is important for photofunctional hybrid materials based on organically modified mesoporous silica. On the basis of the above research on rare earth sol–gel-derived hybrid materials with ORMOSILs, it is natural to further attempt the assembly of rare earth mesoporous silica hybrids by grafting rare earth complex units with templates. Novel kinds of rare earth mesoporous hybrid materials, which combine the luminescence properties of rare earth complexes and the particular properties of mesoporous materials, have therefore received considerable attention in recent years. The research has involved many kinds of typical mesoporous hosts such as MCM-41(48), SBA-15(16), periodic mesoporous organosilicas (POMs), etc.

3.2 Photofunctional Rare Earth Hybrid Materials Based on Organically Modified MCM-Type Mesoporous Silica

M41S mesoporous silica family consists of hexagonal crystal system MCM-41, cubic crystal system MCM-48, and layer-like structural MCM-50. Among them, MCM-41 mesoporous silica possesses hexagonal arrangement of one-dimensional channels, which is the most popular system in the M41S family due to its easy synthesis and simple structure. This kind of novel mesoporous materials not only breaks the limit of too small pore diameter of old zeolite materials but also shows the new character such as uniform channel, regular hexagonal or order arrangement, continuous tuning in 2–10 nm range of pore diameter, high specific surface area, good thermal stability, etc. [7–9].

Functionalized mesoporous hybrid materials of photoactive rare earth complexes have appeared in recent decades. The primary research is originated from MCM-41 mesoporous hybrids fabricated with rare earth complexes. There have been extensive studies of the encapsulation and assembly of guest molecules in mesoporous channels [24–44]. Xu et al. study the direct encapsulation of rare earth complexes into MCM-41 host to prepare the hybrid materials, mainly with β-diketonates [24–27]. For example, rare earth complex $[C_5H_5NC_{16}H_{33}][Eu(TTA)_4]$ is incorporated into surface-modified mesoporous molecular sieve Si-MCM-41 via reactions of the surface Si–OH with different silylation agents such as $(C_2H_5O)_3Si(CH_2)_2NH(CH_2)_2NH_2$ (NSED), $(C_2H_5O)_3Si(CH_2)_3NH_2$ (APTES), and $(C_2H_5O)_3Si(CH_2)_3CN$ (TSBT), whose photophysical properties are studied [24].

The results show that the surface silylation of Si-MCM-41 provides a unique chemical environment for the incorporated $[C_5H_5NC_{16}H_{33}][Eu(TTA)_4]$ complex. The content of the rare earth complex in the final products, obtained from chemical analysis, is 6.61% in NSED-Si-MCM-41, 1.84% in APTES-Si-MCM-41, 1.83% in TSBT-Si-MCM-41, and 0.42% in Si-MCM-41, respectively. Hydrogen bonding interactions of the rare earth complex with its surrounding silylating agents alter the photophysical properties of the rare earth complex, whose emission intensity and color purity in these surface-silylated Si-MCM-41 materials increase in the order of Si-MCM-41 < TBST-Si-MCM-41 < APTES-Si-MCM-41 < NSED-Si-MCM-41. Because of the strongest hydrogen bonding in NSED-Si-MCM-41, the rare earth complex only emits light with a single wavelength, corresponding to $^5D_0$-$^7F_2$, which is rarely seen in the luminescence of rare earth complexes. Similarly, considering the suitable match between the pore diameter of MCM-41 host and the size of rare earth complex guest, the other rare earth β-diketonates can also be introduced to assembly the hybrid materials [25–27].

Besides, Carlos's group also study the MCM-41 hybrid materials with special pyrazolylpyridine-derived ORMOSIL linkage [28–31]. Gago et al. use mesoporous silica MCM-41 functionalized with a chelating pyrazolylpyridine ligand (MCM-41-L2) (L2 = (3-triethoxysilylpropyl)[3-(2-pyridyl)-1-pyrazolyl] acetamide) as a support for the immobilization of tris(β-diketonate) complexes $RE(NTA)_3$ (RE = Eu, Gd; NTA = 1-(2-naphthoyl)-3,3,3-trifluoroacetone) [28]. The spectroscopic studies supported by ab initio calculations evident that the immobilized Eu^{3+} complex is an eight-coordinate with a local coordination environment similar to that for a model complex containing ethyl[3-(2-pyridyl)-1-pyrazolyl]acetate (L1). No emission from the pyrazolylpyridine ligands is observed in the room-temperature emission spectrum of MCM-41-L2/Eu in spite of only about one-third engaged in coordination with Eu^{3+} ions, while the pyrazolylpyridine groups in the precursor ligand–silica can exhibit efficient emission. Furthermore, the radiance value measured for MCM-41-L2/Eu (0.33 $\mu W \cdot cm^{-2}$) is only about one-half of that measured for the complex $Eu(NTA)_3 \cdot L1$ (0.73 $\mu W \cdot cm^{-2}$), even though the concentration of emitting centers in the MCM material is much lower, which suggests the existence of an unusual two-step intermolecular energy transfer between "free" and "coordinated" ligands in MCM-41-L2/Eu to culminate in the observation of enhanced Eu^{3+} luminescence. Bruno et al. prepare hybrid ligand–silica by reaction of the ordered mesoporous silica MCM-41 with 3-triethoxysilylpropyl 4-pyridylacetamide (L3) [29]. Elemental analysis indicates a pyridyl group loading of 0.93 $mmolg^{-1}$. Pyridyl-functionalized MCM-41(L3) is treated with chloroform solutions of rare earth tris-β-diketonate complexes $Ln(NTA)_3(H_2O)_2$ (RE = Eu, Gd) to give the surface-bound monosubstituted species $Ln(NTA)_3(H_2O)(L3)$, whose residual coordinated water molecules are subsequently replaced by pyridine (py) or methyl phenyl sulfoxide (mpso) to give immobilized $RE(NTA)_3(py)(L)$ and $RE(NTA)_3(mpso)(L3)$ species. Variation of the excitation wavelength confirms that all of the Eu^{3+} occupies the same average local environment within each sample. The interaction between the host and guest has a strong effect on the excited states of the organic ligands. They further investigate a luminescent hybrid material by impregnating the Eu^{3+} β-diketonate complex $Eu(NTA)_3L0$ within the channels of MCM-41 (L0 = 2-(3(5)-pyrazolyl)pyridine) [30]. The low- (14 K) and room-temperature emission spectra of the Eu-modified mesoporous material display the typical Eu^{3+} intra-$4f^6$ lines, whose $^5D_0$ quantum efficiency is estimated to be 21.1%, which is lower than 46.1% for the model complex $Eu(NTA)_3L0$. This difference is ascribed to the presence of an excited state of the organic ligands in the MCM-41, which lies approximately resonant with the $^5D_1$ intra-$4f^6$ level to open up an additional non-radiative channel.

Recently, Felício et al. directly prepare MCM-41 hybrids incorporated with $Eu(TTA)_3$ephen [31]. The combination of UV–Vis and photoluminescence spectroscopy shows that the complex incorporation seems to modify essentially the second Eu^{3+} coordination shell. The impregnated hybrid material shows maximum $^5D_0$ quantum yield value of 0.31, which is almost in the same scale as covalently bonded one. To deeply understand the photoluminescence process, the ligand-to-Eu^{3+} intramolecular energy transfer and back-transfer rates are also predicted, which are in good agreement. The dominant pathway involves the energy transfer between the lowest energy ligand triplet and the $^5D_0$ level (9.70×10^7 s^{-1}).

Zhang's group study MCM-41-based hybrids with pyridine derivative linkages in detail [32–34]. Firstly, Li et al. prepare organo-functionalized MCM-41 containing non-covalently linked 1,10-phenanthroline (phen-MCM-41) [32]. The one-step synthesis presents an alternative to postsynthesis grafting methods. The high affinity toward various cations and the blue emission of the modified phenanthroline that is proven to be within the channel renders phen-MCM-41a promising candidate both for optical devices and the removal of anions. The desired properties of MCM-41 can be tailored by an appropriate choice of the precursors and the metal ions. Their emphasis has been on NIR-luminescent mesoporous hybrids [33, 34]. For instance, Sun et al. prepare NIR-luminescent mesoporous materials by linking ternary rare earth (Er^{3+}, Nd^{3+}, Yb^{3+}, Sm^{3+}, Pr^{3+}) complexes to MCM-41 through a functionalized phen group, 5-[*N*,*N*-bis-3-(triethoxysilyl)propyl] ureyl-1,10-phenanthroline on the basis of Li's work. Here, two β-diketonates HFTH (4,4,5,5,6,6,6-heptafluoro-1-(2-thienyl)hexane-1,3-dionate and TFNB (4,4,4-trifluoro-1-(2-naphthyl)-1,3-butanedione) are used as the second ligands [33]. Upon excitation at the absorption wavelength of the organic ligands, all these materials show the characteristic NIR luminescence of the corresponding rare earth ions. They further prepare mesoporous hybrid material, Q-MCM-41 based on a bifunctional ligand, 8-hydroxyquinoline-functionalized organosilane (Q-Si) [34]. Furthermore, through ligand exchange reactions, new NIR-luminescent mesoporous REQ_3-MCM-41 (RE = Er, Nd, Yb) materials are prepared by linking rare earth quinolinate complexes to Q-MCM-41. In addition, Feng et al. focus on the Tm mesoporous MCM-41 hybrid materials. Still using phen-Si as linkage, they prepare three NIR-luminescent thulium complexes covalently bonded to the ordered mesoporous material MCM-41 ($Tm(L)_3$phen–MCM-41 (L = TTA, TFNB, DBM)] [36, 37]. The full widths at half maximum (fwhm) of the 1474 nm emission band are 96 nm, 100 nm, and 110 nm for $Tm(TTA)_3$phen–MCM-41, $Tm(TFNB)_3$phen–MCM-41,

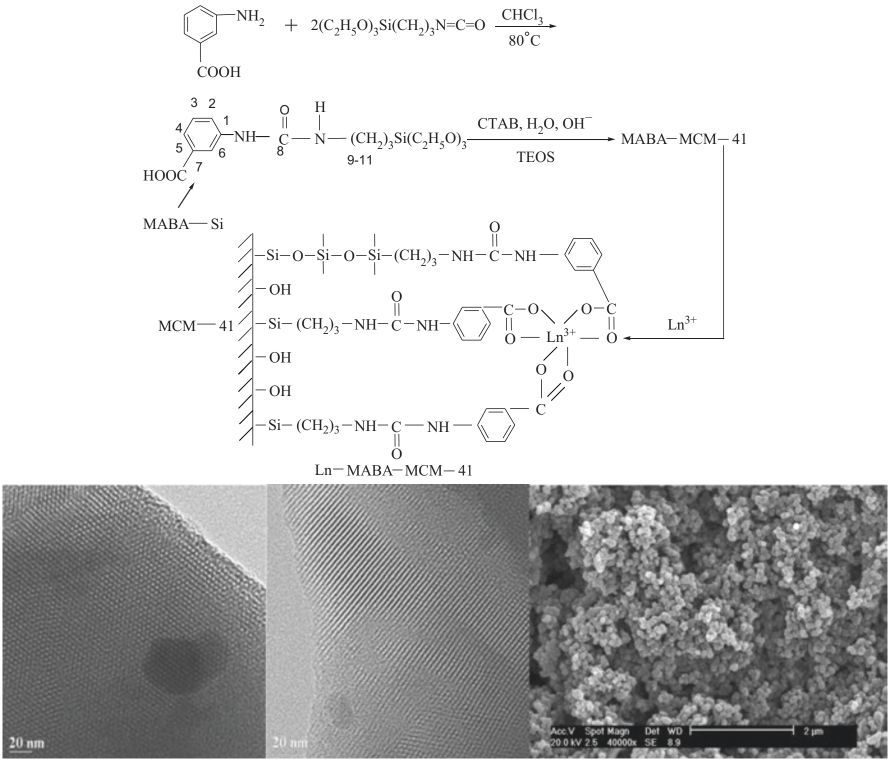

Fig. 3.1 The scheme for synthesis procedure and predicted structure of RE-MABA-MCM-41(RE = Tb, Eu) (*Top*); selected HRTEM recorded along the [100], [110] zone axes (left, middle) and SEM image (*Right*) of Tb-MABA-MCM-41 (*Bottom*) (Reprinted with permission from Ref. [39]. Copyright 2010, Elsevier Publisher Ltd)

and Tm(DBM)$_3$phen-MCM-41, respectively. The good luminescent performances enable these materials to have potential applications in optical amplification (broadening amplification band from C band (1530–1560 nm) to S* band (1450–1500 nm)).

Yan's group has also prepare some rare earth mesoporous hybrids of MCM-41 hosts based on their previous work on the ORMOSILs introduced in Chap. 2 [37–44]. Li et al. prepare a series of aromatic carboxylic acids (with amino, hydroxyl, and methyl substituted groups) grafted ORMOSILs modified MCM-41 hybrid materials through the different modification paths [37–39]. Here, an example is given for the aminobenzoic acid grafted ORMOSILs modified MCM-41 hybrid materials. The rare earth (Tb^{3+}, Eu^{3+}) complexes are covalently immobilized in MCM-41 through the modification of MBA (*meta*-aminobenzoic acid) with TESPIC, using a co-condensation method (Fig. 3.1 (Top)) [39]. The final luminescent mesoporous materials have high surface area, uniformity in the mesopore structure, and good crystallinity. The HTEM images (Fig. 3.1(Bottom) left and middle)) of

Tb-MABA-MCM-41 suggest that the ordered pore structure is still substantially conserved after the complexation, which shows *p6mm* symmetry and well-ordered hexagonal structure in agreement with the SAXRD and N_2 adsorption/desorption isotherms. The distance between the centers of the mesopore is estimated to be 3.91 nm, which is in good agreement with the value determined from the corresponding XRD data. Moreover, Tb-MABA-MCM-41 exhibits the stronger characteristic emission of Tb^{3+} and longer lifetime than Eu-MABA-MCM-41. Compared with pure $Tb(MABA)_3$ complex, the increase of luminescence intensity in Tb-MABA-MCM-41 shows that the mesoporous MCM-41 is an excellent host for the luminescence $Tb(MABA)_3$ complex. Similarly, other kinds of aromatic carboxylic acid ligands can be grafted onto an MCM-41 host [39, 40].

MCM-41 materials directly covalently bonded with modified β-diketones have also been obtained [41–43]. Zhou et al. report MCM-41 mesoporous hybrids with dibenzoylmethane (DBM) and acetylacetone (ACAC) ORMOSILs [40]. The hybrid materials with covalently bonded MCM-41 have higher intensities and longer lifetimes than those of pure complexes (Eu-DBM and Tb-ACAC), suggesting that covalently bonded MCM-41 host can decrease the concentration quenching effect and enhance the luminescent stability. Moreover, the luminescence properties of mesoporous hybrids are comparable to those of sol–gel-derived hybrids with the same ORMOSILs (TTA-Si) [41]. In addition, Li et al. functionalize MCM-41 mesoporous silica with two kinds of macrocyclic calixarene derivatives Calix [4] and Calix [4]Br (Calix [4] = P-tert-butylcalix[4]arene, Calix [4]Br = 5,11,17,23-tetra-tert-butyl-25,27-bihydroxy-26,28-bibromopropoxycalix[4]arene) [43]. More recently, Gu et al. report the synthesis of organic ligands (9-hydroxyphenalenone (HPO), 2-methyl-9-hydroxyphenalenone (MHPO), 6-hydroxybenz[de]anthracen-7-one (HBAO)) and their assembly with phen-Si-functionalized mesoporous MCM-41 to obtain the ternary Eu^{3+} hybrid materials, EuL_3phen-MCM-41 (L = HPO, MHPO, HBAO) [44]. It is worth noting that the excitation spectra of these hybrid materials have a broad absorption, which occupies from UV to visible region (250–475 nm) consisting of two absorption centers from phen-MCM-41 and three ligands (HPO, MHPO, HBAO), respectively. Upon ligand-mediated excitation with the visible light, the low efficient energy transfer occurs between the organic ligands and europium(III) ion under visible excitation, but the maximum wavelength (456 nm/457 nm/451 nm) locates at blue light region, which is in consistent with the blue LED light. Then this hybrid material may be a feasible alternative in producing time-resolved luminescence under LED excitation.

Besides MCM-41 hybrids, Meng et al. report the studies on functionalized MCM-48 mesoporous hybrids with europium β-diketonate complexes ($Eu(DBM)_3{\cdot}2H_2O$) using a simple wet impregnation method [44, 45]. MCM-48 has a very high surface area, large pore volume, and narrow pore size distribution, adjustable in the 1.5–10 nm range. The high surface area exhibited by MCM-48 makes it an attractive host for the insertion of large amounts of bulky molecules with functional properties. Shifts in the absorption maxima are observed in the excitation spectra, which is in relation to host–guest interactions between the organic complex and the silica matrix. The role of the O^{2-}–Eu^{3+} charge-transfer band and the impact of silylation on the luminescence properties at room and high temperatures are demonstrated.

3.3 Photofunctional Rare Earth Hybrid Materials Based on Organically Modified SBA-Type Mesoporous Silica

SBA series belongs to mesoporous silica materials containing cage structures, which is synthesized in strong acidic condition using double-chain surfactant as template. Among the series, the most important system is pure mesoporous silica material SBA-15 with hexagonal structure (P6mm), prepared using special hydrophilic tri-block copolymer (poly (oxyethylene)-poly (oxypropylene)-poly (oxyethylene) (PEO-PPO-PEO) as template. Besides, another SBA-16 mesoporous silica material with cubic cage structure can be synthesized using large PEO chain block copolymer [10–14].

There are many reports on photofunctional rare earth SBA-15 mesoporous hybrids [46–61]. Zhang's group concentrate on SBA-15-type hybrid materials with ORMOSILs derived from pyridine derivatives (bpy, phen, etc.) as the first ligand and second ligand such as β-diketones (DBM, HFTH, TFNB) [46, 47]. In Peng et al.'s work on phen-Si modified SBA-15 hybrids (Eu(TTA)3phen-SBA-15) [47], and they confirm that these chemically bonded mesoporous hybrids show more favorable luminescence performances than the corresponding doped systems. The thermal stability of the rare earth complex is also evidently improved. Corriu et al. prepare ordered mesoporous silica containing 3-chloropropyl groups by a direct synthetic approach [48]. Nucleophilic displacement of chloro groups by cyclam moieties (cyclam = 1,4,8,11-tetraazacyclotetradecane) is then achieved almost quantitatively. Subsequent treatment of solids containing different amounts of cyclam moieties with an ethanolic solution of Eu^{3+} chloride gives rise to 1:1 EuIII/cyclam complexes. The EXAFS studies have shown that Eu(III) adopts an octahedral geometry.

Besides, Sun et al. prepare the dual–functional ligand Q-Si and the mesoporous hybrid material REQ_3-SBA-15 (Q = 8-hydroxyquinoline; RE = Er, Nd, Yb) (Fig. 3.2) [49]. After ligand-mediated excitation, all of the emission spectra of the LnQ_3-SBA-15 materials show the characteristic NIR luminescence of the corresponding rare earth ions. As both the organic ligands and the emission of the rare earth ions can be tuned, a variety of mesoporous materials exhibiting a wide range of optical properties can be envisaged useful for optical applications. Besides, they further realize the attachment of ternary rare earth complexes ($RE(HFTH)_3phen$) (RE = Er, Nd, Yb, Sm) and ($Pr(TFNB)_3phen$) to the ordered SBA-15 mesoporous materials via a functionalized phen-Si linker, all of which also display the characteristic NIR luminescence of the corresponding RE^{3+} ions [50]. Based on their work on visible-luminescent SBA-15 mesoporous hybrids, it can be expected that the luminescence

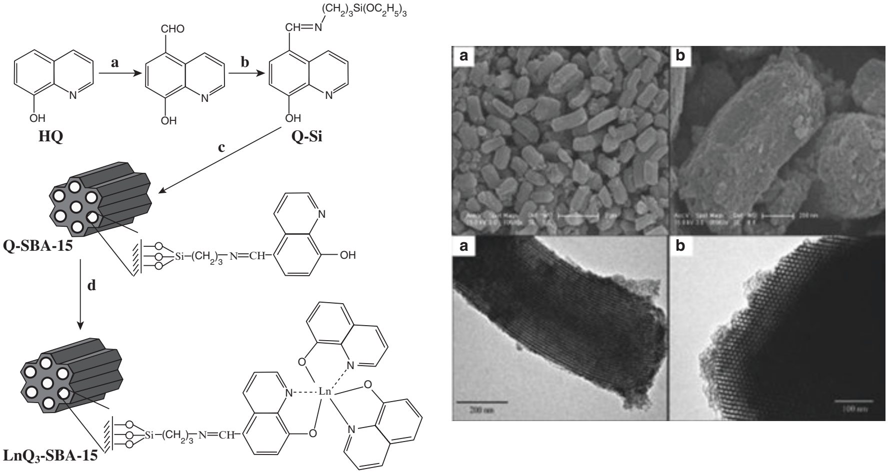

Fig. 3.2 The scheme for synthesis procedure and predicted structure of REQ$_3$-SBA-15 (RE = Nd, Er, Yb) hybrids (*Left*); SEM images of surfactant-extracted Q-SBA-15 material (*middle*) and TEM images of surfactant-extracted Q-SBA-15 material along the [110] (*a*) and [100] (*b*) zone axes (*Right*) (Reprinted with permission from [49]. Copyright 2008, The American Chemical Society)

spectral region from 1300 to 1600 nm is of particular interest for telecommunications applications.

Yan's group also study the functionalized SBA-15 mesoporous host with ORMOSILs derived from different organic precursors, including β-diketones (1-(2-naphthoyl)-3,3,3-trifluoroacetone (NTA), TTA, DBM, ACAC, calixarene derivatives (Calix, Calix-NH$_2$, Calix-NO$_2$), aromatic carboxylic acids, and sulfoxide ligands (oxobenzyldimethyl sulfoxide, benzylsulfinylacetylbenzene, porphyrin and hydroxyphenalen-1-one derivatives, etc.) [51–61]. They all have high surface areas and uniform mesostructures and crystallinities. The efficient intramolecular energy transfer in mesoporous materials mainly occurs between the modified ligand and the central RE^{3+} ion. For example, Li et al. prepare mesoporous hybrid materials by linking the binary and ternary Eu^{3+} complexes to the functionalized ordered mesoporous SBA-15 with the modified 1-(2-naphthoyl)-3,3,3-trifluoroacetone (NTA) (Fig. 3.3) [51]. Among these, Eu(NTA-SBA-15)$_3$bpy exhibited the characteristic emission of Eu^{3+} ion under UV irradiation with higher $^5D_0$ luminescence quantum efficiency than the pure Eu(NTA)$_3$bpy complex and other hybrid materials. This work can be extended to other β-diketone-grafted ORMOSIL-modified SBA-15 hybrid materials [52–56]. Li et al. synthesize the mesoporous hybrid materials phen-RE(OBDS)$_3$-SBA-15 and phen-RE(BSAB)$_3$-SBA-15 (RE = Eu, Tb) by linking the ternary rare earth (Eu^{3+}, Tb^{3+}) complexes to the functionalized ordered mesoporous SBA-15 with the modified sulfoxide (OBDS–Si and BSAB–Si) [57]. The resulted mesoporous hybrids exhibit a strong, nearly monochromatic emission of Eu^{3+} ions, and good thermal stability. Li et al. prepare three types of ternary rare earth mesoporous hybrid materials ((RE(Calix-S15)phen, RE(Calix-NO$_2$-S15)

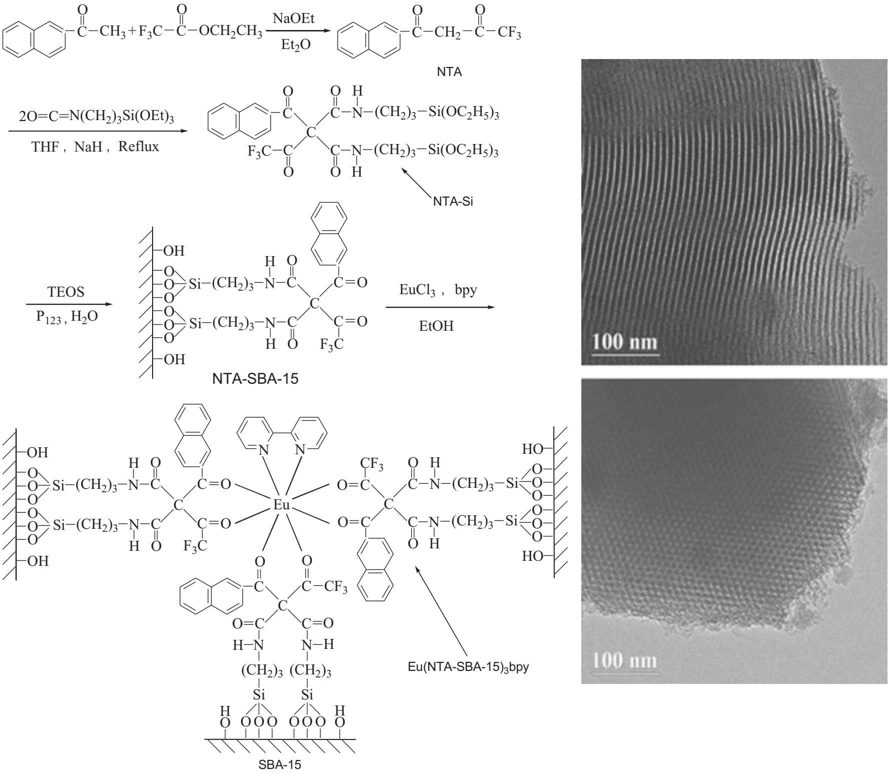

Fig. 3.3 Scheme of the synthesis process of NTA–Si and predicted structure of hybrid mesoporous material Eu(NTA-SBA-15)$_3$bpy (*Left*); and HRTEM images of Eu(NTA-SBA-15)$_3$bpy recorded along the [100] (*top*) and [110] (*bottom*) zone axes (*Right*) (Reprinted with permission from Ref. [51]. Copyright 2008 the American Chemical Society

phen, and RE(Calix-NH$_2$-S15)phen) using modified macrocycle organic ligands (Calix-Si, Calix-NO$_2$-Si, and Calix-NH$_2$-Si) as a linker [58]. Li et al. also functionalize SBA-15 mesoporous silica with two kinds of macrocyclic porphyrin derivatives (meso-(tetra(p-hydroxyphenyl)porphyrin (THPP), protoporphyrin IX (PPIX)) through condensation approach of TEOS [59]. They exhibit the characteristic NIR luminescence of Nd^{3+} and Yb^{3+}.

Li et al. synthesize two kinds of binary and ternary rare earth (Nd^{3+} or Yb^{3+}) hybrid materials using 9-hydroxyphenalen-1-one (HPNP)-modified silane as bridge molecule and phen as assistant ligand, which display the characteristic NIR luminescence of Nd^{3+} and Yb^{3+} under the excitation at visible region [60]. Furtherly, Gu et al. modify MHPO (2-methyl-9-hydroxyphenalenoe) with TESPIC to achieve linkage (MHPOSi) and prepare photoconversion RE^{3+} (Eu^{3+}, Nd^{3+}, Yb^{3+}) mesoporous hybrid materials [61]. The functionalized mesoporous SBA-15 network still presents excitation capability in visible region in spite of the modification of organic silane. Subsequently, they can exhibit characteristic visible (for Eu^{3+}) and NIR

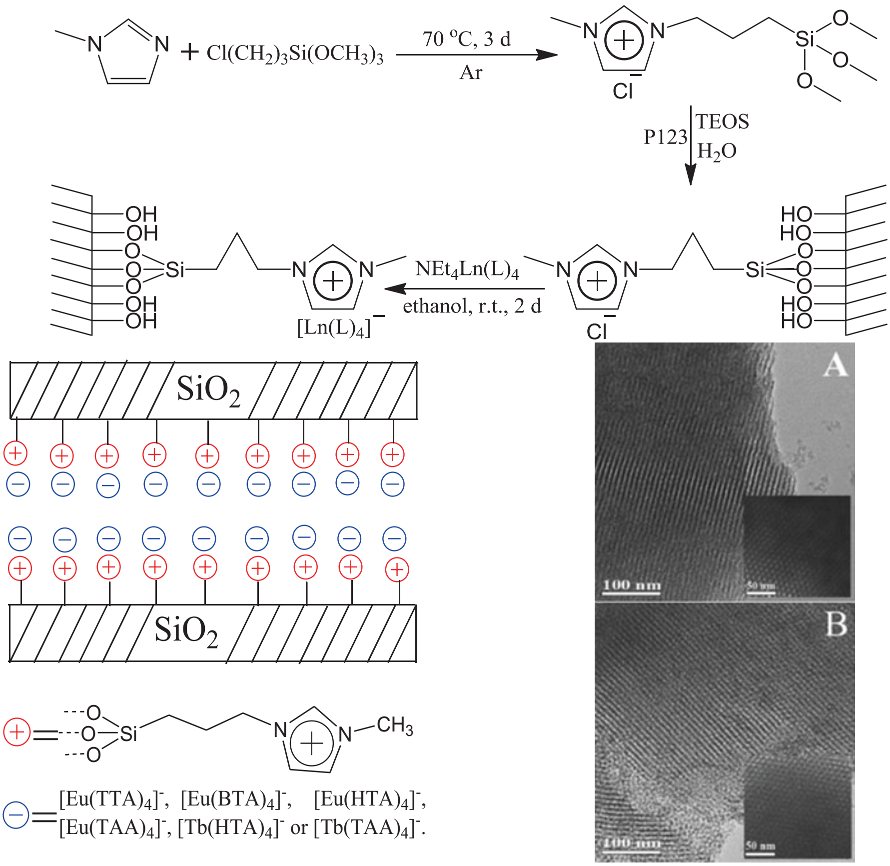

Fig. 3.4 The scheme for the synthesis process and possible structure of the resulted materials (*Top* and *Bottom*, *left*); TEM images of SBA-15-IM$^+$Cl$^-$ (*A*) and SBA-15-IM$^+$[Eu(TTA)$_4$]$^-$ (*B*) (*Bottom, right*) (Reprinted with permission from Ref. [63]. Copyright 2012 the Royal Society of Chemistry)

luminescence for (Nd$^+$ and Yb^{3+}). The photo conversion between the visible and NIR light can be expected to have potential application in the practical fields. Moreover, Gu et al. synthesize a series of new visible and near-infrared (NIR) luminescent rare earth complexes of hydroxybenz[de]anthracen derivatives (RE(HBAN)$_3$(H$_2$O)$_2$(NO$_3$)$_3$, RE(HBAN)$_3$phen(NO$_3$)$_3$) (HBAN-6-hydroxybenz[de]anthracen-7-one, RE = Eu, Yb, Nd) and prepare the chemically bonded rare earth hybrids of functionalized mesoporous silica (SBA-15) using HBAN-functionalized alkoxysilane (HBAN-Si) as linker [62]. Worth noting here is that the excitation spectra of these hybrid materials are extended to visible light region (439–535 nm). Upon ligand-mediated excitation with the ultraviolet and visible light, the visible luminescence for europium hybrids and NIR luminescence for Yb^{3+} and Nd^{3+} hybrids are obtained.

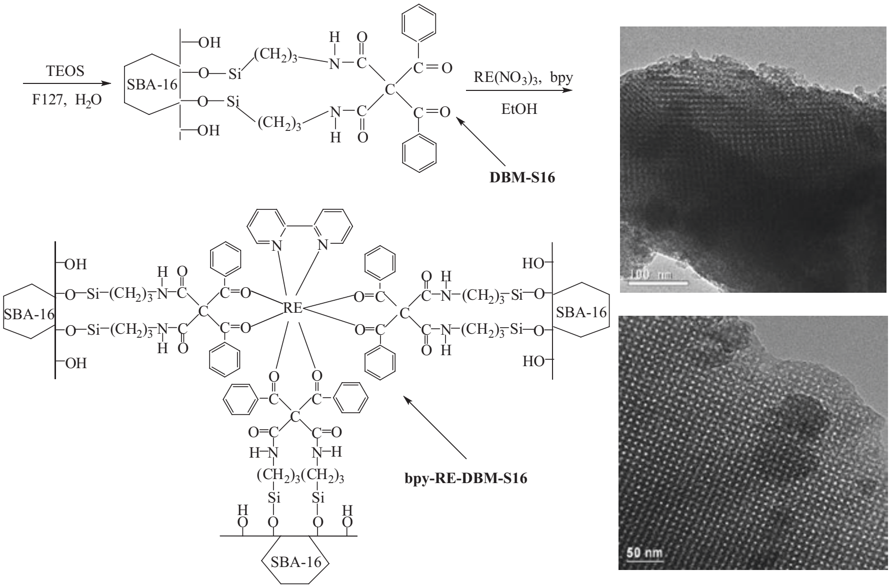

Fig. 3.5 Scheme for synthesis process and predicted structure of mesoporous hybrid materials bpy-RE-TTA-S16 (RE = Eu, Tb) (Left); TEM images of pure SBA-16 (Top) and mesoporous hybrid bpy-Eu-TTA-S16 (Bottom) (Right). Reprinted with permission from [64]. Copyright 2010 Elsevier

Li et al. put forward a novel method to construct the luminescent mesoporous materials, in which the ionic liquid 1-methyl-3-[3-(trimethoxysilyl)propyl] imidazolium chloride is incorporated into mesoporous SBA-15 framework by an in situ sol–gel processing (Fig. 3.4) [63]. Then, an anion metathesis processing is performed for introducing the rare earth β-diketonate complexes anion. Four kinds of commercially available β-diketonate are used in here, which are benzoyltrifluoroacetone (BTA), hexafluoroacetylacetone (HTA), TTA, and trifluoroacetylacetone (TAA), respectively. Subsequently, four europium-based mesoporous materials SBA-15-IM$^+$[Eu(L)$_4$]$^-$ (L = TTA, BTA, HTA, or TAA) are obtained after anchoring the europium β-diketonate complexes anion onto the SBA-15 framework. All the resulting materials through ionic exchange possess higher quantum yields than those covalently bonded mesoporous hybrid materials. This may be due to the fact that ion exchange reaction forming the hybrid system through static force is beneficial for the energy transfer and sensitized luminescence of rare earth ions.

Yan's group prepare mesoporous SBA-16-type hybrids, TTA-S16, and DBM-S16, by co-condensation of a modified β-diketone in the presence of Pluronic F127. Novel mesoporous luminescent hybrids containing RE^{3+} (Eu^{3+}, Tb^{3+}) complexes covalently attached to the functionalized ordered mesoporous SBA-16 (TTA-S16 and DBM-S16), denoted by bpy-Ln-TTA-S16 and bpy-RE-DBM-S16, are obtained by a sol–gel process (Fig. 3.5). The luminescence properties of these resulting materials have been characterized in detail, and the results reveal that the mesoporous hybrid material bpy-Eu-TTA-S16 has a stronger luminescence intensity, longer lifetime, and higher luminescence quantum efficiency than the corresponding DBM-containing material bpy-Eu-DBM-S16, and bpy-Tb-DBM-S16 exhibits a stronger characteristic emission of Tb^{3+} and a longer lifetime than the corresponding TTA-containing material bpy-Tb-TTA-S16 [64]. Further, Gu et al. synthesize rare earth complex functionalized mesoporous SBA-16-type hybrid materials by co-condensation of modified 2-methyl-9-hydroxyphenalenoe (MHPOSi, from the modification of TESPIC and TEOS) [65]. Among them, Eu^{3+} hybrid system shows the ultraviolet excitation and visible emission, and Nd^{+} and Yb^{3+} hybrids exhibit the visible excitation and NIR emission.

3.4 Photofunctional Rare Earth Hybrid Materials Based on POMs-Type Mesoporous Silica

PMOs (periodic mesoporous organosilicas) belong to hybrid materials with organic functional groups that functionalized mesoporous silica host, in which organic groups are contained within the mesoporous pore walls. The organic functional groups are distributed in the mesoporous frameworks and cannot block the channel or occupy the pore volume, whose flexibility can enhance the mechanical strength of materials. Besides, the different organic groups can tune the hydrophilicity/hydrophobicity of the materials surface and also can derive the new active center through further reactions. PMOs realize the uniform distribution and high loading amount of organic groups [15–17].

For mesoporous hybrids with PMO hosts, Guo et al. report novel periodic mesoporous organosilica covalently grafted with phen-derived ORMOSILs (phen-PMO), which is synthesized via co-condensation of 1,2-bis(triethoxysilyl)ethane and phen-Si using a polyoxyethylene stearyl ether surfactant as a template (under acidic conditions) [66]. Compared with the pure complex, the resulting hybrid material exhibits better thermal stability and a similar emission quantum efficiency. Besides, the PMO material is further synthesized through one-step co-condensation of 1,2-bis(triethoxysilyl)ethane (BTESE) and benzoic acid-functionalized organosilane (BA-Si) using cetyltrimethylammonium bromide (CTAB) as a structure-directing agent under basic conditions (Fig. 3.6, Bottom) [67]. XRD and N_2 adsorption–desorption isotherms reveal the characteristic mesoporous structure with highly uniform pore size distributions. FESEM confirms that the morphology of the PMOs is significantly dependent on the molar ratio of two organosilica precursors. In addition, BA-PMO is attempted as a supporter to link the Tb^{3+} ions via impregnation of $TbCl_3$ into BA-PMO through a ligand exchange reaction. Under the UV radiation, it exhibits a strong characteristic of emitting Tb^{3+} ions.

More recently, Sun et al. prepare periodic mesoporous organosilica material (named as bpd-PMO) through co-condensation of bis(triethoxysilyl)ethane (BTEE)

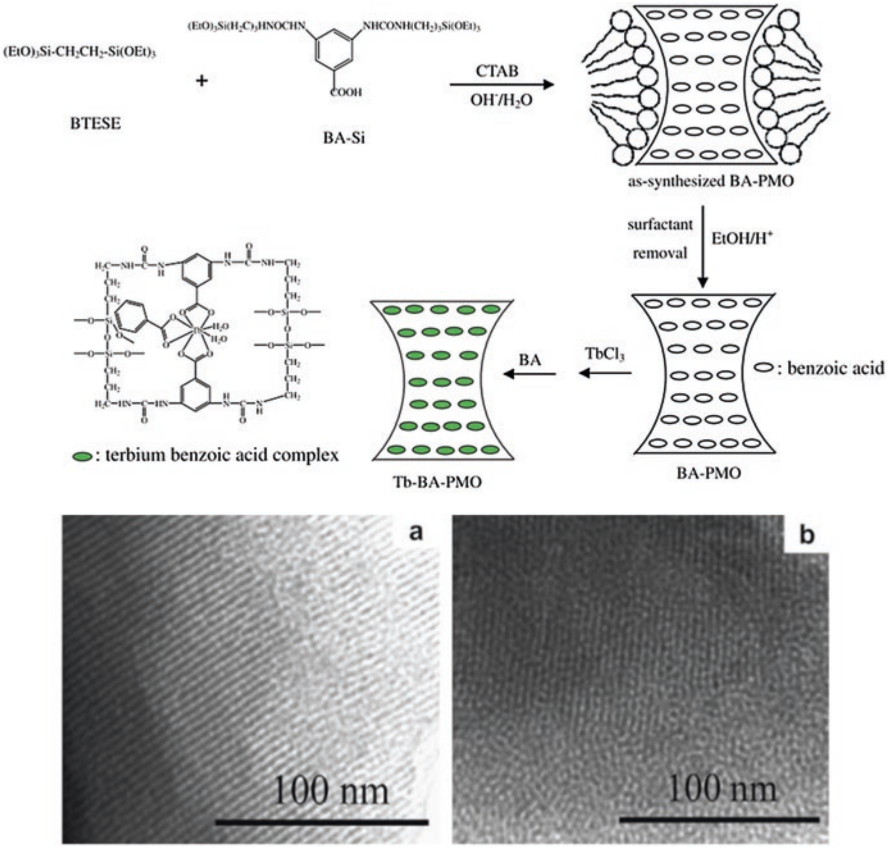

Fig. 3.6 (*Top*) Schematic diagram for synthesis of the novel PMO via a co-condensation of 1,2-bis(triethoxysilyl)ethane (BTESE) and benzoic acid-functionalized organosilane (BA-Si) and its application in incorporation of the Tb^{3+} ions as matrix. (*Bottom*) TEM images of hybrid Tb-BA(0.07)-PMO material recorded along the [100] (*a*) and [110] (*b*) zone axes (Reprinted with permission from Ref. [67]. Copyright 2009 Elsevier)

and a synthesized silsesquioxane precursor 4,4′-bis[$Si(OEt)_3(CH_2)_4$]-2,2′-bipyridine (bpd-Si) [68]. Subsequently, three NIR-luminescent PMO hybrid materials (named as $RE(DBM)_3$bpd-PMO, RE = Er, Nd, Yb) covalently linked with rare earth complexes are prepared via a ligand exchange reaction. The excitation spectra of the $RE(DBM)_3$bpd-PMO extend to the visible light range, whose visible light excitation produces the characteristic NIR luminescence of the corresponding RE^{3+} ions.

In recent years, Li et al. synthesize PMOs by linking rare earth (Tb^{3+}, Eu^{3+}) complexes to mesoporous frameworks through modified 4-mercaptobenzoic acid (MCBA) [69]. From the 29Si MAS NMR spectra, the peaks corresponding to the organosiloxane T_n [$T_n = RSi(OSi)_nOH_{3-n}$, n = 2–3] species can be identified clearly, which indicates the existence of the Si–C bond in the hybrids. Besides, the relative intensity of T_3 NMR signal is obviously stronger than T_2, resulting in the degree of

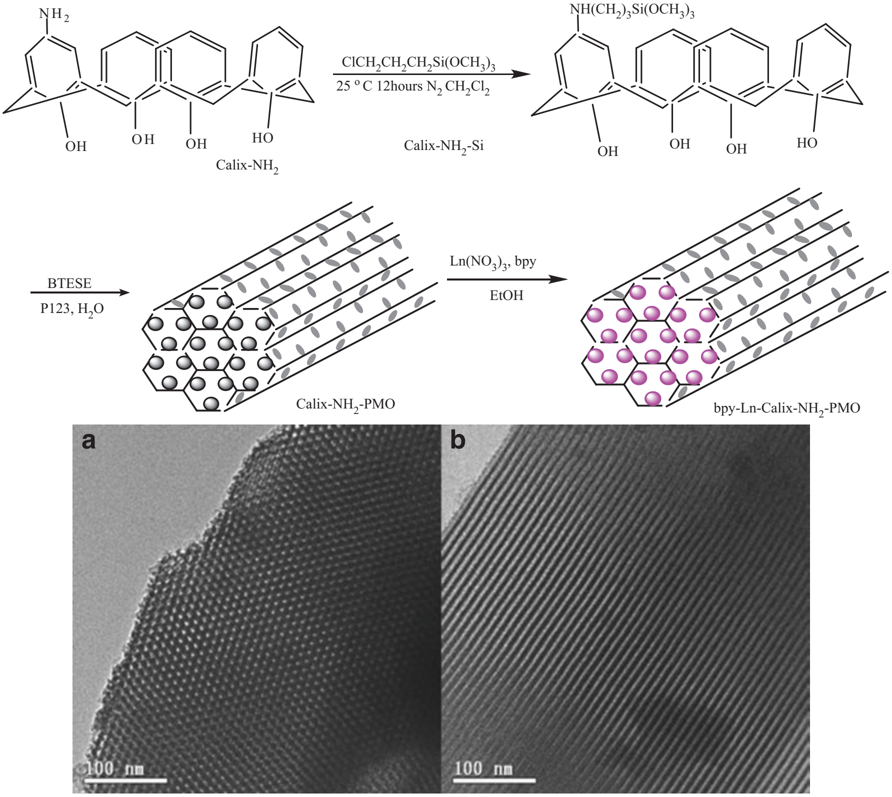

Fig. 3.7 Scheme for synthesis (*Top*) and high-resolution transmission electron microscopy images (*Bottom*) of ternary mesoporous hybrid bpy-Tb-Calix-NH_2-PMO recorded along the [100] (*A*) and [110] (*B*) zone axes (Reprinted with permission from Ref. [70]. Copyright 2011 the Royal Society of Chemistry Publishing Company)

hydrolysis–condensation between BTESE and MCBA is completely. The absence of various siloxane Q_m [$Q_m = Si(OSi)_m(OH)_{4-m}$, m = 2–4] around −90 to −120 ppm suggests that Si–C bond is not decomposed in the process of hydrolysis–condensation. Recently, Li et al. prepare the ternary mesoporous hybrid material bpy-Ln-Calix-NH_2-PMO (Ln = Eu, Tb) by linking ternary rare earth (Eu^{3+}, Tb^{3+}) complexes to PMOs through functionalized Calix-NH_2 ligands [70]. The luminescence properties show that the triple-state energy level of Calix-NH_2 is more suitable for the sensitization of Eu^{3+} than of Tb^{3+}, and the luminescence intensity of the $^5D_0 \rightarrow {}^7F_2$ transition and the $^5D_0$ luminescence quantum efficiency of this material are higher than that of the pure bpy-Eu-Calix-NH_2 complex, further confirming that the ternary complex bpy-Ln-Calix-NH_2 is covalently bonded to the PMO silicon network (see Fig. 3.7).

Gu et al. use molecular linkage phen-Si to construct the phen-NH_2-functionalized periodic mesoporous organosilica (PMOs) hybrids by linking ternary europium complexes with phen-Si linkage and MHPO [71]. It is worth pointing out that the europium hybrids show emission of both europium ion and phen-functionalized PMOs, which can be integrated into the close white luminescence. This provides us a strategy to obtain white emissive rare earth hybrids.

3.5 Photofunctional Rare Earth Hybrid Materials Based on Organically Modified Mesoporous Silica and Other Inorganic Hosts

From above introduction to the three main kinds of organically modified mesoporous silica hybrid materials, we can draw a conclusion that the covalent linker still plays an important role in preparing these mesoporous hybrids by postsynthetic modification and in situ assembly approach. Besides, some work report the comparison of different mesoporous hosts except for the assembly process using different templates. For example, Sun et al. achieve the NIR-luminescent RE(DBM)$_3$phen complexes covalently bonded to the ordered mesoporous materials MCM-41 and SBA-15 via a functionalized phen group phen-Si (RE = Er, Nd, Yb) [72]. The synthesis parameters $X = 12$ and $Y = 6$ h (X denotes RE(DBM)$_3$(H$_2$O)$_2$/phen-MCM-41 molar ratio or RE(DBM)$_3$(H$_2$O)$_2$/phen-SBA-15 molar ratio and Y is the reaction time for the ligand exchange reaction) are selected through a systematic and comparative study. The derivative materials are denoted as RE(DBM)$_3$phen-MCM-41 and RE(DBM)$_3$phen-SBA-15 (RE = Er, Nd, Yb). In addition, RE(DBM)$_3$phen-SBA-15 hybrids show an overall increase in relative luminescent intensity and lifetime compared to the RE(DBM)$_3$phen-MCM-41 materials, which is explained by the comparison of the rare earth ion content and the pore structures of the two kinds of mesoporous materials. Li et al. also prepare rare earth mesoporous hybrid l materials by introducing the ternary rare earth (Eu^{3+}, Tb^{3+}) β-diketonate (TTA, TAA) into the functionalized mesoporous hosts through the coordination bond and covalent bond by using 3-chloropropyltriethoxysilane modified 1,4,7, 10-tetraazacyclododecane (Cyclen-Si) as an organic bridge molecule [73]. Gu et al. prepare a series of hybrid materials by linking rare earth (Eu^{3+}, Sm^{3+}) complexes to mesoporous SBA-15/SBA-16 through 8-hydroxybenz[de]anthracen-7-one modified silane (HBA-Si) as linker [74]. The luminescence properties of these covalently bonded materials (denoted as RE(HBA-SBA-15)$_3$phen and RE(HBA-SBA-16)$_3$phen) are compared with ternary complexes (RE(HBA)$_3$phen) (RE = Eu, Sm). Eu(HBA-SBA-15(16))$_3$phen hybrids display better thermal stability; their luminescent lifetimes and quantum efficiencies are comparable to those of Eu(HBA)$_3$phen complex in spite of its much less effective condensation of Eu^{3+} species. In addition, the luminescent performance of functionalized SBA-15 hybrids is more favorable than that of functionalized SBA-16 hybrids, revealing that SBA-15 is a better host material for rare earth complex than mesoporous silica SBA-16. Guo et al. prepare ternary Eu(TTA)$_3$phen covalently bonded with the general mesoporous material

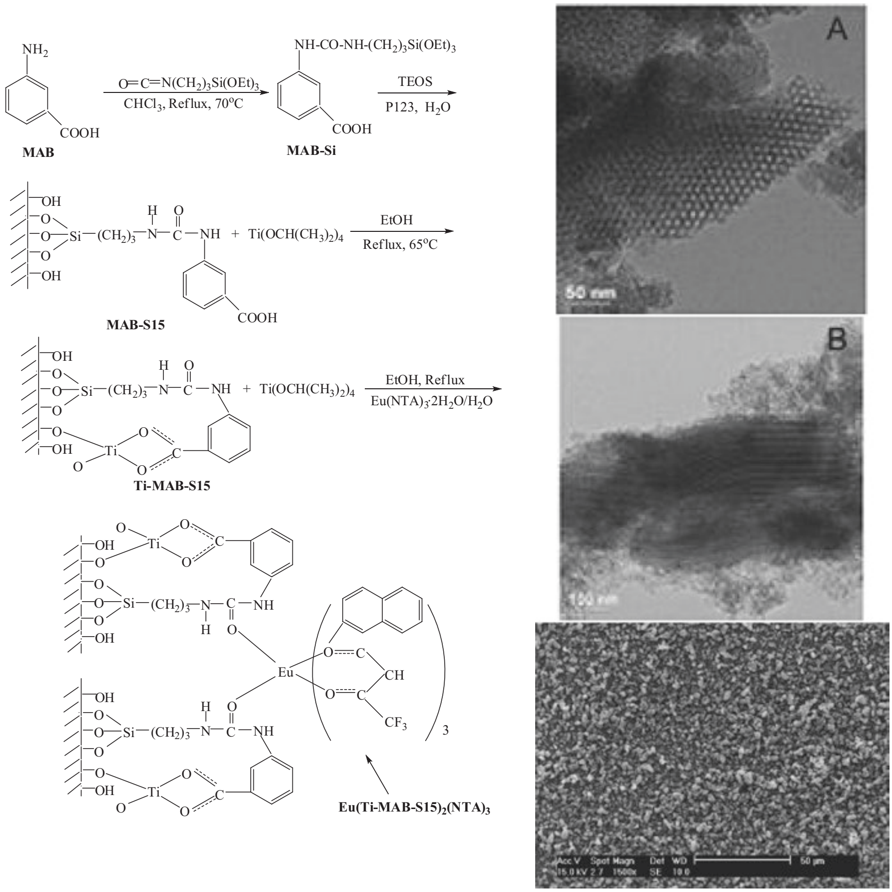

Fig. 3.8 The scheme for synthesis procedure and predicted structure of the (*Left*), TEM images (*top, middle*) recorded along the [100] (*A*) and [110] (*B*) zone axes and SEM image (*bottom*) of mesoporous ternary hybrid titania materials Eu(Ti-MAB-S15)$_2$(NTA)$_3$ (*Right*) (Reprinted with permission from Ref. [76]. Copyright 2011 the Royal Society of Chemistry Publishing Company)

SBA-15 and SBA-15-type of periodic mesoporous organosilica (PMO) material via impregnation of Eu(TTA)$_3$·2H$_2$O into phen-S15 and phen-PMO, respectively, through a ligand exchange reaction [75]. Compared with the sample of Eu(TTA)$_3$phen-PMO, the mesoporous hybrid material Eu(TTA)$_3$phen-S15 exhibits longer luminescent decay time and higher luminescence intensity, emission quantum efficiency, and absolute quantum yield. Meanwhile, the result of thermal treatment demonstrates that the europium complex in Eu(TTA)$_3$phen-S15 material possesses a better thermal stability than that in Eu(TTA)$_3$phen-PMO.

Li et al. prepare multifunctional precursor Ti-MAB-S15 (MAB = meta-aminobenzoic acid) through the reaction of the carboxylic group with titanium alkoxide, and the amino group is modified with the coupling agent TESPIC and covalently bonded to mesoporous silica SBA-15 (Fig. 3.8) [76]. The selection of ligand is the key point for the preparation of this hybrid material. Herein, the organic ligand MAB is selected as multifunctional linker, which not only can be covalently bonded to the framework of mesoporous silica and coordinate to lanthanide ions as well as sensitize the luminescence of them, but also can modify the reactivity of titanium precursor and introduce titania matrix to the hybrid system. Then, novel luminescent mesoporous hybrid titania materials Eu(Ti-MAB-S15)$_2$(NTA)$_3$ are obtained by introducing the Eu(NTA)$_3$·2H$_2$O complex into the hybrid materials Ti-MAB-S15 via a ligand exchange reaction. Compared to the pure complex Eu(NTA)$_3$·2H$_2$O, the mesoporous hybrid titania material Eu(Ti-MAB-S15)$_2$(NTA)$_3$ presents longer luminescent lifetime and higher quantum efficiency, which indicates that the introduction of the multifunctional ligand Ti-MAB-S15 can sensitize the luminescence emission of Eu^{3+} ions.

In addition, they further put forward a novel method to assemble luminescent rare earth hybrid materials containing ordered mesoporous Si–O network and amorphous Ti–O (Al–O) network simultaneously (Fig. 3.9) [77]. Firstly, NTA-functionalized SBA-15 mesoporous hybrid material (NTA-S15) is prepared, in which NTA is covalently bonded to the framework SBA-15 by co-condensation of modified NTA (denoted as NTA–Si) and TEOS. Subsequently, nicotinic acid (NA) is selected as the second ligand, whose carboxylic acid group can react with metallic alkoxide to moderate the reactivity toward hydrolysis and condensation, and the heterocyclic group can coordinate to rare earth ions as well as sensitize the luminescence of them. Finally, after the coordination reaction between rare earth ions and functionalized organic ligand (NTA-S15 and NA-M (M = Ti, Al)) together with the hydrolysis cross-linking reaction, the final mesoporous hybrids Ln(NA-M)$_2$(NTA-S15)$_3$ (Ln = Eu, Tb; and M = Ti, Al) are obtained. Further investigation on the luminescence properties shows that the lanthanide mesoporous material containing Al–O network presents stronger luminescence intensities, longer lifetimes, and higher luminescence quantum efficiencies than the lanthanide mesoporous hybrids containing Ti–O network, which indicates Al–O network is a better candidate host for supporting the lanthanide complex than Ti–O network.

Pang et al. recently prepare the luminescent mesoporous hybrids, Eu(M-BDA)$_2$(TTA-SBA-15)$_3$ and Eu(M-BDA)$_2$(TTA-MCM41)$_3$ (M = Ti, Al) through the coordination reaction between Eu^{3+} ions and a functionalized organic ligand (TTA-SBA-15 or TTA-MCM41 and M-BDA (M = Ti, Al)) followed by the hydrolysis cross-linking reaction [78]. Results show that SBA-15-type mesoporous hybrid Eu(M-BDA)$_2$(TTA-SBA-15)$_3$, with larger pore sizes than the corresponding MCM-41-type hybrids Eu(M-BDA)$_2$(TTA-SBA-15)$_3$, presents longer luminescent lifetimes and higher quantum efficiency than the latter because of spatial confinements of mesoporous matrix nanochannels. The Al–O-based mesoporous hybrids also exhibit more excellent luminescent properties than the corresponding Ti–O-based hybrids, suggesting that the Al–O host is more beneficial to Eu^{3+} ion luminescence than the Ti–O host. The quantum efficiency of Eu(Al-BDA)(TTA-SBA-15)$_3$ is high, even up to 43%.

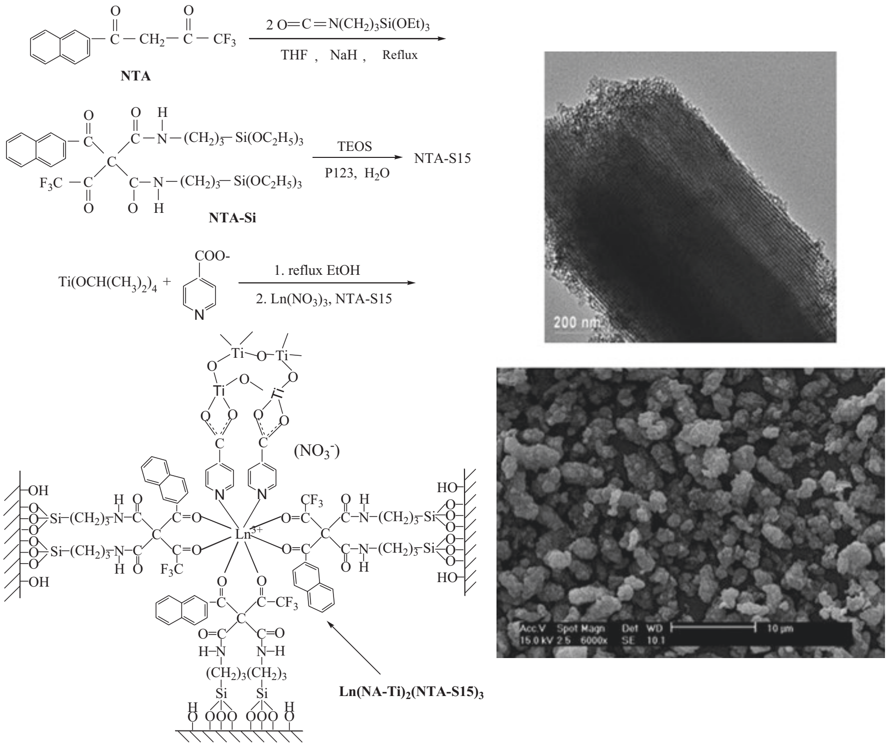

Fig. 3.9 The scheme for synthesis procedure and predicted structure (*Left*), TEM and SEM images (*Right*) of mesoporous hybrid materials RE(NA-Ti)$_2$(NTA-S15)$_3$ (RE = Eu, Tb) (Reprinted with permission from Ref. [77]. Copyright 2011 the Royal Society of Chemistry Publishing Company)

3.6 Photofunctional Rare Earth Hybrid Materials Based on Organically Modified Mesoporous Silica and Polymer Units

Fu et al. incorporate diurea cross-linked poly(oxyethylene) (POE)/siloxane hybrid structure (di-ureasil) into the hexagonal array of one-dimensional channels of mesoporous silica MCM-41 [79]. The hybrids display the intrinsic green emission of MCM-41 superposed to the blue and purplish-blue di-ureasil components. Time-resolved spectroscopy provides further support from energy transfer between the mesoporous silica and the di-ureasil matrix.

Yan's group focus on the research of ternary assembly of organically modified mesoporous silica and polymer unit by means of the postsynthetic technology [80–83]. Li et al. first assemble the mesoporous luminescent polymeric hybrid materials containing rare earth (Eu^{3+}, Tb^{3+}) complexes covalently bonded to mesoporous silica SBA-15 [81]. The detailed luminescence studies on all the materials show that the ternary rare earth mesoporous polymeric hybrid materials present stronger luminescent intensities, longer lifetimes, and higher luminescent quantum efficiencies than the binary rare earth mesoporous hybrid materials, indicating that the introduction of the organic polymer chain is beneficial for the luminescence properties of the overall hybrid system. Further, they conduct the systematic and comparative study of the mesoporous materials covalently bonded with rare earth complexes containing organic polymeric chains, designated as Ln(DBM-SBA-15)$_3$PMAA and Ln(DBM-SBA-16)$_3$PMAA (Ln = Eu, Tb; DBM-SBA-15 and DBM-SBA-16 denote DBM-functionalized SBA-15 mesoporous material and DBM-functionalized SBA-16 material, respectively) (Fig. 3.10) [81]. In addition, for further comparison, SBA-15 and SBA-16 covalently bonded with the binary Ln^{3+} complex with DBM ligand are also synthesized, denoted as Ln(DBM-SBA-15)$_3$ and Ln(DBM-SBA-16)$_3$ (Ln = Eu, Tb), respectively. The luminescence properties of all synthesized materials are comprehensively characterized and compared.

Li et al. further compare a series of ternary mesoporous polymeric hybrids, TTA-S16-Eu-PMMA, TTA-S16-Eu-PMAA, and TTA-S16-Eu-PVP (PVP = polyvinylpyrrolidone), which are assembled by the Eu^{3+} complex covalently attached to the TTA directly functionalized ordered mesoporous SBA-16 and three organic polymers [82]. The ternary rare earth mesoporous polymeric hybrids show an overall increase in luminescent lifetime and quantum efficiency compared to binary rare earth mesoporous hybrid TTFA-S16-Eu, especially the mesoporous hybrid with PVP exhibits the highest luminescence quantum efficiency and longest lifetime. Gu et al. prepare polymeric mesoporous hybrid materials containing europium (III) complexes incorporated to mesoporous silica SBA-15/SBA-16 by simple physical doping (impregnation) methods, followed by the additional polymerization reaction of the monomer 4-vinylpyridine (vpd) extending along the mesoporous channels [83]. After the physical doping and the polymerization reaction, the final ternary materials Eu(β-diketonate)$_3$pvpd-SBA-15/Eu(β-diketonate)$_3$pvpd-SBA-16 are obtained. The XRD and BET results reveal that all of these hybrid materials have uniformity in the mesostructure. The detailed luminescence investigation on all the materials shows that Eu(TAA)$_3$pvpd-SBA-16 has the highest luminescence intensity and the materials with TAA ligands have longer lifetimes.

Li et al. realize the linkage of the binary and ternary Eu^{3+} complexes to the functionalized ordered mesoporous SBA-15 with the modified polymer poly(ethylene glycol) (PEG) as a “bifunctional bridge,” where PEG is firstly modified with the coupling agent TESPIC and covalently bonded to mesoporous silica SBA-15 (designated as PEG-SBA-15) [84]. They further prepare polymer-functionalized mesoporous SBA-16-type hybrid materials with encapsulated rare earth (Eu^{3+} and Tb^{3+}) complexes for luminescence. The organic molecule acrylamide (AM) is modified by a silane coupling agent TESPIC to form an alkene precursor, which is then covalently bonded to a mesoporous SBA-16 backbone [85]. Then, the flexible polymer chain polyacrylamide (PAM) within the pores of SBA-16 can be formed by initiating the monomer. The luminescent mesoporous hybrids (denoted as RE(S16-PAM-Si)$_3$ and RE(S16-PAM-Si)$_3$phen, respectively) with the organic polymer acting as a flexible linker between the mesoporous framework and the rare earth complex are finally attained.

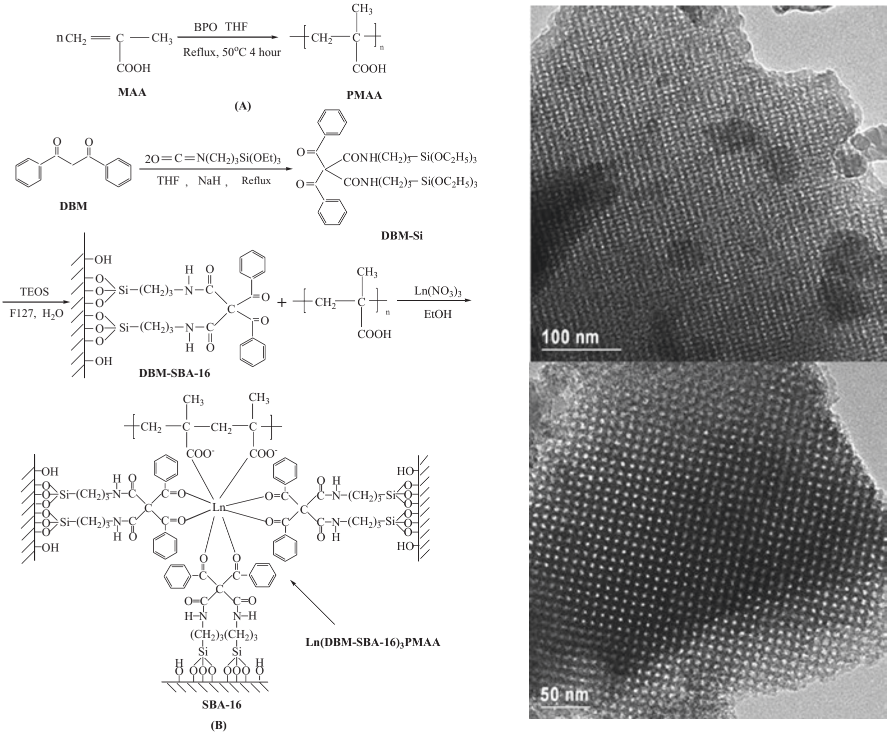

Fig. 3.10 Selected scheme of synthesis process of PMAA (*A*) and the mesoporous polymeric hybrids Ln(DBM-SBA-16)$_3$PMAA (*B*) (*Left*); HRTEM images of Eu(DBM-SBA-15)$_3$PMAA (*top*) and Eu(DBM-SBA-16)$_3$PMAA (*bottom*) (*Right*) (Reprinted with permission from Ref. [81]. Copyright 2010 the Royal Society of Chemistry)

3.7 Conclusion and Outlook

In conclusion, recent research progress in the photofunctional rare earth hybrid materials based on mesoporous silica has been summarized, which mainly consist of three important classes with the different mesoporous hosts to be functionalized. The first is the rare earth hybrids based on MCM-41(or 48). The second is the rare earth hybrids based on SBA-51(or 16). The third is the rare earth hybrids based on POMs. Among all the results, it is suggested that SBA-15 is the most favorable host for the luminescence of rare earth ions, whose mesoporous hybrids display the best luminescent performance. Besides, both inorganic host and organic polymer host can be introduced to the mesoporous hybrid materials, providing new opportunities to obtain new systems and new applications. However, some problems still exist in the field of photofunctional rare earth materials based on mesoporous silica. The most important one is how to develop the practical applications of these materials.

References

1. Lebeau B, Galarneau A, Linden M (2013) Introduction for 20 years of research on ordered mesoporous materials. Chem Soc Rev 42:3661–3662
2. Kresge CT, Roth WJ (2013) The discovery of mesoporous molecular sieves from the twenty year perspective. Chem Soc Rev 42:3663–3670
3. Chong ASM, Chong ZXS (2003) Functionalization of SBA-15 with APTES and characterization of functionalized materials. J Phys Chem B 107:12650–12657
4. Sayari A, Yang Y, Kruk M, Jaroniec M (1999) Expanding the pore size of MCM-41 silicas: use of amines as expanders in direct synthesis and postsynthesis procedures. J Phys Chem B 103:3651–3658
5. Mehdi A, Reye C, Corriu R (2011) From molecular chemistry to hybrid nanomaterials. Design and functionalization. Chem Soc Rev 40:563–574
6. Mizoshita N, Tani T, Inagaki S (2011) Syntheses, properties and applications of periodic mesoporous organosilicas prepared from bridged organosilane precursors. Chem Soc Rev 40:789–800
7. Kresge CT, Leonowicz ME, Roth WJ, Vartuli JC, Beck JS (1992) Ordered mesoporous molecular sieves synthesized by a liquid-crystal template mechanism. Nature 359:710–712
8. Beck JS, Vartuli JC, Roth WJ, Leonowicz ME, Kresge CT, Schmitt KD, Chu CT, Olson DH, Sheppard EW, McCullen SB, Higgins JB, Schlenker JL (1992) A new family of mesoporous molecular sieves prepared with liquid crystal templates. J Am Chem Soc 114:10834–10843
9. Scott J, Wirnsberger G, Stucky GD (2001) Mesoporous and mesostructured materials for optical applications. Chem Mater 13:3140–3150
10. Lim MH, Stein A (1999) Comparative studies of grafting and direct synthesis of inorganic-organic hybrid mesoporous materials. Chem Mater 11:3285–3295
11. Zhao DY, Feng JP, Huo QS, Melosh N, Fredrickson CH, Chmelka BF, Stucky GD (1998) Triblock copolymer syntheses of mesoporous silica with periodic 50 to 300 angstrom pores. Science 279:548–552
12. Zhao DY, Sun JY, Li QZ, Stucky GD (2000) Morphological control of highly ordered mesoporous silica SBA-15. Chem Mater 12:275–278
13. Newalkar BL, Komarneni S, Katsuki H (2000) Rapid synthesis of mesoporous SBA-15 molecular sieve by a microwave– hydrothermal process. Chem Comm:2389–2390
14. Zhao DY, Huo QS, Feng JP, Chmelka BF, Stucky GD (1998) Nonionic triblock and star diblock copolymer and oligomeric surfactant syntheses of highly ordered, hydrothermally stable, mesoporous silica structures. J Am Chem Soc 120:6024–6036
15. Melde BJ, Holland BT, Blanford CF, Stein A (1999) Mesoporous sieves with unified hybrid inorganic/organic frameworks. Chem Mater 11:3302–3308
16. Inagaki S, Guan S, Fukushima Y, Ohsuna T, Terasaki O (1999) Novel mesoporous materials with a uniform distribution of organic groups and inorganic oxide in their frameworks. J Am Chem Soc 121:9611–9614
17. Asefa T, MacLachlan MJ, Coombs N, Ozin GA (1999) Periodic mesoporous organosilicas with organic groups inside the channel walls. Nature 402:867–871
18. Smith JV (1988) Topochemistry of zeolites and related materials. I. Topology and geometry. Chem Rev 88:149–182
19. Mann S (1993) Molecular tectonics in biomineralization and biomimetic materials chemistry. Nature 365:499–505
20. Shephard DS, Zhou WS, Maschmeyer T (1998) Site directed surface derivatization of electron microscopy MCM-41: use of high-resolution transmission and molecular recognition for determining the position of functionality within mesoporous materials. Angew Chem Int Edi 37:2719–2723
21. Burket SL, Sims SD, Mann S (1996) Synthesis of hybrid inorganic–organic mesoporous silica by co-condensation of siloxane and organosiloxane precursors. Chem Comm:1367–1368

22. Fowler CE, Burkett SL, Mann S (1997) Synthesis and characterization of ordered organo–silica–surfactant mesophases with functionalized MCM-41-type architecture. Chem Comm:1769–1770
23. Stein A, Melde BJ, Schroden RC (2000) Hybrid inorganic-organic mesoporous silicates - nanoscopic reactors coming of age. Adv Mater 12:1403–1419
24. Xu QH, Li LS, Li B, Yu JH, Xu RR (2000) Encapsulation and luminescent property of tetrakis(1-(2-thenoyl)-3,3,3-triuoracetate) europium N-hexadecyl pyridinium in modi®ed Si±MCM-41. Microp Mesop Mater 38:351–358
25. Fu LS, Xu QH, Zhang HJ, Li LS, Meng QG, Xu RR (2002) Preparation and luminescence properties of the mesoporous MCM-41s intercalated with rare earth complex. Mater Sci Eng B 88:68–72
26. Xu QH, Li LS, Liu XS, Xu RR (2002) Incorporation of rare-earth complex $Eu(TTA)_4C_5H_5NC_{16}H_{33}$ into surface-modified Si-MCM-41 and its photophysical properties. Chem Mater 14:549–555
27. Xu QH, Dong WJ, Li HW, Li LS, Feng SH, Xu RR (2003) Encapsulation and luminescent property of $[C_5H_5NC_{16}H_{33}][Eu(TTA)_4]$ (TTA: tetrakis(1-(2-thenoy)-3,3,3-trifluoracetate) in chiral Si-MCM-41. Solid State Sci 5:777–782
28. Gago S, Fernandes JA, Rainho JP, Ferreira RAS, Pillinger M, Valente AA, Santos TM, Carlos LD, Ribeiro-Claro PJA, Goncalves IS (2005) Highly luminescent tris(β-diketonate) europium(III) complexes immobilized in a functionalized mesoporous silica. Chem Mater 17:5077–5084
29. Bruno SM, Coelho AC, Ferreira RAS, Carlos LD, Pillinger M, Valente AA, Ribeiro-Claro P, Gonçalves IS (2008) MCM-41 derivatised with pyridyl groups and its use as a support for luminescent europium(III) complexes. Eur J Inorg Chem 2008:3786–3795
30. Bruno SM, Ferreira RAS, Carlos LD, Pillinger M, Ribeiro-Claro P, Gonçalves IS (2008) Synthesis, characterization and luminescence properties of MCM-41 impregnated with an Eu^{3+} β-diketonate complex. Microp Mesop Mater 113:453–462
31. Felício MR, Nunes TG, Vaz PM, Botas AMP, Ribeiro-Claro P, Ferreira RAS, Freire RO, Vaz PD, Carlos LD, Nunes CD, Nolasco MM (2014) Modelling the luminescence of extended solids: an example of a highly luminescent MCM-41 impregnated with a Eu^{3+} β-diketonate complex. J Mater Chem C 2:9701–9711
32. Li HR, Lin J, Fu LS, Guo JF, Meng QG, Liu FY, Zhang HJ (2002) Phenanthroline-functionalized MCM-41 doped with europium ions. Microp Mesop Mater 55:103–107
33. Sun LN, Yu JB, Zhang HJ, Meng QG, Ma E, Peng CY, Yang KY (2007) Near-infrared luminescent mesoporous materials covalently bonded with ternary rare earth [Er(III), Nd(III), Yb(III), Sm(III), Pr(III)] complexes. Microp Mesop Mater 98:156–165
34. Sun LN, Zhang Y, Yu JB, Yu SY, Dang S, Peng CY, Zhang HJ (2008) Design and synthesis of near-IR luminescent mesoporous materials covalently linked with tris(8-hydroxyquinolinate) rare earth(III) complexes. Microp Mesop Mater 115:535–540
35. Feng J, Song SY, Xing Y, Zhang HJ, Li ZF, Sun LN, Guo XM, Fan WQ (2009) Synthesis, characterization, and near-infrared luminescent properties of the ternary thulium complex covalently bonded to mesoporous MCM-41. J Solid State Chem 182:435–441
36. Feng J, Song SY, Fan WQ, Sun LN, Guo XM, Peng CY, Yu JB, Yu YN, Zhang HJ (2009) Near-infrared luminescent mesoporous MCM-41 materials covalently bonded with ternary thulium complexes. Microp Mesop Mater 117:278–284
37. Li Y, Yan B (2008) Hybrid materials of MCM-41 functionalized by rare earth (Tb^{3+}, Eu^{3+}) complexes of modified *meta*-methylbenzoic acid: covalently bonded assembly and photoluminescence. J Solid State Chem 181:1032–1039
38. Li Y, Yan B (2009) Photophysical properties of rare earth hybrids covalently bonded to functionalized MCM-41 by modified aromatic carboxylic acids. J Fluorescence 19:191–201
39. Li Y, Yan B (2010) Rare earth (Tb^{3+}, Eu^{3+}) functionalized MCM-41 through modified *meta*-aminobenzoic acid linkage: covalently bonding assembly, physical characterization and photoluminescence. Microp Mesop Mater 128:62–70

40. Yan B, Zhou B (2008) Two photoactive rare earth (Eu^{3+}, Tb^{3+}) hybrid materials of modified beta-diketone bridge directly covalently bonded mesoporous host (MCM-41). J Photochem Photobiol A Chem 195:314–322
41. Yan B, Li Y, Zhou B (2009) Covalently bonding assembly and photophysical properties of luminescent molecular hybrids Eu-TTA-Si and Eu-TTASi-MCM-41 by modified thenoyltrifluoroacetone. Microp Mesop Mater 120:317–324
42. Li YJ, Yan B, Wang L (2011) Rare earth (Eu^{3+}, Tb^{3+}) Mesoporous hybrids with calix[4]arene derivative covalently linking MCM-41: physical characterization and photoluminescence property. J Solid State Chem 184:2571–2579
43. Gu YJ, Yan B (2013) Europium (III) complex functionalized Si-MCM-41 hybrid materials with visible-light-excited luminescence. Inorg Chim Acta 408:96–102
44. Meng QG, Boutinaud P, Franville AC, Zhang HJ, Mahiou R (2003) Preparation and characterization of luminescent cubic MCM-48 impregnated with an Eu^{3+} β-diketonate complex. Microp Mesop Mater 65:127–136
45. Meng QG, Boutinaud P, Zhang HJ, Mahiou R (2007) Luminescence properties of Eu^{3+} β-diketonates incorporated in cubic mesoporous silica. J Lumin 124:15–22
46. Peng CY, Zhang HJ, Meng QG, Li HR, Yu JB, Guo JF, Sun LN (2005) Synthesis and luminescence properties of SBA-15 functionalized with covalently bonded ternary europium complex. Inorg Chem Comm 8:440–443
47. Peng CY, Zhang HJ, Fu LS, Meng QG, Fu LS, Li HR, Sun LN, Guo XM (2005) Synthesis, characterization, and luminescence properties of the ternary europium complex covalently bonded to mesoporous SBA-15. J Phys Chem B 109:15278–15287
48. Corriu RJP, Mehdi A, Reye C, Thieuleux C, Frenkel A, Gibaud A (2004) Preparation of ordered SBA-15 mesoporous silica containing chelating groups. Study of the complexation of EuIII inside the pore channels of the materials. New J Chem 28:156–160
49. Sun LN, Zhang HJ, Yu JB, Yu SY, Peng CY, Dang S, Guo XM, Feng J (2008) Near-infrared emission from novel tris(8-hydroxyquinolinate)rare earth(III) complexes-functionalized mesoporous SBA-15. Langmuir 24:5500–5507
50. Sun LN, Zhang Y, Yu JB, Peng CY, Zhang HJ (2008) Ternary rare earth (Er^{3+}, Nd^{3+}, Yb^{3+}, Sm^{3+}, Pr^{3+}) complex-functionalized mesoporous SBA-15 materials that emit in the near-infrared range. J Photochem Photobiol A Chem 199:57–63
51. Li Y, Yan B, Yang H (2008) Construction, characterization, and photoluminescence of mesoporous hybrids containing europium (III) complexes covalently bonded to SBA-15 directly functionalized by modified *beta*-diketone. J Phys Chem C 112:3959–3968
52. Kong LL, Yan B, Li Y (2009) Hybrid materials of SBA-15 functionalized by Tb^{3+} complexes of modified acetylacetone: covalently bonded assembly and photoluminescence. J Alloys Compds 481:549–554
53. Kong LL, Yan B, Li Y (2009) Mesoporous hybrids containing Eu^{3+} complexes covalently bonded to SBA-15 functionalized: assembly, characterization and photoluminescence. J Solid State Chem 182:1631–1637
54. Yan B, Li Y (2010) Luminescent ternary inorganic-organic mesoporous hybrids Eu(TTASi-SBA-15)phen: covalent linkage in TTA directly functionalized SBA-15. Dalton Trans 39:1480–1487
55. Li YJ, Yan B, Li Y (2010) Luminescent rare earth (Eu^{3+}, Tb^{3+}) ternary mesoporous hybrids with functionalized β-diketones (TTA, DBM) covalently linking SBA-15 and 2,2′-bpyridine (bpy). Microp Mesop Mater 131:82–88
56. Li YJ, Yu XD, Wang XJ, Yang ML (2014) Rare earth (Eu^{3+}, Tb^{3+}) functionalized SBA-15 through modified hexafluoroacetylacetone linkage: covalently bonding construction, physical characterization, and luminescent properties. J Mater Res 29:675–683
57. Li YY, Yan B, Guo L, Li YJ (2012) Ternary rare earth sulfoxide-functionalized mesoporous hybrids Phen-RE(OBDS(BSAB))$_3$-SBA-15 (RE = Eu, Tb): covalently bonded assembly, characterization, and photoluminescence. Microp Mesop Mater 148:73–79

58. Li YJ, Yan B, Wang L (2011) Calix[4]arene derivative functionalized rare earth (Eu, Tb) SBA-15 mesoporous hybrids with covalent bond: assembly, characterization and photoluminescence. Dalton Trans 40:6722–6731
59. Yan B, Li YY, Qiao XF (2012) Photofunctional metalloporphryns functionalized mesoporous hybrids phen-ln(LSi)-SBA-15 (ln = Nd, Yb, L = porphyrin derivatives). Microp Mesop Mater 158:129–136
60. Li YY, Yan B, Qiao XF (2013) Visible light excitation and near-infrared luminescence of rare earth mesoporous hybrids through 9-hydroxyphenalen-1-one linkage by chemical bonds. Microp Mesop. Mater 169:60–66
61. Gu YJ, Yan B (2013) Novel photoversion rare earth functionalized SBA-15 mesoporous hybrids: ultraviolet-visible excitation and visible-NIR emission. Eur J Inorg Chem:2963–2970
62. Gu YJ, Yan B (2013) Rare earth mesoporous SBA-15 hybrids through functionalized 6-hydroxybenz[de]anthracen-7-one linkage: UV-visible light sensitization and visible-NIR luminescence. J Coll Interf Sci 393:36–43
63. Li QP, Yan B (2012) Luminescent hybrid materials of rare earth β-diketonate and mesoporous host through the covalent and ion bonding with anion metathesis. Dalton Trans 41:8567–8574
64. Li YJ, Yan B, Li Y (2010) Hybrid materials of SBA-16 functionalized by rare earth (Eu^{3+}, Tb^{3+}) complexes of modified *β*-diketone (TTA and DBM): covalently bonding assembly and photophysical properties. J Solid State Chem 183:871–877
65. Gu YJ, Yan B, Qiao XF (2013) Novel light conversion hybrids of SBA-16 functionalized by rare earth (Eu^{3+}, Nd^{3+}, Yb^{3+}) complexes of modified 2-methyl-9-hydroxyphenalenoe and 1,10-phenanthroline. J Solid State Chem 199:116–122
66. Guo XM, Wang XM, Zhang HJ, Fu LS, Guo HD, Yu JB, Carlos LD, Yang KY (2008) Preparation and luminescence properties of covalent linking of luminescent ternary europium complexes on periodic mesoporous organosilica. Microp Mesop Mater 116:28–35
67. Guo XM, Guo HD, Fu LS, Zhang HJ, Deng RP, Sun LN, Feng J, Dang S (2009) Novel hybrid periodic mesoporous organosilica material grafting with Tb complex: synthesis, characterization and photoluminescence property. Microp Mesop Mater 119:252–258
68. Sun LN, Mai WP, Dang S, Qiu YN, Deng W, Shi LY, Yan W, Zhang HJ (2012) Near-infrared luminescence of periodic mesoporous organosilicas grafted with rare earth complexes based on visible-light sensitization. J Mater Chem 22:5121–5127
69. Li Y, Yan B, Li YJ (2010) Sulfide functionalized rare earth (Eu/Tb) periodic mesoporous organosilicas (PMOs) hybrids with covalent bond: physical characterization and photoluminescence. Microp Mesop Mater 132:87–93
70. Li YJ, Wang L (2011) Photoactive rare earth hybrids covalently bonded to functionalized periodic mesoporous organosilica (PMO) by calix[4]arene derivative. J Mater Chem 21:1130–1138
71. Yan B, Gu YJ (2013) A novel white-luminescent ternary europium hybrids with phenanthroline functionalized periodic mesoporous organosilicas (PMOs) and 2-methyl-9-hydroxyphenalenone. Inorg Chem Comm 34:75–78
72. Sun LN, Zhang HJ, Peng CY, Yu JB, Meng QG, Fu LS, Liu FY, Guo XM (2006) Covalent linking of near-infrared luminescent ternary rare earth (Er^{3+}, Nd^{3+}, Yb^{3+}) complexes on functionalized mesoporous MCM-41 and SBA-15. J Phys Chem B 110:7249–7258
73. Yan B, Li QP (2014) Photofunctional hybrids of rare earth (Eu^{3+}, Tb^{3+})/beta-diketonate functionalized MCM-41/ SBA-15 mesoporous host prepared with 1,4,7,10-tetraazacyclododecane modified siloxane as covalent linkage. Microp Mesop Mater 196:284–291
74. Guo XM, Guo HD, Fu LS, Deng RP, Chen W, Feng J, Dang S, Zhang HJ (2009) Synthesis, spectroscopic properties, and stabilities of ternary europium complex in SBA-15 and periodic mesoporous organosilica: a comparative study. J Phys Chem C 113:2603–2610
75. Gu YJ, Yan B (2016) Eu^{3+}/Sm^{3+} hybrids based with 8-hydroxybenz[de]anthracen-7-one organically modified mesoporous silica SBA-15/16. Solid State Sci 50:9–17
76. Li YJ, Yan B (2011) Preparation, characterization and luminescence properties of the ternary europium complexes covalently bonded to titania and mesoporous SBA-15. J Mater Chem 21:8129–8136

77. Yan B, Li YJ (2011) Photoactive rare earth (Eu^{3+}, Tb^{3+}) centered hybrid systems with titania-mesoporous silica / aluminum mesoporous silica based hosts. J Mater Chem 21:18454–18461
78. Pang XL, Zhang HL, Yu XD, Wang T, Geng LJ, Wang YQ, Li YJ (2015) Synthesis and characterization of novel luminescent europium(III) hybrid materials with a host based on titania–mesoporous silica or alumina–mesoporous silica. RSC Adv 5:84790–84796
79. Fu LS, Ferreira RAS, Valente A, Rocha b LDC (2006) Optically functional nanocomposites with poly(oxyethylene)-based di-ureasils and mesoporous MCM-41. Microp Mesop Mater 94:185–192
80. Li YJ, Yan B (2009) Rare earth (Eu^{3+}, Tb^{3+})/beta-diketone modified mesoporous SBA-15/organic polymer hybrids: chemically bonded construction, physical characterization, and photophysical properties. Inorg Chem 48:8276–8285
81. Li YJ, Yan B (2010) Photoactive europium(III) centered mesoporous hybrids with 2-thenoyltrifluoroacetone functionalized SBA-16 and organic polymers. Dalton Trans 39:2554–2562
82. Li YJ, Yan B, Li Y (2010) Rare earth (Eu^{3+}, Tb^{3+}) centered mesoporous hybrids with 1,3-diphenyl-1,3-propanepione covalently linking SBA-15 (SBA-16) and poly(methylacrylic acid). Chem Asi J 5:1642–1651
83. Gu YJ, Yan B, Li YY (2012) Ternary europium mesoporous polymeric hybrid materials Eu(β-diketonate)$_3$pvpd-SBA-15(16): host-guest construction, characterization and photoluminescence. J Solid State Chem 190:36–44
84. Li Y, Wang JL, Chain W, Wang X, Jin Z, Lia XQ (2013) Coordination assembly and characterization of europium(III) complexes covalently bonded to SBA-15 directly functionalized by modified polymer. RSC Adv 3:14057–14065
85. Li Y, Zhu RD, Wang JL, Wang X, Liu SH (2015) Polyacrylamide modified mesoporous SBA-16 hybrids encapsulated with a rare earth (Eu^{3+}/Tb^{3+}) complex. New J Chem 39:8658–8666

Chapter 4
Photofunctional Rare Earth Hybrid Materials Based on Functionalized Microporous Zeolites

Abstract This chapter mainly focuses on recent research progress in photofunctional rare earth hybrid materials based on functionalized microporous zeolites. It covers photofunctional rare earth hybrid materials based on zeolite X, zeolite A, and zeolite L, respectively. Among them the emphasis is put on the hybrid systems based on zeolite L because they are most intensively studied.

Keywords Rare earth ion • Photofunctional hybrid material • Functionalized zeolite • Luminescence

4.1 Zeolite, Rare Earth Ion-Functionalized Zeolites, and Their Photophysical Properties

Molecular sieves are microporous solids with pores of the size of molecular or nanoscale dimensions, 0.3–2.0 nm in diameter. Some are crystalline with a uniform pore size delineated by their crystal structure, for example, zeolites. Most molecular sieves in practice today are zeolites [1].

Zeolites are natural or synthetic crystalline aluminum silicate of group IA and group IIA elements, such as sodium (Na), potassium (K), magnesium (Mg), and calcium (Ca), whose pores are of molecular dimensions [2]. Chemically, they are represented by the empirical formula: $M_{2n}O \cdot Al_2O_3 \cdot ySiO_2 \cdot wH_2O$ where y is 2–200, *n* is the cation valence, and *w* represents the water contained in the voids of the zeolite. Structurally, they are complex crystalline inorganic polymers based on an infinitely extending three-dimensional, four-connected framework of AlO_4 and SiO_4 tetrahedra linked to each other by the sharing of oxygen ions. Each AlO_4 tetrahedron in the framework bears a net negative charge which is balanced by an extra-framework cation. The framework structure contains intracrystalline channels or interconnected voids that are occupied by the cations and water molecules. The cations are mobile and ordinarily undergo ion exchange. The water may be removed reversibly, generally by the application of heat, which leaves intact a crystalline host structure permeated by the micropores and voids which may amount to 50% of the crystals by volume. The intracrystalline channels or voids can be one-, two-, or three-dimensional. The preferred type has two or three dimensions to facilitate

B. Yan, *Photofunctional Rare Earth Hybrid Materials*,
Springer Series in Materials Science 251, DOI 10.1007/978-981-10-2957-8_4

intracrystalline diffusion in widespread application such as catalysis, gas absorption, water filtration, etc. [1, 2]. The structures of zeolite comprise of a three-directional network of $[AlO_4]^{5-}$, and $[SiO_4]^{4-}$ tetrahedron linked via bridging oxygen atoms are assembled into secondary building units which may be simple polyhedra, such as cubes, hexagonal prisms, or cubo-octahedra. The secondary units in the final framework structure generate different kinds of holes of negative charge density due to the presence of Al^{3+}, and the net negative charge can be balanced by metallic cations, protons, or cationic complex. Cages and channels of discrete size in the zeolite are normally occupied by water molecules [1, 3].

More than 70 novel, distinct framework structures of zeolites are known, which exhibit pore sizes from 0.3 to 1.0 nm and pore volumes from about 0.10 to 0.35 cm^3/g. Typical zeolite pore sizes include small-pore zeolites with 8-ring pores, free diameters of 0.30–0.45 nm (e.g., zeolite A); medium-pore zeolites with 10-ring pores, 0.45–0.60 nm in free diameter (ZSM-5); large-pore zeolites with 12-ring pores of 0.6–0.8 nm (e.g., zeolites X, Y); and extra-large-pore zeolites with 14-ring pores (e.g., UTD-1), respectively. Some important types of zeolite have been used in commercial applications, including the zeolite minerals mordenite, chabazite, erionite, clinoptilolite, and the synthetic zeolite types A, X, Y, and L [1, 2]. The low silica zeolites represented by zeolites A and X are aluminum-saturated, have the highest cation concentration, and give optimum adsorption properties in terms of capacity, pore size, and three-dimensional channel systems. They represent highly heterogeneous surfaces with a strongly hydrophilic surface selectivity. The intermediate Si/Al zeolites (Si/Al of 2–5) consist of the natural zeolites erionite, chabazite, clinoptilolite, and mordenite and the synthetic zeolites Y, mordenite, omega, and L. These materials are still hydrophilic in this Si/Al range. The high silica zeolites with Si/Al of 10–100 can be generated by either thermochemical framework modification of hydrophilic zeolites or by direct synthesis. In the modification route stabilized, siliceous variants of Y, mordenite, and erionite and over a half-dozen other zeolites have been prepared by steaming and acid extraction. These materials are reported to be hydrophobic and organophilic and represent a range of pore sizes from 0.4 to 0.8 nm.

Zeolites are endowed with uniform cavities and channels, which have opened new possibilities for numerous application fields, not only in catalysis and absorption but also for the utility of host materials for photoluminescence center. One of the earliest applications of zeolite photoluminescence is to probe coordination environments of ions [4]. Among all the paths used to functionalize zeolite, ion exchange method should be the most popular one. Because zeolite has many cages and channels, cations are free to migrate in and out zeolite structures. The luminescence properties of rare earth ion-exchanged zeolite are exploited to probe microenvironment of zeolite [5–7]. Rare earth ions have large ion size so that a hydrated ion cannot migrate from a supercage to a small sodalite to replace the residing Na^+ ions. The ion exchange saturated level of La-NaY is 0.69 ± 0.01 at 25 °C. Rare earth ions can only replace Na^+ ions in the supercage unless the temperature of exchange is raised much more higher. Higher temperature of treatment facilitates rare earth ions going into the sodalite cages and double hexagonal prisms [8, 9]. Luminescence spectra are usually used to track the transfer of energy on solid surface from absorber to an emitter, and lifetime experiments are used to obtain the number of coordinated water molecules [10].

Chen et al. investigate the photoluminescence and photostimulated luminescence of Tb^{3+} and Eu^{3+} co-doped in zeolite Y [11]. The luminescence from the hydrated zeolite containing Tb^{3+} and Eu^{3+} prepared at room temperature is very weak due to the dissipation of excitation energy by OH vibrations. However, the luminescence is enhanced greatly when the sample is treated at 800 °C, which is due to the loss of water and the migration of the ions from the supercages to the sodalite cages. Strong photostimulated luminescences of both Tb^{3+} and Eu^{3+} are firstly detected in the sample prepared at 800 °C. The photostimulated luminescence of Tb^{3+} is due to the recombination of electrons with Tb^{4+} ions, while the photostimulated luminescence of Eu^{3+} is caused by energy transfer from Tb^{3+} to $Eu^{3}.^{+}$ The existence of Tb^{4+} and Eu^{2+} ions confirmed by EPR measurements is due to charge transfer from Tb^{3+} to $Eu^{3}.^{+}$ The occurrence of photostimulated luminescence and discrete emission lines in blue (434 nm), green (543 nm), and red (611 nm) colors indicate that this material has potential applications in white light-emitting devices and erasable optical storage. The photoluminescence intensity of Eu^{3+} is higher than the photoluminescence intensity of Tb^{3+}, but it is contrary to their photostimulated luminescence intensity.

Jüstel et al. study the optical properties of Tb^{3+}/Ce^{3+}-doped zeolites in the UV and green spectral emission range, with an emphasis on ultraviolet (UV) and vacuum ultraviolet (VUV) excitation and luminescence [12]. Ce^{3+}-sensitized Tb^{3+} green emission possesses a quantum yield of 85% under 330 nm excitation, which is from an efficient $Ce^{3+} \rightarrow Tb^{3+}$ energy transfer. Unfortunately, low absorptivity at 254 nm due to low Ce^{3+} concentrations or low Tb^{3+}/Ce^{3+} ratios restricts their applicability as phosphors for Hg-based discharges such as in conventional fluorescent lamps. Near band edge excitation at 172 nm reveals an immediate quantum yield of 50% enabled by a zeolite $\rightarrow Ce^{3+}(5d^1) \rightarrow Tb^{3+}(4f^7 5d^1)$ energy transfer channel, which may be exploited for the down-conversion of the Xe_2 excimer emission. In VUV investigations the optical bandgap of zeolite X is located at 6.9 eV. The introduction of Ce^{3+} into Tb-X zeolites results in a remarkable increase of the green quantum yields upon near band edge excitation, which is due to the Ce^{3+} d-states in resonance to the optically generated excitons in the zeolite. The capability of the zeolite host lattice to transfer excitation energy into sensitizer or rare earth ion levels may be of immediate interest in applications such as $Xe_2{}^*$ excimer discharge-driven lighting systems.

Zeolite L (ZL) is a cylindrically shaped, porous aluminosilicate having a one-dimensional channel system oriented along the c-axis. Mech et al. show how the intentionally generated oxygen vacancies can be used to indirectly excite the Er^{3+} ions loaded in ZL and generate the 1.54 μm emission [13]. The PL is effectively produced by a photoinduced energy transfer from the oxygen vacancies, which act as a light-harvesting antenna and can be excited in a very broad spectral range (from 355 nm to 700 nm in the whole UV and visible region) with common light sources to the rare earth ion. The role of the vacancies is clearly evidenced by the decay time of the obtained NIR emission, which results to be three times longer than that mea-

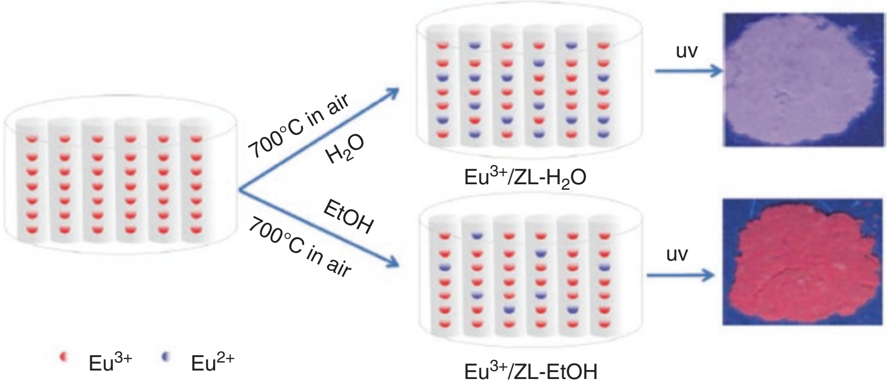

Fig. 4.1 Schematic of the preparation procedure and digital photo of samples irradiated under UV light (Reprinted with permission from Ref. [14]. Copyright 2012 the Royal Society of Chemistry)

sured in the same dehydrated host without oxygen defects. So it is possible to obtain sensitization of the Er^{3+} NIR emission, using white light excitation, by incorporation of Er^{3+} into the ZL structure, whereby oxygen vacancies have been created.

Li et al. have found that annealing of Eu^{3+}-functionalized ZL (Eu^{3+}/ZL) at 400 to 800 °C can produce a strong and bright violet-blue emission, [14] whose real origin of the emission is still not clear and needs to be identified. They confirm the reduction of Eu^{3+} to Eu^{2+} in the annealed Eu^{3+}/ZL crystals during the annealing process at 700 °C under an air atmosphere, and both Eu^{3+} and Eu^{2+} ions are present in the annealed Eu^{3+}/ZL crystals. Washing Eu^{3+}/ZL crystals with water followed by annealing can give them a strong violet–blue luminescence, while ethanol can give them bright red luminescence, which results from the strong quenching of Eu^{3+} luminescence in the water-washed samples (Fig. 4.1). So zeolite crystals can be used as an ideal host to obtain Eu^{2+} ions that can emit from the UV region to the red region depending on the symmetry and crystal field strength around Eu^{2+}.

They further study the red emission and NIR emission from a RE^{3+}- and Bi^{3+}-cofunctionalized ZL (RE^{3+}/Bi^{3+}-ZL, RE = Eu, Nd) by a simple ion exchange process and subsequent annealing. The morphology and size distribution of the RE^{3+}/Bi^{3+}-ZL remain almost unchanged during the synthesis process as revealed by SEM images and can easily be tuned by an appropriate choice of ZL crystals (Fig. 4.2) [15]. It is interesting that Eu^{3+} in the Eu^{3+}/Bi^{3+}-ZL has a lifetime of 1.93 ms and a $^5D_0$ quantum efficiency of 67%, which is suitable for cooperation with UV-emitting LEDs because of its ability of near UV excitation. Nd^{3+} in the annealed Nd^{3+}/Bi^{3+}-ZL also attains in a lifetime of 0.196 ms, which may make it a potential candidate for generating laser emission at 1060 nm for optical device application.

Duan et al. synthesize a great diversity of ion-exchanged zeolite Y processing high ion-exchanged capability and numerous hospitable cavities and sites. As for zeolite modified with Y^{3+} or Zn^{2+}, investigations of doping monometal ions and bimetal ions are carried out to enrich the theoretical knowledge of the photoluminescence of ion-exchanged zeolite Y [16]. The metal ion-exchanged zeo-

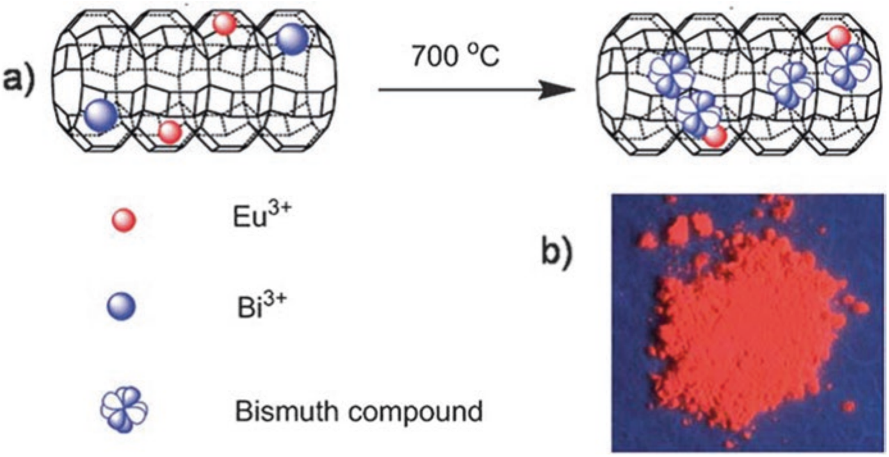

Fig. 4.2 The scheme for (*a*) synthetic strategy pursued to obtain luminescent materials; (*b*) digital photo of Eu^{3+}/Bi^{3+}-ZL under UV irradiation (365 nm). Reprinted with permission from Ref. [15]. Copyright 2011, the Royal Society of Chemistry

lites are conveniently prepared through suspending zeolite into certain nitrate aqueous solution (Fig. 4.3 (top)). Most of them are octahedral NaY zeolite nanocrystals with a small amount of gmelinite as impurity (SEM image in Fig. 4.3 (bottom)), which have a regular and uniform structure with the diameter of about 250 nm. The morphology of zeolite NaY crystals and their size are largely dependent on the preparation conditions such as temperature, time, and the composition and molar ratio of the starting gels. The time-dependent experiment is carried out to study the morphology transformation of zeolite. When prolonging synthesis time, the morphology of zeolite transforms from zeolite NaY to gmelinite. When ion exchange is performed at low temperature and low pressure, the exchanged ions are located in the β supercage of NaY zeolite, which includes (1,1,1) crystal plane, since it is the maximum ion exchange window of NaY zeolite. The intensity of (1,1,1) crystal plane of rare earth ion-exchanged zeolite is relatively low than that of transition metal ion-exchanged zeolite, mainly because the ion radius of rare earth is much larger than that of transition metal ion, which leads to partly inevitable damage on (1,1,1) plane. The emission in EuNaY following laser excitation at 394 nm contains the $^5D_0 \rightarrow {}^7F_J$ (J = 0, 1, 2, 3, 4) transition at 579, 590, 614, 653, and 698 nm and also includes $^5D_5 \rightarrow {}^7F_J$ transition (J = 0, 1, 2) at 524, 535, and 555 nm, together with a broadband around 478 nm due to the emission of excited zeolite structure. The Ce^{3+} emission in CeNaY zeolite shows a broadband at 350 nm due to the transition of 5d → $^2F_{5/2}$ and 5d → $^2F_{7/2}$ ground states. Tb^{3+} emission in TbNaY contains the $^5D_4 \rightarrow {}^7F_J$ (J = 3, 4, 5, 6) transition at about 621, 583, 545, and 489 nm as well as the broadband around 437 nm due to the emission of excited zeolite structure. The emission spectra of rare earth ion-exchanged zeolites reveal that the characteristic rare earth emission peaks are generated by its nature 4f (or 5d) energy level

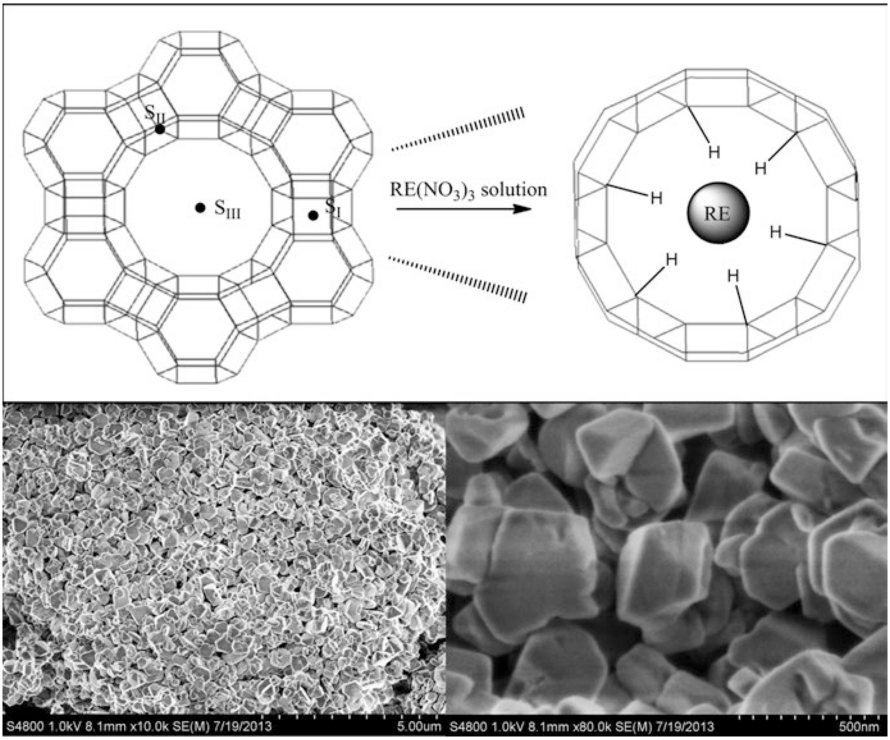

Fig. 4.3 (*Top*) The scheme for synthesis of the rare earth ion-exchanged zeolite: ion exchange process to introduce rare earth ions into NaY zeolite under the condition of 373 K. The rare earth ions are mainly on the S_{III} site because of relatively low heating treatment temperature. (*Bottom*) Selected SEM images of synthesis NaY zeolite (Reprinted with permission from Ref. [16]. Copyright 2014 Wiley Publisher)

transition, but not by the excitation band of zeolite. It's remarkable that EuNaY exhibits white light which shows strong applied value in luminescent devices.

4.2 Photofunctional Rare Earth Hybrid Materials Based on Functionalized Zeolite-FAU

To get some novel materials, it is advantageous to introduce substance of interest by ion exchange, vapor impregnation, solid-state diffusion, or ship-in-bottle synthesis. Herein the photofunctional rare earth hybrids based on functionalized zeolite faujasite type (FAU, including Y type) are firstly introduced.

Wada et al. succeed in drastically enhancing the near-infrared (NIR) emission of Nd^{3+} by ligating it with bis(perfluoromethylsulfonyl)amine in cages of a nanocrystalline, large-pore zeolite FAU (Fig. 4.4) [17]. The octahedral shape of each particle

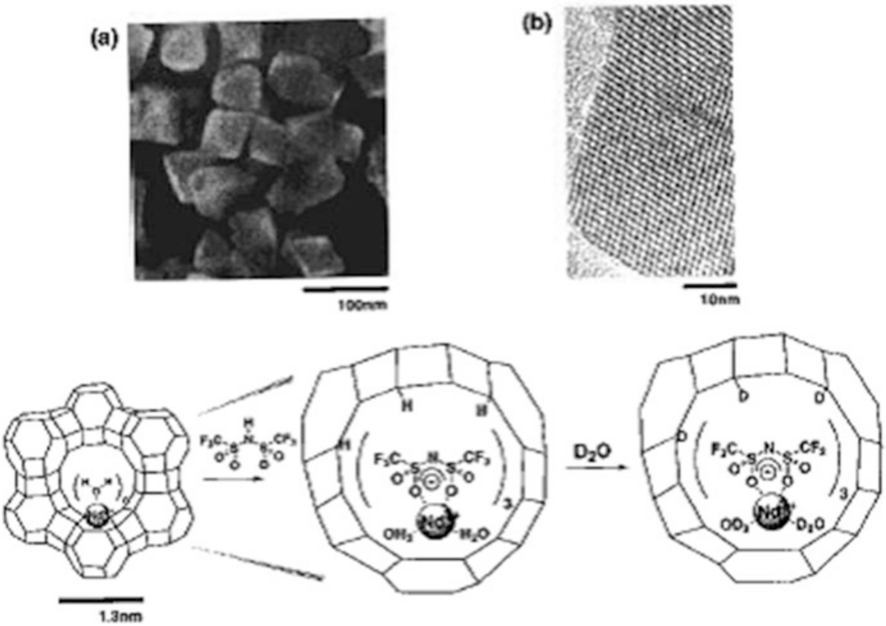

Fig. 4.4 FE-SEM (*a*) and TEM (*b*) views of the nanosized zeolite FAU prepared. The scheme displayed below the photos shows the conceptual process of the ship-in-bottle synthesis and the treatment with D_2O (Reprinted with permission from Ref. [17]. Copyright 2000 American Chemical Society)

and the fine structure of the zeolite cage are shown in Figure 4.5a and b, respectively. The particle sizes of the crystallites are 50–80 nm. The Nd-exchanged n-FAU powder is confirmed to have the composition of Si/Al = 2.8 and the exchange degree of (Na^+ by Nd^{3+}) 85–95%. After being degassed and kept in contact with vapor of bis(perfluoromethylsulfonyl)amine (PMS-H), the final hybrid (Nd(PMS)-n-FAU) is prepared, whose differential scanning calorimetry analysis shows an endothermic peak above the decomposition temperature of the neodymium with PMS and supports the formation of the complex inside the cages. The quantum yield for the emission of Nd(PMS)-n-FAU is determined to be $(9.5 \pm 1.0) \times 10^{-2}$ under excitation at 585 nm, being the highest value ever observed for Nd^{3+} emission in organic media. Nd-(PMS)-n-FAU particles aggregate to some extent with particle size distribution ranging from 100 to 175 nm. The strong emission for the hybrid system should be attributed to suppression of the relaxation of the excitation energy of Nd^{3+} through the vibrational excitation by the low-vibrational zeolite cage wall and the energy migration at collisions by locating Nd^{3+} separately in the cages. Furthermore, ligation of the emitting Nd^{3+} center with PMS in the zeolite cages should play an important role in retarding the vibration excitation caused by -OD groups surrounding the emitting centers.

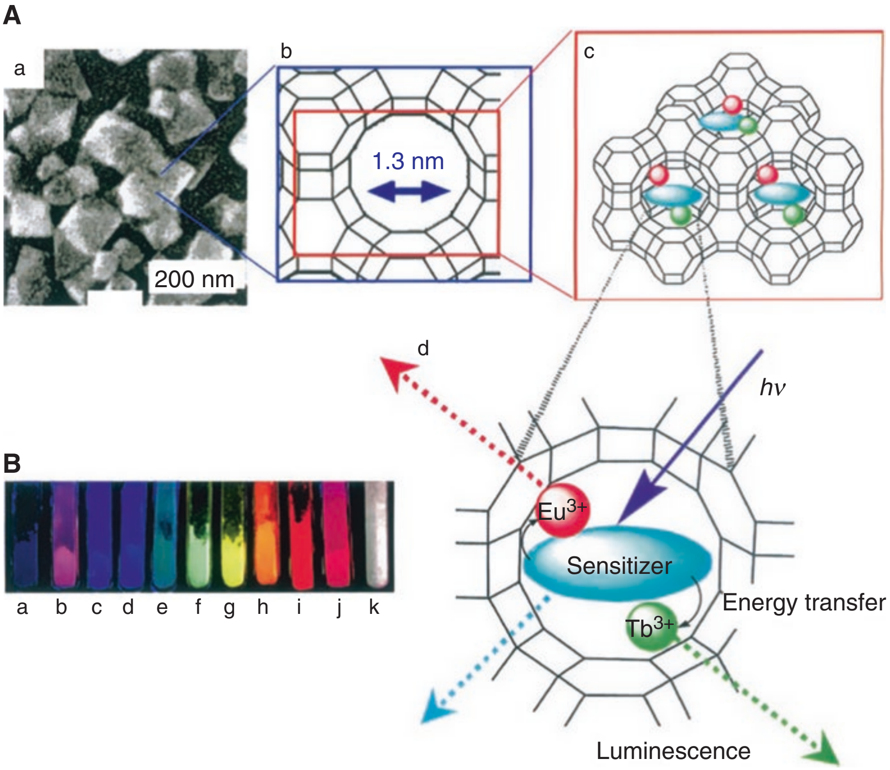

Fig. 4.5 (**a**) (*a*) SEM image of faujasite zeolite; (*b*, *c*) views of the framework structure of the ZX crystal; the sizes of the 12-ring open window and inner cage are 0.7 and 1.3 nm, respectively; (*d*) luminescence from the sensitizer molecule and emission of Tb^{3+} and Eu^{3+} ions through energy transfer from the sensitizer molecule. (**b**) Photographs of the photoluminescence from ZX samples, with colors varying from violet to red depending on the incorporated amounts of Tb^{3+} and Eu^{3+} ions, the type of photosensitizer (bzp or acbp), and the excitation wavelength (Reprinted with permission from Ref. [18]. Copyright 2006 Wiley)

They further investigate the rare earth ion-exchanged zeolites FAU incorporated with a photosensitizer (Figure 4.5A) that exhibit successful RGB photoluminescence depending on which rare earth ions and photosensitizers are used (Figure 4.5B) [18]. The color can also be finely tuned by varying the temperature and the excitation wavelength. The RE^{3+}-exchanged zeolite X is degassed for dehydration and is then either exposed to benzophenone (bzp) vapor or stirred in a solution of 4-acetylbiphenyl (acbp) in ethanol at room temperature. The reaction sequence is carried out on a vacuum line to avoid exposure of the zeolites to the atmosphere. The colors obtained varied from violet (b) to red (j) through blue (c, d) and green (e) by changing the amounts of the RE^{3+} and the nature of the sensitizer (bzp or acbp) (Figure 4.5B). The encapsulation of acbp in the zeolite cavity gives rise to blue emission besides the red and green colors emitted by Eu^{3+} and Tb^{3+} ions, respectively, leading to simultaneous RGB photoluminescence, while it is contrary to bzp.

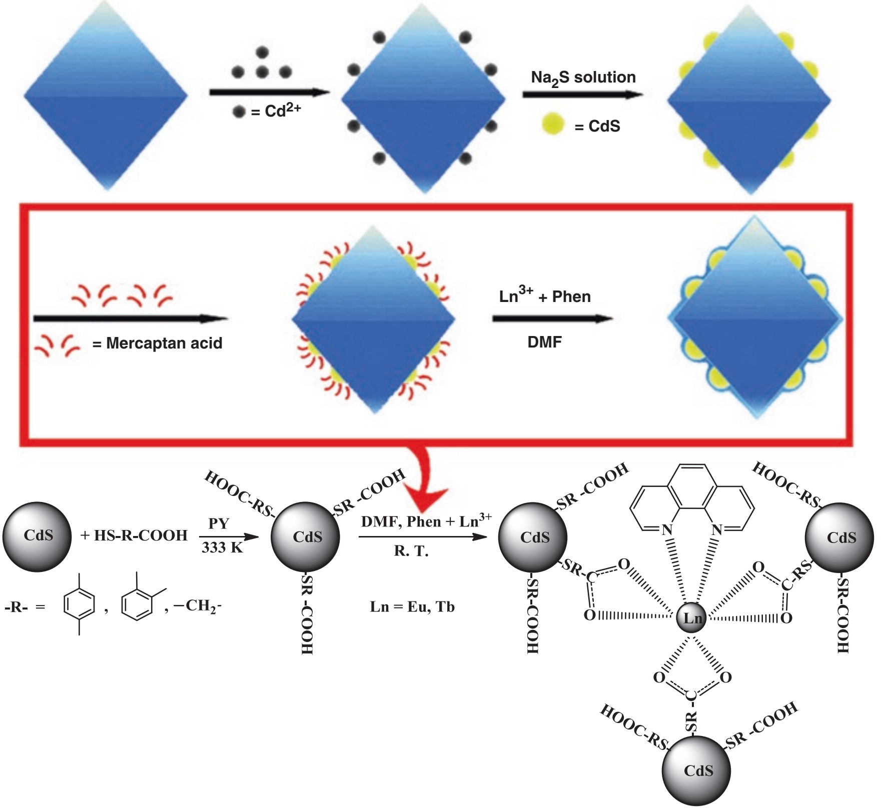

Fig. 4.6 The scheme for the synthesis procedure of rare earth complexes functionalized CdS-ZY and the predicted structure of the rare earth ternary complex functionalized CdS-ZY hybrid materials. Reprinted with permission from Ref. [19]. Copyright 2014 the Royal Society of Chemistry

The ratio of the intensities of the red and green emissions increases gradually with the increase of Eu^{3+} content (Figure 4.5B parts f–i). Furthermore, changes in the ratio of the three colored components as a function of the excitation wavelength and temperature are attained only by using zeolites as a host. The zeolite supercage incorporated with various amounts of three colored components provides an ideal environment to control the energy transfer processes that take place between them as a function of the excitation wavelength and temperature.

Recently, Duan et al. prepare a series of CdS-ZY hybrid materials via a mild coordination reaction (ZY = zeolite Y). The synthesis procedure and the predicted structure of the CdS-ZY hybrid material are shown in Fig. 4.6 [19]. In the first step, the synthesized zeolite Y crystal is loaded with Cd^{2+} ions through ion exchange process, and then an ethanol solution of sodium sulfide is used to react with cadmium ion-loaded zeolite, resulting in the CdS-zeolite Y hybrids. CdS QDs are proved by TEM images not only in the pores of zeolite but also on the surface of ZY

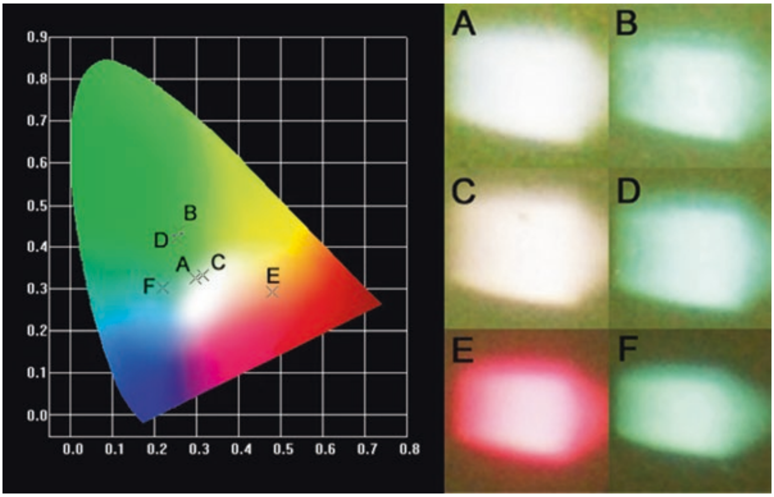

Fig. 4.7 CIE x-y chromaticity diagrams of hybrid materials. (*A*) Eu(phen)(*o*-MBA)$_3$-CdS-ZY (λ_{ex} = 296 nm) (*B*) Tb(phen)(*o*-MBA)$_3$-CdS-ZY (λ_{ex} = 297 nm) (*C*) Eu(phen)(*p*-MBA)$_3$-CdS-ZY (λ_{ex} = 321 nm) (*D*) Tb(phen)(*p*-MBA)$_3$-CdS-ZY (λ_{ex} = 323 nm) (*E*) Eu(phen)(MAA)$_3$-CdS-ZY (λ_{ex} = 298 nm) (*F*) Tb(phen)(MAA)$_3$-CdS-ZY (λ_{ex} = 298 nm) (Reprinted with permission from Ref. [19]. Copyright 2014 the Royal Society of Chemistry)

crystal. The aggregation of CdS QDs exists on the external surface of zeolite since a small amount of Cd^{2+} ions cling to the zeolite surface during introduction of S^{2-} ions. In the next step, three different mercaptan acids are performed separately on the CdS-ZY hybrids to modify CdS QDs, from which a coordination reaction is performed among mercaptan acid-modified CdS-ZY, phen, and rare earth ion.

The distribution of CdS QDs can be confirmed by the UV–vis diffusion reflection spectra. In the case of CdS QDs, the absorption maxima wavelength of the isolated QDs, interconnected QDs, and mesosized QDs appear in the 200 ~ 300 nm, 300 ~ 380 nm, and 380 ~ 480 nm regions, respectively. Therefore, it can be predicted from UV–vis reflection spectra that intrazeolite CdS QDs exist in zeolite Y crystals in three types, isolated, interconnected, and mesosized. Interestingly, the photoluminescence color can be tuned from white and pink to red by changing the coordination mercaptan acid. Figure 4.7 shows the corresponding CIE chromaticity diagram of europium or terbium complexes functionalized CdS-ZY with different coordination mercaptan acid. The corresponding luminescence color can be seen clearly from the photographs of europium or terbium complexes functionalized CdS-ZY samples, where an appropriate wavelength is used as the excitation source.

Sendor et al. load Eu^{3+} complexes of TTA to the supercages of zeolite X to improve the luminescence intensity of Eu^{3+}, in which lattice atoms participate in the luminescence mechanism via polar interaction and coordination [20]. But isolated complex within the large cavities of ZX structure may be observed, depending on composition and spatial consideration. The strong excitation band in near ultraviolet region is matchable to ultraviolet excited LED, enabling the potential applications of this material in sensors or lighting devices.

4.3 Photofunctional Rare Earth Hybrid Materials Based on Functionalized Zeolite A

Zeolite A (abbreviated as ZA) has a three-dimensional network of cavities, and the composition of its Na^+ form is $Na_{12}[(SiO_2)_{12}(AlO_2)_{12}]$. Yan's group first assemble the photofunctional rare earth hybrid materials through the functionalization of ZA host. Hao et al. prepare the host–guest assemblies of ZA and their thin films [21]. The assembly of zeolite A is done by first embedding rare earth complexes ($Eu(TTA)_n$ or $Tb(TAA)_n$) into the cages of ZA and then grafting another lanthanide complexes (Eu(L) or Tb(L), L = bpy or phen) onto the surface of functionalized ZA via 3-methacryloyloxypropyltrimethoxysilane (γ-MPS) (Fig. 4.8 (Top)). Firstly, the dependence of the crystal stability of ZA as the host of rare earth complexes on the level of ion exchange is studied by XRD, indicating that the degradation and partial collapse of ZA framework occur upon doping high amount of lanthanide complexes into its channels. While through properly controlling ion exchange extent, the integrity of ZA framework is well maintained after fabrication. Secondly, the obtained thin films of ZA assemblies are provided with the property of homogeneous dense packing and the high coverage degree of the crystals on the ITO glass, as displayed in SEM images (Fig. 4.8(Middle) c,d). The surface of the crystal becomes cruder, which may be caused by the follow-up surface modifications. Figure 4.8 (Middle) d reveals the homogeneous dense packing and the high coverage degree of the crystals on the ITO glass. The method to prepare the thin films of ZA assembly is by spin-coating via molecular linker, thus probably leading to the stronger interaction between the crystal base and the substrates, which is more conducive to make the crystals to stay on the glass tightly through chemical bonds. Thirdly, white light-emitting materials are obtained from a three-component system that comprises a blue-emitting ZA matrix, a red-emitting europium complex, and a green-emitting terbium complex. Various photoluminescence colors from the uniform thin films of ZA assembly can be fine-tuned both by purposely selecting the rare earth complexes inside and outside of ZA and by varying the excitation wavelength. Four red–green–blue (RGB) photoluminescence materials display white lights. Photographs of the photoluminescence colors from thin films are shown in Fig. 4.8 (Bottom).

Chen et al. introduce Eu/Tb complex and rare earth (Eu, Tb, Dy) polyoxometalates (REW_{10}) to functionalize ZA and titania through an inside–outside double modification path [22]. Eu/Tb complex-modified ZA (TTA-Eu(AA-Tb) ⊂ ZA) is achieved by ionic exchange reaction and gas dispersion. REW_{10}-modified titania (Ti-IM-REW_{10}) is obtained with the ionic liquid compound as the linker. Then multicomponent hybrids TTA-Eu(AA-Tb) ⊂ ZA-Ti-IM-REW_{10} are assembled through condensation reaction between hydroxyl groups on the surface of ZA and titania (Fig. 4.9 (top)). The selected SEM image of the cylindrical structure of these hybrids indicates that the crystal framework belonging to ZA still can be observed except that it becomes irregular as pure ZA due to the introduction of other functionalized components in the hybrid system. Figure 4.9 (Bottom) shows the selected digital photos of hybrid materials TTA-Eu ⊂ ZA-Ti-IM-EuW_{10} and AA-Tb ⊂ ZA-Al-IM-

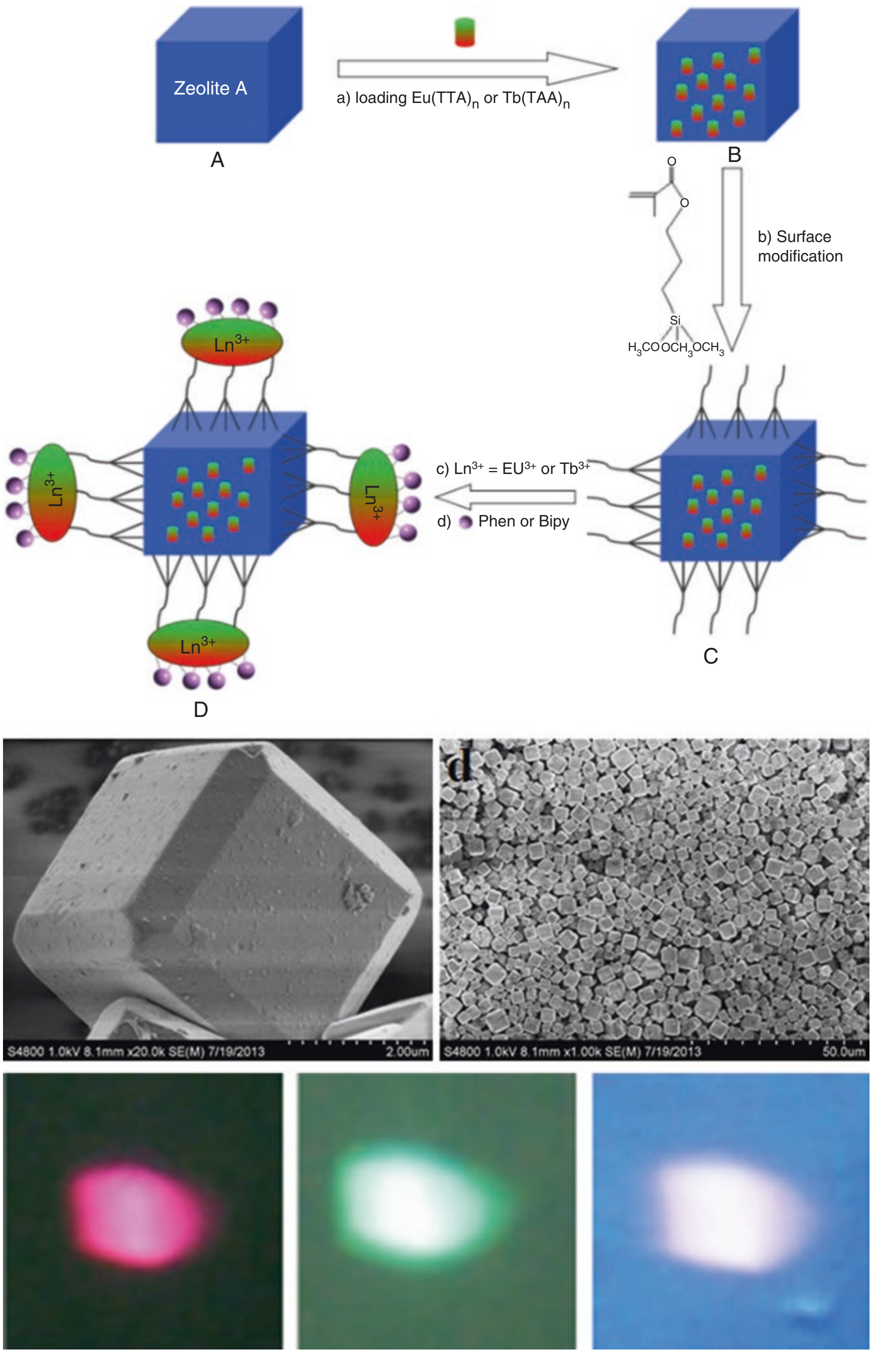

Fig. 4.8 (*Top*) The scheme for synthesis procedure and predicted structure of the hybrid materials of RE(L_2)-γ-MPS-[RE(L_1)$_n$-ZA]: (*a*) inserting lanthanide complexes into the cages of zeolite A; (*b*) fixing γ-MPS on the external surface of RE(L_1)$_n$-ZA through Si-O-Si; (*c*) further anchoring Ln^{3+} via C = O groups of γ-MPS; and (*d*) introducing phen or bpy ligands to coordinate with RE^{3+}.

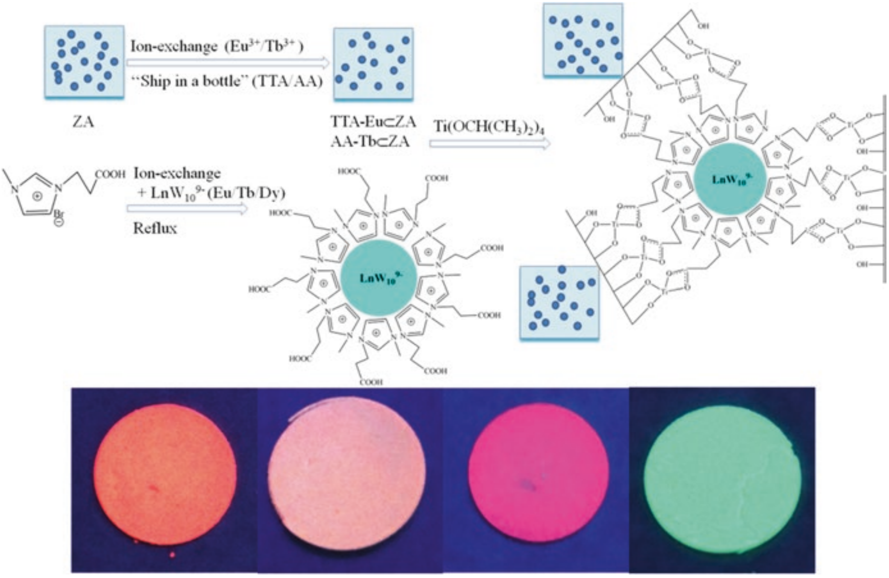

Fig. 4.9 (*Top*) The scheme for synthesis process and composition for the hybrid materials TTA-Eu(AA-Tb) ⊂ ZA-Ti-IM-LnW$_{10}$ (Ln = Eu, Tb, Dy). (*Bottom*) The selected digital photos of hybrid materials TTA-Eu ⊂ ZA-Ti-IM-EuW$_{10}$ (*left* two, λ_{ex} = 254 and 365 nm, respectively) and AA-Tb ⊂ ZA-Ti-IM-EuW$_{10}$ (*right* two, λ_{ex} = 254 and 365 nm, respectively) under UV irradiation (Reprinted with permission from Ref. [22]. Copyright 2015, Springer)

EuW$_{10}$ under UV irradiation of two wavelengths (254, 365 nm). For TTA-Eu ⊂ ZA-Ti-IM-EuW$_{10}$ hybrids, the color of the hybrids changes from orange–red to violet–red for the different dominant europium luminescent species. More apparent for AA-Tb ⊂ ZA-Al-IM-EuW$_{10}$ hybrids, its color changes from light purple–red to light blue–green. So the selective excitation of the hybrids can realize the color tuning for the two luminescent species.

Hao et al. prepare the PEMA-P4VP polymer thin films co-doped with the rare earth-ZA via coordination bond by a two-step procedure (Fig. 4.10 (Top)) [23]. Firstly, rare earth complexes are embedded into the cages of ZA, leading to RE-ZA host–guest materials with a marked enhancement of thermal stability or photostability as well as attractive luminescent properties. They choose two trialkoxysilyl derivatives of polydentate ligands as bridging molecules to graft the rare earth complexes which coordinate to the polymer chain on the external surface of rare earth-

◄

Fig. 4.8 (continued) (Middle) SEM images of thin films of the final hybrid materials. (*Bottom*) The photographs of the photoluminescence colors from the thin films with the UV excitation using a Xe lamp as the excitation source: the images from left to right stand for Eu(L)-γ-MPS-[Eu(TTA)$_n$-ZA] (*red light*), Tb(L)-γ-MPS-[Tb(TAA)$_n$-ZA] (*green light*), and Tb(L)-γ-MPS-[Eu(TTA)$_n$-ZA] or Eu(L)-γ-MPS-[Tb(TAA)$_n$-ZA] (*white light*), respectively (Reprinted with permission from Ref. [21]. Copyright 2014 the Royal Society of Chemistry)

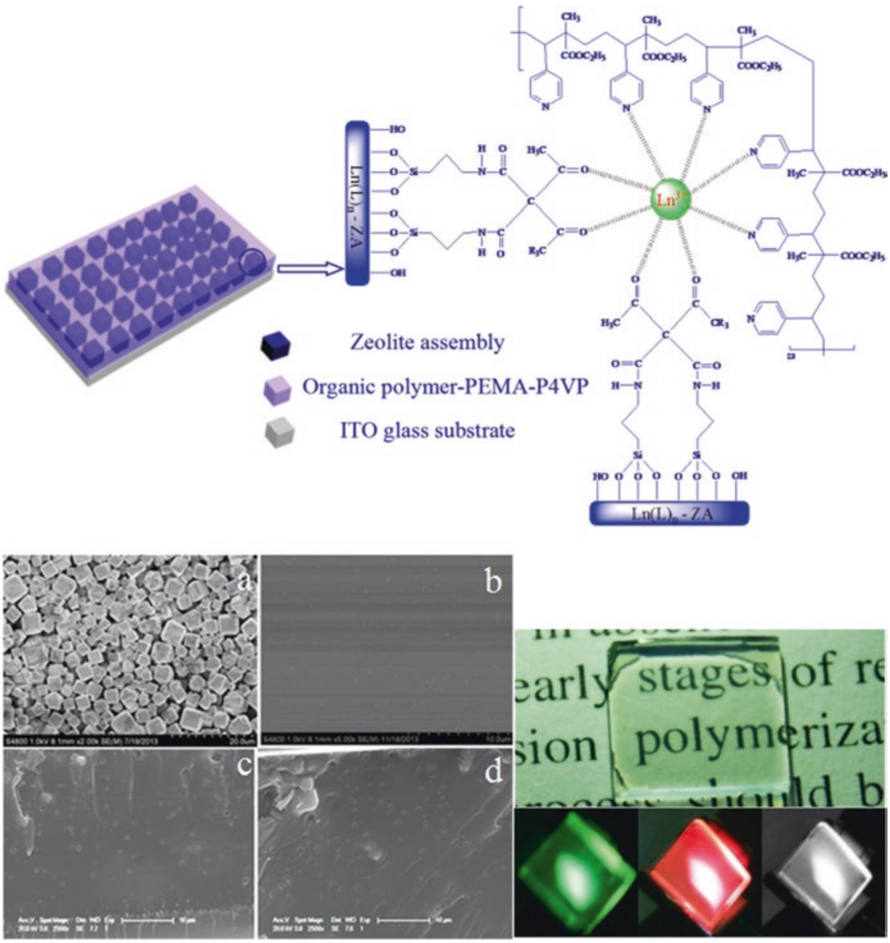

Fig. 4.10 (*Top*) The scheme for the synthesis procedure and predicted structure of the polymer thin films of PEMA-P4VP-RE-TAA-Si/AA-Si-[RE(L)-ZA]. (*Bottom*) SEM images of (*a*) ZA and a typical (*b*) surface and (*c*, *d*) cross-sectional SEM images of hybrid polymer thin film (*left*); and photographs of the transparent thin films and the photoluminescence colors from the organic polymer thin films with the UV excitation using a Xe lamp as the excitation source: *green* for terbium, *red* for europium, and *white* for Eu^{3+}/Tb^{3+} hybrids, respectively (*right*) (Reprinted with permission from [23]. Copyright 2014 the Royal Society of Chemistry Publishing Company)

doped ZA, thus dispersing RE-functionalized ZA into the organic polymer. The SEM image and the size distribution histogram in Fig. 4.10 (top, a) show that the ZA particles are monodispersed with an average particle size of 2.0 μm. Dispersion of the RE^{3+} complex-loaded ZA in the polymer matrix through chemical bond is investigated by surface and cross-sectional SEM (Fig. 4.10 (Bottom), left b, c, d). Several white spots in the images which are even distributed on the smooth background of the PEMA-P4VP polymer originate from zeolite A. And from the surface and cross-sectional images, it can be further inferred that there exists a homogeneous dispersion of zeolite crystals throughout a polymer matrix. In this system, three kinds of photoluminescence colors are obtained, green, red, and white light from Eu^{3+} hybrids, Tb^{3+} hybrids, and Eu^{3+}/Tb^{3+} co-doped hybrids, respectively (Fig. 4.10 (Bottom), right). The bright white light is expected to have the potential and significant applications in optoelectronic devices in the future.

Chen et al. prepare some multicomponent hybrids based on zeolite L/A [24]. Firstly zeolite A/L is loaded with rare earth complexes (Eu-DBM or Tb-AA into their channels. Secondly, γ-MPS is used to covalently graft onto the surface of functionalized zeolite A/L (Si-[ZA/L ⊃ Eu-DBM(Tb-AA)]). Thirdly, rare earth ions (Eu^{3+}/Tb^{3+}) are coordinated to the functionalized zeolite A/L and ligands (phen or bipy). Some hybrids display white or near-white light emission. Further, above-selected hybrids are fabricated into PEMA/PMMA (poly ethyl methacrylate/polymethyl methacrylate) host to prepare luminescent polymer films. Chen et al. assemble a series of multicomponent photofunctional hybrid materials based on lanthanide polyoxometalates ($Na_9LnW_{10}O_{36}\cdot 32H_2O$, LnW_{10}, Ln = Eu, Tb, Sm and Dy), ionic liquids (IMCl), and functionalized ZA/ZL through an inside–outside double modification path [25]. Here 1-methyl-3-(trimethoxysilylpropyl)imidazolium chloride (IM^+Cl^-) is covalently grafted onto the functionalized zeolite A/L and linked to lanthanide polyoxometalates as a double linker. These hybrids own two luminescence centers, one is rare earth complexes, and the other is lanthanide polyoxometalates. By adjusting the different components of the hybrids, the luminescent tuning and integration of various colors (white, warm white, green, and red light) can be realized.

4.4 Photofunctional Rare Earth Hybrid Materials Based on Functionalized Zeolite L

Zeolite L (ZL) crystals feature strictly parallel channels arranged in a hexagonal symmetry, and the particle size and aspect ratio of the colorless crystallites can be tuned over a wide range. The one-dimensional channels of ZL can be filled with suitable guests and geometrical constraints imposed by the host structure lead to supramolecular organization of the guests in the channels. Three main stages exist in the organization to form guest–host hybrid materials: supramolecular organization of dyes inside the ZL channels allowing light harvesting within the volume of a dye-loaded ZL crystal and radiationless energy transport to either the cylinder ends or to the center of the channel through one-dimensional excitation energy transport, the coupling of an external acceptor or donor stopcock fluorophore to the ends of the ZL channels to trap or inject electronic excitation energy, and interfacing the material to an external device through a stopcock intermediate. It is worth pointing out that Calzaferri's group has done the pioneering work on the functionalization of ZL-based hybrids for photophysical application [26].

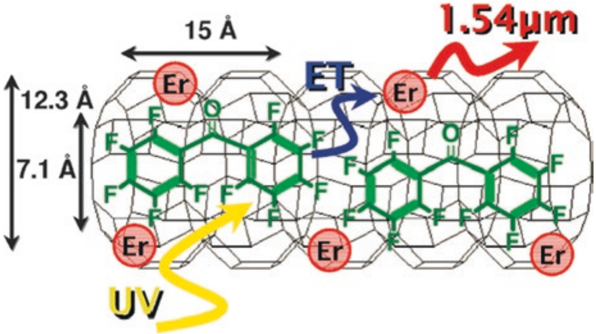

Fig. 4.11 Sketch showing the dimension of the ZL pore and schematic illustration of the energy transfer between dye and Er^{3+} inside the zeolite nanochannel (Reprinted with permission from Ref. [28]. Copyright 2010 the American Chemical Society)

For example, Monguzzi et al. use the ZL with highly crystalline microcrystals consisting of parallel arrays of nanometric channels to produce the desired confinement between the sensitizer and the emitting ion [27]. Ionic exchange of positive counterions with Er^{3+} and then benzophenone is introduced to form the final hybrid system. Subsequently, they obtain microcrystals suitable for NIR light emission by ion exchange of the zeolite charge-compensating cations (Na^+, Ca^{2+}) with Er^{3+} ions. Benzophenone is used as a light-harvesting molecule, which is a well-known triplet emitter for Er^{3+} sensitization. This approach has a number of potentially useful advantages. Inclusion of antenna molecules into the pores can provide an indirect excitation for the ion through a RET process. Optical pumping using LED or lamps rather than laser becomes feasible using this broadband sensitization. Through proper chemical functionalization, zeolites can be made compatible with polymer matrix to open the possibility of fabricating plastic photonic devices. The pump power required for population inversion in Er^{3+}-based optical amplifiers can then be lowered from more than 10^3 W/cm^2 to less than 1 W/cm^2, thus opening the way for important telecom applications.

Mech et al. demonstrate the possibility to obtain sensitized, highly efficient NIR emission of Er^{3+} ions exchanged within a ZL matrix [28]. The 1.5 μm emission is excited via energy transfer from loaded decafluorobenzophenone (DFB) molecules that upon filling the zeolite, nanochannels act as light-harvesting antenna (Fig. 4.11). Removal of water molecules from ZL structure and the use of perfluorinated organic molecules result in a strongly enhanced NIR emission (1.54 μm, $^4I_{13/2} \rightarrow {}^4I_{15/2}$ of Er^{3+}) with a longer lifetime (>2 orders of magnitude longer) than in erbium complexes with organic, nonfluorinated ligands. The full width at half maximum (fwhm) of the 1.54 μm PL band (~86 nm) is substantially broader than those observed for the Er^{3+} doped into inorganic hosts and most of the erbium (III) organic complexes, which is beneficial for wave division multiplexed signal amplifications. The intrinsic quantum yield of the sensitized luminescence is estimated to be 2.5%, which is one of the highest values reported for the 1.54 μm emission of Er^{3+} ions sensitized by organic dyes. This approach may open a new way of manufacturing efficient NIR-emitting plastic-compatible devices useful in a broad spectrum of communication applications, because functionalized zeolites can be successfully incorporated into polymer matrices.

In recent years, on the basis of work of Calzaferri's group, Li's group has done an extensive and deep investigation on the functionalized ZL to assemble the photofunctional rare earth host–guest hybrid materials. Their research involves the control of morphology and size of ZL microcrystals, the assembly of rare earth complexes in the channel of ZL, the self-assembly of ZL induced by rare earth complexes, the ZL–polymer transparent hybrid materials, etc. [29]. For example, Wang et al. graft terbium complexes onto nanozeolite L material and prepare the hybrid material by first functionalizing ZL with (3-aminopropyl)triethoxysilane (APES) and then grafting carboxyphenyl isothiocyanate via the reaction of amino group covered on ZL surface and isothiocyanate groups. The functionalized ZL is at last reacted with Tb^{3+} ions [30]. They also realize the striking increase of Eu^{3+} and Tb^{3+} emission for the formation of $RE^{3+}(bpy)_n$ complexes (RE = Eu, Tb) inside the nanochannel of ZL upon gas-phase insertion of bpy into RE^{3+}-exchanged ZL crystals [31]. The new host–guest materials are suited to cooperate with UV-emitting LEDs because they can be excited in the near UV region. Furthermore, these materials can be tested for fabrication of different plastic photonic devices based on the recently published procedure of realizing transparent zeolite–polymer hybrid materials by means of a suitable functionalization of the external surfaces. Li et al. prepare luminescent rare earth complexes loaded ZL/silica core-shell hybrids and demonstrate the ability to further functionalize the core-shell hybrids for the luminescence sensing of dipicolinic acid (DPA), which is a major constituent of many pathogenic spore-forming bacteria [32]. This study also extends the application of ZL-based hybrid materials to the field of biosensors. Owing to the versatility of zeolite crystals and the luminescent dyes, the present approach should allow for the synthesis of novel core-shell hybrid materials for future sensing. The advantage of ZL compared to silica is that it can prevent the self-aggregation of dyes and superimpose a specific organization (the anisotropic intense luminescence with a high concentration of monomers).

Furthermore, Wang et al. achieve higher organization and additional functionality by a functional linker that has the ability to coordinate and sensitize lanthanide ions RE^{3+} and that is also able to self-assemble on a surface through hydrogen bonding (Fig. 4.12) [33]. They synthesize the triethoxysilylated molecule and test its ability to bind on a quartz substrate, to coordinate RE^{3+} ions and sensitize their luminescence. The flexible linker has two urea groups capable of forming hydrogen bridges. Substrate functionalized by the linker should then be able to form monolayers of oriented ZL microcrystals, resulting in the functionalized quartz plates, which can then be immersed in a suspension of ZL crystals to form the final hybrid monolayers. These hybrid materials present densely packed ZL monolayers, all of which stand on the substrate with their c axis perpendicular to the surface. This orientation and the high degree of coverage imply that the interaction between the crystal base and the substrate is much stronger than any other interactions.

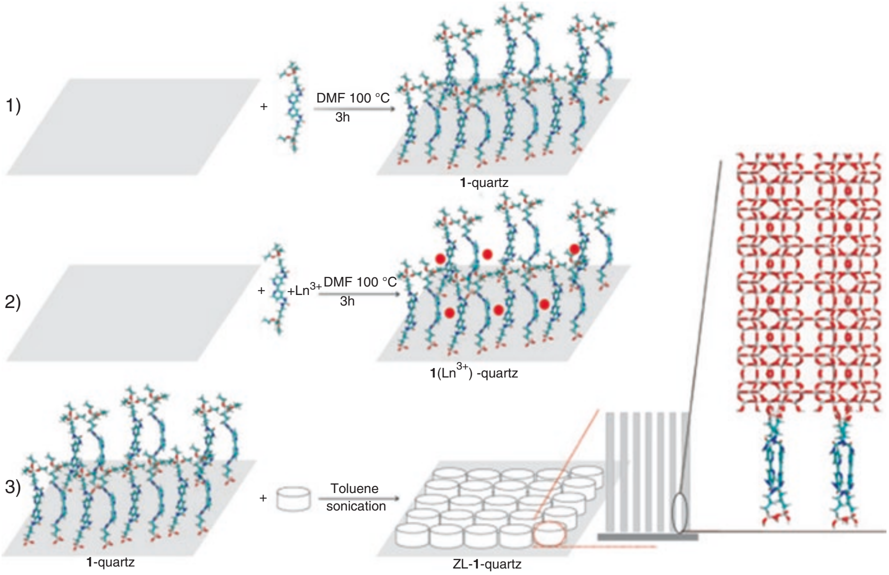

Fig. 4.12 Scheme for the bonding of ORMOSILs to the hydroxyl groups of a quartz substrate and subsequent formation of oriented open-channel monolayers (Reprinted with permission from Ref. [33]. Copyright 2010 Wiley)

Cao et al. further try the self-assembling ZL crystals into uniformly oriented layers with both the transition metal cations Zn^{2+}/Cu^{2+} and the lanthanide cations Eu^{3+}/Tb^{3+} that work effectively in binding and organizing the ZL crystals (Fig. 4.13) [34]. The cooperative interaction of terpy and metal cations is successful to assemble the uniformly oriented monolayer. Two different strategies, the S-L(M) and S-(L-M-L) methods, have been applied for lanthanide ions. The outlined principle is expected to be successful also for organizing other nano- or microsized objects bearing nanochannel. The self-assembly procedure is so versatile and robust that tailoring the properties of layers for meeting desired functionalities for a specific application is possible.

Ding et al. prepare photostable and efficient red-emitting host–guest hybrid materials employing a ship-in-bottle procedure by loading TTA or TTA and phen from gas phase into the channels of Eu^{3+}-ZL crystals that exhibit disk-shaped morphology followed by treatment with ammonia gas [35]. The emission intensity and the lifetime of Eu^{3+} ions of the host–guest materials can be significantly increased by treatment with ammonia gas, and the encapsulated Eu^{3+} complexes in ZL crystals show remarkably increased photostability; the insertion of organic ligand into the Eu^{3+}-ZL crystals leads to a striking increase in the emission intensity of Eu^{3+} ions as a result of the formation of Eu–TTA complexes. Furthermore, the significant increase in both the emission intensity and the decay times of Eu^{3+} ions by ammonia

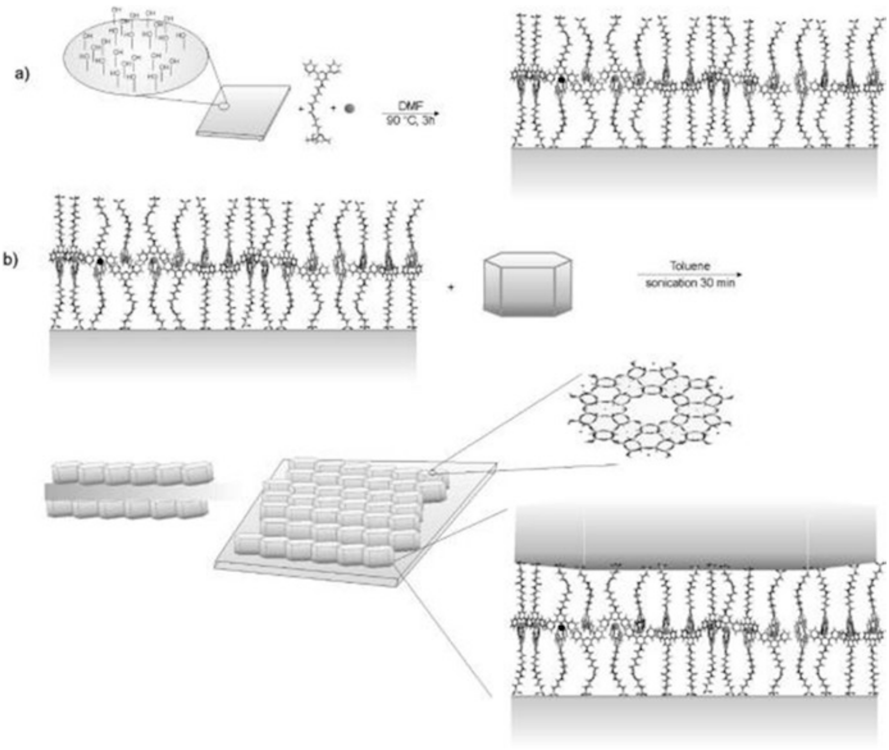

Fig. 4.13 S-(L-M-L) method for synthesizing ZL-L(M^{n+})L-S-L(M^{n+})L-ZL c-ocMLs. (*a*) The ligand is attached to the substrate in the presence of metal cations (indicated as *spheres*, e.g., Zn^{2+}, Cu^{2+}, or lanthanide Ln^{3+}), thus forming a L(M^{n+})L-S-L(M^{n+})L layer. (*b*) ZL crystals are attached to this layer. Conditions are such that they react preferentially with their base (Reprinted with permission from Ref. [34]. Copyright 2011 the American Chemical Society)

gas treatment may imply a potential use in ammonia sensing. Wen et al. investigate the acidity of Eu^{3+}-exchanged ZL and its influence on the luminescent performances of encapsulated Eu^{3+}–β-diketonate complexes [36]. The acidity of Eu^{3+}/ZL is determined roughly by using a dye (thionine) as the probe molecule. The luminescence behavior of the host–guest materials can be tuned by changing the acidity inside the channels of the zeolite L crystals and can potentially be used as a sensor for detecting ammonia.

Li et al. design a simple and robust platform to detect basic molecule vapors based on the encapsulation of Eu^{3+}–β-diketonate complexes within a nanozeolite L framework, which shows a condition selective luminescence turn-on response to basic molecule vapors [37]. The stationary and time-resolved spectroscopy studies suggest that the mechanism responsible for the turn-on response to basic molecule vapors is that basic molecules are favorable for the formation of Eu^{3+}–β-diketonate complexes with high coordination numbers by decreasing the proton strength of the channels. The turn-on luminescence response can be switched off by acidic vapors.

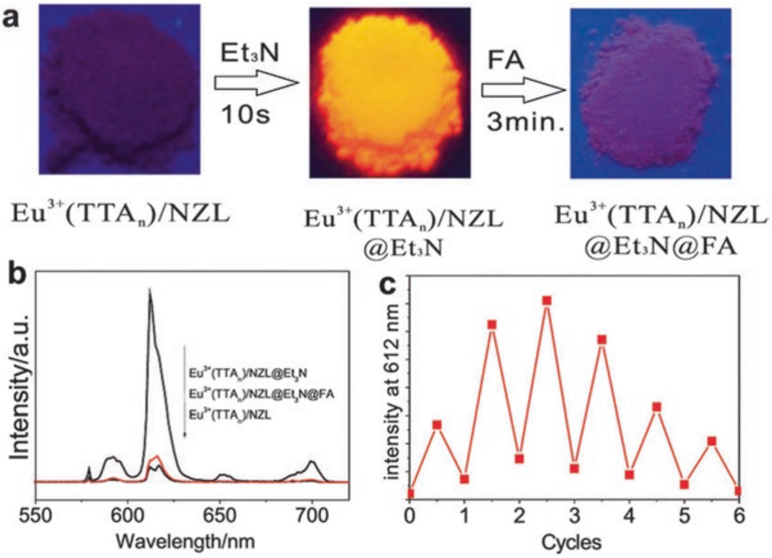

Fig. 4.14 Acid–base vapor-induced luminescence switching of Eu^{3+}(TTA)$_n$–NZL. (*a*) Digital photos of Eu^{3+}(TTA)$_n$–NZL during the exposure to Et_3N–FA vapor; (*b*) emission spectra of Eu^{3+}(TTA)$_n$–NZL showing spectral changes before and after exposure to Et_3N–FA vapor; (*c*) responses of emission intensity at 612 nm of Eu^{3+}(TTA)$_n$–NZL during the Et_3N–FA vapor exposure cycles (Reprinted with permission from Ref. [37]. Copyright 2012 the Royal Society of Chemistry)

Interestingly, when the used Eu^{3+}(TTA)$_n$–NZL samples are exposed to a formic acid (FA)–gas-enriched environment for several seconds, red luminescence disappears and is not visible to the naked eye, while upon subsequent exposure to Et_3N vapor for 5 sec, red luminescence can be seen by the naked eye (Fig. 4.14). The emission spectra of the Eu^{3+}(TTA)$_n$–NZL film are recorded upon alternate exposure to FA gas and Et_3N over at least six cycles in order to examine the reversibility. The high selectivity toward basic molecules, the fast response and good reversibility, and the outstanding robustness are another merit of this method.

Stopper molecules attached to nanozeolite L (NZL) boost the luminescence of confined Eu^{3+}–β-diketonate complexes (Fig. 4.15) [38]. The mechanism responsible has been elucidated by comparing two different diketonate ligands with different pKa values and two aromatic imines, bpy and phen, and by applying stationary and time-resolved spectroscopy. They have found that all of the data support the interpretation that the presence of stopper is favorable to the sustainable formation of Eu^{3+}–β-diketonate complexes with high coordination numbers by decreasing the proton strength inside of the channels of NZL, the main influence being exerted by the stoppers directly bound to the channel entrance. The strongly luminescent transparent films can be prepared using aqueous suspension.

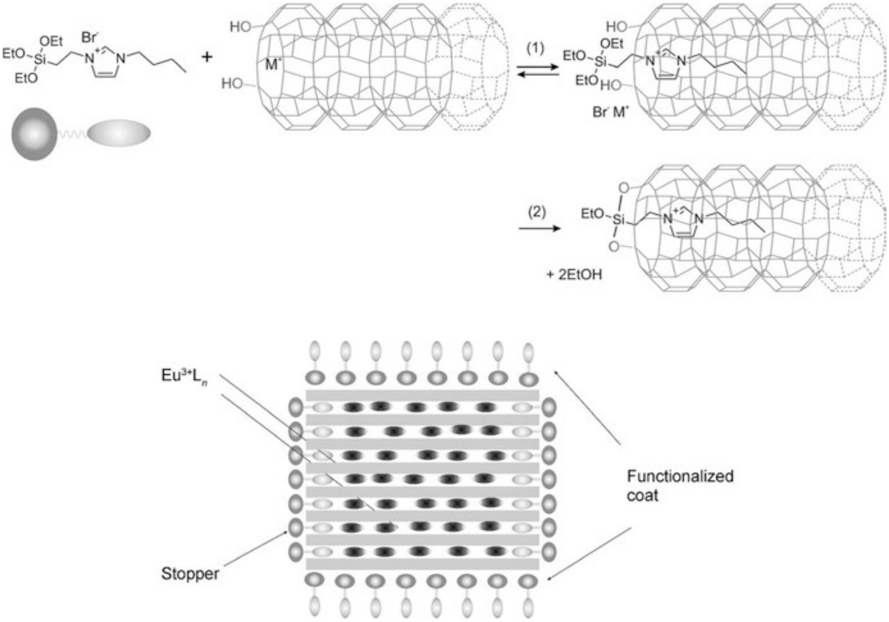

Fig. 4.15 *Upper*: selective modification of the ZL channel entrance; (*1*) sonication and (*2*) reflux. *Lower*: stopper- and coat-functionalized NZL crystal containing inside Eu^{3+} complexes as guests (Reprinted with permission from [38]. Copyright 2014 Wiley)

Li et al. obtain a luminescent and transparent hybrid material by embedding $Ln(L)_n$/ZL nanocrystals into a polymer (polymethyl methacrylate, PMMA) by means of a suitable functionalization of the external surface. In these hybrid materials, lanthanide complexes are encapsulated into the channels of nanosized ZL which are wrapped inside the polymers [39]. PMMA can prevent water molecules from quenching the luminescence of Eu^{3+}/Tb^{3+} inside the channels of nanosized ZL crystals. Functionalization of $Ln(L)_n$/ZL with methacryloxymethyltrimethoxysilane (MATMS) leads to $Ln(L)_n$/ZL-MATMS, and the transparent hybrids ($Ln(L)_n$/ZL-PMMA) are finally prepared from the radical polymerization of the monomer methyl methacrylate (MMA) and the $Ln(L)_n$/ZL-MATMS. Photographs show that the hybrid materials with a ZL content of 2 W/W% are highly transparent and show bright emission under UV illumination.

Liu et al. modify the photoluminescence properties of the $Eu(DBM)_3$ bath complexes by encapsulating it into the sub-nanometer pores of aluminosilicates zeolites L and Y [40]. The outer quantum efficiency of the Eu^{3+} emission and the photostability of Eu^{3+} are both improved considerably. Zeolite L is a more ideal host material for modification of lanthanide complexes. Besides, Chen et al. also functionalize ZL by some rare earth complexes of hydroxybenzene ketone derivatives [41, 42] and realize the multicomponent assembly of ZL with different rare earth luminescence species [43].

4.5 Conclusion and Outlook

In conclusion, recent research progress in the photofunctional rare earth materials based on nanoporous zeolite host has been summarized. The inside–outside double functionalization strategy and the self-assembly method have a special significance for zeolite-based photofunctional rare earth hybrid materials. It needs to mention that the crystal framework of zeolite is important for practical applications. The luminescent devices and sensors based on these hybrid materials should be developed extensively in the future.

References

1. Flanigen EM, Broach RW, Wilson ST (2010) Introduction, zeolites and molecular sieves. 1: zeolites in industrial separation and catalysis. Edited by Santi Kulprathipanja WILEY-VCH Verlag GmbH & co. KGaA, Weinheim
2. Breck DW (1974) Zeolite molecular sieves, structure, chemistry and use. Wiley, New York; Reprinted by Krieger, Malabar, Florida, 1984
3. Flanigen EM (2001) Zeolites and molecular sieves. An historical perspective, in Introduction to zeolite science and practice, 2nd edn (eds H. Van Bekkum, E.M. Flanigen, Jacobs PA, Jensen JC). Stud Surf Sci Catal 137:11–35
4. Devaux A, Minkowski C, Calzaferri G (2004) Electronic and vibrational properties of fluorenone in the channels of zeolite L. Chem Eur J 10:2391–2408
5. Baugis GL, Brito HF, de Oliveira W, de Castro FR, Sousa-Aguiar EF (2001) The luminescent behavior of the steamed EuY zeolite incorporated with vanadium and rare earth passivators. Microp Mesop Mater 49:179–187
6. Nakamura Y, Hasaegawa M, Katsuki K (2005) Microenvironments in faujasite-type Fe-al zeolites probed by europium luminescence. Chem Lett 34:490–491
7. Abry S, Lux F, Albela B, Artigas-Miquel A, Nicolas S, Jarry B, Perriat P, Lemercier G, Bonneviot L (2009) Europium(III) complex probing distribution of functions grafted using molecular stencil patterning in 2D hexagonal mesostructured porous silica. Chem Mater 21:2349–2359
8. Chen SH, Chao KJ, Lee TY (1990) Lanthanum-NaY zeolite ion exchange. 1. Thermodynamics and thermochemistry. Ind Eng Chem Res 29:2020–2023
9. Lee TY, TS L, Chen SH, Chao KJ (1990) Lanthanum-NaY zeolite ion exchange. 2. Kinetics. Ind Eng Chem Res 29:2024–2027
10. Atienzar P, Corma A, Garcia H, Serra JM (2004) High-throughput characterisation of materials by photoluminescence spectroscopy. Chem Eur J 10:6043–6047
11. Chen W, Sammynaiken R, Huang Y (2000) Photoluminescence and photostimulated luminescence of Tb^{3+} and Eu^{3+} in zeolite-Y. J Appl Phys 88:1424–1431
12. Justel T, Wiechert DU, Lau C, Sendor D, Kynast U (2001) Optically functional zeolites: evaluation of UV and VUV stimulated photoluminescence properties of Ce^{3+}- and Tb^{3+}-doped zeolite X. Adv Funct Mater 11:105–110
13. Mech A, Monguzzi A, Cucinotta F, Meinardi F, Mezyk J, De Cola L, Tubino R (2011) White light excitation of the near infrared Er^{3+} emission in exchanged zeolite sensitised by oxygen vacancies. Phys Chem Chem Phys 13:5605–5608
14. Li HR, Ding YX, Wang Y (2012) Photoluminescence properties of Eu^{3+}-exchanged zeolite L crystals annealed at 700 °C. CrystEngComm 14:4767–4771

15. Zhang HH, Li HR (2011) Efficient visible and near-infrared photoluminescence from lanthanide and bismuth functionalized zeolite L. J Mater Chem 21:13576–13580
16. Duan TW, Yan B (2014) Photophysical properties of metal ion functionalized NaY zeolite. Photochem Photobiol 90:503–510
17. Wada Y, Okubo T, Ryo M, Nakazawa T, Hasegawa Y, Yanagida S (2000) High efficiency near-IR emission of Nd(III) based on low-vibrational environment in cages of nanosized zeolites. J Am Chem Soc 122:8583–8584
18. Wada Y, Sato M, Tsukahara Y (2006) Fine control of red–green–blue photoluminescence in zeolites incorporated with rare-earth ions and a photosensitizer. Angew Chem Int Ed 45:1925–1928
19. Duan TW, Yan B (2014) Novel luminescent hybrids by incorporating a rare earth ternary complex into CdS QDs loaded zeolite Y crystals through coordination reaction. CrystEngComm 16:3395–3402
20. Sendor D, Kynast U (2002) Efficient red-emitting hybrid materials based on zeolites. Adv Mater 14:1570–1574
21. Hao JN, Yan B (2014) Photofunctional host-guest hybrid materials and thin film of lanthanide complexes covalently linked to functionalized zeolite a. Dalton Trans 43:2810–2818
22. Chen L, Yan B (2015) Photofunctional hybrid materials with polyoxometalates and benzoate modified mesoporous silica through double functional imidazolium ionic liquid linkage. Coll Polym Sci 293:1847–1853
23. Hao JN, Yan B (2014) Hybrid polymer thin films with a lanthanide-zeolite a host-guest system: coordination bonding assembly and photo-integration. New J Chem 38:3540–3547
24. Chen L, Yan B (2015) Multi-component lanthanide hybrids based on zeolite a/L and zeolite a/L-polymer for tunable luminescence. Photochem Photobiol Sci 14:358–365
25. Chen L, Yan B (2015) Multi-component assembly and luminescence tuning of lanthanide hybrids through the inside-outside double modification of zeolite A/L. New J Chem 39:4154–4161
26. Calzaferri G, Huber S, Maas H (2002) Host–guest antenna materials. Angew Chem Int Ed 42:3732–3758
27. Monguzzi A, Macchi G, Meinardi F, Tubino R, Calzaferri G (2008) Sensitized near infrared emission from lanthanide-exchanged zeolites. Appl Phys Lett 92:123301
28. Mech A, Monguzzi A, Meinardi F, Mezyk J, Macchi G, Tubino R (2010) Sensitized NIR erbium(III) emission in confined geometries: a new strategy for light emitters in telecom applications. J Am Chem Soc 132:4574–4576
29. Li HR, Wang Y, Cao PP, Ding YX, Zhang HH, Hu XJ, Wen TT (2012) Recent progress in host–guest luminescent functional materials based on lanthanide/zeolite L. Sci Chin-Chem (in Chinese) 42:1–18
30. Wang YG, Li HR, Zhang WJ, Liu BY (2008) Luminescence properties of nanozeolite L grafted with terbium organic complex. Mater Lett 62:3167–3170
31. Wang YG, Li HR, LJ G, Gan QY, Li YN, Calzaferri G (2009) Thermally stable luminescent lanthanide complexes in zeolite L. Microp Mesop Mater 121:1–6
32. Li HR, Cheng WJ, Wang Y, Liu BY, Zhang WJ, Zhang HJ (2010) Surface modification and functionalization of microporous hybrid material for luminescence sensing. Chem Eur J 16:2125–2130
33. Wang Y, Li HR, Feng Y, Zhang HJ, Calzaferri G, Ren TZ (2010) Orienting zeolite L microcrystals with a functional linker. Angew Chem Int Ed 49:1434–1438
34. Cao PP, Li HR, Zhang PM, Calzaferri GA (2011) Self-assembling zeolite crystals into uniformly oriented layers. Langmuir 27:12614–12620
35. Ding YX, Wang YG, Li HR, Duan ZY, Zhang HH, Zheng YX (2011) Photostable and efficient red-emitters based on zeolite L crystals. J Mater Chem 21:14755–14759
36. Wen TT, Zhang WJ, Hu XJ, He L, Li HR (2013) Insight into the luminescence behavior of europium(III) β-diketonate complexes encapsulated in zeolite L crystals. ChemPlusChem 78:438–442

37. Li HR, Zhang HH, Wang LY, Mu D, Qi ST, Hu XJ, Zhang L, Yu JS (2012) Highly luminescent Eu^{3+}-exchanged zeolite L crystals resulting from modification with silylated β-diketone. J Mater Chem 22:9338–9342
38. Li P, Wang YG, Li HR, Calzaferri G (2014) Luminescence enhancement after adding stoppers to europium(III) nanozeolite L. Angew Chem Int Ed 53:2904–2909
39. Li HR, Ding YX, Cao PP, Liu HH, Zheng YX (2012) Preparation and luminescence of transparent zeolite L-polymer hybrid materials. J Mater Chem 22:4056–4059
40. Liu HH, Song HW, Li SW, Ren XG, Lv SZ, Yu HQ, Pan GH, Zhang H, Hu LY, Dai QL, Qin RF, Yu JH, Wang GM, Jiang JX (2008) Preparation, characterization and photoluminescence properties of ternary europium complexes $Eu(DBM)_3$bath encapsulated into aluminosilicate zeolites. J Nanosci Nanotechnol 8:3959–3966
41. Chen L, Yan B (2014) Novel cool-white luminescent hybrids through host-guest assembly of 6-hydroxybenz[de]anthracen-7-one and europium ion exchanged zeolite L. Inorg Chem Comm 43:75–77
42. Chen L, Yan B (2014) Luminescent hybrid materials based on zeolite L crystals and lanthanide complexes: host-guest assembly and ultraviolet-visible excitation. Spectrochim Acta A 131:1–8
43. Chen L, Yan B (2015) Novel multi-component hybrids through of double luminescent lanthanide unit functionalized zeolite L and titania. Spectrochim Acta A 151:1001–1003

Chapter 5
Photofunctional Rare Earth Hybrid Materials Based on Functionalized Metal–Organic Frameworks

Abstract This chapter mainly focuses on recent research progress in photofunctional rare earth hybrid materials based on metal–organic frameworks (MOFs) or porous coordination polymers (PCPs), with an emphasis on rare earth ion-functionalized hybrid systems. It covers photofunctional rare earth hybrid materials based on functionalized MOFs through ion substitution, ionic exchange, coordinated postsynthetic modification, and composition of MOFs and other functional units, respectively. The single MOFs or PCPs including pure rare earth MOFs (or PCPs) are not covered here.

Keywords Rare earth ion • Photofunctional hybrid materials • Metal–organic frameworks • Luminescence • Porous coordination polymers

5.1 Introduction to Metal–Organic Frameworks (MOFs)

Metal–organic frameworks (MOFs) or porous coordination polymers (PCPs) themselves are considered as a class of hybrid materials. Their simple synthesis and versatility originate from organic linkers, which bring the renaissance of coordination chemistry. The highly porous and crystalline frameworks of MOFs with large surface area, together with their inherent functionality hosted by both organic and inorganic building blocks, endow them with suitable properties or functions for practical applications such as adsorption, gas storage and separation, catalysis, sensors, light output, bioimaging, drug delivery, etc.

The most popular organic linker to construct MOFs is carboxylic acids, especially the aromatic carboxylic acids with multi-carboxylic groups. MOFs possess sufficiently robust and porous structure, which allows late-stage transformations without compromising overall framework integrity, resulting in a variety of chemical reactions available to modify the framework components. Postsynthetic modification (PSM) of MOFs can so be broadly defined as chemical derivatization of MOFs after their formation. It may refer only to those modifications involving covalent bond formation with the framework [1–3]. The potential advantages of PSM approach to functionalize MOFs are proposed by Cohen et al. [1]:

B. Yan, *Photofunctional Rare Earth Hybrid Materials*,
Springer Series in Materials Science 251, DOI 10.1007/978-981-10-2957-8_5

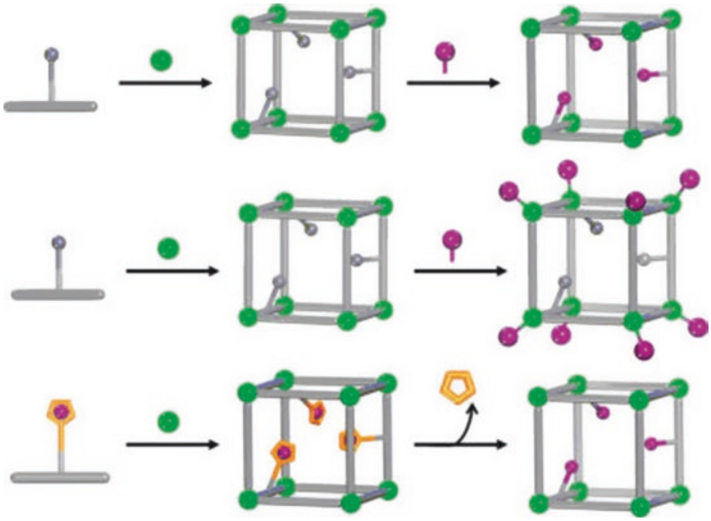

Fig. 5.1 Generic schemes for (*a*) covalent PSM, (*b*) dative PSM, and (*c*) PSD (Reprinted with permission from Ref. [3]. Copyright 2011 the American Chemical Society)

1. A more diverse range of functional groups, freed of the restrictions posed by MOF synthetic conditions.
2. Purification and isolation of modified products are facile because the chemical derivatization is performed directly on crystalline solids.
3. A given MOF structure can be modified with different reagents to generate a large number of topologically identical but functionally diverse MOFs.
4. Control over both the type of substituent and the degree of modification introduces multiple functional units into a single framework in a combinatorial manner to be an effective way for systematically fine-tuning and optimizing MOF properties.

There are a variety of different ways to modify a MOF in a postsynthetic manner, and each of these forms of modification has the capacity to alter the physical and chemical properties of the framework. Postsynthetic modification of MOFs is broadly divided into three areas (Fig. 5.1) [3]: (a) covalent PSM, (b) dative PSM (coordinate covalent PSM), and (c) postsynthetic deprotection (PSD). These postsynthetic methods provide the high complexity and functionality for modified MOFs hybrid materials; the desired chemical transformation should not destroy the MOFs under the reaction conditions used. Subsequently, some new hybrid materials based on MOFs can be obtained by postsynthetic methods, which still retain the characteristic features of MOFs such as high crystallinity, high surface areas, and a structure comprising highly regular coordination bonding. Among covalent PSM is the most extensive, which uses a reagent to modify a component of the MOF in a heterogeneous, postsynthetic manner to form a new covalent bond (Fig. 5.1a). Covalent PSM has provided a powerful and versatile method to introduce a broad

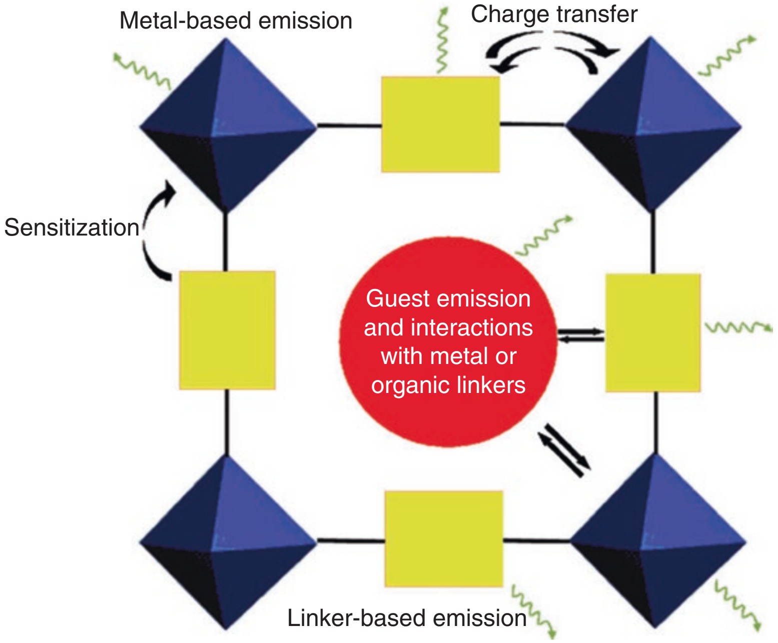

Fig. 5.2 Representation of emission possibilities in a porous MOF, wherein metal clusters (*blue octahedra*) is linked by organic linkers (*yellow rectangles*) with an incorporated guest (*red circle*) (Reprinted with permission from Ref. [4]. Copyright 2014 The Royal Society of Chemistry)

range of chemical groups into MOFs. Dative PSM using a reagent to form a dative (i.e., metal-ligand) bond with a component of the MOF in a heterogeneous, postsynthetic manner, a ligand is either added to the framework that coordinates to the SBU of the MOF or is added to the MOF by binding to the organic linker of the MOF (Fig. 5.1b). PSD is performed on the MOF in a postsynthetic manner that results in the cleavage of a chemical bond within an intact framework (Fig. 5.1c).

The hybrid nature of MOFs materials involving both an organic ligand and a metal ion within a special porous structure enables a wide range of emissive phenomena. Luminescence mainly comes from five components in MOFs (Fig. 5.2) [4]:

1. Linkers or ligands with luminescent groups, typically conjugated organic compounds, absorb in the UV and visible region. Emission can be directly from the linker or can involve a charge transfer with the coordinated metal ions or clusters. The typical system is transition metal-centered MOF.
2. Framework metal ions: proximity to an organic fluorophore, either within the framework or adsorbed within the pore, can produce an antenna effect and a pronounced increase in the luminescence intensity of metals. As transition metal ions with unpaired electrons often quench the luminescence efficiently, lanthanide ion (Ln(III)) MOFs are the typical system, which emit sharp, but weak

luminescence from characteristic transitions of Ln(III) that are forbidden by electric dipole selection rules.

3. Adsorbed lumophores: MOF nanopores provide an opportunity to entrap luminescent molecules in an otherwise non-emissive MOF.
4. Exciplex formation: π–π interactions between adjacent conjugated linkers or between a linker and a guest molecule can produce an excited complex that typically exhibits broad, featureless luminescence.
5. Lumophores bound to the MOF surface: this represents a largely unexplored opportunity to create multifunctional MOFs.

Among them the linkers' luminescence and metal ions' luminescence are most important and extensive. The organic ligands such as carboxylic acids enter the MOF system and become the linkers to construct MOFs with metal ions. So the linker's luminescence may be affected by metal ions' coordination, even the charge-transfer state (CTS) transition is formed. Lanthanide ions' luminescence is mainly sensitized through the intramolecular energy transfer from linkers or ligands. MOFs offer a unique platform for the development of solid-state luminescent materials because they have a degree of structural predictability and well-defined environments for lumophores in crystalline form [5]. The favorable luminescence of the MOFs is expected to have potential application in sensing [6, 7].

All the features allow to develop photofunctional hybrid materials based on rare earth ion-functionalized MOFs. For non-rare earth MOFs, RE^{3+} ions can be introduced into MOF systems by doping, dative, or coordination bonding PSM or ionic exchange. The coordination bonding PSM of MOFs by rare earth ions depends on the free active groups in their organic linkers. The ionic exchange modification of MOFs by RE^{3+} ions requires the cation existence in some anionic MOFs. For rare earth MOFs, the most convenient method to modify them is rare earth ionic substitution, just like the rare earth doping of rare earth solid-state phosphors. The RE^{3+} ion functionalization of MOFs may provide the double luminescence centers in the hybrid systems: one is from linkers and the other is from RE^{3+}ions, whose different luminescence colors in the visible region may be expected to realize the luminescence tuning and white light integration. Moreover, the double luminescence center also gives rise to different sensing behavior, which is useful for fluorescence sensing, especially the ratiometry sensing.

5.2 Photofunctional Rare Earth Hybrid Materials Based on the Ionic Substitution Functionalized Metal–Organic Frameworks

Duan et al. prepare a series of MOF-76(Y):Ln (Ln = Eu, Tb, Sm, Dy) through ionic exchange [8]. The structure of MOF-76(Y) is that the central Y is seven-coordinated by six oxygen atoms from the carboxylate groups of 1,3,5-BTC ligands to form a tetragonal porous framework [9]. As illustrated in Fig. 5.3(Top)(left), the CIE

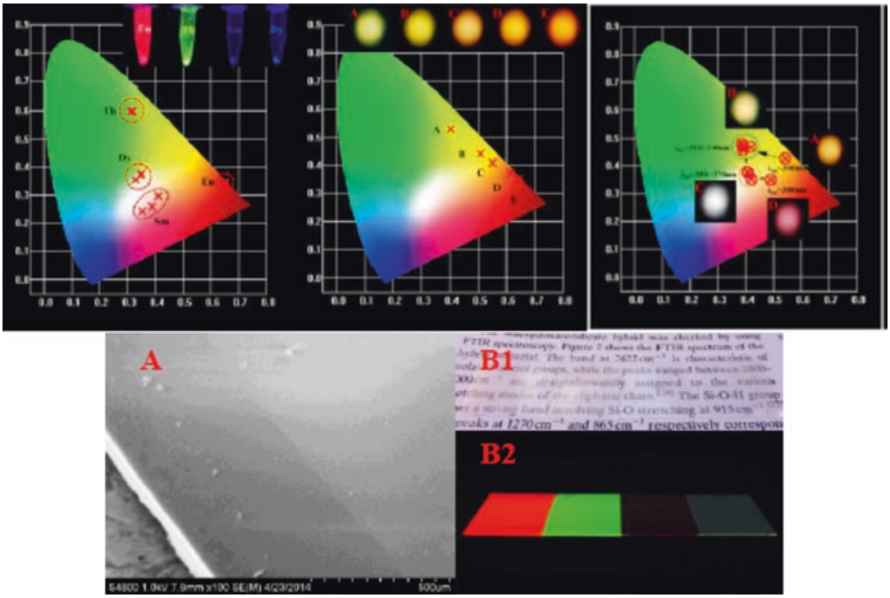

Fig. 5.3 (*Top*) CIE x-y chromaticity diagram of (*left*) MOF-76(Y):Ln (Ln = Eu, Tb, Sm, Dy) with different doping ratios (1, 5, and 10 mol%) using the excitation wavelength of 300 nm, the inset is MOF-76(Y):Ln under the excitation wavelength of 254 nm; (*middle*) MOF-76(Y): x mol% Eu/y mol% Tb. (*A*) MOF-76(Y): 1 mol% Eu/10 mol% Tb; (*B*) MOF-76(Y): 5 mol% Eu/10 mol% Tb; (C) MOF-76(Y): 10 mol% Eu/10 mol% Tb; (*D*) MOF-76(Y): 10 mol% Eu/5 mol% Tb; (*E*) MOF-76(Y): 10 mol% Eu/1 mol% Tb; and (*right*) MOF-76(Y):10 mol% Eu/10 mol% Tb under different excitation wavelengths. The inset shows luminescence of 10 mol% Eu/10 mol% Tb under the excitation of (*A*) 300 nm, (*B*) 330 nm, (*C*) 360 nm, and (*D*) 380 nm. (*Bottom*) (*A*) SEM image of NMOF-76:Eu polymer film; Images of the NMOF-76:Ln (Ln = Eu, Tb, Sm, Dy) polymer film (*B1*) under sunlight and (*B2*) in the ultraviolet box (under 254 nm excitation) (Reprinted with permission from Ref. [8]. Copyright 2014 The Royal Society of Chemistry)

chromaticity coordinates for MOF-76: Ln^{3+} fall in red-orange, green-yellow, pink, and light green regions, respectively. Under 300 nm excitation, MOF-76(Y):Eu and MOF-76(Y):Tb both show fairly bright luminescence. Therefore, changing the doping ratio hardly causes the movement of the coordinates of MOF-76(Y):Eu or MOF-76(Y):Tb, which remains the bright luminescence of red or green. When it comes to MOF-76(Y):Dy or MOF-76(Y):Sm, different doping ratio (1 mol%, 5 mol%, 10 mol%) causes slightly shift of coordinates. With the decrease of doping concentration of Sm^{3+} or Dy^{3+}, the coordinates gradually move toward the blue region. The co-doped MOF-76(Y):x mol% Eu/y mol% Tb under 297 nm excitation displays emission of yellow-green, yellow, warm yellow, orange, and red, respectively (Fig. 5.3(Top)(middle)). The photoluminescence color of MOF-76(Y):10 mol% Eu/10 mol% Tb can be tuned from yellow, yellow-green, and warm white to orange by changing excitation wavelength from 300–380 nm. MOF-76(Y):10 mol %Eu/10 mol% Tb under different excitation wavelengths (300–380 nm) yields various photoluminescence colors (Fig. 5.3(Top)(right)). The surface of the

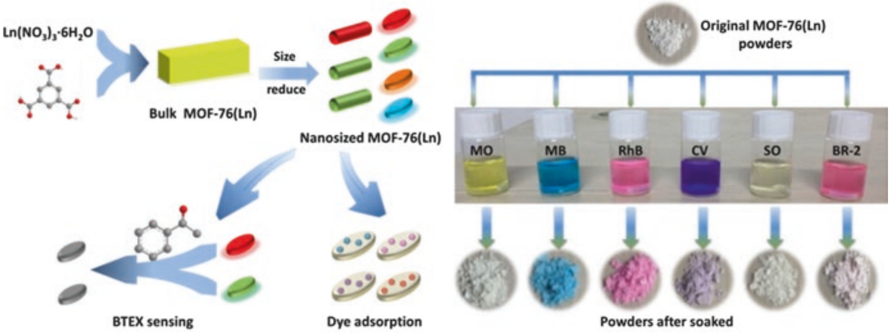

Fig. 5.4 (*Left*) Schematic diagrams of dye adsorption and sensing process of MOF-76(Ln). (*Right*) The schematic diagram and photographs of dye adsorption experiment. The original MOF-76(Ln) powders were immersed in different dye solutions include methyl orange (MO), methylene blue (MB), rhodamine B (RhB), crystal violet (CV), semixylenol orange (SO), and basic red 2 (BR-2) for 48 h, respectively (Reprinted with permission from ref. [10]. Copyright 2016 the Royal Society of Chemistry)

NMOF-76:Eu-fabricated polymer film is smooth, continuous, and defect-free over a large area (Fig. 5.3(Bottom)A), which is transparent under the sunlight (Fig. 5.3(Bottom)B1) and shows emission of red, green, pink, and cold white in the ultraviolet box (254 nm excitation) (Fig. 5.3(Bottom)B2).

Lian et al. further prepare a series of MOF-76(Ln) (Ln = Eu, Tb, Sm, Dy, Yb and Nd) through the similar ionic substitution approach and evaluate the adsorption ability toward different dyes (various solutions of methyl orange (MO), methylene blue (MB), rhodamine B (RhB), crystal violet (CV), semixylenol orange (SO), and basic red 2 (BR-2), respectively) (See Fig. 5.4(Left)). Subsequently, these suspensions are stirred at room temperature for about 48 h, indicating the hybrid system represent different adsorption behaviors, and this difference can be found just by the naked eye (Fig. 5.4(Right)). Samples which are soaked in the MB, RhB, CV, and BR-2 are dyed blue, red, violet, and pink, respectively. But the other two samples soaked in the MO and the SO are remained colorless. That means the cationic dyes, such as MB, RhB, CV, and BR-2, can be adsorbed over a period of time with the colorless crystals gradually becoming colored. However, the anionic dyes like MO and SO could not be adsorbed. This selective adsorption of different dyes is due to the interaction of the dye molecules and framework of hybrid system. The electrostatic interaction makes it possible for dye molecules to combine with the framework. So MOF-76(Ln) can be developed as a potential adsorbent to remove the cationic dyes in aquatic environment.

5.3 Photofunctional Rare Earth Hybrid Materials Based on the Ion Exchange Functionalized Metal–Organic Frameworks

There are a lot of anionic MOFs systems with dimethylammonium (DMA) cations in their porous structure, which can be expected to introduce other cations including metal ions through ionic exchange with DMA, just like traditional zeolite molecular sieves discussed in Chap. 4. This is a versatile and universal strategy to functionalize these kinds of anionic MOFs to obtain hybrid materials.

Among the Bio-MOFs, metal-adeninate organic frameworks reported by Rosi's group are appealing candidates for practical applications because of their permanent microporosity, high surface areas, and chemical stability due to the presence of basic biomolecule building units [11]. Among them, $Zn_8(ad)_4(BPDC)_6O{\cdot}2Me_2NH_2$ (where ad = adeninate, BPDC = biphenyldicarboxylate, denoted as bio-MOF-1) is interconnected via biphenyldicarboxylate linkers, which can be further functionalized via postsynthetic cation exchange of luminescent lanthanide ions [12]. An et al. employ a versatile strategy to generate luminescent lanthanide MOFs compatible for applications in aqueous solutions. They show that a MOF can serve as both a host and an antenna for protecting and sensitizing extra-framework lanthanide cations emitting in the visible (Tb, Sm, and Eu) and NIR (Yb) that are encapsulated within the MOF pores (Fig. 5.5). Ln^{3+} loading does not impact the crystalline integ-

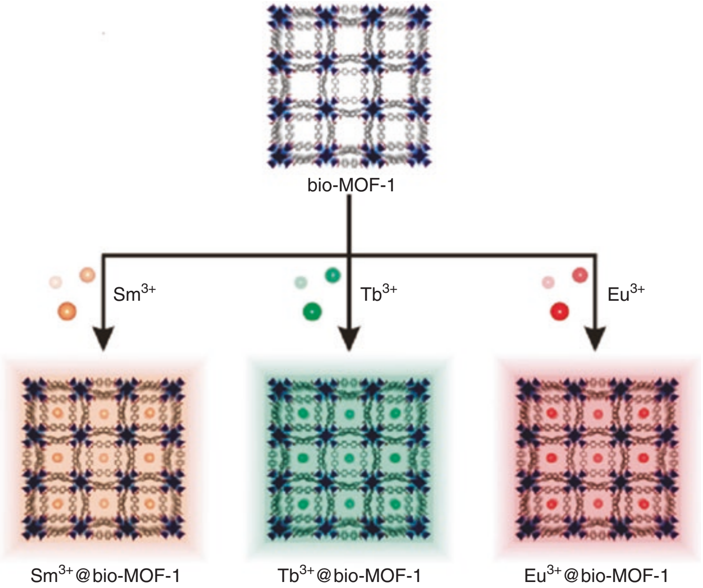

Fig. 5.5 Bio-MOF-1 encapsulation and sensitization of lanthanide cations. Schematic illustration of Ln^{3+} incorporation into bio-MOF-1 and subsequent Ln^{3+}@bio-MOF-1 sensitization by the framework (Reprinted with permission from Ref. [12]. Copyright 2011 the American Chemical Society)

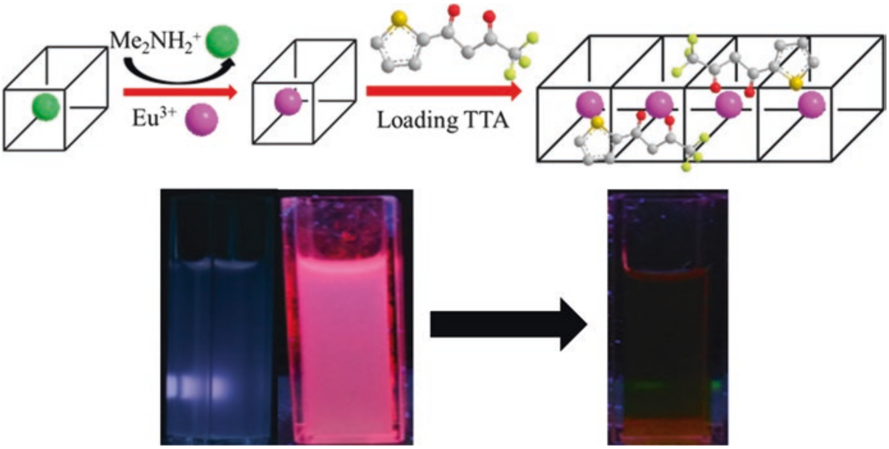

Fig. 5.6 (*Top*)The selected scheme for the synthesis procedures of Eu^{3+} functionalized bio-MOF-1 (Eu^{3+}@bio-MOF-1)) via cation exchange and the encapsulation of TTA with "ship-in-bottle" method; (*Bottom*)the photograph (*Left*) for Eu^{3+}/Tb^{3+}@bio-MOF-1 hybrid system; and the photograph of Eu^{3+}@bio-MOF-1 to sense Fe^{3+} (*Right*) (Reprinted with permission from Ref. [13]. Copyright 2015 Elsevier)

rity of bio-MOF-1. Under irradiation of a standard laboratory UV lamp (365 nm), the distinctive colors (Eu, red; Tb, green; Sm, orange-pink) can be readily observed with the naked eye. The individual samples excited with 340 nm light exhibit the characteristic sharp emission corresponding to the respective encapsulated Ln^{3+} cations.

Yan's group further carries out the research on bio-MOF-1 for photofunctional hybrid materials [13–15]. Firstly, Shen et al. introduce TTA to Eu^{3+} (or Eu^{3+}/Tb^{3+}) exchanged bio-MOF-1 by "ship-in-bottle" method (Fig. 5.6(Top)) [13]. They check the luminescence of bio-MOF-1 itself, whose excitation spectrum shows a similar broad excitation band ranged in 250 ~ 400 nm, and emission spectrum presents a broad band covering 350 ~ 550 nm with maximum peak at around 400 nm to display deep blue color. The introduction of TTA ligand to Eu^{3+}@bio-MOF-1 hybrid system can improve the luminescent intensity of Eu^{3+}, while the emission intensity of bio-MOF is hardly changed because TTA can be dispersed into bio-MOF-1 to link with Eu^{3+} through coordination bonds. The emission spectrum of double lanthanide ion (Eu^{3+}/Tb^{3+})-functionalized bio-MOF-1 hybrid system contains the characteristic emissions of the two lanthanide ions together with bio-MOF-1, showing CIE coordinate close to white region (Fig. 5.6(Bottom)(Left)). Besides, the energy transfer efficiency of Eu^{3+}@bio-MOF-1 is similar to that of TTA-Eu^{3+}@bio-MOF-1, indicating the energy transfer between bio-MOF-1 and Eu^{3+} is similar, and so the enhancement of the emission in TTA-Eu^{3+}@bio-MOF-1 is due to TTA ligand. Further, it is found that the introduction of Fe^{3+} almost quenches the luminescence of Eu^{3+}@bio-MOF-1 hybrids (photograph in Fig. 5.6(Bottom), Right).

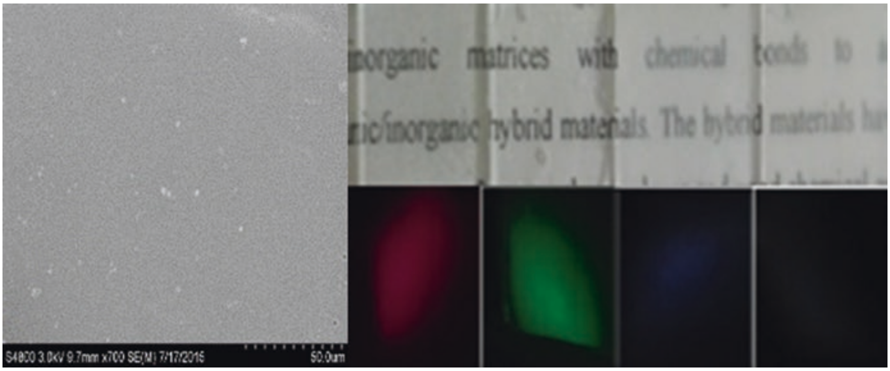

Fig. 5.7 (*Left*) SEM image of Eu^{3+}@Cd-MOF-2; and (*Right*) the images of Ln^{3+}@Cd-MOF-2 polymer films under sunlight (*top*), images of Ln^{3+}@Cd-MOF-2 polymer films under xenon lamp when excited at 293 nm (*bottom*) (Reprinted with permission from Ref. [16]. Copyright 2016 the Royal Society of Chemistry)

Weng et al. prepare a series of luminescent Ln^{3+}@Cd-MOF (Ln = Eu, Sm, Tb, Dy) hybrid system via postsynthetic cation exchange, while Ln^{3+} ions substitute $(Me_2NH_2)^+$ cations in the porous structure [16, 17]. The emission of both Eu^{3+}@Cd-MOF and Tb^{3+}@Cd-MOF can be easily observed by the naked eye, and the emission of ligand is hardly detected, while the ligand-centered emission bands at 365 nm of Sm^{3+}@Cd-MOF and Dy^{3+}@Cd-MOF are obvious. Meanwhile, they also obtain white light by introducing two kinds of lanthanide ions into the Cd-MOF. The introduction of both Sm^{3+} and Tb^{3+} displays the characteristic peaks of them to integrate white light. While for the introduction of Eu^{3+} and Tb^{3+}, the emission color presents a change from green to yellow gradually. Moreover, the Ln^{3+}@Cd-MOF hybrid polymer film is prepared with the assistance of EMA and BPO. The SEM image of Eu^{3+}-fabricated polymer is shown in Fig. 5.7(Left), the surface of the film is smooth and defect-free over a large area. The lanthanide ion-fabricated polymer films are transparent under sunlight, while showing red, green, blue, and white colors when excited at 293 nm under Xenon lamp (Fig. 5.7(Right)).

Zhao et al. present a anionic MOF $\{[Me_2NH_2]_{0.125}[In_{0.125}(H_2L)_{0.25}]\cdot xDMF\}_n$ (1) with a large 1D channel (13.06 × 13.06 Å^2), by the treatment of 4,8-disulfonyl-2,6-naphthalenedicarboxylic acid (H_4L) with $InCl_3$ under solvothermal condition. Through the postsynthetic cation exchange process, Ln^{3+}-modified MOF hybrid system is easily prepared, which can be used as a potential luminescent probe toward different Ln^{3+} ions. The emission spectra of the as prepared Ln^{3+}-loaded MOF materials indicate that they are suitable for the sensitization of Eu^{3+} emitter rather than Tb^{3+}, Dy^{3+}, and Sm^{3+} emitters. [18].

5.4 Photofunctional Rare Earth Hybrid Materials Based on the Coordinated Metal–Organic Frameworks

MOF-253 with a bipyridine derivative in the ligand, reported by Yaghi and co-workers, is famous in the inherent advantage of postsynthetic method (PSM) [19–24]. In the structure of MOF-253, one-dimensional infinite chains of AlO_6 corner-sharing octahedra are built by connecting bpydc (bpydc = 2,2′-bipyridine-5,5′-dicarboxylic) linkers to construct rhombic-shaped pores. The representative structure of MOF-253 has been resolved by PXRD and a Pawley refinement using the Al(OH)(bpdc) ($bpdc^{2-}$ = 4,4-biphenyldicarboxylate) unit cell parameters in the reported work [19]. With PSM, the application of modified MOF-253 has been extended to luminescent material and fluorescent sensing [20–22].

Lu et al. present a new strategy for preparing MOF-based monolayer luminescent thin film [23]. MOF-253-Ln is prepared through PSM, in which lanthanide ions (Eu^{3+}, Tb^{3+} or Yb^{3+}) are firstly encapsulated to a fabricated MOF (MOF-253) host by coordination effect between Ln^{3+} ion and bipyridine of ligand, and then the second ligand TTA or TAA (TAA = 1,1,1-trifluoropentane-2,4-dione) is introduced to sensitize the incorporated Ln^{3+} ion. The functionalized plates, 1(Eu^{3+})-quartz, can be further immersed in a suspension of MOF-253 in toluene to realize the formation of MOF-1(Eu^{3+})-quartz (Fig. 5.8(Top)). Here, Eu^{3+} ion is used as linker to connect the MOF-253 and the functionalized plates. The transparent Eu-HBA-functionalized quartz plates (1(Eu^{3+})-quartz) turn opaque upon contact with the suspension of MOF-253 in dry toluene under vigorous sonication. The SEM images of the modified quartz plates (MOF-1(Eu^{3+})-quartz) reveal that the coverage degree and packing degree are both highly satisfactory, although some spots with less surface coverage can be observed in Fig. 5.8(Bottom, a). And then, the thin film is transparent in the photograph (Fig. 5.8(Bottom, c)); the thickness of the thin film should be less than 100 nm. The point of emission spectrum of MOF-1(Eu^{3+})-quartz under 390 nm in CIE chromaticity diagram is in the area of yellow color. So the white light can be archived by the yellow light (from MOF) and the violet light (from the excited light). And every point of this line can be achieved by different contents of phosphors. A cold white light can be achieved by the combination of blue (from substrate) and yellow light (from phosphor). For MOF-1(Eu^{3+})-quartz, the CIE points is $X = 0.36$ and $Y = 0.50$. The line of CIE point and 390 nm (round the color area) is cross the white light. That means the white light can be achieved by MOF-1(Eu^{3+})-quartz under 390 nm. In the photograph of MOF-1(Eu^{3+})quartz, the thin film can emit white light under 390 nm (Fig. 5.8(Bottom, b)).

Lu et al. further report a new method for luminescent lanthanide barcode based on postsynthetic modified nanoscale MOFs (MOF-253). Multiple visible-emitting lanthanide ions (Eu^{3+}, Tb^{3+} and Sm^{3+}) are introduced to MOF-253 by PSM to realize barcoding (Fig. 5.9(Top)) [24]. The luminescent intensities of the two emitting lanthanide ions can be quantitatively controlled by controlling the lanthanide composition. Their relative intensities can be reflected as unique and visible color which is corresponding to three distinct barcodes. The points of emission of

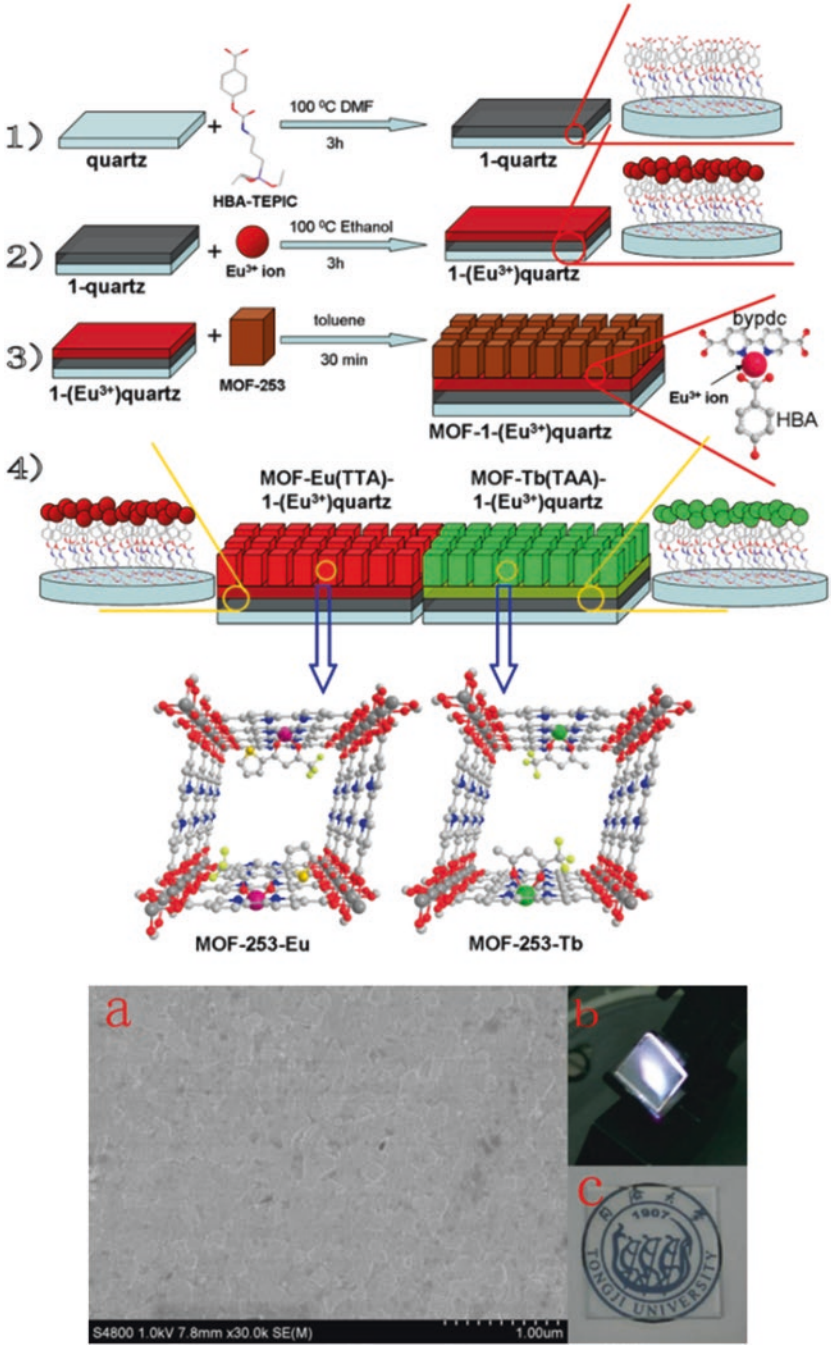

Fig. 5.8 (*Top*) The procedure to prepare the thin-film materials based on PSM and functional linker: (*1*) 1-quartz, (*2*) 1-(Eu^{3+})quartz, (*3*) MOF-1(Eu^{3+})quartz and (*4*) MOF-Eu(TTA)-1(Eu^{3+})quartz and MOF-Tb(TAA)-1(Tb^{3+})quartz. (*Bottom*) SEM images of MOF-1(Eu^{3+})quartz thin film (*a*) viewed from surface, the white light from MOF-1(Eu^{3+})quartz under the light of 390 nm (*b*) and the photograph of MOF-1(Eu^{3+})quartz thin film (*c*) (Reprinted with permission from Ref. [23]. Copyright 2016 the Royal Society of Chemistry)

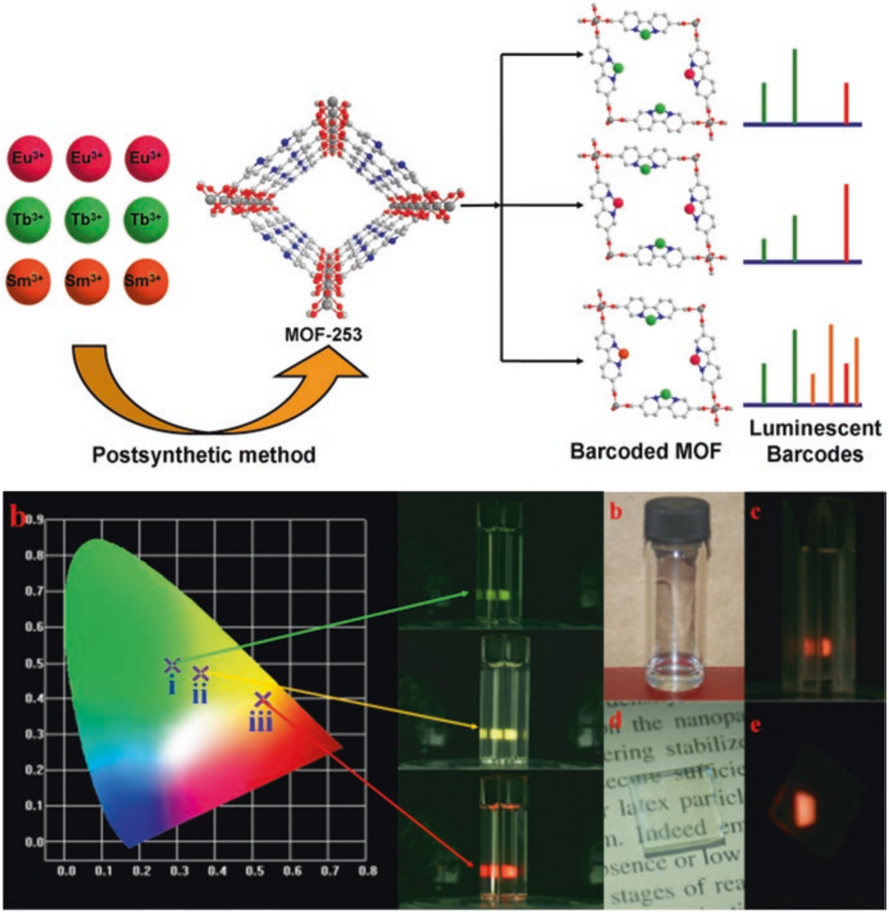

Fig. 5.9 (*Top*) The scheme for luminescent lanthanide barcodes based on PSM; (*bottom*) color-coded of the barcode readout in CIE chromaticity diagram and the photograph of the MOF-253-based barcoded material (dispersed in ethanol) under excitation at 330 nm, *i*, *ii*, and *iii* is MOF-253-$Tb_{0.999}Eu_{0.001}$, MOF-253-$Tb_{0.995}Eu_{0.005}$, and MOF-253-$Tb_{0.99}Eu_{0.01}$, respectively (*left*) and (*right*)the photograph of IL-MOF-Ln (*b*) and under excitation at 330 nm (*c*), the photograph of thin film constructed by MOF-253-Ln-1(*d*) and the red light from the thin film under excitation at 330 nm (*e*) (Reprinted with permission from Ref. [24]. Copyright 2015 the Royal Society of Chemistry)

MOF-253-$Tb_{0.95}Eu_{0.05}$, MOF-253-$Tb_{0.99}Eu_{0.01}$, and MOF-253-$Tb_{0.995}Eu_{0.005}$ in CIE chromaticity diagram are green (X = 0.2876, Y = 0.4915), yellow (X = 0.3630 Y = 0.4698), and red (X = 0.5276, Y = 0.3980), respectively (Fig. 5.9(Bottom,a)). The synthesized nanoscale barcoded material can be used in marking functional ionic liquid (1-(2-hydroxyethyl)-3-methylimidazolium bromide) and preparing thin film on ITO glass by direct spin coating (Fig. 5.9(Bottom)). The IL-MOF-Ln is clear (about 70 °C) and can emit the luminescent barcoded signal under 330 nm

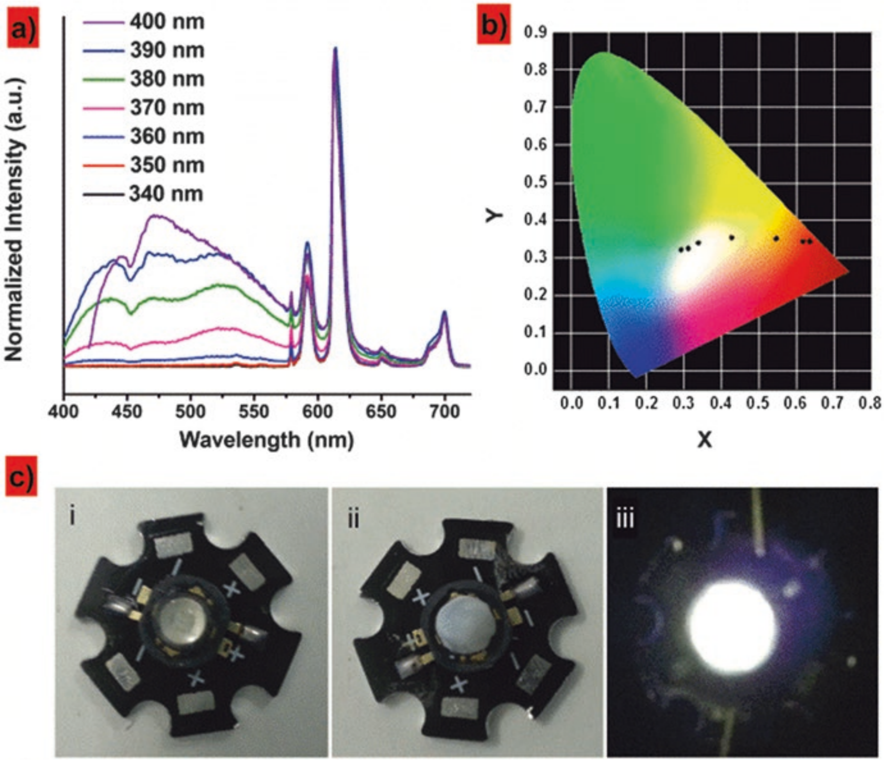

Fig. 5.10 (**a**) Emission spectra of Eu^{3+}@ MOFUiO-67-bpydc when excited by the wavelength at 340–400 nm. Spectra were normalized to the $^5D_0 \rightarrow {}^7F_2$ transition of Eu^{3+}. (**b**) CIE chromaticity diagram showing the luminescent color of Eu^{3+}@ MOFUiO-67-bpydc under various excitation wavelengths. (**c**) Photographs of a UV (375 nm) InGaAsN LED chip (*i*), the same LED coated with a thin layer of nanocrystals of Eu^{3+}@ MOFUiO-67-bpydc (*ii*), and the coated LED turned on and illuminating bright white light (*iii*) (Reprinted with permission from Ref. [28]. Copyright 2016 the Royal Society of Chemistry)

(Fig. 5.9(Bottom, b, c)). ITO glass-supported luminescent thin films of MOF-253-Ln-1 are transparent (Fig. 5.9(Bottom, d)) and emit the luminescent barcoded signal under 330 nm (Fig. 5.9(Bottom, e)).

Research work can be extended to the MOFs which have similar linker, H_2bpydc, as MOF-253 [25–27]. MOFUiO-67-bpydc also has the linker H_2bpydc [28] with high stability, so it can be modified through the similar coordination path [29–31]. In Eu^{3+}@ MOFUiO-67-bpydc hybrid system, both the framework MOFUiO-67-bpydc and the incorporated Ln^{3+} cations contribute to the compound's luminescence, so it can be expected to achieve a fine tuning of emission color by modulating the excitation wavelength. Figure 5.10a depicts the emission spectra of Eu^{3+}@ MOFUiO-67-bpydc with excitation wavelength from 340 to 400 nm, whose excitations at different wavelengths give rise to different emission intensity ratios of these two kinds of luminescence (Eu^{3+} emission and the ligand-centered emission), leading to a shift of the chromaticity coordinate in the chromaticity diagram. As shown in Fig. 5.10b, the calculated chromaticity from the emission spectra of Eu^{3+}@MOFUiO-67-bpydc moves from the red region to the white region as the excitation wavelength varying from 340 to 400 nm. Notably, the coordinates are (0.4267, 0.3557), (0.3372, 0.3419), and (0.3102, 0.3265) when the sample is excited at 370, 380, and 390 nm, respectively, which closely approach the optimum white light chromaticity coordinates (0.33, 0.33) established by the CIE. Figure 5.10c demonstrates the white LED fabricated by combining Eu^{3+}@MOFUiO-67-bpydc nanophosphors with a UV LED chip. A thin layer of Eu^{3+}@MOFUiO-67-bpydc prepared from a methanol solution is coated onto a commercially available UV LED chip through a simple and efficient dip-coating procedure. Upon illumination, it generates bright white light. The electroluminescence spectrum of the white LED under a drive current of 150 mA presents a broad emission band in the range of 400–550 nm band and several sharp lines ranging from 570 to 710 nm. The CIE and CCT values are (0.3481, 0.3292) and 4914 K, respectively. The CRI is determined as 75 and the luminous efficiency of the fabricated LED is 32 lm W^{-1} [29].

Another typical MOF is Al-MIL-53 derivative or its analogues with a high crystalline framework and regular one-dimensional channels, which shows high structural flexibility [32]. The presence of non-coordinating carboxyl group, as well as the high thermal and chemical stabilities of the Al-MIL-53 derivatives, makes these compounds a good candidate to incorporate with Ln^{3+} ions and sensitize the Ln^{3+} luminescence [33]. Zhou et al. introduce Ln^{3+} cations into the pores of compound Al-MIL-53-COOH. After the postsynthetic functionalization of Ln^{3+}, the products emitted their distinctive colors (Eu^{3+}, red; Tb^{3+}, green; Eu^{3+}/Tb^{3+}, yellow), which can be readily observed with the naked eye as a qualitative indication of lanthanide sensitization. The Eu^{3+} emission collected at the excitation wavelength of 318 nm continually improves when further raising the concentration of Eu^{3+}. In contrast, the ligand-centered emission decreases with the increase of Eu^{3+} concentration due to the enhancement of the energy transfer probability from organic linkers to Eu^{3+} (Fig. 5.11(Top, a)). The emission colors can be modulated from blue to white to red (Fig. 5.11(Top, b)). The white luminescence can be further confirmed by the photograph irradiated under 318 nm wavelength (the inset in Fig. 5.11(Top, a)), which is from the single-component Eu^{3+}@Al-MIL-53-COOH balanced on synergetic contribution from Eu^{3+} and ligand-centered dual emission. Figure 5.11(Bottom, a) presents the emission spectra of Eu^{3+}@Al-MIL-53-COOH, the intensity of the broad band arising from the framework increases with the excitation wavelength varying from 320 to 360 nm contrary to the Eu^{3+} emission. The corresponding CIE chromaticity diagram in Fig. 5.11(Bottom, b) shows a tunable chromaticity of emission from red to blue, verifying that the white light emitting from Eu^{3+}@Al-MIL-53-COOH is caused by the broad blue emission of Al-MIL-53-COOH and red emission of incorporated Eu^{3+} simultaneously. It indicates a potential approach to manage the white light emission by means of such dual emissive single-phase compound, which opens the way to practical applications such as pellets, membranes or sensors. The transparent, continuous, and homogenous thin film of Eu^{3+}@Al-MIL-53-COOH is prepared and shows white light emission under 350 nm excitation.

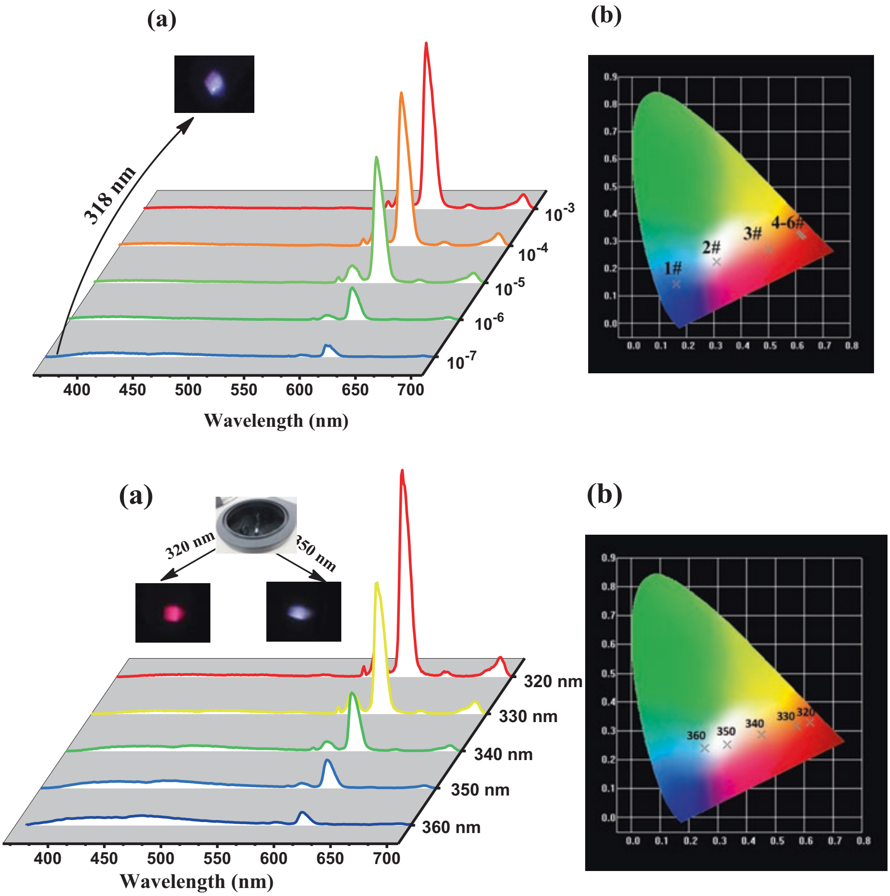

Fig. 5.11 (*Top*) Emission spectra ($\lambda_{ex} = 318$ nm) (**a**) and CIE chromaticity (**b**) of Eu^{3+}@**1** products resulted from $EuCl_3$ ethanol solutions with concentrations in the range of 10^{-7}–10^{-3} $molL^{-1}$. (*Bottom*) Emission spectra (**a**) and CIE chromaticity diagram (**b**) of Eu^{3+}@**1** collected at different excitation wavelengths (Reprinted with permission from Ref. [33]. Copyright 2016 the Royal Society of Chemistry)

MIL-124 ($Ga_2(OH)_4(C_9O_6H_4)$) with adjacent chains are linked to each other through the carboxylate functional groups at 1,2 positions of 1,2,4-H_3btc with a bidentate mode bridging the two gallium atoms. It results in the formation a layer-like network developed in the (a,c) plane. The hydrogen bond interactions between the terminal carboxylic acid from one gallium hydroxide trimellitate layer and the bridging hydroxy groups from an adjacent one lead to the three-dimensional cohesion of the MIL-124 structure [34]. Xu et al. choose MIL-124 as a parent framework to load Ln^{3+} cations with the purpose of getting a new class of lanthanide luminescent MOFs [35]. After postsynthetic functionalization of Ln^{3+} (Ln = Eu, Tb, Eu/Tb), the products yield their corresponding emissions, while emission intensities from

1,2,4-H_3btc still remain. Considering that MIL-124 provides blue light, by means of the Eu^{3+} ion (red emission) singly doped in to the MIL-124 framework, it will therefore be possible to construct white emitting material, whose CIE chromaticity diagram shows a tunable chromaticity of emission from red to white to blue by varying the excitation wavelength from 310 to 340 nm and the color is confirmed by the photographs irradiated under 299 nm. The optimized chromaticity coordinates can be tuned to (0.3693, 0.3362) when excited at 297 nm, which is very close to the value for ideal white light (0.333, 0.333).

Besides, according to the similar postsynthetic modification path of uncoordinated carbonyl groups, Cao et al. prepare the 3D microporous compound $[Zn_3(Httca)_2(4,4'\text{-bpy})(H_2O)_2]_n$(MOF–COOH, H_4ttca = 1,1′:2′,1″-terphenyl-‘4,4′,4″,5′-tetracarboxylic acid) and the lanthanide ion-exchanged hybrid systems. It is shown that it can effectively and selectively serve as an antenna for sensitizing the visible-emitting Tb^{3+} cation [36].

5.5 Photofunctional Rare Earth Hybrid Materials Based on the Covalent Postsynthetic Modification of Metal–Organic Frameworks

There are many examples on the covalent postsynthetic modification of MOFs, but the usage of them for rare earth hybrid systems is few. The main reason may be due to the stability of post-synthetically modified MOFs is hard to maintain.

Recently, Abdelhameed et al. show that postsynthetic modification of MOFs is an excellent route to prepare infrared and visible light emitters [37], and here our group wish to extend our studies to modifications with other linkers, in order to firmly establish the general characteristics of this approach [38, 39]. Isoreticular IRMOF-3 is chosen due to its high porosity and the presence of non-coordinating amino groups on the benzenedicarboxylate linker, which may be easily modified [37]. Thus, the amino groups of IRMOF-3 are post-synthetically modified by nucleophilic substitution (chloroacetic acid), nucleophilic addition (glyoxylic acid), reductive amination (glyoxylic acid), and a- and b-additions to a,b-unsaturated carbonyl compounds and subsequently coordinated to Eu^{3+} and Nd^{3+} ions (as shown in Fig. 5.12). The presence of a second aromatic ring on the b-diketonate may further enhance the Ln^{3+} sensitization. In the visible spectral range, the emission spectra of the Nd^{3+}-containing samples consist of a broad band ascribed to the hybrid host. A very similar broad band has been reported for Nd^{3+}-complexes of β-diketonates also bearing aromatic ligands and is assigned to π–π^* and/or n–π^* transitions.

Liu et al. construct the MOF-based microsized chemosensor from a pyrene-functionalized organic building block (H_2L) and 2-(pyrene-1- imine)terephthalic acid (Fig. 5.13) [40]. The structure of H_2L includes three important parts: (a) terephthalic acid moiety for MOF structure construction, (b) imine moiety for supplying binding site of metal ions, and (c) pyrene moiety for the use as a fluorophore.

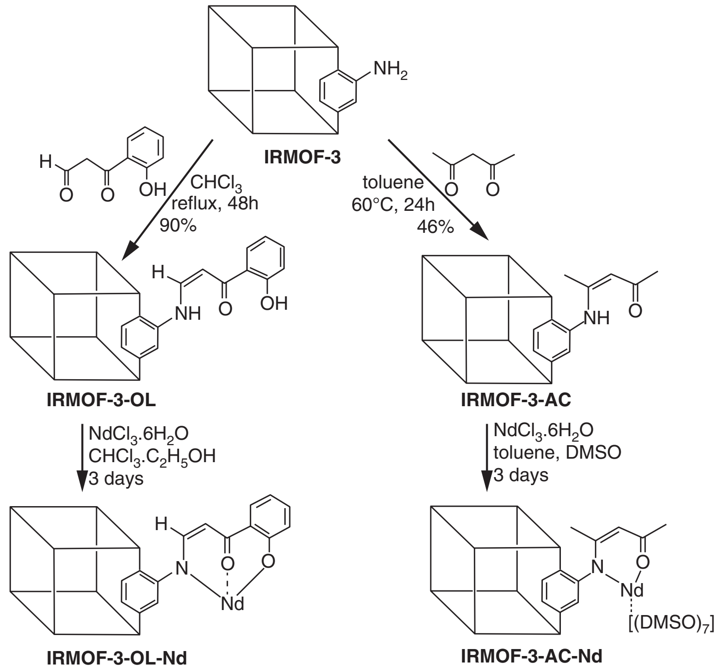

Fig. 5.12 Scheme for postsynthetic covalent modification of IRMOF-3 with pentane-2,4-dione and 3-(2-hydroxyphenyl)-3-oxopropanal and ensuing Nd^{3+} coordination (Reprinted with permission from Ref. [37]. Copyright 2013 the Royal Society of Chemistry)

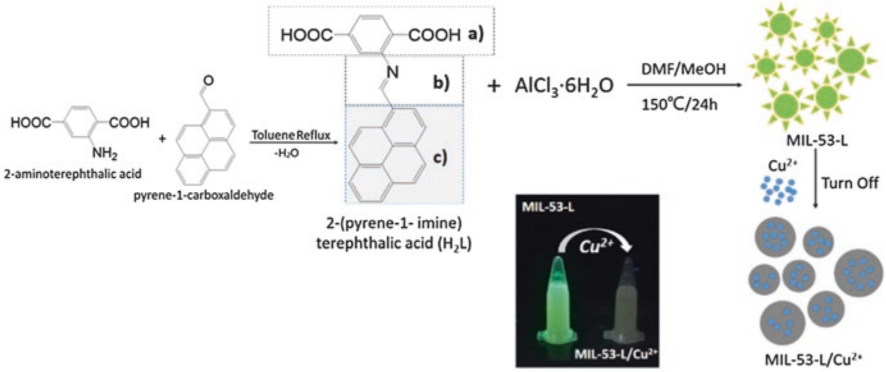

Fig. 5.13 Schematic representation for turnoff fluorescent chemosensor of microsized MIL-53-L on Cu^{2+}. In the organic ligand of H$_2$L, (*a*) framework construction part, (*b*) detecting part, (*c*) fluorophore part (Reprinted with permission from Ref. [40]. Copyright 2016 Elsevier Publisher Ltd)

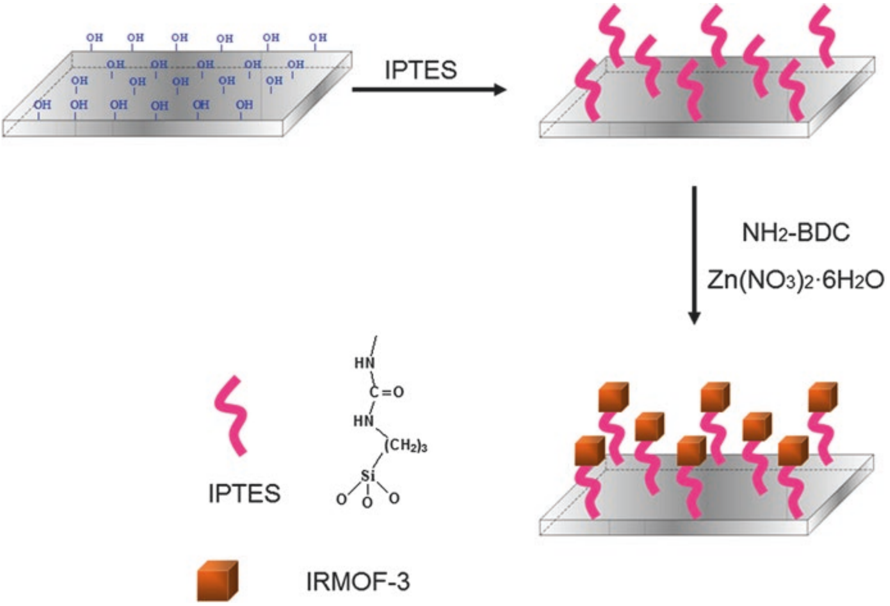

Fig. 5.14 The selected scheme for the composition of hybrid materials Ln-SBA-15-Si-IRMOF-3 (Ln = Eu, Tb, Nd, Yb) (*top*) and (*bottom*) (Reprinted with permission from Ref. [41]. Copyright 2015 the Royal Society of Chemistry)

The structure of MIL-53-L material is made up of chains of corner sharing $AlO_4(OH)_2$ octahedra interconnected by H_2L groups. And all of the pyrene groups are present in the form of excimer in MIL-53-L. After the formation of MIL-53-L, the initial emission band of H_2L (480 nm) disappears completely and new emission band is located at 567 nm, when excited at 337 nm in aqueous suspension, and it shows an intense yellow color under UV light irradiation. These new bands are attributed to the excimer species of pyrene moieties; the main reason is that pyrene units overlap and result in intramolecular π–π stacking interactions. There may be a confinement effect that makes all pyrene moieties exist in the excimer form instead of the monomer form after MOF formation. As a result of the limited space in the inner of MOF structure, pendant pyrene groups will be forced to move in together and form the excimer. This discovery reveals an inevitable confinement effect within MOF, which causes a conformational adjustment of dangled groups. The hybrid system MIL-53-L shows the high selectivity for the sensing and specific recognition of Cu^{2+} in aqueous media.

Lian et al. prepare a series of lanthanide hybrid materials containing both MOFs and SBA-15 through the multicomponent assembly strategy-based covalent post-synthetic modification, which is named as Ln-SBA-15-Si-IRMOF-3 (Ln = Eu, Tb, Nd, Yb) (Fig. 5.14) [41]. SBA-15 can be easily modified by the cross-linking reagent IPTES to form the Si-SBA-15 through the cohydrolysis and co-polycondensation process between the alkoxyl groups of IPTES and hydroxyl groups of SBA-15. On

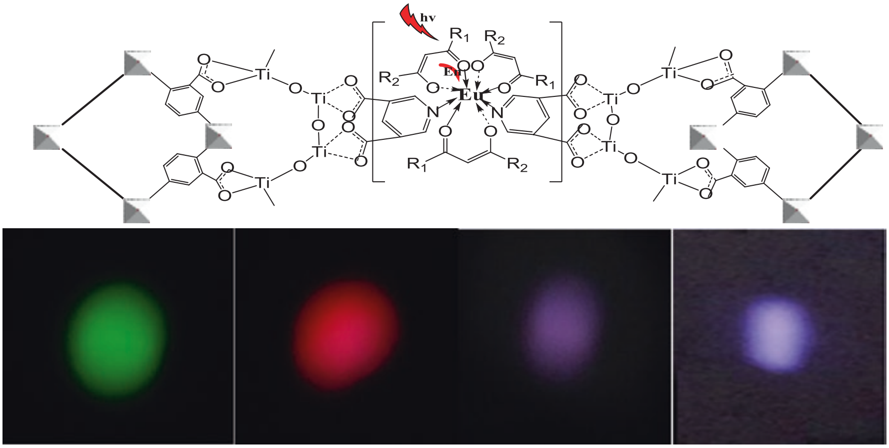

Fig. 5.15 (*Top*) The selected scheme for the synthesis process, composition, and proposed structure of TTA/TAA-Eu-PDA-Ti-MOF, other hybrid systems show the similar scheme except for different beta-diketonates or alumina unit. (*Bottom*) Photographs of the photoluminescence color from power with the UV excitation using a Xe lamp as the excitation source. The images from left to right stand for hybrid materials TAA-Tb-PDA-Al-MOF, TAA-Eu-PDA-Al-MOF, TTA-Eu-PDA-Al-MOF and TAA-Eu-PDA-Ti-MOF, respectively (Reprinted with permission from Ref. [42]. Copyright 2014 the Royal Society of Chemistry)

the other hand, IRMOF-3 is in situ synthesized and then is covalently grafted to Si-SBA-15 through the addition reaction between its amino group and inner ester group of Si-SBA-15. Finally, lanthanide ions (Eu^{3+}, Tb^{3+}, Nd^{3+}, Yb^{3+}) are introduced into SBA-15-Si-IRMOF-3 host through the coordination reaction. The selected small angel X-ray diffraction patterns (SAXRD) of the prepared SBA-15, and IPTES modified Si-SBA-15 shows the typical character of highly uniform mesoporous materials. Both SBA-15-Si-IRMOF-3 and Eu SBA-15-Si-IRMOF-3 present a regular hexagonal array of uniform channels, which is the characteristic of mesoporous SBA-15 material. The mesostructure of the micro-mesoporous complex materials can be substantially conserved after the coordination process. The characteristic luminescence of Ln^{3+} in both visible and near-infrared regions can be obtained and even white luminescence can be integrated.

Xu et al. fabricate Al-MIL-53-COOH and rare earth complexes in inorganic matrices (alumina or titania) through coordination bonds to assemble the multicomponent hybrid materials (Fig. 5.15(Top)). [42] Metallic alkoxides ($Ti[OCH(CH_3)_2]_4$, $Al[OCH(CH_3)_2]_3$) can be modified by reagents with carboxylic groups such as PDA. Then the rare earth beta-diketonates can further coordinate to PDA-modified metallic alkoxides for the high coordination number and remained nitrogen atom of PDA. On the other hand, Al-MIL-53-COOH can be also introduced in the courses of sol–gel reaction process to form alumina and titania for its uncoordinated COOH group. Subsequently, after the hydrolysis and polycondensation process of metallic alkoxides, the final hybrid materials based on alumina or titania are prepared, and the photoactive units of MOF and rare earth complexes are chemically linked.

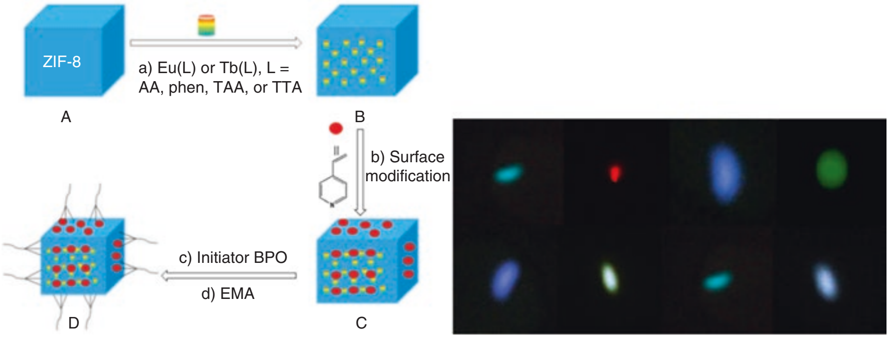

Fig. 5.16 (*Left*) Synthesis procedure and predicted structure of the hybrid polymer films of PEMA-PVPD ⊃ Ln-L/ZIF-8 (Ln = Eu, Tb; L = AA, phen, TAA): (*A*) composing lanthanide complexes both into the cages and onto the surface of ZIF-8 to form Ln-L/ZIF-8; (*B*) linking VPD with Ln-L/ZIF-8 through coordination bond; (*C*) introducing EMA and BPO (as initiator) in this system; (D) copolymerization reaction and film anchoring to the final hybrid films; (*Right*) photograph of selected hybrid films for luminescence color change from ZIF to hybrids from *left* to *right* and *top* to *bottom*: PEMA-PVPD ⊃ Eu-TTA/ZIF-8 (*blue* → *red*, λ_{ex} = 400 nm → 370 nm), PEMA-PVPD ⊃ Tb-AA/ZIF-8 (*blue* → *green*, λ_{ex} = 395 nm → 319 nm), PEMA-PVPD ⊃ Eu/Tb/ZIF-8 (*blue* → *light yellow*, λ_{ex} = 395 nm → 280 nm) and PEMA-PVPD ⊃ Eu/Tb-phen/ZIF-8 (*blue* → *white*, λ_{ex} = 395 nm → 300 nm) (Reprinted with permission from Ref. [46]. Copyright 2015 Wiely Publisher)

Three hybrids based on alumina, and the TAA-Tb-PDA-Al-MOF and TAA-Eu-PDA-Al-MOF hybrids show the typical bright green for Tb^{3+} and red emission for Eu^{3+}, while Eu-TTA-Al-MOF hybrids present the pink-white emission (Fig. 5.15(Bottom)). For Eu-TAA-Ti-MOF hybrid, it presents the close white luminescence. So these hybrids can realize the multicolor light output by adjusting the component and excitation wavelengths. Further, the uniform and transparent hybrid thin films are prepared for further optical application, whose luminescent spectra consist of the emission both europium β-diketonates (TTA, TAA) and MOF functionalized titania host in the red region and blue-green region, respectively, integrating the white color luminescence.

5.6 Photofunctional Rare Earth Hybrid Materials Based on the Composition of Metal–Organic Frameworks with Other Species

ZIFs are a class of metal–organic frameworks that are topologically isomorphic with zeolites, which are composed of tetrahedrally coordinated transition metal ions connected by organic imidazole linkers [43]. ZIFs are chemically and thermally stable materials, especially ZIF-8 ($Zn(MeIM)_2$, MeIM = 2-methylimidazole) that is a kind of chemically robust and thermally stable material, which belongs to the

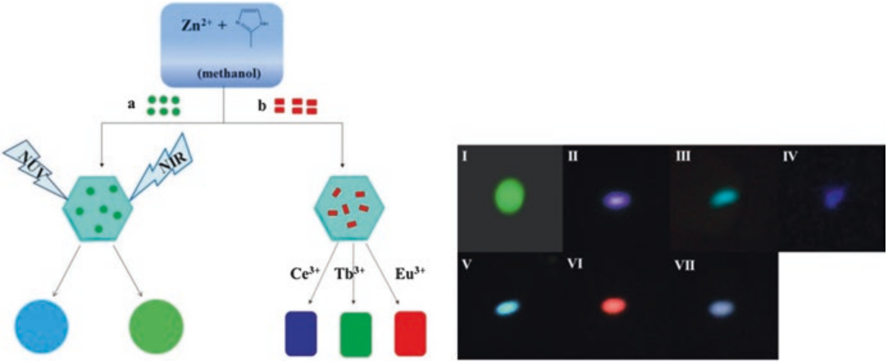

Fig. 5.17 (*Left*) Scheme for the preparation of nanocomposites of luminescent nanoparticles and ZIF-8 crystals, (*a*) upconversion nanoparticles, (*b*) $LaPO_4:Ln^{3+}$ nanoparticles. (Right) Digital photographs of nanocomposite: (*I*) $NaYF_4:Yb^{3+}/Er^{3+}$@ZIF-8 (λ_{ex} = 980 nm), (*II*) $NaYF_4:Yb^{3+}/Tm^{3+}$@ZIF-8 (λ_{ex} = 980 nm), (*III*) $NaYF_4:Yb^{3+}/Er^{3+}$@ZIF-8 (λ_{ex} = 396 nm), (*IV*) $LaPO_4:Ce^{3+}$@ZIF-8 (λ_{ex} = 280 nm), (*V*) $LaPO_4:Tb^{3+}$@ZIF-8(λ_{ex} = 320 nm), (*VI*) $LaPO_4:Eu^{3+}$@ZIF-8 (λ_{ex} = 320 nm) (*VI*) and $LaPO_4:Ce^{3+}$@ZIF-8 (λ_{ex} = 393 nm) (Reprinted with permission from Ref. [47]. Copyright 2015 the Royal Society of Chemistry)

sodalite zeolite-type structure with large cavities and small pore apertures [44]. ZIF-8 holds an intersecting three-dimensional structural feature, high thermal stability, large pore size, and large surface area, which make it a suitable host to compose all kinds of nanoparticles [45].

Liu et al. assemble the multicomponent hybrid films PEMA-PVPD ⊃ Ln-L/ZIF-8 (Ln = Eu, Tb; L = AA (acetylacetonate), phen, TAA (trifluoroacetylacetonate), or TTA; PEMA-PVPD copolymers of 4-vinylpyridine ethylene-methyl acrylate) (Fig. 5.16(Left)) [46]. This provides the possibility to adjust the luminescence of different units in the whole hybrid systems. For Eu^{3+}/Tb^{3+}-phen complex co-fabricated hybrid films, the luminescent color can change from blue (ZIF-8) to close white (Eu^{3+}/Tb^{3+} composed with PEMA-PVPD). In order to show the discrete luminescence for different hybrid films for the selective excitation with two luminescent centers (ZIF-8 and lanthanide complexes), they give the comparison of the photograph of the emission of four hybrid films with two kinds of excitation wavelengths (Fig. 5.16(Right)). For PEMA-PVPD ⊃ Eu-TTA/ZIF-8 and PEMA-PVPD ⊃ Tb-AA/ZIF-8 hybrid system, it changes from blue for ZIF-8 to red for Eu^{3+} and to green for Tb^{3+}. For PEMA-PVPD ⊃ Eu/Tb-ZIF/8 hybrid films, the emission color changes from blue for ZIF-8 to light yellow for the integration of both Eu^{3+} and Tb^{3+}. While for PEMA-PVPD ⊃ Eu/Tb-phen/ZIF-8 hybrid system, the contribution of the emission of PEMA-PVPD polymer host modifies the emission color to white region. Therefore, the selective excitation of these hybrid films can realize the discrete luminescence of ZIF-8 center (blue) or lanthanide center (red, green, yellow and white).

Liu et al. also have tried the assembly strategy that surfactant-capped nanoparticles (upconversion $NaYF_4:Yb^{3+},Er^{3+}/Tm^{3+}$ and downconversion $LaPO_4:Ln^{3+}$

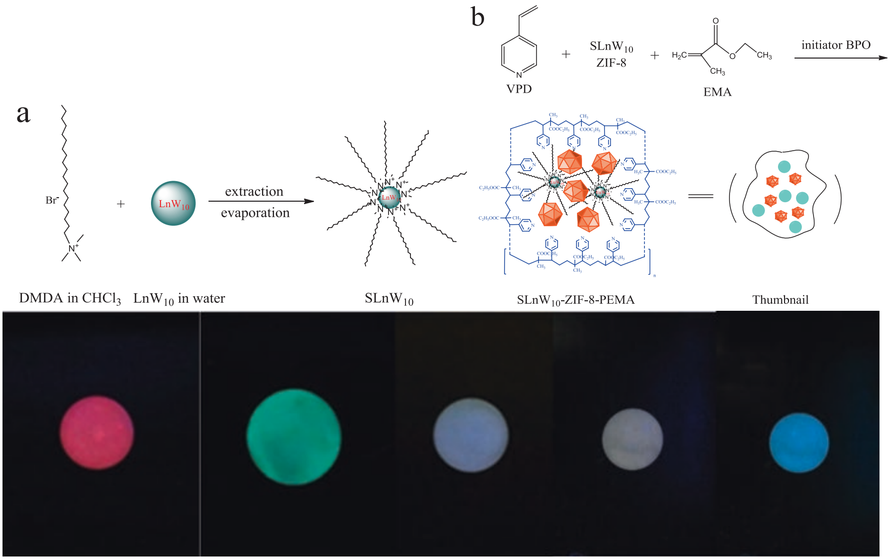

Fig. 5.18 (*Top*) Selected scheme of the synthesis process of SLnW$_{10}$ (*a*) and SLnW$_{10}$-ZIF-8-PEMA (*b*). (*Bottom*) Digital photograph (from *left* to *right*) of SLnW$_{10}$-ZIF-8-PEMA: Ln = Eu (λ_{ex} = 395 nm), Tb(λ_{ex} = 377 nm), Sm (λ_{ex} = 403 nm), Dy (λ_{ex} = 297 nm, 397 nm) in dark (*bottom*) (Reprinted with permission from Ref. [48]. Copyright 2015 the Royal Society of Chemistry)

(Ln = Ce, Eu, Tb)) can be covered by a readily synthesized ZIF-8 through in situ composing method (Fig. 5.17 (Left)), which involves two steps, the functionalization of nanoparticle surfaces with PVP and the crystallization of ZIF-8 [47]. The TEM image verifies that the product is composed of the core of nanoparticles and the shell of ZIF-8, whose particle size is in the range of 100–120 nm. Under 980 nm laser diode excitation (power density = 100 W/cm^2), $NaYF_4:Yb^{3+}/Er^{3+}$@ZIF-8 $NaYF_4:Yb^{3+}/Tm^{3+}$@ZIF-8 nanocomposite show yellow-green and light violet-white color, respectively, which is due to a combination of green/red emissions from Er^{3+} ion and the overlap of blue/red emission from Tm^{3+} in visible region (Fig. 5.17(Right) I,II)). At ambient temperature, the emission spectrum of $NaYF_4:Yb^{3+}/Er^{3+}$@ZIF-8 nanocomposite displays a blue emission at 450 nm under near ultraviolet (NUV) excitation at 396 nm (Fig. 5.17(Right, III)). Therefore, $NaYF_4:Yb^{3+}/Er^{3+}$@ZIF-8 nanocomposite can give rise to luminescence both up- and downconversion by selective excitation of near-infrared 980 nm laser and NUV light, respectively, which is interesting for the luminescence color tuning to have application. For $LaPO_4:Ce^{3+}$@ZIF-8 nanocomposite, it shows two emissions of 380 nm (strong) for parity-allowed 5d → 4f electronic transitions of Ce^{3+} and 460 nm (weak) of ZIF-8, respectively, showing blue color (Fig. 5.17(Right) IV). For $LaPO_4:Tb^{3+}$@ZIF-8 nanocomposite, it shows strong green emission of Tb^{3+} together with blue emission of ZIF-8, whose final luminescence appears light blue in color (Fig. 5.17(Right)V). Both excitation spectra of ZIF-8 and $LaPO_4:Eu^{3+}$ have the same wavelength at

390 nm approximately, displaying warm white in color due to a combination of blue and red emissions from them under excitation of 393 nm (Fig. 5.17 (Right)VI,VII).

Liu et al. also assemble the hybrid system including lanthanide POMs ($Na_9LnW_{10}O_{36}\cdot 32H_2O$ (LnW_{10})), ZIF-8, and polymer (Fig. 5.18(Top)a, b)). Surfactant-capped LnW_{10} ($SLnW_{10}$) is prepared with the ion exchange between the surfactant HTAB and the LnW_{10} for the electrostatic attraction force between their different charges. After ion exchange, VPD is added into the compounds of HTAB-modified LnW_{10} and ZIF-8 to blend through its coordination to Ln^{3+}. The digital photograph of $SEuW_{10}$-ZIF-8-PEMA hybrid system under excitation at 395 nm (Fig. 5.18(Bottom, left 1)) shows weak blue emissions between 430 and 500 nm for ZIF-8 and a dominant red emission between 580 and 710 nm for EuW_{10}, and the integrated luminescence shows the pink color. The digital photograph of the $SEuW_{10}$-ZIF-8-PEMA hybrid (Fig. 5.18(Bottom, left 2)) under excitation of 377 nm displays light blue color for a combination of green and blue emissions from the TbW_{10} and ZIF-8, respectively. The digital photograph of the hybrids $SSmSiW_{11}$-ZIF-8-PEMA (Fig. 5.18(Bottom, left 3)) under excitation at 403 nm exhibits the integrated white color luminescence, owing to a combination of blue and red emissions from SmW_{10} and ZIF-8 units in the hybrid system. The emission spectrum of $SDyW_{10}$-ZIF-8-PEMA only shows white luminescence by the excitation of LMCT at 297 nm (Fig. 5.18(Bottom, left 4)). The emission wavelength of the other component, ZIF-8, is monitored at 397 nm, which is its characteristic peak (blue photograph in Fig. 5.18(Bottom, left 5)) [48].

Liu et al. prepare new hybrids with silica@lanthanide complex@MOF heterostructure, whose synthetic process is shown in Fig. 5.19(Left) [49]. The PXRD patterns of SiO_2@EuTTA@ZIF-8 show the existence of the characteristic signal at $2\theta = 20–25°$ for SiO_2 and the characteristic peaks for ZIF-8, confirming successful formation of the ZIF-8 layer on SiO_2@EuTTA microspheres. The peaks of SiO_2@EuTTA@ZIF-8 blanket the ground of SiO_2@EuTTA, which means that most of the SiO_2@EuTTA is dispersed into the inner of the layer. Figure 5.19(Right)a, b are the SEM and TEM images of bare SiO_2 microsphere, and the diameter of particles is in the range of 100 to 110 nanometer. ZIF-8 nanocrystals are observed on the surface of SiO_2@ETTA@ZIF-8 microspheres by controlling ZIF-8 growth (Fig. 5.19(Right) d). The diameter of SiO_2@EuTTA@ZIF-8 heterostructure composite microspheres increases from 130 mm for SiO_2@EuTTA microspheres to 170 nm, thus indicating that a 20 nm thickness of ZIF-8 was grown on the SiO_2@EuTTA microspheres.

The hybrids based on rare earth ion or complex functionalized MOFs and silica may be assembled to form core-shell microstructure, which can be applied in the photophysical sensing [50, 51]. Besides, it is interesting to study the synthetic chemistry and function of the in situ assembly of MOF and nanoparticles from the special sources. Duan et al. present zinc oxide-embedded metal–organic framework (ZnO@Zn(pdc)) [52]. The structure of Zn(pdc)-1 is in blocks of irregular shape under the temperature of 80 °C (Fig. 5.20(Left)A). With the temperature up to 120 °C, Zn(pdc)-3 exhibits grasslike morphology distributed on the bulk structure of MOF due to formation of less ZnO (Fig. 5.20(Left)B). As the system heats at

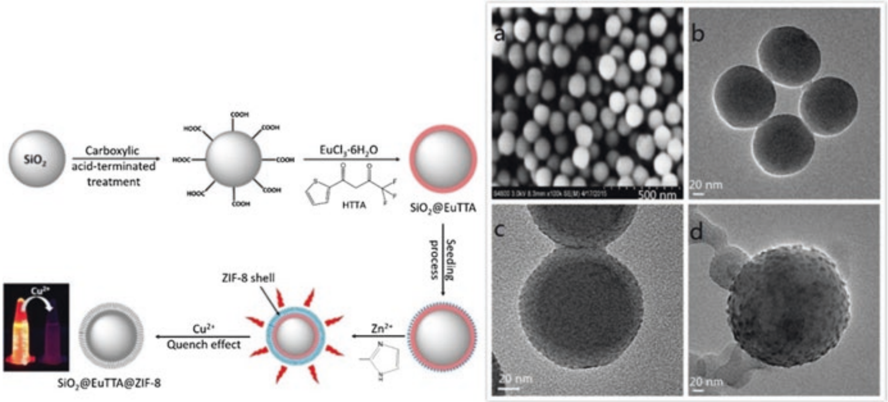

Fig. 5.19 (*Left*) Schematic representations for the synthetic progress of SiO_2@EuTTA@ZIF-8 and the fluorescent quenching phenomenon of Cu^{2+} to SiO_2@EuTTA@ZIF-8. (*Right*) SEM images: (*a*) SiO_2; TEM images: (*b*) SiO_2, (*c*) SiO_2@EuTTA, and (*d*) SiO_2@EuTTA@ZIF-8 (Reprinted with permission from ref. [49]. Copyright 2015 the Royal Society of Chemistry)

160 °C, the morphology of Zn(pdc)-6 presents rodlike morphology with manifest agglomeration owing to the formation of a large amount of ZnO (Fig. 5.20(Left) C). Moreover, they can acquire various emission light via incorporating lanthanide into ZnO-loaded MOF. Lanthanide ion (Eu^{3+}, Tb^{3+}, Sm^{3+}, Dy^{3+})-activated ZnO shows distinct characteristic emission under ultraviolet excitation. In addition to that, Eu activated MOF displays interesting white light emission under near ultraviolet excitation through a dual-emitting pathway: the metal-centered (MC) $f-f$ emission characteristic of Ln^{3+} ion and defect emission of ZnO. Furthermore, obtained white light emission materials (ZnO@Zn(pdc)-Eu), which show the CIE coordinates of (0.35, 0.41) and the quantum efficiency of 10.2% under the excitation of 375 nm, can be fabricated into WLED for potential utility. The procedure employs a commercially available ultraviolet LED of 375 nm (Fig. 5.20(Right)A) and a ZnO@Zn(pdc)-Eu sample as phosphor (Fig. 5.20(Right)C). The resultant WLED shows bright warm white light at an applied voltage of 3.8 V (Fig. 5.20(Right) D). Under ambient condition, this fabricated WLED displays CIE, CCT values of (0.35, 0.41) and 5018 K, respectively. On the basis of these results, it is clear that the ZnO@Zn(pdc)-Eu has potential for practical lighting applications under excitation of 375 nm.

5.7 Conclusion and Outlook

In conclusion, recent research progress in the photofunctional rare earth hybrid materials based on metal–organic frameworks are summarized. The content is divided into five parts according to the modification paths of MOFs and the

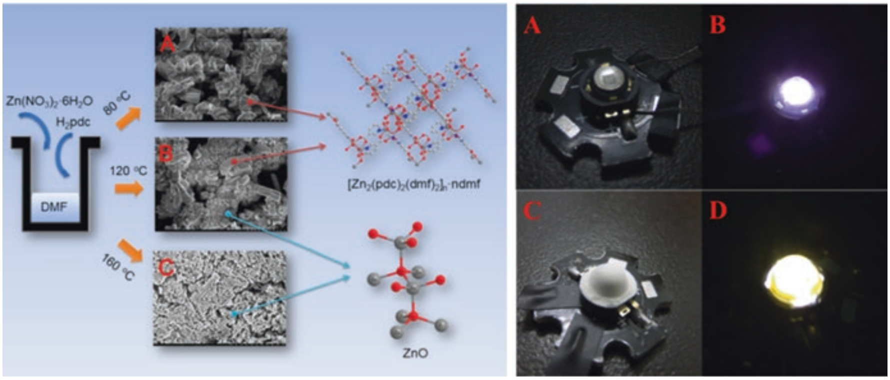

Fig. 5.20 (*Left*) Illustration of temperature dependence of product morphology and composition; (*A*) Zn(pdc)-1, (*B*) Zn(pdc)-3, (*C*) Zn(pdc)-5. (*Right*) Photo of (*A*) LED emitting 375 nm (not turned on); (*B*) LED emitting 375 nm light (turned on); (*C*) LED coated with a thin layer of ZnO@Zn(pdc)-Eu (not turned on); (*D*) the coated LED turned on (Reprinted with permission from Ref. [52]. Copyright 2015 the Royal Society of Chemistry)

interactions between the rare earth ions or complexes and MOFs. Rare earth ion doping or substitution is a simple and common method to achieve the hybrid materials. Besides, rare earth ion exchange for anionic MOFs and rare earth ion coordination for MOFs with free active groups in linkers together with covalently bonding are effect approaches to assemble the hybrid materials. Certainly, considering the assembly of whole hybrid materials, the simple physical assembly or covalent bonding method also can be applied to some special hybrid systems. However, some problems still exist in the field of photofunctional rare earth materials based on MOFs. The first one is how to realize the controlled synthesis of microstructures with regular morphology or suitable particle size of the hybrid materials. The second one is the controlled preparation and fabrication of thin films of hybrid materials. Both of them are important and necessary for the further applications in optical devices or sensors. Besides, the photostability of this hybrid system needs to be enhanced, especially in aqueous environment.

References

1. Wang ZQ, Cohen SM (2009) Postsynthetic modification of metal–organic frameworks. Chem Soc Rev 38:1315–1329
2. Cohen SM (2010) Modifying MOFs: new chemistry, new materials. Chem Sci 1:32–36
3. Cohen SM (2012) Postsynthetic methods for the functionalization of metl-organic frameworks. Chem Rev 112:970–1000
4. Allendorf MD, Bauer CA, Bhakta RK, Houk RJT (2009) Luminescent metal–organic frameworks. Chem Soc Rev 38:1330–1352
5. Cui YJ, Yue YF, Qian GD, Chen BL (2012) Luminescent functional metal-organic frameworks. Chem Rev 112:1126–1162

6. Rocha J, Carlos LD, Almeida Paz FA, Ananiasa D (2011) Luminescent multifunctional lanthanides-based metal–organic frameworks. Chem Soc Rev 40:926–940
7. Kreno LE, Leong K, Farha OK, Allendorf M, Van Duyne RP, Hupp JT (2012) Metal-organic framework materials as chemical sensors. Chem Rev 112:1105–1125
8. Duan TW, Yan B (2014) Hybrids based on lanthanide ions activated yttrium metal organic frameworks: functional assembly, polymer film preparation and luminescence tuning. J Mater Chem C 2:5526–5532
9. Jiang HL, Tsumori N, Xu Q (2010) A series of (6,6)-connected porous lanthanide organic framework enantiomers with high thermostability and exposed metal sites: scalable syntheses, structures, and sorption properties. Inorg Chem 49:10001–10006
10. Lian X, Yan B (2016) A lanthanide metal–organic framework (MOF-76) for adsorbing dyes and fluorescence detecting aromatic pollutants. RSC Adv 6:11570–11576
11. An J, Geib SJ, Rosi NL (2009) Cation-triggered drug release from a porous zinc-adeninate metal-organic framework. J Am Chem Soc 131:8376–8380
12. An J, Shade CM, Chengelis-Czegan DA, Petoud S, Rosi NL (2011) Zinc-adeninate metal-organic framework for aqueous encapsulation and sensitization of near-infrared and visible emitting lanthanide Cations. J Am Chem Soc 133:1220–1223
13. Shen X, Yan B (2015) Photofunctional hybrids of lanthanide functionalized bio-MOF-1 for fluorescence tuning and sensing. J Coll Interf Sci 451:63–68
14. Shen X, Yan B (2015) A novel fluorescence probe for sensing organic amine vapors from Eu^{3+} β-diketonate functionalized bio-MOF-1 hybrid system. J Mater Chem C 3:7038–7046
15. Shen X, Yan B (2016) Anionic metal-organic framework hybrids: double functionalization with lanthanides/cationic dyes and fluorescent sensing small molecules. RSC Adv 6:28165–28170
16. Weng H, Yan B (2016) Cadmium metal–organic frameworks: Ln^{3+} ions functionalized assembly, fluorescence tuning and polymer film preparation. New J Chem 40:3732–3737
17. Weng H, Yan B (2016) A flexible Tb(III) functionalized cadmium metal-organic framework as fluorescent probe for highly selectively sensing ions and organic small molecules. Sensors Actuator B Chem 228:702–708
18. Zhao SN, Song XZ, Zhu M, Meng X, Wu LL, Feng J, Song SY, Zhang HJ (2015) Encapsulation of ln(III) ions/dyes within a microporous anionic MOF by post-synthetic ionic exchange serving as a ln(III)ion probe and two-color luminescent sensors. Chem Eur J 21:9748–9752
19. Bloch ED, Britt D, Lee C, Doonan CJ, Uribe-Romo FJ, Furukawa H, Long JR, Yaghi OM (2010) Metal insertion in a microporous metal-organic framework lined with 2,2′-bipyridine. J Am Chem Soc 132:14382–14834
20. Lu Y, Yan B, Liu JL (2014) Nanoscale metal-organic framework as highly sensitive luminescent sensors for Fe^{2+} in aqueous solution and living cells. Chem Comm 50:9969–9972
21. Lu Y, Yan B (2014) A ratiometric fluorescent pH sensor based on nanoscale metal-organic frameworks (MOFs) modified by europium (III) complex. Chem Comm 50:13323–13326
22. Lu Y, Yan B (2014) Lanthanide organic-inorganic hybrids based on functionalized metal-organic frameworks (MOFs) for near-UV white LED. Chem Comm 50:15443–15446
23. Lu Y, Yan B (2014) A novel luminescent monolayer thin film based on postsynthetic method and functional linker. J Mater Chem C 2:5098–5104
24. Lu Y, Yan B (2014) Luminescent lanthanide barcodes based on postsynthetic modified nanoscale metal-organic frameworks. J Mater Chem C 2:7411–7416
25. Zhou Y, Yan B, Lei F (2014) Postsynthetic lanthanides functionalization of nanosized metal-organic frameworks for highly sensitive ratiometric luminescent nanothermometers. Chem Comm 50:15235–15238
26. Hao JN, Yan B (2015) Simultaneous determination of indoor ammonia pollution and its biological metabolite in human body by use of a recyclable nanocrystalline lanthanide functionalized MOF. Nanoscale 8:2881–2886
27. Xu XY, Yan B (2016) Fabrication and application of ratiometric and colorimetric fluorescent probe for Hg^{2+} based on dual-emissive metal-organic framework hybrids with carbon dots and Eu^{3+}. J Mater Chem C 4:1543–1549

28. Fei HH, Cohen SM (2014) A robust, catalytic metal–organic framework with open 2,2′-bipyridine sites. Chem Comm 50:4810–4812
29. Zhou Y, Yan B (2015) Lanthanides post-functionalized nanocrystalline metal-organic frameworks for tunable white-light emission and orthogonal multi-readout thermometry. Nanoscale 7:4063–4069
30. Zhou Y, Yan B (2016) A responsive MOF nanocomposite for decoding volatile organic compounds. Chem Comm 52:2265–2268
31. Zhou Y, Yan B (2015) Ratiometric detection of temperature using responsive dual-emissive MOF hybrids. J Mater Chem C 3:9353–9358
32. Reimer N, Gil B, Marszalek B, Stock N (2012) Thermal post-synthetic modification of al-MIL-53–COOH: systematic investigation of the decarboxylation and condensation reaction. CrystEngComm 14:4119–4125
33. Zhou Y, Yan B (2014) Imparting tunable and white-light luminescence to a nanosized metal-organic framework by controlled encapsulation of lanthanide cations. Inorg Chem 53:3456–3463
34. Hajjar R, Christophe V, Loiseau T, Guillou N, Marrot J, Férey G, Margiolaki I, Fink G, Morais C, Taulelle F (2011) ^{71}Ga slow-CTMAS NMR and crystal structures of MOF-type gallium carboxylates with infinite edge-sharing octahedra chains (MIL-120 and MIL-124). Chem Mater 23:39–47
35. Xu XY, Yan B (2015) Intercalation of lanthanide cations to a layer-like metal-organic framework for color tunable and white light emission. Dalton Trans 44:1178–1185
36. Cao JW, Gao YF, Wang YQ, Du CF, Liu ZL (2013) A microporous metal–organic open framework containing uncoordinated carbonyl groups as postsynthetic modification sites for cation exchange and Tb^{3+} sensing. Chem Comm 49:6897–6899
37. Abdelhameed RM, Carlos LD, Silva AMS, Rocha J (2013) Near-infrared emitters based on post-synthetic modified Ln^{3+}-IRMOF-3. Chem Comm 49:5019–5021
38. Abdelhameed RM, Carlos LD, Rabu P, Santos SM, Silva AMS, Rocha J (2014) Designing near-infrared and visible light emitters by postsynthetic modification of Ln^{3+}–IRMOF-3. Eur J Inorg Chem:5285–5295
39. Abdelhameed RM, Carlos LD, Silva AMS, Rocha J (2015) Engineering lanthanide-optical centres in IRMOF-3 by post-synthetic modification. New J Chem 39:4249–4258
40. Liu C, Yan B (2016) A novel photofunctional hybrid material of pyrene functionalized metal-organic framework with conformation change for luminescence sensing of Cu^{2+}. Sensors &Actuators B-Chem 235:541–546
41. Lian X, Yan B (2015) Multi-component luminescent lanthanide hybrids of both functionalized IR-MOF-3 and SBA-15. New J Chem 39:5898–5901
42. Xu XY, Yan B (2014) Novel photofunctional hybrid materials (alumina and titania) functionalized with both MOF and lanthanide complexes through coordination bonds. RSC Adv 4:38761–38768
43. Yaghi OM, O'Keeffe M, Ockwig NW, Chae HK, Eddaoudi M, Kim J (2003) Reticular synthesis and the design of new materials. Nature 423:705–714
44. Cravillon J, Lohmeier SJ, Feldhoff A, Huber K, Wiebcke M (2009) Rapid room-temperature synthesis and characterization of nanocrystals of a prototypical zeolitic imidazolate framework. Chem Mater 21:1410–1412
45. Lu G, Li SZ, Guo Z, Farha OK, Hauser BG, Qi XY, Wang Y, Wang X, Han SY, Liu XG, DuChene JS, Zhang H, Zhang QC, Chen XD, Ma J, Loo SCJ, Wei WD, Yang YH, Hupp JT, Huo FW (2012) Imparting functionality to a metal-organic framework material by controlled nanoparticle encapsulation. Nat Chem 4:310–316
46. Liu C, Yan B (2015) Photoactive hybrid polymer films incorporated with both lanthanide complex and ZIF-8 for selectively excited multi-color luminescence. Eur J Inorg Chem:279–287
47. Liu C, Yan B (2015) Photofunctional nanocomposites based on the functionalization of metal-organic framework by up/downconverion luminescent nanophosphors. New J Chem 39:1125–1131

48. Liu C, Yan B (2015) Multicomponent hybrids of surfactant-capped lanthanide polyoxometalates and ZIF-8 with tuneable luminescence. RSC Adv 5:11101–11108
49. Liu C, Yan B (2015) Highly effective chemosensor of luminescent silica@lanthanide complex@MOF heterostructure composite for metal ion sensing. RSC Adv 5:101982–101988
50. Lian X, Yan B (2016) Novel core-shell structure microspheres based on lanthanide complexes for white light emission and fluorescence sensing. Dalton Trans 45:2666–2673
51. Shen X, Yan B (2016) Barcoded materials based on photoluminescent hybrid system of lanthanide ions-doped metal organic framework and silica via ion exchange. J Coll Interf Sci 468:220–226
52. Duan TW, Yan B (2015) Lanthanide ions (Eu^{3+}, Tb^{3+}, Sm^{3+}, Dy^{3+}) activated ZnO embedded zinc 2,5-pridinedicarboxylic metal organic frameworks for luminescent application. J Mater Chem C 3:2823–2830

Chapter 6

Photofunctional Rare Earth Hybrid Materials Based on Polymer and Polymer/Silica Composite

Abstract This chapter mainly focuses on recent research progress in photofunctional rare earth hybrid materials based on polymer and polymer/silica composite. The emphasis is put on the rare earth hybrids with polymer as the main building units. It covers photofunctional rare earth hybrid material based on organic polymers, mainly the rare earth complexes with polymers; photofunctional rare earth hybrid materials based on organically modified silica and organic polymers, with both of the two units behaving as ligands coordinated to rare earth ions and no direct interaction between them; and photofunctional rare earth hybrid materials based on organically modified silica covalently bonded organic polymers. Herein, it focuses on the work of our group in the recent years.

Keywords Rare earth ion • Photofunctional hybrid material • Polymer • Polymer/silica composite • Luminescence

The introduction of rare earth ions or their complexes into polymer hosts has been carried out for a long time [1–3]. In general, there are four methods for preparing rare earth-fabricated polymers:[4–10] blending, polymerization, sol–gel methods, and solution mixing, which can be more simply classified as chemical and physical incorporations. It has been shown that if a rare earth ion is chemically bonded to the chains of a polymer, factors such as the content of rare earth ion, the type of chemical interaction between the rare earth ion and the polymer chain, and the distribution of rare earth ions along the polymer chain will strongly influence the luminescence properties of the materials obtained.

For rare earth hybrids based on polymers, rare earth complexes may be fabricated into polymer host through simple doping or chemical bonds (coordination and covalent bonds) [11]. For rare earth hybrids based on polymer/silica composite host, two main strategies can be classified according to the interaction between polymer and silica units: one is that both polymer and organically modified silica are coordinated to rare earth ions, and there is no direct interaction between them. The other is that polymer is covalently grafted to organically modified silica and they behave as an integrated ligand to be coordinated to rare earth ion. So in this chapter, four aspects are introduced on photofunctional rare earth hybrid materials based on polymers or polymer/silica composites. The first is focused on the photofunctional rare earth hybrid materials with pure polymer. The second is on the photofunctional rare

B. Yan, *Photofunctional Rare Earth Hybrid Materials*,
Springer Series in Materials Science 251, DOI 10.1007/978-981-10-2957-8_6

earth hybrid materials with polymer/silica composites with both polymer and silica as ligands without interaction between them. The third is on the photofunctional rare earth hybrid materials with polymer/silica composites with both polymer covalently grafted silica as ligand. Besides, works of Carlos's group on diuresil and polymer are emphatically reviewed as the fourth.

6.1 Photofunctional Rare Earth Hybrid Materials Based on Organic Polymers

Chen et al. synthesize the luminescent linear Eu^{3+} Schiff-base polyelectrolytes with Eu^{3+} in the polymer backbone [12]. New $[NaY(tstm)]_n$ polyelectrolytes, where $tstm^{4-}$ is the anionic ligand derived from *N*,*N*′,*N*′′,*N*′′′-tetrasalicylidene-3,4,3′,4′-tetraaminodiphenylmethane, are synthesized with *M*n values up to 21,600 based on NMR end-group analysis. Intrinsic viscosities provide Mark–Houwink constants of $a = 0.52$ and $K = 0.066$ cm^3/g for $[NaY(tstm)]_n$. Mixed-metal $[NaY_xEu_{1-x}(tstm)]_n$ polyelectrolytes display enhanced emission over $[NaEu(tstm)]_n$, among which polyelectrolytes with Y:Eu ratios between 1:2.5 and 1:9 present the most enhanced intensity for intrachain energy transfer from the yttrium units of the polyelectrolytes to the Eu(III) ions. $[NaY_{0.2}Eu_{0.8}(tstm)]_n$ (Y:Eu = 1:4) hybrid system possesses the highest quantum yield of 0.74 at 77 K.

Zhao et al. synthesize a polymer–inorganic hybrid material from terephthalic acid and rare earth (Tb^{3+}, Eu^{3+}) complexes, in which RE^{3+} ions are connected to the polymer by coordination bonds [13]. The luminescent hybrids PET-Tb and PET-Eu [PET = poly(ethyl terephthalate)] are formed through in situ low-temperature solution polycondensation process (Fig. 6.1). SEM images show a homogeneous microstructure with typical polymeric aggregation, similar to synthetic tissue. The coordinated groups of the PET polymer chains only provide two coordinated O atoms, to limit hindrance; thus, there are two carbonyl groups of another PET polymer unit coordinating to Ln^{3+}. In addition, the balancing three NO_3^- may also coordinate with Ln^{3+}. In these polymer hybrid systems, Ln^{3+} ions behave as bridges, linking the different adjacent PET polymer chain units through coordination. Finally, all the PET polymer chains can be assembled into an interpenetrating polymer network structure by Tb or Eu ions (Fig. 6.1).

Bender et al. report a series of polymeric Eu^{3+} complexes with polyester ligands and the Eu^{3+} block copolymer film (Fig. 6.2) [14]. Dibenzoylmethane (DBM) is derived with a hydroxyl initiator site (DBMOH) for tin octoate-catalyzed ring opening polymerization of DL-lactide. The resulting poly(lactic acid) macroligand DBMPLA is combined with $EuCl_3$ to generate $Eu(DBMPLA)_3$. Chelation of both DBMPLA and a polycaprolactone-functionalized bipyridine ligand ($bpyPCL_2$) leads to the Eu^{3+}-centered heteroarm star hybrid system $Eu(DBMPLA)_3(bpyPCL_2)$. Relative amounts of the longer lifetime component increase in the series $Eu(dbm)_3$ solutions to $Eu(DBMPLA)_3$ solutions to $Eu(DBMPLA)_3$ films perhaps suggest ben-

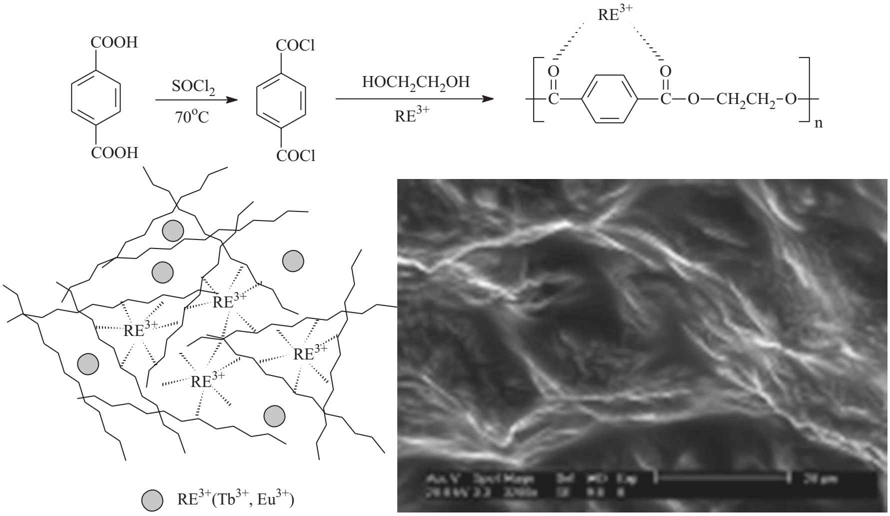

Fig. 6.1 Scheme for synthesis and SEM images of rare earth hybrid materials with PET (Reprinted with permission from Ref. [13]. Copyright 2008, Elsevier)

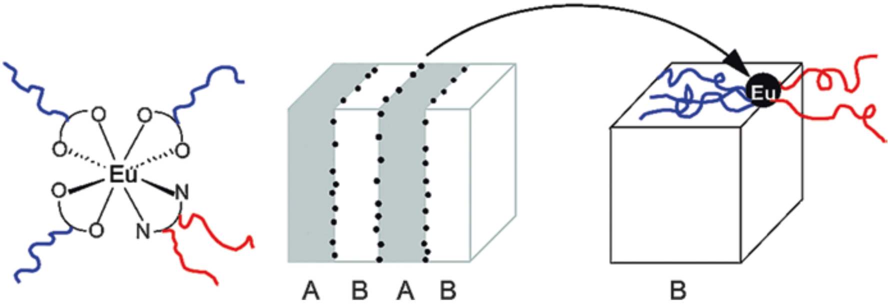

Fig. 6.2 The schematic representation of composition (*left*) and the lamellar morphology (A = PCL, B = PLA, • = Eu center) and of the Eu polymer complex system (*right*). (Reprinted with permission from Ref. [14]. Copyright 2008, American Chemical Society)

efits of the “polymer shell effect” and the diminishment of aquo adducts. AFM study on Eu(DBMPLA)$_3$(bpyPCL$_2$) thin films reveals a lamellar structure with a 17.5 nm repeat.

Shunmugam et al. use terpy containing homo, block, and statistical copolymers PS-r-MAterpy synthesized by themselves to coordinate with Ln^{3+} (Ln = Dy, Tb, Eu) ions; the obtained hybrid material shows characteristic emission bands in blue, green, and red region [15, 16]. Interestingly, when Eu^{3+}, Dy^{3+}, and Tb^{3+} are incorporated into the same polymer backbone in equimolar ratio, irradiation of the hybrids at 350 nm results in white color emission. The emission curve for this white color shows the simple addition of spectra from the three metal centers, and its CIE coordinate values are tabulated in the region of “white-like” or “near-white” emission.

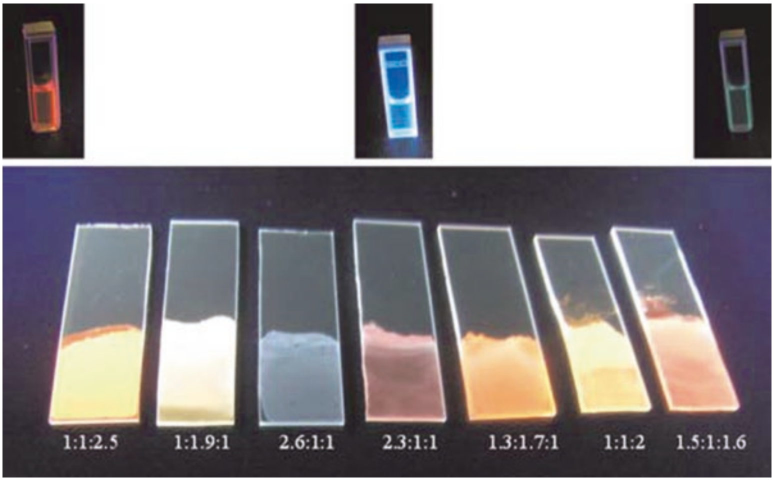

Fig. 6.3 Films fabricated with copolymers PS-r-MAterpy on a glass surface by drop casting. The metal ratios of Dy^{3+}, Tb^{3+}, and Eu^{3+} are shown, respectively, below each color (Reprinted with permission from Ref. [16]. Copyright 2007 Wiley)

The ratio of metal ions is carefully varied to mix the three rare earth ions in the ratio of 1.1:1:1 (Dy^{3+}:Tb^{3+}:Eu^{3+}), producing white light with CIE coordinates $x = 0.3124$ and $y = 0.3295$. A metal ratio of 1.8:1:1 of Dy, Eu, and Tb, gives “true” white emission films with CIE coordinate values $x = 0.3112$ and $y = 0.3281$, extremely close to the theoretical values of $x = 0.3127$ and $y = 0.3291$. To demonstrate the easy “dial in” of colors, the metal ratios are varied to obtain colors from the drop cast on a glass slide (Fig. 6.3). The metal ratios of the three Ln^{3+} ions are shown, respectively, below each color [16].

Wang et al. synthesize a series of Eu-containing copolymers by the direct copolymerization of Eu complex monomers containing β-diketones with methyl methacrylate (Fig. 6.4) [17]. Euacrylate-β-diketonate complexes as monomers are synthesized by the reaction of europium isopropoxide with β-diketone (acac, BA, DBM, TTA) and acrylic acid in anhydrous organic solvents. In comparison with the water-phase synthetic approach using oxide as the starting material, this synthetic method utilizing highly reactive rare earth alkoxide in organic phase has the advantage of affording the desired complex without inner-coordinated water molecules, especially for preparing a rare earth-mixed ligands complex. Eu copolymers are prepared by the radical copolymerization using AIBN as an initiator, which are fully soluble in common organic solvents and can be easily cast into transparent, uniform, thin films. The number-average molecular weights (Mn) and the polydispersity indexes (PDI) of the resulting polymers are measured by gel permeation chromatography (GPC) using THF as eluent and polystyrene as the standard; the Mn and PDI of the Eu copolymers are in the range of 53,700–72,600 and 4.79–5.96, respectively. However, the Mn values of all Eu copolymers are smaller, and the PDI are larger than that of PMMA, which may be due to the lower polymerization reac-

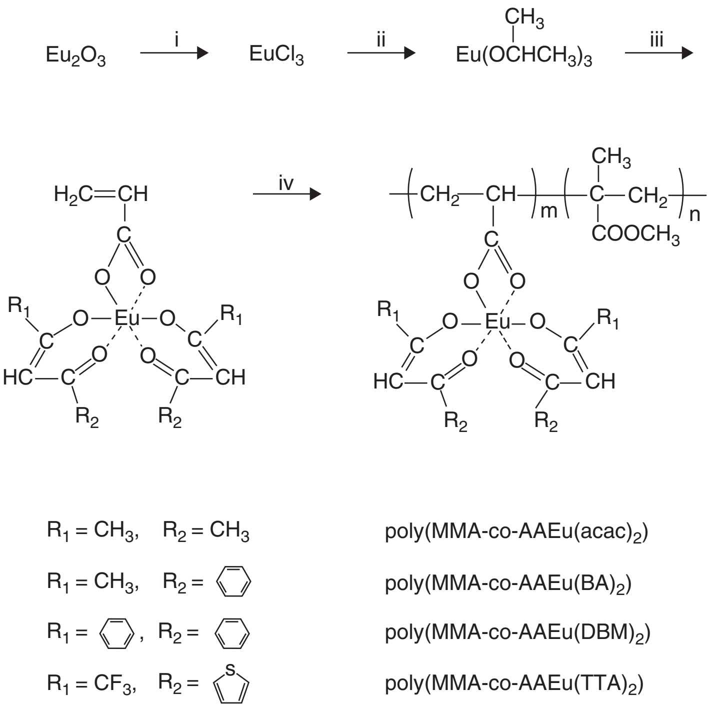

Fig. 6.4 The scheme for synthetic route for the Eu-containing copolymer (Reagents and conditions: (*i*) HCl/NH_4Cl, (*ii*) $Na(O^iPr)/{}^iPrOH$/benzene, (*iii*) β-diketone/AA/^{i}PrOH/benzene, (*iv*) MMA/AIBN/DMF) (Reprinted with permission from ref. [17]. Copyright 2000 American Chemical Society)

tivities of Eu-complex monomers than that of MMA. The luminescence intensities, lifetimes, and monochromaticities [$^5D_0 \rightarrow {}^7F_2/{}^5D_0 \rightarrow {}^7F_1$)] of the Eu-copolymers are much higher than that of the corresponding Eu-complex monomers and Eu-complex/PMMA blends, whose improvement is ascribed to the microenvironment effects. Furthermore, the luminescence intensities of the Eu-copolymers are found to depend strongly on the substituents of the β-diketone ligands, increasing with the β-diketones in the order acac < BA < DBM < TTA.

Liu et al. in situ synthesize two luminescent temperature-sensitive poly(N-isopropylacrylamide) hydrogels fabricated with rare earth (Eu, Tb) picolinic acid within the interpenetration networks [18]. At the temperature range from 5 to 33 °C, the emission has been reduced along with the increase of temperature, until 33 °C for sharply quenching. Two possible reasons may account for such phenomenon. Firstly, high temperature will make relaxed excited state return to the ground state in a nonradiative manner (thermal quenching of luminescence). Secondly, when phase separation takes place (reaching LCST), the delicate hydrophilic/hydrophobic balance within P-NIPAA backbones is affected and dehydration in the P-NIPAA net appears, which may accelerate the aggregation of P-NIPAA chains and large volume shrinkage. No corresponding intensity differences are observed in the non-thermosensitive poly(acrylamide) hydrogels that also bear amide groups, suggesting that conformational change of P-NIPAA chains is a prevalent factor determining fluorescence quenching. They also prepare a series of Eu-containing copolymers through the direct coordination coprecipitation that occurs among 4-vinylpyridine units, benzoic acids (ortho- and meta-methylbenzoic acids), and europium ions [19]. The resulting hybrids can be soluble in common organic solvents like butanone or acetone and can be cast into thin films with excellent mechanical flexibility and thermal stability [20].

Guo et al. synthesize two new chemical linkages (BPDA-PAM, BPDA-DG) through the reaction between 4,4′-biphthalic anhydride (BPDA), acrylamide (AM), diethylene glycol (DG), respectively, and assemble two series of rare earth (Eu^{3+}, Tb^{3+}, Sm^{3+}) polymeric hybrids through the coordination bonding. One is from the linkage BPDA-PAM to form the hybrids BPDA-PAM-RE-phen(bipy) (bipy and phen), and the other is from the linkage BPDA-DG to compose the hybrids BPDA-DG-RE-PVP and PVP [21].

6.2 Photofunctional Rare Earth Hybrid Materials Based on the Polymer Composite of Other Units Consisting Di-ureasils

The urethanesils are hybrid materials composed of poly(oxyethylene) (POE) chains covalently bonded to a siliceous network by means of urethane (−NHC(=O)O-) moieties [22–36]. These xerogels are introduced with the primary goal of serving as model compounds of a class of advanced nanohybrids known as di-ureasils. In the host matrix of the di-ureasils, POE segments are grafted at both ends to a siliceous backbone through urea (−NHC(O)NH-) groups. Classical doping procedures with adequate salt species transform these POE/siloxane composites into excellent candidates for the fabrication of multipurpose and one-material based devices. The di-ureasils incorporating lanthanide ions represent one of the best examples of the relevance of the di-ureasil strategy for the production of materials, whose behavior is intimately related to several factors: (1) the di-urea cross-linked host framework possesses a unique coordinating ability toward cations, since the activation of its donor centers (the ether oxygen atoms of the polymer chains and the carbonyl oxygen atoms of the cross-links (two per organic segment)) may be tailored by varying either the guest salt content at constant chain length or the length of the organic segments at constant salt concentration. (2) The Ln^{3+} ions have high charge/ionic radius ratios and are characterized by high coordination numbers (typically 12). Carlos’s group has carried out detailed investigations of the hybrid materials based on diurea-cross-linked siloxane – POE (poly(oxyethylene) nanohybrids whose main unit is represented as $U(2000)_nREL_n$. Rare earth species (salts such as $Eu(CF_3SO_3)_3$ or complexes with β-diketones) can be introduced into the hybrid system by doping or coordination interaction. The corresponding sol–gel reaction chemistry, structure, and photophysical properties are discussed deeply here.

One work is on the di-ureasils identified by $U(2000)_nEu(CF_3SO_3)_3$, where U originates from the word "urea," 2000 indicates the average molecular weight of the oligopolyoxyethylene chains, and n = O/Eu represents the number of monomer units per Eu^{3+} cation [22], whose salt concentrations in the present work are n = 400, 200, 100, 80, 60, 40, and 20, respectively. The broad green ± blue band can be observed in the luminescence spectra of both the undoped di-ureasil and Eu^{3+}-based xerogels, corresponding to the emission from NH groups of the urea bridges, which is originated from electron ± hole recombinations in the siliceous domains in the inorganic backbone. The relative intensity and the energy range of the broad green ± blue emission for $U(2000)_{200}Eu(CF_3SO_3)_3$ hybrids are strongly dependent on the excitation wavelength used between 330 and 420 nm. To the naked eye, the hybrid's emission appears to be white, as shown in the CIE (x, y) chromaticity diagram for $U(2000)_{200}Eu(CF_3SO_3)_3$, n = 200 and 80. The ability to tune the di-ureasil's emission to colors across the chromaticity diagram is readily achieved, either by changing the amount of Eu^{3+} incorporated in the ureasil host and/or the excitation wavelength. The (x, y) coordinates of $U(2000)_{80}Eu(CF_3SO_3)_3$ change from (0.36, 0.28) to (0.47, 0.51) as the excitation wavelength increases from 280 to 501 nm. Furthermore, for the same excitation wavelength (395 nm, for instance), where the Eu^{3+} content increases from n = 400 to 80, the chromaticity coordinates vary from (0.22, 0.20) to (0.25, 0.30). This white light emission has been nicely illustrated very recently for $U(2000)_{80}Eu(CF_3SO_3)_3$ at 14 K in a set of frames (extracted from a split video film) recorded for 1 s after the excitation laser beam (UV Ar ion) is turned off. Carlos et al. also reported a fine-tuning of the emission chromaticity from red to green for di-ureasil nanostructured hybrids ($U(2000)_{80}(Eu_{0.05}Tb_{0.15}Tm_{0.80}(BTFA)_3\cdot H_2O$, BTFA = 4,4,4-trifluoro-1-phenyl-1,3-butanedione). Raising the temperature from 200 to 300 K changes the color coordinates smoothly from the yellowish-green region of the chromaticity diagram toward the red. This is discussed in terms of thermally activated energy transfer mechanisms from Tb^{3+} energy states to the hybrid's emitting levels [23].

Dahmouche et al. investigate the aggregation, gelation, and aging of urea-cross-linked siloxane-POE nanohybrids containing two different amounts of $Eu(CF_3SO_3)_3$ by in situ small-angle X-ray scattering (SAXS) [24]. For both low (n = [O]/[Eu] = 80) and high (n = 25) Eu^{3+} contents, the SAXS intensity is attributed to the formation of siloxane clusters of about 8–11 Å in size. Siloxane cluster formation and growth are a rapid process in hybrids with low Eu contents and slow in Eu-rich hybrids. By fitting a theoretical function for this model to the experimental SAXS curves, relevant structural parameters are determined as functions of time during the sol–gel transition and gel aging. For hybrids with low europium contents (n = 80), the size of the siloxane clusters remains essentially invariant, whereas the dense segregation domains progressively grow. For these hybrids, the segregation of siloxane clusters forming dense domains occurs only during advanced stages of the process. Two different mechanisms are responsible for the sol–gel transformation and gel aging of europium-doped siloxane-POE nanocomposites. The first is the

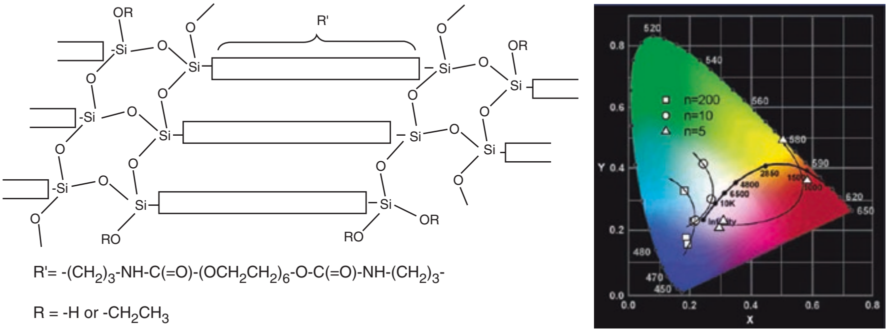

Fig. 6.5 The scheme for representation of the structure (*left*) of the d-Ut(300)$_n$Eu(CF_3SO_3)$_3$ di-urethanesils hybrids. (*Right*) CIE chromaticity diagram showing the excitationdependence of the RT (*x*, *y*) color coordinates for the d-Ut-(300)$_n$Eu(CF_3SO_3)$_3$ di-urethanesils with $n = 200$, 10, and 5. The *arrows* indicate variations in the excitation wavelength between 350 and 420 nm (Reprinted with permission from Ref. [25]. Copyright 2004 American Chemical Society)

formation and growth of primary siloxane clusters, with a final average radius of gyration of around 10 Å, grafted to the extremities of the polymer chains. The second mechanism is the formation of rather large siloxane cluster-rich domains embedded in a cluster-depleted matrix. The kinetics of the sol–gel transformation depends on the europium content. For low europium doping ($n = 80$), the growth of individual siloxane clusters is fast, which evolves by increasing the size and/or number of the domains containing siloxane clusters. For high europium doping ($n = 25$), the polycondensation reaction is a slow process, where the growth of siloxane clusters is the preponderant mechanism of structural transformation during the gelation process.

Goncalves et al. prepare the poly(oxyethylene)/siloxane hybrids (di-urethanesils) doped with Eu(CF_3SO_3)$_3$ complex [25]. The host framework of these materials consists of a siliceous network grafted through urethane linkages to both ends of polymer chains with 6 oxyethylene repeat units. The compounds with $n \geq 10$ (n = molar ratio OCH_2CH_2)/Eu^{3+}) are amorphous. In the di-urethanesils with $n \geq 10$, the cations interact with the urethane carbonyl oxygen atoms. The complexation of the polyether chains to the cations is initiated at approximately $n \geq 10$. At $n \leq 10$, both types of cation bonding situations occur. Ionic aggregates are formed in samples with $n = 5$ and 1. The empirical formula deduced on the basis of the ^{29}Si and ^{13}C MAS NMR spectra of the d-Ut(300)-based samples suggests that the structure of the di-urethanesils may be tentatively represented in the scheme of Fig. 6.5(left). These data support the claim that in this set of samples, the main environment present is the T_3 site, typically associated with the existence of functional -$(CH_2)_3SiO_{3/2}$ groups, a proof that the condensation process favored branched structures rather than linear segments. For $200 \geq n \geq 20$, the emission quantum yields range from 0.7 to 8.1%, and the decrease in the quantum yield with the increase of the Eu^{3+} concentration markedly depends on the activation of the energy transfer between the hybrid hosts' emitting centers and the cations, which permits a fine-tuning of the emission chromaticity across the CIE diagram (e.g., (x, y) color coordinates from (0.19, 0.18) to (0.50, 0.49), for $n = 200$ and 5, respectively). The color of the emission changes from the blue to the red spectral region with the increase in the Eu^{3+} content from $n = 200$ to 5. Within each sample, an increase in the excitation wavelength from 350 to 420 nm induces variations in the color coordinates. In particular, the color coordinates of the most dilute sample ($n = 200$) change from the blue (0.19, 0.18) to the blue-green region (0.18, 0.33), and the (x, y) coordinates of the emission of the most concentrated sample ($n = 5$) are shifted from the red-purple (0.30, 0.21) to the yellow (0.50, 0.49) spectral region (Fig. 6.5(Right)). For the di-urethanesil with $n = 10$, the color coordinates change from the white region (0.22, 0.23) for the 350 nm excitation wavelength to the green region (0.25, 0.41) at the 420 nm excitation wavelength. The dependence of the relative intensity between the hybrid host band and the Eu^{3+} emission lines is associated with the activation/deactivation of the energy transfer processes that take place between the di-urethanesil emitting centers and Eu^{3+} ions.

Bermudez et al. carry out the FT-IR and FT-Raman spectroscopic studies of ion association in mono-urethanesils doped with $Eu(CF_3SO_3)_3$. Their study points out the presence of “free” $CF_3SO_3^-$ ions, weakly coordinated anions located in two different sites, and cross-link-separated ion pairs over the whole range of salt composition examined ($\infty > n \geq 5$) [26]. At $20 \geq n \geq 5$, “free” ions, the ionic configurations detected at lower salt concentration and contact ion pairs, coexist. The PL and PLE data suggest the presence of three distinct cation local sites in the m-Ut(350)$_n$Eu$(CF_3SO_3)_3$ compounds. Goncalves et al. discuss the local structure and NIR emission features of Nd-based amine functionalized hybrids of diurea and di-urethane cross-linked POE/siloxane host incorporating $Nd(CF_3SO_3)_3$ [27]. The analysis of the specific vibrational modes of the POE chains and of the urea and urethane cross-links provided evidences that in these materials the coordination of the lanthanide ions takes place in the following way: (1) at $n > 10$ for the d-U(600)$_n$ $Nd(CF_3SO_3)_3$ di-ureasils and $n > 20$ for the d-Ut(300)$_n$Nd$(CF_3SO_3)_3$ and d-Ut(600)$_n$Nd$(CF_3SO_3)_3$ di-urethanesils, the cations interact exclusively with the carbonyl oxygen atoms of the urea and urethane linkages, respectively; (2) at $n \leq 10$ for the d-U(600)$_n$ $Nd(CF_3SO_3)_3$ di-ureasils and $n \leq 20$ for the d-Ut(300)$_n$Nd$(CF_3SO_3)_3$ and d-Ut(600)$_n$Nd$(CF_3SO_3)_3$di-urethanesils, the coordination of the cations to the oxygen atoms of the polyether chains occurs. Thus, for low Nd^{3+} concentrations, the cation preferential coordination site is the carbonyl group located at the organic/inorganic interface, which is independent of the organic chain length and the nature of the cross-link. The siloxane domains are spatially correlated at a mean distance that depends mainly on the chain length and conformation. The formation of Nd^{3+}/carbonyl group interactions at the expense of the destruction of some POE/urethane and urethane/urethane interactions also influences the POE chains local order of the d-Ut(600) hybrids, promoting more disordered arrangements. Nd^{3+} hybrids present both purple–blue–green and infrared luminescence, originating from recombinations in the host matrix and the ${}^4F_{3/2} \rightarrow {}^4I_{9/2-13/2}$ transitions, respectively.

Lima et al. discuss quantitatively the energy transfer mechanisms that occur in sol–gel-derived d-U(600)-[Eu(btfa)$_3$(4,4′-bpy)] and d-U(2000)nEu$(CF_3SO_3)_3$

(n = 200, 80, and 40) di-ureasils [28]. The ground-state geometries of d-U(600)-[Eu(btfa)$_3$(4,4′-bpy)] and d-U(2000)$_{40}$Eu(CF$_3$SO$_3$)$_3$ are predicted by the Sparkle/AM1 model. Host-to-Eu^{3+} energy transfer occurs either via ligand excited states or directly from the hybrid emitting centers through the dipole-dipole, dipole-2$^{\lambda}$ pole (λ = 2, 4, and 6), and exchange mechanisms. The ligand-to-Eu^{3+} energy transfer rate is typically one order of magnitude larger than the value estimated for the direct transfer from the hybrids emitting centers, 3.75×10^{10} and 3.26×10^{9} s^{-1}, respectively, to the $^5D_1$ level. The most efficient luminescence channel is (S_0)Hybrid → (T) Hybrid → (T)Ligand → $(^5D_1,^5D_0) \rightarrow {}^7F_{0\text{–}6}$. The predicted room temperature emission quantum yield lies in excellent agreement with the corresponding experimental value (53 and 50 ± 5%, respectively), pointing out that the Sparkle/AM1 model could, under certain conditions, be applied to Eu^{3+} hybrids. The Forster and Dexter classic approaches are applied to the d-U(2000)$_n$Eu(CF$_3$SO$_3$)$_3$ (n = 200 and 40) di-ureasils where the singlet and triplet excited states of the complex could not be predicted because of a higher computational effort necessary for this type of calculation in big structures. The evidence points out that the exchange (Dexter) mechanism accounted for energy transfer.

Fu et al. synthesize europium complexes with phen in the formation of di-ureasil hosts by carboxylic acid solvolysis process [29]. The maximum crystal field splitting allows for the $^5D_0$–$^7F_1$ transition, suggesting at least two different Eu^{3+} complexes with phen in situ synthesized during the formation of di-ureasil hosts by AA solvolysis process. Fernandes et al. report the hybrid matrix built by co-condensation of two di-ureasil frameworks [d-U(900) and d-U(600)], one for incorporating POE chains with about 15.5 oxyethylene repeating units and the other for about 8.5 oxyethylene repeating units [30]. The co-condensed di-ureasil network has been doped with a europium triflate complex, and the effective interactions between the rare earth ions and the host hybrid structure result in the increased overall emission quantum yield (36%) and $^5D_0$ quantum efficiency (57%) compared with those of the complex alone (29% and 27%, respectively). Pecoraro et al. prepare d-U(2000) Eu^{3+}-doped thin films [31]. Fernandes et al. incorporated the Eu(TTA)$_3$phen complex into the *d*-Ut(600) hybrid matrix to yield an amorphous material [32], whose emission depends on the excitation wavelength. The photoluminescence data point out effective interaction between di-urethanesil host and Eu^{3+} complex.

Molina et al. prepare Er^{3+}-containing d-U(600) di-ureasils by carboxylic acid (AA, VA, and FA) solvolysis, with a siliceous network grafted to both ends of a polymer chain containing about 8.5 oxyethylene units [33]. Er^{3+} ions have been incorporated as erbium triflate salt, Er(CF$_3$SO$_3$)$_3$, with n = 5, 10, and 20, where n denotes the ratio of (OCH$_2$CH$_2$) moieties of the hybrid organic counterpart per Er^{3+} ion. FT-IR results reveal the Er^{3+} coordination of both types of oxygen atoms of the hybrid host and free and coordinated triflate ions. From absorption spectra $\Omega_{\lambda,}$ intensity parameters are evaluated together with the Er^{3+} 4I$^{13/2}$ state radiative lifetime and the peak emission cross section, whose values ($\Omega_2 = 12.3 \times 10^{-20}$, $\Omega_4 = 5.6 \times 10^{-20}$, and $\Omega_6 = 3.6 \times 10^{-20}$ cm^2; $\tau_{RAD} = 3.6$ ms; σ_{EM}(1537 nm) = 1.0×10^{-20} cm^2; Δ_{λ} = 78 nm) denote the strong coordination ability of the hybrid host.

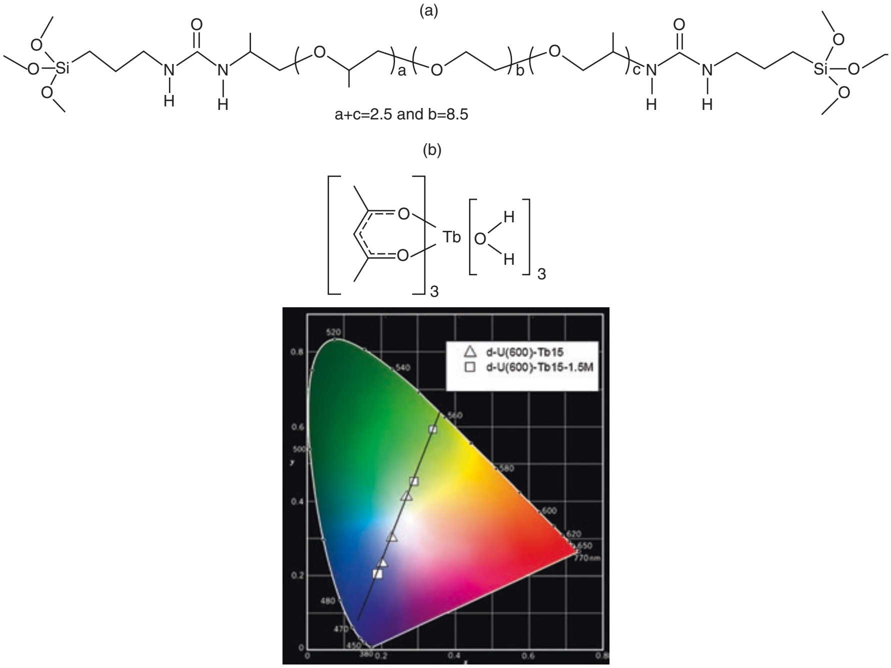

Fig. 6.6 (*Top*) Scheme for chemical structures of (*a*) the di-ureasil organic–inorganic hybrid and the (*b*) Tb(acac)$_3$·3H$_2$O complex (top). (*Bottom*) and partial 1931 CIE (*x*,*y*) diagram displaying emission color coordinates of d-U(600)-Tb15 and d-U(600)-Tb15–1.5 M excited at (1) 300 nm, (2) 320 nm, and (3) 360 nm (room temperature) (Reprinted with permission from Ref. [35]. Copyright 2009 Elsevier)

Mesquita et al. add a europium dipicolinate complex to the short-chain d-U(600) di-ureasil POE/siloxane hybrid structure prepared by the sol–gel method [34]. The addition of the Na$_3$[Eu(dipic)$_3$]·xH$_2$O complex to d-U(600) has major consequences in terms of hydrogen-bonding interactions, leading to a significant breakdown of the most disordered hydrogen-bonded aggregates of d-U(600) and to the concomitant formation of stronger aggregates. The hybrid sample is thermally stable up to 145°C and has a nonporous texture, being composed of a homogeneous, smooth surface of the hybrid host material and spherical particles of complex. In spite of the low complex concentration, a crystalline phase of unknown nature is formed in the doped xerogel. Upon incorporation of the complex into the di-ureasil matrix, they show an increase of both the $^5D_0$ lifetime and quantum efficiency values (1.950 ± 0.007 ms and 0.50, respectively) and enhanced absolute emission quantum yield value (0.66 excited at 280 nm).

Lima et al. incorporate Tb(acac)$_3$·3H$_2$O complex into the di-ureasil hybrid host via conventional hydrolysis sol–gel reactions in the presence and absence of an acid catalyst, HCl (0.5, 1.0, 1.5 and 2.0 mol L^{-1}) (Fig. 6.6(Top)) [35]. The acid catalyst contributes in the decrease of the gelation time for all samples (between 5 and 20

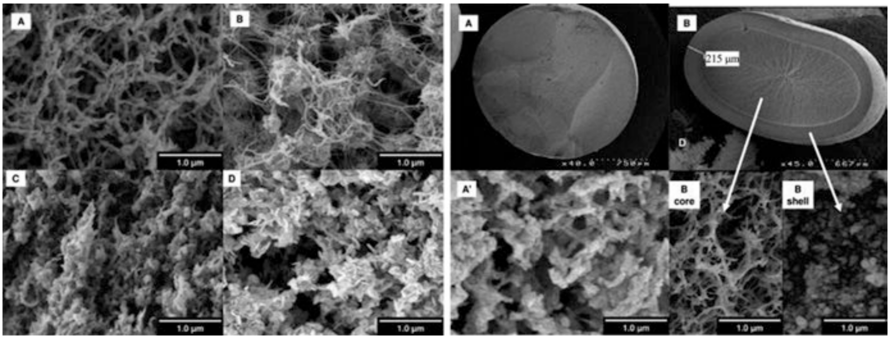

Fig. 6.7 (*Left*) SEM pictures of the cross section of aerogels prepared using the procedure of Eu^{3+} incorporation: (*A*) chitosan; (*B*) Eu–Ch; (*C*) Eu-ChS-b-H; (*D*) Eu-ChS-"*in-situ*"-H. (*Right*) SEM of cross sections of EuChS-H (A, A2) and EuChS-CS (*B*, Bcore, Bshell) (Reprinted with permission from Ref. [36]. Copyright 2010 American Chemical Society)

min). The emission quantum yields measured for the undoped samples (between 8.7 and 10.6%) although similar to those of the d-U(600) hybrids prepared by carboxylic acid solvolysis are higher than those obtained by conventional hydrolysis (in fact the value for d-U(600)-1.5 M is the highest one reported for the d-U(600) host). All the Tb^{3+}-based di-ureasils prepared with HCl present the emission quantum yield and lifetime higher than that prepared without HCl. Particularly for d-U(600)-Tb15-2 M, the profile of the excitation spectrum, the energy, and the *fwhm* of the $^5D_4 \rightarrow {}^7F_{6-3}$ transitions suggest that the $Tb(acac)_3{\cdot}3H_2O$ lost one or more of its acac ligands after incorporation into the di-ureasil host. The emission color varies along the chromaticity diagram from the blue to the green spectral regions crossing the white area, and this is achieved either by changing the HCl or Tb^{3+} concentration or the excitation wavelength (Fig. 6.6(Bottom)).

Liu et al. prepare three types of hybrid materials containing RE^{3+}, chitosan, and silica, with different structural features [36]. Two procedures of silica incorporation are used: the sol–gel procedure with the open macroporous texture chitosan gel allows an easy penetration of partially hydrolyzed ethoxysilane species into the core of the gel beads, leading to condensation of silica throughout the bead and formation of a homogeneous composite (ChS-H); the formation of composite (ChS-CS) by aggregation of silica particles through the reaction between the alcogel spheres of chitosan and Ludox colloidal silica. The resulting composites present a core–shell morphology, whose shell thickness may be tuned by changing the reaction time. The rare earth ions may be embedded either (i) before the silica incorporation, (ii) *in situ*, during the sol–gel processing, or (iii) by a postsynthesis treatment. In the first procedure, the Eu–chitosan (EuCh) alcogel hybrid is formed by impregnating the corresponding chitosan alcogel spheres with RE^{3+} to affect the structure of the chitosan network (Fig. 6.7(Left) A and B), whose morphology is highly modified (Fig. 6.7(Left) C). In the *in situ* synthesis, RE^{3+} ions are introduced concomitantly with TEOS and NaF, which presents EuF_3 to prevent the catalytic reaction (Fig. 6.7(Left)D). The two different morphologies of the Eu^{3+}-containing chitosan–

silica hybrid materials are described in Fig. 6.7(Right). The homogeneous hybrid (Fig. 6.7(Right)A) presents an open network of fibrils embedded with silica. The core-shell hybrid presents the two different components (Fig. 6.7(Right)B). The magnification reveals the presence of silica aggregates in the shell (6.7(Right)B shell) and the fibrillary structuring of chitosan in the core of the composite (6.7(Right)B core). The emission features of the core–shell materials are characterized by the distinct local environments of two Eu^{3+} ions, one associated with the chitosan core and the other with the silica shell. A distinct emission is observed for a silica-related Eu^{3+} local coordination. The local sensing features of hybrids combined with their drug-delivery control may be expected to have in vivo biological applications in diagnostics and therapy.

6.3 Photofunctional Rare Earth Hybrid Material-Based Polymer/Silica Composite Through Coordination Bonding Assembly

Both polymer and rare earth complexes can be embedded into silica gel [37]. On the basis of sol–gel-derived silica hybrid materials with ORMOSILs as linkers in Chap. 2, Yan's group further extends the multicomponent photofunctional rare earth hybrid materials with polymer/silica composite host. In these hybrid systems, rare earth ions are assembled with both silica and polymer with coordination bonds. Silica and polymer both can be directly coordinated to rare earth ions separately. On the other hand, silica and polymer are covalently linked together and then behave as a whole ligand to be coordinated to rare earth ions. Here the former is firstly discussed, whose hybrids are assembled with both silica and polymer behaving as ligands to coordinate to rare earth ions.

Wang et al. prepare polymer–inorganic hybrids (phen-Ln-MMA-co-MAL-Si) through polyhydrolysis and condensation between the triethoxysilyl group of a modified copolymer (MMA-co-MAL-APES) and TEOS, resulting in the characteristic red or green emissions of Eu or Tb ions [38]. The introduction of copolymer chains provides a template to induce the formation of a regular microstructure. The 2phen-Tb-MMA-co-MAL-Si hybrids have ordered particles of size 100–200 nm, which suggests that the terminal ligand of phen also affects the micromorphology of the hybrid system. AFM images show that the covalent composites exhibit relatively regular column shapes (diameter range of around 200 nm) within rough upper surfaces, which may be caused by mutual influences originating from the polymer soft chains and silica coupling agent (Fig. 6.8).

Zhao et al. prepare a series of quaternary and ternary polymer hybrid materials from 3-methacryloxypropyltrimethoxysilane (MS), MAA (methacrylic acid), phen, and rare earth (Eu^{3+}, Tb^{3+}, Dy^{3+}) precursors [39]. MS and MSMAA (a copolymer of MS and MAA) behave as structural functional components to form an inorganic polymer network or polymer host through coordination to rare earth ions, whereas

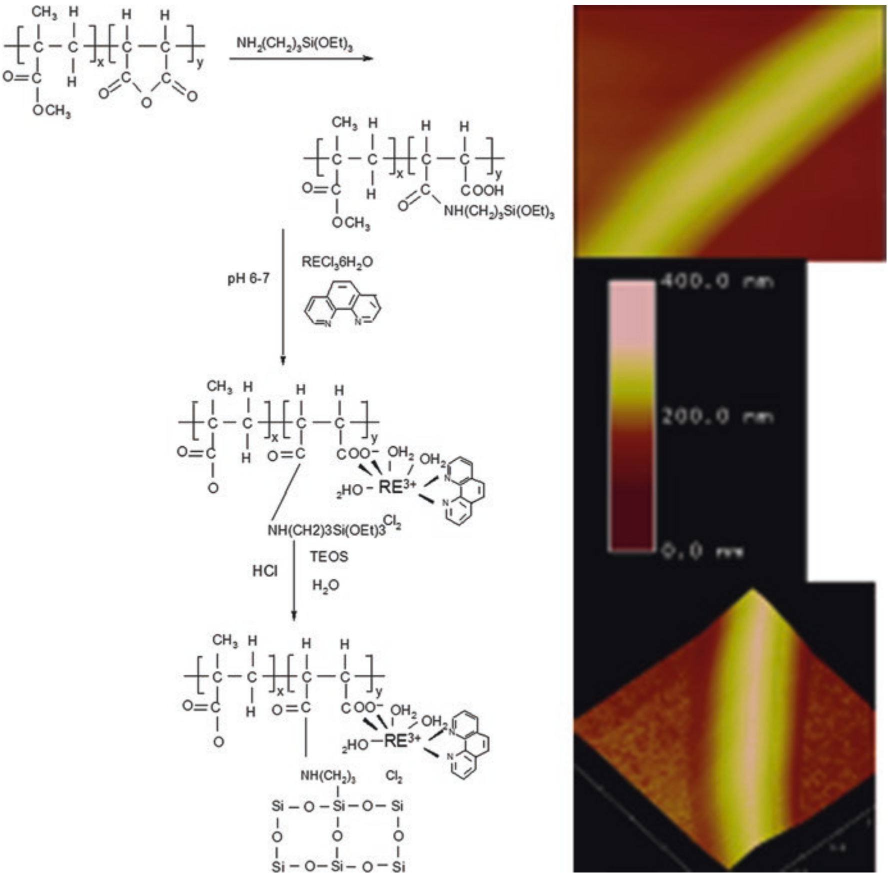

Fig. 6.8 Scheme for synthesis and atomic force microscopy photographs of the surface of 2phen-Eu-MMA-co-MAL-Si (Reprinted with permission from Ref. [38]. Copyright 2008, Elsevier)

phen acts as an energy sensitizer for the luminescence of Ln^{3+} ions. It is found that the introduction of organic polymer units influences the microstructure and, in particular, the luminescence properties of hybrid materials. It is worth pointing out that quaternary hybrid materials phen-Eu^{3+}(Tb^{3+}, Dy^{3+})-MSMA with an organic polymer unit (MAA) have larger luminescence intensities and longer lifetimes than those of ternary materials without MAA (phen-Eu^{3+}(Tb^{3+}, Dy^{3+})-MS), suggesting that the introduction of an organic chain (MAA) is beneficial to the photophysical properties of the hybrids.

Qiao et al. use 2-hydroxynicotinic acid (HNA)-grafted TESPIC to achieve the HNA-Si and then construct the rare earth polymeric hybrids by the introduction of three different polymeric chains (poly-(methacrylic acid) (PMAA) or poly-(methacrylic and acrylamide) (PMAALM) and polyvinylpyrrolidone (PVP)) [40]. All these hybrid materials exhibit homogeneous, regular, and ordered microstructure, suggesting the existence of self-assembly of inorganic network and organic chain. Both rare earth ions and organic polymer are the important factors. Seen from Fig. 6.9a(b), a large number of regular columns and cuboids are dispersed on the hierarchies homogenously with the same size of about 200–500 nm. The hybrids HNA-Si-Tb-PMAA possess the bulk dendritic stripe microstructure, while they are very complicated for HNA-Si-Eu-PMAA hybrid material (Fig. 6.9d), which exhibits the homogenous sandwich structure composed of plentiful planar circular disks on the face with the same diameter size of about 5 μm. Besides, a large number of pinholes with the uniform diameter size of about 500 nm are in the circles. For HNA-Si-RE-PMAALM, it induces that the dominant growth tendency is along the direction of Si-O-Si polymeric network, different from the dominant growth tendency in HNA-Si-RE. Moreover, it is presumed that there is less steric hindrance in the conjugated system in the rare earth complexes (HNA-Si-RE-PMAALM) than that in HNA-Si-RE or that in HNA-Si-RE-PMAA, as the result of the formation of the larger polymeric chains of PMAALM formed through the addition reaction Fig. 6.9(e,f). HNA-Si-Tb-PVP (Figure 6.9g) is composed of many layers regularly, which are full of foursquare blocks on the faces. HNA-Si-Eu-PVP (Figure 6.9h) reveals that there exist many acicular clusters distributed homogenously, which are composed of plentiful needle-like columned configurations with the same size of the width of 100 nm and the length of 1 μm. Qiao et al. also prepare the polymeric hybrids HBA-TESPIC-RE-PVP/PMAA/PMAALM with regular microstructure [41]. The path can be utilized for other hybrids with carboxylic acid-derived ORMOSILs and polymer unit [42].

Qiao et al. further prepare the hybrid materials with 1-(2-naphthoyl)-3,3,3-trifluoroacetonate (NTA)-grafted silica and polymer (PVPD, PMAA, and PVPDMAA) [43]. The NTA-Si-Eu-PVPD hybrid is composed by many regular and uniform hiberarchy and dendritic stripe microstructure, and there are many granules with the same size of about 200 nm around the hiberarchy disposed in order. Therefore, it is speculated that the longer coordination reaction with rare earth ions or the complete aging procedure is good for the growth of the granules. Besides, polymer precursor is synthesized through the copolymerization reaction between the 4-vinylpyridine and methacrylic acid to form the longer chains, bringing in more polymeric units in certain space. Therefore, the growth of these granules is hard or slow in such crowded circumstance with the unordered array. This path can also be applied to other hybrid materials with polymer/silica composite through β-diketones-derived linker [44–47]. Besides, Guo et al. synthesize polysilsesquioxane bridge (PPSSi) with methylene group modification of phenylphenacylsulfoxide by isocyanate group of TESPIC. Then ternary lanthanide (Eu, Tb) hybrids of polysilsesquioxane bridge (PPSSi) and four kinds of polymer chain (PA), PVP, PMMA, and PEMA are assembled with coordination bonding [48]. The microstructure and photoluminescent properties of these polymer hybrids (PPSSi-Ln-PAM (PVP, PMMA, PEMA)) are studied in detail. The different structure of the polymers induces the different microstructure and the different photoluminescent behavior of hybrid materials; the PPSSi-Ln-PMMA hybrid represents the longest lifetime and highest quantum efficiency.

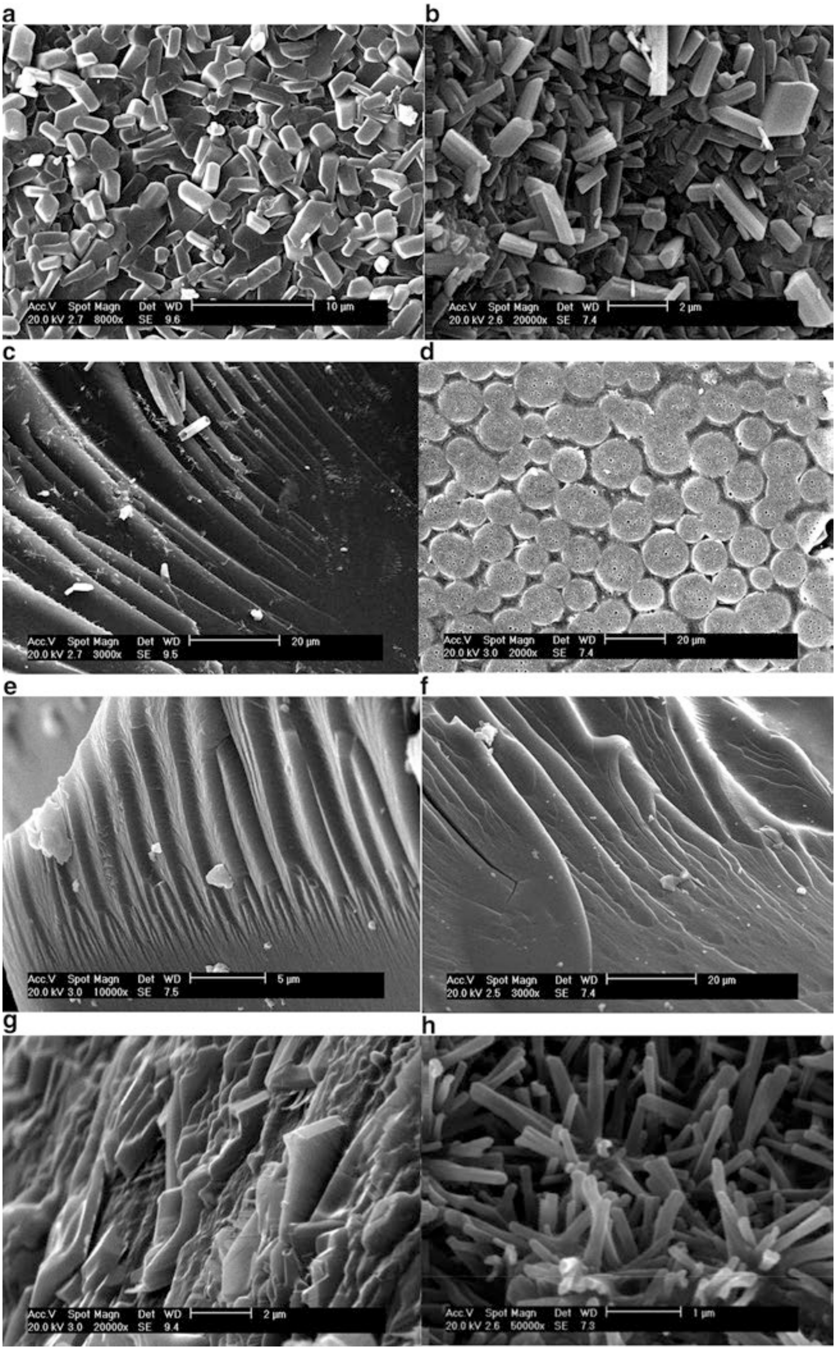

Fig. 6.9 SEM images for molecular-based hybrid materials with organic and inorganic networks: (**a**) HNA-Si-Tb, (**b**) HNA-Si-Eu, (**c**) HNA-Si-Tb-PMAA, (**d**) HNA-Si-Eu-PMAA, (**e**) HNA-Si-Tb-PMAAALM, (**f**) HNA-Si-Eu-PMAALM, (**g**) HNA-Si-Tb-PVP, and (**h**) HNA-Si-Eu-PVP (Reprinted with permission from Ref. [40]. Copyright 2007 American Chemical Society)

Qiao et al. further use calixarene derivative-grafted linkages (Calix-Br-Si and Calix-AC-Si) to assemble binary and ternary hybrid materials with chemical bonds, which are composed of lanthanide ion centers (Eu^{3+}, Tb^{3+}, Nd^{3+}), precursors Calix-Br-Si (or Calix-AC-Si), and polymers PVPD, PMMA [49]. Different polymer chains also affect the luminescence properties of hybrid systems, and Calix-Br-Si-Eu(Tb)-PMMA shows the longest luminescence decay time and largest emission quantum efficiency. The hybrid Calix-Br-Si-Eu(Tb) (Figure 6.10a,b) shows a mass of transparent thin-layer protuberance with the same radium of 3 μm, derived from the large difference in the thermal expansion coefficient among different components or the evaporation of solvent through the aging procedure. When PVPD is added into the hybrid Calix-Br-Si-Eu(Tb,Nd) as the second ligand, the microstructure has changed (Fig. 6.10c,d,e). On the surface of Calix-Br-Si-Eu(Tb,Nd)-PVPD are regularly dispersed bulk stripes. The hybrid Calix-Br-Si-Eu(Tb)-PMMA shows the homogeneous planar pleats with the same size on the surface, different from the bulk stripe in Calix-Br-Si-Eu(Tb,Nd)-PVPD, since they contain different polymers coordinated to the center ions (Fig. 6.10g,h). Moreover, besides the long carbon chain in the horizontal direction in polymer PVPD, the pyridine ring occupies the crucial vertical direction with the larger volume, which makes the hybrids grow according to the vertical direction to construct the bulk stripes. PMMA contains the carbon chain in horizontal direction and methyl and ester groups in vertical direction with smaller volume, so the hybrid with PMMA can not only grow according to the vertical direction but also along every direction on the plane to construct the planar pleat microstructure. Similar morphology can be observed in the micrographs of Calix-AC-Si-Eu(Tb) and Calix-AC-Si-Eu (Tb)-PVPD hybrids (Fig. 6.10g(h), i(j)). For hybrid Calix-AC-Si-Eu(Tb), there exist many thin-layer protuberances and clusters displaced on the surfaces uniformly with the same radium of 3 μm. Besides, Calix-AC-Si-Eu has the extra trunk-like stripes microstructure. Thus, the hybrids Calix-AC-Si-Eu(Tb,Nd)-PVPD show the tiny different microstructures after the addition of the polymer PVPD. On the surface of Calix-AC-Si-Eu/Tb-PVPD, many sheets of fold with few clusters are regularly dispersed in Fig. 6.10c and d. In Calix-AC-Si-Nd-PVPD, many particles with the radius of 1 μm are on the surface of the bulk trunk-like stripes microstructure. The final photoluminescence of them is also affected correspondingly.

Yan and Sheng et al. also fabricate the rare earth polymeric hybrids Eu/Tb-(PHA-Si)-PMMA through chemically bonding assembly technology [50, 51]. The photoactive ligand PHA (*o*-phthalic anhydride) modified by silane coupling agent APES is used as a double-functional bridge molecule to link the RE^{3+} ions and the silica with covalent bonds to form the inorganic Si-O networks. Compared to the binary hybrid materials Eu/Tb-(PHA-Si) without PMMA, the ternary hybrid materials Eu/Tb-(PHA-Si)-PMMA exhibit the improvement on the luminescence property of the hybrid system due to the introduction of the polymer PMMA.

Wang et al. prepare hybrid materials phen-Si-RE using the phen-Si as a bridge molecule that can both coordinate to rare earth ions (Sm^{3+} and Eu^{3+}) and form an inorganic Si–O network with TEOS [52]. Nicotinic acid (NA) and the polymers (PMMA and PVP) as the second ligands are introduced into the above system to prepare the hybrid materials phen-Si-RE-NA, phen-Si-RE-PVP, and phen-Si-RE-

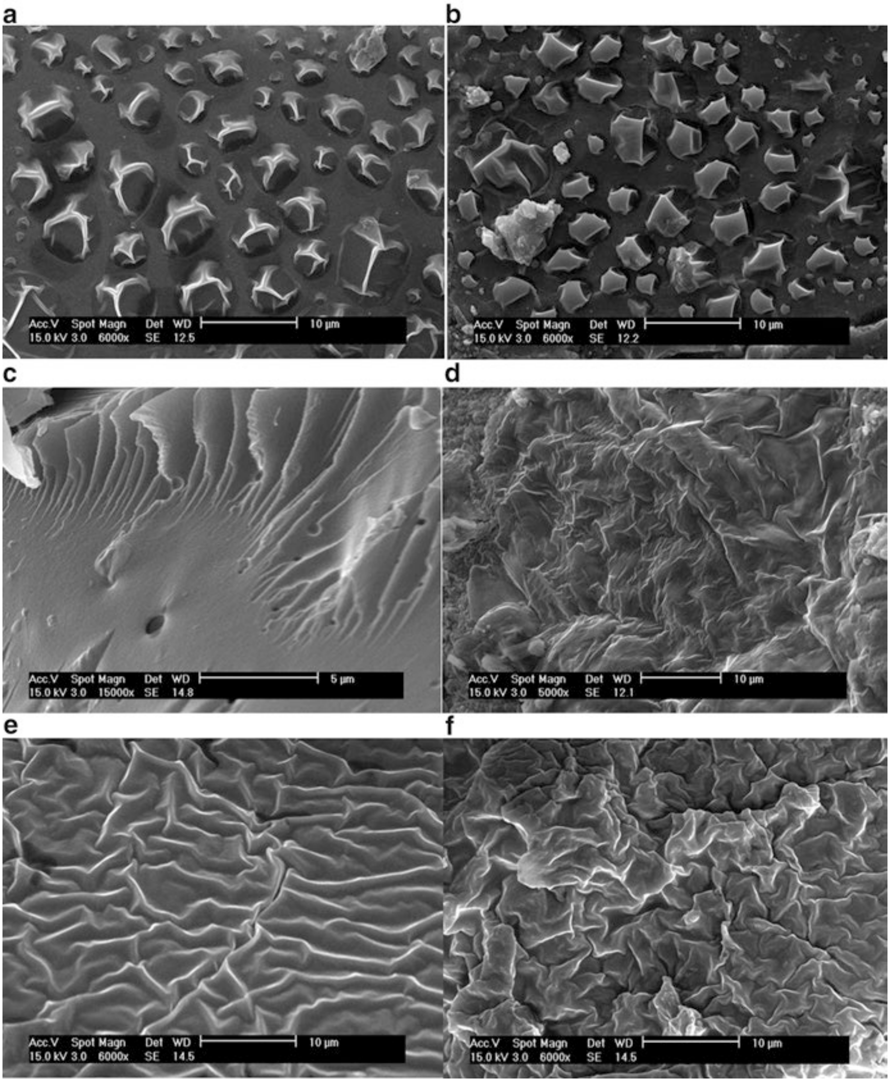

Fig. 6.10 SEM images of the hybrid materials: **a** and **b** for Calix-Br-Si-Eu (Tb); **c**, **d**, and **e** for Calix-Br-Si-Eu (Tb, Nd)-PVPD; **f** and **g** for Calix-Br-Si-Eu (Tb)-PMMA; **g**(**h**) for Calix-AC-Si-Eu (Tb); and **i**(**j**) for Calix-AC-Si-Eu (Tb) –PVPD (Reprinted with permission from Ref. [49]. Copyright 2010 the Royal Society of Chemistry)

PMMA, respectively. Yan et al. construct a series of ternary lanthanide-centered hybrid systems through coordination bonds [53]. Among them one component (ligand) is organically modified, Si-O network, which is originates from the functional molecular bridge (BFPPSi) by the functionalization of 1,3-bis(2-formylphenoxy)-2-propanol (BFPP) with TESPIC. In the second component (ligand), three different organic polymeric chains are introduced PMMA, PMAA,

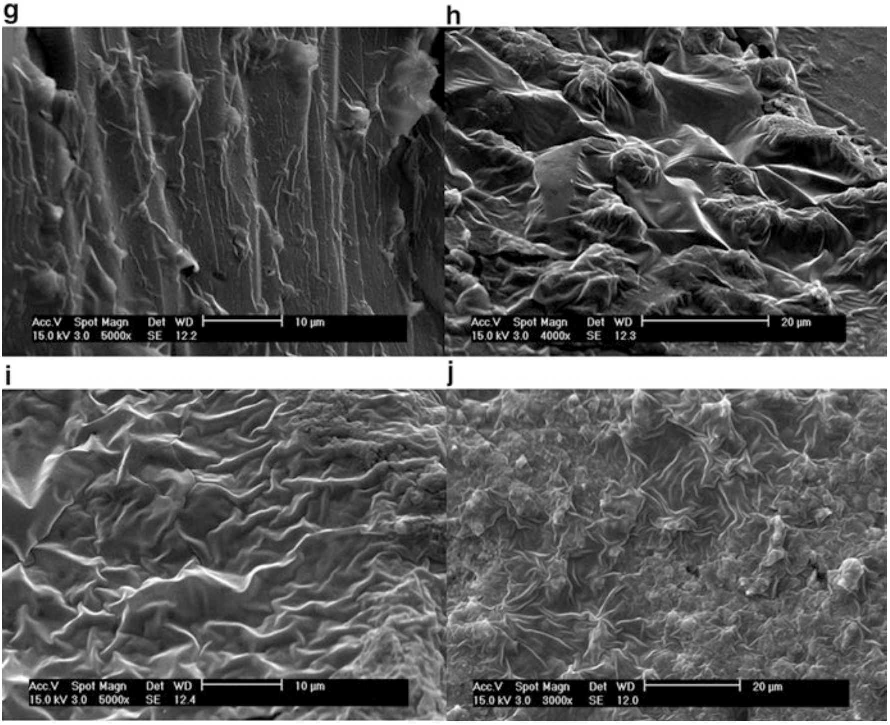

Fig. 6.10 (continued)

and PVPD, respectively. Sheng et al. prepare ternary molecular hybrid material by immobilization of Eu-Salen complex into silica matrix and poly(methyl methacrylate) (PMMA) matrix [54]. Here, the Salen-type Schiff-base ligand H2Salen (N,N′-bis(salicylidene)ethylenediamine) grafted by TESPIC is used as a flexible linker and the antenna. The obtained solid hybrid material shows not only the characteristic red emission of Eu^{3+} but also the blue emission of Salen-Si host arising from the inefficient energy transfer from antenna to Eu^{3+}, leading to the unexpected near-white light color of the material.

6.4 Photofunctional Rare Earth Hybrid Materials Based on Polymer/Silica Composite Through Covalent Bonding Assembly

In the above hybrid materials, both ORMOSIL linker and polymer units behave as the ligands to coordinate to rare earth ions, and there is no direct interaction between the two main units [38–54]. On the other hand, both ORMOLISLs and polymer units can be functionalized and then covalently linked together, which behave as a whole ligand to coordinate to rare earth ions.

Yao et al. firstly modify polyethylene glycol (PEG) with TESPIC to form the polymeric functional bridge precursor to assemble polymer hybrids [55]. Qiao et al. use TTA and the polyethylene glycol (PEG400 with the molecular weight of 380–430) as precursors to graft onto the coupling agent TESPIC, respectively, to construct two precursors TTA-Si and PEG-Si (Fig. 6.11(Top)) [56]. Then TTA-Si and the terminal ligand phen are coordinated to the rare earth ions by the carbonyl group or nitrogen atom to obtain binary or ternary hybrid polymeric materials via sol–gel process. The hybrid TTA-Si-Eu is composed by many regular and uniform spheres with the same diameter of about 2 μm (Fig. 6.11(Bottom)a). The hybrid TTA-Si-Eu-PEG is also composed by many particles with the diameter about 2 μm (Fig. 6.11(Bottom)b). However, in the overall view, the microstructure has shown less orderly arrangement, and the particles have not grown into the regular sphere. The hybrid TTA-Si-Eu-phen is also composed by many homogenous spheres with the same diameter of about 5 μm (Fig. 6.11(Bottom)c), which has the larger configuration in the wider space and accelerates the sphere to grow to form the final microstructure with the larger size than TTA-Si-Eu. The hybrid TTA-Si-Eu-Phen-PEG (Fig. 6.11(Bottom)d) has shown many particles, which have not grown into spheres as the hybrid TTA-Si-Eu-PEG, even there exist many uniform hiberarchy and dendritic stripes on the surface. The addition of the polymer PEG has the significant influence on the hydrolysis and copolycondensation process due to its long carbon chains on the vertical level and brings the expansive extensity, which is propitious to the growth of the polymeric stripe-like structure of Si-O-Si due to the decrease of the steric hindrance effect. Therefore, the growth trend to construct the polymeric network with stripes has become the major trend.

Yan et al. discuss a polymer polyacrylamide (PAM) without effective photoactive groups for energy transfer to rare earth ions, which mainly behaves as a structural host unit rather than a functional one [57]. 5-Hydroxyisophthalic acid (HIPA) is modified by TESPIC through an addition reaction, so the two *meta* carboxylate groups chelate with the rare earth ions, and the remaining amide can react with the functional PAM, modified by CPTMS, through cohydrolysis and copolycondensation. Finally, the hybrids show a relatively regular trunk or stripe. When PAMSi is introduced into the Eu-HIPA-Si hybrid material through a hydrolysis/polycondensa tion process, the emergence of circular particles is observed, whose number of particles increases and the particle size decreases with increasing PAMSi content. The dual control of orientation and copolymerization affect the formation and growth of particles in the hybrid systems. The SEM images show that the particle sizes are on the nanometer scale and the microstructures tend to be regular and homogenous (Fig. 6.12).

Wang et al. graft BFPP to TESPIC to prepare the organic precursor BFPP-Si. Then, the organic precursor BFPP-Si is coordinated to rare earth ion to obtain the luminescent center RE-BFPP-Si. Allylamine monomer (AM) is modified by TESPIC to form the precursor (AM-Si) which is then polymerized to form the polymer precursor PAM-Si. The other polymer precursor PEG-Si is achieved through the grafting reaction between polyethylene glycol (PEG) and TESPIC [58]. Yan and

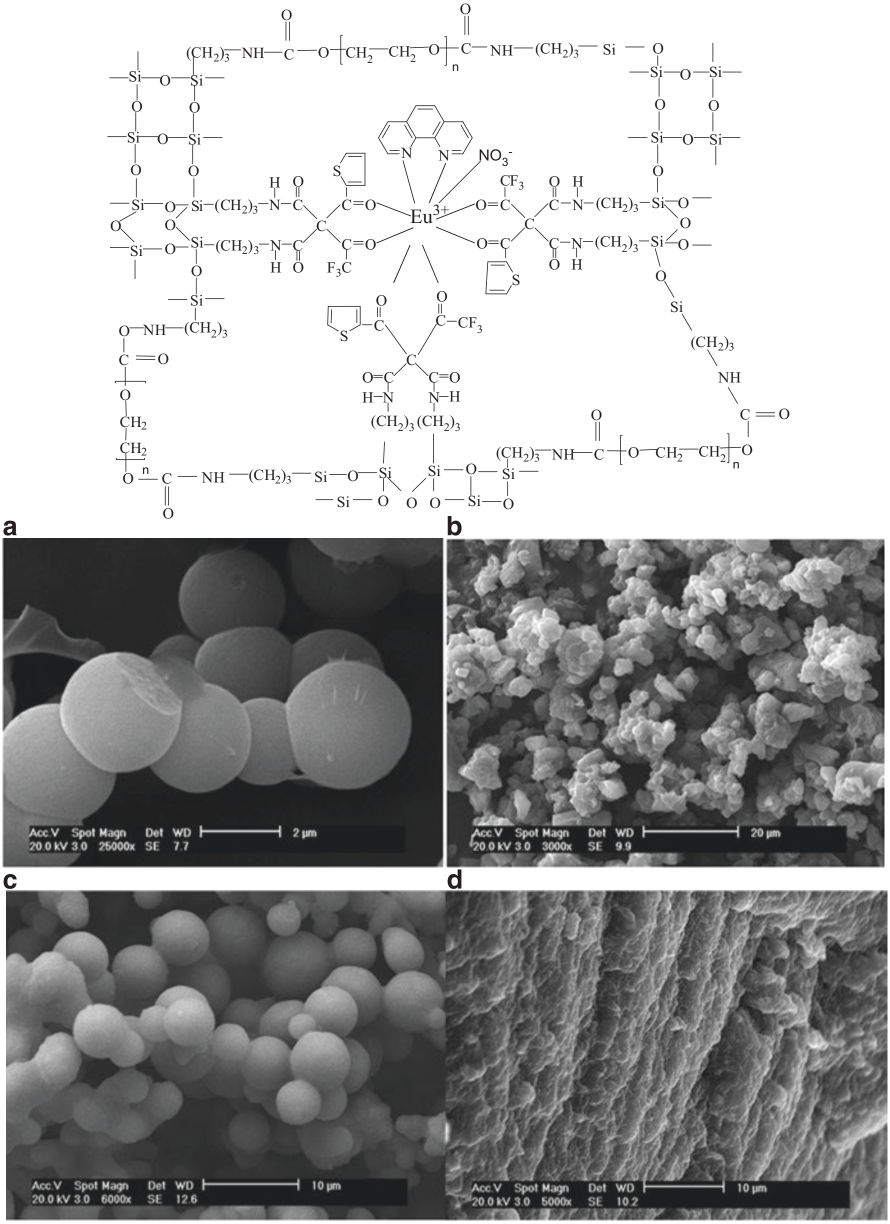

Fig. 6.11 (*Top*) Scheme of synthesis processes of hybrid polymeric materials TTA-Si-Eu-Phen and TTA-Si-Eu–Phen-PEG (*top*). (*Bottom*) SEM images of the hybrid materials TTA-Si-Eu (**a**), TTA-Si-Eu-PEG (**b**), TTA-Si-Eu-Phen (**c**), and TTA-Si-Eu–Phen-PEG (**d**) (Reprinted with permission from Ref. [56]. Copyright 2009 American Chemical Society)

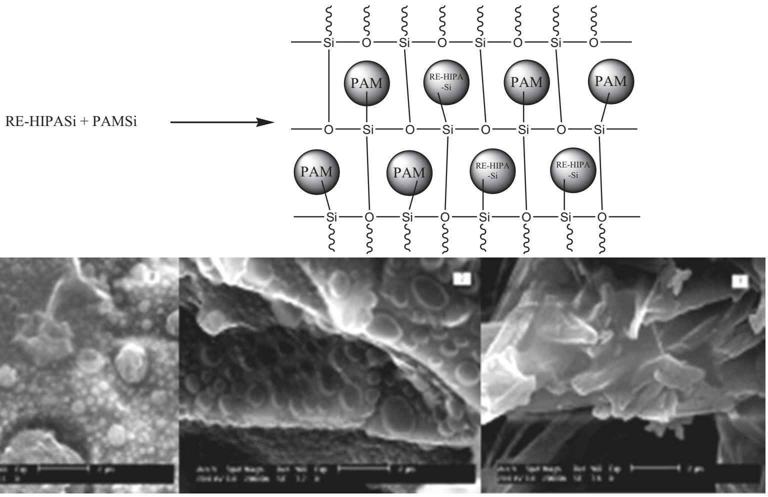

Fig. 6.12 Scheme of the synthesis of the final hybrids RE-1HIPA-Si-1PAM and comparison of the SEM images of (*1*) Eu-HIPA-Si composite material, (*2*) Eu-2HIPA-Si-1PAM composite material with a PAM/HIPA molar ratio of 1:2, and (*3*) Eu-1HIPA-Si-1PAM composite material with a PAM/HIPA molar ratio of 1:1 (Reprinted with permission from Ref. [57]. Copyright 2011 the Royal Society of Chemistry)

Wang et al. modify 2-thiosalicylic acid (TSA) with two cross-linking reagents to achieve two kinds of sulfide bridges (abbreviated as TSA-CSi and TSA-TSi, respectively). And two organic PAM and PEG are also functionalized with TESPIC to form their polymeric silane derivatives PAMSi and PEGSi. Then a series of multicomponent Eu^{3+}/Tb^{3+} hybrid materials are assembled with inorganic silica covalently linking organic polymer through the sulfide bridges [59]. Qiao et al. further synthesize the polymer-modified linkers G-Si, DG-Si, and PG-Si to prepare the hybrid materials with covalently polymer composite host [60]. Through the reaction between the hydroxyl groups of 2-hydroxyl-3-methylbenzoic acid (HMBA), the glycol (G), the diglycol (DG), or the polyethylene glycol (PEG) and the isocyanate groups of TESPIC, the hybrid precursors HMBA-Si, G-Si, DG-Si, and PEG-Si are obtained [61]. And then the precursors HMBA-Si and G-Si (DG-Si, PEG-Si) are coordinated to the rare earth ions with the carbonyl group of G-Si (DG-Si, PEG-Si) and the carboxyl group of HMBA-Si to form the hybrid materials HMBA-G-RE-Si (HMBA-DG-RE-Si, HMBA-PEG-RE-Si).

The direct polymerization process can also be used to assemble rare earth polymer hybrids [62]. A new functional polysilsesquioxane linkage (VPBA-Si) has been achieved through a hydrogen transfer addition reaction between 4-vinylphenylboronic acid and TESPIC. Three kinds of Eu^{3+}- and Tb^{3+}-centered hybrid materials are assembled with VPBA-Si and copolymers through radical addition polymerization of VPBA-Si, trans-styrylacetic acid, and N-vinylphthalimide; hydrolysis and copolycondensation between the VPBA-Si unit and TEOS; and a coordination reaction between the ligand and rare earth ions. At the same time, another kind of rare earth (Eu^{3+}, Tb^{3+}) hybrid is constructed through addition polymerization of *trans*-styrylacetic acid and vinyltrimethoxysilane, without the VPBA-Si precursor. The photoluminescence properties are studied in depth, and the results show that the hybrids with trans-styrylacetic acid exhibit the most favorable luminescence (long lifetime and high quantum efficiency). Using the similar strategy, Guo et al. realize the cooperative assembly of rare earth hybrids with 4-vinylbenzeneboronic acid (VBBA)-functionalized linkers of silane or polymer [63–66].

6.5 Photofunctional Rare Earth Hybrid Materials Based on Polymer Composite and Other Units

Nicotinic acid (NA) is grafted to titanium alkoxide to achieve functional precursor Ti-NA and further assembles two types of ternary titania hybrid materials Ti-NA-Ln-PMAA/Ti-NA-Ln-PVP by the introduction of the organic polymers PMAA/PVP into the above system [67]. Luminescence spectra and lifetime record of these titania hybrids reveal that the hybrids with organic polymers exhibit longer luminescence lifetimes and higher quantum efficiencies.

Series of alumina and titania hybrid gels are assembled with both RE^{3+} (RE = Eu, Tb) pyridine-3,5(4)-dicarboxylate complexes (3,5- for M1 and 3,4 for M2) and polymer unit (polyacrylic acid, PA) through coordination bonds [68]. Generally, pyridine carboxylates are coordinated to RE^{3+} with their carboxylates while not the nitrogen atoms because the former possesses the stronger coordination ability than the latter. So in the reaction process, the two carboxlyates of pyridine–dicarboxylates ligands (M1 and M2) are firstly controlled to be coordinated to Al or Ti ions and then the remaining pyridine nitrogen atoms are coordinated to RE^{3+}. Three β-diketonate ligands (TFAA and AA) are further chelated to RE^{3+} to form the eight-coordination number structure for RE^{3+}. M1 and M2 not only coordinate to rare earth ions to sensitize their luminescence but also anchor rare earth complexes to the framework of hybrid gels. Besides, polymer unit is introduced to the hybrid system through their dicarboxylates coordinated to Al or Ti ions. Photoluminescence property indicates that hybrid alumina gels are more favorable for the luminescence of RE^{3+} than hybrid titania gels, while different linkages (M1, M2) only have little influence on the luminescence of hybrid gels.

More recently, Li et al. prepare an organic precursor, Ti-DHBA-Si (DHBA = 3,5-dihydroxybenzoicacid), via the reaction of a carboxylic group with titanium alkoxide and the modification of the double hydroxyl groups with TESPIC. The organic precursor Ti-DHBA-Si and polymer PMMA are then simultaneously coordinated with europium ion, resulting in the final polymeric hybrids, $Eu(Ti\text{-}DHBA\text{-}Si)_3PMMA$, which shows the characteristic luminescence of europium ions [69]. Li et al. incorporate some rare earth (Eu^{3+}, Tb^{3+}, and Sm^{3+}) tetrakis(β-diketonate) complexes into polymer matrices through the anion–cation interaction, where the rare earth luminophores are non-covalently attached to the

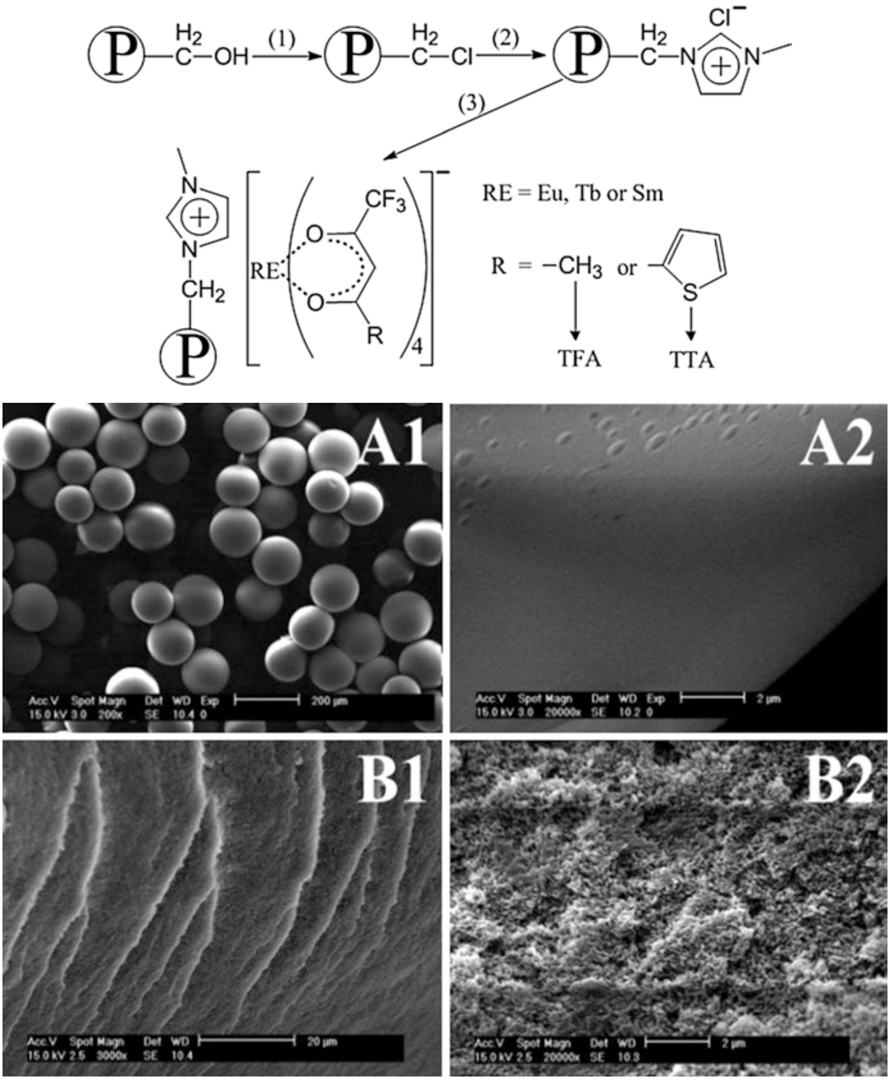

Fig. 6.13 (*Top*) The scheme for the synthesis of the rare earth tetrakis(β-diketonate) complex-functionalized polymers (or copolymers). Conditions: (1) thionyl chloride, reflux for 12 hrs; (2) 1-methylimidazole, 100 °C for 48 h; and (3) rare earth tetrakis(β-diketonate) complexes, ethanol, room temperature for 48 h. (*Bottom*) Selected SEM images of the WR-IM$^+$[Sm(TTA)$_4$]$^-$ (A1, A2) and poly(St-HEMA)-IM$^+$[Sm(TTA)$_4$]$^-$ (B1, B2) (Reprinted with permission from [70]. Copyright 2013, the European Society for Photobiology, the European Photochemistry Association, and the Royal Society of Chemistry)

polymer backbone through electrostatic interactions (Fig. 6.13(Top)) [70]. Commercially available polymer (Wang resin) and homemade copolymer Poly(St-HEMA) containing less hydroxyl groups are used here as the host materials. Polymers containing hydroxyl groups are firstly converted to chloric substituent and then cross-linked with 1-methylimidazole to form imidazolium salt molecular bridge. After that, the rare earth tetrakis(β-diketonate) complexes are introduced into polymer matrices using a mild anion metathesis reaction. Both of the Wang resin-based and HEMA-based materials present regular and uniform structure, indicating the uniform distribution of the rare earth complex unit in the polymer matrix (Fig. 6.13(Bottom)). The simple and mild functionalization operation makes it possible to substantially conserve the microstructure of polymers after the introduction of rare earth complex units through the anion–cation interaction.

Guo et al. construct polymeric hybrid microspheres with rare earth complexes into polymer matrix through covalent bonds [71]. Functional covalent polymer linkages (PAAR(MR)-M1(M2, M3)) are achieved from the functionalization of three 4-substituted aromatic carboxylic acid derivatives (4-aminobenzoic acid (M1)), 4-mercapto benzoic acid (M2), 4-hydroxybenzoic acid (M3)) with two polymer resins (*para*-alkoxy-benzyl alcohol resin (PAAR) or Merrifield resin (MR)). They present the regular microsphere morphology and characteristic photoluminescence.

6.6 Conclusion and Outlook

In conclusion, recent research progress in the photofunctional rare earth hybrid materials based on polymer or polymer/silica composite has been summarized, with an emphasis placed on the polymer/silica composite. The hybrid mainly consists of two important classes: in one class the polymer and silica both behave as the ligands to coordinate with rare earth ion and there is no direct interaction between the two units; in the other class, the polymer is covalently grafted with silica and forms a whole ligand to coordinate with rare earth ions. At present, the research of these hybrid materials should be extended to thin film or gel preparation and the control of the physical properties. Certainly, the further application should also be explored deeply.

References

1. Ueba Y, Banks E, Okmoto Y (1980) Investigation on the synthesis and characterization of rare earth metal-containing polymers. II. Fluorescence properties of Eu^{3+}–polymer complexes containing β-diketone ligand. J Appl Polym Sci 25:2007–2017
2. Okmoto Y, Ueba Y, Zhanibekov NFD, Banks E (1981) Rare earth metal containing polymers. 3. Characterization of ion-containing polymer structures using rare earth metal fluorescence probes. Macromolecules 14:17–22
3. Bekiari V, Pistolis G, Lianos P (1999) Intensely luminescent materials obtained by combining lanthanide ions, 2,2′-bipyridine, and poly(ethylene glycol) in various fluid or solid environments. Chem Mater 11:3189–3195
4. Parra EF, Brito HF, Matos JDR, Dias LC (2002) Enhancement of the luminescent intensity of the novel system containing Eu^{3+} beta-diketonate complex doped in the epoxy resin. J Appl Polym Sci 83:2716–2726
5. Zucchi G, Murugesan V, Tondelier D, Aldakov D, Jeon T, Yang F, Thuery P, Ephritikhine M, Geffroy B (2011) Solution, solid state, and film properties of a structurally characterized highly luminescent molecular europium plastic material excitable with visible light. Inorg Chem 50:4851–4856
6. Lunstroot K, Driesen K, Nockemann P, Viau L, Mutin PH, Vioux A, Binnemans K (2010) Ionic liquid as plasticizer for europium(III)-doped luminescent poly(methyl methacrylate) films. Phys Chem Chem Phys 12:1879–1885
7. Tanner PA, Yan B, Zhang HJ (2000) Preparation and luminescence properties of sol-gel hybrid materials incorporated with europium complexes. J Mater Sci 35:4325–4328
8. Yan B (2003) Sol-gel preparation and luminescence of silica/polymer hybrid material incorporated with terbium complex. Mater Lett 57:2535–2539
9. Yan B, Wang QM (2004) In-situ composition and luminescence of terbium coordination polymers/PEMA hybrid thick films. Opt Mater 27:533–537
10. Wang HF, Wang YG, Zhang L, Li HR (2013) Transparent and luminescent ionogels based on rare earth-containing ionic liquids and poly(methyl methacrylate) prepared through an environmentally friendly method. RSC Adv 3:8535–8540
11. Yan B, Qiao XF, Sheng K, Wang XL, Guo M, Shao YF (2012) Recent progress in the research of chemical assembled rare earth/inorganic/polymeric hybrid photofunctional materials. Sci China Chem (in Chinese) 42:1278–1288.
12. Chen HY, Archer RD (1996) Synthesis and characterization of linear luminescent Schiff-base polyelectrolytes with europium(III) in the backbone. Macromolecules 29:1957–1964
13. Zhao LM, Yan B (2007) Novel polymer-inorganic hybrid materials fabricated with in situ composition and luminescent properties. J Non-Cryst Sol 353:4654–4659
14. Bender JL, Corbin PS, Fraser CL, Metcalf DH, Richardson FS, Thomas EL, Urbas AM (2002) Site-isolated luminescent europium complexes with polyester macroligands: metal-mentered heteroarm stars and nanoscale assemblies with labile block junctions. J Am Chem Soc 124:8526–8527
15. Shunmugam R, Tew GN (2008) Polymers that contain ligated metals in their side chain: building a foundation for functional materials in opto-electronic applications with an emphasis on rare earth ions. Macromol Rapid Comm 29:1355–1362
16. Shunmugam R, Tew GN (2007) Dialing in color with rare earth metals: facile photoluminescent production of true white light. Polym Adv Technol 18: 940–945
17. Wang LH, Wang W, Zhang WG, Kang ET, Huang W (2000) Synthesis and luminescence properties of novel Eu-containing copolymers consisting of Eu(III)-acrylate-β-diketonate complex monomers and methyl methacrylate. Chem Mater 12:2212–2218
18. Liu Y, Wang QM, Xiang YQ, Yan B (2006) Luminescent behavior of two novel thermosensitive poly(N-isopropylacrylamide) hydrogels incorporated with rare earth complexes. J Fluorescence 16:723–726

19. Wang QM, Yan B (2006) Assembly of luminescent hybrids from co-polymers bearing functional 4-vinyl pyridine and europium aromatic carboxylate. J Photochem Photobiol A Chem 177:1–5
20. Yan B, Wang QM (2007) Molecular fabrication and photoluminescence of novel terbium co-polymer using 4-vinyl pyridine as the efficient second ligand. Opt Mater 30:617–621
21. Yan B, Guo M, Li QP (2012) Two series of multi-component rare earth (Eu^{3+}, Tb^{3+}, Sm^{3+}) polymeric hybrids: chemically bonded assembly and photophysical properties. Photochem Photobiol 88:242–249
22. Carlos LD, Messaddeq Y, Brito HF, Ferreira RAS, Bermudez VDZ, Ribeiro SJL (2000) Full-color phosphors from europium(III)-based organosilicates. Adv Mater 12:594–598
23. Carlos LD, Ferreira RAS, Rainho JP, Bermudez VDZ (2002) Fine tuning of the chromaticity of the emission color of organic-inorganic hybrids co-doped with Eu^{III}, Tb^{III} and Tm^{III}. Adv Funct Mater 12:819–823
24. Dahmouche K, Carlos LD, Santilli CV, Bermudez VDZ, Craievich AF (2002) Small-angle x-ray scattering study of gelation and aging of Eu^{3+}-doped sol-gel-derived siloxane-poly(oxyethylene) nanocomposites. J Phys Chem B 106:4377–4382
25. Goncalves MC, Bermudez VDZ, Ferreira RAS, Carlos LD, Ostrovskii D, Rocha J (2004) Optically functional di-urethanesil nanohybrids containing Eu^{3+} ions. Chem Mater 16:2530–2543
26. Bermudez VDZ, Ostrovskii D, Goncüalves MC, Lavoryk S, Carlos LD, Ferreira RAS (2005) Eu^{3+} coordination in an organic/inorganic hybrid matrix with methyl end-capped short polyether chains. J Phys Chem B 109:7110–7119
27. Goncalves MC, Silva NJO, Bermudez VDZ, Ferreira RAS, Carlos LD, Dahmouche K, Santilli CV, Ostrovskii D, Correia Vilela IC, Craievich AF (2005) Local structure and near-infrared emission features of neodymium-based amine functionalized organic/inorganic hybrids. J Phys Chem B 109:20093–20104
28. Lima PP, Nobre SS, Freire RO, Junior SA, Ferreira RAS, Pischel U, Malta OL, Carlos LD (2007) Energy transfer mechanisms in organic-inorganic hybrids incorporating europium(III): a quantitative assessment by light emission spectroscopy. J Phys Chem C 111:17627–17634
29. Fu LS, Ferreira RAS, Nobre SS, Carlos LD, Rocha J (2007) In situ synthesis of rare earth complex in urea cross-linked organic/inorganic di-ureasil hybrids via carboxylic acid solvolysis. J Lumin 122–123:265–267
30. Fernandes M, Bermudez VDZ, Ferreira RAS, Carlos LD, Martins NV (2008) Incorporation of the $Eu(tta)_3(H_2O)_2$ complex into a co-condensed d-U(600)/d-U(900) matrix. J Lumin 128:205–212
31. Pecoraro E, Ferreira RAS, Molina C, Ribeiro SJL, Messsaddeq Y, Carlos LD (2008) Photoluminescence of bulks and thin films of Eu^{3+}-doped organic/inorganic hybrids. J Alloys Compds 451:136–139
32. Fernandes M, Goncalves MC, Bermudeza VDZ, Ferreira RAS, Carlos LD, Charas A, Morgado J (2008) Optical material composed of a di-urethanesil host hybrid and a europium complex. J Alloys Compds 451:201–205
33. Molina C, Ferreira RAS, Poirier G, Fu LS, Ribeiro SJL, Messsaddeq Y, Carlo LD (2008) Er^{3+}-based diureasil organic-inorganic hybrids. J Phys Chem C 112:19346–19352
34. Mesquita ME, Nobre SS, Fernandes M, Ferreira RAS, Santos SCG, Rodrigues MO, Carlos LD, Bermudez VDZ (2009) Highly luminescent di-ureasil hybrid doped with a Eu(III) complex including dipicolinate ligands. J Photochem Photobiol A Chem 205:156–160
35. Lima PP, Ferreira RAS, Júnior SA, Malta OL, Carlos LD (2009) Terbium(III)-containing organic–inorganic hybrids synthesized through hydrochloric acid catalysis. J Photochem Photobiol A Chem 201:214–221
36. Liu FY, Carlos LD, Ferreira RAS, Rocha J, Ferro MC, Tourrette A, Quignard F, Robitzer M (2010) Synthesis, texture, and photoluminescence of lanthanide-containing chitosan-silica hybrids. J Phys Chem B 114:77–83

37. Huang XG, Wang Q, Yan XH, Xu J, Liu WS, Wang Q, Tang Y (2011) Encapsulating a ternary europium complex in a silica/polymer hybrid matrix for high performance luminescence application. J Phys Chem C 115:2332–2340
38. Yan B, Wang QM (2007) Covalently bonded assembly and photoluminescent properties of rare earth/silica/poly(methyl methacrylate-co-maleic anhydride) hybrid materials. J Photochem Photobiol A Chem 197:213–219
39. Yan B, Zhao LM, Liu JL (2008) Molecular assembly and photophysical properties of covalently bonded rare earth polymeric hybrid materials phen-RE-MSMA (MS). J Photochem Photobiol A Chem 199:50–56
40. Yan B, Qiao XF (2007) Rare earth/inorganic/organic polymeric hybrid materials: molecular assembly, regular microstructure and photoluminescence. J Phys Chem B 111:12362–12374
41. Qiao XF, Yan B (2009) Binary and ternary lanthanide centered hybrid polymeric materials: coordination bonding construction, characterization, microstructure and photoluminescence. Dalton Trans 38:8509–8518
42. Sheng K, Yan B, Lu HF, Guo L (2011) Ternary rare earth inorganic/organic hybrids with a mercapto-functionalized Si-O linkage and a polymer chain: coordination bonding assembly and luminescence. Eur J Inorg Chem:3498–3505
43. Qiao XF, Yan B (2008) Assembly, characterization, and photoluminescence of hybrids containing europium (Ш) complexes covalently bonded to inorganic Si-O networks/organic polymers by modified beta-diketone. J Phys Chem B 112:14742–14750
44. Qiao XF, Yan B (2009) Hybrid materials of rare earth centers/functionalized 2-thenoyltrifluoroacetone/silicon-oxygen network/polymeric chain: coordination bonded assembly, physical characterization, and photoluminescence. Inorg Chem 48:4714–4723
45. Qiao XF, Yan B (2009) Luminescent polymeric hybrids functionalized by beta-diketone with silicon-oxygen networks and carbon chains: assembly and characterization. Eur Polym J 45:2002–2010
46. Sheng K, Yan B (2010) A new luminescent molecular based terbium hybrid material containing both organic polymeric chains and inorganic silica networks. J Mater Sci Mater Electr 21:65–71
47. Sheng K, Yan B (2009) Coordination bonding assembly and photophysical properties of europium organic/inorganic/polymeric hybrid materials. J Photochem Photobiol A Chem 206:140–147
48. Guo L, Yan B, Sheng K, Wang XL (2011) Coordination bonding construction, characterization and photoluminescence of ternary rare earth (Eu^{3+}, Tb^{3+}) hybrids with phenylphenacylsulfoxide modified bridge and polymer units. Dalton Trans 40:632–638
49. Qiao XF, Zhang HY, Yan B (2010) Photoactive binary and ternary rare earth (Eu^{3+}, Tb^{3+}, Nd^{3+}) hybrids with p-tert-butylcalix[4]arene derived Si-O linkages and polymers. Dalton Trans 39:8882–8892
50. Yan B, Sheng K, Yao RF (2009) Novel luminescent rare earth hybrids covalently trapped through phthalic anhydride linkage. J Non-Cryst Sol 355:1008–1011
51. Sheng K, Yan B, Qiao XF, Guo L (2010) Rare earth (Eu/Tb)/phthalic acid functionalized inorganic Si-O/organic polymeric hybrids: chemically bonded fabrication and photophysical property. J Photochem Photobiol A Chem 210:36–43
52. Wang XL, Yan B, Liu JL (2011) Photophysical properties of ternary rare earth (Sm^{3+}, Eu^{3+}) centered hybrid systems with N-heterocyclic modified Si-O bridge and terminal ligands. Photochem Photobiol Sci 10:580–586
53. Yan B, Wang XL, Liu JL (2011) Photophysical properties of ternary organometallic hybrid system of rare earth center linking organically modified silica and polymeric chain. Photochem Photobiol 87:602–610
54. Sheng K, Li HT, Jin Z, Li Y (2014) Near-white light luminescent material from Eu(III) complexes encapsulated in silica/PMMA matrices. J Mater Sci Mater Electron 25:4562–4567
55. Yan B, Yao RF, Wang QM (2006) Molecular assembly and photoluminescence of novel rare earth/inorganic/polymeric hybrid materials with functional covalent linkages. Mater Lett 60:3063–3067

56. Qiao XF, Yan B (2009) Covalently bonded assembly of rare earth/silicon-oxygen network/polyethylene glycol hybrid materials through functionalized 2-thenoyltrifluoroacetone linkage. J Phys Chem B 113:11865–11875
57. Yan B, Zhao LM, Qiao XF, Wang XL, Zhao Y (2011) Sol-gel preparation, microstructure and luminescence of rare earth / silica / polyacrylamide hybrids through double functionalized covalent Si-O linkage. RSC Adv 1:1064–1071
58. Wang XL, Yan B, Liu JL (2010) Photoactive rare earth (Eu^{3+}, Tb^{3+}) hybrids with organically modified silica covalently bonded polymeric chain. Coll Polym Sci 288:1139–1150
59. Yan B, Qian K, Wang XL (2011) Photofunctional Eu^{3+}/Tb^{3+} hybrids with inorganic silica covalently linking polymer chain through their double functionalization. Inorg Chim Acta 376:302–309
60. Qiao XF, Yan B (2008) Molecular construction and photophysics of luminescent covalently bonded hybrids by grafting the rare earth ions into the silicon-oxygen networks and carbon chains. J Photochem Photobiol A Chem 199:188–196
61. Qiao XF, Yan B (2009) Chemically bonded assembly and photophysical properties of luminescent hybrid polymeric materials embedded into silicon-oxygen network and carbon unit. J Organomet Chem 694:3232–3241
62. Qiao XF, Yan B (2011) Rare earth (Eu^{3+}, Tb^{3+}) centered polymeric hybrids: composite assembly of radical addition polymerization and condensation reaction, physical characterization and photoluminescence. New J Chem 35:568–575
63. Guo M, Yan B, Guo L, Qiao XF (2011) Cooperative sol-gel assembly, characterization and photoluminescence of rare earth hybrids with novel covalent linkages and 1,10-phenanthroline. Coll Surf A 380:53–59
64. Yan B, Guo M, Qiao XF (2011) Luminescent rare earth (Eu3+, Tb3+) hybrids with 4-vinylbenzeneboronic acid functionalized Si-O bridge and beta-diketones. Photochem Photobiol 87:786–794
65. Wang XL, Yan B (2012) Photofunctional binary and ternary Eu^{3+}/Tb^{3+} hybrid materials with copolymer linkage methacrylic acid–vinyltrimethoxysilane and 1,10-phenanthroline. Coll Surf A 399:18–24
66. Li Y, Guo M, Yan B (2012) Photoluminescent Eu^{3+}/Tb^{3+} hybrids from the copolymerization of organically-modified silane. Coll Polym Sci 290:1765–1775
67. Wang XL, Yan B (2011) Ternary luminescent rare earth-centered hybrids with organically modified titania and polymer units. Coll Polym Sci 289:423–431
68. Yan B, Guo M (2013) Photoluminescent hybrid aluminum and titanium gels linked with Eu^{3+}/Tb^{3+} complexes and polymer units through coordination bond. Inorg Chim Acta 399:160–165
69. Li YJ, Ge XT, Pang XL, Yu XD, Zhen XL, Geng LJ, Wang YQ (2015) Molecular assembly and luminescent properties of europium polymeric hybrid material based on Si–O–Ti hosts. Mater Lett 152:170–172
70. Li QP, Yan B (2013) Novel luminescent hybrids by incorporating rare earth β-diketonates into polymers through ion pairing with an imidazolium counter ion. Photochem Photobiol Sci 12:1628–1635
71. Yan B, Guo M (2013) Photofunctional Eu^{3+}/Tb^{3+} organic-inorganic polymeric hybrid microspheres with covalently bonded resin host. J Photochem Photobiol A Chem 257:34–43

Part III
Multicomponent Assembly

Chapter 7

Photofunctional Rare Earth Hybrid Materials Based on Multicomponent Assembly

Abstract This chapter mainly focuses on recent research progress in photofunctional rare earth hybrid materials based on multicomponent assembly. On the basis of the previous chapters on all kinds of typical rare earth hybrid materials, a lot of chemical modification paths are obtained. These paths can be further utilized to introduce other functional units including luminescent units such as another rare earth species or other photoactive species to assemble the multicomponent hybrid systems. This chapter covers photofunctional rare earth hybrid materials based on modified clay, ionic gel, inorganic nanocomposite, polyoxometalate, and multi-host assembly. Herein, it mainly focuses on the work of our group in recent years.

Keywords Rare earth ion • Photofunctional hybrid material • Multicomponent assembly • Luminescence

In Chaps. 2, 3, 4, 5 and 6, rare earth ions or their complexes can be introduced into all kinds of host materials (silica or mesoporous silica, microporous zeolite or metal-organic framework, polymer or polymer composite) through chemical bonds or other interactions. In fact, the hybrid systems involving photoactive rare earth species are not limited to these; they cover a very extensive range. Besides the single structural or functional unit, the composite units are also assembled through similar postsynthetic paths, such as the polymer–silica composite in Chap. 6. In addition to the multicomponent host in the hybrid materials, the multi-photofunctional species can be also introduced into the same hybrid system, whose luminescence color may be tuned or integrated. These luminescent species can be other rare earth compounds as well as non-rare earth photoactive compounds. So in this context, we focus on the photofunctional rare earth hybrid materials involving new host units or new photofunctional units. Here five types are emphatically selected: photofunctional rare earth hybrid materials based on modified clay, ionic gel, inorganic nanocomposite, polymetallate, and multi-host assembly. The main emphasis is placed on the work of our group in photofunctional hybrid materials.

B. Yan, *Photofunctional Rare Earth Hybrid Materials*,
Springer Series in Materials Science 251, DOI 10.1007/978-981-10-2957-8_7

7.1 Photofunctional Rare Earth Hybrid Materials Based on Modified Clay

Layered matrices can be modified by intercalation and/or functionalization of organic molecule, anion, or ligands, thereby producing hybrid materials with specific properties, which in turn depend on the interaction, covalent bond in functionalization, and intermolecular forces in intercalated compounds.

Xu et al. intercalate two kinds of rare earth complexes into zirconium bis(monohydrogen phosphate) (α-ZrP) by exchanging the RE complexes into the p-methoxyaniline (PMA) preintercalated compound $Zr(O_3POH)_2 \cdot 2PMA$ (α-ZrP·2PMA) [1]. Intercalation of RE complexes into α-ZrP is performed, resulting in the insertion of a RE complex into bulk α-ZrP. α-ZrP·2PMA is a useful starting material for the intercalation of bulky and weakly basic guests, in that it combines a large interlayer spacing with easily exchanged groups. The luminescent lifetimes of the assemblies are longer than those of the corresponding pure complexes, suggesting the improved photostabilities after intercalating RE complexes into α-ZrP.

Gago et al. use Zn–Al layered double hydroxide (LDH) pillared by 2,2-bipyridine-5,5-dicarboxylate (BDC) anions as a porous matrix to intercalate $LnCl_3$ (Ln = Eu, Gd) (Fig. 7.1) [2]. Metal loadings of 9.0 wt% for Eu and 11 wt% for Gd suggest about two lanthanide ions for every three BDC ions. The fitting of the room-temperature EuL_3-edge EXAFS for the Eu hybrids reveals one shell of 7 ± 1 oxygen/nitrogen atoms at 2.41 Å and no evidence for a Eu–Cl bond. The emission spectra for this material display the typical Eu^{3+} red emission and a large broad band

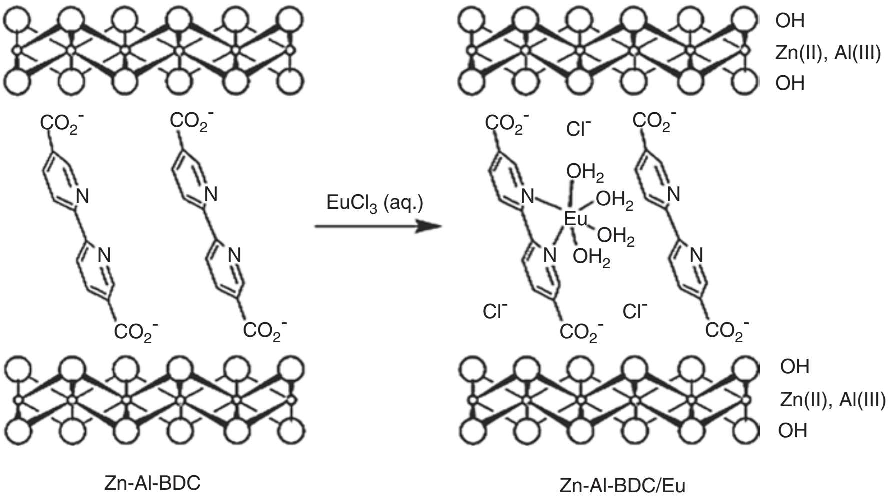

Fig. 7.1 Scheme for the preparation of Zn-Al-BDC/Eu, showing the proposed coordination environment of Eu^{3+} ions within the interlayer region (Reprinted with permission from Ref. [2]. Copyright 2005 American Chemical Society)

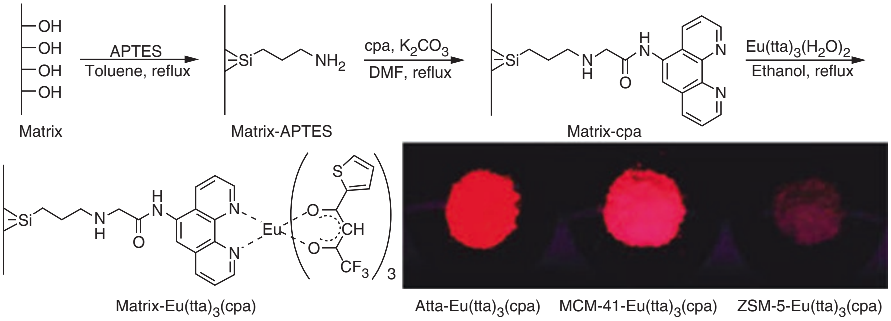

Fig. 7.2 Synthesis procedure and predicted structure of matrix-Eu(TTA)$_3$(cpa). The photography shows the composites under UVA irradiation (365 nm) (Reprinted with permission from Ref. [3]. Copyright 2009 American Chemical Society)

with the peak at 460 nm corresponding to the emission from free ligands. Selected excited spectra and low-temperature spectra both show only one type of Eu^{3+} binding site. The $^5D_0$ quantum efficiency is estimated to be low (7.7%), and the number of water molecules is calculated as 3.6 ± 1.

Attapulgite clay as natural silicate nanorods can form nanocomposites with extreme chemical stability and remarkable exposure durability. Ma et al. prepare the hybrids with covalently coupled europium complex Eu(tta)$_3$(H$_2$O)$_2$ on attapulgite (and MCM-41 or ZSM-5 for comparison) via ligand exchange reaction (Fig. 7.2) [3]. Eu^{3+} complexes either covalently bond to the outer surfaces of attapulgite or permeate the channels. The hybrids display more efficient emission, enhanced thermal stability, and improved exposure durability in comparison with the isolated complexes, due to interactions of the complexes with the matrices. The complexes bonded to attapulgite are superior to that introduced to the other matrices, not only for the natural availability of the clay but also for its stronger luminescence and similar stability.

Domínguez et al. prepare Eu and Nd-doped hydrocalumite by a coprecipitation method [4], which (with Eu^{3+} and Nd^{3+} contents up to 4% molar ratio) shows a single crystallographic phase, without segregation of secondary Eu/Nd-containing phases. The photoluminescence spectra of the noncalcined hybrids consist of both visible Eu^{3+} or NIR Nd^{3+} and a broad band corresponding to Al-related defects. High-temperature stable ceramic pigments prepared from Eu^{3+}/Nd^{3+}-doped hydrocalumite precursors present multiwavelength emission covering a large vis/NIR spectral region, which has potential applications as barcodes or broad band amplifiers. The emission spectra of the calcined samples evidence the presence of two Eu^{3+} local environments (CaO and mayenite). Upon calcination, the absolute emission quantum yield of the Eu^{3+} hybrid material increases from less than 0.01 to 0.06.

de Faria et al. prepare luminescent hybrid materials by grafting terbium picolinate complexes on kaolinite c matrix by intercalation and immersion (Fig. 7.3) [5]. Treatment of kaolinite (Ka) with picolinic acid (pa) increases the basal distance of the clay (7.2 ~ 13.5 Å), suggesting that the acid molecules are inserted into the

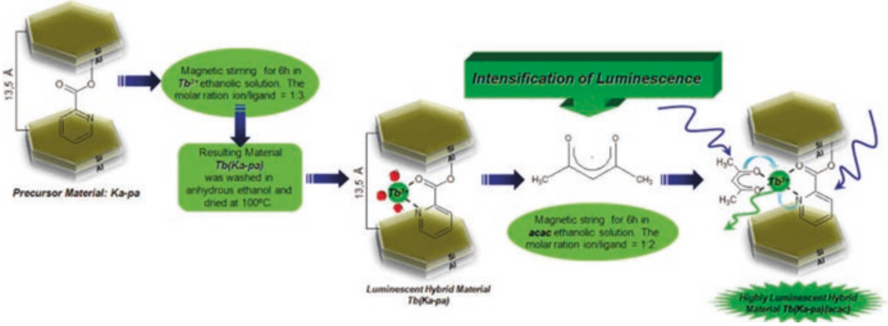

Fig. 7.3 Scheme of the procedure employed for the preparation of luminescent hybrid materials based on kaolinite (Reprinted with permission from Ref. [5]. Copyright 2011 American Chemical Society)

interlayer region of the clay. Further insertion of Tb^{3+} into Ka-pa does not provoke any further variation in the basal distance but provoke the removal of some pa molecules. The final solid material has 49% of intercalated layers. Addition of a secondary ligand (acac) promotes the curling of the kaolinite layers because of the decreased interaction between them. The curling process is known to be favorable when the hydrogen bonds of the kaolinite structure are weakened by intercalation or grafting of polar molecules.

Li et al. design and synthesize a new organic salt capable of coordinating and sensitizing both Eu^{3+} and Tb^{3+} ions with quantum yields of 0.34 and 0.43, respectively. They also prepare the corresponding hybrid materials by electrostatic adsorption of the ionic complex on Laponite [6]. XRD patterns suggest that the complexes are mainly adsorbed on the outer surfaces of the Laponite disks rather than intercalated within the interlayer spaces. Wang et al. use Na_2Bipydc (Bpydc = 2,2′-bipyridine-5,5′-dicarboxylic) (Fig. 7.4 (Top) a) as the organic ligand for Ln^{3+}, whose negatively charged carboxylate anions can interact electrostatically with the positively charged amino groups of amino clay (AC) in aqueous system to achieve a white hybrid hydrogel AC–Bipy (Fig. 7.4 (Top) b). Finally luminescent hybrid hydrogels AC–Bipy–Ln are prepared [7], whose powders have various emission colors and satisfied color purity (Fig. 7.4 (Top) c). Transparent luminescent thin films are prepared by simply drop casting the dilute hydrogels of AC–Bipy–Ln (about 1% in mass ratio) onto 2 cm × 2 cm quartz substrate (Fig. 7.4 (Bottom) a) followed by dehydration at 40 °C in air. Similarly, the emission colors can be tuned by varying the molar ratio of Eu^{3+} and Tb^{3+} and the excitation wavelength. The films of AC–Bipy–Eu_1Tb_{24}, AC–Bipy–Eu_1Tb_{49}, and AC–Bipy–Eu_1Tb_{99} are all able to emit white light under 350 nm UV light illumination, especially the AC–Bipy–Eu_1Tb_{24}, with a satisfied CIE coordinate of (0.32, 0.33) (Fig. 7.4 (Bottom) b). These luminescent thin films are possibly available for application in the fields of optoelectronics and sensing.

More recently, Yao et al. observe a remarkable increase of luminescence efficiency of a hybrid material by loading of Eu^{3+}–β-diketonate complexes into the

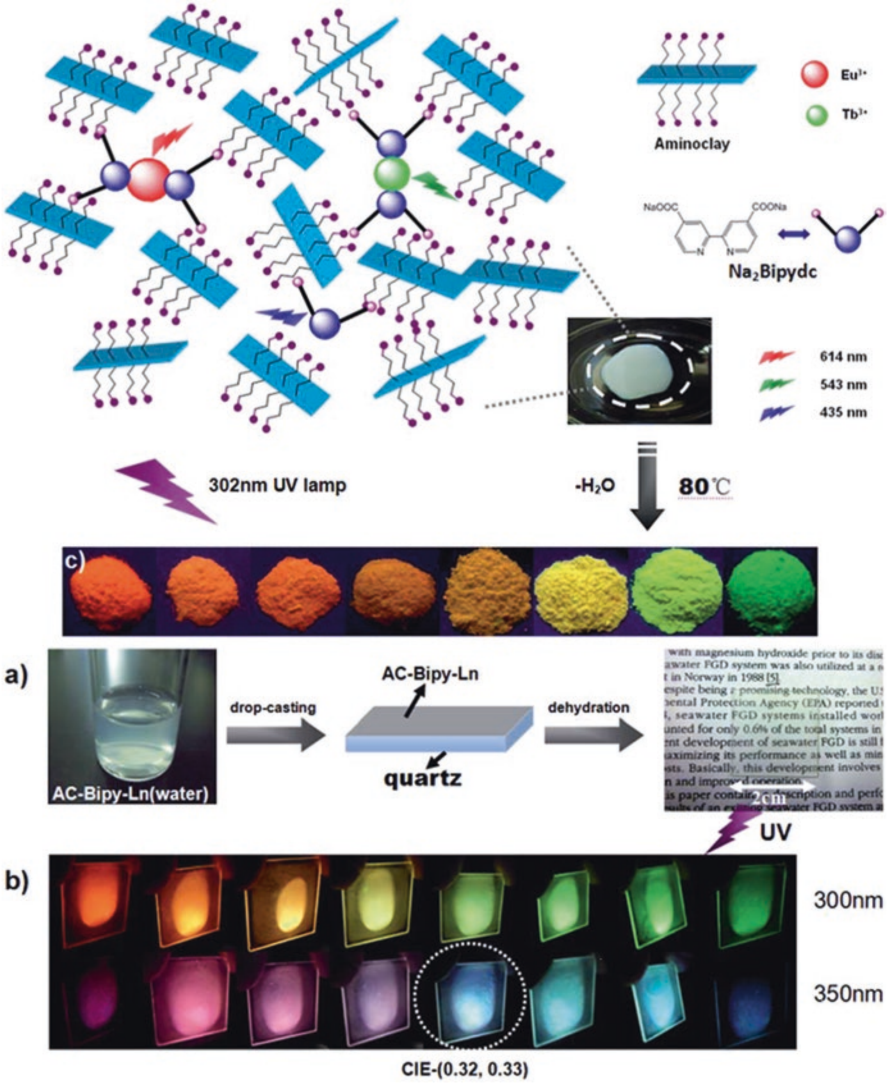

Fig. 7.4 (*Top*) (**a**) Illustration of the predicted structure of the AC–Bipy–Ln hybrid luminescent materials. The molar ratio of the components is AC: Na_2Bipydc: $LnCl_3$ = 3.46: 2: 1; (**b**) AC–Bipy–Ln hydrogel; (**c**) luminescent powders of AC–Bipy–Eu, AC–Bipy–Eu_1Tb_1, AC–Bipy–Eu_1Tb_4, AC–Bipy–Eu_1Tb_{14}, AC–Bipy–Eu_1Tb_{24}, AC–Bipy–Eu_1Tb_{49}, AC–Bipy–Eu_1Tb_{99}, and AC–Bipy–Tb, from left to right in the order, respectively (under 302 nm UV lamp illumination). (Bottom) (**a**) Preparation of the transparent luminescent thin films on quartz substrate; (**b**) digital photographs of the thin films under 300 and 350 nm UV light irradiation (AC–Bipy–Eu, AC–Bipy–Eu_1Tb_1, AC–Bipy–Eu_1Tb_4, AC–Bipy–Eu_1Tb_{14}, AC–Bipy–Eu_1Tb_{24}, AC–Bipy–Eu_1Tb_{49}, AC–Bipy–Eu_1Tb_{99}, and AC–Bipy–Tb, from left to right in the order, respectively) (Reprinted with permission from Ref. [7]. Copyright 2015 the Royal Society of Chemistry)

LAPONITE® interlayers using a two-step procedure, after modification with tpy-IL [8]. The presence of tpy-IL can fully protect Eu^{3+} ions from the water molecule quenching and remove the abundant protons on the platelets, resulting in luminescent enhancement. Wang et al. report a fascinating multicolored photoluminescent and white light-emitting hybrid materials by simple supramolecular co-assembly of organoclay (cationic aminoclay, AC), sensitizer, as well as Ln^{3+} in aqueous medium at room temperature (Fig. 7.5) [9]. The XRD pattern (Fig. 7.5c) reveals a disordered structure of the as-synthesized aminoclay. Sodium 1,2,4,5-benzenetetracarboxylate (Na-BTC) (Fig. 7.5b) is employed as the anionic organic sensitizer for Ln^{3+} ions, whose negatively charged carboxylate groups are expected to interact electrostatically with the positively charged organoclay to form a hybrid hydrogel. The final hybrid materials AC-BTC display blue fluorescence under UV lamp illumination (Fig. 7.5g).

Yang et al. realize the tunable emission colors in both powders (Fig. 7.6a) and transparent films through the assembly of Eu^{3+}/Tb^{3+} complex and AC (Fig. 7.6b) [10]. The gels can be easily coated on round-shaped objectives like an UV–LED cell, and then a bright white light is achieved (Fig. 7.6c).

Yang et al. also use a simple two-step strategy to fabricate $Eu(TTA_n)$@Lap hybrids by Eu^{3+}–β-diketonate complex, Laponite platelets, and imidazolium salt [11], whose self-standing film is also fabricated. $Eu(TTA_n)$@Lap-1 hybrid film presents a bright emission under UV light illumination (inset of Fig. 7.7a). Bright-red emission under a UV light illumination is then observed (Fig. 7.7b). The aqueous solution can be easily casted on a round-shaped objective such as an LED cell, also showing bright-red light (Fig. 7.7c). Red-emitting luminescent materials excited effectively by near UV light are highly desirable for white light-emitting LED. The resultant flexible film shows bright-red light even under daylight (Fig. 7.7d (top)). Strong bright-red emission light is observed when it is illuminated with a UV light (Fig. 7.7d).

Li et al. prepare a Eu^{3+}/Tb^{3+} AcAc complex co-doped Laponite hybrids ($Eu_1Tb_9(ACAC)_n$@Lap) and utilize it for ratiometric detection of low-level water in organic solvents [12]. Such a luminescence detector represents excellent fingerprint correlation between water content in solvents and emission intensity ratio (I_{Eu}/I_{Tb}), whose variable emissive light colors can be observed as water concentration in common organic solvents (MeCN, EtOH, and THF) increases (0–5% v/v) clearly and directly with the naked eye.

7.2 Photofunctional Rare Earth Hybrid Materials Based on Ionogels

Room temperature ionic liquids are salts which have melting points below room temperature and compose entirely of ions. They have received numerous attentions for their potential application due to their low melting points, negligible volatility, non-flammability, increased thermal stability, high electrochemical window and

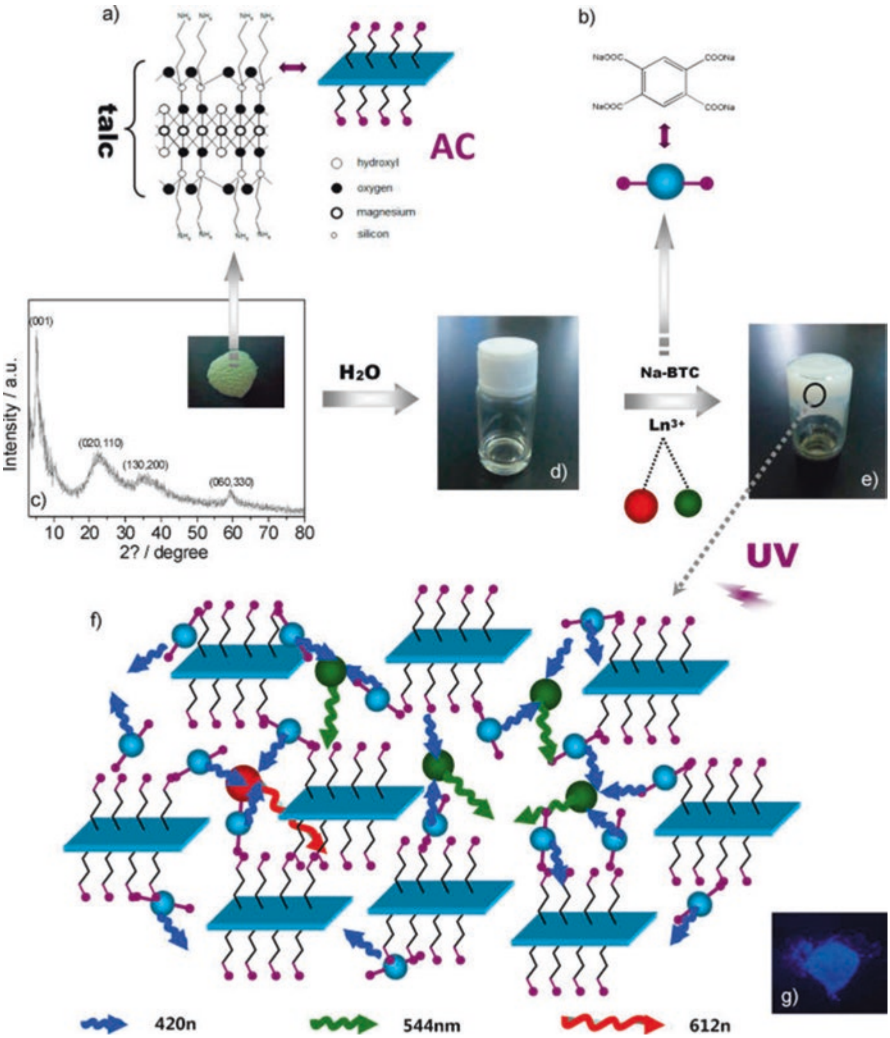

Fig. 7.5 (**a**) A single AC unit; (**b**) Na-BTC; (**c**) digital photo and XRD pattern of AC; (**d**) AC aqueous solution; (**e**) AC-BTC-Ln (hydrogel), with approximate molar ratio of AC:Na-BTC = 13:7 and Na-BTC:Ln^{3+} = 3:4; (**f**) schematic representation of the luminescent materials consists of AC, Na-BTC, and $LnCl_3$, under UV light illumination; (**g**) image of the dehydrated fine powder of AC-BTC (254 nm UV illumination) (Reprinted with permission from Ref. [9]. Copyright 2014 American Chemical Society)

ease of recycling etc. For material field applications, one of the important strategies for using ionic liquids is by confining them into some porous solids to obtain so-called "ionogels".

Lunstroot et al. have shown that lanthanide complexes (1-hexyl-3-methylimidazolium tetrakis(naphthoyltrifluoroacetonato)-europate(III)) can be efficiently confined in the ionic liquid component of solid-state ionogels [13]. This

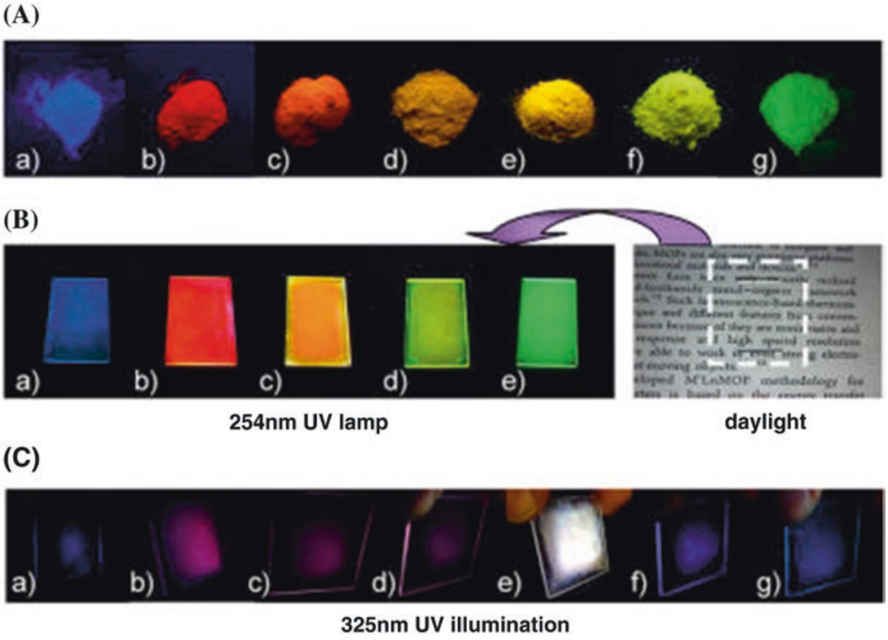

Fig. 7.6 (**a**) Images of luminescent materials with tunable emission colors under 254 nm UV lamp illumination: (*a*) AC-BTC; (*b*) AC-BTCEu; (*c*) AC-BTC-Eu_1Tb_2; (*d*) AC-BTC-Eu_1Tb_4; (*e*) AC-BTC-Eu_1Tb_7; (*f*) AC-BTC-Eu_1Tb_{19}; and (*g*) AC-BTC-Tb. (**b**) Images of transparent and luminescent films on quartz substrate: (*a*) AC-BTC; (*b*) AC-BTC-Eu; (*c*) AC-BTC-Eu_1Tb_2; (*d*) AC-BTC-Eu1Tb7; and (e) AC-BTC-Tb, with excitation wavelength of 254 nm. (**c**) Images of the films on quartz substrate: (*a*) AC-BTC; (*b*) AC-BTC-Eu; (*c*) AC-BTC-Eu_1Tb_2; (*d*) ACBTC-Eu_1Tb_4; (*e*) AC-BTC-Eu_1Tb_7; (*f*) AC-BTC-Eu_1Tb_{19}; and (*g*) AC-BTC-Tb, under 325 nm UV light illumination (Reprinted with permission from Ref. [9]. Copyright 2014 American Chemical Society)

method of immobilization of luminescent complexes in hybrid materials is a general powerful alternative to immobilization of the complexes by covalent linking to the silica network, and it expands the types of known functional hybrids. The luminescent ionogels offer the advantages over other luminescent hybrid materials that their 80 vol% ionic liquid content exhibits a high ionic conductivity. Ru et al. synthesize a special linker by the reaction of TESPIC with an amino-functionalized imidazolium salt and prepare the hybrid organosilica-fabricated lanthanide complexes [14]. The hybrid organosilicas exhibit thermally reversible behavior. Heating can make the materials fluid at 60 °C, and cooling of the solution to room temperature regenerates the gels. These two procedures can be repeated several times.

Wen et al. prepare the hybrid ionogels with IL-ACC and Eu^{3+},Tb^{3+} complexes (Fig. 7.8) [15]. The final hybrid ionogels emit red emissions irradiated by UV lamp (λ_{max} = 254 nm). Substitution of results in similar gels (Gel–Tb) shows bright-green emission under UV light. It is found that precipitates rather than gels are obtained without addition of Ln^{3+} ions, implying the vital role of Ln^{3+} in the formation of these ionogels. Both the coordination of Ln^{3+} ions to organic salts and the presence

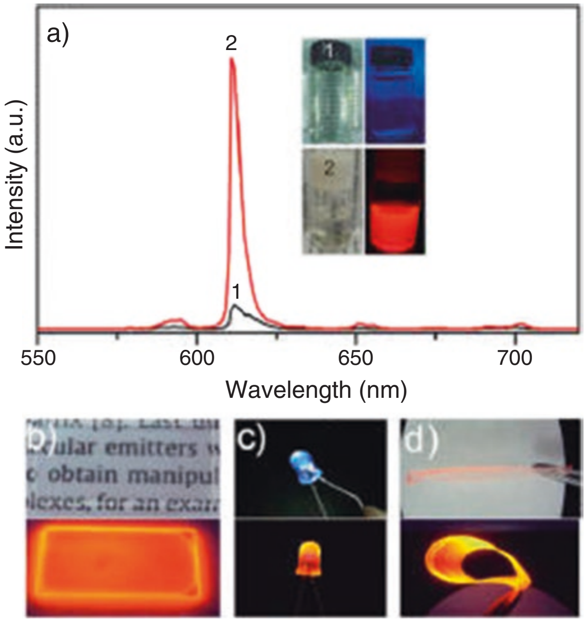

Fig. 7.7 Demonstrations of the aqueous solution processability of the luminescent nanohybrid. (*a*) Emission spectra of aqueous solution of Eu(TTA_n)@Lap (*1*) and Eu(TTA_n)@Lap-1 (*2*), (*inset*) Photographs of the same under daylight (*top*) and UV light irradiation (*bottom*); (*b*) A luminescent and transparent film results from casting the aqueous solution of Eu($TTA_{n)}$@Lap-1 on a glass substrate; (*c*) The commercially available UV–LED (λ_{max} = 395 nm) and that coated with Eu(TTA_n)@Lap-1; (*d*) The flexible film casting aqueous solution of the Eu(TTA_n)@Lap-1 with a small amount of water-soluble organic polymer like PVA (Reprinted with permission from Ref. [10]. Copyright 2015 American Chemical Society)

of hydrogen bonding within it are believed to be responsible for the formation of the ionogels. The ionogels display bright luminescence irradiated with UV light; the luminescence color of the ionogels can be tuned by exchanging Eu^{3+}, Tb^{3+} ions, or Eu^{3+}/Tb^{3+} with various molar ratios.

Wang et al. report the luminescent soft materials based on the coordination of Eu^{3+} with task-specific ionic liquids consisting terpyridine moieties to coordinate and sensitize Eu^{3+} ions and imidazolium rings [16]. It is observed that the anions of the carboxyl-functionalized ILs can influence the physical state of the obtained soft materials. Typically, soft luminescent materials obtained from [Carb-C1mim]Br are paste-like samples, while substitution of [Carb-C1mim]Br with [Carb-C1mim]NTf_2 leads to viscous transparent soft luminescent materials, a fluid at room temperature regardless of the anions used for Terpy-TSILs. These hybrid soft materials show bright-red emissions under UV light (Fig. 7.9). The content of the ionic liquid in the soft materials can be up to 97% by weight. These soft hybrid materials present some virtues such as a high content of ILs, easy coating on surfaces, and excellent luminescence, which may render them valuable for various optical applications such as flexible displays.

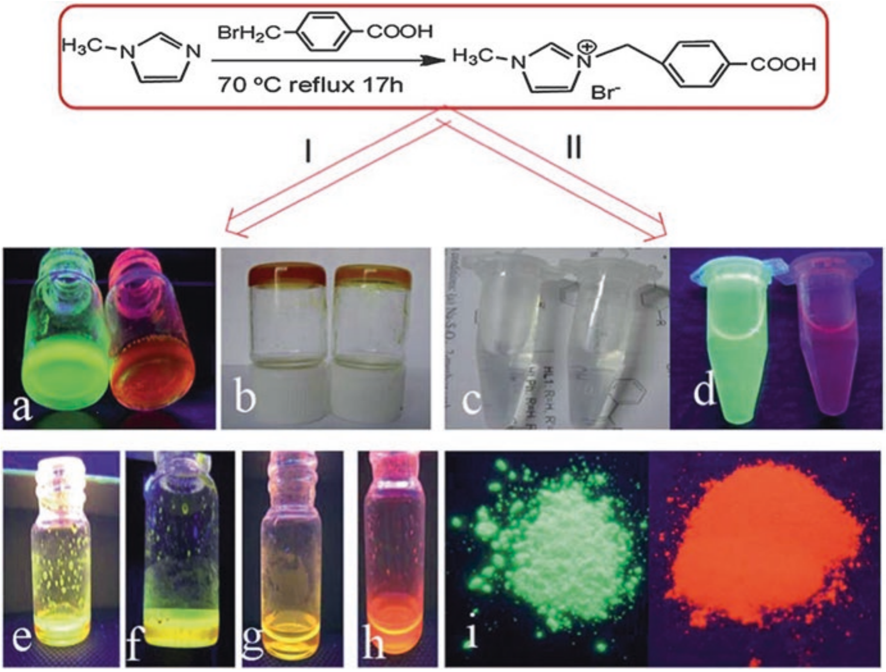

Fig. 7.8 Synthesis of IL-ACC and digital photos of the samples. Gel–Eu and Gel–Tb under UV light (*a*) and daylight (*b*); precipitate dissolved in water under daylight (*c*) and UV light (*d*); gel with increased molar ratio of Tb^{3+}/Eu^{3+} (*e–h*) under UV light and the precipitate under UV light (*i*). (*I*) Without NaOH; (*II*) with NaOH. The UV light used in this study is 254 nm (Reprinted with permission from Ref. [15]. Copyright 2013 the Royal Society of Chemistry)

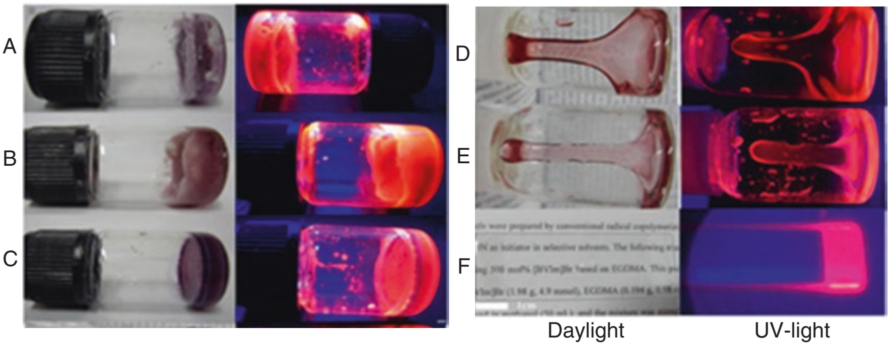

Fig. 7.9 Digital photos of the soft materials: (*A*) Eu/([Carb-C_1mim]Br-[C_1terpyim]Br), (*B*) Eu/([Carb-C_1mim]Br-[C_4terpyim]Br), (*C*) Eu/([Carb-C_1mim]Br-[C_{16}terpyim]Br), (*D*) Eu/([Carb-C_1mim]NTf_2-[C_4terpyim]Br), (*E*) Eu/([Carb-C_1mim]NTf_2-[C_4terpyim]NTf_2), and (*F*) a glass slide coated with Eu/([Carb-C_1mim]NTf_2-[C_4terpyim]NTf_2) (Reprinted with permission from Ref. [16]. Copyright 2013 American Chemical Society)

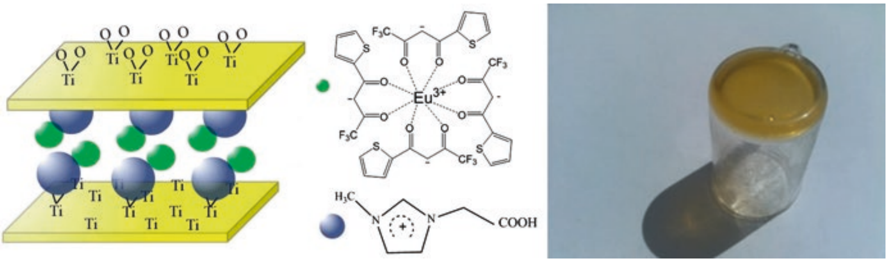

Fig. 7.10 The fabrication scheme of the synthesis process of hybrid soft xerogel material [Eu(L)$_4$]-IM$^+$-Ti: (*Left*) the scheme for sandwich composition and structure and (*Right*) the photograph for soft gels [Ln(L)$_4$]-IM$^+$-Ti1. Here we only set [Eu(TTA)$_4$]$^-$IM$^+$-Ti as an example, and for other [Ln(L)$_4$]-IM$^+$-Ti (Ln = Eu, Tb, Sm; L = TTA or TAA) systems, the scheme is similar except: Eu is replaced by Tb or Sm, TTA is replaced by TAA, and titania (Ti) is replaced by alumina (Al) (Reprinted with permission from Ref. [21]. Copyright 2014 the Centre National de la Recherche Scientifique (CNRS) and the Royal Society of Chemistry)

Li et al. assemble luminescent hybrid soft gels by introducing the lanthanide (Eu^{3+}, Tb^{3+}) tetrakis β-diketonate into the imidazolium-based silica through electrostatic interactions [17], in which the imidazolium cations are strongly anchored within the silica matrices while anions can still be exchanged following functionalization of lanthanide complexes functionalization. Mei et al. put forward a convenient method to synthesize luminescent lanthanide hybrid materials using 1-methyl-3-(2-(thiocarboxyoxy)ethyl)-2H-imidazole-1,3-diium bromide (SHIL) as functional linkage or bridge [18]. Mercapto-ion liquid compound such as SHIL has the ability to link semiconductor nanoparticles due to the chemical affinity between S and metal element component (Zn, Cd) of semiconductor sulfides. So SHIL can be used as effective medium to disperse II–VI group semiconductor. On the other hand, it can also interact with tetrakis europium β–diketonate complexes through the ion exchange reaction. So the ionic liquid SHIL behaves as double functional linker to construct the whole soft hybrids. As a result, close white luminescence of the soft hybrids can be observed by integrating different photoactive species. Similarly, this work can be extended to other hybrid systems containing ZnO nanoparticles or Ag_2S ones [19, 20]. For example, both ZnO-SH-IL-Eu5.0 and SH-IL-Eu2.5-Tb1 hybrids show the white color, which is achieved by integrating two components (blue (ZnO), red (Eu^{3+})) and three components (blue (ZnO), green (Tb^{3+}), and red (Eu^{3+}) light), respectively.

Yan et al. provide the strategy to prepare luminescent sandwich-structured hybrids [Ln(L)$_4$]$^-$IM$^+$-Al/Ti (Ln = Eu, Sm; L = TTA; Ln = Tb, L = TAA) based on sol–gel-derived hosts of Ti–O or Al–O networks [21]. Ln(III) tetrakis β-diketonate complexes are introduced to replace Br^- of the above system, resulting in the hybrid system by the static electric interaction of the positive (IM$^+$) and negative charge ([Ln(β-diketonate)$_4$]$^-$). On the other hand, the IM$^+$ fragment can link alumina and titania xerogel matrices through the coordination interaction between its carboxylic groups and Al^{3+} or Ti^{4+}. So the liquid compound behaves as the double functional linker to connect lanthanide complexes and xerogels, just like sandwich mode

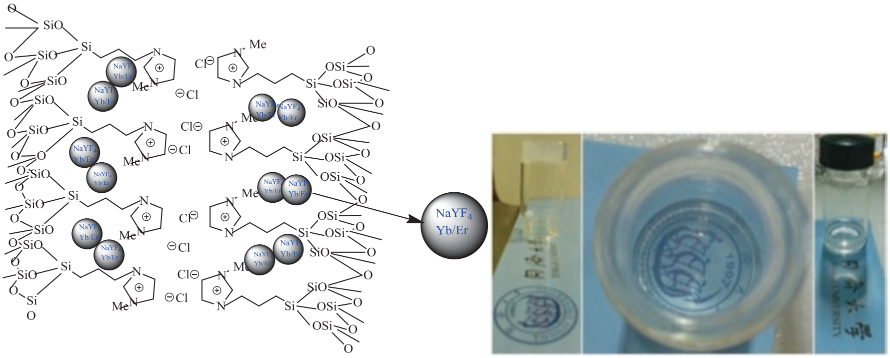

Fig. 7.11 The scheme for the possible structure (*Left*) of the ionogels and the photos of the ionogels from different angles (*Right*) (Reprinted with permission from Ref. [22]. Copyright 2013 Wiley)

(Fig. 7.10 (Left)). Figure 7.10 (Right) presents the selected photograph of the final xerogels of $[Ln(L)_4]$-IM^+-Ti hybrids, revealing the formation of transparent and stable xerogel forms. For europium hybrid soft xerogel, the luminescence color can be changed to the yellow zone from the green zone, according to the CIE chromaticity diagram. For samarium one, the luminescence color can be adjusted and the white luminescence can be integrated.

Yan et al. also realize the assembly of ionic liquid (IM^+Cl) and fluoride nanocrystals to prepare the transparent hybrid soft gels (Fig. 7.11) [22]. Firstly, the fluoride nanocrystals can be dispersed in IM^+Cl homogenously through the electrostatic force among the ionic liquid solutions. Further, the ionogels can be prepared after the sol–gel process based on cohydrolysis and copolycondensation reaction of the alkoxy groups of IM^+ component and TEOS. It is worth mentioning that the decentralized good samples are placed after a long period of about 1 month, which indicates that fluoride has been stably dispersed in the ionic liquids. It is by no means a simple task to disperse inorganic ionic liquids. The stable dispersion can be the product of interest, although it may also need to be studied further as hybrid material. Plastic crystal from the confinement of imidazolium-based hybrid materials containing silica nanoparticles and hydrogel loaded with upconversion $NaYF_4$ nanoparticles have all attracted wide attention.

7.3 Photofunctional Rare Earth Hybrid Materials Based on Multicomponent Nanocomposite

Inorganic semiconductor nanocrystals are another kind of important optical materials, which have been extensively utilized in optic–electric fields. The composition in the hybrid system of both rare earth species and semiconductor nanocrystals can be expected to produce new applications. Some studies have achieved the

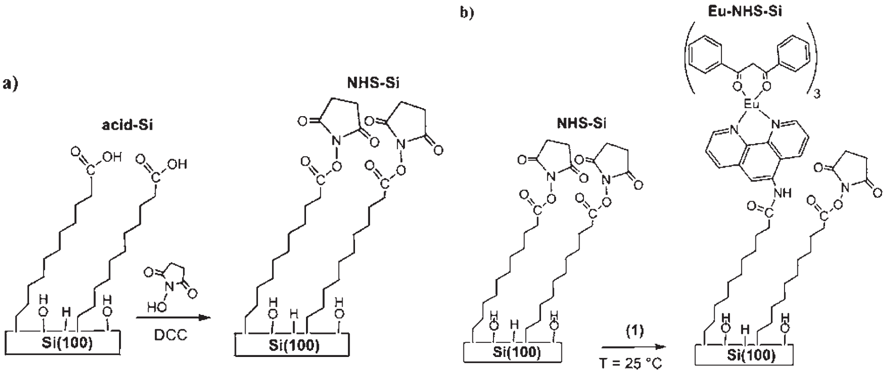

Fig. 7.12 The scheme 1 for (**a**) formation of NHS–Si species on Si(100) and (**b**) subsequent anchoring of the Eu complex (Reprinted with permission from Ref. [23]. Copyright 2010 Wiley)

introduction of various semiconductors, such as Si, ZnO, TiO_2, ZnS, CdS, Ag_2S, ZnSe, and GaN, into luminescent lanthanide hybrids [23–30].

Condorelli et al. develop a multistep synthetic strategy to anchor the Eu complex on the silicon surface through the nucleophilic attack of primary amine groups of aminophenanthrolinic ligands to NHS-activated carboxylic acid groups of prefunctionalized Si surfaces (Fig. 7.12) [23]. Si(100) surfaces functionalized with NHS–ester-activated carboxylic groups contain three steps: grafting of methyl-protected 10-undecenoic acid on Si, hydrolysis of the methyl ester to undecanoyl acid-functionalized Si (acid Si), and formation of NHS–ester (NHS–Si), respectively. Covalent anchoring of the Eu complex is performed by the treatment of NHS–Si with an ethyl acetate solution of the Eu complex. Therefore, results obtained for Eu–NHS–Si are consistent with the anchoring of the complex through a nucleophilic attack of its $-NH_2$ group to the NHS-activated carboxylic acid terminations (Fig. 7.12b). The surface reaction on NHS-activated carboxylic groups does not significantly change the ligand arrangement of the complex during the anchoring process, whereas direct reaction on the carboxylic acid leads to the exchange/dissociation of some ligands, thus changing the Eu coordination environment. Especially photoluminescence properties are retained in the monolayer, which suggests the hybrid is suitable for application in the photonic field.

Maggini et al. report the end-octahedral functionalization of MWCNTs with a neutral and hydrophobic tris-hexafluoro acetylacetonate EuIII complex (1; Fig. 7.13). They try to unravel the intimate interaction between the CNTs and the encapsulated Eu(III) complex and the influence on the luminescence of the resulting hybrid material [24]. To evaluate the contribution of externally bound traces of 1 to the luminescent output of 1@MWCNTs, they perform the same functionalization procedure with untreated pMWCNTs to prepare hybrid 1@MWCNTs, the closed analogue of 1@MWCNTs. In spite of some quenching, the luminescence quantum yield of the selected luminophore remains reasonably high (7%). These results provide the possibility to develop visible light-emitting CNT-based hybrids. It is the first proof of principle that visible light-emitting host–guest MWCNT

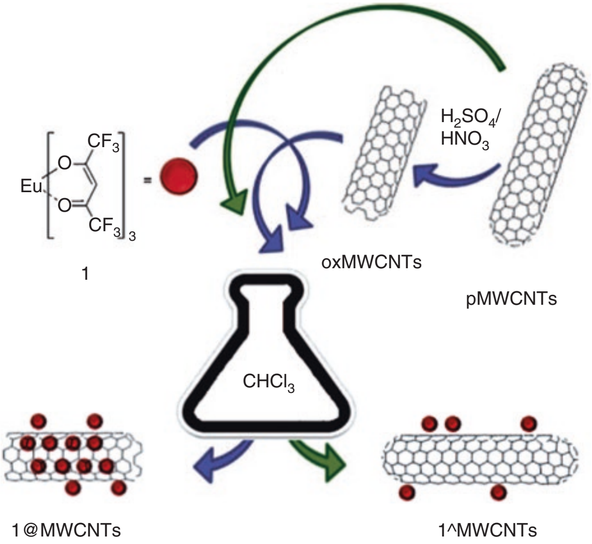

Fig. 7.13 Schematic representation of the nano-extraction technique. The structure of complex 1 and the products of the functionalization of MWCNTs (Reprinted with permission from Ref. [24]. Copyright 2011 Wiley)

hybrids with supramolecular host–guest approach through appropriate organic functionalization of the external carbon wall, which has potential applications in biological and material sciences or biodiagnostics. Li et al. report the synthesis of multi-walled carbon nanotube (MWCNT)-based hybrid materials with in situ sol–gel method [25]. The MWCNT is primarily covalently functionalized with 3-aminopropyltriethoxysilane, and then the rare earth complex is introduced onto the silylated MWCNT surface using the bifunctional silylated monomer TTA-Si and TAA-Si as a siloxane network precursor. The photoluminesce measurements indicated that these hybrids exhibit characteristic red and green luminescence originating from the corresponding ternary rare earth ion (Eu^{3+}, Tb^{3+}). The luminescence quenching effect of MWCNT networks has been successfully restrained by coating a relatively thicker silica–oxygen-based organic–inorganic complex.

Zhao et al. select mercaptobenzoic acid (MBA) as organic ligand and modify it with TESPIC to form the precursor (MBA-Si). Then, titanium dioxide is coordinated with carboxyl group of MBA-Si to form MBA-Si-TiO_2. After that, the modified organic ligand (MBA-Si-TiO_2) coordinated to rare earth ions is introduced to this system via sol–gel process. Phen and bipy are also introduced as the assistant ligands, to improve the quantum yield of the hybrid system. Finally, the hybrid material is achieved after a sol–gel process [26]. Besides, Zhao et al. modify ZnS quantum dot with 3-mercaptopropyltrimethoxysilane (MPTMS) to obtain MPTMS-functionalized SiO_2/ZnS nanocomposite. The hybrid materials are prepared by using TESPIC as an organic bridge molecule that can both coordinate to rare earth ions (Eu^{3+}, Tb^{3+}, Sm^{3+}, Dy^{3+}) and form an inorganic Si–O–Si network with SiO_2/ZnS nanocomposite after cohydrolysis and copolycondensation process [27]. Kwon

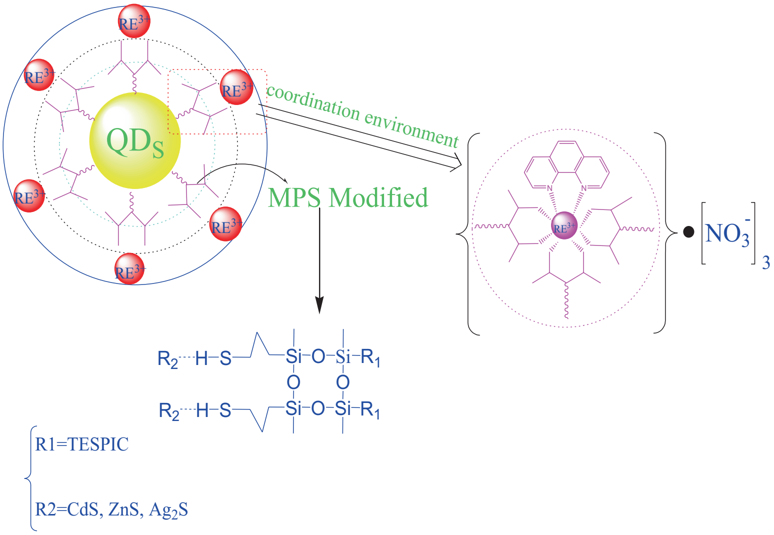

Fig. 7.14 Scheme for synthesis of the hybrids phen-Eu-TAASi-SiO_2-MS-CdS (Reprinted with permission from Ref. [27]. Copyright 2011, Elsevier)

et al. synthesize a color-tunable emitter comprising Eu complex-capped ZnSe quantum dot (QD) hybrid nanocrystals (NCs) by a hot-injection method [28]. The hybrid NCs have the emissions of both Eu complexes and ZnSe QDs, resulting in a bluish-white light, whose emission is enhanced to pristine ZnSe QDs as a result of the sensitization of the Eu complex as an antenna to transfer energy to the ZnSe QDs. The strong excitation band of the hybrid NCs in the near-UV region is expected to be particularly useful in white light-emitting diodes for potential light sources in white displays. Zhao et al. have tried to modify ZnS QDs to obtain SiO_2/ZnS nanohybrids and then prepared lanthanide hybrid materials using TESPIC as an organic bridge [29]. Three kinds of semiconductor metal sulfide nanoparticles (CdS, ZnS, and Ag_2S) have been synthesized and then functionalized with MS to obtain organically modified MS-CdS(ZnS, Ag_2S) composites. Through cohydrolysis and copolycondensation between the TTASi unit of phen(bipy)-Eu-TAASi and the MS unit of MS/CdS(ZnS, Ag_2S), both semiconductor unit and lanthanide complex are sol–gel assembled via covalently bonding Si–O to form the multicomponent inorganic–organic hybrids phen(bipy)-Eu-TAASi-SiO_2-MS-CdS(ZnS, Ag_2S). The luminescence properties of these hybrids show that the introduction of a semiconductor unit is favorable for the luminescence of Eu^{3+} ions (Fig. 7.14).

Li et al. report the covalent functionalization of GaN surfaces with imidazolium salts IL, which bears an organosilane group and can silanize the hydroxylated surfaces of GaN and then can adsorb the tetrakis β-diketonate europium complex anion through the electrostatically driven anion exchange reaction (Fig. 7.15) [30]. GaN powder is treated with piranha solution (H_2SO_4/H_2O_2 (3:1 v/v)) for 30 min and then washed with deionized water and dried under vacuum condition prior to

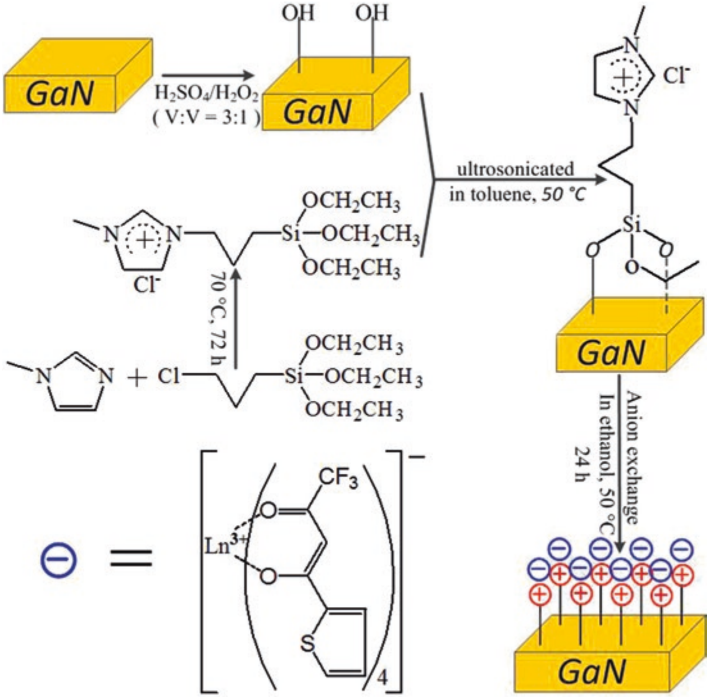

Fig. 7.15 Synthetic scheme for the preparation of lanthanide complexes functionalized GaN (Reprinted with permission from Ref. [30]. Copyright 2012 the Royal Society of Chemistry)

silanization, and the oxidized sample is then silalized by ultrosonicating in the as-prepared 1-methyl-3-[3-(trimethoxysilyl)propyl]imidazolium chloride. At the same time, the tetrakis β–diketonate europium complex $NEt_4Eu(TTA)_4$ is prepared and anchored onto the surface of GaN sample through an anion exchange reaction. The photoluminescent properties reveal that GaN is a favorable matrix to construct luminescent rare earth hybrid materials.

Zhao et al. present three kinds of cross-linking reagent silane as covalent linkage to functionalize both aromatic ligands and GaN to construct multicomponent rare earth hybrids (Phen-RE-NBC-APTES-GaN, Phen-RE-MBA-ICTES-GaN, and Phen-RE-HBA-CPTES-GaN (RE = Eu, Tb)) [31]. They further assemble ternary hybrid materials containing mesoporous silicon SBA-15 and inorganic GaN matrix (Fig. 7.16) [32]. The surface of GaN matrix is modified by oxidation to produce functional hydroxyl groups and then can be introduced into the silica matrices with Si–O bonds after the cohydrolysis and copolycondensation process with the organically modified silane (TAA-Si and BTA-Si). On the other hand, TAA-Si- or BTA-Si-functionalized SBA-15 can also be achieved by co-condensation with TEOS under the P123 template. Then, the organically modified silane-functionalized GaN unit can coordinate to rare earth ions through the chelated oxygen atoms of the diketone groups and occupy the eight coordination spot of RE^{3+} for the molar ratio of

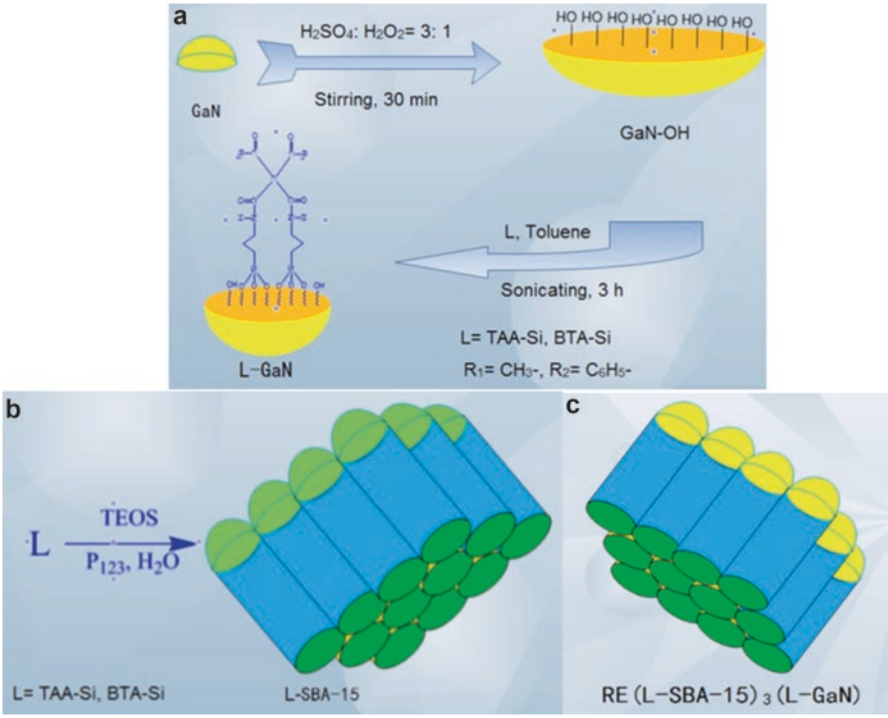

Fig. 7.16 The selected scheme for the synthesis process and predicted structure of the hybrids: (**a**) L-GaN (L = TTA-Si, BTA-Si), (**b**, **c**) RE(L-SBA-15)$_3$(L-GaN) (L = TAA-Si, BTA-Si) (Reprinted with permission from Ref. [32]. Copyright 2013, Elsevier)

1:3:1 for RE/L-SBA-15/L-GaN. The synthesis process can be easily applied to other systems.

Shao et al. prepare the hybrid materials with three kinds of precursors (EMA, HEMA, HFBMA) by covalently bonding the ternary lanthanide (Eu^{3+}, Tb^{3+}, Sm^{3+}, Dy^{3+}) complexes to the methacrylic group-modified ZnO nanoparticle (ZnO-MAA) matrices [33]. MAA-modified ZnO nanoparticles are in situ formed with the controlling reaction of the LiOH and $Zn(MAA)_2$ complex from $Zn(OH)_2$ and MAA. ZnO colloids have methacrylic groups, which are originated from the reagent materials adsorbed on the surface of ZnO. Then the ZnO polymer nanocomposites are assembled with MAA-modified ZnO nanoparticles and monomer EMA (HEMA, HFBMA) through the copolymerization between MAA group and EMA (HEMA, HFBMA). So the polyesters are indirectly connected with ZnO by covalent bonds with MAA unit as bridge. Here the interaction between ZnO and MAA unit can be considered as the coordination effect of Zn^{2+} and carboxylate group of MAA, and the charge of COO- is balanced by Li^+. They further assemble the multicomponent photofunctional systems with ZnO nanocomposite and lanthanide hybrids through the polymer-functionalized mesoporous silica. ZnO is synthesized and further modified with special polymer (poly(methacrylic acid) (PMAA) and poly(2-hydroxyethyl methacrylate) (PHEMA) and then is grafted to lanthanide complex-functionalized mesoporous SBA-15 silica [34]. This strategy can realize the multicomponent composition of ZnO polymer core–shell nanoparticles, mesoporous silica, and lanthanide complexes through the coordination bonds and polymer linkage functionalization of SBA-15. They also used surfactant dodecyl(11-methacryloyloxyundecyl) dimethylammonium bromide (DMDA) as the chemical linkage to assemble multicomponent photofunctional hybrids [35]. Europium (III) tetrakis (β-diketonate) complexes (β-diketonate (L) = TTA, 4, 4, 4-trifluoro-1-phenyl-1, 3-butanedionate (BTA), TAA) are connected with DMDA via anion exchange reaction to form $Eu(L)_4DMDA$. Then $Eu(TTA)_4DMDA$ system is encapsulated into (3-aminopropyl)triethoxysilane-functionalized MCM-41 host, resulting in MCM-41(m)-$Eu(L)_4DMDA$ assembly. It is interesting that the white luminescence is obtained for MCM-41(m)-$Eu(TAA)_4DMDA$-ZnO by the emission integration of ZnO unit and Eu^{3+}.

Yu et al. prepare the bifunctional nanocomposite particles via three consecutive steps by a modified Stober method combined with the layer-by-layer (LbL) assembly technique [36]. The first step involves the controlled addition of TEOS to an aqueous dispersion of Fe_3O_4 nanoparticles in order to cover the nanoparticles with silica layers to obtain the resulting Fe_3O_4 nanoparticle/silica core–shell nanoparticles (Fe_3O_4@SiO_2). The second step is to graft the Tb-PABI (PABI = *N*-(4-benzoic acid-yl),*N′*-(propyltriethoxysilyl) urea) complex onto the surface of Fe_3O_4@SiO_2 core–shell nanospheres (Fig. 7.17 (Top)). Particles with diameter ranging from 120 to 160 nm can be observed from the FESEM picture (Fig. 7.17 (Bottom, left) a). The presence of core Fe_3O_4 nanoparticles is confirmed by the TEM image (Fig. 7.17 (Bottom, left) b, c), which shows obvious difference in terms of contrast between the core and its surroundings. Upon UV light irradiation, well-dispersed aqueous Fe_3O_4@SiO_2@PABI-Tb nanoparticles emit bright-green light to the characteristic emission of Tb^{3+} as shown in the digital photographs of Fig. 7.17 (Bottom, right) b. Besides UV light, the nanocomposites are also inductive to the external magnetic field, whose particles are attracted to the magnet very quickly (Fig. 7.17 (Bottom, left) c). It can easily drag the nanoparticles from the bottom to the middle of the glass vial (Fig. 7.17 (Bottom, left) e) by elevating the magnets. Meanwhile, corresponding bright-green light emissions can be observed at these two positions under UV light irradiation (Fig. 7.17 (Bottom, left) d, f).

Feng et al. synthesize magnetic mesoporous silica nanospheres covalently bonded with near-infrared (NIR) luminescent lanthanide complexes [denoted as $Ln(DBM)_3$phen-MMS (Ln = Nd, Yb)] [37]. Fan et al. also prepare NIR photoluminescent macromaterial and an NIR luminescent/magnetic bifunctional macromaterial using PS (polystyrene) and Fe_3O_4@PS nanoparticles, respectively [38]. Both of them show the characteristic emission of the Er^{3+} ion originating from an intra-4f shell transition ($^4I_{13/2} \rightarrow {}^4I_{15/2}$). Shao et al. design and assemble lanthanide complex-functionalized magnetic mesoporous silica nanospheres covalently bonded with polymer-modified ZnO unit [39]. Here the linker between MMM and Eu(III) β-diketonate complexes is the IM^+ unit, which forms both the Si–O covalent bond to MMM and the static electricity interaction. These multifunctional nanocomposites both have magnetic and luminescent properties by further introducing lanthanide

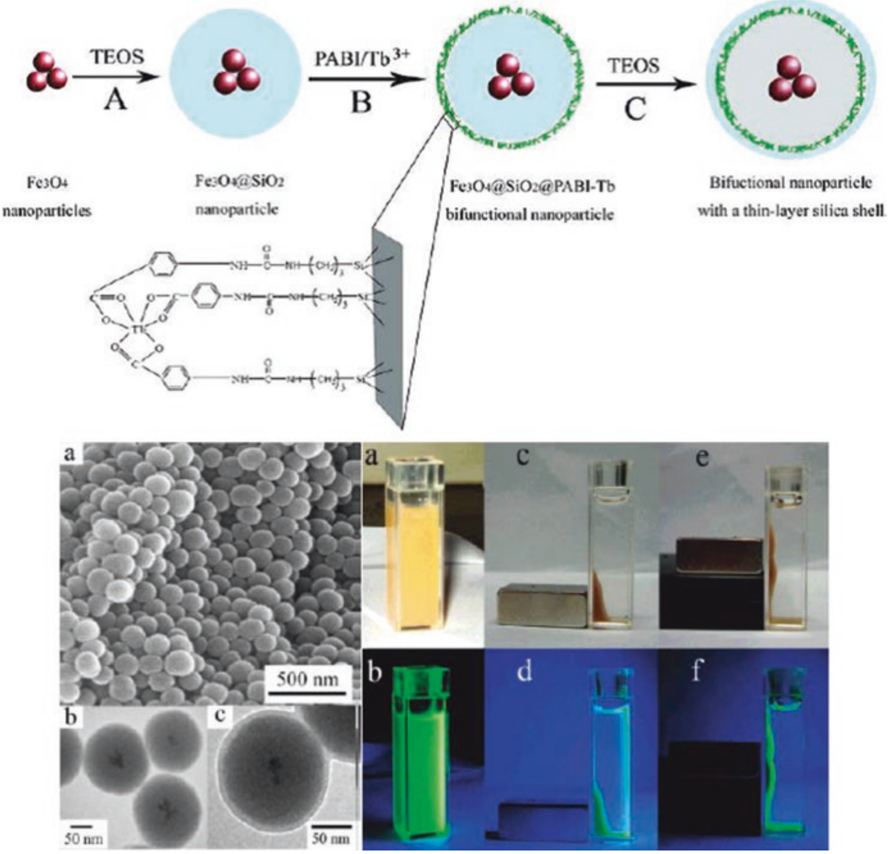

Fig. 7.17 (*Top*) Scheme for synthesis procedure to obtain bifunctional magnetic–optical nanoparticles. (*Bottom, left*) (*a*) SEM and (*b*, *c*) TEM images of obtained bifunctional magnetic–optical nanoparticles. (*Bottom*, *right*) Photographs of the obtained bifunctional magnetic–optical nanoparticles before (*a, c*, *e*) and after (*b*, *d, f*) UV light irradiation. (*a*, *b*) Aqueous suspension of the obtained bifunctional magnetic–optical nanoparticles, (*c*, *d*) after magnetic capture and (*e*, *f*) movement of the magnet dragging the concentrated nanoparticles (Reprinted with permission from Ref. [36]. Copyright 2007 American Chemical Society)

complexes. Especially Eu(ZnO-MMS)(CNTA)$_3$ and Tb(ZnO-MMS)(NTA)$_3$ possess high quantum yield value of 32.2% and 68.5%, respectively. The functional integration of luminescence and magnetism will embody these kinds of multifunctional hybrids to have several advantages for potential applications [40].

7.4 Photofunctional Rare Earth Hybrid Materials Based on Polyoxometalate

For rare earth hybrid materials themselves, the tendency is shifted to introduce the inorganic crystalline building block into hybrid system to further improve their physical and chemical properties. Besides, polyoxometalates are inorganic metal oxide clusters with the dimension of several nanometers, whose crystalline framework structure and versatile function are favorable for the hybrid materials. Especially decatungstoeuropate(9-) anion as a potassium salt is worthy of attention [41], whose sodium salt ($Na_9EuW_{10}O_{36}\cdot 32H_2O$, EuW_{10}) possesses long luminescent lifetime and high luminescent quantum yield for its crystalline structure [42].

Shao et al. synthesize surfactant dodecyl(11-methacryloyloxyundecyl) dimethylammonium bromide (DMDA) and POMs and then prepare DMDA-encapsulated polyoxometalloeuropate (SEP). At the same time, methacrylic group-modified ZnO nanoparticles (ZnO-MAA) are prepared. Then three different ester units with polymerizable groups are chosen to connect with SEP and ZnO-MAA through addition polymerization, resulting in the hybrid system including polyoxometalate, nanoparticles, and polymer (Fig. 7.18) [43]. DMDA is a kind of polymerizable surfactants composed of two equal-length alkyl chains and contains an unsaturated group at the terminal of one chain. Therefore, the surfactant-encapsulated POMs

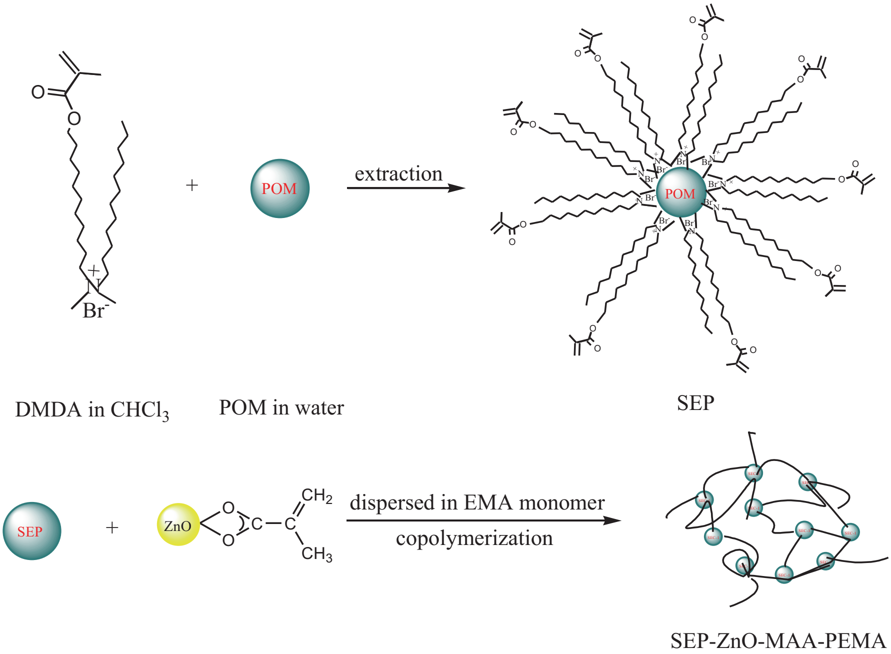

Fig. 7.18 Scheme of the synthesis process of SEP-ZnO-MAA-PEMA (Reprinted with permission from Ref. [43]. Copyright 2014 the Royal Society of Chemistry)

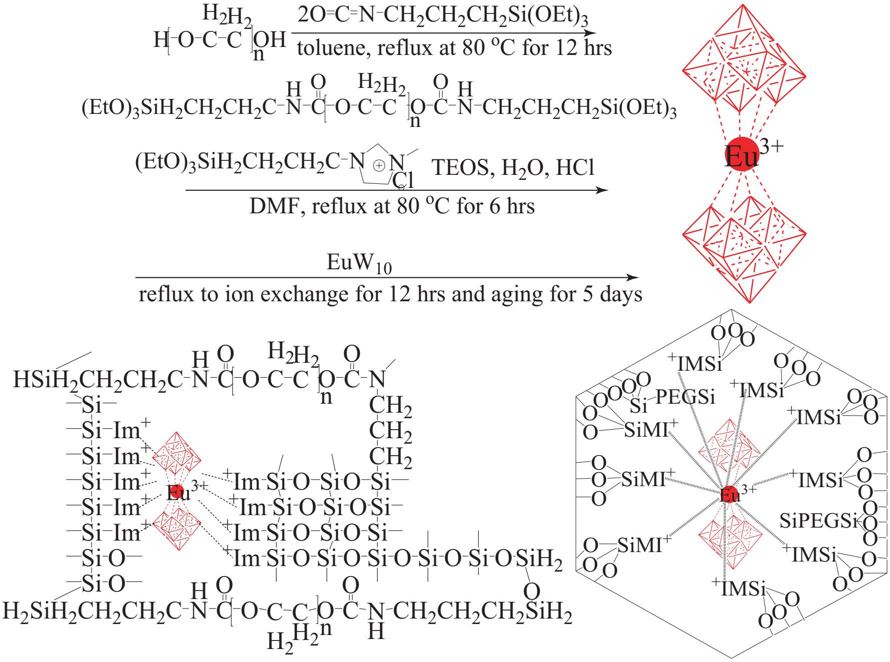

Fig. 7.19 Selected scheme of synthesis process of the precursor and the composition of the hybrid systems. Here we set up P1 as an example; for the hybrids of P2 and P3 polymers, it shows the similar scheme (Reprinted with permission from Ref. [44]. Copyright 2013 the Royal Society of Chemistry)

can further be copolymerized to other substrates such as polymer chains and nanohybrids. SEP is prepared with the ion exchange between the surfactant DMDA and the POMs for the electrostatic attraction force between their different charges. While MAA-modified ZnO nanoparticles are in situ constructed with the reaction of the LiOH and $Zn(MAA)_2$ complex from $Zn(OH)_2$ and MAA. ZnO colloids have methacrylic groups adsorbed on the surface of ZnO. Then the ZnO polymer nanocomposites are assembled with MAA-modified ZnO nanoparticles and monomer EMA (HEMA, HFBMA) through the copolymerization reaction between them. Based on the emission, both at the blue region from ZnO unit and red region for Eu^{3+} from SEP, it is natural to hope to realize the tunable color of luminescence for different excitation wavelengths. Composing the violet–blue excitation and orange or red emission, the white luminescence can be observed for the whole hybrid system. This provides a new strategy to obtain the white luminescence materials with hybrids.

Cuan et al. assemble multicomponent hybrids with building units such as europium polyoxometalates EuW_{10}, ionic liquid linker, polymer unit, and its functionalized silica or mesoporous silica. The coordination environment around europium ion cannot be changed for EuW_{10} crystal framework that is still kept in the hybrid

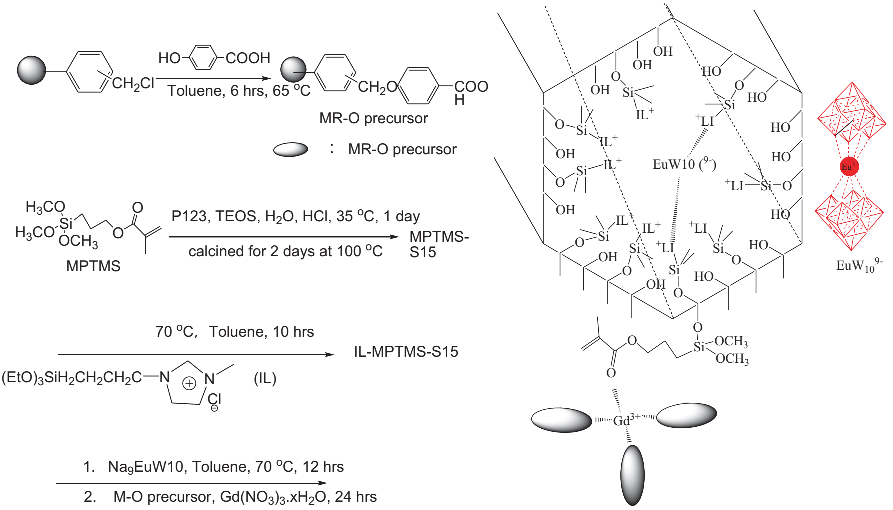

Fig. 7.20 (*Top*) The selected scheme for the synthesis process and basic composition of MR-O-Gd-S15 hybrids; for other hybrids, the scheme is similar except that MR, O, and Gd are replaced by WR, N or S, and Eu, respectively. (*Bottom*) The CIE chromaticity diagrams of MR-O(S, N)-Gd-S15 (1-O, 2-S, 3-N), MR-O(S, N)-Eu-S15 (4-O, 5-S, 6-N), and WR-O(S, N)-Eu-S15 (7-O, 8-S, 9-N) hybrids (Reprinted with permission from Ref. [45]. Copyright 2013 the Royal Society of Chemistry)

system (Fig. 7.19) [44]. TESPIC firstly is grafted onto the three polymers (P1, P2, and P3) through addition reaction between inter ester group of TESPIC and the hydroxyl groups of polymers. On the other hand, IM-functionalized EuW_{10} is prepared with ion exchange reaction between IM^+Cl^- and EuW_{10}. Finally, the whole multicomponent hybrid systems consist of EuW_{10}, and polymer-functionalized silanes (P1-Si, P2-Si, and P3-Si) are linked with Si–O bond after the cohydrolysis and copolymerization process between their alkoxy groups (TESPIC unit and IM^+). For the functionalized mesoporous silica (SBA-15) hybrids, the procedure similar to above is adopted except for the presence of P123 as template. The CIE chromaticity diagrams of these hybrid materials are checked. It can be found that the four hybrid systems (Eu-Si-P2(3) and Eu-SBA-15-P2(3)) emit close white luminescence, whose CIE coordinates ((0.3941, 0.4035), (0.3767, 0.4061), (0.3847, 0.4039), and (0.3799, 0.4046)) are in the cool-white region, close to sunlight, which is useful for the lighting. Combined with the long luminescent lifetimes and higher quantum yields, the two kinds of multicomponent hybrids Eu-Si-P2(3) will be expected to have potential application value.

They also assemble the multicomponent hybrid system (MR(WR)-O(S, N)-Gd(Eu)-S15) using several kinds of building blocks through different linking modes: europium polyoxometalate anions (EuW_{10}), ion liquid linkage, polymer resin unit and lanthanide (Eu, Gd) aromatic carboxylate complexes, and MPTMS-functionalized mesoporous silica, respectively (Fig. 7.20) [45]. Three benzoate derivatives are grafted onto resin (MR or WR) with their substituted groups (−OH, −SH, $-NH_2$) through the condensation reaction, and three carboxylates can occupy chemically equal six coordination spots of Eu^{3+} or Gd^{3+} ion. IL behaves as the linkage to both interact with EuW_{10} ion through ion exchange interaction and chemically bond with functionalized mesoporous silica (MPTMS-S15) after the cohydrolysis and copolymerization process between their alkoxy groups (MPTMS-S15 unit and IL) in the presence of P123 as template. Besides, lanthanide (Eu^{3+} or Gd^{3+}) complexes with three benzoate derivatives are easily understood for lanthanide coordination chemistry principle. The CIE chromaticity diagrams are obtained from the emission spectra within 400–700 nm. Except for MR-N-Gd-S15 and MR-N-Eu-S15 emitting orange or yellow light, the emitted light colors of other seven hybrid systems almost all locate at the nearly white light region (cool light), which is close to the sunlight and should be more useful in practical applications for lighting or optical devices.

Cuan et al. fabricate lanthanide polyoxometalate ($Na_9LnW_{10}O_{36}\cdot 36H_2O$, abbreviated as LnW_{10}, Ln = Eu, Tb, Sm, Dy) into the titania (zirconia, alumina) matrices through special carboxylic-derived ionic liquid 1-methyl-3-propionyloxy imidazolium bromide [46]. IL (IM^+) behaves as the linkage to both interact with $EuW10^{9-}$ ion through ion exchange interaction and coordinate to zirconia, alumina, and titania matrices with carboxylate groups after the hydrolysis and copolymerization process. Besides, the hydrolysis and polycondensation reaction of tetraisopropoxytitanium is much faster than other two alkoxyl precursors (aluminum isopropylate and zirconium butoxide), which is too quick to produce the lower encapsulating content of LnW_{10} in titania than other two systems (alumina and zirconia), affecting the luminescent performance of them. Eu-IL-Ti, Tb-IL-Zr, Tb-IL-Ti, Dy-IL-Ti, Dy-IL-Zr, and Dy-IL-Al locate at warm white light regions, displaying favorable luminescent performance for practical applications. So it can be presumed that different matrices have influence on the luminescence of hybrid system. Alumina/zirconia matrices are more beneficial for the luminescence of polyoxometalates than titania. Besides, hybrid titania xerogels are favorable for the potential to synthesize white light luminous materials. Cuan et al. also achieve the multicomponent assembly of novel kinds of photofunctional hybrid materials with polyoxometalates (POMs, EuW_{10}) and benzoate (4-aminobenzoate, 4-hydroxybenzoate, 4-mercaptobenzoate)-modified mesoporous silica using imidazolium ionic liquid (IL, 1-methyl-3-(trimethoxysilylpropyl)) compound as double functional linkage [47]. They fabricate POM into the framework of functionalized SBA-15 mesoporous silica with IL and Tb^{3+} is further introduced into the above hybrid system through coordination bond to carboxylate group of benzoate unit, which can be expected to modify luminescence color and to obtain close white luminescence. They also prepare task-specified ionic liquid-encapsulating lanthanide polyoxometalates and coordination compounds co-assembled luminescent hybrid materials by convenient synthetic routes [48]. All hybrid materials are amorphous structures, indicating that neither free polyoxometalates salts nor lanthanide inorganic compounds exist. This proves that all these inorganic building blocks are assembled into the hybrids by chemical

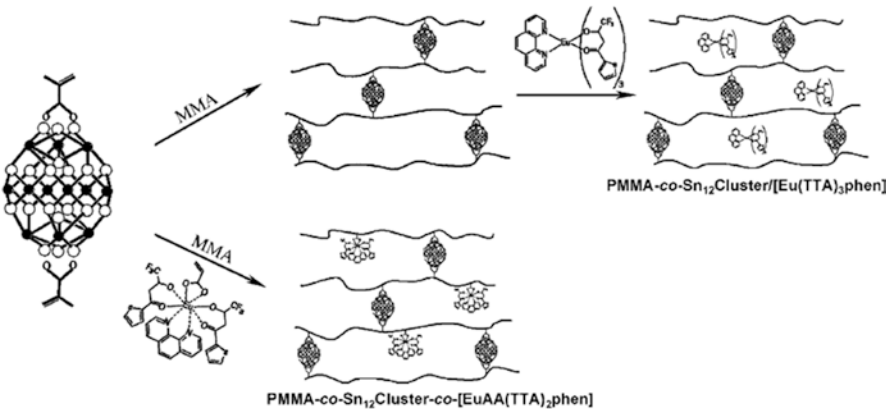

Fig. 7.21 Proposed mechanisms for the formation of PMMA-co-Sn$_{12}$Cluster/[Eu(TTA)$_3$phen] and PMMA-co-Sn$_{12}$Cluster-co-[EuAcAc(TTA)$_2$phen] hybrid materials (Reprinted with permission from Ref. [50]. Copyright 2010, Wiley)

bonds, and the whole system is in a more homogeneous phase. The quantum efficiency of europium polyoxometalates is also excellent, and EuW$_{10}$-IL-Tb-phen possesses the highest quantum efficiency which can reach 92%. Among all obtained hybrids, EuW$_{10}$-IL-Tb-phen, EuW$_{10}$-IL-Tb-bpy, TbW$_{10}$-IL-Tb-phen, and TbW$_{10}$-IL-Tb-bpy can emit high-quality white light which have great potential in white light device.

Considering the reactivity of mercapto group (−SH) of SHIL, Mei et al. try to assemble lanthanide polyoxometalate with polymer resin, in which SHIL behaves as linkage both through the exchange reaction with LnW$_{10}$ (Ln = Eu, Sm) and covalent bonding (condensation reaction) with resins MR or WR [49]. These hybrids present excitation both in ultraviolet and visible region. Under the excitation at visible region, the yellow–orange emission is obtained for LnW$_{10}$ unit, resulting in white luminescence for the excitation at visible region. Because the excitation is in visible region, we can observe the close white light from the hybrids system. Besides, for EuW$_{10}$-SHIL-MR, combined excitation and emission also can exhibit the yellow luminescence.

Fan et al. have prepared luminescent hybrid materials by physically doping (or covalently bonding) europium complexes into PMMA-co-Sn$_{12}$Cluster, which has a high capacity for physical doping with europium complexes. PMMA-co-Sn$_{12}$Cluster shows more extensive absorption spectra than the single PMMA matrix, revealing that it can prevent quenching of Eu^{3+} ions, thereby maintaining the luminescence lifetimes of the Eu^{3+} complexes [50]. Novel NIR luminescent-copolymerized hybrid materials have been prepared by covalently grafting and physically doping Ln complexes (Ln = Er, Sm, Yb, Nd) into a copolymer matrix built from nano building blocks. Transparent films of these materials can be easily prepared through spin coating on indium–tin–oxide glasses, taking advantage of their matrix nature (Fig. 7.21).

7.5 Photofunctional Rare Earth Hybrid Materials Based on Multi-host Assembly

Chen et al. use both zeolite A/L and SBA-15 to assemble multicomponent hybrid materials [51]. Microporous zeolites A/L are firstly functionalized by embedding lanthanide complexes into the pores of zeolite A/L, and then the surface of functionalized zeolite A/L are modified via covalent linkers. Meanwhile, SBA-15 is modified by grafting covalent linker phen–Si. Then another lanthanide ion is used to link both functionalized zeolites A/L and SBA-15 through the coordination with the two covalent linkers, ABS-Si (HBA-Si) and phen-Si, respectively (Fig. 7.22 (Top)). The whole hybrid system shows interesting characters of both mesoporous SBA-15 (for TEM) and microporous ZL/ZA (for SEM). Besides, the luminescent color can be tuned by adjusting the composition of these hybrids, and white light emission can be integrated, whose strong and bright emission color upon irradiation by a UV lamp (254, 365 nm) is shown in Fig. 7.22 (Bottom). Different materials have different light colors under the same conditions due to the imparity of host material, lanthanide ion, and organic ligand-modified linkers. The same material under the different wavelengths of exciting light also displays two kinds of emitting light. Subsequently, four hybrid systems (S-phen-Eu-HBA-[ZA-Zn-bipy], S-phen-Eu-HBA-[ZA-Tb-bipy], S-phen-Eu-ABA-[ZA-Tb-TAA], and S-phen-Eu-ABA-[ZL-Tb-bipy]) emit close white luminescence, whose CIE coordinates ((0.2947, 0.2982), (0.2878, 0.2807), (0.3587, 0.3360), and (0.2984, 0.3502)), respectively, are in the white region.

Lian et al. report a facile route for synthesis of core–shell structure microspheres based on silica and $[H_2NMe_2]_3[Ln(dpa)_3]$ (Ln = Eu, Tb, Sm, Dy, Nd, Yb; $[H_2NMe_2]^+$ = dimethyl amino cation; dpa = 2-dipicolinate) [52]. Nanosized silica sphere (with a diameter of about 210 nm) belongs to a suitable substrate for fluorescence sensors due to the excellent stability and optical transparency. The core–shell structure materials SiO_2@Ln-dpa (Ln = Eu, Tb, Sm, Dy, Yb and Nd) display excellent optical properties for application in development of white light device and small organic molecule or Cu^{2+} sensor (Fig. 7.23 (Left)). The formation of monodisperse SiO_2@Ln-dpa core–shell microspheres is verified by SEM and TEM, respectively (Fig. 7.23 (Right). The TEM images obviously validate the formation of the core–shell structure, as shown in Fig. 7.23 (Right) f), whose page edges and the dark center are the typical feature for core–shell materials. The diameter changes from 210 nm for the raw silica microspheres to 270 nm after the solvothermal reaction, which indicates that the shells of the complexes with a thicknesses of about 30 nm surrounding the core generate (Fig. 7.23 (Right) a–d). SEM images (Fig. 7.23 (Right) c) demonstrate that SiO_2@Ln-dpa is spherical shaped with narrow size distribution.

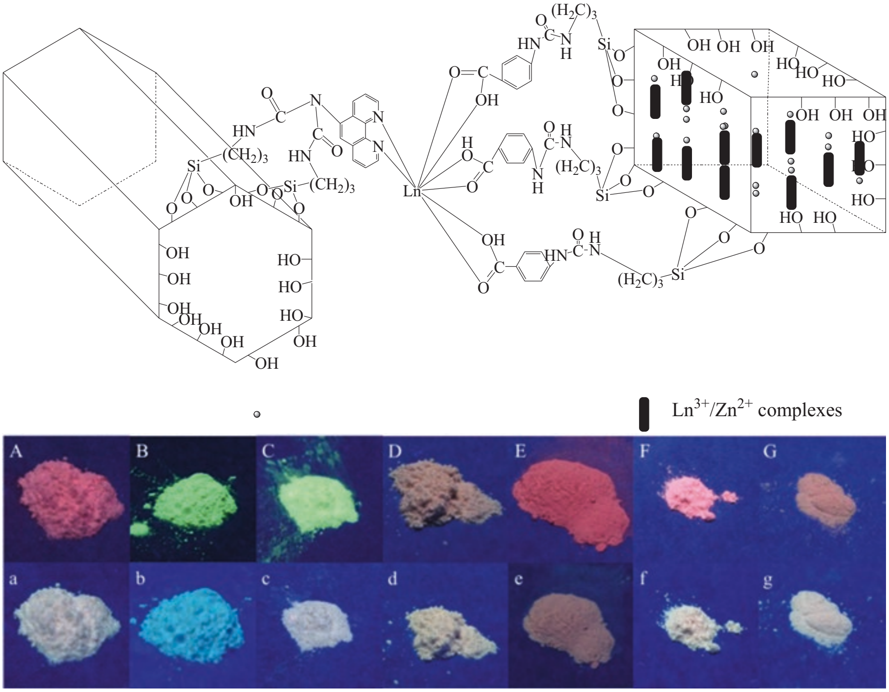

Fig. 7.22 (*Top*) Scheme the selected micro-mesoporous hybrid materials S-phen-Ln-ABA-[ZA-Ln/Zn-L]. (*Bottom*) The digital photos of S-phen-Eu-HBA-[ZA-Tb-bipy] (*A*, *a*), S-phen-Tb-ABA-[ZL-Zn-bipy] (*B*, *b*), S-phen-Tb-HBA-[ZA-Eu-TTA] (*C*, *c*), S-phen-Eu-ABA-[ZL-Tb-bipy] (*D*, *d*), S-phen-Eu-ABA-[ZA-Tb-bipy] (*E*, *e*), S-phen-Eu-HBA-[ZA-Zn-bipy] (*F*, *f*), and S-phen-Eu-ABA-[ZA-Tb-TAA] (*G*, *g*) under UV irradiation (λ_{ex} = 254, 365 nm) (Reprinted with permission from Ref. [51]. Copyright 2014 the Royal Society of Chemistry)

7.6 Conclusion and Outlook

In conclusion, recent research progress in the photofunctional rare earth hybrid materials based on multicomponent assembly of different structural or functional units is summarized, among which some typical types are discussed in detail. The first is the photofunctional hybrid materials based on modified clay for intercalation assembly, which is an important host–guest hybrid system in nature and has practical application value. The second is photofunctional rare earth hybrid materials based on ionogels, most of which is formed using ionic liquids both as the chemical linkers and hosts. The third is photofunctional rare earth hybrid materials based on nanocomposite, involving the rare earth species and other photofunctional species such as semiconductor nanoparticles. The fourth is based on the photofunctional rare earth polyoxometalate as the important luminescent center like EuW_{10}. The fifth is based on the multi-host assembly. Because of the diversity of the components within these hybrid systems, the exact control of the composition and structure or

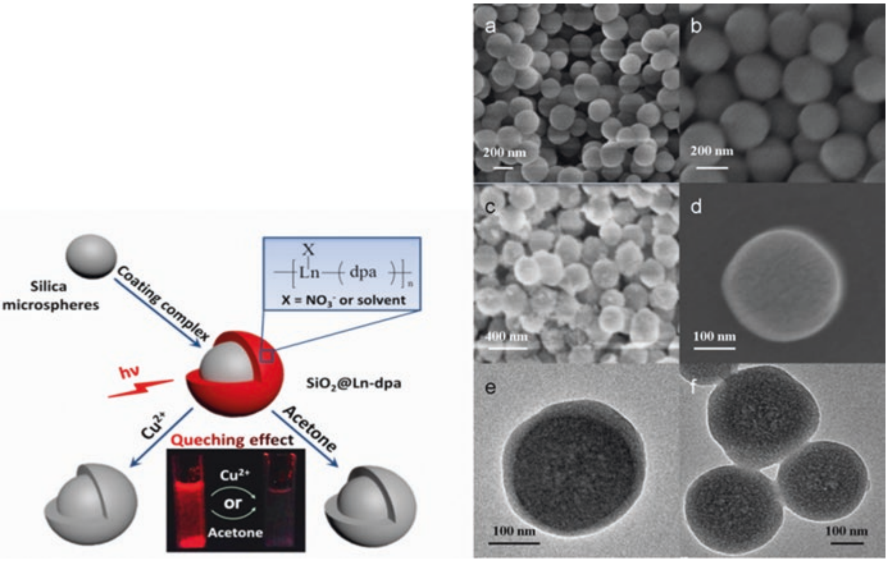

Fig. 7.23 (*Left*) Schematic diagrams of synthesis and sensing process of SiO$_2$@Ln-dpa core–shell microspheres. (Right) (*a–b*) SEM images of carboxylate-terminated silica spheres with an average diameter of 210 ± 20 nm. (*c–d*) SEM and (*e–f*) TEM images of SiO$_2$@Ln-dpa core–shell microspheres with an average diameter of 270 ± 20 nm. The average diameters were measured from SEM images (Reprinted with permission from Ref. [52]. Copyright 2016 the Royal Society of Chemistry)

microstructure is the key factor to achieve ideal hybrid materials. Besides, the thin films and other special aggregates of these hybrid materials are also important for the practical application. Naturally, the photophysical properties and applications of these hybrids are always the concern.

References

1. Xu QH, Fu LS, Li LS, Zhang HJ, Xu RR (2000) Preparation, characterization and photophysical properties of layered zirconium bis(monohydrogenphosphate) intercalated with rare earth complexes. J Mater Chem 10:2532–2536
2. Gago S, Pillinger M, Ferreira RAS, Carlos LD, Santos TM, Goncüalves IS (2005) Immobilization of lanthanide ions in a pillared layered double hydroxide. Chem Mater 17:5803–5809
3. Ma YF, Wang HP, Liu WS, Wang Q, Xu J, Tang Y (2009) Microstructure, luminescence, and stability of a europium complex covalently bonded to an attapulgite clay. J Phys Chem B 113:14139–14145
4. Domínguez M, Perez-Bernal ME, Ruano-Casero RJ, Barriga C, Rives V, Ferreira RAS, Carlos LD, Rocha J (2011) Multi-wavelength luminescence in lanthanide-doped hydrocalumite and Mayenite. Chem Mater 23:1993–2004

5. de Faria EH, Nassar EJ, Ciuffi KJ, Vicente MA, Trujillano R, Rives V, Calefi PS (2011) New highly luminescent hybrid materials: terbium pyridine –picolinate covalently grafted on kaolinite. ACS Appl Mater Interf 3:1311–1318
6. Li HR, Li M, Wang Y, Zhang WJ (2014) Luminescent hybrid materials based on Laponite clay. Chem Eur J 20:10392–10396
7. Wang TR, Yu XY, Li ZQ, Wang J, Li HR (2015) Multi-colored luminescent light-harvesting hybrids based on aminoclay and lanthanide complexes. RSC Adv 5:11570–11576
8. Yao YL, Li ZQ, Li HR (2015) Modification of Eu^{3+}-beta-diketonate complex intercalated Laponite with a terpyridine functionalized ionic liquid. RSC Adv 5:70868–70873
9. Wang TR, Li P, Li HR (2014) Color-tunable luminescence of organoclay-based hybrid materials showing potential applications in white LED and thermosensors. ACS Appl Mater Interf 6:12915–12921
10. Yang DQ, Wang YG, Wang Y, Li ZQ, Li HR (2015) Luminescence enhancement after adding organic salts to nanohybrid under aqueous condition. ACS Appl Mater Interf 7:2097−2103
11. Yang DQ, Wang J, Li HR (2015) Photo- and thermo-stable luminescent nanocomposite resulting from hybridization of Eu(III)-β-diketonate complexes with laponite. Dyes Pigments 118:53–57
12. Li P, Li ZQ, Li HR (2016) Emission fingerprint relationships of low-level water in organic solvents based on Ln^{3+}-β-diketonate complexes in Laponite. Adv Opt Mater 4:156–161
13. Lunstroot K, Driesen K, Nockemann P, Gorller-Walrand C, Binnemans K, Bellayer S, Le Bideau J, Vioux A (2006) Luminescent ionogels based on europium-doped ionic liquids confined within silica-derived networks. Chem Mater 18:5711–5715
14. Ru QR, Wang YG, Zhang WJ, Yu XY, Li HR (2013) Thermally reversible, flexible, transparent, and luminescent ionic organosilica gels. Eur J Inorg Chem:2342–2349
15. Went TT, Li HR, Wang YG, Wang LY, Zhang WJ, Zhang L (2013) Ln^{3+}-mediated formation of luminescent ionogels. J Mater Chem C 1:1607–1612
16. Wang DY, Wang HF, Li HR (2013) Novel luminescent soft materials of terpyridine-containing ionic liquids and europium(III). ACS Appl Mater Interf 5:6268–6275
17. Li QP, Yan B (2014) Photophysical properties of lanthanide (Eu^{3+}, Tb^{3+}) hybrid soft gels of double functional linker of ionic liquid-modified silane. Photochem Photobiol 90:22–28
18. Mei Y, Lu Y, Yan B (2013) Multi-component hybrid soft gels containing Eu^{3+} complexes and MS (M = Zn, cd) nanoparticles assembled with mercapto- ion liquid linkage: adjustable color and white luminescence. New J Chem 37:2619–2623
19. Mei Y, Lu Y, Yan B (2014) Soft materials composed with lanthanide (Eu^{3+}, Tb^{3+}) beta-diketonates and ZnO nanoparticles through thio-functionalized ionic liquid bridge to integrate white luminescence. J Photochem Photobiol A Chem 280:1–4
20. Mei Y, Yan B (2014) White hybrid soft materials of lanthanide (Eu^{3+}, Sm^{3+}) beta-diketonates and ag/Ag_2S nanoparticles based with thiol-functionalized ionic liquid bridge. Inorg Chem Comm 40:39–42
21. Yan ZY, Yan B (2014) Novel organic inorganic hybrid soft xerogels with lanthanide complexes through an ionic liquid linkage. New J Chem 38:2604–2610
22. Yan ZY, Yan B (2013) Luminescent hybrid ionogels functionalized with rare earth fluoride up-conversion nanocrystals dispersing in ionic liquid. Photochem Photobiol 89:1262–1268
23. Condorelli GG, Tudisco C, Motta A, Di Mauro A, Lupo F, Gulino A, Fragalà IL (2010) Multistep anchoring route of luminescent (5-amino-1,10-phenanthroline)-tris(dibenzoylmethane) europium(III) on Si(100). Eur J Inorg Chem:4121–4129
24. Maggini L, Mohanraj J, Traboulsi H, Parisini A, Accorsi G, Armaroli N, Bonifazi D (2011) A luminescent host–guest hybrid between a EuIII complex and MWCNTs. Chem Eur J 17:8533–8537
25. Li QP, Yan B (2012) Multi-walled carbon nanotube based ternary rare earth (Eu^{3+}, Tb^{3+}) hybrid materials with organically modified silica-oxygen bridge. J Coll Interf Sci 380:67–74

26. Zhao Y, Yan B (2012) Photoluminescent properties of novel rare earth organic-inorganic nanocomposite with TiO_2 modified silica via double crosslinking units. Photochem Photobiol 88:21–31
27. Yan B, Zhao Y, Li QP (2011) Europium hybrids / SiO_2 / semiconductor: multi-component sol-gel composition, characterization and photoluminescence. J Photochem Photobiol A Chem 222:351–359
28. Kwon BH, Jang HS, Yoo HS, Kim SW, Kang DS, Maeng S, Jang DS, Kimand H, Jeon DY (2011) White-light emitting surface-functionalized ZnSe quantum dots: europium complex-capped hybrid nanocrystal. J Mater Chem 21:12812–12818
29. Yan B, Zhao Y, Li YJ (2011) Novel photofunctional multi-component rare earth (Eu^{3+}, Tb^{3+}, Sm^{3+}, Dy^{3+}) hybrids with functionalized TESPIC covalently bonded to SiO_2/ZnS nanocomposite. Photochem Photobiol 87:757–765
30. Li QP, Yan B (2012) Luminescent GaN semiconductor based on surface modification with lanthanide complexes through an ionic liquid bridge. RSC Adv 2:10840–10843
31. Zhao Y, Yan B (2012) Rare earth hybrid materials of organically modified silica covalently bonded GaN matrix: multicomponent assembly and multi-color luminescence. Dalton Trans 41:5334–5342
32. Zhao Y, Yan B (2013) Rare earth (Eu^{3+}, Tb^{3+})/β-diketonate functionalized mesoporous SBA-15/GaN nanocomposites: multi-component chemical bonding assembly, characterization and luminescence. J Coll Interf Sci 395:145–153
33. Shao YF, Yan B (2012) Photofunctional hybrids of rare earth complexes covalently bonded to ZnO core-shell nanoparticles substrate through polymer linkage. Dalton Trans 41:7423–7430
34. Shao YF, Yan B, Jiang ZY (2012) Multicomponent assembly of luminescent hybrid materials of ZnO-lanthanide polymer complex functionalized SBA-15 mesoporous host by chemical bonds. RSC Adv 2:9192–9200
35. Shao YF, Yan B (2014) Multi-component hybrids of surfactant functionalized europium tetrakis(β-diketonate) in MCM-41(m) and polymer modified ZnO for luminescence integration. Microp Mesop Mater 193:85–92
36. Yu SY, Zhang HJ, Yu JB, Wang C, Sun LN, Shi WD (2007) Bifunctional magnetic-optical nanocomposites: grafting lanthanide complex onto core-shell magnetic silica nanoarchitecture. Langmuir 23:7836–7840
37. Feng J, Song SY, Deng RP, Fan WQ, Zhang HJ (2010) Novel multifunctional nanocomposites: magnetic mesoporous silica nanospheres covalently bonded with near-infrared luminescent lanthanide complexes. Langmuir 26:3596–3600
38. Fan WQ, Feng J, Song SY, Lei YQ, Xing Y, Deng RP, Dang S, Zhang HJ (2008) Erbium-complex-doped near-infrared luminescent and magnetic macroporous materials. Eur J Inorg Chem:5513–5518
39. Yan B, Shao YF (2013) Multifunctional nanocomposites of lanthanide (Eu^{3+}, Tb^{3+}) complex functionalized magnetic mesoporous silica nanospheres covalently bonded with ZnO-polymer. Dalton Trans 42:9565–9573
40. Shao YF, Yan B, Li QP (2013) Magnetic mesoporous silica nanospheres-supported europium (III) tetrakis(β-diketonate) complexes using ionic liquid compound as linker. Eur J Inorg Chem:381–387
41. Coronado E, Gomez-Garcıa CJ (1998) Polyoxometalate-based molecular materials. Chem Rev 98:273–296
42. Peacock RD, Weakley TJR (1971) Heteropolytungstatecomplexes the lanthanide elements. J Chem Soc A:1836–1839
43. Yan B, Shao YF (2014) Multicomponent hybrids with surfactant-encapsulated europium polyoxometalate covalently bonded ZnO and tunable luminescence. RSC Adv 4:3318–3325
44. Cuan J, Yan B (2013) Multi-component assembly and photophysical property of europium polyoxometalates and polymer functionalized (mesoporous) silica through double functional ionic liquid linker. Dalton Trans 42:14230–14239

45. Cuan J, Yan B (2013) Cool-white light emitting hybrid materials of resin-mesoporous silica composite matrix encapsulating europium polyoxometalates through ionic liquid linker. RSC Adv 3:20077–20084
46. Cuan J, Yan B (2014) Luminescent lanthanide-polyoxometalates assembling zirconia/alumina/titania hybrid xerogels through task-specified ionic liquid linkage. RSC Adv 4:1735–1743
47. Cuan J, Yan B (2014) Photofunctional hybrid materials with polyoxometalates and benzoate modified mesoporous silica through double functional imidazolium ionic liquid linkage. Microp Mesop Mater 183:9–16
48. Cuan J, Yan B (2014) Co-assembly and luminescence tuning of hybrids with task-specified ionic liquid encapsulating and linking lanthanide-polyoxometalates and complexes. Photochem Photobiol Sci 13:1469–1475
49. Mei Y, Yan B (2015) Photofunctional polymer hybrid materials of lanthanide (Eu^{3+}, Sm^{3+}) polyoxometalates and resin through ionic liquid linker. Coll Polym Sci 293:817–822
50. Fan WQ, Feng J, Song SY, Lei YQ, Zheng GL, Zhang HJ (2010) Synthesis and optical properties of europium-complex-doped inorganic/organic hybrid materials built from oxo–hydroxo organotin nano building blocks. Chem Eur J 16:1903–1910
51. Chen L, Yan B (2014) Multi-component assembly and luminescence tuning of lanthanide hybrids based with both zeolite L/a and SBA-15 through two organically grafted linkers. Dalton Trans 43:14123–14131
52. Lian X, Yan B (2015) Multi-component luminescent lanthanide hybrids of both functionalized IR-MOF-3 and SBA-15. New J Chem 39:5898–5901

Part IV
Photophysical Application

Chapter 8
Photophysical Applications of Photofunctional Rare-Earth Hybrid Materials

Abstract This chapter mainly focuses on recent research progress in the photophysical applications of photofunctional rare-earth hybrid materials, which include the luminescent solar energy concentrators (or optical amplifiers), the luminescent devices or barcoding, and the luminescent sensors for cations, anions, molecules or species, and physical properties such as temperature or pH value. Since the research on the luminescent sensors is very active, the emphasis is put on this topic. As the hybrids based on rare-earth functionalized metal–organic frameworks (MOFs) have the characteristics of molecules, their application in the practical fields are most extensively studied and will be discussed in detail. Herein it mainly focuses on the work of our group in the recent years.

Keywords Rare-earth ion • Photofunctional hybrid material • Photophysical application • Luminescence sensing

Photofunctional rare-earth hybrid materials have great potential for practical applications due to their unique photophysical properties, the relevant research of which is becoming more and more active. For example, Sun et al. synthesize a ternary $Er(DBM)_3phen$ (EuDP) complex and prepare its gels [1]. The erbium complex is in situ synthesized in the ErDP gel, showing the typical near-infrared (NIR) luminescence (centered at around 1.54 μm) originated from the $^4I_{13/2} \rightarrow {}^4I_{13/2}$ transition of Er^{3+} ion, whose full width at half maximum (FWHM) is 72 nm. Combined with the theoretical analysis, it can be expected to be a candidate for tunable lasers and planar optical amplifiers. They also extend their work to other hybrid gels fabricated from $Ln(DBM)_3phen$ complexes (Ln = Nd, Yb). Both experimental data and Judd-Ofelt analysis suggest that the $^4F_{3/2} \rightarrow {}^4I_{11/2}$ transition of Nd^{3+} ion in the Nd-D-P gel has the potential to be used for a solid-state laser transition [2].

In this context, we focus on the popular applications of photofunctional rare-earth hybrid materials, with an emphasis placed on the sensors. The photofunctional hybrid materials based on rare-earth functionalized metal–organic frameworks (MOFs) are also discussed in detail, while the single MOFs including rare-earth-centered MOFs are not covered here.

B. Yan, *Photofunctional Rare Earth Hybrid Materials*,
Springer Series in Materials Science 251, DOI 10.1007/978-981-10-2957-8_8

8.1 Photofunctional Rare-Earth Hybrid Materials for Luminescent Solar Concentrators (LSC)

Carlos' group has done extensive work on the applications of photofunctional rare-earth hybrid materials for luminescent solar concentrators (LSC). This is an exciting field and needs to be developed.

Graffion et al. have prepared luminescent bridged silsesquioxanes (M5-Eu and M6-Eu) from two new urea-bipyridine derived bridged organosilanes (P5 and P6) under nucleophilic catalysis (Fig. 8.1 (Top)) [3]. M6-Eu can be loaded 11% w Eu^{3+} with highest absolute emission quantum yield value (0.18 ± 0.02), whose photoluminescence properties show a significantly different complexation mode of Eu^{3+} ions from M5-Eu. The modification of the sol composition upon the addition of a malonamide derivative can increase its quantum yield (0.26 ± 0.03). Besides, the thin film fabricated with M6-Eu by spin coating on glass substrates exhibits one of the highest emission quantum yields reported so far for films of Eu^{3+} hybrids (0.34 ± 0.03), whose optical conversion efficiency of ∼4% makes it have a potential application as new LSCs. The photograph of the F6-Eu film under 365 nm excitation displays red light, which is guided to the film edges through internal reflection to be used as LSC (Fig. 8.1 (Bottom)A). Figure 8.1 (Bottom)B displays one example of such three-dimensional (3D) intensity maps of the red pixel (in the RGB color model) in nonsaturated photographs. The average intensity ratio between corrected Isf and Ie yields C = 6 is consistent with other LSC systems.

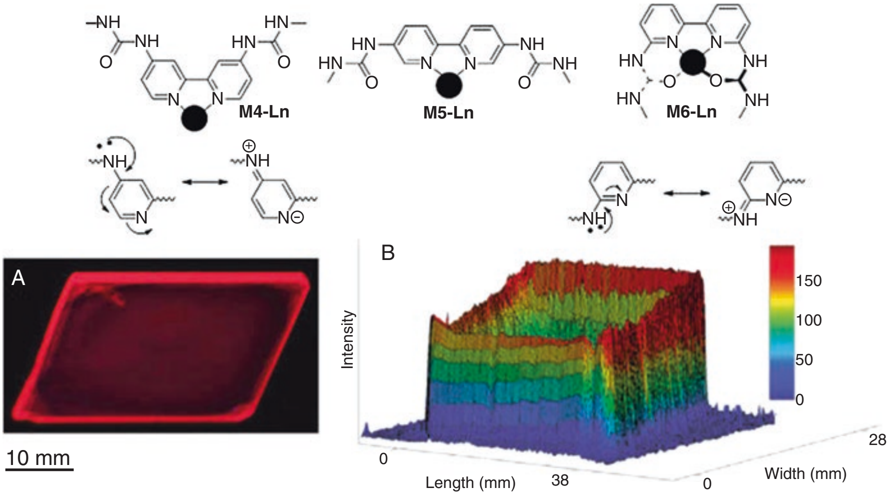

Fig. 8.1 (*Top*) Schematic representation of the possible interactions between the Ln ion (*full circle*) and one diureido-2,2′-bipyridine ligand. (*Bottom*) Mesomeric formulas involving the pyridine nitrogen atoms. (*Bottom*) (**a**) Photograph and (**b**) intensity map of the red pixel of F6-Eu excited at 365 nm. The top edge of the photograph corresponds to the more intense profile in the intensity map (Reprinted with permission from Ref. [3]. Copyright 2011 American Chemical Society)

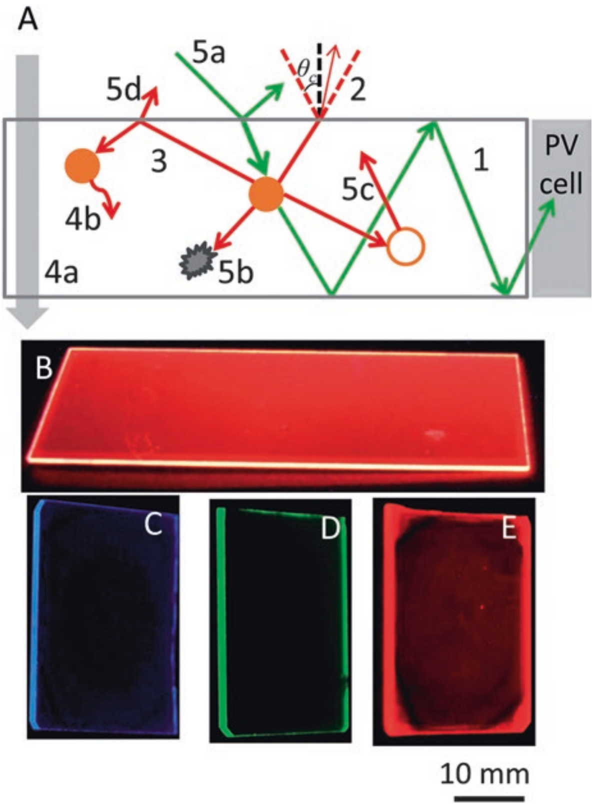

Fig. 8.2 (**a**) Schematic representation of the working principle of a LSC and of the main loss mechanisms: (*1*) total internal reflection, (*2*) radiation emitted through the escape cone, (*3*) reabsorption of the emitted radiation by an optical active center (*solid sphere*), (*4a*) nonabsorbed radiation, (*4b*) non-radiative deactivation, (*5a*) surface reflection, (*5b*) self-absorption, (*5c*) internal waveguide scattering, (*5d*) surface scattering. Photographs of some LSCs under UV irradiation (365 nm) based on (**b**) a di-ureasil organic – inorganic hybrid doped with $[Eu(btfa)_3\text{-}(MeOH)_2]_2bpta_2$, (btfa = 4,4,4-trifluoro-1-phenyl-1,3-butanedionate, bpta = trans-1,2-bis(4-pyridil)ethane, and MeOH = methanol) and on bipyridine-based bridged silsesquioxanes (**c**) lacking metal activator centers and doped with (**d**) Tb^{3+} and (E) Eu^{3+} ions (Reprinted with permission from Ref. [4]. Copyright 2014 The Royal Society of Chemistry)

Correia et al. have found that part of the emitted signal is lost at the surface, and the rest is trapped inside the layer through total internal reaction that will guide it to the edges (Fig. 8.2) [4], which endows an LSC with the ability of concentrating the maximum amount of light energy at its edges for electrical power generation. They summarize that light available at the edges of a LSC depends on four factors: the total surface area of the layer, the total amount of incident light collected on the layer, the type of layer, and the quantum efficiency of the active species, respectively. The usage of LSCs boosts the reduction of the area of the PV cell to decrease the cost associated with energy conversion. But it is estimated that LSCs will only be economically viable if the cost per Watt peak generated can be reduced to about 1 V per Watt peak, meaning that the ratio between the cost of the LSC itself and the cost of the PV material in use should be less than 1/5. Despite the simple mechanism behind the LSC working principle, several factors must be considered to design efficient devices. The first issue is related to the type of the target PV cell, especially the energy bandgap of the material to produce the PV cell. In addition, the knowledge of the material bandgap will determine both the sunlight wavelength region not absorbed by the PV cell and the wavelength emission range of the LSC emissive layer.

Freitas et al. have developed Eu^{3+}-bearing ethane tetracarboxamide-BS hybrids, whose monoliths and thin films with controlled thickness are prepared by drop cast and spin coating, respectively (Fig. 8.3) [5]. The hybrids are synthesized with the new ethane tetracarboxamide based organosilane (P4-m) through the hydrolysis − condensation under nucleophilic catalysis in the presence of Eu^{3+} with and without 2-thenoyltrifluoracetonate (TTA). A Eu^{3+} cooperative complexation by TTA and hybrids leads to a very significant increase of quantum yields. M4-m-2 hybrids are further processed as thin films on glass substrates, where the P4-m concentration, aging time, spinning conditions, and solvent type are varied to optimize the optical properties. Thin films with lower amount of Eu^{3+} centers (3% w/w) as well as high emission quantum yield (up to 0.60) and tuned refractive index are used to fabricate planar LSCs. The potential of hybrids is verified to enhance PV conversion efficiency. The quantitative report provides evidence for potential Ln^{3+}-LSCs using Ln^{3+}-based hybrid coatings.

Nolasco et al. report the synthesis and DFT/TD-DFT calculations of a highly luminescent ternary complex $Eu(TTA)_3$ephen (ephen = 5,6-epoxy-5,6-dihydro-[1, 10] phenanthroline) [6]. The tri-ureasil hybrids immobilized with this complex as a monolith (MtU5Eu-II) and as a thin film (FtU5Eu-II) are prepared and compared with the complexes, resulting in high emission quantum yield (82 ± 8% for complex, 63 ± 6% for monolith, and 48 ± 5% for thin film, respectively). Subsequently, the photostability of the complex in hybrids is significantly improved under UV irradiation. They also evaluate the possibility of hybrid thin film FtU5Eu-II to be used as a luminescent solar concentrator due to its optical conversion efficiency of ±9% and ability to boost up the Si photovoltaic cell output to 0.5%.

Correia et al. report the fabrication of cylindrical LSCs of commercial highly flexible PMMA-based POFs coated with a Eu^{3+}-doped hybrid layer, which is a step forward on the development of lightweight and mechanically flexible high performance waveguiding photovoltaics [7]. Compared with a cylindrical LSC fabricated by Eu^{3+}-doping PMMA, the coating of commercial POFs with an emitting layer is easily to produce long cylindrical LSCs with the consequent cost reduction and scalable fabrication. The optimized FWLSC displays effective opt η and PCE values of 20.77 ± 1.3% and 2.57 ± 0.2%, respectively. Combing the other virtues of the devices, it underlines the great potential of this innovative procedure to fabricate high-efficiency, lightweight, flexible, and cost-effective waveguiding photovoltaics. The use of low attenuation of the POFs envisages the possible fabrication of longer FWLSCs with higher G and F values. The resulting increase in the PV conversion

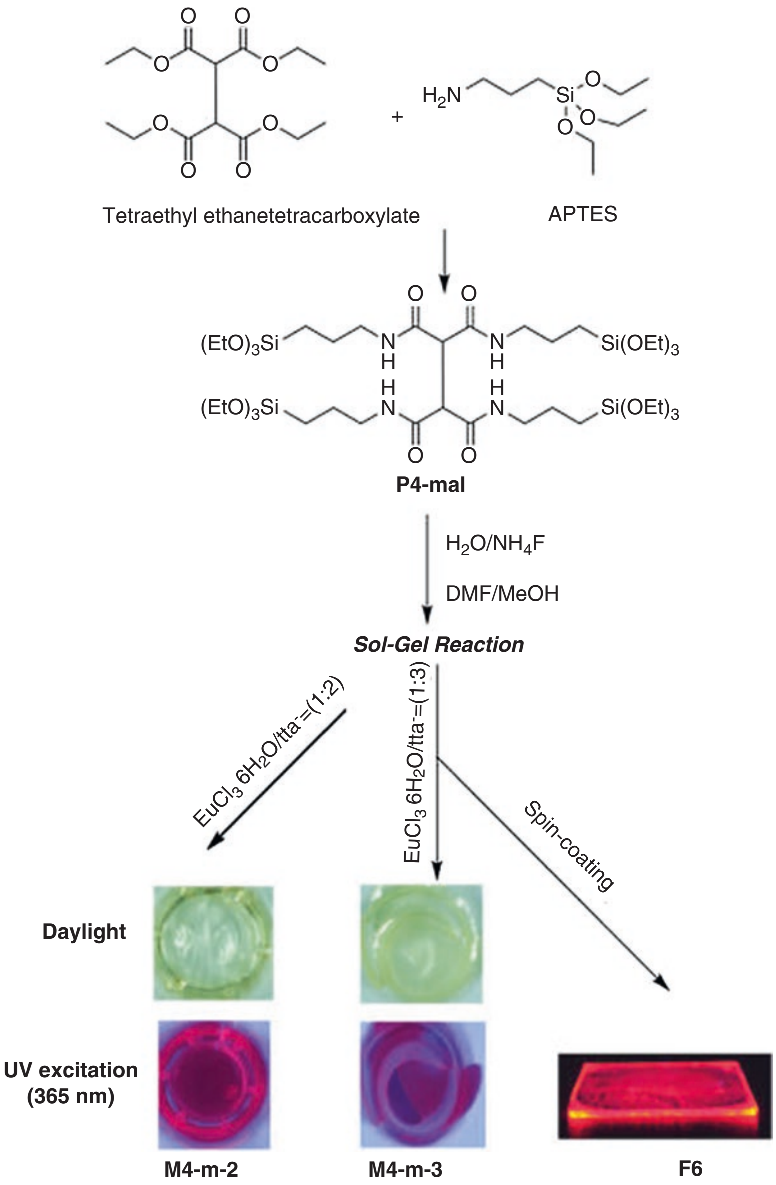

Fig. 8.3 The scheme for representation of the synthesis route of P4-m, M4-m-2, M4-m-3, and F6 and photographs acquired under daylight illumination and UV exposure (spectroline ENF-280C/FE) (Reprinted with permission from Ref. [5]. Copyright 2015 American Chemical Society)

efficiency in the presence of an LSC will also contribute to reduce CO_2 emissions as fewer panels are required to achieve the same efficiency. Unlike conventional LSCs, the FWLSC design can be implemented in ultrathin, mechanically bendable formats allowing high-efficiency flexible waveguiding photovoltaics. The FWLSC structures may open new opportunities for cost-effective sunlight collection and wearable solar-harvesting fabrics for mobile energy, making LSCs market competitive.

8.2 Photofunctional Rare-Earth Hybrid Materials for Luminescent Devices and Barcoding

Wang et al. have prepared luminescent hybrids both in the form of powder and transparent film by simply mixing organic sensitizer, aminoclay (AC), and Ln^{3+} ions in aqueous solution, whose emission color can be fine-tuned by changing various parameters such as the molar ratio of Eu^{3+} to Tb^{3+}, excitation wavelength, and temperature [8]. Especially, the white light output is achieved. The gels can be easily coated on round-shaped objectives like an UV-LED cell, and then a bright white light is achieved (Fig. 8.4). Correspondingly, the emission colors of the luminescent films can be also tuned by changing the molar ratio of Eu^{3+}/Tb^{3+} and excitation wavelength.

They also present luminescent materials by co-doping of deprotonated H_2bipydc (2,2′-bipyridine-5,5′-dicarboxylic), AC, and Ln^{3+} in aqueous medium at room temperature, whose tunable luminescence is obtained by changing the molar ratio of Eu^{3+}/Tb^{3+} in AC-bipy-Ln excited at 300 nm (Fig. 8.5) [9]. With the decrease of molar ratio of Eu^{3+} and Tb^{3+}, the relative emission intensity of Eu^{3+} and Tb^{3+} reduces consistently, leading to a series of the emission colors from red to green through orange and yellow (Fig. 8.5c). Further, the emission color of the hybrids also highly depends on their excitation wavelengths. The emission spectra of the hybrids (Fig. 8.5b) are composed of both line-like bands to f-f transition of Eu^{3+}/Tb^{3+} and broad band (400 to 500 nm) to bipyridine moieties under excitation of 350 nm. AC-bipy-Eu_1Tb_{99} has a coordinate of (0.30, 0.30) located in the "white region" of

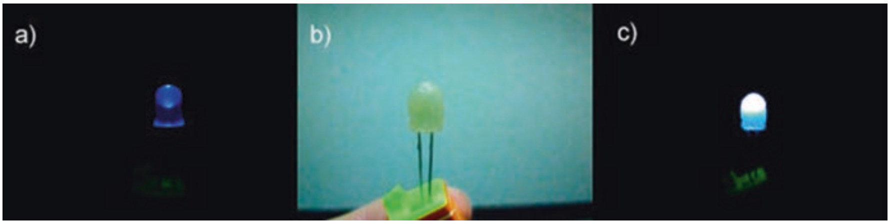

Fig. 8.4 Images of (**a**) commercial available UV-LED cell (λ_{em} = 365–370 nm, 3.2–3.8 V, 20 mA) and (**b**) UV LED coated with the AC-BTC-Eu_1Tb_7 hydrogel, a bright white light when the LED is on in image (**c**) (Reprinted with permission from Ref. [8]. Copyright 2014 American Chemical Society)

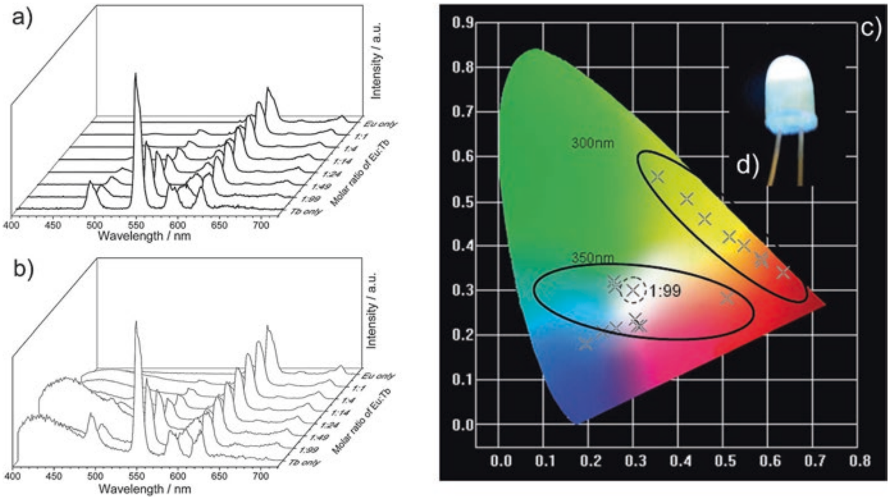

Fig. 8.5 Emission spectra of the AC-bipy-Ln (powder) excited at 300 (**a**) and 350 nm (**b**) and the CIE 1931 chromaticity diagram within the coordinates of AC-bipy-Ln (powder) excited at various wavelength (**c**) within an image of 365 nm UV-LED cell (0.06 W) coated with AC-bipy-Eu1Tb99 (**d**) (Reprinted with permission from Ref. [9]. Copyright 2014 The Royal Society of Chemistry)

CIE close to the ideal coordinate of white light (0.33, 0.33). They further coat the hydrogel of AC-bipy-Eu_1Tb_{99} on a commercial available UV-LED cell, and bright white light is obtained (Fig. 8.5d).

Lu et al. present a new method for fabrication of near-UV white LED based on rare-earth functionalized MOFs hybrids [10]. Rare-earth complex is firstly encapsulated to MOF-253 by postsynthetic method (PSM) and then introduced into polymer (poly ethyl methacrylate, PEMA) by suitable monomer functionalization to achieve polymer hybrids based on MOFs. Finally, the hybrid system is assembled on near-UV GaN chip to realize near-UV white LED (Fig. 8.6 (Top)). The excitation spectrum of MOF-253 is dominated by a broad band centered at about 380–400 nm and the emission spectra of MOF-253 present broad bands centered at about 550 nm under excitation at 395 nm. The point of emission spectra in CIE chromaticity diagram is in the yellow color area of (X = 0.33, Y = 0.47), so white light can be observed under excitation by bluish violet light (λ_{ex} = 395 nm) for the integration of bluish violet light and yellow light. This is similar to commercial white LED based on yellow-emitting YAG: Ce^{3+} phosphor and also endows MOF-253-based hybrid material with inherent advantage in the application in near-UV white LED. The selected hybrid material has high transparency and can emit bright white light under excitation by 395 nm GaN chip (Fig. 8.6 (Bottom)). The MOF-PEMA-10 white LED operated at 350 mA shows warm white light with CCT of 3742 K ($X = 0.39$, $Y = 0.38$) and a promising CRI (R_a) of 87.34, higher values than the commercial YAG: Ce^{3+} white LED (whose R_a is 78). The LED assembled by MOF-PEMA-3.5 shows natural white light, the color coordinates are $X = 0.33$ and $Y = 0.34$, and CCT is 5603 K. Hence, the white light operated by MOF-PEMA LED can be changed

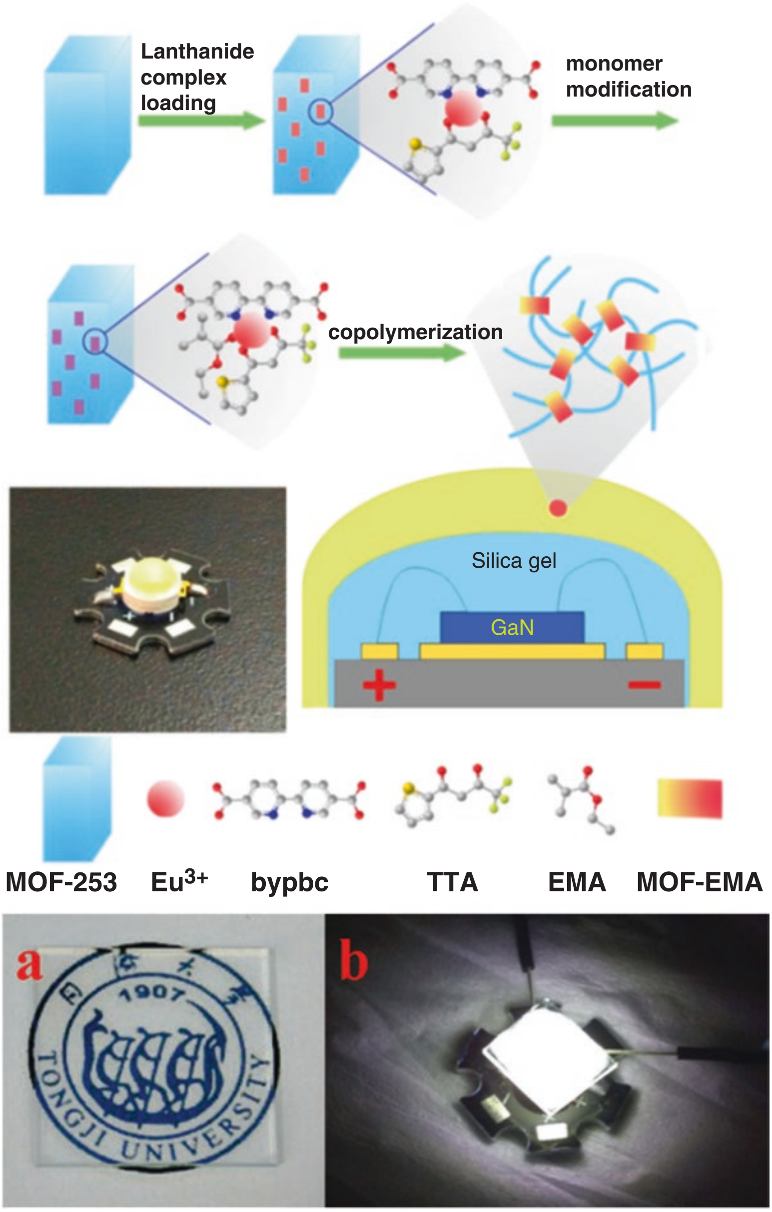

Fig. 8.6 (*Top*) Procedure for MOF-PEMA LED, the inset is LED based on MOF-PEMA. (*Bottom*) The photograph of MOF-PEMA-3.5 and bright white light from MOF-PEMA-3.5 under excitation by 395 nm GaN chip (Reprinted with permission from Ref. [10]. Copyright 2014 The Royal Society of Chemistry)

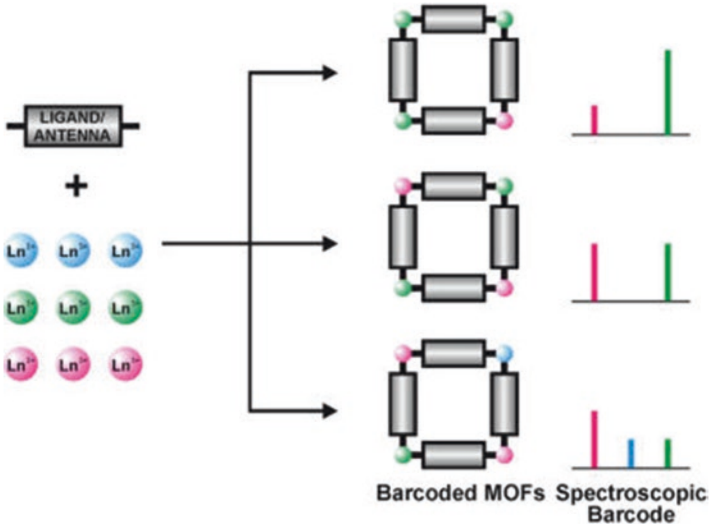

Fig. 8.7 The scheme for controlled preparation of barcoded MOFs (Reprinted with permission from Ref. [12]. Copyright 2009 American Chemical Society)

from natural white to warm white. Zhou et al. also prepared the white LED by combining Eu^{3+}@MOFUiO-67-bpydc nanophosphors with a UV-LED chip [11]. The correlated color temperature (CCT) of MOF-253 is 5627, and the quantum yield (QY) is 33% ($\lambda_{ex} = 395$ nm).

White et al. report a new conceptual approach to create luminescent barcoded systems based on multiple NIR-emitting lanthanides modified MOFs that contain multiple near-IR (NIR)-emitting lanthanides (Fig. 8.7) [12]. The functionalized MOFs hybrid systems display sharp signals from both Er^{3+} and Yb^{3+} ions. The excitation spectrum of either Er^{3+} or Yb^{3+} emission band contains two similar bands with apparent maxima at 370 and 470 nm, as observed for Yb-PVDC-1. Excitation through either of these bands simultaneously produces the characteristic Yb^{3+} emission band centered at 980 nm and the Er^{3+} band centered at 1530 nm, respectively. They demonstrate the quantitatively control the resulting luminescence intensities of the individual signals of the two NIR-emitting RE^{3+} cations. They generate a color-coded barcode readout because Er^{3+} and Yb^{3+} luminescence bands in the NIR range cannot be detected by the naked eye. Their relative intensities are reflected in the display, creating four distinct barcodes. The number and diversity of barcodes can be increased by using a larger number of ratios or by incorporating additional RE^{3+} cations.

Lu et al. use the same method to yield barcoded MOF-253 with varying Tb^{3+} and Eu^{3+} ion stoichiometries MOF-253-Tb_xEu_{1-x}, [13] which demonstrates the different RE^{3+} compositions can result in unique and discernible barcoded signals. The emission of MOF-253-Tb_xEu_{1-x} displays the characteristic transition of Eu^{3+} and Tb^{3+} ion with excitation at 330 nm (Fig. 8.8a). With an increase in the amount of

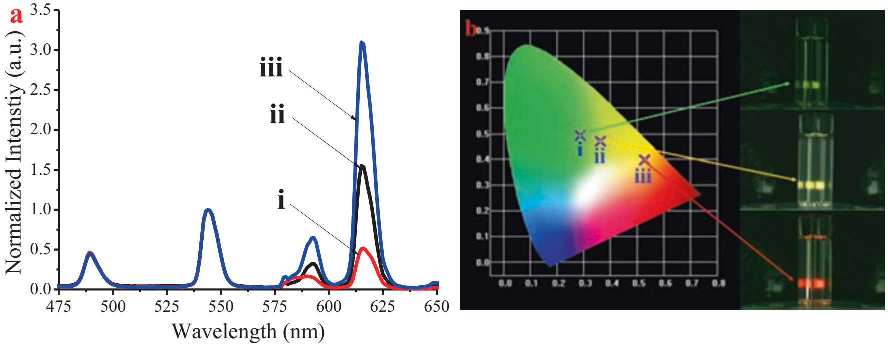

Fig. 8.8 (**a**) Eu^{3+} and Tb^{3+} emission spectra recorded under excitation at 330 nm, normalized to the Tb^{3+} signal. (**b**) Color-coded of the barcode readout in CIE chromaticity diagram and the photograph of the MOF-253-based barcoded material (dispersed in ethanol) under excitation at 330 nm, i, ii, and iii is MOF-253-$Tb_{0.999}Eu_{0.001}$, MOF-253-$Tb_{0.995}Eu_{0.005}$, and MOF-253-$Tb_{0.99}Eu_{0.01}$, respectively (Reprinted with permission from Ref. [13]. Copyright 2014 The Royal Society of Chemistry)

Eu^{3+} ion and a decrease in the amount of Tb^{3+} ion, their characteristic emission intensities increase and decree accordingly. So they can quantitatively control the luminescent intensities of the two emitting RE^{3+} by controlling their composition. A plot of the ratio of the integrated intensities of the transition of $^5D_0 \rightarrow {}^7F_2$ (Eu^{3+}) and the transition of $^5D_4 \rightarrow {}^7F_5$ (Tb^{3+}) reveals a linear relationship between 1:99 and 0.1:99.9 Eu^{3+}/Tb^{3+} (molar ratio). This can be reflected as unique and visible color corresponding to three distinct barcodes. The points of emission of MOF-253-$Tb_{0.95}Eu_{0.05}$, MOF-253-$Tb_{0.99}Eu_{0.01}$, and MOF-253-$Tb_{0.995}Eu_{0.005}$ in CIE chromaticity diagram are green ($X = 0.2876$, $Y = 0.4915$), yellow ($X = 0.3630$ $Y = 0.4698$), and red ($X = 0.5276$, $Y = 0.3980$), respectively (Fig. 8.8b).

Zhou et al. develop a new barcoded system based on lanthanide photofunctionalized MIL-100 (In) films containing multiple emission bands [14], whose encoding strategy relies on tuning the emission intensities of Ln^{3+} in multiple bands through luminescence reabsorbed processes and is significantly different from that of the two previously reported MOF barcoded systems [12, 13]. Varying the filtered dye loading generates distinct ratiometric optical signatures or codes. Ratiometric luminescence measurements are independent of excitation power fluctuations, optoelectronic drift of the detectors, and material's inhomogeneities. This strategy allows the construction of MOF luminescence barcodes in a reproducible and robust way. Specifically, Ln^{3+}@MIL-100 (In) films display multiple emission bands with far less spectra overlap than quantum dots or organic dyes, hence the relative intensity of these emissions can be determined accurately. By loading with a screen layer that contains different amounts of organic dyes, some of these emission bands can be reabsorbed to various degrees, while the others are not absorbed by the filtered dyes and serve as ratiometric references to the reabsorbed emission bands. This permits the establishment of a very large number of ratiometric optical signatures or codes (Fig. 8.9 (Left)). Subsequently, it exhibits dual emissions of Eu^{3+} and Tb^{3+}

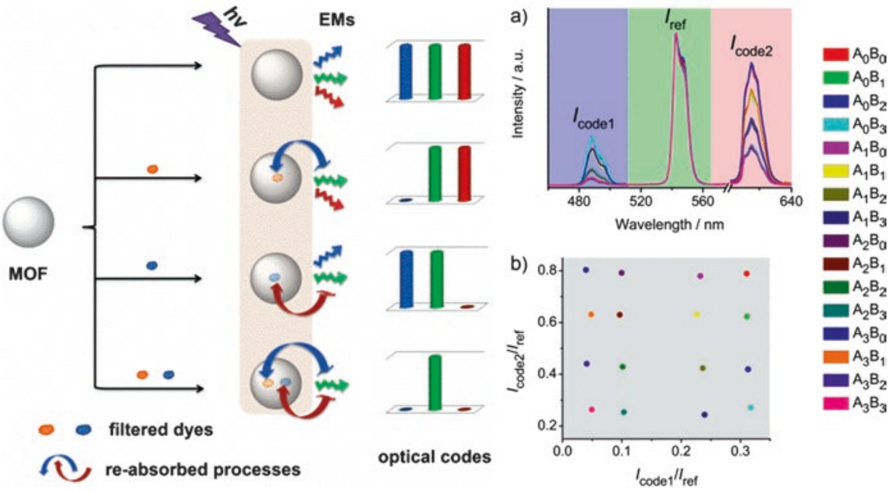

Fig. 8.9 (*Left*) Schematic illustration of the encoding strategy based on tuning the multiple emission bands of lanthanides luminescent MOFs. Blue and red emissions can be tuned by controlling filtered dye loading, while the green emission is not adsorbed and serves as an internal reference to generate ratiometric optical codes. (*Right*) (*a*) Emission spectra of Eu^{3+}/Tb^{3+}@MIL-100 (In) films with various dye (FL and MB) loading combinations. The loading concentration of both FL and MB is set as four levels, leading to 4^2 ratiometric codes. (*b*) Two-dimensional matrix of the ratiometric codes derived from (*a*), revealing that the ratiometric codes can be well separated and identified (Reprinted with permission from Ref. [14]. Copyright 2015 The Royal Society of Chemistry)

upon excitation at the same wavelength. Three emission bands (488, 544, and 615 nm) of Eu^{3+}/Tb^{3+}@MIL-100 (In) film are chosen as the spectral signals for realizing the barcoding function (Fig. 8.9 (Right) a). Of them, 488 (I_{code1}) and 615 nm (I_{code2}) emissions are filtered by FL and MB dyes, respectively. On the contrary, 615 nm emission is unfiltered and served as reference (I_{ref}) to the filtered emissions. Similarly, the concentration of FL and MB dyes is both set as four levels, leading to 16 combinations in total. Since the information of the combinations can be carried by their emission intensities in multiple bands, each of the combinations correlates to one two-dimensional ratiometric code (I_{code1}/I_{ref}, I_{code2}/I_{ref}), which is calculated by the ratios of two filtered intensities (I_{code1} and I_{code2}) to one reference intensity (I_{ref}) (Fig. 8.9 (Right) b). The optical codes can be well separated and identified.

Shen et al. report a new system based on rare-earth ion (red-Eu, green-Tb, and orange-Sm) functionalized bio-MOF-1 hybrid system by cation exchange [15]. The $Tb_{1-x}Eu_x$@**1** barcoded materials with varying Tb^{3+} and Eu^{3+} stoichiometry are obtained as $Tb_{1-x}Eu_x$@ bio-MOF-1. A barcoded readout based on color code is generated with green for Tb^{3+} signal and red for Eu^{3+} signal, whose relative intensities are reflected in the display to create three distinct barcodes and can be detected by the naked eyes. The colors of three samples in the CIE chromaticity diagram are as follows: green for $Tb_{0.999}Eu_{0.001}$@bio-MOF-1, yellow for $Tb_{0.99}Eu_{0.01}$@bio-MOF-1, and red for $Tb_{0.9}Eu_{0.1}$@bio-MOF-1, respectively. Photographs of these three materials display various colors under a xenon lamp. Sm^{3+} is introduced to increase the diversity of the barcodes and enrich the luminescent signals. With the increasing amount of Sm^{3+} in $Sm_{0.85}Tb_{0.125}Eu_{0.025}$@bio-MOF-1, the emission of Sm^{3+} at 598 nm has been obviously enhanced at the excitation of 327 nm compared with $Sm_{0.8}Tb_{0.17}Eu_{0.03}$@bio-MOF-1. From the CIE chromaticity diagram, both of two samples are located at pink area, displaying pink color under a xenon lamp.

8.3 Photofunctional Hybrid Materials as Probes or Sensors for Metal Cations

8.3.1 Photofunctional Hybrid Materials as Probes or Sensors for Fe^{3+} and Fe^{2+}

Iron species are essential for virtually all organisms due to their functions as a cofactor in central cellular process such as respiration, DNA synthesis and repair, ribosome biogenesis, metabolism, etc. In this regard, how to effectively probe iron ion becomes a challenging issue, particularly with the emergence of fluorescent imaging technology. Biological iron is most commonly found in the +2 (ferrous) and +3 (ferric) oxidation states. Designing a sensor with specificity for ferrous over ferric is difficult due to its propensity for oxidation within aqueous and aerobic conditions. To face this challenge, there are only a few fluorescent sensors selective for Fe^{2+} over Fe^{3+}, all of which are small molecule sensors. Moreover, some flaws still remain due to their selectivity and solubility in water solvents. The luminescence probe to detect Fe^{3+} in environmental and biological systems mainly depends on the quenching effect on luminescence of MOFs by metal cations, which is originated from three approaches: the interaction between metal cations and organic ligands, the collapse of the crystal structure by metal cations, and the cation exchange of central cations in framework with targeted cations. The sensing of Fe^{2+} and even both Fe^{2+} and Fe^{3+} or Fe^{2+} against Fe^{3+} is expected to study deeply.

Zhou et al. have demonstrated an alternative approach to fabricate a highly luminescent nanosized MOF by encapsulating Eu^{3+} cations in MIL-53-COOH (Al) nanocrystals (Fig. 8.10 (Left)) [16], which is developed as a highly selective and sensitive fluorescence probe targeting Fe^{3+} cations in aqueous solution. They examine the potential of Eu^{3+}@**1** to detect metal cations, the luminescent responses of which toward aqueous solutions of various metal cations are shown in Fig. 8.10 (Right) a. Only Fe^{3+} gives significant quenching effect on the luminescence, which can be further confirmed by the photograph of Eu^{3+}@**1** suspension under UV-light irradiation (Fig. 8.10 (Left)). In addition, the quenching effect of Fe^{3+} on the luminescence of Eu^{3+}@**1** is evaluated by fluorescence decay time of Eu^{3+} (Fig. 8.10 (Right) b). Cu^{2+} and Fe^{3+} exhibit varying degrees of decline in the fluorescence lifetime. Especially in the case of Fe^{3+}, the decay time of Eu^{3+}@1 is undetectable of 5 mM Fe^{3+}. This observation agrees well with the responses of luminescence

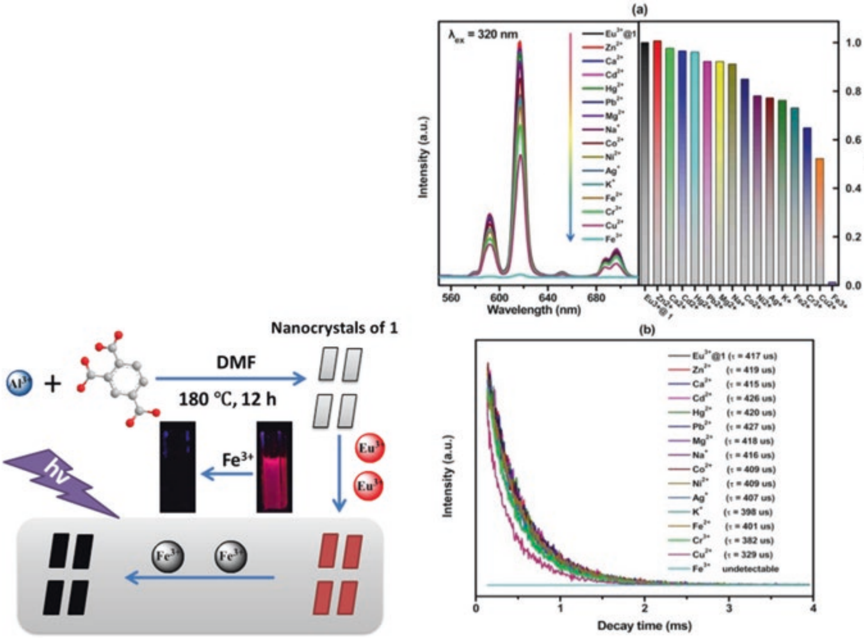

Fig. 8.10 (*Left*) The scheme for fabricated MIL-53-COOH (Al) nanocrystals by post-functionalization with Eu^{3+}, possessing super selectivity and sensitivity in detection of Fe^{3+} in aqueous solution. (Right) Responses of the fluorescence (*a*) and lifetime (*b*) of Eu^{3+}@**1** (0.4 mg·L^{-1}) toward aqueous solution of various metal cations (5 mM). Both the emission spectra and lifetimes are collected at the excitation wavelength of 320 nm. I and I_0 denote the fluorescence intensity of Eu^{3+}@**1** with and without metal ions of interest, respectively (Reprinted with permission from Ref. [16]. Copyright 2014 The Royal Society of Chemistry)

Eu^{3+}@**1** to various metal cations. The good fluorescence stability in aqueous environment, the low-detection limit, and the broad linear range suggest it has the potential for intracellular sensing and imaging of Fe^{3+}.

Xu et al. prepare a layer-like MOF (MIL-124, or $Ga_2(OH)_4(C_9O_6H_4)$) to encapsulate Eu^{3+} cations by one uncoordinated carbonyl group in its pores, whose hybrid system (Eu^{3+}@MIL-124) shows excellent luminescence and good fluorescence stability in water or other organic solvents. Subsequently, it is chosen as a sensitive probe for sensing metal ions, suggesting a highly selective and sensitive probe for detection of Fe^{3+} (detection limit, 0.28 μM) and Fe^{2+} ions through fluorescence quenching of Eu^{3+} and MOF over other metal ions [17]. For the Fe^{2+} and Fe^{3+} ions, although they all seriously quench the emission of Eu^{3+}, their emission colors are different and easy to distinguish under UV light in Fig. 8.11 (Top). Therefore, Eu^{3+}@MIL-124 can selectively sense Fe^{2+} and Fe^{2+} ions though the different quenching effects to Eu^{3+} and MOF. To detect Fe^{2+} and Fe^{3+} in water, the test paper is immersed in the aqueous solution of metal ions for 1 min and then exposes to air for drying under the irradiation of UV light of 254 nm, the fluorescent colors of the test paper change from red to dark red, faint dark red, and finally black with the increase

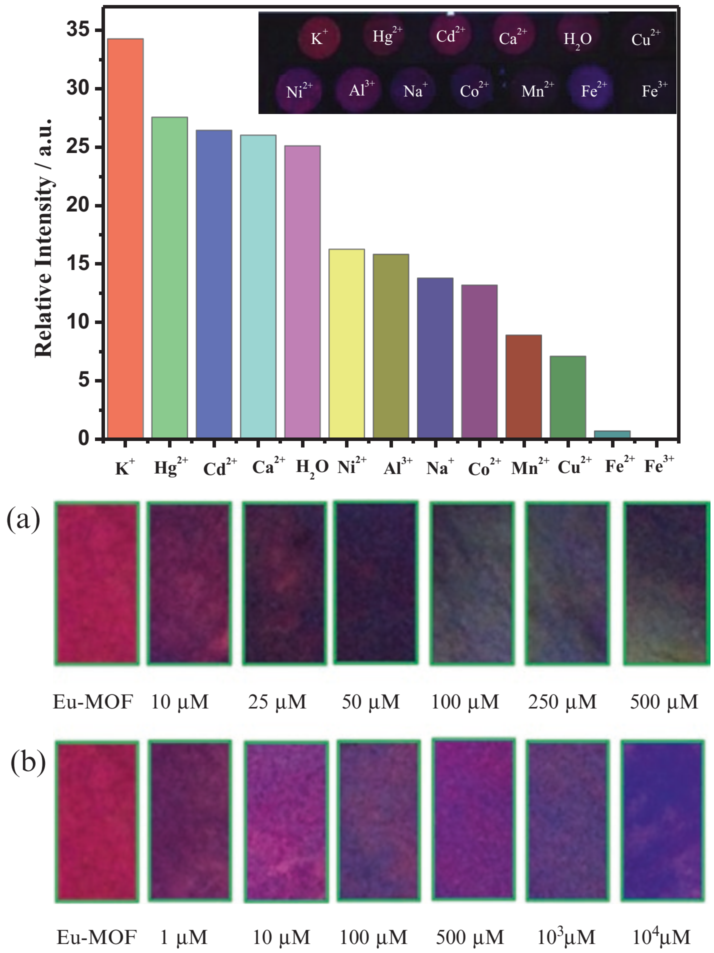

Fig. 8.11 (*Top*) The luminescence intensity of the $^4D_0$-$^7F_2$ of Eu^{3+}@MIL-124 interacting with different metal ions in 10^{-2} mol L^{-1} aqueous solution of MCl$_n$ (excited monitored at 298 nm). The inset is the corresponding photographs under UV-light irradiation at 254 nm. (*Bottom*) Optical images of the Eu^{3+}@MIL-124 test paper after immersion into solution with different concentrations of Fe^{3+} (**a**) and Fe^{2+} (**b**) for 1 min (Reprinted with permission from Ref. [17]. Copyright 2015 American Chemical Society)

of Fe^{3+} (Fig. 8.11 (Bottom) a). The least concentration of detection for Fe^{3+} by fluorescence test paper is 50 μM. At the same time, when immersing the test paper in various concentrations of Fe^{2+} aqueous solution, the color changes from red to blue, as shown in Fig. 8.11 (Bottom) b, which is obviously different from Fe^{3+}. So the colors of different intensities can be distinguished by the naked eyes. The quenching effect of Eu^{3+}@MIL-124 by Fe^{3+} can be attributed to the partial replacement of Ga^{3+} and substitution of Eu^{3+} while substitution of Eu^{3+} is the main reason for the fluorescence quenching by Fe^{2+}.

Shen et al. check the sensing property of Eu^{3+}@bio-MOF-1 hybrid system for different metal ions (in DMF solution) [18]. Al^{3+},Na^{+}, Mg^{+}, and Co^{2+} have slight quenching effects of luminescence of Eu^{3+}@bio-MOF-1 hybrids, while Zn^{2+} shows a slight enhancement of luminescent intensity of Eu^{3+}@bio-MOF-1 hybrids. Both Cr^{3+} and Cu^{2+} produce the markedly quenching of the luminescent intensity of Eu^{3+}@bio-MOF-1 hybrids. Especially the introduction of Fe^{3+} almost quenches the luminescence of Eu^{3+}@bio-MOF-1 hybrids. These results may be related to the interaction between different metal ions and bio-MOF-1 and exchange of Eu^{3+}. Weng et al. examined the potential of Tb^{3+}@Cd-MOF for sensing metal cations [19]. The luminescent intensity of the complex depends on the DMF solutions of different metal cations to various degrees. They monitor the luminescent intensity at the wavelength of 547 nm, which can be assigned to the $^5D_4 \rightarrow {}^7F_5$ transition of Tb^{3+}. It is worth noting that Fe^{3+} can quench the fluorescence intensity remarkably. Sun et al. examine the potential of [DBM-Yb-ZA]-NTASi-Eu hybrids for sensing metal ions [20]. It can be seen the introduction of Ag^{+}, K^{+}, Pb^{2+}, Al^{3+}, Na^{+}, Mg^{2+}, Zn^{2+}, Cd^{2+}, and Hg^{2+} slightly changes the luminescent intensity of [DBM-Yb-ZA]-NTASi-Eu. Co^{2+}, Fe^{2+}, Ni^{2+}, and Cu^{2+} have different quenching effects on the luminescent intensity of [DBM-Yb-ZA]-NTASi-Eu. It is worth pointing out that Fe^{3+} shows the high selectivity, which quenches the luminescent intensity of bio-MOF-1 remarkably. The selectivity for sensing metal ions may be due to the exchange interaction between different metal ions and ZA host. In addition, the quenching effect of M^{Z+} on the luminescence of [DBM-Yb-ZA]-NTASi-Eu hybrid system evaluated by the fluorescence decay time of Eu^{3+}’ $^5D_0 \rightarrow {}^7F_2$ transition is in good agreement with the luminescence responses to various metal ions.

8.3.2 Photofunctional Hybrid Materials as Probes or Sensors for Cd^{2+} and Hg^{2+}

Among various heavy metal ions, cadmium (Cd(II)) and mercury (Hg(II)) are the most dangerous ions due to their high toxicity and carcinogenicity. It is widely used in many fields, such as industry, agriculture, military affairs, etc. These sources lead to high level of (Cd(II) and Hg(II)) exposure and contamination. Further, toxic Cd(II) can be easily absorbed and accumulated in plants and other organisms, which may result in serious diseases and even certain forms of cancers. Hg(II) is attracting particular attention due to its significant threat to the environment and public health, such as Minamata disease. Bearing in mind the elevated risks related to human health, the qualitative and quantitative detection of (Cd(II) and (Hg(II) ions can be considered to be an aspiration of primary importance.

Hao et al. encapsulate Eu^{3+} cations into the pores of Uio-66(Zr)-$(COOH)_2$ for its sufficiently porous structure and available free carboxyl on the ligand amenable to coordination with metal cations [21]. The Eu^{3+} incorporated hybrids (Eu^{3+}@Uio-66(Zr)-$(COOH)_2$) is developed as a fluorescent probe and sensor for Cd^{2+}, showing

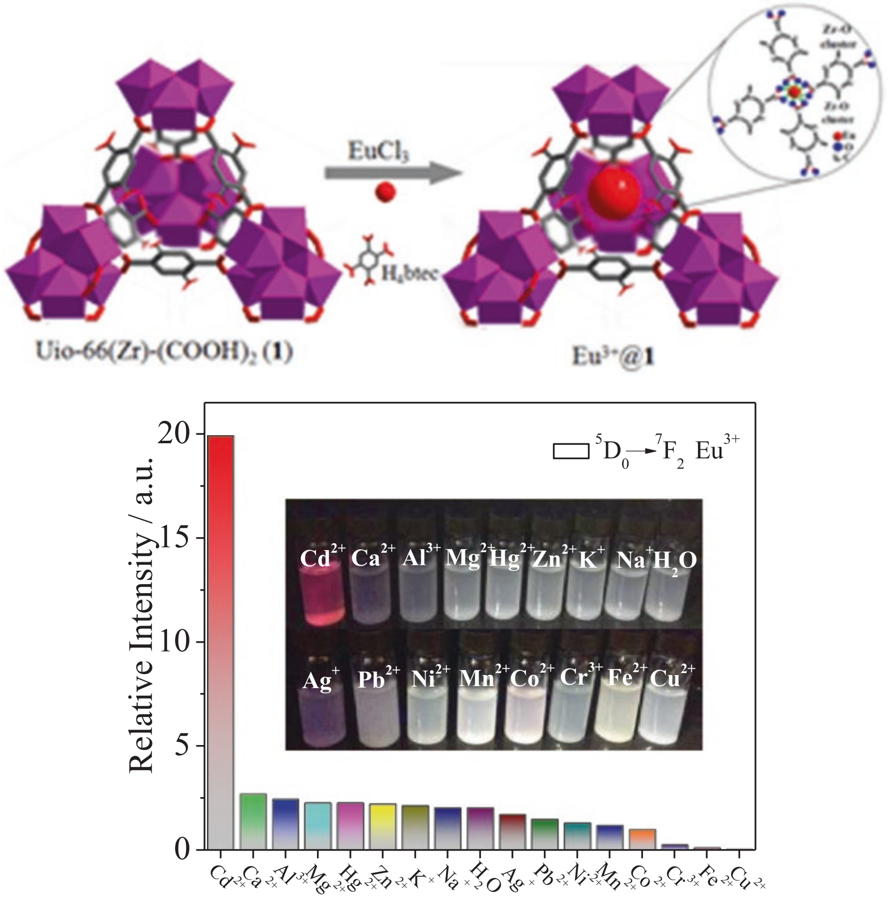

Fig. 8.12 (*Top*) Synthetic scheme and representative structure of Eu^{3+}@1, the inset is schematic representation of Eu^{3+} tethered to the free carboxyl sites of 1. (*Bottom*) the relative intensities of $^5D_0 \rightarrow {}^7F_2$ at 614 nm for Eu^{3+}@1 dispersed in various metal ions aqueous solutions (10 mM) when excited at 322 nm. Inset is the corresponding photographs under UV-light irradiation (Reprinted with permission from Ref. [21]. Copyright 2015 The Royal Society of Chemistry)

high selectivity, excellent sensitivity and fast detection time. The representative structure of Eu^{3+}@1 is depicted in Fig. 8.12 (Top), whose XPS and ICP-MS analysis prove that four non-coordinating carboxyl groups are coordinated with one Eu^{3+} cation (inset of Fig. 8.12 (Top)). As shown in Fig. 8.12 (Bottom), when irradiated under UV light, only Cd^{2+} can induce a red-colored luminescence which can be clearly seen by naked eye, while no visible change can be observed upon the addition of other metal ions. Cd^{2+} ions interact with the Lewis basic carboxylic oxygen sites within hybrid system and facilitate the efficiency of energy transformation from ligands to Eu^{3+} ions. This facilitates ligand-to-Eu energy transfer, and thereof benefits Eu emissions. Cd^{2+} ion also has heavy atom effect to promote intersystem crossing energy transfer from ligands to Eu^{3+}, while its d-d transitions are impossible

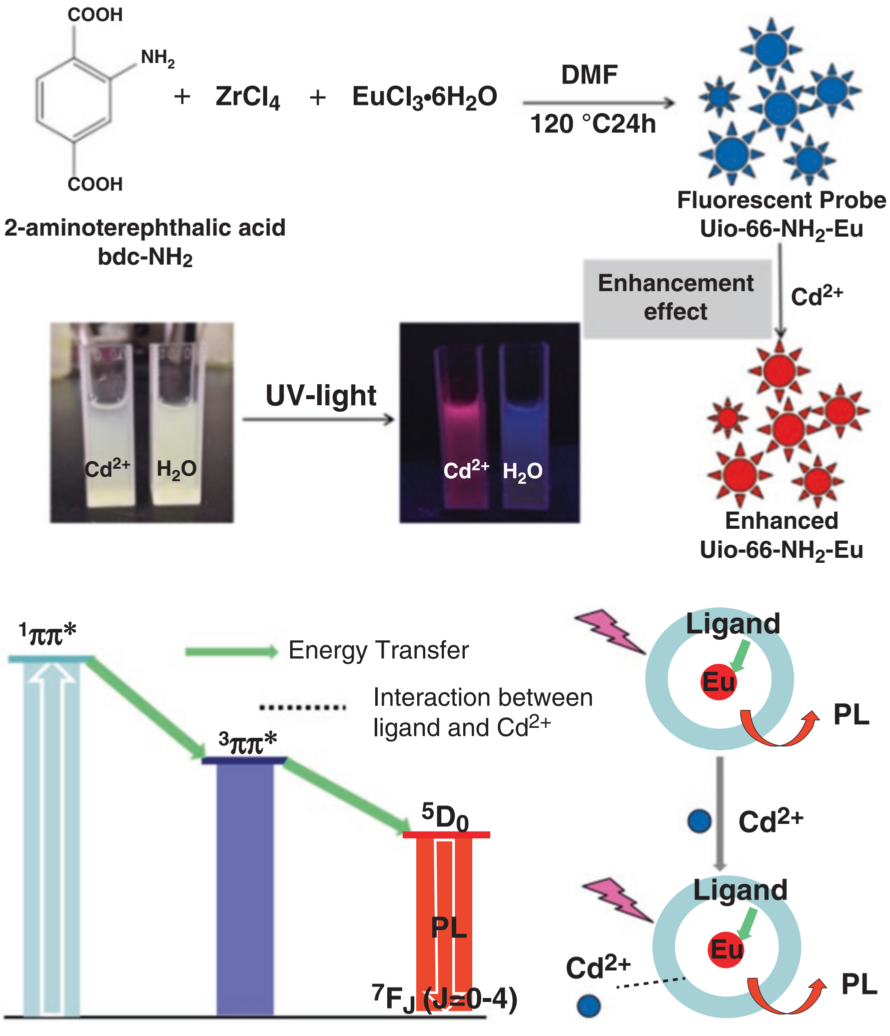

Fig. 8.13 (*Top*) Schematic representation for and fluorescent enhancement chemosensor of Uio-66-NH$_2$-Eu on Cd^{2+}. The inset is clear photograph under UV-light irradiation at 365 nm for sensing effect. (*Bottom*) Simplified Schematic Diagrams Showing Ligand-Metal Energy Transformation (LMET) for Luminescence Emission ($^1\pi\pi^*$ and $^3\pi\pi^*$ are the Singlet State and Triplet State of Ligands) and Influence of Cd^{2+} on LMET (Reprinted with permission from Ref. [22]. Copyright 2016 Elsevier)

and LMCT will change the energy level of the excited state of the ligands. All these factors lead to an enhanced emission intensity of hybrids upon Cd^{2+}-binding.

Xu et al. prepare new Eu-based MOFs (Uio-66-NH$_2$-Eu) hybrid and choose it as highly selective and sensitive fluorescence probe targeting Cd^{2+} ions in aqueous solutions through an impressive enhancing phenomenon upon the typical Eu-luminescence, which is successfully applied to determine the concentration of Cd^{2+} in environmental samples (Fig. 8.13 (Top)) [22]. The scheme for a simplified

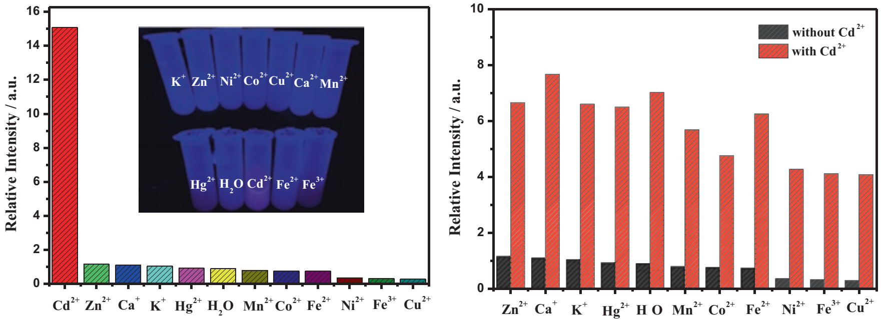

Fig. 8.14 (*Left*) Variation of fluorescence intensity of Uio-66-NH_2-Eu at 617 nm with different immersion time in Cd^{2+} solution (0.01 mol L^{-1}) (λ_{ex} = 395 nm). (*Right*) Luminescence intensity of Uio-66-NH_2-Eu (1.5 mg/mL) upon the without and with of Cd^{2+} (0.01 mol L^{-1}) in the presence of background of metal cations in aqueous solution (λ_{ex} = 395 nm; λ_{em} = 617 nm) (Reprinted with permission from Ref. [22]. Copyright 2016 Elsevier)

ligand ($^1\pi\pi^*$) → ligand ($^3\pi\pi^*$) → Eu* energy transformation is shown in Fig. 8.13 (Bottom). The enhancement of luminescent intensity of Uio-66-NH_2-Eu to Cd^{2+} is ascribed to its more efficient energy transfer from ligands to Eu^{3+}. UV-Vis measurements also support the participation of nitrogen in MOF in the coordination to Cd^{2+}, which affects the electric density of the ligand and thus affect the electronic transitions. The histogram shows about 13 times as much as that of the original one after immersing into 0.01 mol L^{-1} Cd^{2+} aqueous solution for a few minutes (Fig. 8.14 (Left)). The remarkable enhancement effect by Cd^{2+} can be further confirmed by the photograph of Uio-66-NH_2-Eu suspension under UV-light irradiation as shown in the inset of Fig. 8.14 (Left). The emitted visible red light of Uio-66-NH_2-Eu suspension is completely enhanced when in contact with aqueous solution of Cd^{2+}. Moreover, the influence of other metal cations (Zn^{2+}, Ca^{2+}, K^+, Mn^{2+}, Co^{2+}, Fe^{2+}, Ni^{2+}, Fe^{3+}, Hg^{2+} and Cu^{2+}) on the detection of Cd^{2+} is also determined. As shown in Fig. 8.14 (Right), every metal ion shows similar fluorescence enhancement after introducing Cd^{2+}. It is quite cheerful that the enhancement effect of Cd^{2+} ion on Eu-luminescence is not influenced by the addition of other metal ions, further convincing the high selectivity of Uio-66-NH_2-Eu for Cd^{2+} detection in practical use.

Liu et al. prepare a new Eu^{3+} functionalized MOF (CPM-17-Zn-Eu) hybrid (Fig. 8.15). Its available functional group could coordinate to metal cations to recognize Cd^{2+} ions in aqueous solutions with an enhancing Eu^{3+} characteristic luminescence [23]. The fluorescence intensity of CPM-17-Zn-Eu does not show obvious change during diffusion in different pH solutions due to its excellent fluorescence stability. The luminescence intensity of CPM-17-Zn-Eu is enhanced by about 4.0 times with the addition of Cd^{2+} compared with that of the aqueous solutions. Only Cd^{2+} can induce a red-colored luminescence and can be clearly seen under UV-light irradiated.

Xu et al. report encapsulating CDs (carbon dots) with strong fluorescence activity into MOF-25, [24] both of which (CDs@MOF-253) remain the excellent optical properties of CDs and can take on Eu^{3+} to form dual-emissive Eu^{3+}/CDs@MOF-

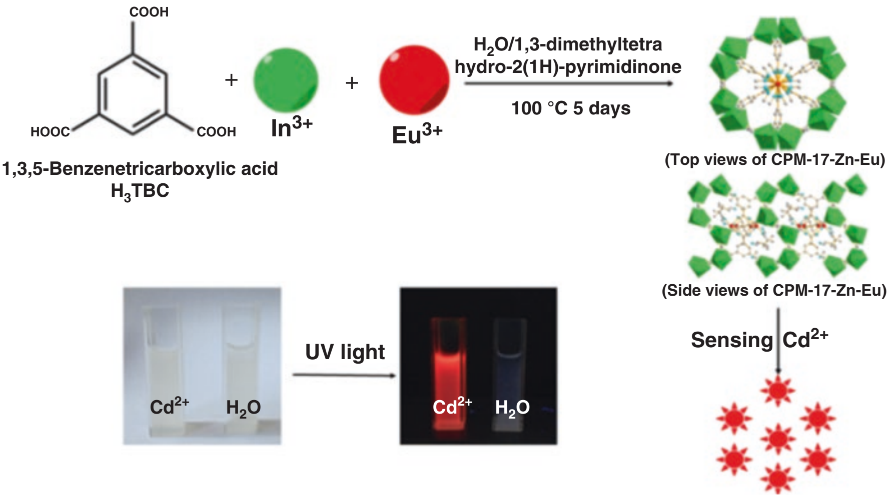

Fig. 8.15 The scheme for the synthetic procedure of CPM-17-Zn-Eu and the fluorescent enhancement of CPM-17-Zn-Eu by Cd^{2+} (Reprinted with permission from Ref. [23]. Copyright 2015 Elsevier)

253. Eu^{3+}/CDs@MOF-253 is developed to a ratiometric and colorimetric fluorescent sensor to detect Hg^{2+} with high sensitivity and selectivity. Eu^{3+}/CDs@MOF-253 shows its good adsorbent for Hg^{2+} removal for its coordination to the organic functional groups, which can change the surface traps or electron-hole recombination annihilation via electron or energy transfer process, resulting in the quenching of fluorescence of CDs efficiently. Eu^{3+}/CDs@MOF-253 solution in the absence of Hg^{2+} exhibits both characteristic emission of CDs and Eu^{3+} (I_{Eu}/I_{CD} = 1.5) with a faint blue light (Fig. 8.16 (Top) a). In contrast, it changes from blue to red under UV light, corresponding to the quenching of the CDs emission. Then less effect on emission of Eu^{3+} in Eu^{3+}/CDs@MOF-253 leads to the colorimetric and ratiometric fluorescence Hg^{2+} sensor. The quenching effect of Hg^{2+} brought on CDs in Eu^{3+}/CDs@MOF-253 attributes to the coordination between Hg^{2+} and some functional groups in CDs. Figure 8.16 (Bottom) presents the relative PL intensities (I_{Eu}/I_{CD}) versus the concentration of Hg^{2+}. A good linear correlation (R^2 = 0.99324) is observed over the concentration range of 0–150 μM and the detection limit (LOD) is estimated to be 13 nM at a signal-to-noise ratio of 3, which is nearly close to the maximum level for mercury in drinking water permitted by the US Environmental Protection Agency (2 ppb, 10 nM). The relative standard deviation (RSD) for nine replicate measurements of 50 and 100 μM Hg^{2+} is 2.8% and 1.8%, respectively. To make the detection simple and portable, they prepare a test plate for rapid Hg^{2+} sensing. Under the irradiation of UV light of 365 nm, the fluorescent colors of test plate changing from blue to faint blue, dark red and finally red as concentrations increasing from 0 to 100 μM of Hg^{2+}. Noted that to the naked eyes, the change of different colors is easier to identify than that of single color. Therefore the dual-emission detection system for Hg^{2+} sensing has greater advantage in practical application than other systems.

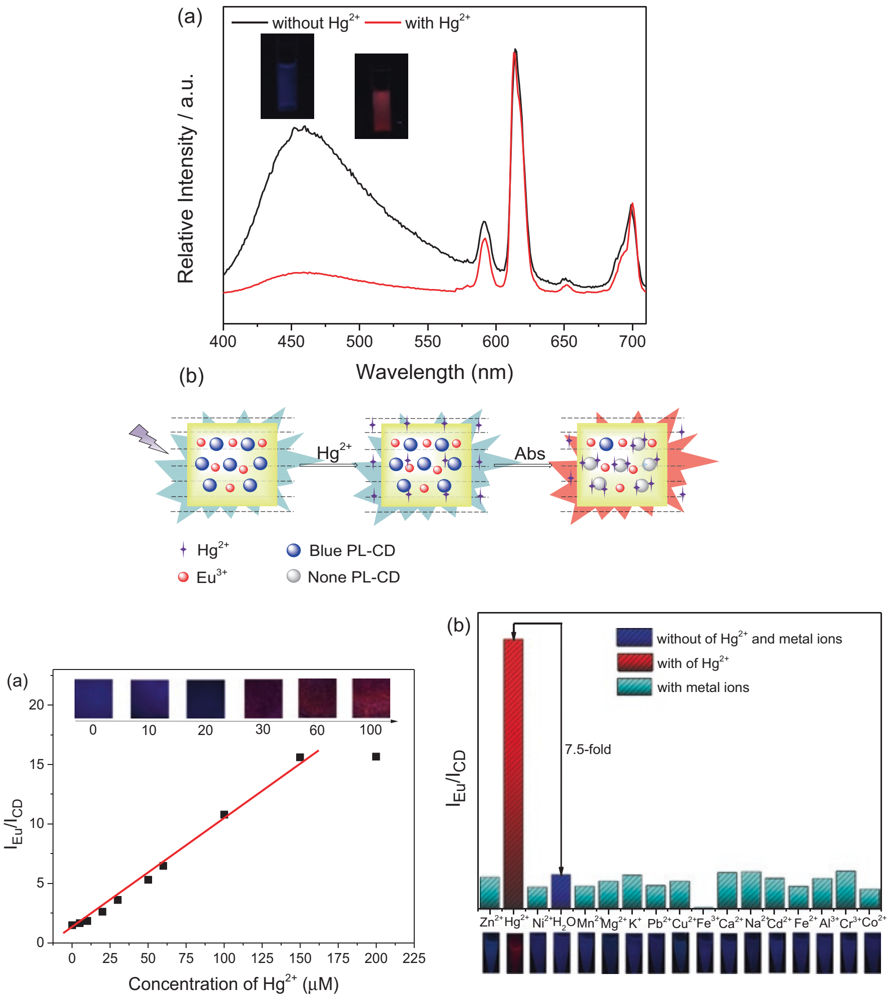

Fig. 8.16 (*Top*) (**a**) PL emission spectra of the Eu^{3+}/CDs@MOF-253 in the absence (*blue line*) and presence (*red line*) of 100 μM Hg^{2+} when excited by the wavelength of 360 nm and corresponding photographs under UV-light irradiation at 365 nm; (**b**) Schematic illustration of the Hg^{2+} detection mechanism using Eu^{3+}/CDs@MOF-253. (*Bottom*) (**a**) Line relationship between I_{Eu}/I_{CD} and $C_{Hg}{}^{2+}$ (λ_{ex} = 360 nm). Inset shows photographs of the test plates treated by different concentration of Hg^{2+}; (**b**) Comparison of the PL intensity of I_{Eu}/I_{CD} for Eu^{3+}/CDs@MOF-253 (3 mg) dispersed in aqueous solutions containing different metal ions (100 μM) when excited at 360 nm and corresponding photographs under UV-light irradiation at 360 nm (Reprinted with permission from Ref. [24]. Copyright 2016 The Royal Society of Chemistry)

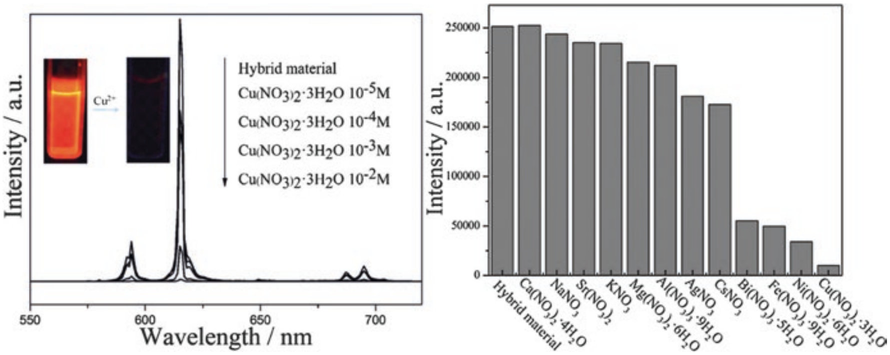

Fig. 8.17 The PL spectra of Eu(dpa)$_3$@POSS-NH$_2$ in Cu(NO$_3$)$_2$ aqueous solution at different concentrations (excited at 290 nm). The inset shows the luminescence change after the addition of Cu^{2+} ions in the suspension under UV light (254 nm). Comparison of the luminescence intensity of different metal ions incorporated in the hybrid composites activated in M(NO$_3$)$_x$ aqueous solution (Reprinted with permission from Ref. [26]. Copyright 2016 Wiley)

8.3.3 Photofunctional Hybrid Materials as Probes or Sensors for Cu^{2+} and Ag$^+$

The detection of Cu^{2+} in the human body is an essential issue in medicine, because Cu^{2+} plays considerable roles in living organisms, particularly in the brain. The sensing of Cu^{2+} in the environment and biological systems is extremely important. For example, Alzheimer's disease and Wilson's disease are related to the homeostasis of Cu^{2+}. Ag$^+$ can accumulate in the human body through the food chain and drinking water. Therefore, the deficiency of Ag$^+$ will result in a number of pathological disorders, such as cell toxicity and organ failure.

Zhou et al. introduce Eu(TTA)$_3$·L into tetramethoxysilane (TMOS) and assemble a luminescent hybrid (H) into PUF to fabricate a europium containing polyurethane foam (Eu-PUF) by the polycondensation of soy polyol and 2,4-toluene diisocyanate (TDI) [25]. It is used as a sensory material to detect copper ions in water, displaying a highly selective and sensitive luminescence quenching effect to Cu^{2+}, which is considered as the coordination interaction between Cu^{2+} and EDTA resulted in the "off–on" process. Eu-PUF can be recycled more than 10 times. Xu et al. report water-soluble hybrids formed by linking Na3[Ln(dpa)3] (dpa = 2,6-pyridinedicarboxylic acid) to octa-amino functionalized polyhedral oligomeric silsesquioxane (POSS-NH2) through hydrogen bonding [26]. The emission color of the resulting EuxTby(dpa)3@POSS-NH$_2$ can be finely tuned by changing the value of x/y. The luminescence sensing selectivity of Eu(dpa)$_3$@POSS-NH$_2$ shows a dramatically decrease in intensity due to the addition of Cu^{2+}, which is quenched significantly even in the presence of very low Cu^{2+} concentration, allowing for the identification of trace amounts of Cu^{2+} ions in aqueous solution (Fig. 8.17). The luminescence lifetime of Eu^{3+} (1.49 ms) in the aqueous suspension is dramatically reduced to 0.11 ms in the presence of 0.01 M Cu^{2+}, whereas the other metal ions

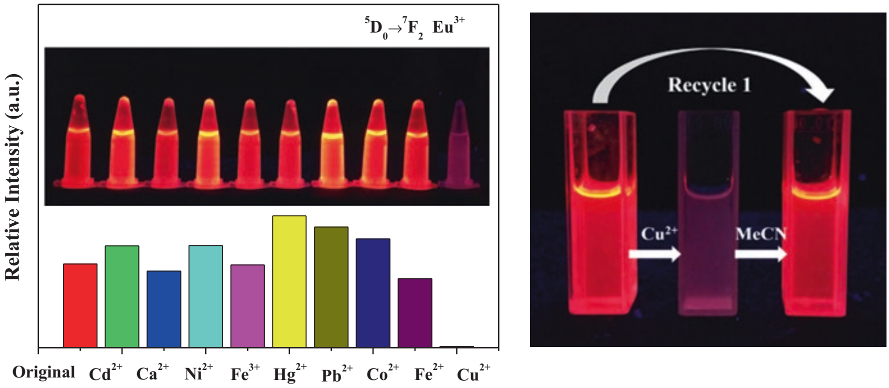

Fig. 8.18 (*Left*) The relative intensities of $^5D_0$-$^7F_2$ at 613 nm for SiO_2@EuTTA@ZIF-8 dispersed in various metal ion aqueous solutions upon excitation at 396 nm. The inset is in the corresponding photographs under UV-light irradiation(*top*); (*Right*) Photograph of SiO_2@EuTTA@ZIF-8 microspheres recycled 1 times for Cu^{2+} sensing (*right*) (Reprinted with permission from ref. [29]. Copyright 2016 The Royal Society of Chemistry)

have negligible effects. The interaction between the Cu^{2+} ions and dpa may reduce the energy transfer efficiency from dpa to Eu^{3+} ions.

Besides, Tan et al. demonstrate the $Eu(DPA)_3$ and Tb $(DPA)_3$) based cellulose hydrogel films for the rapid and selective detection of Cu^{2+} in aqueous solution with a rapid luminescence quenching effect [27]. The biodegradable and environmentally friendly property endows them with potential in practical applications. Zhang et al. prepare two novel silica-based lanthanide complexes with 2-phenyl-4,5-imidazoledicarboxylic acid into poly(acrylic acid) host, which give unique quenching to Cu^{2+} (detection limit 10^{-5} M) (tested cations: Cu^{2+}, Pd^{2+}, Cd^{2+}, Co^{2+} and Mn^{2+}) and recycles more than ten times [28].

Liu et al. examine the potential sensing of SiO_2@EuTTA@ZIF-8 for metal ions [29]. Only Cu^{2+} can quench the red light emission and can be clearly seen under UV-light excitation; the addition of other metal ions can not induce visible change. The microspheres have high selectivity for the specific recognition and sensing of Cu^{2+} in aqueous solutions. They examine the recyclability of SiO_2@EuTTA@ZIF-8 microspheres for sensing processes. SiO_2@EuTTA@ZIF-8 microspheres can be reused several times by simply washing the chemsensors with fresh MeCN after the sensing process (Fig. 8.18). Lian et al. utilize SiO_2@Eu-dpa core-shell hybrid material as a luminescent sensor for metal ion detection [30]. Only Cu^{2+} reveals a conspicuous quenching effect on the luminescence originated from the f-f transition of Eu^{3+}. The well-dispersed DMF suspensions of the core-shell microspheres with various concentrations of Cu^{2+} exhibit a decrease of the luminescence intensity of SiO_2@Eu-dpa microspheres with increasing contents of Cu^{2+} from 0 to 500 μM, whose luminescent turn-off effect on Cu^{2+} of SiO_2@Eu-dpa is also easily observed by the naked eye. In addition, the quenching effect coefficient K_{sv} value (2.93×10^4 M^{-1}) of core-shell materials exhibits more than 20% improvement over the pure Eu-dpa complex (2.29×10^4 M^{-1}).

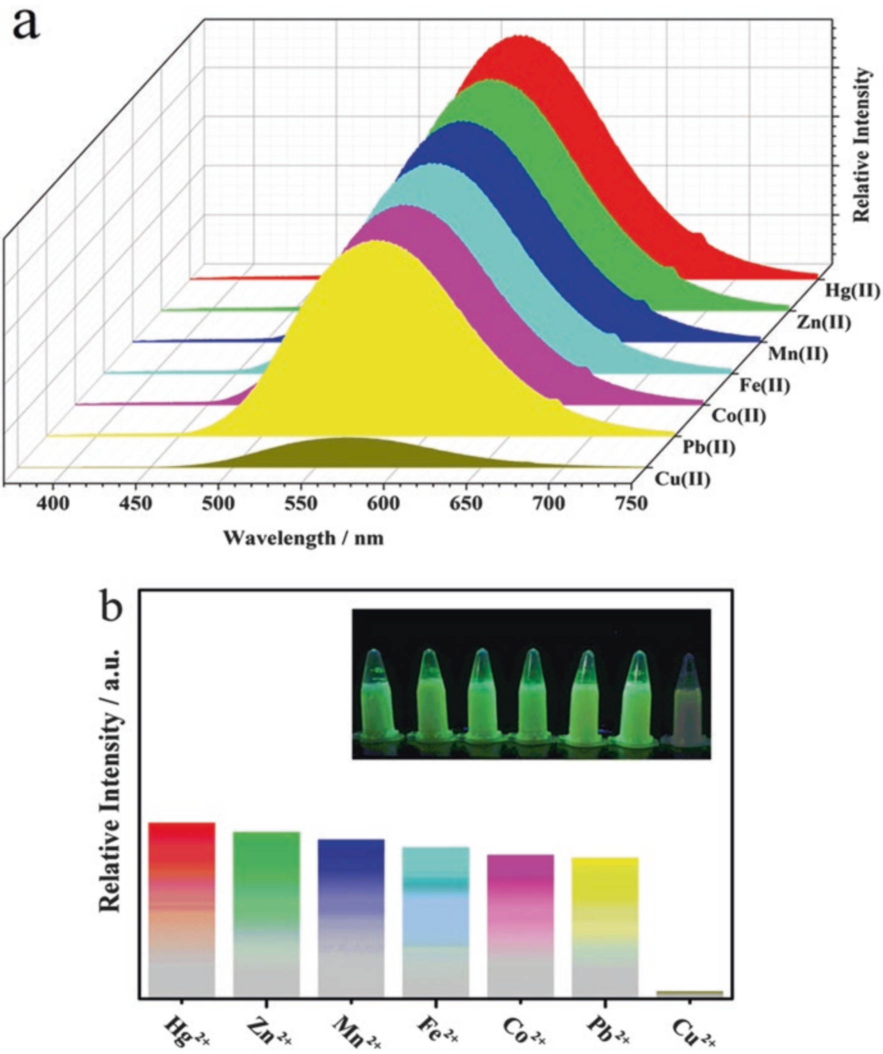

Fig. 8.19 **(a)** Suspension-state PL spectra and **(b)** the relative intensities of MIL-53-L dispersed in various metal ions aqueous solutions (10^{-2} M) when excited at 337 nm. *Inset* in (**b**): the corresponding photographs under UV-light irradiation (Reprinted with permission from Ref. [31]. Copyright 2016 Elsevier)

Liu et al. also examine the potential of MIL-53-L as a fluorescent probe for metal ions in aqueous media [31]. Seen from Fig. 8.19, only Cu^{2+} shows a quenched effect, indicating the high selectivity of MIL-53-L for the sensing and specific recognition of Cu^{2+} in aqueous media. Some additional metal ions have the heavy atom effect, which can promote intersystem crossing energy transfer and thus lead to a more effective intramolecular energy transfer from ligands to framework metal

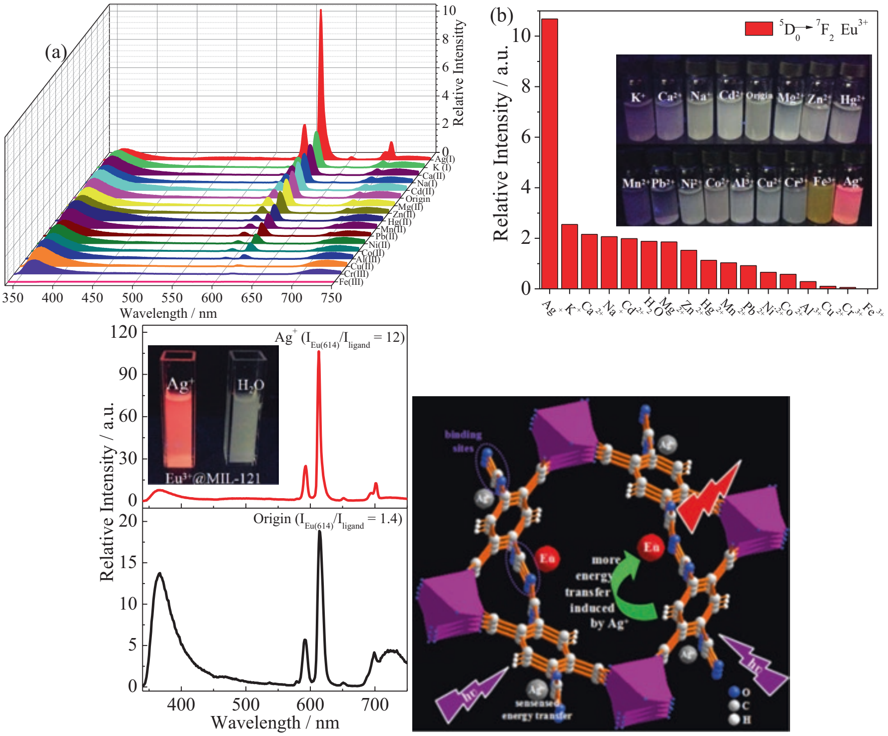

Fig. 8.20 (*Top*) (**a**) Suspension-state PL spectra and (**b**) the relative intensities of $^5D_0 \rightarrow {}^7F_2$ at 614 nm for Eu^{3+}@MIL-121 dispersed in aqueous solutions containing different metal ions (10 mM) when excited at 315 nm. The *inset* in Fig. (**b**) is the corresponding photographs under UV-light irradiation at 254 nm. (*Bottom*) The excitation spectra of Eu^{3+}@MIL-121 in the absence (*black*) and presence of Ag^+ (*red*) in aqueous solution. The *insert* is the corresponding photographs under UV-light irradiation at 254 nm (*Left*). Illustration of the fluorescence enhancement of Eu^{3+}@MIL-121 by Ag^+ (*Right*) (Reprinted with permission from Ref. [30]. Copyright 2015 The Royal Society of Chemistry)

ions. But the coordination to Cu^{2+} ion herein can enhance various non-radiative activations and increase energy loss, reducing ligand-to-metal energy transfer to quench luminescence.

Hao et al. have found the luminescent enhancement of Ag^+ on Eu^{3+}@MIL-121, which can be utilized for sensing Ag^+ ion [32]. Ag^+ drastically enhances the luminescence intensity with a maximum of more than 5.0 times as much as that of the original one, showing direct information of visibly red luminescent color to naked eyes when irradiated under UV light of 254 nm (in set of Fig. 8.20 (Top)b). These results indicate that Eu^{3+}@MIL-121 can selectively sense Ag^+ ions through fluorescence enhancement, which is quite rare in luminescent MOFs. They conclude that the enhancement of luminescent intensity of Eu^{3+}@MIL-121 is because Ag^+ causes more efficient energy transfer from ligands to Eu^{3+} ions, as depicted in Fig. 8.20 (Bottom, Right). This is consistent with the results of suspension-state PL spectra of

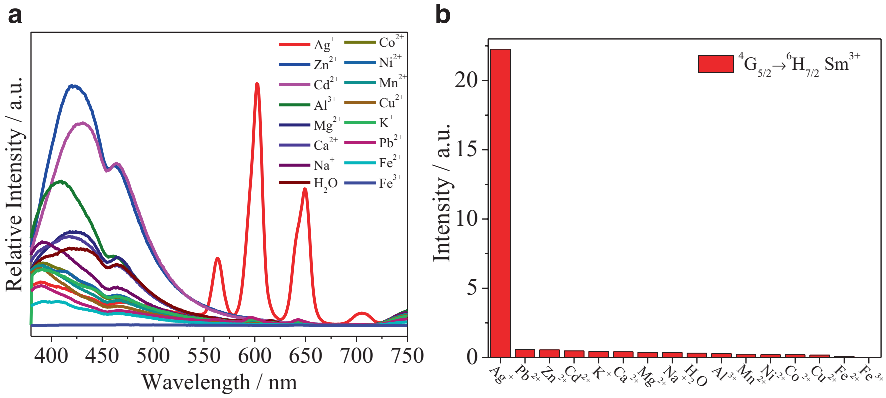

Fig. 8.21 (**a**) Suspension-state PL spectra and (**b**) the relative intensities of $^5G_{5/2} \rightarrow {}^6H_{7/2}$ at 603 nm for Sm^{3+}@MIL-121 dispersed in aqueous solutions containing different metal ions (10 mM) when excited at 320 nm (Reprinted with permission from Ref. [33]. Copyright 2015 The Royal Society of Chemistry)

Eu^{3+}@MIL-121 in the absence and presence of Ag^+. The PL emission spectrum (Fig. 8.20 (Bottom) left, up) of the Eu^{3+}@MIL-121 suspension features both Eu^{3+} sharp emissions and the broad ligand-centered emission (370 nm). By contrast, the basically diminished LC emission and the enhanced Eu^{3+}-luminescence of Eu^{3+}@MIL-121 in the presence of Ag^+ (Fig. 8.20 (Bottom) left, down) indicate the energy transfer is more effective. As a result, with the addition of Ag^+, the fluorescent color of Eu^{3+}@MIL-121 suspension changes from colorless to intense red under a 254 nm UV lamp (inset), observed by the naked eyes. They also extend the research to other rare-earth ions functionalized MIL-121 hybrid systems and obtain the similar results [33]. Seen from Fig. 8.21, the luminescent measurements illustrate that only Ag^+ can induce a significant fluorescence enhancement of Sm^{3+}, and no remarkable fluorescence responses are observed upon the addition of other metal ions, indicating Sm^{3+}@MIL-121 can be a potential sensor with excellent selectivity for Ag^+ in the aqueous solution.

8.3.4 Photofunctional Hybrid Materials as Probes or Sensors for Other Cations

Weng et al. modify $[H_2NMe_2]_3[Y(DPA)_3]$ to $RE^{3+} \subset [Y(DPA)_3]$ by ion exchange and select $Tb^{3+} \subset [Y(DPA)_3]$ to detect sensing properties [34]. They are surprised to see it shows high selectively toward Cr^{3+}. Hao et al. examine the potential of the Eu-MOF for the sensing of metal ions; the as-synthesized samples are ground and suspended in DMF solutions containing different metal ions (Li^+, Mn^{2+}, Fe^{2+}, Fe^{3+}, Ni^{2+}, Cu^{2+}, Zn^{2+}, Cd^{2+}, Al^{3+}) [35]. The different quenching effects lead to the changes

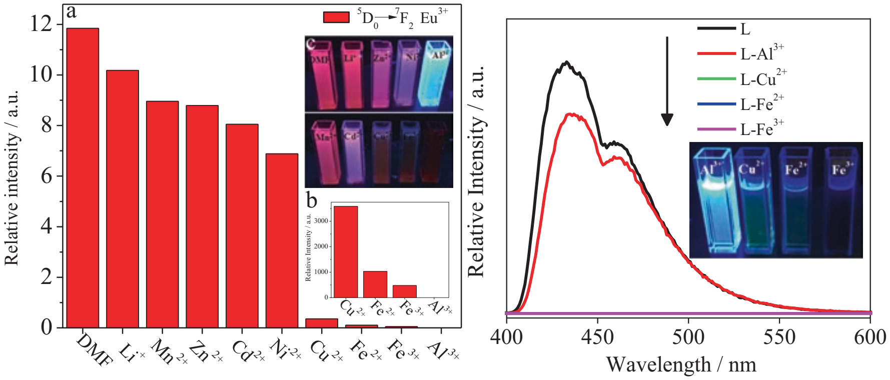

Fig. 8.22 (*Bottom*) The luminescence intensity of the $^5D_0 \rightarrow {}^7F_2$ transition of Eu-MOF interacting with different metal ions in 10^{-2} mol·L^{-1}DMF solution of MCl$_z$ (excited and monitored at 365 nm). The *insets* show the relative intensity of Eu-MOF with respect to Cu^{2+}, Fe^{2+}, Fe^{3+}, and Al^{3+}(*b*) and the photographs of M^{z+}·Eu-MOF under UV-light irradiation at 365 nm (*c*), respectively. (*Right*) Responses of the fluorescence of pure ligand (NH$_2$-BDC) toward DMF solution of various metal cations and the inset are the corresponding photograph under UV-light irradiation (Reprinted with permission from Ref. [35]. Copyright 2014 The Royal Society of Chemistry)

of emitting color under the UV-light irradiation, and the luminescent color changes are completely consistent with the variation tendency of the emission spectra in Fig. 8.22 (Left). For the Cu^{2+}, Fe^{2+}, Fe^{3+}, and Al^{3+} ions, although they all seriously quench the emission of Eu^{3+}, their emission colors are different and easy to distinguish under UV light. This is because Al^{3+} ion completely quenches the emission of Eu^{3+}, while the emission of the ligand still exists, causing the bright blue light as shown in Fig. 8.22 (Left) c. However, unlike Al^{3+}, the Cu^{2+}, Fe^{2+}, and Fe^{3+} ions cannot only quench the emission of Eu^{3+} but also have quenching effect on the emission of ligand; as a result, their emission colors under UV light are dark. The luminescent properties of pure ligand in DMF solutions are recorded and compared in Fig. 8.22 (Right). As expected, Cu^{2+}, Fe^{2+}, and Fe^{3+} totally quench the emission of pure ligands, while the Al^{3+} has no significant quenching effect. These results indicate the Eu-MOF can selectively sense Al^{3+} ions through quenching the luminescence of Eu^{3+} rather than that of the ligand.

8.4 Photofunctional Hybrid Materials as Probes or Sensors for Anions

8.4.1 Photofunctional Hybrid Materials as Probes or Sensors for F$^-$

Detection of fluoride is significant in the fields of water environment and biochemical monitor. Fluoride is considered as a serious health hazard in the environment because it may lead to bone disease or be widely used in organic synthesis. So many

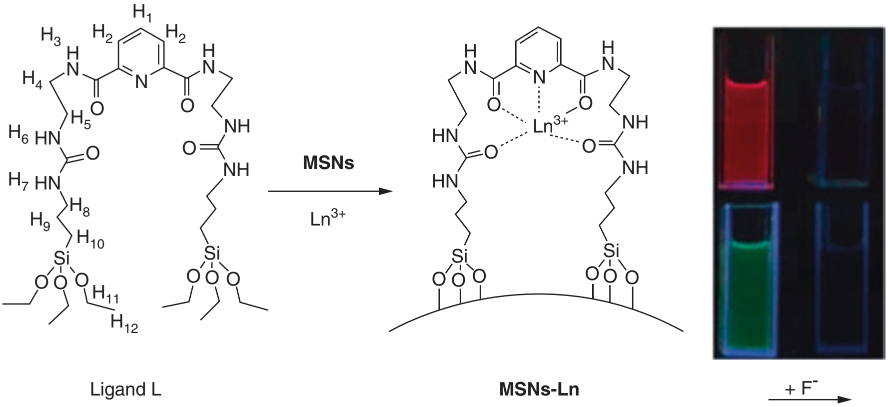

Fig. 8.23 Schematic representation of MSNs-Eu and MSNs-Tb. Photo: MSNs-Eu (*top*) and MSNs-Tb (*bottom*) in DMSO excited by UV light at 254 and 365 nm with (*right*) and without (*left*) fluoride (10^{-5} M) (Reprinted with permission from ref. [37]. Copyright 2014 American Chemical Society)

efforts have been made to design simple and low-cost sensors to detect F^-, such as solid-state ion-selective electrodes or devices, especially the fabrication of a group of anion-selective electrodes based on chemical interaction processes. Certainly, the development on fluoride-selective optical sensing is potentially important to provide possible alternatives to the ion electrodes.

Wang et al. prepare a hybrid system as a fluorescent receptor based on mesoporous silica, which shows significant changes in fluorescence upon hydrogen bonding to F^- in DMSO/H_2O (volume ratio) with color change from green to blue. Proton NMR titration studies indicate that the organic ligand is participating in hydrogen-bonding interactions with fluoride guest anions. The detection limit for F^- reached 1 μM, and reusability cycles are performed more than ten times [36]. Zhou et al. design a novel polydentate-type ligand derived from N,N′-bis(4,4-diethoxy-9-oxo-3-oxa-8,10-diaza-4-siladodecan-12-yl)pyridine-2,6-dicarboxamide (L) to assemble a new hybrid material (ASNs-Eu and ASNs-Tb, MSNs-Eu, MSNs-Tb) [37], whose multiple amide groups are coordinated to Eu^{3+}/Tb^{3+} firmly to sensitize, and two silylated arms induce the sol−gel reaction. The hydrogen-bond donor units in the hybrid system show strong affinity to guest F^-. Mesoporous hybrids (MSNs-Eu and MSNs-Tb) present much enhanced thermal stability, and lower detection limits for the fluoride ion (Fig. 8.23).

Li et al. synthesize 2-(2-hydroxyphenyl)-imidazo[4,5-f]-1,10-phenanthroline (L) modified linker (L-Si) and assembled the Eu^{3+} SBA15 hybrids ($Eu(L–S15)_2TTA$) with TTA as second ligand [38]. It displays a high-sensitivity sensing function with respect to fluoride for a significant quenching effect on its luminescence, which can be easily observed by the naked eye under UV-light irradiation (Fig. 8.24 (Top)). Moreover, the interference studies of other anions on the detection of F^- are also conducted. As can be seen in Fig. 8.24 (Bottom), the emission intensity of the Eu^{3+} hybrid only exhibits slight changes in the presence of other anions. The sensing

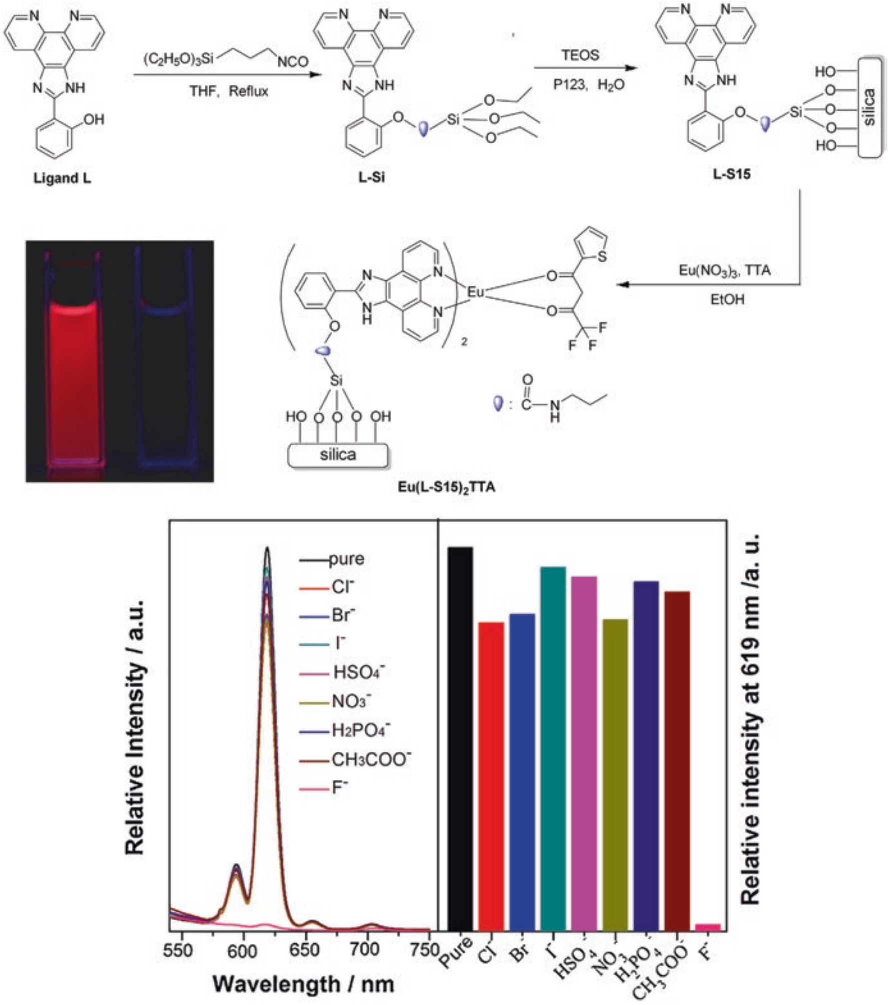

Fig. 8.24 Scheme for the synthetic process and predicted structure of europium-containing mesoporous hybrid Eu(L–S15)$_2$TTA. Photo: Eu(L–S15)$_2$TTA in DMSO excited by UV light at 365 nm with (*right*) and without (*left*) fluoride (10^{-6} M). (*Bottom*) Emission spectra of Eu(L-S15)$_2$TTA in DMSO solutions upon addition of10 − 6 mol L^{-1} different anions (*left*); emission intensity at 619 nm of Eu(L–S15)$_2$TTA in the presence of 10^{-6} mol L^{-1} different anions. The emission spectra were collected at the excitation wavelength of 355 nm (Reprinted with permission from Ref. [38]. Copyright 2016 Elsevier)

mechanism for the luminescence quenching can be ascribed to the formation of hydrogen-bonding interaction between NH of organic ligand L-Si and F$^-$ demonstrated by^{1}HNMR experiments.

Zhou et al. use tetra-n-butyl titanate (TNBT) as the host and Tb^{3+} 2-isopropylim idazole-4,5-dicarboxylic acid complex to assemble a novel terbium hybrid titania xerogel [39]. The hybrids present a highly sensitive fluorescence response toward F^- to quench the luminescence of Tb^{3+} through the hydrogen-bonding interaction between the ligand and F^-.

8.4.2 *Photofunctional Hybrid Materials as Probes or Sensors for CrO_4^{2-} or $Cr_2O_7^{2-}$*

With the development of modern industry, contamination of water resource is causing a concern, especially toxic anion pollutants because of their biological hazard. Among common toxic anion pollutants, Cr (VI) species, i.e., CrO_4^{2-} and $Cr_2O_7^{2-}$, have been a core concern because it causes serious damage to human health and environment.

Xu et al. carry out the anion-sensing function by immersing Eu^{3+}@MIL-124 in different anion aqueous solutions (anion = F^-, Cl^-, Br^-, I^-, NO_3^-, SO_4^{2-}, CrO_4^{2-}, $Cr_2O_7^{2-}$) [17]. It is found that $Cr_2O_7^{2-}$ has the largest quenching effect on the luminescent emission which leads to a dark emission and has reduced the luminescent lifetime of Eu^{3+}@MIL-124 from 0.4 ms to 0.1 ms. The fluorescence of Eu^{3+}@MIL-124 is gradually quenched as the $Cr_2O_7^{2-}$ concentration increased. The quenched fluorescence intensity (I_0/I) of Eu^{3+}@MIL-124 has a good linear relationship to the $Cr_2O_7^{2-}$ concentration ($R = 0.99343$) in the concentration range of 10–500 μm $Cr_2O_7^{2-}$. Eu^{3+}@MIL-124 shows high selectivity to $Cr_2O_7^{2-}$(detection limit, 0.15 μM). Hao et al. investigate anion recognition of the Eu^{3+}@MIL-121 [40], whose intensity shows the quenching effect for most anions, while the quenching degree is heavily dependent on the species of anions (Fig. 8.25). Among the anions studied, the quenching effects of F^- and $Cr_2O_7^{2-}$ are very pronounced, especially for $Cr_2O_7^{2-}$ ion. Although both F^- and $Cr_2O_7^{2-}$ can seriously quench the emission of Eu^{3+}, they can be distinguished by Eu^{3+}@MIL-121. This is because F^- ion only has quenching effect on the Eu-luminescence but not on the LC emission, while $Cr_2O_7^{2-}$ cannot only quench the emission of Eu^{3+} but also have quenching effect on the emission of ligand, as shown in the inset of Fig. 8.25a. As a result, in the presence of $Cr_2O_7^{2-}$ and F^-, the luminescent color of Eu^{3+}@MIL-121 changes from red to blue and dark, respectively. To clearly illustrate the different degrees of quenching effects on the ligand emission by the F^- and $Cr_2O_7^{2-}$ ions, the pure ligands are immersed in the aqueous solutions containing F^- and $Cr_2O_7^{2-}$, respectively. As expected, $Cr_2O_7^{2-}$ totally quenches the emission of pure ligands, while F^- has no significantly quenching effect. These results imply that the Eu^{3+}@MIL-121 can selectively sense F^- and $Cr_2O_7^{2-}$ ions. The detection limit of Eu^{3+}@MIL-121 for $Cr_2O_7^{2-}$ and F^- is estimated to be 0.054 μM and 0.063 μM, respectively, which meets the requirement for pollutant sensing.

Weng et al. also study the potential of the Tb^{3+}@Cd-MOF for sensing anions [41], which shows the high selectivity to $Cr_2O_7^{2-}$ compared to other anions including MnO_4^-. The introduction of $Cr_2O_7^{2-}$ can affect the antenna effect to a certain

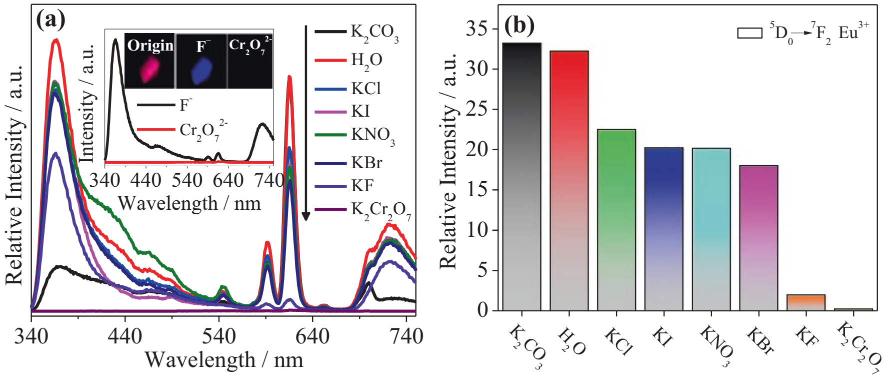

Fig. 8.25 (**a**) Suspension-state PL spectra and (**b**) the relative intensities of $^5D_0 \rightarrow {}^7F_2$ at 614 nm for Eu^{3+}@MIL-121 dispersed in aqueous solutions containing different anion ions (10 mM) when excited at 315 nm (Reprinted with permission from ref. [40]. Copyright 2014 The Royal Society of Chemistry)

extent, since the antenna effect plays an important role in the emission of lanthanide. The absorption of the ligand of Tb^{3+}@Cd-MOF almost overlaps with the DMF solution of $Cr_2O_7^{2-}$. The competition between the ligand and $Cr_2O_7^{2-}$ in the absorption of energy hinders the absorption of ligand directly and then affects the efficiency of energy transfer between the ligand and Tb^{3+} to lead to the luminescent quenching in the presence of $Cr_2O_7^{2-}$. Shen et al. select various anions (NO_3^-, SO_4^{2-}, Br^-, Cl^-, F^-, I^-, CrO_4^{2-}, $Cr_2O_7^{2-}$) to carry out the anion-sensing experiments in aqueous solutions of the hybrids $Y_{0.99}Eu_{0.01}$/Ad/BPDC [42]. $Cr_2O_7^{2-}$ has the largest quenching effect on the luminescent emission, showing the color change from red in original aqueous to dark in $Cr_2O_7^{2-}$ solution under the irradiation of UV light of 365 nm, completely quenching the $^5D_0 \rightarrow {}^7F_2$ of Eu^{3+}.

Duan et al. study the hybrids $[Y(BTC)(H_2O)_6]_2$:0.1Eu in sensing Cr (VI) anion species [43]. Under the high-anion concentration-sensing procedure, Cr (VI) anion species show remarkable quenching effect on europium emission (Fig. 8.26 (Left)). The luminescence quenching caused by $Cr_2O_7^{2-}$ along with CrO_4^{2-} is understandable for hydrolysis process, resulting in transformation between $Cr_2O_7^{2-}$ and CrO_4^{2-}. The selectivity of $[Y(BTC)(H_2O)_6]_2$:0.1Eu is tested by performing quenching experiments in pH = 7 aqueous suspensions, using both CrO_4^{2-} and $Cr_2O_7^{2-}$, as well as interferents, F^-, Cl^-, Br^-, I^-, NO_3^-, and SO_4^{2-} (Fig. 8.26 (Right)). The fluorescence is of the same quenched degree as the introduction of CrO_4^{2-}/$Cr_2O_7^{2-}$ to aqueous solution. Only in the low-concentration range, such as 0–300 mM, $[Y(BTC)(H_2O)_6]_2$:0.1Eu can be explored as an effectively selective sensing probe for $Cr_2O_7^{2-}$ and CrO_4^{2-} anions. The quenching mechanism of its luminescence caused by $Cr_2O_7^{2-}$ or CrO_4^{2-} anions can be probably ascribed to static quenching.

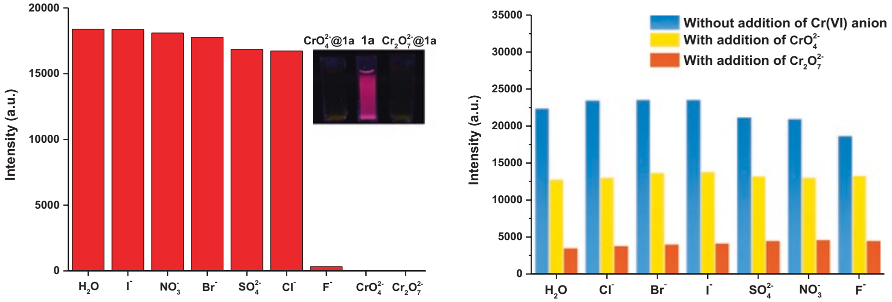

Fig. 8.26 (*Left*) Suspension-state PL spectra intensities of $^5D_0 \rightarrow {}^7F_2$ at 616 nm for **1a** dispersed in different anions in aqueous solution when excited at 295 nm. (*Right*) Intensity of $^5D_0 \rightarrow {}^7F_2$ at 616 nm of **1a** and **1a** with interferents (Reprinted with permission from Ref. [43]. Copyright 2016 Elsevier B.V)

8.4.3 Photofunctional Hybrid Materials as Probes or Sensors for Other Anions

Tan et al. prepare a hybrid silica-encapsulated terbium complex of 2-methylimidazole-4,5-dicarboxylic, showing strong green emission in pure water [44]. It is found that the luminescence of the hybrids is selectively and rapidly turned off by hydrogen sulfate HSO_4^-, whereas the addition of anions such as F^-, Cl^-, Br^-, and I^- did not change the luminescence. Tan et al. prepare two novel silica-based terbium complexes with 2-ethylimidazole-4,5-dicarboxylic acid (a) or 2-propylimidazole-4,5-dicarboxylic acid (b) in the poly(acrylamide) host with green emission in water [45]. It is interesting that they can selectively recognize H2PO4$^-$ (detection limit 10^{-5} M) and HSO4$^-$ (detection limit 5×10^{-5} M) compared with other anions, such as F^-, Cl^-, Br^-, and I^-. Zhou et al. prepare two silica-based lanthanide complexes (Eu^{3+},Tb^{3+}) with 2-(2-furyl)-4,5-imidazoledicarboxylic acid, which is incorporated into poly(N-isopropylacrylamide) to develop novel lanthanide luminescent hydrogels (Ha and Hb) as anion sensors [46]. It is interesting to discover that these target materials only give rise to luminescence response to HSO_4^- and can be reversibly used more than ten times, which is ascribed to anion's acidity for the emission quenching and the hydrogen-bonded forces between NH of imidazole. Upon addition of hydrogen sulfate from 10^{-6} to 10^{-5} M, the characteristic emission of Eu^{3+} decreases gradually and is quenched at last. The sharp and distinguished changes can be seen by the naked eye under the excitation of the ultraviolet light.

Wang et al. demonstrate that the sensing species (europium complex) can be covalently grafted onto the surface of SWNT [47]. It is interesting that only ClO^- can generate unique fluorescence quenching toward this sensing material in comparison with other anions. None of these anions can generate obvious fluorescence changes (less than 10%) for this sensing material. This nanoprobe provides a new example for the fabrication of a luminescent sensor used for the recognition of hypochlorite in water (Fig. 8.27). Zheng et al. have prepared a covalent lanthanide

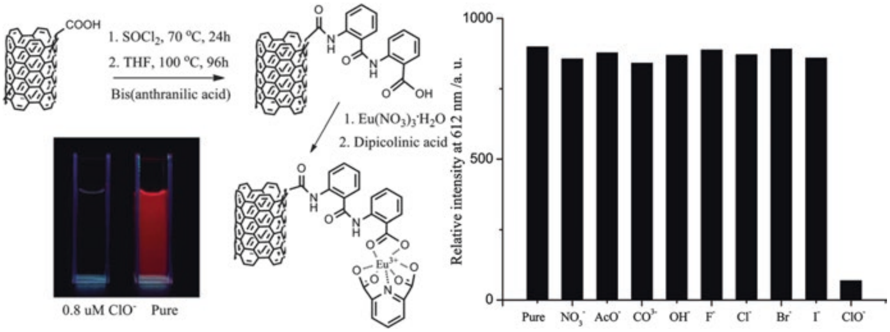

Fig. 8.27 (*Left*) Synthetic scheme for the single-walled carbon nanotube covalently modified with a luminescent europium complex (SWNT-4). (*Right*) Emission spectra of SWNT-4 (1 mg L^{-1} in water) excited at 280 nm in the presence of 10^{-5} $molL^{-1}$ of anions (Reprinted with permission from Ref. [47]. Copyright 2012 The Royal Society of Chemistry)

silica hybrid material Ha and a co-doped lanthanide silica hybrid material Hb, both of which possess strong green luminescence and can be used as smart sensors for the detection of nitrite ion NO_2^- upon addition of interference anions such as NO_3^-, Cl^-, $H_2PO_4^-$, F^-, HCO_3^-, Br-, ClO_3^-, AcO^-, I^-, and $C_2O_4^{2-}$ in pure water [48]. Zhou et al. synthesize two novel luminescent cellulose hydrogel films, which can be used for detecting of nitrite [49]. The excellent hydrogels can be served as easily applicable and portable tools to monitor nitrite in the fields of biology and environment.

Sun et al. present a facile, rapid selective strategy for the ratiometric sensing toward carbonate ions based on robust and porous Eu/Pt-MOFs [50]. The hybrid system shows dual-emission spectrum, ligand-centered broad bands, and characteristic $^5D_0 \rightarrow {}^7F_J$ ($J = 0 \sim 4$) transitions of Eu^{3+}, respectively, which lay the foundation for ratiometric sensing. The sensing property toward a variety of environmentally and biologically relevant anions is further checked. It reveals that the interaction with CO_3^{2-} drastically enhances the luminescence intensity of Eu^{3+}, contributing to the maximum ratio of two fluorescence intensity ($I_{Eu(614)}/I_{Ligand}$) upon addition of carbonate ion. It is believed that the proposed sensing methodology might be an efficient tool for analytical monitoring of trace CO_3^{2-} in real sample analysis. Moreover, the proposed method is superior to the previously reported sensor as it possesses high orientation selectivity toward CO_3^{2-}.

8.5 Photofunctional Hybrid Materials as Probes or Sensors for Molecules

The most common molecules are organic pollutants, which are increasingly concerned for their environmental biological hazards.

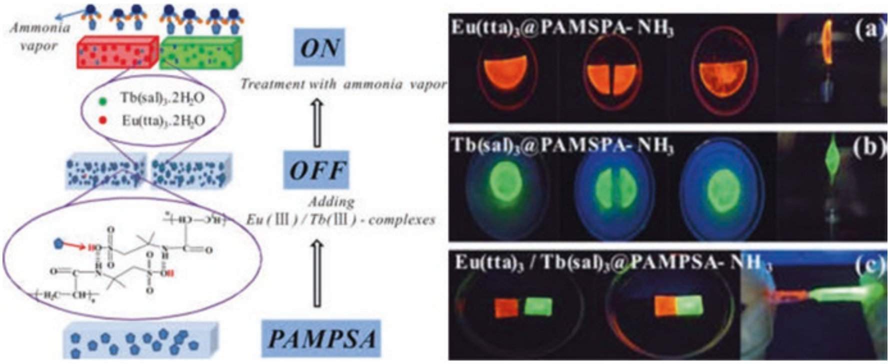

Fig. 8.28 Luminescence switching mechanism of the hybrid hydrogels (*Left*). Self-healing process of hybrid hydrogels after exposure to NH_3 vapor under a UV lamp (λ_{ex} = 365 nm) (*Right*) (Reprinted with permission from Ref. [51]. Copyright 2015 American Chemical Society)

Yao et al. prepare responsive hydrogels by simply doping lanthanide complexes into a polymer hydrogel, poly(2-acrylamido-2-methyl-1-propanesulfonicacid) (PAMPSA) [51]. They exhibit effectively self-healing performance without any external stimulus and reversible "on – off" luminescence switching triggered by exposure to acid – base vapor, whose key is that the protonation of the organic ligands competes with full coordination to Ln^{3+} and that incomplete coordination affects the luminescence yield. The high proton strength in the resulting hydrogels makes the doped lanthanide complexes unstable, and ammonia (or triethylamine) vapor can dramatically decrease the proton strength through neutralization, driving the full coordination of the ligand to Ln^{3+} (Fig. 8.28 (Left)). The characteristic emission color of both hybrid hydrogels is "switched on." Further treatment with HCl gas increases the acidity of the hydrogel to "switch off" the emission color again. Furthermore, they also examine the self-healing process of NH_3-treatment hybrid hydrogels by cutting both hybrid hydrogels with different shapes into two pieces. For 30 min, the two pieces heal as a single one through self-healing, and no obvious damage to the healed area is observed, which is strong enough to carry a 1 kg weight without damage. So the dynamic hydrogen bond is not obviously decomposed by NH_3 vapor (Fig. 8.28 (Right)a, b). Both $Eu(TTA)_3$@PAMPS-NH_3 and $Tb(sal)_3$@PAMPSA-NH3 can merge together with slight pressing (Fig. 8.28 (Right) c). These results suggest that the hybrid hydrogels after treatment with NH3 vapor also display effective self-healing ability.

Li et al. design a simple and robust platform for detecting basic molecule vapors based on the encapsulation of Eu^{3+}-β-diketonate complexes within a nanozeolite L framework [52]. The stationary and time-resolved spectroscopy studies suggest that the mechanism responsible for the turn on response to basic molecule vapors is that basic molecules are favorable for the formation of Eu^{3+}-β-diketonate complexes with high coordination numbers by decreasing the proton strength of the channels. The turn on luminescence response can be switched off by acidic vapors.

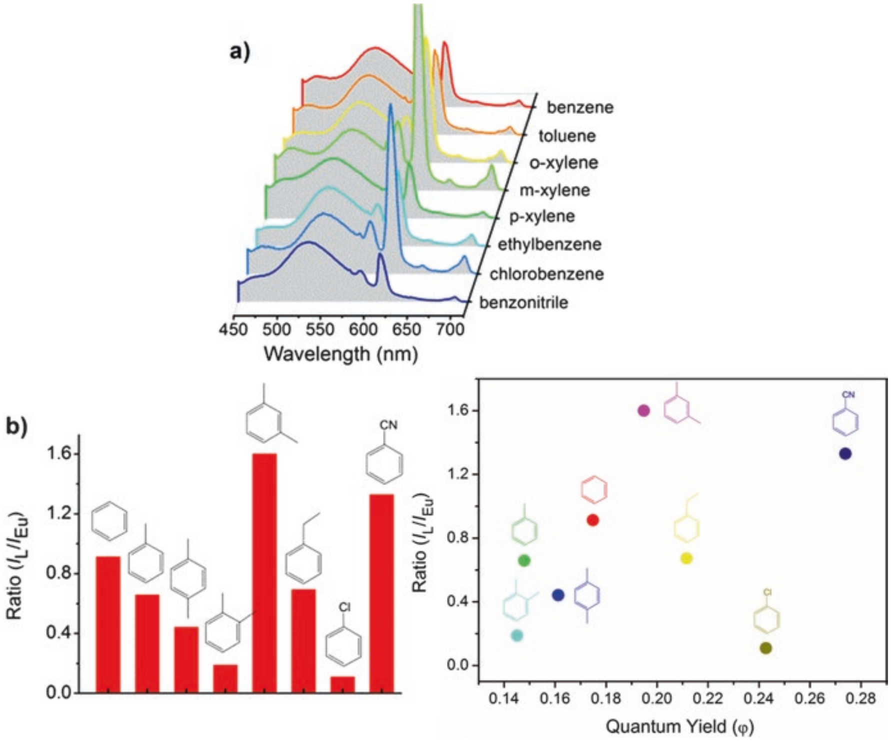

Fig. 8.29 (*Left*) The emission spectra (**a**) and I_L/I_{Eu} intensity ratios (**b**) of Eu^{3+}@UiO-bpy after the encapsulation of different aromatic VOCs. The emission spectra ($\lambda_{ex} = 355$ nm) are normalized to the intensity of the ligand emission. (*Right*) A 2D decoded map of the aromatic VOCs based on the emission intensity ratio (I_L/I_{Eu}) and quantum yield (Φ) responses of Eu^{3+}@bpy-UiO nanohybrid toward the VOCs accommodation (Reprinted with permission from Ref. [53]. Copyright 2016 The Royal Society of Chemistry)

Zhou et al. check the capability of Eu^{3+}@bpy-UiO nanohybrids in volatile organic compounds (VOCs) sensing [53]. Figure 8.29 (Left) a presents the emission spectra of Eu^{3+}@bpy-UiO after different VOCs accommodation, which shows sensitive ratiometric luminescence responses toward various VOCs. The intensity ratio of the ligand-based emission to Eu^{3+} emission (I_L/I_{Eu}) significantly depends on the included VOCs. Moreover, the ratiometric luminescence of Eu^{3+}@bpy-UiO is highly responsive to different concentrations of VOCs and mixed VOCs. As shown in Fig. 8.29 (Left) b, there is a one-to-one correspondence between the resulting I_L/I_{Eu} and the encapsulated VOCs. Therefore, these VOCs can be readily decoded by monitoring the ratiometric emission intensity (I_L/I_{Eu}) of the host MOF composite. Such a self-referencing strategy can circumvent the complications existing in intensity measurement of a single emission, such as the errors introduced by optical occlusion, concentration inhomogeneities, excitation power fluctuations, or environment-induced non-radiative relaxation, thus is more accurate and reliable. In

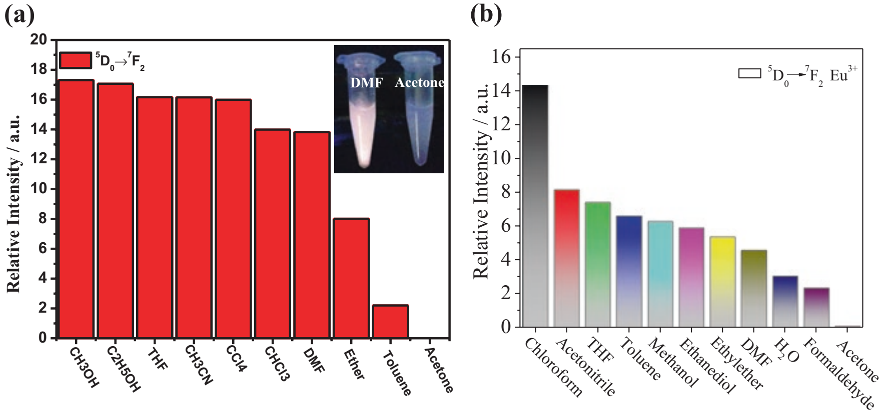

Fig. 8.30 Luminescence intensity of the $^4D_0$-$^7F_2$ of Eu^{3+} Eu^{3+}@MIL-124 (**a**) and Eu^{3+}@MIL-121 (**b**) dispersed into different organic small molecules (Reprinted with permission from Ref. [17, 40]. Copyright 2015 American Chemical Society, Copyright 2016 the Centre National de la Recherche Scientifique (CNRS) and the Royal Society of Chemistry)

addition, the luminescence quantum yield of the Eu^{3+}@bpy-UiO nanohybrid is also responsive to the accommodation of VOCs. Since the information of the VOCs can be carried by the ratiometric emission intensity and luminescence quantum yield (Φ) of the VOCs included Eu^{3+}@bpy-UiO, each of the VOCs is related to one unique two-dimensional (2D) readout (I_L/I_{Eu}, Φ) arranged in a decoded map (Fig. 8.29 (Right)). These readouts are well separated and identified in the decoded map, suggesting that one can precisely differentiate these VOCs through a ratiometric emission intensity and luminescence quantum yield-dual readout process.

Xu et al. examine the potential of Eu^{3+}@MIL-124 for the sensing of organic small molecules [17]. The photoluminescent spectra are significantly dependent on the solvent molecules, particularly in the case of acetone, which exhibit clearly quenching effects. The remarkable quenching effect can be further confirmed by the photograph of the Eu^{3+}@MIL-124 suspension under UV-light irradiation (Fig. 8.30a). Hao et al. examine the potential of Eu^{3+}@MIL-121 for the sensing of organic small molecules, whose luminescent recognition and selectivity in different solvent suspensions are investigated [40]. Figure 8.30b shows that the luminescence of Eu^{3+} is significantly dependent on the solvent molecules, particularly in the case of chloroform and acetone, which exhibit the most noticeable enhancing and quenching effects, respectively. Such solvent-dependent luminescent properties are of interest for the sensing of chloroform and acetone, harmful to human beings. It is noticeable that the luminescent intensity of the suspension of Eu^{3+}@MIL-121 increases with the addition of chloroform, and the enhancement is nearly proportional to the content of chloroform. Conversely, addition of acetone into the standard suspension of Eu^{3+}@MIL-121 leads to a significant decrease of the fluorescence intensity, which almost disappears at 8 vol % acetone content.

Weng et al. select Tb^{3+}@Cd-MOF hybrid system for sensing a series of small organic molecules [41]. Comparing to other organic molecules, pyridine and acetone show clearly quenching effects. The absorption band of the ligand of Tb^{3+}@Cd-MOF is completely overlaid by the absorption band of acetone, which reduces the absorption of light by organic ligand. Meanwhile, energy exchange occurs between the MOF, and acetone molecules can result in the decrease of luminescent intensity, even quenching. To elucidate the possible mechanism for the luminescent quenching induced by the pyridine solvent, they perform guest-replacement experiment by refluxing the Tb^{3+}@MOF with low-boiling solvent methanol to get guest-solvent-free MOF, whose crystal transformation causes the change of coordination environment by pyridine.

Shen et al. investigate Eu^{3+}-β-diketonate modified bio-MOF-1 hybrid material for sensing volatile organic molecule, especially volatile amines, which is of great significance in environment and industrial monitor [54]. Histogram in Fig. 8.31a shows a remarkable enhancement in luminescence intensity can be observed for vapors of NH_3 and ethylenediamine. A series of organic amines and one kind of organic acid are selected in order to further study the luminescent trend and inherent mechanism (Fig. 8.31b). The enhancement in emission intensity by a factor of 14, 9, and 4 for vapors of diethylamine ($(C_2H_5)_2NH$), triethylamine (Et_3N), and NH_3, respectively, whereas an intense quench effect occurs when exposed to formic acid (FA)V. Another interesting phenomenon in the embedded luminescent spectrum is that the formic acid only quenches the characteristic emission of europium ions, while the emission of the host material retains. The digital photographs of theses samples in the insets of Fig. 8.32a have changed accordingly. It is visual that the color has shifted from bright red in diethylamine to pink in NH_3 and then light purple in the acidic environment under UV excitation of 365 nm.

Shen et al. select $[HDMA]_2[Zn_2(BDC)_3(DMA)]\cdot 6DMF$ (**1**) ($HDMA^+$: dimethylamonnium, BDC^{2-}: 1,4-benzenedicarboxilate, DMA: dimethylamine, and DMF: N,N′-dimethylformamide) as host materials to exchange cation with external ions, such as lanthanides and cationic organic dyes [55]. It displays the luminescent response for sensing organic solvent molecules, including 1,4-dioxane, acetone, methanol, ethanol, acetonitrile, diethyl ether, $CHCl_3$, $CHCl_2$, THF, ethyl acetate, and DMF (Fig. 8.32a). Among them acetone has the strongest quenching effect, indicating that 2%RhB@**1** can only selectively sense acetone solvent. When it comes to several volatile organic benzenes with very similar structural motifs (Fig. 8.32b), quenching effect is observed in aniline with sharply decreased luminescent intensity.

Weng et al. prepare highly luminescent hybrids N-GQDs/Eu^{3+}@Mg-MOF (N-GQDs = N atom-doped graphene quantum dots, Mg-MOF = $\{[Mg_3(ndc)_{2.5}(HCO_2)_2(H_2O)][NH_2Me_2]\cdot 2H_2O\cdot DMF\}$), whose 349 nm and 394 nm excitations are both used to explore the capability in BTEX sensing [56]. When excited at 349 nm, the intensity ratio of the ligand-based emission to Eu^{3+} emission (I_L/I_{Eu}) depends on the encapsulated BTEX vapors in a certain degree. Toluene included N-GQDs/Eu^{3+}@Mg-MOF has the largest value of I_L/IEu, while phenylethane has the lowest value of I_L/I_{Eu}. When excited at 394 nm, the intensity ratio of the emission peak located at

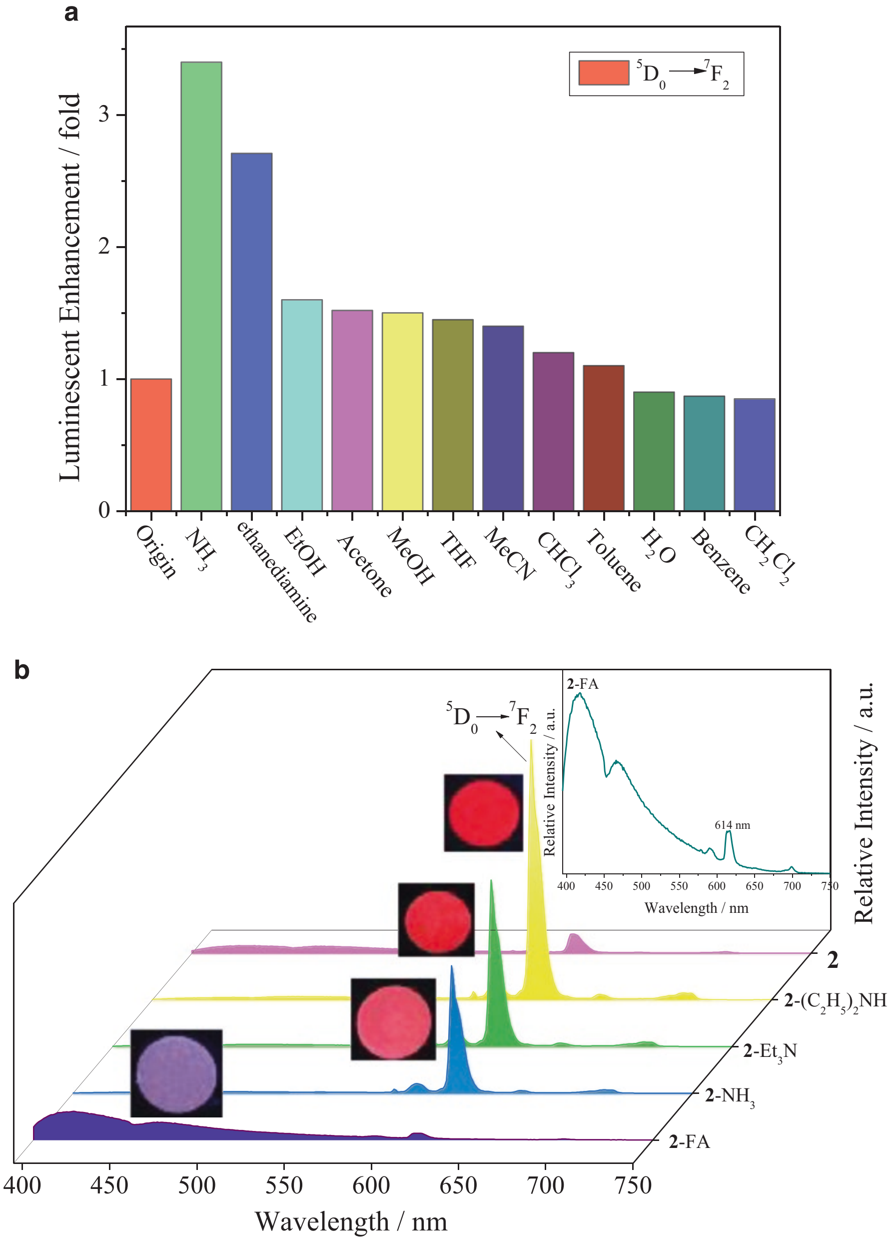

Fig. 8.31 (**a**) Histogram of an enhancement in the emission intensity of $^5D_0 \rightarrow {}^7F_2$ transition at 614 nm after exposure to vapors of various organic molecule solvents. (**b**) The luminescent spectra and digital photos (under UV irradiation of 365 nm) when exposed to vapors of three kinds of organic amines such as $(C_2H_5)_2NH$, Et_3N, and NH_3 and one kind of organic acid, formic acid. Inset is an enlarged spectrum of **2**-FA from 400 nm to 750 nm (Reprinted with permission from Ref. [54]. Copyright 2015 The Royal Society of Chemistry)

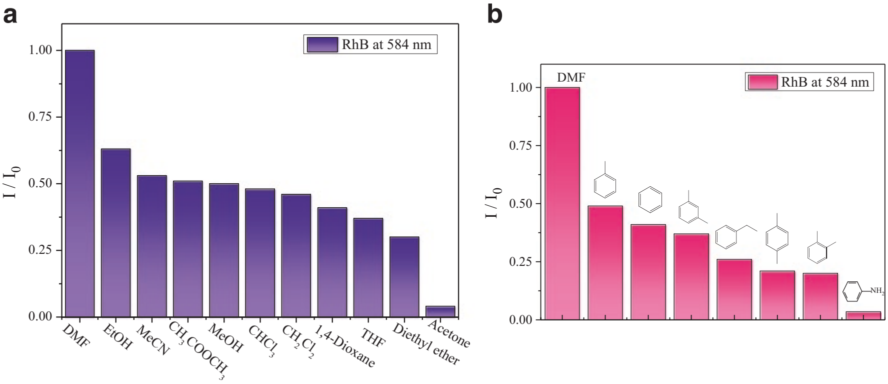

Fig. 8.32 The solvent-dependent luminescent intensity of 2%RhB@**1** dispersed into several organic small molecules (**a**) as well as volatile organic benzenes (**b**) (Reprinted with permission from Ref. [55]. Copyright 2016 The Royal Society of Chemistry)

618 nm to 443 nm is varying with different BTEX vapor. However, when the hybrid system is exposed to the vapors of BTEX for 1 hour, the ratio of the QD-based emission to Eu^{3+} emission (I_{Eu}/ $I_{N\text{-}GQDs}$) has changed, where m-xylene has the largest I_{Eu}/ $I_{N\text{-}GQDs}$ and acetophenone has the lowest one. Unfortunately it is hard to distinguish benzene and toluene relying on the ratio merely.

Lian et al. examine the potential of the MOF-76(Eu) hybrids for the sensing of BTEX molecules (Fig. 8.33) [57], whose intensities at 614 nm are strongly influenced by the solvent, especially in the case of acetophenone showing the conspicuous significant quenching effects. The different effects on the emission between acetophenone and other solvents are clearly observed, indicating that MOF-76(Eu) can be considered as a promising luminescent probe for acetophenone. Analogous materials MOF-76(Tb) exhibits similar behavior with MOF-76(Eu), and its luminescence intensity is responding to acetophenone, reducing rapidly with the increasing content of acetophenone. However, it is notable that the fluorescence of MOF-76(Tb) disappears just as an acetophenone content of 2.0 Vol % (Fig. 8.33c). This indicates that nanosized MOF-76(Tb) shows a high capacity to discriminate acetophenone molecule among other BTEX volatiles.

Xu et al. prepare a portable luminescent LnMOF film by in situ growing nanoscale SUMOF-6-Eu on oxidation-treated nonwoven polypropylene surface (NMOFs@O-PP) (Fig. 8.34) [58]. Upon polydimethysiloxane (PDMS)-coating treatment, the film shows good water resistance without employing any surface area and crystalline structure changes. By controlling the excitation wavelength, they can predict and tune the emission of coated NMOFs@O-PP film in dual-emission bands (I_L and I_{Eu}). Due to the disturbance of energy transfer processes from ligand to Eu^{3+} in NMOFs by O_2, coated NMOFs@O-PP film can be used in ratiometric O_2 sensing. With new assembly method for O_2 sensing, coated NMOFs@O-PP film shows high O_2 sensitivity ($K_{sv} = 6.73$, LOD = 0.45%), short response/recovery time (10/60 s), and good reversibility. The combination of nanoscale SUMOF-Eu-6 is

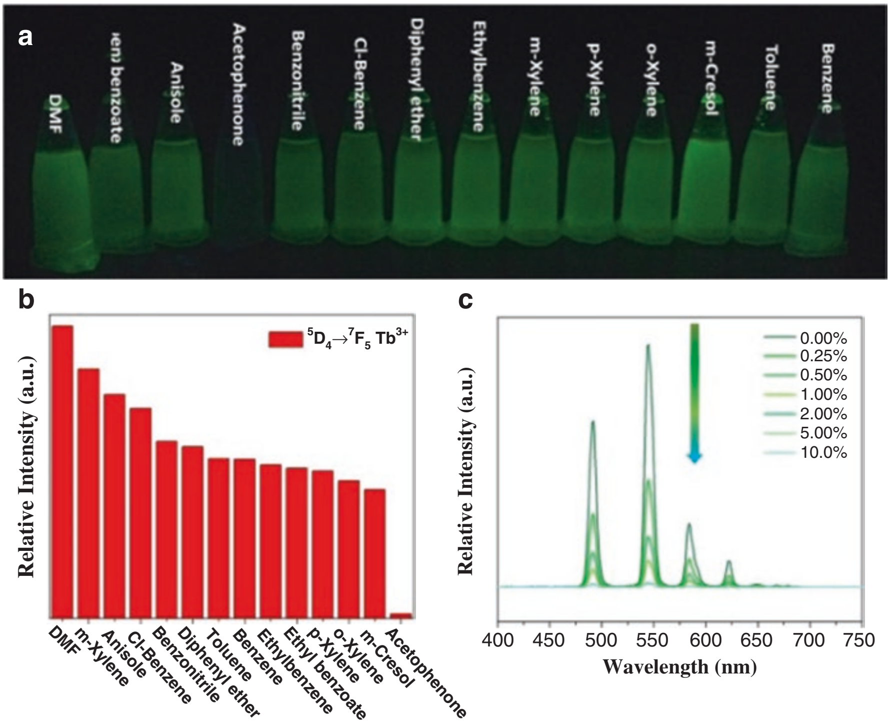

Fig. 8.33 (**a**) Photograph of the various mixtures consisting of MOF-76(Tb) and different BTEX solvents; (**b**) the $^5D_4 \rightarrow {}^7F_5$ transition intensity ratios from the emission spectra of MOF-76(Tb) introduced into various pure BTEX solvents when excited at 296 nm; (**c**) emission spectra of MOF-76(Tb) dispersed in different content acetophenone-DMF mixed solvent (Reprinted with permission from Ref. [57]. Copyright 2016 The Royal Society of Chemistry)

expected to be more reliable and powerful in O_2 sensing in comparison with the conventional detection systems for its advantages such as ideal luminescence characteristics and high porosity, flexible substrate with good O_2 permeability, and low-density and PDMS-coated layer as water-resistant protective layer to maximize the available information.

8.6 Photofunctional Hybrid Materials as Probes or Sensors for Special Molecule Species or Indices

Urine can reflect physiological and biochemical parameters, urine constituents' measurements as evaluation of Biological Exposure Indices (BEIs) are used in several fields of occupations. Among them, urine hippuric acid (HA) is the ultimate and major metabolites of toluene, which is considered as the biological indicators of toluene exposure. Approximately 80% of the inhaled toluene is excreted in urine as

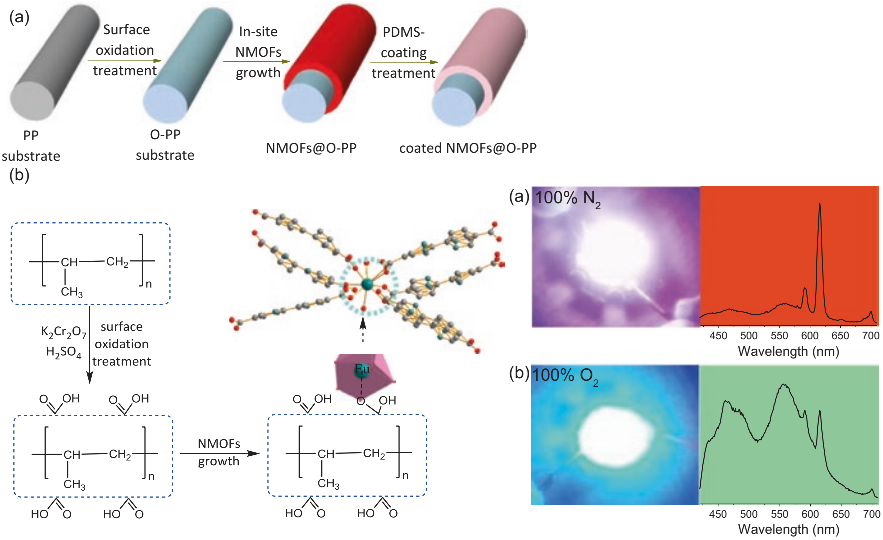

Fig. 8.34 (*Left*) (***a***) Schematic of O_2 sensor's synthesis route: nonwoven polypropylene (PP) carboxylation, nanoscale SUMOF-6-Eu (NMOFs) growth, and hydrophobic polydimethysiloxane (PDMS) coating; (*b*) carboxylation of PP substrate and a proposed mechanism of SUMOF-6-Eu formation and immobilization on the surface of PP; and (*Right*) photographs of 395 nm LED modified by coated NMOFs@O-PP and emission spectra of coated NMOFs@O-PP under 100% N_2 (*a*) and 100% O_2 (*b*) (Reprinted with permission from Ref. [58]. Copyright 2016 The Royal Society of Chemistry)

HA, and the urinary concentration of HA is proportional to the level of toluene exposure. Therefore, simple monitoring of exposure to toluene is very important in occupational health care. However, the heterogeneous factors of individuals, monitoring the environmental toluene, could not accurately estimate people's real intoxication level, so it is more significant to determine the concentration of toluene's metabolites (HA) in human body. This can better reflect the real toluene exposure and intoxication of human beings.

Hao et al. report a new method based on a fluorescent sensor for determination of urinary HA [59]. A Eu-functionalized MIL-121 hybrid with extremely high water toleration is presented as a highly selective and sensitive luminescent probe for HA. The sensor for detection of HA simultaneously realizes easy preparation, short response time, broad linear range, and quick regeneration. The above excellent performances of the sensor make it capable of determining HA in human urines with recoveries in the range of 93.5–102.9%. Through soaking of the freshly prepared samples in ethanol solutions of europium chloride, Eu^{3+} ions are introduced into the channels of **1**, yielding Eu^{3+}@**1** (Fig. 8.35 (Top)). The ingredients of human urine mainly include H_2O, creatinine (Cre), creatine, urea, uric acid (UA), hippuric acid (HA), SO_4^{2-}, Na^+, K^+, NH_4^+, Cl^-, or glucose (Glu). Hence, in chemistry, urine can be defined as water solutions containing various chemicals. Eu^{3+}@ MIL-121 are insoluble and stable in these various chemicals' aqueous solutions. Only HA induced a remarkable reduction (84%) of luminescence intensity of Eu^{3+}@**1** at

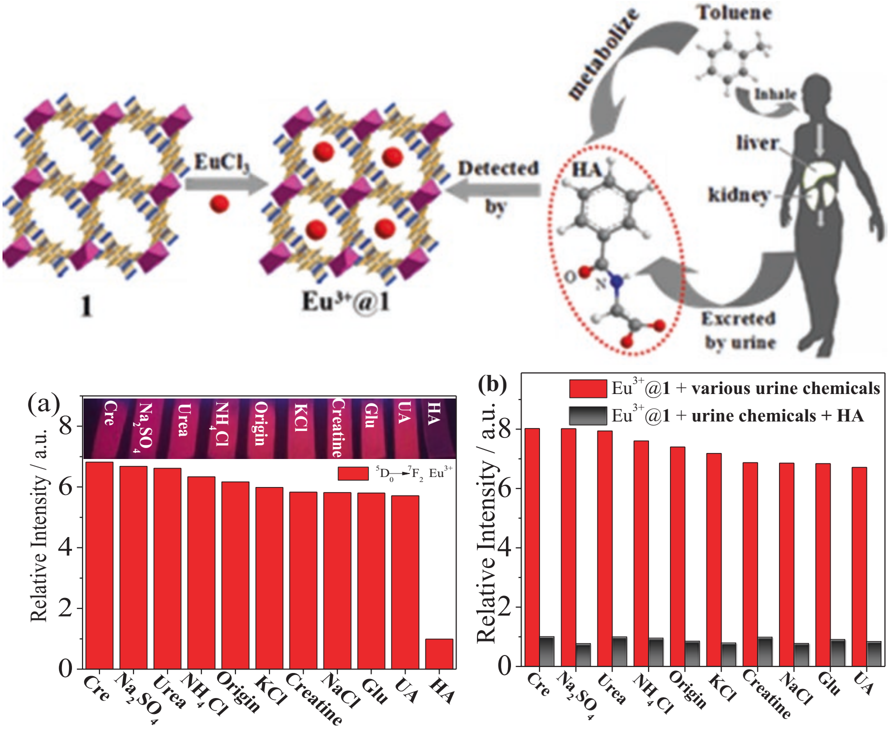

Fig. 8.35 (*Top*) Schematic representation of the fabricated Eu^{3+}@**1** as a fluorescent sensor for urinary HA. (*Bottom*) (**a**) Luminescent intensities of $^5D_0 \rightarrow {}^7F_2$ at 614 nm for Eu^{3+}@**1** dispersed in various metal ions aqueous solutions (10 mM) (λ_{ex} = 315 nm). *Inset*: the corresponding photographs under 254 nm UV-light irradiation. (**b**) Luminescence responses of Eu^{3+}@**1** (1 mg/mL) upon the addition of HA (0.01 M) in the presence of background of various urine chemicals (0.02 M) in aqueous solution (λ_{ex} = 315 nm) (Reprinted with permission from Ref. [59]. Copyright 2015 The Royal Society of Chemistry)

614 nm. Under the irradiation of a UV lamp, only HA-incorporated Eu^{3+}@ MIL-121 shows a significantly darker luminescence than that from the original one, which can be distinguished easily by the naked eyes (inset of Fig. 8.35 (Bottom) a). So the high selectivity of the hybrid is attained to HA in aqueous media. As shown in Fig. 8.35 (Bottom) b, when HA is added into the solution of Eu^{3+}@ MIL-121 with excess amount of other urine chemicals, the intensity change at 614 nm displays a similar pattern to that with HA only, suggesting the quenching effect of HA on the emission of Eu^{3+} is not influenced by the coexisting components, further confirming that Eu^{3+}@**1** acts as a promising sensor for HA.

The distribution diagrams of HA levels in the nonexposed and exposed individuals are depicted in Fig. 8.36 (Top). The average level of HA in nonexposed urine specimens determined by the sensor is 0.366 ± 0.243 mg/mL. The HA level in the 15 studied organic chemistry researchers varies from 0.19 to 4.3 mg/mL (Fig. 8.36 (Top) B). Among the analysis results of specimens, three of them turn out to be positive (HA level $>$ 2.0 mg/mL), indicating these three students have high probability of

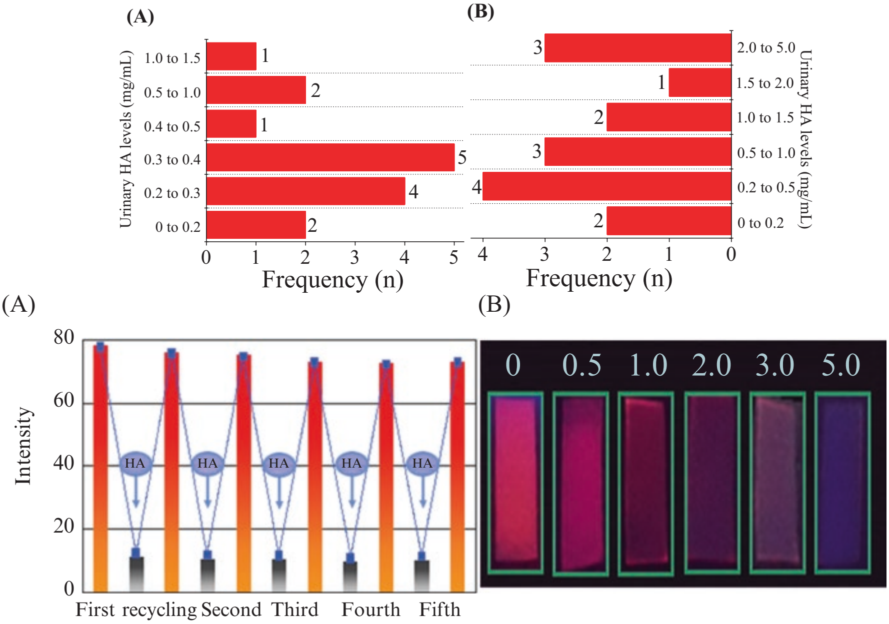

Fig. 8.36 (*Top*) Distributions of HA concentration in the urines of nonexposed (*A*) and exposed (*B*) individuals. (*Bottom*) The luminescence intensity of Eu^{3+}@**1** at 614 nm after five recycles. (λ_{ex} = 315 nm) (*A*) and Optical images under 254 nm UV-light irradiation of the test paper after immersing into urines with different concentrations (mg/mL) of spiked HA for 1 min.(*B*) (Reprinted with permission from Ref. [59].Copyright 2015 The Royal Society of Chemistry)

being overexposed to toluene. The regenerable performance of a sensor plays an important role in its applications. After the fluorescence reduction induced by HA, the following ultrasonic washing will make the fluorescence intensity recover to the level before HA addition (Fig. 8.36 (Bottom) A). After five runs performed by sequential addition of HA and ultrasonic washing, the luminescent intensity of the recycled Eu^{3+}@1 is well consistent with that of the original one, suggesting that Eu^{3+}@**1** can be reused to detect HA. Additionally, the fast and simple regeneration method also implies that the interaction between Eu^{3+}@**1** and HA should be weak and the luminescence of Eu^{3+}@**1** recovered by ultrasonic washing is due to the removal of HA. All the above results demonstrate that the newly designed method is suitable for analysis of HA in human urine. Furthermore, a fluorescent test paper for rapid detection of urinary HA is developed. Under the irradiation of UV light of 254 nm, the fluorescent colors of the test paper changed from bright red to dark red, faint red, and finally black as soaked in 0.5, 1.0, 2.0, 3.0, and 5.0 mg/mL of HA-spiked urines (Fig. 8.36(Bottom)B). With the naked eyes, one can distinguish the colors of different intensities, thus judging the degree of toluene intoxication.

The indoor air quality has great effect on people's health. Indoor air pollution (IAP) is gaining more and more attention with the improvement of living standard and indoor decoration gradually becoming popular. Ammonia (NH_3) has higher over-standard rate and ranks highest in the indoor air pollution. Such a colorless,

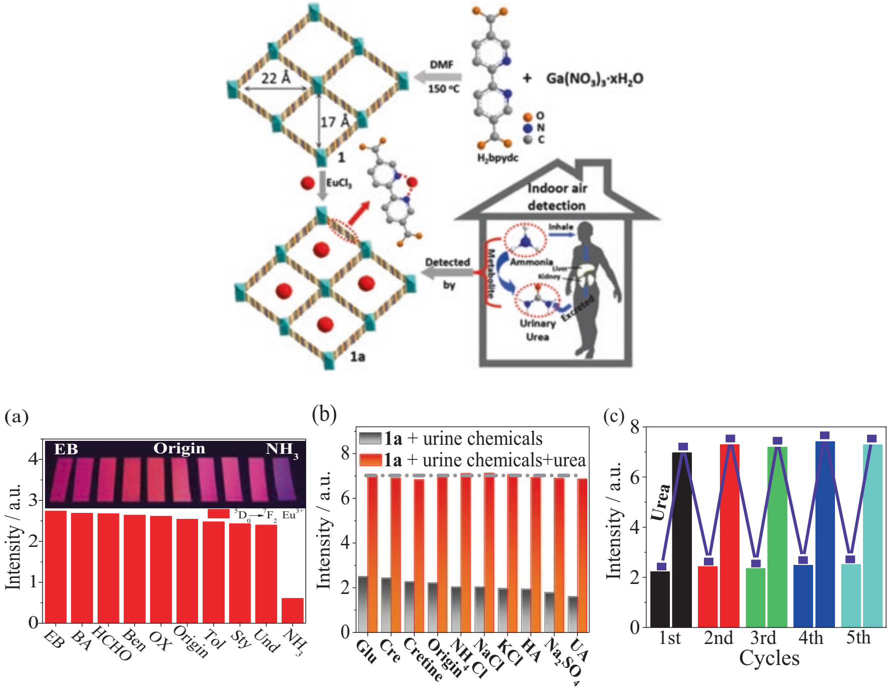

Fig. 8.37 (*Top*) Schematic representation of synthesis route of nanocrystal 1a as a fluorescent sensor for indoor ammonia and its biological metabolite (urinary urea) in human body. (*Bottom*) (*a*) The relative emission intensities at 614 nm (λ_{ex} = 338 nm), the inset shows the corresponding photographs under 365 nm UV-light irradiation. (*b*) Luminescence responses of **1a** (1 mg/mL) upon the addition of urea (0.01 M) in the presence of background of various urine chemicals (0.02 M) in aqueous solution (λ_{ex} = 338 nm). (*c*) The regeneration cycles of **1a** sensor used in detecting urea (Reprinted with permission from Ref. [60]. Copyright 2016 The Royal Society of Chemistry)

volatile, and corrosive gas with a pungent odor is toxic and harmful to humans' health. So it is highly necessary to design and fabricate a long-term reliable, highly sensitive, miniaturized, room-temperature-efficient, and no-humidity-impact ammonia gas sensor, which can detect and monitor indoor NH_3 concentration in real time. The main outlet of inhaled ammonia in human body is mainly excreted by the kidneys as urea and urinary ammonium compounds. What's more, researches have shown that exposure to 13 mg/m^3 ammonia for 8 h will lead to the increase of urea content in human urine. Therefore, besides monitoring indoor ammonia, it is also necessary to determine the concentration of ammonia's metabolite (urinary urea) in human body by the probe to comprehensively reflect the real ammonia exposure and intoxication of human beings.

Hao et al. develop a luminescent sensor for both ammonia and urea based on a europium-functionalized Ga(OH)(bpydc) via coordination to the accessible 2,2′-bipyridine sites on the linker molecule (Fig. 8.37 (Top)) [60]. Under the irradiation of a UV lamp, only the hybrid film-absorbed NH_3 shows a significantly darker luminescence than that from the original one, which can be distinguished easily by the naked eyes (inset of Fig. 8.37 (Bottom) a). The different effects on the emission between NH_3 and other vapors are clearly observed, which is indicative of the fact that Eu^{3+} hybrid film can be considered as a promising luminescent probe for NH_3. Figure 8.37 (Bottom) b shows the fluorescence response of the hybrid system to urea in the presence of other urine chemicals. The emission intensity enhancement induced by urea is not affected by the coexisting components, further confirming that the hybrid system is a highly selective probe for urea. In order to quantitatively describe the relationship between the enhancing efficiency and the concentration, the responses of the sensor to increasing urea concentration are investigated. The hybrid sensor for urea can also be regenerated and reused by centrifuging the dispersed powder in urea aqueous solutions and washing with water for several times. After five consecutive cycles of enhancing and recovery, its luminescent intensity in water is comparable to the initial state (Fig. 8.37 (Bottom) c).

Formaldehyde (FA), as one of the typical indoor air pollutants, is classified as a human carcinogen, which is mainly released from building and indoor decorative materials such as pressed wood, coated paper products, paints, and so on. Such a colorless, volatile, and deleterious gas with a pungent and suffocating odor poses a serious health hazard to human beings by causing central nervous system damage, blood and immune system disorders, respiratory disease, etc. In order to protect people from excessive FA exposure, the indoor FA detection is of great importance and in huge demand for human health.

Hao et al. fabricate a dual-emissive Ag(I)-Eu(III) functionalized MOF nanohybrid (Ag^+/Eu^{3+}@Uio-66) and utilize it as a self-calibrated and ratiometric luminescent sensor for detecting indoor FA [61]. The centered Eu^{3+} and organic ligands of this hybrid material are the two luminescent centers for self-calibrating purpose. Their luminescent characters are governed by the coordinated Ag^+ because of its ability to alter the electronic structure and energy transfer process in the compound. FA can interact with Ag^+ and change the luminescent behaviors of the nanohybrid by weakening the Ag^+ ions' influence on the energy transfer process in the compound. Gas sensors for practical applications are required not only to have high sensing response but also very good selectivity to the targeted gases. Therefore, under the same conditions as used above for FA, the fluorescent responses of these hybrid sensors toward other typical indoor polluted gases such as benzene (Ben), ammonia (NH_3), toluene (Tol), TVOC {butyl acetate (BA), ethylbenzene (EB), n-Undecane (Und), o-xylene (OX)} are also tested, as shown in Fig. 8.38 (Top). Their I_{Eu}/I_L data of the above sensors are shown as the bar diagrams in Fig. 8.38 (Bottom) a. It can be found that the pure Eu^{3+}@Uio-66 does not show obvious selectivity for FA vapors. On the contrary, the Ag^+-loaded film sensors exhibit excellent selectivity for FA, which can be proved by the fact that only FA induced an obvious enhancement and all other vapors did not cause evident changes of the I_{Eu}/I_L values. To further explore the anti-interference ability for FA sensing, the competition experiments are performed by exposing the sensing films to the mixed vapors of FA and other typical interference indoor gases for 1 h at 25 °C. The fluorescence responses (I_{Eu}/I_L) of this sensor to FA with various disturbed gases are similar to that

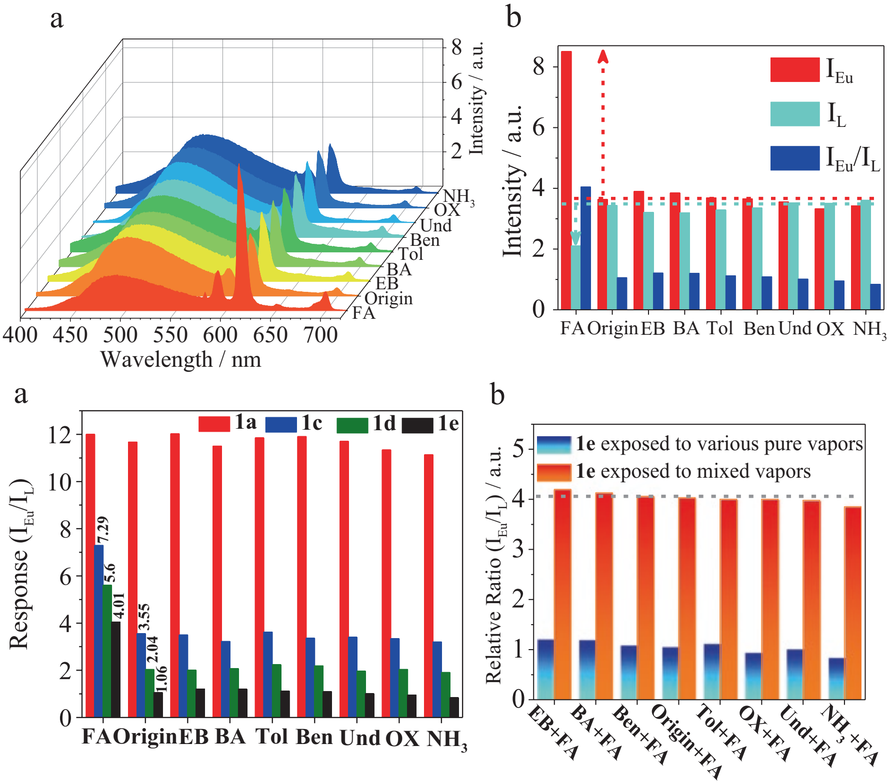

Fig. 8.38 (*Top*) The fluorescent spectra (*a*) and the intensities (I_{Eu}, I_L, and I_{Eu}/I_L) (*b*) of **1e** films after treated with various indoor polluted gases. (*Bottom*) (*a*) The responses of different sensors (**1a**, **1c**, **1d**, and **1e** films) to various indoor-polluted gases; (*b*) luminescence responses of **1e** films toward FA gas in the presence of background of other various indoor air pollutants ($\lambda_{ex} = 330$ nm) (Reprinted with permission from Ref. [61]. Copyright 2016 The Royal Society of Chemistry)

with FA only (Fig. 8.38 (Bottom) b), indicating the enhancement effect of FA on the I_{Eu}/I_L is not influenced by the coexisting gas pollutants.

More recently, Xu et al. fabricate a ZnO-doped Uio-MOFs heterostructures (ZnO@Uio-MOFs) through a facile solvothermal reaction. After introducing the Eu^{3+} fluorescent center using a postsynthetic method, the heterostructures have been tuned to a dual-emitting material (I_{614} and I_{470}) by controlling the excitation wavelength [62]. When exposing the material to aldehyde gases, the excellent selective, sensitive, and reusable fluorescent responses are obtained, which could be ascribed to the following reasons: firstly, the reduced aldehyde molecules can build the bridge from the charge transfer from ZnO to Eu^{3+} to increase the intensity of I_{614} and realize selective sensing; secondly, the open-connected channels and high-surface area of Uio-MOFs can facilitate the effective adsorption of aldehydes leading to a low-detection limit (42 ppb for FA, 58 ppb for AA and 66 ppb for ACA); and, thirdly, efficient charge transfer from MOFs to ZnO gives the possibility of reusable detection of aldehyde gases. In addition, the proposed sensing method also shows stable and reliable fluorescent response for aldehydes in different exposing temperature (25–65 °C). The excellent sensing property of Eu^{3+}-functionalized heterostructures for polluted aldehyde gases will make it suitable for practical application in vehicle detection.

PAHs are of the largest class of chemical contaminants known to be cancer-causing agents and have been ranked the ninth most threatening chemical compounds to human health. Due to their formation during incomplete combustion or pyrolysis of organic materials, PAHs are found ubiquitously not only in all different environmental media (such as air, soil, and water) but also in various foods we encounter in our everyday life. Human exposure is from both inhalation of contaminated air and consumption of contaminated food and water. Extremely high exposure occurs through the cigarette smoking and ingestion of certain foods. Tobacco smoke contributes to 90% of indoor PAHs levels in the homes of smokers. For the general population, dietary intake is the dominant route of human exposure to PAHs. However, those external monitoring methods of PAHs cannot actually reflect people's real PAH intoxication due to the heterogeneous factors of individuals and multiple routes of external exposure.

Recently, Hao et al. prepare a luminescent Eu-functionalized MOF sensor for specific detection of urinary 1-HP as the metabolite of inhaled PAHs in human body and considered as a biomarker of human exposure to PAHs carcinogens, which is designed through a fluorescence resonance energy transfer (FRET) process [63]. As the first example of luminescent sensors for 1-HP, the developed sensor exhibits a fluorescence quenching effect, fast response, and high sensitivity to 1-HP without the interference by other coexisting species in urine (Fig. 8.39). The sensor also has excellent reusability and is applicable for 1-HP detection in human urine. Moreover, a convenient method of evaluating people's intoxication degree of PAHs is achieved by developing a portable 1-HP urine test paper based on the sensor. This fast, sensitive, and selective probe possesses the potential to serve as a powerful diagnostic tool for PAHs-related disease in future clinical medicine.

8.7 Photofunctional Hybrid Materials as Probes or Sensors for Physical Properties

Brites et al. provide a general overview of recent examples of luminescent and non-luminescent thermometers working at nanometric scale in two reviews [64, 65]. Luminescent thermometers involve complex thermometric systems formed by polymer and organic–inorganic hybrid matrices encapsulating Ln^{3+} ions as emitting centers. There are few examples reporting thermometers encompassing mixtures of organic dyes with Ln^{3+} β-diketonate complexes and Eu^{3+}/Tb^{3+} β-diketonate complexes embedded into siloxane matrices [65–72]. These examples are among the few involving Ln^{3+} ions that effectively illustrate the temperature sensing/mapping at micron and submicron scale.

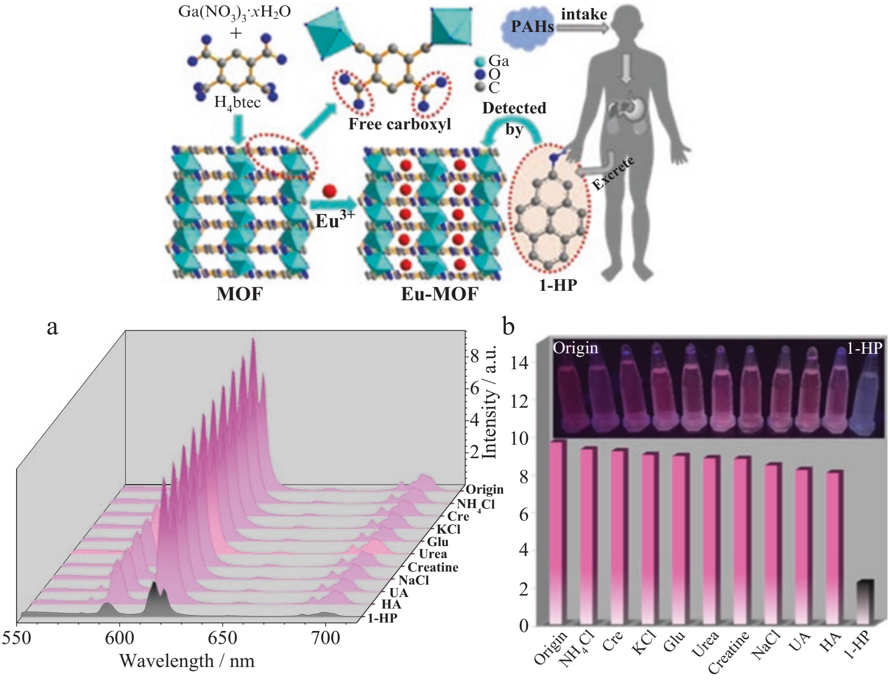

Fig. 8.39 (*Top*) Synthetic scheme and representative structure of Eu-MOFs probe for 1-HP; (*Bottom*) (*a*) Fluorescent spectra and (*b*) intensities (the $^5D_0 \rightarrow {}^7F_2$ transition) of Eu-MOFs suspensions with various urine components. Inset in (*b*) the corresponding photographs under a UV-lamp (254 nm) (Reprinted with permission from Ref. [63]. Copyright 2017 Wiley)

Peng et al. report the incorporation of the Eu-DT complex into siloxane hybrid NPs (formed by a BTD–PMMA hybrid matrix with a silica outer layer) [66]. The NPs display strong temperature dependence, in both luminescence intensity and $^5D_0$ lifetime of Eu^{3+}, over the physiological range with a good resolution (typically to ±0.3 K). Tan et al. present another example of a non-ratiometric thermometer involving a dual luminophore probe based on a mixture of several Eu^{3+} and Tb^{3+} complexes ($Eu(dbm)_3·2H_2O$, $Eu(acac)_3·2H_2O$, $Tb(acac)_3·2H_2O$ and Tb(ca) ca = citric acid) [67]. The polymeric hydrogels (based on PAA and OTES) are able to measure the temperature in the range 283–323 K. It is found that the two europium hydrogels can be excited at visible wavelength. Ratiometric thermometers are demonstrated by Peng et al. [68] using siloxane hybrid NPs formed by a BTD–PMMA core – incorporating the Eu-DT complex and a OASN reference – covered with a silica outer layer and by Brites et al. using magnetic hybrid NPs co-doped with Eu^{3+} and Tb^{3+} chelates [69]. In the former work, the resulted ratiometric fluorescence is found to be highly temperature dependent in the physiological range (298–318 K), with an intensity temperature sensitivity of −4.0%/K. In the latter examples, siloxane-based hybrid magnetic nanoclusters (size ranging from 100 to 400 nm) are formed by a g-Fe_2O_3 maghemite core (hydrodynamic size of 21.0 ± 4.0 nm) coated with a TEOS–APTES organosilica shell and co-doped with [Eu(btfa)$_3$(MeOH)(bpeta)] and [Tb(btfa)$_3$(MeOH)(bpeta)] β-diketonate chelates by combining self-referencing allowing absolute measurements. Self-referenced luminescent thermometers are also demonstrated using di-ureasil hybrid films embedding the superparamagnetic maghemite NPs and the Eu^{3+}/Tb^{3+} chelates. The temperature operation range with Sm up to 1.0% K^{-1} is extended to 300–350 K, relative to that of the maghemite covered TEOS–APTES NPs incorporating the same complexes.

Brites et al. continue the discussion on the absolute temperature sensing/mapping of the hybrid thermometers, relatively to the initial work and with an emphasis on the di-ureasil films, the extension of the temperature operation range with a sensitivity up 1%K^{-1} to 300–350 K, and the improvement of both the spatial resolution and the long-term stability of the thermometric systems [70]. They describe the tuning of the performance of thermometer based on hybrids co-doped with Eu^{3+} and Tb^{3+} tris(β-diketonate) and dipicolinate chelates through the adjustment of the energy mismatch between the triplet states of the ligands and of the hybrid host. Ideally the ligand triplet energy should occupy such a position in the partial energy diagram, which is close enough to that of the hybrid host triplet (to ensure thermally driven host-ligand energy transfer) and far enough from that of the Ln^{3+}-emitting levels to avoid a decrease of the integrated intensities close to the noise levels. This will permit that the operating temperature range of highly sensitivity thermometers can be extended wider temperature ranges [71].

Brites et al. present two luminescent ratiometric nanothermometers based on a magnetic core coated with an organosilica shell co-doped with Eu^{3+} and Tb^{3+} chelates [72]. The hybrid host and chelate ligands permit the working of the nanothermometers in a nanofluid at 293–320 K with an emission quantum yield of 0.38 ± 0.04, a maximum relative sensitivity of 1.5% K^{-1} at 293 K and a spatiotemporal resolution (constrained by the experimental setup) of 64×10^{-6} m/150×10^{-3} s (to move out of 0.4 K – the temperature uncertainty). The heat propagation velocity in the nanofluid, $(2.2 \pm 0.1) \times 10^{-3}$ ms^{-1}, is determined at 294 K using the nanothermometers' Eu^{3+}/Tb^{3+} steady-state spectra. There is no precedent of such an experimental measurement in a thermographic nanofluid, where the propagation velocity is measured from the same nanoparticles used to measure the temperature.

Li et al. report the fabrication of a sensitive ratiometric and colorimetric luminescent thermometer with a wide operating temperature range, from cryogenic temperatures up to high temperatures, through the combination of metal complexes [73]. Benefiting from the transition metal complex as a self-reference, the lanthanide content in the mixed-coordination complex, $Eu_{0.05}$(Mebip-mim bromine)$_{0.15}$ $Zn_{0.95}$(Mebip-mim bromine)$_{1.9}$, is lowered to 5%.

Cui et al. firstly realize a new mixed lanthanide MOF thermometer Tb0.9Eu0.1PIA with the significantly high sensitivity of 3.53% per K by making use of an organic ligand, 5-(pyridin-4-yl) isophthalate (PIA), with higher-triplet state energy [74]. The representative mixed lanthanide MOF (Tb0.9Eu0.1PIA) exhibits a significantly different temperature-dependent luminescent behavior with respect to the emissions of Eu^{3+} at 615 nm and Tb^{3+} at 546 nm. With the temperature increases, the emission intensity of both Tb^{3+} and Eu^{3+} ions remain unchanged in the low-temperature range (14–100 K). However, in the 100–300 K temperature range, the emission intensity of the Tb^{3+} ions decreases, while that of the Eu^{3+} increases. The absolute temperature measurement can be linearly correlated to an experimental parameter Δ (Δ = ITb/ IEu from 100 to 300 K Δ = 11.671–0.0353 *T*) and suggests that Tb0.9Eu0.1PIA is an excellent luminescent thermometer in this temperature range. The sensitivity of this new M'LnMOF is about 9 times higher than that of our recently developed Eu0.0069 Tb0.9931-DMBDC: 3.53% per K in Tb0.9Eu0.1PIA versus 0.38% per K in Eu0.0069 Tb0.9931-DMBDC. Besides the enhanced sensitivity to highly sensitize the temperature changes, it does not require any additional calibration of luminescence intensity and thus is much more instantaneous than other types of solid luminescent thermometers. The sensitivity can be increased to be about 6% and 20% for theTb0.95Eu0.05PIA and Tb0.99Eu0.01PIA luminescent thermometers, respectively. The $Tb_{0.95}Eu_{0.05}PIA$ with sensitivity of about 6% is also a potentially useful luminescent thermometer. The temperature-dependent luminescent colors of $Tb_{0.9}Eu_{0.1}PIA$ can be systematically tuned from green to yellow from 14 to 300 K, which can be clearly and directly observed even by the naked eye or camera. Based on the CIE coordinates change from (0.3064, 0.5923) at 14 K to (0.4155, 0.4823) at 300 K. The high-temperature sensitivity of $Tb_{0.9}Eu_{0.1}PIA$ is related to both different temperature-dependent emissions of Tb^{3+} and Eu^{3+} ions, and temperature-dependent energy transfer probability from the Tb^{3+} and Eu^{3+} ions [75].

Zhou et al. discover the potential of Ln^{3+}@In(OH)(bpydc) hybrid materials in temperature sensing; the temperature-dependent luminescent spectra and lifetimes of Ln^{3+}@**1** are performed [76]. The temperature-dependent luminescent behavior of Eu^{3+} and Tb^{3+} in Eu^{3+}/Tb^{3+}@In(OH)(bpydc) is significantly different from those in Eu^{3+}@In(OH)(bpydc) and Tb^{3+}@ In(OH)(bpydc), respectively (Fig. 8.40 (Left) a). When the temperature increased from 10 to 60 °C, Tb^{3+} emission exhibited a much more decrease of 60%, as compared to 33% for Tb^{3+}@In(OH)(bpydc) (Fig. 8.40 (Left) b). The Eu^{3+} emission in Eu^{3+}/Tb^{3+}@In(OH)(bpydc) is enhanced, which is contrary to that in Eu^{3+}@In(OH)(bpydc). The different variation of emissions of Eu^{3+} and Tb^{3+} in Eu^{3+}/Tb^{3+}@In(OH)(bpydc) with temperature enables this Ln^{3+}-functionalized MOF to serve as a nanoplatform for temperature sensing. The ratiometric thermometric parameter of Eu^{3+}/Tb^{3+}@In(OH)(bpydc) can be defined as the intensity ratio of $^5D_4 \rightarrow {}^7F_5$ (Tb^{3+}, 545 nm) and $^5D_0 \rightarrow {}^7F_2$ (Eu^{3+}, 613 nm) transitions (I_{Tb}/I_{Eu}). Figure 8.40 (Left) c plots the dependence of I_{Tb}/I_{Eu} on temperature, which reveals a good linear relationship between I_{Tb}/I_{Eu} and temperature within the range of 10 to 60 °C. The thermal sensitivity of Eu^{3+}/Tb^{3+}@**1** is 4.97%°C^{-1}, which is more than 35 times higher than that of the MOF nanothermometer $Tb_{0.99}Eu_{0.01}(BDC)_{1.5}(H_2O)_2$ (0.14% °C^{-1}). To verify the applicability of this mechanism to Eu^{3+}/Tb^{3+}@**1**, the temperature-dependent emission spectra of Eu^{3+}/Tb^{3+}@**1** excited at 488 nm of the $^7F_6 \rightarrow {}^5D_4$ transition of Tb^{3+} displayed gradually enhanced Eu^{3+} emission, confirming the Tb^{3+} to Eu^{3+} energy transfer occurred and enhanced with the increase in temperature (Fig. 8.40 (Left)). Another indication provided by Fig. 8.40 (Right) is that Eu^{3+}/Tb^{3+}@**1** nanoparticles can also be developed as ratiometric optical thermometers when the excitation wavelength is fixed at 487 nm. The

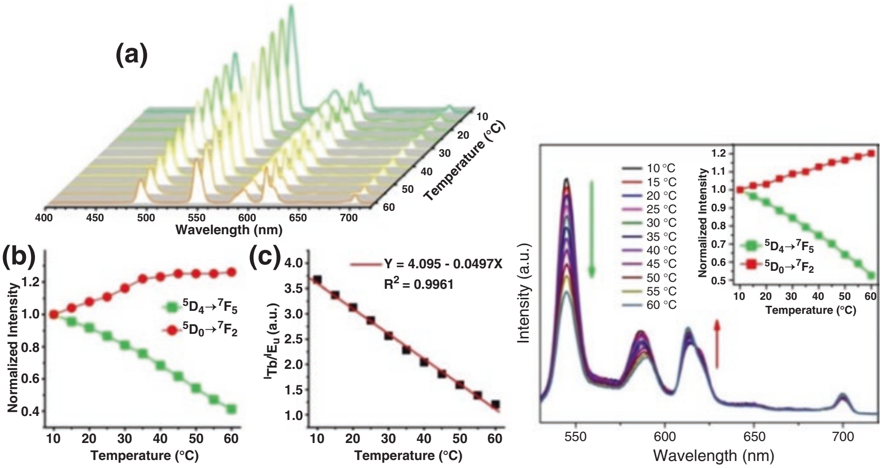

Fig. 8.40 (*Left*) Eu^{3+}/Tb^{3+}@**1** nanocrystals show sensitive spectra changes in response to temperature: (*a*) emission spectra (λ_{ex} = 312 nm) recorded in the temperature range of 10–60 °C, (*b*) temperature-dependent intensity of $^5D_4 \to ^7F_5$ and $^5D_0 \to ^7F_2$ transition, (*c*) the dependence of I_{Tb}/I_{Eu} on temperature. The red line plotted in (*c*) is the linear fitted curve. (*Right*) Emission spectra (λ_{ex} = 487 nm) of Eu^{3+}/Tb^{3+}@**1** recorded between 10 and 60 °C. The inset is the temperature-dependent normalized intensity of Eu^{3+} ($^5D_0 \to ^7F_2$) and Tb^{3+} ($^5D_4 \to ^7F_5$) (Reprinted with permission from Ref. [76]. Copyright 2016 The Royal Society of Chemistry)

temperature (10–60 °C) can be related to I_{Tb}/I_{Eu} by a linear calibration curve with a slope of −3.69%. This thermometric sensitivity is lower than that of Eu^{3+}/Tb^{3+}@**1** when employing 312 nm excitation (4.97% $°C^{-1}$). Nevertheless, 487 nm excitation is much less cytotoxic than 320 nm, thus is preferred in biotechnology.

Zhou et al. also examine the feasibility of the Eu^{3+}@UiO-bpydc for ratiometric thermometry by studying its temperature-dependent photoluminescence properties (Fig. 8.41a) [77]. When temperature increases, the Eu^{3+} emission intensity declines, while the ligand-centered emission significantly increases. The luminescence intensity of $EuCl_3$ barely changes over the temperature range from 293 to 353 K. These results suggest that the significant luminescence enhancement of bpydc as well as the decrease in Eu^{3+} emission in Eu^{3+}@UiO-bpydc hybrid may be attributed to the back energy transfer (BEnT) from Eu^{3+} cations to bpydc linkers. These results indicate the occurrence of the back energy transfer from Eu^{3+} to the bpydc linkers embedded in framework. It is established that the thermal dependence of the BEnT rate follows an Arrhenius-type equation with an energy barrier E_a. To study the BEnT mechanism in detail, the energy back-transfer rates from Eu^{3+} to bpydc linkers (K_{BEnT}) are estimated by Arrhenius-type equation. Temperature-dependent emission lifetimes (Eu^{3+}) of the MOF hybrid are recorded for the determination of K_b and E_a (Fig. 8.41 (Right)a). The calculated K_{BEnT} enhances with the increase of temperature, as presented in Fig. 8.41 (Right)b. The slope of Arrhenius plots for K_{BEnT} is 1.98, resulting in a value of 44 kJ mol^{-1} for activation energy E_a (Fig. 8.41 (Right) c). To quantitatively determine the temperature-sensing function of Eu^{3+}@UiO-

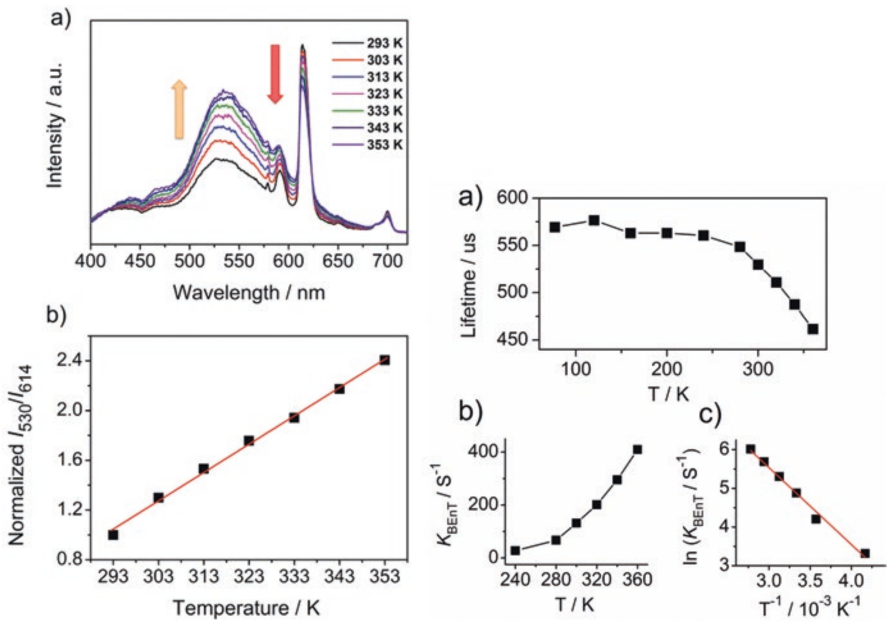

Fig. 8.41 (*Left*) (*a*) Temperature-dependent emission spectra of Eu^{3+}@UiO-bpydc. (*b*) The intensity ratio of bpydc (530 nm) to Eu^{3+} (614 nm) as a function of temperature. Ratios were normalized to the value at 293 K. (*Right*) (*a*) Temperature dependence of luminescence lifetime of Eu^{3+} in Eu^{3+}@UiO-bpydc. (*b*) Thermometric response curve plotting back energy transfer rate (K_{BEnT}) versus temperature. (*c*) Arrhenius plots for back K_{BEnT} constants of Eu^{3+}@UiO-bpydc. (Reprinted with permission from Ref. [77]. Copyright 2016 The Royal Society of Chemistry)

bpydc, the ratiometric parameter is defined as the intensity ratio of 530 nm (bpydc) to 614 nm (Eu^{3+}) emission (I_{530}/ I_{614}). Figure 8.41 (Right)b plots the response of I_{530}/I_{614} (normalized to the 293 K value) to temperature in 10 K increment. It is found I_{530}/I_{614} changed linearly with temperature in the range of 293–353 K. The linear relationship is fitted with correlation coefficient (R^2) of 0.996.

Shen et al. prepare polymer thin film based on the $Tb_{0.999}Eu_{0.001}$–**2** and used it as luminescent thermometer due to the energy transfer from Tb^{3+} to Eu^{3+} [78]. The temperature-dependent luminescent color is tuned from blue-green to pink cross the white light area from 100 K to 320 K, systematically. Based on CIE chromaticity diagram, the corresponding CIE coordinates change from (0.2194, 0.3198) at 100 K to (0.3719, 0.2657) at 320 K. The different temperature-dependent luminescent emissions of $^5D_4 \rightarrow {}^7F_5$ (Tb^{3+}, 545 nm) and $^5D_0 \rightarrow {}^7F_2$ (Eu^{3+}, 616 nm) have enabled this film to be excellent candidates for self-referencing luminescent thermometers. The absolute temperature measurement can be linearly correlated to $lg(I_{Tb}/I_{Eu})$ from 160 K to 320 K, and the thermal sensitivity is $1.05\%K^{-1}$. Shen et al. also studied the temperature dependence of the emission spectra (80–300 K) of $Tb_{0.999}Eu_{0.001}$ [79]. The temperature-dependent emission spectra are transformed to CIE diagram coordinates, which is systematically tuned from green-yellow (0.3384, 0.5517) at 100 K to red (0.6273, 0.3584) at 300 K. The energy transfer efficiency of Tb^{3+}-to-Eu^{3+} ($\eta_{Tb\rightarrow Eu}$) can be determined from the $^5D_4$ donor lifetime in the presence (τ) and absence (τ_0) of the Eu^{3+} acceptors. The value of $\eta_{Tb\rightarrow Eu}$ is estimated to be 85% at room temperature, a very high efficiency. The linear relationship can be fitted as a function of Eq. (2) with a correlation coefficient (R^2) of 0.994, and the thermal sensitivity is 1.23%K^{-1}. The luminescent color change of $Tb_{0.999}Eu_{0.001}$ together with the high-energy transfer efficiency makes it easy to use as sensitive luminescent thermometer over a wide temperature range.

Lin et al. present a type of Eu(III) ofloxacin complex as the fluorescent pH indicator [80]. During the concentration-dependence experiments, the photoluminescence studies on the complex showed that the excitation of this pH probe can occur at a very long wavelength which extends to visible range (Ex = 427 nm). Furthermore, the functional complex is successfully incorporated into soft networks, and two novel luminescent hydrogels (rod and film) are fabricated. The soft materials also exhibit specific responses toward the pH variation. Finally, the onion cell-stain experiments are carried out to further confirm the validity of pH dependence. Li et al. construct a structurally simple, promptly responsive, and widely applicable thin film pH detector Eu $(TTA)_n$@Lap by loading Eu-β-diketonate complexes to LAPONITEs [81]. The hybrid pH detector is highly sensitive to acid sites over a wide pH range and exhibited pH-dependent luminescence behaviors, which can be observed directly by the naked eye. In addition, the hybrid pH detector can be easily recovered and reused by treating with Et_3N vapor. Considering that LAPONITEs is a very important coating additive, they believe that this host-gust hybrid pH detector will be an appealing alternative for the in situ and real-time detection of pH in many special areas such as reaction kettle linings and aircraft/ship surface coating materials.

Lu et al. report a new ratiometric pH sensor based on nanoscale PSM MOF-253 [82]. By PSM, two types of Eu^{3+} with different characteristic excitation wavelength are realized in MOF-253 simultaneously (Fig. 8.42 (Top)), and then one of them is insensitive to pH; another one is sensitive to pH. In PSM, the amount of Eu^{3+} ion is 4 times of TTA (according to feed ratio) for building two different coordination environments of Eu^{3+} ion: one of them is only linked by bipyridine, named as Eu1; the other one has two ligands (bipyridine and TTA), named as Eu2. The broad band at 330 nm can be chiefly assigned to excitation of Eu1. And then, the broad band at 375 nm should mostly belong to the excitation of Eu2 due to the energy absorption of TTA. The different intensity ratios of $^5D_0 \rightarrow {}^7F_2$ to $^5D_0 \rightarrow {}^7F_1$ could be indicated; the intensity ration of $^5D_0 \rightarrow {}^7F_2$ to $^5D_0 \rightarrow {}^7F_1$ for Eu1 is 7.1 (λ_{ex} = 330 nm) and that for Eu2 is 10.3 (λ_{ex} = 375 nm). The sensor has a linear response in the pH range 5.0–7.2, which is required for work with biological fluids such as blood and culture cell media. The free TTA will be still in the pore after the broken of the six-member chelate ring because MOFs have the adsorption capacity to hold those molecules (TTA). As a consequence, the sensitization from TTA is still existence, but the effect is lessened. More importantly, the weakened sensitization can keep the excitation wavelength of Eu2 is still at 375 nm and not changed to 330 nm, even if the six-member chelate ring is broken (Fig. 8.42 (Bottom)). This is why the luminescent

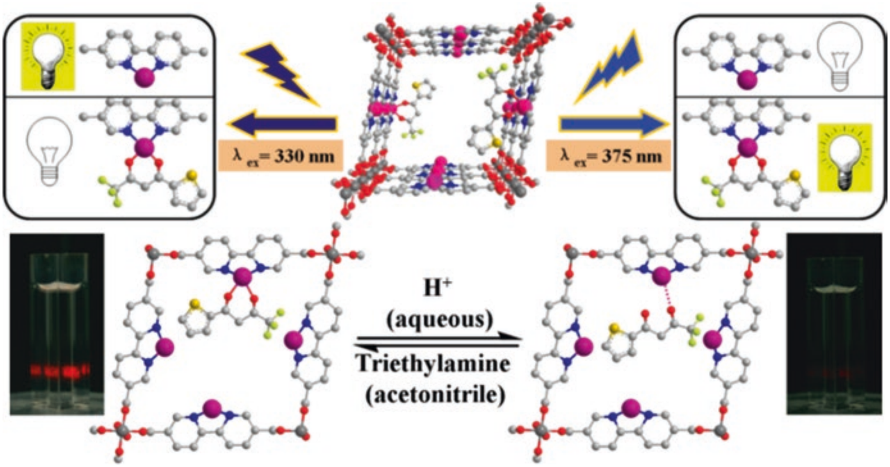

Fig. 8.42 (*Top*) Schematic diagram of MOF-253 modified by Eu^{3+} complex with TTA; there are two types of Eu^{3+} with different ligand in the modified MOF-253 (Eu1 and Eu2): Eu1 could emit Eu^{3+} characteristic light under the excitation at 330 nm, and Eu2 could emit Eu^{3+} characteristic light under the excitation at 375 nm. (*Bottom*) Schematic representation of the pH sensor based on MOF-253: H^+ proton could impair the sensitization of TTA to Eu^{3+} through breaking the six-member chelate ring, and the thriethylamine could recover the sensitization; the insets are the photograph of MOF-253-Eu-TTA in pH = 5 aqueous solution (*right*) and in pH = 7.2 aqueous solution (lift) ($\lambda_{ex} = 375$ nm) (Reprinted with permission from ref. [82]. Copyright 2016 The Royal Society of Chemistry)

intensity of Eu1 is not enhanced after the broken of six-member chelate ring, and the luminescent intensity of Eu2 is only weakened, not vanished. To further prove that the free TTA is in the pore, triethylamine is used to recover the luminescent intensity ($\lambda_{ex} = 375$ nm) of MOF-253-Eu-TTA which has been soaked in pH = 5 aqueous solution. But this will not affect the application of MOF-253-Eu-TTA in pH sensing because that most of luminescent sensors are irreversible, especially for use in biomedicine.

8.8 Conclusion and Outlook

In conclusion, recent research progress in the photophysical applications of photofunctional rare-earth hybrid materials are summarized, which mainly consist of three parts: the first is the application in solar energy concentrators, the second is the application in optical device or barcode, and the third is the application in sensors. The emphasis is put on the photofunctional rare-earth hybrid materials for sensing because the research in this field is very active and extensive. Herein only a limited number of topics are covered. Although preliminary understanding of the fluorescence-sensing mechanism has been achieved, it still needs deep investigation, especially the theoretical calculation of the sensing process. On the other hand, the disadvantage of fluorescence sensing should be avoided to improve its low-detection limit compared to other chemical-sensing approach. In addition, the real application should be explored to solve the practical problem.

References

1. Sun LN, Zhang HJ, Fu LS, Liu FY, Meng QG, Peng CY, Yu JB (2005) A new so-gel material doped with an erbium complex and its optical-amplification application. Adv Funct Mater 15:1041–1048
2. Sun LN, Zhang HJ, Meng QG, Liu FY, Fu LS, Peng CY, Yu JB, Zheng GL, Wang SB (2005) Near-infrared luminescent hybrid materials doped with lanthanide (ln) complexes (ln = Nd, Yb) and their possible laser application. J Phys Chem B 109:6174–6182
3. Graffion J, Cattoen X, Chi Man MW, Fernandes VR, Andre PS, Ferreira RAS, Carlos LD (2011) Modulating the photoluminescence of bridged silsesquioxanes incorporating Eu^{3+}-complexed n,n'-diureido-2,20-bipyridine isomers: application for luminescent solar concentrators. Chem Mater 23:4773–4782
4. Correia SFH, Bermudez VDZ, Ribeiro SJL, Andre PS, Ferreira RAS, Carlos LD (2014) Luminescent solar concentrators: challenges for lanthanide-based organic–inorganic hybrid materials. J Mater Chem A 2:5580–5596
5. Freitas VT, LS F, Cojocariu AM, Cattoën X, Bartlett JR, Le Parc R, Bantignies J, Chi Man MW, André PS, Ferreira RAS, Carlos LD (2015) Eu^{3+}-based bridged silsesquioxanes for transparent luminescent solar concentrators. ACS Appl Mater Interf 7:8770−8778
6. Nolasco MM, Vaz PM, Freitas VT, Lima PP, Andre PS, Ferreira RAS, Vaz PD, Ribeiro-Claro P, Carlos LD (2013) Engineering highly efficient Eu(III)-based tri-ureasil hybrids toward luminescent solar concentrators. J Mater Chem A 1:7339–7350
7. Correia SFH, Lima PP, André PS, Ferreira RAS, Carlos LD (2015) High-efficiency luminescent solar concentrators for flexible wave-guiding photovoltaics. Solar Energy Mater Solar Cells138:51–57
8. Wang TR, Li P, Li HR (2014) Color-tunable luminescence of organoclay-based hybrid materials showing potential applications in white LED and thermosensors. ACS Appl Mater Interf 6:12915–12921
9. Wang TR, Yu XY, Li ZQ, Wang J, Li HR (2015) Multi-colored luminescent light-harvesting hybrids based on aminoclay and lanthanide complexes. RSC Adv 5:11570–11576
10. Lu Y, Yan B (2014) Lanthanide organic-inorganic hybrids based on functionalized metal-organic frameworks (MOFs) for near-UV white LED. Chem Comm 50:15443–15446
11. Zhou Y, Yan B (2015) Lanthanides post-functionalized nanocrystalline metal-organic frameworks for tunable white-light emission and orthogonal multi-readout thermometry. Nanoscale 7:4063–4069
12. White KA, Chengelis DA, Gogick KA, Stehman J, Rosi NL, Petoud S (2009) Near-infrared luminescent lanthanide MOF barcodes. J Am Chem Soc 131:18069–18071
13. Lu Y, Yan B (2014) Luminescent lanthanide barcodes based on postsynthetic modified nanoscale metal-organic frameworks. J Mater Chem C 2:7411–7416
14. Zhou Y, Yan B (2015) Ratiometric multiplexed barcodes based on luminescent metal-organic framework films. J Mater Chem C 3:8413–8418
15. Shen X, Yan B (2016) Barcoded materials based on photoluminescent hybrid system of lanthanide ions-doped metal organic framework and silica via ion exchange. J Coll Interf Sci 468:220–226
16. Zhou Y, Chen HH, Yan B (2014) An Eu^{3+} post-functionalized nanosized metal-organic framework for cation exchange-based Fe^{3+}-sensing in aqueous environment. J Mater Chem A 2:13691–13697

17. Xu XY, Yan B (2015) Eu(III)-functionalized MIL-124 as fluorescent probe for highly selectively sensing ions and organic small molecules especially for Fe(III) and Fe(II). ACS Appl Mater Interf 7:721–729
18. Shen X, Yan B (2015) Photofunctional hybrids of lanthanide functionalized bio-MOF-1 for fluorescence tuning and sensing. J Coll Interf Sci 451:63–68
19. Weng H, Yan B (2016) Lanthanide coordination polymers for multi-color luminescence and sensing of Fe^{3+}. Inorg Chem Comm 63:11–15
20. Sun NN, Yan B (2016) Lanthanide complexes inside-outside double functionalized zeolite a hybrid materials for luminescent sensing. New J Chem 40:6924–6930
21. Hao JN, Yan B (2015) A water-stable lanthanide-functionalized MOF as a highly selective and sensitive fluorescent probe for Cd^{2+}. Chem Comm 51:7737–7740
22. Xu XY, Yan B (2016) Eu (III) functionalized Zr-based metal-organic framework as excellent fluorescent probe for Cd^{2+} detection in aqueous environment. Sensors Actuators B-Chem 222:347–353
23. Liu C, Yan B (2015) Zeolite-type metal organic frameworks immobilized Eu^{3+} for cation sensing in aqueous environment. J Coll Interf Sci 459:206–211
24. Xu XY, Yan B (2016) Fabrication and application of ratiometric and colorimetric fluorescent probe for Hg^{2+} based on dual-emissive metal-organic framework hybrids with carbon dots and Eu^{3+}. J Mater Chem C 4:1543–1549
25. Zhou Z, Wang QM, Zeng Z, Yang LT, Ding XP, Lin N, Cheng ZS (2013) Polyurethane-based Eu(III) luminescent foam as a sensor for recognizing Cu^{2+} in water. Anal Methods 5:6045–6050
26. Xu QQ, Li ZQ, Li HR (2016) Water-soluble luminescent hybrid composites consisting of oligosilsesquioxanes and lanthanide complexes and their sensing ability for Cu^{2+}. Chem Eur J 22:3037–3043
27. Tan CL, Wang QM (2012) Luminescent Cu^{2+} probes based on rare-earth (Eu^{3+} and Tb^{3+}) emissive transparent cellulose hydrogels. J Fluorescence 22:1581–1586
28. Zhang LG, Tan CL, Wang QM, Zhang CC (2011) Anion/cation induced optical switches based on luminescent lanthanide (Tb^{3+} and Eu^{3+}) hydrogels. Photochem Photobiol 87:1036–1041
29. Liu C, Yan B (2015) Highly effective chemosensor of luminescent silica@lanthanide complex@MOF heterostructure composite for metal ion sensing. RSC Adv 5:101982–101988
30. Lian X, Yan B (2016) Novel core-shell structure microspheres based on lanthanide complexes for white light emission and fluorescence sensing. Dalton Trans 45:2666–2673
31. Liu C, Yan B (2016) A novel photofunctional hybrid material of pyrene functionalized metal-organic framework with conformation change for luminescence sensing of Cu^{2+}. Sensors Actuator B-Chem 235:541–546
32. Hao JN, Yan B (2014) Highly sensitive and selective fluorescent probe for ag^{+} based on a Eu^{3+} post-functionalized metal-organic framework in aqueous media. J Mater Chem A 2:18018–18025
33. Hao JN, Yan B (2015) Ag^{+}-sensitized lanthanide luminescence in Ln^{3+} post-functionalized metal-organic framework and ag^{+} sensing. J Mater Chem A 3:4788–4792
34. Weng H, Yan B (2016) Multi-color luminescence and sensing of rare earth hybrids by ionic exchange functionalization. J Fluorescence 26:1497–1504
35. Hao JN, Yan B (2014) Amino-decorated lanthanide (III) – organic extended frameworks for multi-color luminescence and fluorescence sensing. J Mater Chem C 2:6758–6764
36. Wang QM, Tan CL, Chen HY, Tamiaki H (2010) A new fluoride luminescence quencher based on a nanostructured covalently bonded terbium hybrid material. J Phys Chem C 114:13879–13883
37. Zhou Z, Zheng YH, Wang QM (2014) Extension of novel lanthanide luminescent mesoporous nanostructures to detect fluoride. Inorg Chem 53:1530−1536
38. Li YJ, Xie DY, Pang XL, Yu XD, Yu T, Ge XT (2016) Highly selective fluorescent sensing for fluoride based on a covalently bonded europium mesoporous hybrid material. Sensors Actuators B Chem 227:660–667
39. Zhou Z, Wang QM, Huo SM, Yan YQ (2012) Luminescent terbium(III) complex-based titania sensing material for fluoride and its photocatalytic properties. Photochem Photobiol Sci 11:738–743

40. Hao JN, Yan B (2016) Ln^{3+} post-functionalized metal-organic frameworks for color tunable emission and highly-sensitivity sensing of toxic anions and small molecules. New J Chem 40:4556–4661
41. Weng H, Yan B (2016) A flexible Tb(III) functionalized cadmium metal-organic framework as fluorescent probe for highly selectively sensing ions and organic small molecules. Sensors Actuator B Chem 228:702–708
42. Shen X, Yan B (2015) Photoactive rare earth complexes for fluorescent tuning and sensing cations (Fe^{3+}) and anions ($Cr_2O_7^{2-}$). RSC Adv 5:6752–6757
43. Duan TW, Yan B, Weng H (2015) Europium activated yttrium hybrid system for sensing toxic anion of Cr (VI) species. Microp Mesop. Mater 217:196–202
44. Tan CL, Wang QM, Ma LJ (2010) Fluorescent-based solid sensor for HSO_4^- in water. Photochem Photobiol 86:1191–1196
45. Tan CL, Wang QM (2011) Reversible terbium luminescent polyelectrolyte hydrogels for detection of $H_2PO_4^-$ and HSO_4^- in water. Inorg Chem 50:2953–2956
46. Zhou Z, Wang QM, Tan CL (2014) Soft matter anion sensing based on lanthanide (Eu^{3+} and Tb^{3+}) luminescent hydrogels. Soft Mat 12:98–102
47. Wang QM, Tan CL, Cai WS (2012) A targetable fluorescent sensor for hypochlorite based on a luminescent europium complex loaded carbon nanotube. Analyst 137:1872–1875
48. Zheng YH, Tang K, Wang QM (2015) Two novel luminescent metallic based organic–inorganic functionalized silica hybrid materials. Synth Met 209:262–266
49. Zhou Z, Wang QM (2012) Two emissive cellulose hydrogels for detection of nitrite using terbium luminescence. Sensors & Actuators B-Chem 173:833–838
50. Sun NN, Yan B (2017) Rapid and facile ratiometric detection of CO_3^{2-} based on heterobimetallic metal-organic frameworks (Eu/Pt-MOFs). Dyes Pigments 42:1–7
51. Yao YL, Wang YG, Li ZQ, Li HR (2015) Reversible on−off luminescence switching in self-healable hydrogels. Langmuir 31:12736–12741
52. Li P, Zhang YZ, Wang YG, Wang YJ, Li HR (2014) Luminescent europium(III)–β-diketonate complexes hosted in nanozeolite L as turn-on sensors for detecting basic molecules. Chem Comm 50:13680–13682
53. Zhou Y, Yan B (2016) A responsive MOF nanocomposite for decoding volatile organic compounds. Chem Comm 52:2265–2268
54. Shen X, Yan B (2015) A novel fluorescence probe for sensing organic amine vapors from Eu^{3+} β-diketonate functionalized bio-MOF-1 hybrid system. J Mater Chem C 3:7038–7046
55. Shen X, Yan B (2016) Anionic metal-organic framework hybrids: double functionalization with lanthanides/cationic dyes and fluorescent sensing small molecules. RSC Adv 6:28165–28170
56. Weng H, Yan B (2016) N-GQDs and Eu^{3+} co-encapsulated anionic MOF: two-dimensional luminescent platform for decoding benzene homologues. Dalton Trans 45:8795–8801
57. Lian X, Yan B (2016) A lanthanide metal–organic framework (MOF-76) for adsorbing dyes and fluorescence detecting aromatic pollutants. RSC Adv 6:11570–11576
58. Xu XY, Yan B (2016) Nanoscale LnMOF-functionalized nonwoven fiber protected by polydimethysiloxane coating layer as highly sensitive ratiometric oxygen sensor. J Mater Chem C 4:8514–8521
59. Hao JN, Yan B (2015) Recyclable lanthanide-functionalized MOF hybrids to determine hippuric acid in urine as biological indices of toluene exposure. Chem Comm 51:14509–14512
60. Hao JN, Yan B (2016) Simultaneous determination of indoor ammonia pollution and its biological metabolite in human body by use of a recyclable nanocrystalline lanthanide functionalized MOF. Nanoscale 8:2881–2886
61. Hao JN, Yan B (2016) A dual-emitting 4d-4f metal-organic framework as a self-calibrating luminescent sensor for indoor formaldehyde pollution. Nanoscale 8:12047–12053
62. Xu XY, Yan B (2017) Eu(III)-functionalized ZnO@MOFs heterostructures: integration of pre-concentration and efficient charge transfer as ppb-level sensing platform for volatile aldehyde gases in vehicles. J Mater Chem A 5:2215–2223

63. Hao JN, Yan B (2017) Determination of urinary 1-hydroxypyrene for biomonitoring of human exposure to polycyclic aromatic hydrocarbons carcinogens by a lanthanide-functionalized metal-organic framework sensor. Adv Funct Mater 27:1603856
64. Brites CDS, Lima PP, Silva NJO, Mill A, Amaral VS, Palacio F, Carlos LD (2012) Thermometry at the nanoscale. Nanoscale 4:4799–4829
65. Brites CDS, Lima PP, Silva NJO, Millan A, Amaral VS, Palacio F, Carlos LD (2011) Lanthanide-based luminescent molecular thermometers. New J Chem 35:1177–1183
66. Peng HS, Stich MIJ, Yu JB, Sun LN, Fischer LH, Wolfbeis OS (2010) Luminescent europium(III) nanoparticles for sensing and imaging of temperature in the physiological range. Adv Mater 22:716–719
67. Tan CL, Wang QM (2011) Photophysical studies of novel lanthanide (Eu^{3+} and Tb^{3+}) luminescent hydrogels. Inorg Chem Comm 14:515–518
68. Peng HS, Huang SH, Wolfbeis OS (2010) Ratiometric fluorescent nanoparticles for sensing temperature. J Nanopart Res 12:2729–2733
69. Brites CDS, Lima PP, Silva NJO, Millan A, Amaral VS, Palacio F, Carlos LD (2011) A luminescent molecular thermometer for long-term absolute temperature measurements at the nanoscale. Adv Mater 22:4499–4504
70. Brites CDS, Lima PP, Silva NJO, Millan A, Amaral VS, Palacio F, Carlos LD (2013) Thermometry at the nanoscale using lanthanide-containing organic–inorganic hybrid materials. J Lumin 133:230–232
71. Brites CDS, Lima PP, Carlos LD (2016) Tuning the sensitivity of Ln^{3+}-based luminescent molecular thermometers through ligand design. J Lumin 169:497–502
72. Brites CDS, Lima PP, Silva NJO, Millan A, Amaral VS, Palacio F, Carlos LD (2013) Ratiometric highly sensitive luminescent nanothermometers working in the room temperature range. Applications to heat propagation in nanofluids. Nanoscale 5:7572–7580
73. Li ZQ, Hou ZH, Ha ZH, Li HR (2015) A ratiometric luminescent thermometer co-doped with lanthanide and transition metals. Chem Asi J 4:2720–2724
74. Rao XT, Song T, Gao JK, Cui YJ, Yang Y, Wu CD, Chen BL, Qian GD (2013) A highly sensitive mixed lanthanide metal−organic framework self-calibrated luminescent thermometer. J Am Chem Soc 135:15559–15564
75. Meng X, Song SY, Song XZ, Zhu M, Zhao SN, Wu LL, Zhang HJ (2014) A Tb-codoped coordination polymer luminescent thermometer. Inorg Chem Front 1:757–760
76. Zhou Y, Yan B, Lei F (2014) Postsynthetic lanthanides functionalization of nanosized metal-organic frameworks for highly sensitive ratiometric luminescent nanothermometers. Chem Comm 50:15235–15238
77. Zhou Y, Yan B (2015) Ratiometric detection of temperature using responsive dual-emissive MOF hybrids. J Mater Chem C 3:9353–9358
78. Shen X, Yan B (2015) Polymer hybrid thin films based on rare earth ion-functionalized MOF: photoluminescence tuning and sensing as thermometer. Dalton Trans 44:1875–1881
79. Shen X, Lu Y, Yan B (2015) Lanthanide complex hybrid system for fluorescent sensing as thermometer. Eur J Inorg Chem:916–919
80. Lin JT, Zheng YH, Wang QM, Zeng Z, Zhang CC (2014) Novel lanthanide pH fluorescent probes based on multiple emissions and its visible-light-sensitized feature. Anal Chim Acta 839:51–58
81. Li ZQ, Li P, Xu QQ, Li HR (2015) Europium(III)–β-diketonate complex-containing nanohybrid luminescent pH detector. Chem Comm 51:10644–10647
82. Lu Y, Yan B (2014) A ratiometric fluorescent pH sensor based on nanoscale metal-organic frameworks (MOFs) modified by europium (III) complex. Chem Comm 50:13323–13326

Index

B. Yan, *Photofunctional Rare Earth Hybrid Materials*,
Springer Series in Materials Science 251, DOI 10.1007/978-981-10-2957-8